frontiers | Research Topics

Smart nanomaterials for biosensing and therapy applications

Edited by
Qitong Huang, Miaomiao Yuan, Youbin Zheng, Zhe Wang and Ziqiang Xu

Published in
Frontiers in Bioengineering and Biotechnology

ISSN 1664-8714
ISBN 978-2-83251-507-5
DOI 10.3389/978-2-83251-507-5

About Frontiers

Frontiers is more than just an open access publisher of scholarly articles: it is a pioneering approach to the world of academia, radically improving the way scholarly research is managed. The grand vision of Frontiers is a world where all people have an equal opportunity to seek, share and generate knowledge. Frontiers provides immediate and permanent online open access to all its publications, but this alone is not enough to realize our grand goals.

Frontiers journal series

The Frontiers journal series is a multi-tier and interdisciplinary set of open-access, online journals, promising a paradigm shift from the current review, selection and dissemination processes in academic publishing. All Frontiers journals are driven by researchers for researchers; therefore, they constitute a service to the scholarly community. At the same time, the *Frontiers journal series* operates on a revolutionary invention, the tiered publishing system, initially addressing specific communities of scholars, and gradually climbing up to broader public understanding, thus serving the interests of the lay society, too.

Dedication to quality

Each Frontiers article is a landmark of the highest quality, thanks to genuinely collaborative interactions between authors and review editors, who include some of the world's best academicians. Research must be certified by peers before entering a stream of knowledge that may eventually reach the public - and shape society; therefore, Frontiers only applies the most rigorous and unbiased reviews. Frontiers revolutionizes research publishing by freely delivering the most outstanding research, evaluated with no bias from both the academic and social point of view. By applying the most advanced information technologies, Frontiers is catapulting scholarly publishing into a new generation.

What are Frontiers Research Topics?

Frontiers Research Topics are very popular trademarks of the *Frontiers journals series*: they are collections of at least ten articles, all centered on a particular subject. With their unique mix of varied contributions from Original Research to Review Articles, Frontiers Research Topics unify the most influential researchers, the latest key findings and historical advances in a hot research area.

Find out more on how to host your own Frontiers Research Topic or contribute to one as an author by contacting the Frontiers editorial office: frontiersin.org/about/contact

Smart nanomaterials for biosensing and therapy applications

Topic editors

Qitong Huang — Gannan Medical University, China
Miaomiao Yuan — Sun Yat-sen University, China
Youbin Zheng — Technion Israel Institute of Technology, Israel
Zhe Wang — Nanyang Technological University, Singapore
Ziqiang Xu — Hubei University, China

Citation

Huang, Q., Yuan, M., Zheng, Y., Wang, Z., Xu, Z., eds. (2023). *Smart nanomaterials for biosensing and therapy applications*. Lausanne: Frontiers Media SA.
doi: 10.3389/978-2-83251-507-5

The authors declare that the research was conducted in the absence of any commercial or financial relationships that could be construed as a potential conflict of interest.

Table of contents

frontiers | Frontiers in Bioengineering and Biotechnology

TYPE Editorial
PUBLISHED 17 January 2023
DOI 10.3389/fbioe.2023.1137508

OPEN ACCESS

EDITED AND REVIEWED BY
Gianni Ciofani,
Italian Institute of Technology (IIT), Italy

*CORRESPONDENCE
Xiaofeng Lin,
Linxf@gmu.edu.cn
Qitong Huang,
hqt@gmu.edu.cn

SPECIALTY SECTION
This article was submitted to Nanobiotechnology, a section of the journal Frontiers in Bioengineering and Biotechnology

RECEIVED 04 January 2023
ACCEPTED 06 January 2023
PUBLISHED 17 January 2023

CITATION
Lin X and Huang Q (2023), Editorial: Smart nanomaterials for biosensing and therapy applications.
Front. Bioeng. Biotechnol. 11:1137508.
doi: 10.3389/fbioe.2023.1137508

Editorial: Smart nanomaterials for biosensing and therapy applications

Xiaofeng Lin[1]* and Qitong Huang[1,2]*

[1]Key Laboratory of Prevention and Treatment of Cardiovascular and Cerebrovascular Diseases of Ministry of Education, Key Laboratory of Biomaterials and Biofabrication in Tissue Engineering of Jiangxi Province, Key Laboratory of Biomedical Sensors of Ganzhou, School of Medical and Information Engineering, Science Research Center, Gannan Medical University, Ganzhou, China, [2]Oil-Tea in Medical Healthcare and Functional Product Development Engineering Research Center in Jiangxi, Gannan Medical University, Ganzhou, China

KEYWORDS

nanomaterials, biosensing, bioimaging, nanozyme, cancer therapies, triggering immune system

Editorial on the Research Topic
Smart nanomaterials for biosensing and therapy applications

At present, medical science is facing many challenges in early diagnosis and effective treatment of diseases. How to carry out effective diagnosis and treatment of diseases is very important for the improvement of people's health level (Cao et al., 2022; Diaz et al., 2022; Kathe et al., 2022; Vistain et al., 2022; Xue et al., 2022). Smart nanomaterials have received extensive attention in the field of bioengineering and biotechnology due to their unique structural and functional properties. Compared with traditional materials, smart nanomaterials with special optical, magnetic, electrical and mechanical properties show great potential for applications in biosensing and therapy (Huang et al., 2020; Liu et al., 2022a; Zhang et al., 2022a; Yi et al., 2022). The successful development of the smart nanomaterials has greatly improved the accuracy of disease diagnosis and treatment efficiency.

To present state-of-the-art research in this field, we launched a Research Topic in Frontiers in Bioengineering and Biotechnology entitled "*Smart Nanomaterials for Biosensing and Therapy Applications*." A total of 20 articles have been published in this Research Topic, including 11 original research articles, 7 review articles and 2 mini review articles, which represents the recent advances in investigations on biosensing, bioimaging, nanozyme, cancer therapies and triggering immune system.

As known, biosensor is an analytical instrument composed of biological-receptors, transducers and signal-processors. The main principle of the biosensor is to combine biometric elements with sensors to produce a measurable signal proportional to the concentration of the analyte, which can be used to detect, transmit and record the physical, chemical and biological reactions of the analytes. Over the past few decades, biosensors have been used to replace traditional analytical techniques because they are reusable, specific, sensitive, and allow for rapid and multiple assays. Therefore, the biosensors have been widely used in disease diagnosis, drug analysis, environmental monitoring, food safety and other fields (Lin et al., 2021; Mei et al., 2022a; Huang Q et al., 2022). Due to the smart nanomaterials have good catalytic, conductive and optical properties, they can greatly improve the detection performance of biosensors.

Liu et al. constructed a fiber-based triboelectric nanogenerators with good stability, washability, flexibility and stretchability, which can be attached to the human body to monitor the finger, arm, and leg activities. What's more, the fiber-based triboelectric

nanogenerators can be used as the power supply of the temperature sensor in a self-powered sensing-system. This work is expected to be applied in multi-functional motion-sensors and human health monitoring.

The sensitive and accurate analysis of circulating tumor cells (CTCs) plays an important role in the early diagnosis and prognosis of cancer patients. Li et al. reviewed the application of microfluidics in detection of CTCs and the potential clinical application of CTCs. At the same time, the application prospect of microfluidics in the treatment of tumor metastasis had been prospected, the development prospect of microfluidic-biosensors had been also discussed.

Electrochemical biosensors have been applied in many fields because of their advantages of economy, environmental protection, simplicity and high sensitivity. Mei et al. summarized the detection of SARS-CoV-2 based on electrochemical DNA biosensors. The development trend of the electrochemical DNA biosensors for SARS-CoV-2 detection is prospected, which can provide reference for researchers in the establishment of different detection methods. Zhang et al. reviewed and discussed the basic principle, nanomaterials, actuality and future development trend of electrochemical biosensors for the detection of lipid hormone.

How to achieve effective treatment and prevention of disease is one of the key factors related to human health and enhance human wellbeing. With the development of science and technology, smart nanomaterials have been widely used in the treatment and prevention of diseases because of their advantages in biocompatibility, targeted-therapy, drug-delivery, photothermal-therapy, etc.

Li et al. reviewed the advances in nanomaterials for immunotherapy, including nanoparticle-based delivery systems, nanoparticle-based photothermal and photodynamic immunotherapy, nanovaccines, nanoparticle-based T Cell cancer immunotherapy and photodynamic immunotherapy, and nanoparticle-based bacterial cancer immunotherapy. Zhu et al. used self-emulsifying nanotechnology to link iodized oil and indocyanine green (ICG), then used Tween-80 and lecithin to emulsify the mixture of iodized oil and ICG to produce a new type of smart nanomaterials. Comparing with the free ICG, the fluorescence intensity of the prepared smart nano-composite is obviously enhanced, and the fluorescence stability and photobleaching resistance of the nanoemulsion were greatly improved under the shielding action of iodol, and the nanoemulsion had the ability of long-term continuous real-time *in vivo* imaging. In addition, the smart nanomaterial can successfully localize tumor tissue and has good tumor-to-normal contrast. Under the fluorescence guidance of the smart nanomaterial, the tumor tissues of orthotopic liver cancer mice can be clearly visualized and accurately delineated, which can achieve effective resection.

It is well-known that the level of reactive oxygen species (ROS) in the body is closely related to the related diseases of the human body. The imbalance of ROS secretion can cause cancer, dry eye disease, cardiovascular disease and so on. Therefore, it is possible to achieve the treatment of related diseases by adjusting the level of ROS in the body with appropriate therapeutic methods. Li et al. synthesized a viable and efficient tantalum-carbon nanozyme with excellent catalase-like (CAT) activity and radiosensitivity by *in situ* reduction of an ultra-small tantalum nanase in a metal-organic framework material (MOF)-derived carbon nanase. The above smart nanomaterials can significantly improve the CAT activity of carbon nanomases and promote the production of more ROS. By improving ROS levels, more DNA double-strand breaks were present at the cellular level, which in turn increased radiotherapy sensitivity, resulting in the excellent antitumor activity of this smart nanomaterial (Li et al.). Zha et al. successfully encapsulated the NLRP3 inhibitor in polydopamine-based microgel for the treatment of dry eye. The results showed that the smart nanomaterial had good biocompatibility, which could prolong the retention time of the drug on the ocular surface, and could effectively inhibit the corneal epithelial injury and apoptosis. In addition, due to the synergistic effects, the NLRP3 inhibitor-loaded microgels exert stronger ROS clearance at lower doses to suppress inflammation. Li et al., summarized a variety of metal-based nanozymes that regulate ROS levels in the body to achieve treatment of related inflammatory diseases, they also discussed the potential applications of metal-based nanozymes as biomedical materials. Li et al. fixed superoxide dismutase (SOD) in zeolite imidazolate framework-8 (SOD@ZIF-8) by biomimetic mineralization method to treat nerve injury by eliminating ROS . The ROS scavenging activity of SOD@ZIF-8 plays a key role in protecting SHSY-5Y cells from MPP + induced cell model damage and alleviating apoptosis, suggesting that SOD@ZIF-8 can effectively treat ROS-mediated nerve damage by removing excess ROS produced *in vitro*.

In order to improve the therapeutic effect of tumors, many therapeutic methods have been developed. Photodynamic therapy (PDT) and photothermal therapy (PTT) have been widely used in the treatment of many solid tumors in recent years due to its advantages of light-triggered, less trauma and high space-time selectivity. Chen et al. summarized the advantages and disadvantages of PDT based on metal nanomaterials, providing a reference for the application of nanomaterials in PDT therapy. Li et al. prepared Cu_2MoS_4@MXene smart nanocomposite, which has obvious photothermal conversion efficiency (η = 87.98%). Based on the electron transfer regulation effect and local surface plasmon resonance effect, a mechanism is proposed to promote non-radiation recombination and generate more heat, and the material has a very good effect in the treatment of cancer. The synthesis method, photothermal mechanism and cancer treatment scheme of the above smart nanomaterial can be extended to other photothermal agents to achieve more effective treatment of cancer.

Because of the excellent biological properties of smart nanomaterials, their applications in drug delivery are getting more and more attention. Yang et al. developed an exosome-loaded camptothecin nano-drug delivery platform as a personalized treatment modality for the treatment of cervical cancer. This method can significantly improve the sensitivity of tumors to ionizing radiation, which can improve the overall efficacy of radiotherapy without the need for higher radiation doses. Chen et al. developed a self-powered drug delivery system consisting of a disk TENG (D-Teng), a rectifying bridge and two gold electrodes. The D-Teng has good performance and provides long-term stable current. The output current of the D-Teng is converted to direct current by the rectifier bridge to stimulate the cells/tissues between the gold electrodes. *In vitro* experiments showed that the system can significantly improve the utilization of doxorubicin. Wang et al. summarized the opportunities and challenges of biomimetic exosomes in drug delivery systems over the past few decades. The design, synthesis, and biomedical applications of stimulus-responsive polymeric prodrugs of paclitaxel are reviewed by Zhou et al., they also summarized the opportunities and challenges of the field. Tian et al. reviewed the application of hydrogels in osteosarcoma inhibition and bone regeneration, and made some suggestions for future development.

Aluminum adjuvants have been widely used in some vaccines and can induce strong human immunity. However, deficiencies in cellular immunity limit its use in some vaccines. Therefore, there is an urgent need to develop novel adjuvants to enhance humoral and cellular immune responses. Shan et al. designed and prepared a novel nano adjuvant (PF3) by microfluidization by combining saponins (ginsenoside Rg1) with oil-in-water nanoemulsion (NE). The PF3 has a stronger humoral and cellular immune induction effect than aluminum adjuvants because of its higher cellular uptake and ability to activate immune response pathways. In addition, the size and zeta potential of PF3 did not change significantly after being stored at 4°C and 37°C for 12 weeks, indicating high stability *in vitro*. This study provides an adjuvant platform for the design of recombinant vaccines instead of traditional aluminum adjuvants.

Zika virus (ZIKV) seriously affects the normal development of the fetus. Visualizing the pathogenic activity of ZIKV from the route of infection to the immune process is critical. However, accurate labeling of ZIKV remains challenging due to the lack of reliable labeling techniques. Zheng et al. designed a new fluorescent quantum dots (QD)-based probe for reliable labeling and visualization of ZIKV. The probe conjugates ZIKV and QD with high efficiency by photo-activated bio-orthogonal cycloaddition. The labeling process is simple and has no effect on the permeability. The results show that the combination of ZIKV and QD probe can localize and track the function of the virus during infection. Therefore, this bio-orthogonal QD probe may be a promising method for detecting the pathogenic activity of ZIKV.

Mesoporous dopamine nanoparticles (MPDA NPs) are a kind of antitumor nanomaterials with broad clinical application prospects, but their biosecurity remains unclear. Huang et al. analyzed the toxicity of RNA-Seq-based MPDA NPs in mice following different exposure routes. The results showed that RNA-Seq-based MPDA NPs of different administration routes had no obvious or serious toxic effect on mice. The authors elucidate the toxic effect of RNA-Seq-based MPDA NPs from the molecular mechanism, which provides a new insight for the further clinical application of MPDA NPs.

Smart nanomaterials have a wide range of applications. The contributions in this Research Topic provide a variety of smart nanomaterials and their applications in biosensing and therapeutics, including biosensors, bioimaging, nanozyme, cancer therapies and triggering immune system. We believe that this Research Topic will provide new ideas and technologies for the application of smart nanomaterials in biosensing and therapy. More importantly, in order to get the latest achievements in this field, the Research Topic has launched the second Research Topic, entitled "*Smart Nanomaterials for Biosensing and Therapy Applications* II," welcome to submit!

Author contributions

All authors listed have made a substantial, direct, and intellectual contribution to the work and approved it for publication.

Acknowledgments

We very much appreciate the contributions of all authors to this Research Topic and are grateful for the time and dedication of those who contributed to the peer review process. This work has been supported by the National Natural Science Foundation of China (No. 82060599), the Natural Science Foundation of Jiangxi (20224BAB206091), the Science and Technology Project of Jiangxi Health Committee (No. 202131033), the Natural Science Foundation of Ganzhou (No. 202101034482), the Plan Post-subsidy Project of Ganzhou (No. 2019-60-174) and the Special Fund for Graduate Innovation in Jiangxi Province (No. YC2021-S796).

Conflict of interest

The authors declare that the research was conducted in the absence of any commercial or financial relationships that could be construed as a potential conflict of interest.

Publisher's note

References

Cao, S., Wang, J. R., Ji, S., Yang, P., Dai, Y., Guo, S., et al. (2022). Estimation of tumor cell total mRNA expression in 15 cancer types predicts disease progression. *Nat. Biotechnol.* 40 (11), 1624–1633. doi:10.1038/s41587-022-01342-x

Diaz, P. A., Bracaglia, S., Ranallo, S., Patino, T., Porchetta, A., and Ricci, F. (2022). Programmable cell-free transcriptional switches for antibody detection. *J. Am. Chem. Soc.* 144 (13), 5820–5826. doi:10.1021/jacs.1c11706

Huang, Q., Lin, X., Chen, D., and Tong, Q.-X. (2022). Carbon Dots/α-Fe_2O_3-Fe_3O_4 nanocomposite: Efficient synthesis and application as a novel electrochemical aptasensor for the ultrasensitive determination of aflatoxin B1. *Food Chem.* 373, 131415. doi:10.1016/j.foodchem.2021.131415

Huang, Q., Lin, X., Tong, L., and Tong, Q.-X. (2020). Graphene quantum dots/multiwalled carbon nanotubes composite-based electrochemical sensor for detecting dopamine release from living cells. *ACS Sustain. Chem. Eng.* 8 (3), 1644–1650. doi:10.1021/acssuschemeng.9b06623

Kathe, C., Skinnider, M. A., Hutson, T. H., Regazzi, N., Gautier, M., Demesmaeker, R., et al. (2022). The neurons that restore walking after paralysis. *Nature* 611 (7936), 540–547. doi:10.1038/s41586-022-05385-7

Lin, X., Xiong, M., Zhang, J., He, C., Ma, X., Zhang, H., et al. (2021). Carbon dots based on natural resources: Synthesis and applications in sensors. *Microchem. J.* 160, 105604. doi:10.1016/j.microc.2020.105604

Liu, C., Wang, Y., Li, L., He, D., Chi, J., Li, Q., et al. (2022a). Engineered extracellular vesicles and their mimetics for cancer immunotherapy. *J. Control. Release* 349, 679–698. doi:10.1016/j.jconrel.2022.05.062

Mei, Y., He, C., Zeng, W., Luo, Y., Liu, C., Yang, M., et al. (2022a). Electrochemical biosensors for foodborne pathogens detection based on carbon nanomaterials: Recent advances and challenges. *Food Bioprocess Technol.* 15, 498–513. doi:10.1007/s11947-022-02759-7

Vistain, L., Van Phan, H., Keisham, B., Jordi, C., Chen, M., Reddy, S. T., et al. (2022). Quantification of extracellular proteins, protein complexes and mRNAs in single cells by proximity sequencing. *Nat. Methods* 19, 1578–1589. doi:10.1038/s41592-022-01684-z

Xue, R., Zhang, Q., Cao, Q., Kong, R., Xiang, X., Liu, H., et al. (2022). Liver tumour immune microenvironment subtypes and neutrophil heterogeneity. *Nature* 612, 141–147. doi:10.1038/s41586-022-05400-x

Yi, X., Zeng, W., Wang, C., Chen, Y., Zheng, L., Zhu, X., et al. (2022). A step-by-step multiple stimuli-responsive metal-phenolic network prodrug nanoparticles for chemotherapy. *Nano Res.* 15, 1205–1212. doi:10.1007/s12274-021-3626-2

Zhang, G., Cong, Y., Liu, F.-L., Sun, J., Zhang, J., Cao, G., et al. (2022a). A nanomaterial targeting the spike protein captures SARS-CoV-2 variants and promotes viral elimination. *Nat. Nanotechnol.* 17, 993–1003. doi:10.1038/s41565-022-01177-2

frontiers | Frontiers in Bioengineering and Biotechnology

REVIEW
published: 06 April 2022
doi: 10.3389/fbioe.2022.875034

Recent Advances in Stimuli-Sensitive Amphiphilic Polymer-Paclitaxel Prodrugs

Man Zhou[1,2], Lijuan Wen[2], Cui Wang[2], Qiao Lei[3], Yongxiu Li[1]* and Xiaoqing Yi[2]**

[1]College of Chemistry, Nanchang University, Nanchang, China, [2]College of Pharmacy, Gannan Medical University, Ganzhou, China, [3]School of Basic Medical Sciences, Anhui Medical University, Hefei, China

Paclitaxel (PTX) is a broad-spectrum chemotherapy drug employed in the treatment of a variety of tumors. However, the clinical applications of PTX are limited by its poor water solubility. Adjuvants are widely used to overcome this issue. However, these adjuvants often have side effects and poor biodistribution. The smart drug delivery system is a promising strategy for the improvement of solubility, permeability, and stability of drugs, and can promote sustained controlled release, increasing therapeutic efficacy and reducing side effects. Polymeric prodrugs show great advantages for drug delivery due to their high drug loading and stability. There has been some groundbreaking work in the development of PTX-based stimulus-sensitive polymeric prodrug micelles, which is summarized in this study. We consider these in terms of the four main types of stimulus (pH, reduction, enzyme, and reactive oxygen species (ROS)). The design, synthesis, and biomedical applications of stimulus-responsive polymeric prodrugs of PTX are reviewed, and the current research results and future directions of the field are summarized.

Keywords: paclitaxel, polymer prodrug, stimuli-sensitive, drug delivery, cancer

OPEN ACCESS

Edited by:
Ziqiang Xu,
Hubei University, China

Reviewed by:
Cheng-Xiong Yang,
Nankai University, China
Jinjin Chen,
Tufts University, United States
Yinlong Zhang,
National Center for Nanoscience and Technology (CAS), China

****Correspondence:***
Qiao Lei
qiaolei@ahmu.edu.cn
Yongxiu Li
yxli@ncu.edu.cn
Xiaoqing Yi
keyi0115@126.com

Specialty section:
This article was submitted to Nanobiotechnology, a section of the journal Frontiers in Bioengineering and Biotechnology

Received: *13 February 2022*
Accepted: *11 March 2022*
Published: *06 April 2022*

Citation:
Zhou M, Wen L, Wang C, Lei Q, Li Y and Yi X (2022) Recent Advances in Stimuli-Sensitive Amphiphilic Polymer-Paclitaxel Prodrugs. Front. Bioeng. Biotechnol. 10:875034. doi: 10.3389/fbioe.2022.875034

INTRODUCTION

Paclitaxel (PTX) was first discovered in the late 1960s. It is a natural substance derived from the needles and bark of the Pacific yew tree. It is a mitotic inhibitor used primarily in cancer chemotherapy, which can be used in the treatment of various cancers, including ovarian cancer, esophagus cancer, small and non–small-cell lung cancer, multiple myeloma cancer, bladder cancer, breast cancer, head and neck cancer, colon cancer, and Kaposi's sarcoma (Khalifa et al., 2019; Chen et al., 2021; Peng et al., 2021; Zuo et al., 2021). PTX is a microtubule stabilizing drug, which can prevent cytoskeletal microtubules from depolymerizing into free tubulin. It can also cause tubulin and tubulin dimer of microtubule to lose dynamic balance, leading to cell cycle arrest and stagnation in the G2/M phase, ultimately inhibiting cell growth (Ashrafizadeh et al., 2021; Mosca et al., 2021; Yi et al., 2022). The efficacy of PTX is primarily attributable to its side chain functionalities, A ring, oxetane ring, and C2 benzoyl group. The acyl group of the C3' amide in the C13 chain remains active, and its function is enhanced by the hydroxyl group of C2' (Zhang et al., 2013). PTX is insoluble in water (<0.3 mg/ml), and increasing its solubility by adjusting its pH is difficult. This greatly limits its clinical application. At present, the PTX dosage forms such as Taxol, PTX liposome, and PTX albumin binding are used in clinical treatment of breast cancer and ovarian cancer. However, the adjuvants in current clinical preparations have serious side effects. Moreover, it is difficult to achieve controlled drug release at the tumor site. Therefore, there is an urgent need to develop a novel drug

delivery system that can improve the permeability and solubility of PTX and facilitate controlled targeted drug delivery, reducing side effects, and improving therapeutic efficacy.

In recent years, the use of self-assembling nanoparticles of amphiphilic polymers has become common in drug delivery as they are able to act as carriers for the hydrophobic molecules of insoluble drugs (Cabral and Kataoka, 2014; Ulbrich et al., 2016). Compared with traditional drug delivery systems, polymeric micelles have many merits such as the well-controlled size distribution, improved solubility, the enhanced permeability and retention (EPR) effect, good stability, and reduced toxicity (Chowdhury and Singh, 2020; Majumder et al., 2020). In addition, drug-targeting at the lesion site can be achieved by introducing targeted functional groups on the surfaces of the amphiphilic polymers (Roacho Perez et al., 2021). Amphiphilic polymers can load hydrophobic drugs through physical interaction or chemical bonding. Loading the drug to the polymers through physical interaction usually includes electrostatic interaction, π–π stacking, hydrogen bonding, and hydrophobic interaction (Zhai S. et al., 2017; Gao C. et al., 2021). However, the loading capacity using this approach is low, generally less than 10%, and significantly increases the metabolic burden on the body through the additional adjuvants. In addition, the weak connections between the molecules of the drug and the nanoparticles can lead to the untimely release of the drug after intravenous administration. Direct chemical bonding of the drug with the amphiphilic polymer creates a drug delivery system with high drug loading that has excellent stability in the blood circulation and can inhibit the premature release of the drug (Deng & Liu, 2020; Liu et al., 2021). Such polymeric prodrug delivery systems can not only improve drug loading significantly but can also precisely control drug loading and pharmacokinetics through chemical reaction. The construction of endogenous stimulus-sensitive polymeric prodrug nanoparticles allows the development of on-demand or triggered drug delivery.

Chemical groups sensitive to external signals (temperature, light, magnetic field, and ultrasonic wave) and endogenous signals [pH, reduction, enzyme, and reactive oxygen species (ROS)] have been extensively exploited in the design of polymeric prodrug delivery systems for triggered drug release (Li et al., 2015; Chen et al., 2018). The pH gradient in the tumor microenvironment (e.g., tumor tissue is around 6.5, endosomes are around 5.5, lysosomes are around 5.0) can act as an endogenous stimulus for controlling the drug release in tumor cells (Dai et al., 2019), whereas acidity is a specific feature of the tumor microenvironment; acid-sensitive coupling linkages are often used to construct polymeric prodrug nanoparticles with efficient transformation in tumors. It is reported that there is a significant difference in the concentration of reduced glutathione (GSH) between the microenvironment inside and outside tumor cells. The differences in GSH between intracellular (2–10 mM) and extracellular environments (2–20 μM) of tumor cells, which are often exploited for reduction-sensitive drug delivery system. Therefore, the prodrug with disulfide bonds releases the parent drug effectively in tumor cells and improves the drug utilization (Wang et al., 2020; Zuo et al., 2020). The design and study of

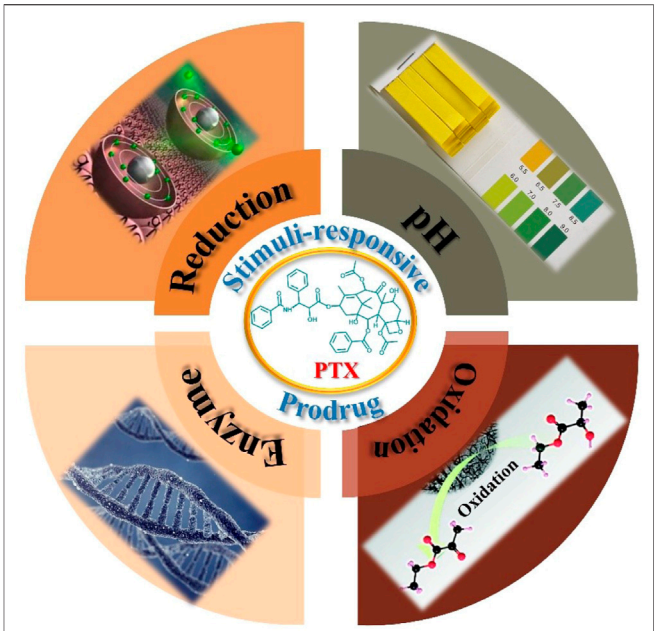

FIGURE 1 | Four types of polymer-PTX prodrug stimuli-sensitives.

enzyme-triggered polymeric prodrugs have potential clinical applications (Srinivasan et al., 2021; Tan et al., 2021). Phospholipases, oxidoreductases, and proteases overexpressed by tumor cells can act as selective triggers for enzyme-sensitive drug delivery vehicles. Nanodrug delivery systems with reactive oxygen species (ROS) sensitivity can also promote the drug release as the level of ROS in tumor cells is ten times higher than that in normal cells (Saravanakumar et al., 2017; Deng et al., 2020; Hong et al., 2021; Tan et al., 2021). For example, the concentration of H_2O_2 is 0.001–0.7 μM in healthy cells, while it is 10–100 μM in tumor cells (Li C. et al., 2021). ROS-sensitive chemical groups such as alkylene sulfides, borate esters, and thioketals (TKs) have been widely exploited to construct efficient stimulus-sensitive drug delivery systems for tumor therapy. However, due to the heterogeneity of tumor cells, the concentration of endogenous ROS is too low to trigger rapid drug release, and few ROS-sensitive drug delivery systems show sufficient sensitivity to tumor cells. Therefore, a ROS-sensitive drug delivery system with the ability to generate ROS would be a promising strategy that could improve selectivity and accelerate drug release to enhance the efficacy of tumor therapy. The construction of the stimulus-sensitive polymeric prodrug will improve the stability and drug loading of PTX, enable its controlled release at the tumor site, enhance the drug utilization, and reduce side effects.

As far as we know, much of the pioneering work on stimulus-sensitive polymeric PTX prodrug nanomedicine has not been well summarized. As shown in **Figure 1**, research on this subject can be categorized by the four different types of polymer-PTX prodrug stimuli: 1) pH-sensitive polymer-PTX prodrug, 2) reduction-sensitive polymer-PTX prodrug, 3) enzyme-sensitive polymer-PTX prodrug, and 4) ROS-sensitive polymer-PTX prodrug. This

TABLE 1 | Summary of representative systems for PTX prodrugs.

Type	Sensitive group	Material	Cancer type	References
pH	Acetal	APPMs	A549	Zhai et al. (2020)
		mPEG-PCL-Ace-PTX_5	MCF-7	Zhai Yinglei et al. (2017)
		PEG-acetal-PTX (PAP)	HeLa and MDA-MB-231	Huang et al. (2018)
	Acyclic-ketal	PEGylated acetone- acyclic-ketal-PTX (PKPs)	A2780 tumor-bearing mice	Mu et al. (2020)
Reduction	Thioether and disulfide	PSMAL and PSSMAL	4T1 tumor-bearing mice	Lou et al. (2021)
	Thioether	PTX-S-BDP.	HeLa and L929	Xia et al. (2021)
	Disulfide	PTX-ss-TMP	A2780 tumor-bearing mice	Zou et al. (2021)
		TB@PMP	HeLa tumor-bearing mice	Yi et al. (2018)
		TB@PMPT	HeLa tumor-bearing mice	Yi et al. (2021)
		diPTX@Fe&TA	HeLa tumor-bearing mice	Yi et al. (2022)
		diPTX@CPGC	NOD/SCID IL2-R-gamma mice	Su et al. (2018)
		PTX-SS-CIT	4T1 tumor-bearing mice	Gao Yuanyuan et al. (2021)
		PTX-SS-Val, PTX-SS-COOH	MCF-7	Li Yanlin et al. (2021)
		FA-DEX-ss-PTX	HCT-8/PTX tumor-bearing mice	Chen et al. (2020)
	Azo	Ce6/PTX2-Azo	HeLa tumor-bearing mice	Zhou et al. (2020b)
Enzyme	GFLG	PEGylated dendrimer-GFLG-PTX	4T1 tumor-bearing mice	Li et al. (2017)
		pGAEMA-PTX-Ppa-Gd	4T1 tumor-bearing mice	Wang Bing et al. (2019)
		dendritic- [(GFLG-polyPTX)-block-polyOEGMA]	4T1 tumor-bearing mice	Luo et al. (2021)
		poly (OEGMA)-PTX@Ce6	PDX tumor bearing mice	Tan et al. (2021)
	Borate ester)benzyl	PEG-B-PTX	MCF-7 tumor-bearing mice	Dong et al. (2020)
ROS	Thioketal	RBC(M(TPC-PTX))	HeLa tumor-bearing mice	Pei et al. (2018)
		PEG-b-P(LL-g-TK-PTX)-(LL-g-DMA)	PC-3 tumor-bearing mice	Xu et al. (2020)
		DEX-TK-PTX	HCT-8/PTX tumor-bearing mice	Chang et al. (2020)
		RLPA-NPs	4T1 cells tumor-bearing mice	Li et al. (2020)
	Thioether	LPC/PTX-S-LA PMs	4T1 tumor-bearing mice	Wang Kaiyuan et al. (2019)
		PPa-S-PTX	KB and 4T1 tumor-bearing mice	Luo et al. (2019)

review focuses on the design, synthesis, and biomedical applications of stimulus-sensitive PTX polymer prodrugs and the latest research progress. Finally, the future development directions and prospects of this field were briefly discussed.

PH-SENSITIVE POLYMER-PTX PRODRUG

Compared with that of normal tissue, the tumor microenvironment is highly acidic, which is due to the high metabolic activity of tumor cells. Therefore, the development of pH-sensitive polymer-PTX prodrugs in which drug release is triggered by the acidity of tumor cells has attracted extensive attention. To achieve this, acid-sensitive organoleptic groups, such as acetals and acyclic ketals, are typically built into polymeric prodrug delivery systems to cause the release of the drug when the delivery system encounters an acidic microenvironment. For instance, Zhai et al. developed pH-sensitive polymer-PTX prodrug micelles by grafting PTX onto the main chain of poly (ethylene glycol) (PEG)-polycarbonate through an acetal-linker to accelerate drug release in tumor cells. The drug loading of PTX reached up to 33% (Zhou et al., 2020a). mPEG-PCL-Ace-PTX is a pH-sensitive PTX prodrug micelle with the PTX content as high as 23.5 wt%. This was constructed using functionalized poly (ethyleneglycol)-poly (ε-caprolactone) (mPEG-PCL) diblock polymer with an acid-cleavable acetal (Ace) linkage (Zhai Y. et al., 2017). Another pH-sensitive amphiphilic polymeric prodrug, PEG-acetal-PTX, has been constructed for the inhibition of tumor cell proliferation. This self-assembled prodrug has excellent stability with drug loading up to 60.3% (Huang et al., 2018). Acyclic ketals are generally more acid-sensitive than acetals, so the development of pH-sensitive polymeric prodrug micelles based on acyclic ketal–coupled linkers are more desirable (Mu et al., 2020). Guo et al. constructed acyclic-ketal–based acid-sensitive PTX prodrug micelles using PEG with different lengths. They found that the length of PEG affects the hydrolysis kinetics, pharmacokinetics, biodistribution, and antitumor activity of the prodrug nanoparticles (Mu et al., 2020).

REDUCTION-SENSITIVE POLYMER-PTX PRODRUG

Due to the high expression of GSH in tumor cells, polymeric prodrugs with reduction-sensitive properties can achieve controlled intracellular drug release. Li et al. constructed a folate-targeted reduction-sensitive polymeric prodrug micelle by coupling PTX with dextrin through disulfide bond and embedded mitochondrial inhibitor of adjudin to overcome any multi-drug resistance of tumor cells (**Figure 2A**) (Chen et al., 2020). Liu et al. demonstrated that the reduction-sensitive PTX prodrug modified with maleimide functional groups was able to rapidly bind the circulating albumin immediately after intravenous administration (Lou et al., 2021). The albumin-bound PTX–maleimide prodrug nanoparticles exhibited longer circulation time and excellent anti-tumor efficacy *in vivo*. This disulfide-bridged prodrug exhibited selective cytotoxicity toward

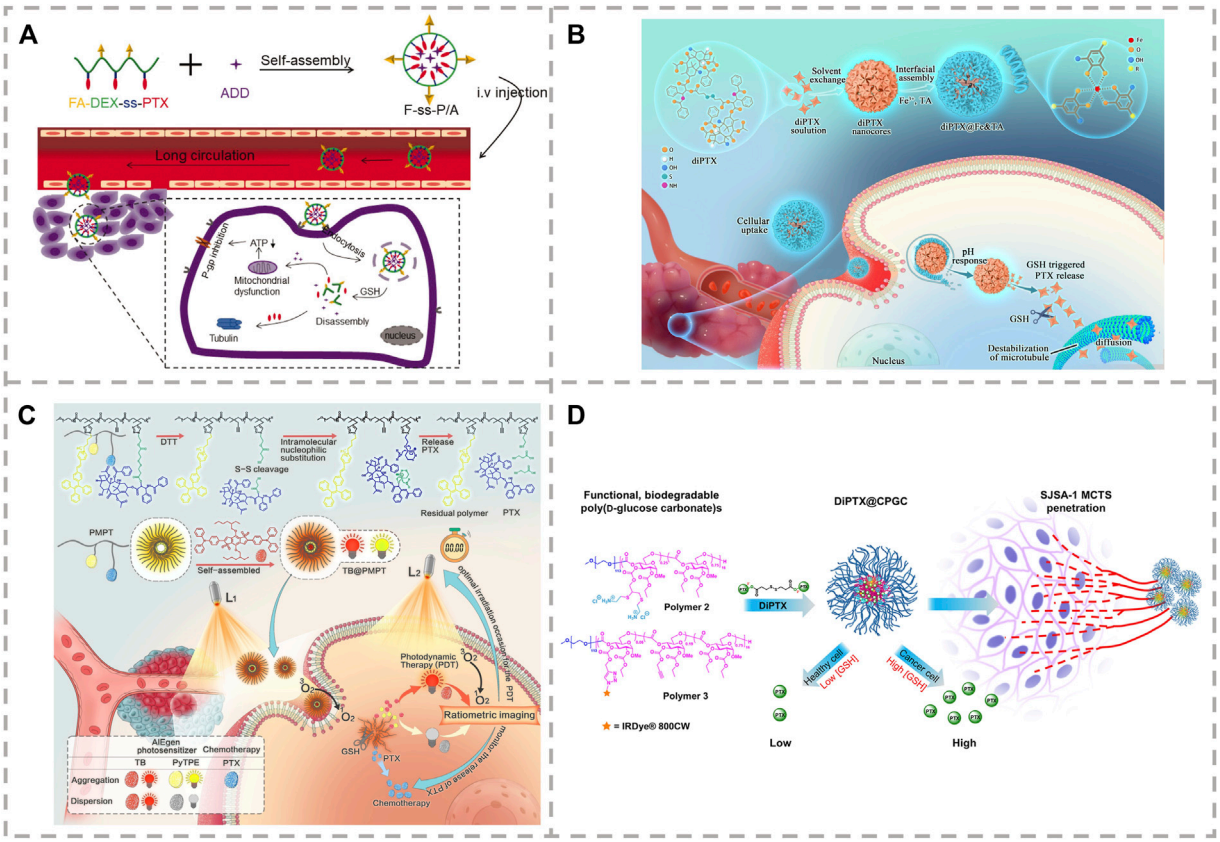

FIGURE 2 | (A) Release and mechanism of the self-assembly of F-ss-P/A micelles (Chen et al., 2020). **(B)** Synthesis and mechanism of PTX release from polymeric prodrug of TB@PMPT (Yi et al., 2021). **(C)** Procedure, intracellular pH, and reduction-sensitive of programmed drug release from dimeric prodrug nanoparticles (Yi et al., 2022). **(D)** Release of PTX from the poly (ethylene glycol) (PEG)-protected reduction-sensitive dimeric PTX (diPTX)-loaded cationic poly (D-glucose carbonate) micelle (diPTX@CPGC) (Su et al., 2018).

tumor cells and enhanced tumor suppression in BALB/C mice bearing 4T1 tumor. Xie et al. reported a reduction-sensitive prodrug of PTX (PTX-S-BDP) by linking PTX and BODIPY (BDP-OH) using a reduction-sensitive linker for fluorescence imaging–guided chemotherapy (Xia et al., 2021). PTX-S-BDP nanoparticles display excellent cellular imaging and good cellular selectivity, with free PTX reserving its cytotoxic effects for cancerous cells. Other studies have endeavored to produce synergistic therapeutic effects by combining two or more agents with different target signaling pathways (Zhou et al., 2020b). Gu et al. synthesized an amphiphilic reduction-sensitive prodrug of PTX-SS-TMP to deliver both PTX and the antiangiogenic agent of tetramethylpyrazine (TMP) to realize the synergistic treatment of A2780 tumor-bearing mice (Zou et al., 2021).

In addition, chemo-photodynamic therapy is an advanced treatment method that researchers are more concerned about (Yi et al., 2018). The combination of chemotherapeutic drugs and photosensitizers can improve therapeutic effects and reduce cytotoxic effects. In the development of this drug, an amphiphilic polymeric prodrug was used as a carrier of the photosensitizer needed for the combined treatment under light irradiation. A further advantage of this synthesis is that the ROS produced by photodynamic therapy can induce lipid peroxidation, increasing the permeability of the cell membrane and enhancing the intracellular internalization of PTX (**Figure 2B**) (Yi et al., 2021). Dimeric prodrugs can achieve high drug loading and inhibit premature drug leakage, so this strategy based on dimeric prodrugs is of great significance for the design of novel nanomedicine (Pei et al., 2018). The nanoparticles, diPTX@Fe&TA (**Figure 2C**), and diPTX@CPGC **Figure 2D** were prepared through co-precipitation of the dimeric prodrug, PTX-SS-PTX (diPTX), with the metal-phenolic network of Fe and tannic acid (Fe&TA) or cationic poly (D-glucose carbonate) (CPGC), respectively (Su et al., 2018; Yi et al., 2022). The drug loading of diPTX was 24.7 and 40% for diPTX@Fe&TA and diPTX@CPGC, respectively. The premature release of PTX and diPTX in the physiological environment was greatly inhibited. Compared with intravenous injection, oral administration is a more preferred choice for PTX administration, which is mainly due to the more convenient, safe, and flexible administration (Du et al., 2020; Gao Y. et al., 2021). The prodrugs, PTX-Cys, PTX-SS-COOH, and PTX-SS-Val were prepared by introducing amino, carboxyl, and

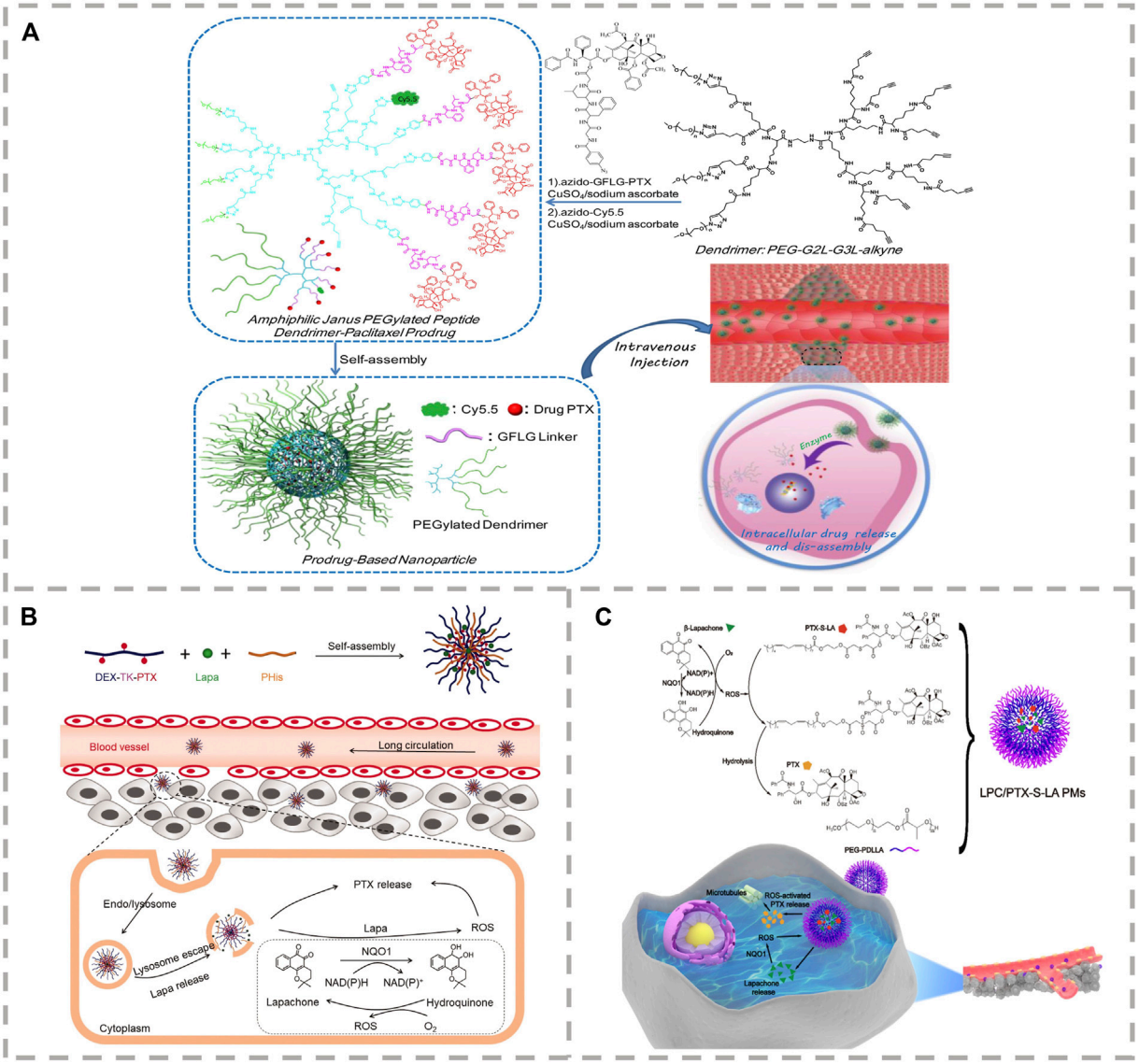

FIGURE 3 | (A) Structure and synthesis of enzyme-sensitive amphiphilic Janus PEGylated dendrimer-GFLG-PTX prodrug and its released PTX from prodrug through intracellular enzymolysis after endocytosis (Li et al., 2017). **(B)** A DEX-TK-PTX–based self-accelerating drug release nanodrug delivery system (PLP-NPs) with pH/ROS cascade response was constructed for the treatment of multidrug resistant colon cancer (Chang et al., 2020). **(C)** Self-strengthened bioactivating prodrug-based NPs are fabricated *via* co-encapsulation of ROS-sensitive thioether-linked linoleic acidpaclitaxel conjugates (PTX-S-LA) and β-lapachone (LPC) into polymeric micelles (PMs) (Wang K. et al., 2019).

valine into the disulfide bond of PTX to improve the solubility and oral bioavailability (Li Y. et al., 2021). Of these three, it was found that PTX-SS-Val can effectively improve the oral bioavailability of PTX.

ENZYME-SENSITIVE POLYMER-PTX PRODRUG

Enzymes have been used extensively as prodrug release triggers for stimulus-sensitive materials due to their high selectivity toward tumor cells (Pei et al., 2021; Zeng et al., 2021). For example, cathepsin B is overexpressed in the cells of various types of tumors, which acts as a lysosomal cysteine protease and can cleave proteins containing an oligopeptide glycylphenylalanylleucylglycine (Gly-Phe-Leu-Gly, GFLG) linker (Cheng et al., 2020; Jin et al., 2020). The GFLG linker between the drug and the polymer in the construction of cathepsin B–based enzyme-sensitive drug carriers is shown in **Figure 3A**. Luo et al. have constructed a series of amphiphilic polymer-PTX prodrugs using the enzyme-sensitive GFLG. They also used the polymeric prodrugs as carriers to load other functional drugs for real-time monitoring, tumor diagnosis, and therapy (Li et al., 2017; Wang B. et al., 2019; Luo et al.,

2021; Tan et al., 2021). For example, the enzyme-sensitive amphiphilic prodrug, Janus PEGylated dendrimer-GFLG-PTX, was prepared by conjugating the GFLG-PTX moiety to the PEGylated peptide dendrimer through click reaction (Li et al., 2017). *In vitro* experiments found that the cytotoxicity of the polymer prodrug on normal cells is far lower than that of free PTX, and it was able to effectively induce the apoptosis of breast cancer cells. A diagnostic and therapeutic platform was created using a PTX saccharide-based prodrug (pGAEMA-PTX-Ppa-Gd polymer) containing enzyme-sensitive GFLG oligopeptide (Wang B. et al., 2019). The T_1 contrast agent of Gadolinium-tetraazacyclododecanetetraacetic (Gd-DOTA) and the NIR fluorescent molecule pheophorbide a (Ppa) were conjugated to the polymer for cancer diagnosis, treatment, and real-time monitoring. In addition, an amphiphilic block copolymer prodrug, poly [oligo (ethylene glycol) methyl ether methacrylate] (polyOEGMA)-functionalized PTX, containing cathepsin B–sensitive GFLG oligopeptide linker between the PTX and the polymer backbone was constructed (Tan et al., 2021). This was then used as a carrier to load the photosensitizer Ce6 for combined chemo-photodynamic therapy. This effectively inhibited the growth of bladder cancer patient-derived tumor xenograft models through the photochemical internalization effect. Delivering the therapeutic agent to the site of the malignancy and activating deep tissue. A polyOEGMA-functionalized dendritic polymer-PTX prodrug with a short peptide GFLG was prepared to encapsulate an imidazole derivative with high energy-transfer efficiency and synergistically enhance the effects of two-photon photodynamic therapy effect for the synergistic effect on inhibition of tumor growth in 4T1 xenograft mice by combined chemo-photodynamic therapy with increased penetration depth (Luo et al., 2021).

ROS-SENSITIVE POLYMER-PTX PRODRUG

It is well known that benzylboronic ester can trigger an elimination response through the high levels of ROS in tumor cells, while the benzylboronic ester linkers have demonstrated excellent stability during blood circulation. For example, Shen et al. constructed the novel ROS-sensitive prodrug micelles based on *p*-(borate ester)benzyl by introducing the benzylboronic ester linker between the PTX and the PEG (PEG-B-PTX) (Dong et al., 2020). The loaded quinone was able to deplete intracellular GSH with the PTX and effectively inhibit the growth of tumor cells. The TK group has excellent stability in a normal physiological environment; the high level of ROS causes the group to cleave to generate acetone and two other thiol-containing fragments. However, the level of ROS expression in tumor cells is insufficient to trigger drug release completely. A promising strategy to address this is the development of drug delivery systems able to provoke intracellular ROS generation. Menadione (VK3) is a quinoid natural molecule with anti-tumor effects in breast, lung, prostate, and liver cancers. VK3 can catalyze ROS production through the specific overexpression of NAD(P)H:quinone oxidoreductase-1 (NQO1) in tumor cells and specifically improve the intracellular ROS level (Yang et al., 2018). Lu et al. developed the dual-responsive pH/ROS polymeric prodrug of PEG-b-P(LL-g-TK-PTX)-(LL-g-DMA) by conjugating the ROS-sensitive PTX prodrug (PTX-TK) and 2,3-dimethylmaleic anhydride (DMA) into the main chain of the amphiphilic polymer, PEG-b-PLL (Xu et al., 2020). Then, they encapsulated VK3 into the core of PEG-b-P((LL-g-TK-PTX)-(LL-g-DMA)) micelles to construct a self-amplifying drug delivery system with charge reversal capability. High levels of NQO1 in tumor cells catalyze the released VK3 to produce ROS, resulting in the amplified release of PTX and reduced side effects. To overcome insufficient intracellular release of nanodrugs and multi-drug resistance (MDR) of chemotherapeutics in the treatment of colon cancer, a ROS-sensitive thioketal (TK) bond combined PTX and dextran (DEX) to synthesize the prodrug DEX-TK-PTX. Then, pH-sensitive poly (L-histidine) and beta-lapachone were loaded into prodrug micelles, creating a self-accelerating drug release nanodrug delivery system (PLP-NPs) with pH/ROS cascade response for the treatment of multidrug-resistant colon cancer (Chang et al., 2020). PLP-NPs can increase the intracellular ROS level and drug concentration and consume the level of ATP in multidrug-resistant tumor cells (**Figure 3B**). To increase the deep penetration ability and intracellular release of nanodrugs at the site of malignancy, Sun et al. synthesized three polymers, the ROS-sensitive (methoxyl poly (ethylene glycol)-thioketal-paclitaxel (mPEG-TK-PTX)), iRGD-PEG-TK-PTX, and the pH-sensitive polymer octadecylaminepoly (aspartate-1-(3-aminopropyl) imidazole) (OA-P(Asp-API)) (Li et al., 2020). The three amphiphilic polymers were then used as carriers to encapsulate the ROS generation agent β-Lapachone (LAP) and construct multifunctional polymeric micelles (RLPA-NPs). RLPA-NPs can penetrate the tumor tissue through iRGD, release LAP in lysosomes, and amplify the release of PTX, ultimately improving the therapeutic effect. Ether is a relatively stable substance, while thioether is easily oxidized into sulphone and sulfoxide, resulting in a strong increase in its hydrophilicity and in the hydrophilic–hydrophobic ratio of polymers. Sun et al. synthesized the ROS-sensitive prodrug of thioether-linked PTX-linoleic acid conjugates (PTX-S-LA) (**Figure 3C**) (Wang K. et al., 2019), and combined it with a ROS generating agent to create a self-strengthening bioactive prodrug nanosystem with powerful anticancer effects. ROS produced by photosensitizers under light can induce tumor cell death and trigger the cleavage of thioether. PTX and the photosensitizer pyropheophytin a (PPa) were linked by a ROS-sensitive thioether linkage to construct a "two-in-one dimer" that was both carrier and cargo (Luo et al., 2019). Under laser irradiation, the overproduction of endogenous ROS and the ROS produced by the PPa synergistically triggered the release of PTX.

SUMMARY AND FUTURE PERSPECTIVES

The presence of the polymer shell stabilizes the polymer-based drug delivery system. Thus, they have the advantages of controlled PTX release, reduced dosage, and reduced systemic side effects. However,

polymer-based drug delivery systems have some limitations. Organic solvents or surfactants, such as those often used in the preparation of polymer nanoparticles, can disrupt biological membranes and have significant interaction with certain proteins. At the cellular level, polymer-based nanodrug delivery systems are not as biocompatible as liposomes. The structure of polymeric nanoparticles is unstable, and the encapsulation of a large amount of PTX can lead to colloidal transformation. There is a main disadvantage that polymer nanoparticles lack selectivity toward tumor cells. Although nanoparticles can passively target solid tumors through the EPR effect, the majority of polymer prodrugs nanoparticles with the size range from 100 to 500 nm will still be cleared by the reticuloendothelial system. Active targeting can achieve specific uptake of tumor cells, further improve drug utilization, and reduce side effects. Polymers are generally modified targeting functional groups by chemical reaction to achieve active targeting.

From the reviewed studies, it can be seen that a number of biocompatible polymers have been used and characterized for PTX prodrug formulation (**Table 1**). Amphiphilic polymer is the most widely studied material, but in fact, proteins are biodegradable, nonantigenic, and metabolizable, which provide a variety of possibilities for drug delivery and is a promising material for adjuvants. Many types of nanoscale drug delivery systems have been used to deliver PTX, including micelles, polysomes, liposomes, and fibers. From these studies, it can be concluded that tumor microenvironment stimulus-responsive polymeric prodrugs not only show outstanding stability and solubility but also have a controlled PTX release profile and biocompatibility. Therefore, prodrug nanoparticles hold exciting promise as a potential PTX delivery tool.

CONCLUSION

The application of nanotechnology to cancer treatment has led to several breakthroughs previously and continues to flourish as a key component of the health care system. Abraxane is the only nano-PTX formulation approved by the FDA and EMEA for the treatment of cancer, and is the most successful PTX formulation in clinical research. In this review, we have focused on amphiphilic polymer-PTX prodrug delivery systems and their ability to provide stimulus-sensitive therapeutic nanoplatforms for intracellular on-demand drug release. Polymeric prodrug nanoparticles can not only greatly improve the drug loading and solubility of PTX but can reduce its toxicity. In the future development of more promising nano-prodrug PTX formulations, some challenges will need to be overcome. Among them, there is the need to improve the efficiency of drug enrichment and the specificity of its release at the lesion site.

Despite this, the efficacy remains low for the prodrugs developed thus far. This may be due to the multilevel and complex biological issues inherent in attempting to eliminate cancerous tissues with minimum harm to the human body. Achieving this end requires targeted nanocarriers with strong specificity. To sum up, the research discussed in this review has made advances but there are still limitations to overcome. We hope that this overview will provide some ideas for future nano-prodrug delivery systems.

AUTHOR CONTRIBUTIONS

MZ, LW, and CW wrote the manuscript. LQ, YL, and XY reviewed and edited the manuscript. All authors revised the manuscript.

FUNDING

This work was financially supported by the Research Fund of Gannan Medical University (No. QD201903) and the Science and Technology Project of the Education Department of Jiangxi Province (No. GJJ211537) the National Natural Science Foundation of China (51864033, 21978127) and the National Key Research Development Program of China (2019YFC0605000).

REFERENCES

Ashrafizadeh, M., Mirzaei, S., Hashemi, F., Zarrabi, A., Zabolian, A., Saleki, H., et al. (2021). New Insight towards Development of Paclitaxel and Docetaxel Resistance in Cancer Cells: EMT as a Novel Molecular Mechanism and Therapeutic Possibilities. *Biomed. Pharmacother.* 141, 111824. doi:10.1016/j.biopha.2021.111824

Cabral, H., and Kataoka, K. (2014). Progress of Drug-Loaded Polymeric Micelles into Clinical Studies. *J. Controlled Release* 190, 465–476. doi:10.1016/j.jconrel.2014.06.042

Chang, N., Zhao, Y., Ge, N., and Qian, L. (2020). A pH/ROS cascade-responsive and Self-Accelerating Drug Release Nanosystem for the Targeted Treatment of Multi-Drug-Resistant colon Cancer. *Drug Deliv.* 27, 1073–1086. doi:10.1080/10717544.2020.1797238

Chen, D., Ge, S., Zuo, L., Wang, S., Liu, M., and Li, S. (2020). Adjudin-loaded Redox-Sensitive Paclitaxel-Prodrug Micelles for Overcoming Multidrug Resistance with Efficient Targeted colon Cancer Therapy. *Drug Deliv.* 27, 1094–1105. doi:10.1080/10717544.2020.1797245

Chen, D., Zhang, G., Li, R., Guan, M., Wang, X., Zou, T., et al. (2018). Biodegradable, Hydrogen Peroxide, and Glutathione Dual Responsive Nanoparticles for Potential Programmable Paclitaxel Release. *J. Am. Chem. Soc.* 140, 7373–7376. doi:10.1021/jacs.7b12025

Chen, E., Wang, T., Zhang, J., Zhou, X., Niu, Y., Liu, F., et al. (2021). Mitochondrial Targeting and pH-Responsive Nanogels for Co-delivery of Lonidamine and Paclitaxel to Conquer Drug Resistance. *Front. Bioeng. Biotechnol.* 9, 787320. doi:10.3389/fbioe.2021.787320

Cheng, Y. J., Qin, S. Y., Liu, W. L., Ma, Y. H., Chen, X. S., Zhang, A. Q., et al. (2020). Dual-Targeting Photosensitizer-Peptide Amphiphile Conjugate for Enzyme-Triggered Drug Delivery and Synergistic Chemo-Photodynamic Tumor Therapy. *Adv. Mater. Inter.* 7 (19), 2000935. doi:10.1002/admi.202000935

Chowdhury, N., and Singh, M. (2020). Current Development of Oral Taxane Formulations: a Review. *Crit. Rev. Ther. Drug Carrier Syst.* 37 (3), 205–227. doi:10.1615/CritRevTherDrugCarrierSyst.2020029699

Dai, Y., Chen, X., and Zhang, X. (2019). Recent Advances in Stimuli-Responsive Polymeric Micelles via Click Chemistry. *Polym. Chem.* 10 (1), 34–44. doi:10.1039/c8py01174e

Deng, C., Zhang, Q., Guo, J., Zhao, X., and Zhong, Z. (2020). Robust and Smart Polypeptide-Based Nanomedicines for Targeted Tumor Therapy. *Adv. Drug Deliv. Rev.* 160, 199–211. doi:10.1016/j.addr.2020.10.019

Deng, Z., and Liu, S. (2020). Controlled Drug Delivery with Nanoassemblies of Redox-Responsive Prodrug and Polyprodrug Amphiphiles. *J. Controlled Release* 326, 276–296. doi:10.1016/j.jconrel.2020.07.010

Dong, C., Zhou, Q., Xiang, J., Liu, F., Zhou, Z., and Shen, Y. (2020). Self-assembly of Oxidation-Responsive Polyethylene Glycol-Paclitaxel Prodrug for Cancer Chemotherapy. *J. Controlled Release* 321, 529–539. doi:10.1016/j.jconrel.2020.02.038

Du, X., Yin, S., Xu, L., Ma, J., Yu, H., Wang, G., et al. (2020). Polylysine and Cysteine Functionalized Chitosan Nanoparticle as an Efficient Platform for Oral Delivery of Paclitaxel. *Carbohydr. Polym.* 229, 115484. doi:10.1016/j.carbpol.2019.115484

Gao, C., Wang, Y., Ye, Z., Lin, Z., Ma, X., and He, Q. (2021a). Biomedical Micro-/Nanomotors: From Overcoming Biological Barriers to *In Vivo* Imaging. *Adv. Mater.* 33 (6), 2000512. doi:10.1002/adma.202000512

Gao, Y., Zuo, S., Li, L., Liu, T., Dong, F., Wang, X., et al. (2021b). The Length of Disulfide Bond-Containing Linkages Impacts the Oral Absorption and Antitumor Activity of Paclitaxel Prodrug-Loaded Nanoemulsions. *Nanoscale* 13 (23), 10536–10543. doi:10.1039/d1nr01359a

Hong, S., Lee, Y., Shin, H., Kim, T., Jung, E., and Lee, D. (2021). Nanoassemblies of Disulfide-Bridged Bile Acid Dimers as Therapeutics Agents for Hepatic Ischemia/reperfusion Injury. *Acs Appl. Bio Mater.* 4 (4), 3145–3154. doi:10.1021/acsabm.0c01554

Huang, D., Zhuang, Y., Shen, H., Yang, F., Wang, X., and Wu, D. (2018). Acetal-linked PEGylated Paclitaxel Prodrugs Forming Free-Paclitaxel-Loaded pH-Responsive Micelles with High Drug Loading Capacity and Improved Drug Delivery. *Mater. Sci. Eng. C* 82, 60–68. doi:10.1016/j.msec.2017.08.063

Jin, X., Zhang, J., Jin, X., Liu, L., and Tian, X. (2020). Folate Receptor Targeting and Cathepsin B-Sensitive Drug Delivery System for Selective Cancer Cell Death and Imaging. *Acs Med. Chem. Lett.* 11 (8), 1514–1520. doi:10.1021/acsmedchemlett.0c00031

Khalifa, A. M., Elsheikh, M. A., Khalifa, A. M., and Elnaggar, Y. S. R. (2019). Current Strategies for Different Paclitaxel-Loaded Nano-Delivery Systems towards Therapeutic Applications for Ovarian Carcinoma: A Review Article. *J. Controlled Release* 311-312, 125–137. doi:10.1016/j.jconrel.2019.08.034

Li, C., Wang, Y., Zhang, S., Zhang, J., Wang, F., Sun, Y., et al. (2021a). pH and ROS Sequentially Responsive Podophyllotoxin Prodrug Micelles with Surface Charge-Switchable and Self-Amplification Drug Release for Combating Multidrug Resistance Cancer. *Drug Deliv.* 28 (1), 680–691. doi:10.1080/10717544.2021.1905750

Li, J., Ke, W., Li, H., Zha, Z., Han, Y., and Ge, Z. (2015). Endogenous Stimuli-Sensitive Multistage Polymeric Micelleplex Anticancer Drug Delivery System for Efficient Tumor Penetration and Cellular Internalization. *Adv. Healthc. Mater.* 4 (15), 2206–2219. doi:10.1002/adhm.201500379

Li, N., Cai, H., Jiang, L., Hu, J., Bains, A., Hu, J., et al. (2017). Enzyme-sensitive and Amphiphilic PEGylated Dendrimer-Paclitaxel Prodrug-Based Nanoparticles for Enhanced Stability and Anticancer Efficacy. *ACS Appl. Mater. Inter.* 9 (8), 6865–6877. doi:10.1021/acsami.6b15505

Li, Y., Chen, M., Yao, B., Lu, X., Song, B., Vasilatos, S. N., et al. (2020). Dual pH/ROS-Responsive Nanoplatform with Deep Tumor Penetration and Self-Amplified Drug Release for Enhancing Tumor Chemotherapeutic Efficacy. *Small* 16 (32), 2002188. doi:10.1002/smll.202002188

Li, Y., Yang, M., Zhao, Y., Li, L., and Xu, W. (2021b). Preparation and *In Vitro* Evaluation of Amphiphilic Paclitaxel Small Molecule Prodrugs and Enhancement of Oral Absorption. *Eur. J. Med. Chem.* 215, 113276. doi:10.1016/j.ejmech.2021.113276

Liu, N., Chen, Q., Zhang, Q., Wang, J., Si, R., Zhang, J., et al. (2021). The Application of Prodrug-Based Drug Delivery Strategy in Anticancer Drugs. *Ctmc* 21 (24), 2184–2204. doi:10.2174/1568026621666210909163108

Lou, X., Zhang, D., Ling, H., He, Z., Sun, J., Sun, M., et al. (2021). Pure Redox-Sensitive Paclitaxel-Maleimide Prodrug Nanoparticles: Endogenous Albumin-Induced Size Switching and Improved Antitumor Efficiency. *Acta Pharmaceutica Sinica B* 11 (7), 2048–2058. doi:10.1016/j.apsb.2020.12.001

Luo, C., Sun, B., Wang, C., Zhang, X., Chen, Y., Chen, Q., et al. (2019). Self-facilitated ROS-Responsive Nanoassembly of Heterotypic Dimer for Synergistic Chemo-Photodynamic Therapy. *J. Controlled Release* 302, 79–89. doi:10.1016/j.jconrel.2019.04.001

Luo, L., Yin, Z., Qi, Y., Liu, S., Yi, Y., Tian, X., et al. (2021). An Intracellular Enzyme-Responsive Polymeric Prodrug with Synergistic Effect of Chemotherapy and Two-Photon Photodynamic Therapy. *Appl. Mater. Today* 23, 2002188. doi:10.1016/j.apmt.2021.100996

Majumder, N., G Das, N., and Das, S. K. (2020). Polymeric Micelles for Anticancer Drug Delivery. *Ther. Deliv.* 11 (10), 613–635. doi:10.4155/tde-2020-0008

Mosca, L., Ilari, A., Fazi, F., Assaraf, Y. G., and Colotti, G. (2021). Taxanes in Cancer Treatment: Activity, Chemoresistance and its Overcoming. *Drug Resist. Updates* 54, 2002188. doi:10.1016/j.drup.2020.100742

Mu, J., Zhong, H., Zou, H., Liu, T., Yu, N., Zhang, X., et al. (2020). Acid-sensitive PEGylated Paclitaxel Prodrug Nanoparticles for Cancer Therapy: Effect of PEG Length on Antitumor Efficacy. *J. Controlled Release* 326, 265–275. doi:10.1016/j.jconrel.2020.07.022

Pei, Q., Hu, X., Zheng, X., Liu, S., Li, Y., Jing, X., et al. (2018). Light-activatable Red Blood Cell Membrane-Camouflaged Dimeric Prodrug Nanoparticles for Synergistic Photodynamic/chemotherapy. *Acs Nano* 12 (2), 1630–1641. doi:10.1021/acsnano.7b08219

Pei, Q., Lu, S., Zhou, J., Jiang, B., Li, C., Xie, Z., et al. (2021). Intracellular Enzyme-Responsive Profluorophore and Prodrug Nanoparticles for Tumor-specific Imaging and Precise Chemotherapy. *ACS Appl. Mater. Inter.* 13 (50), 59708–59719. doi:10.1021/acsami.1c19058

Peng, J., Yin, Y., Liang, H., Lu, Y., Zheng, H., Wu, G., et al. (2021). Tumor Microenvironment Responsive Pepper Mild Mottle Virus-Based Nanotubes for Targeted Delivery and Controlled Release of Paclitaxel. *Front. Bioeng. Biotechnol.* 9, 763661. doi:10.3389/fbioe.2021.763661

Roacho-Pérez, J. A., Garza-Treviño, E. N., Delgado-Gonzalez, P., G-Buentello, Z., Delgado-Gallegos, J. L., et al. (2021). Target Nanoparticles against Pancreatic Cancer: Fewer Side Effects in Therapy. *Life* 11 (11), 1187. doi:10.3390/life11111187

Saravanakumar, G., Kim, J., and Kim, W. J. (2017). Reactive-oxygen-species-responsive Drug Delivery Systems: Promises and Challenges. *Adv. Sci.* 4 (1), 1600124. doi:10.1002/advs.201600124

Srinivasan, S., Roy, D., Chavas, T. E. J., Vlaskin, V., Ho, D.-K., Pottenger, A., et al. (2021). Liver-targeted Polymeric Prodrugs of 8-aminoquinolines for Malaria Radical Cure. *J. Controlled Release* 331, 213–227. doi:10.1016/j.jconrel.2020.12.046

Su, L., Li, R., Khan, S., Clanton, R., Zhang, F., Lin, Y.-N., et al. (2018). Chemical Design of Both a Glutathione-Sensitive Dimeric Drug Guest and a Glucose-Derived Nanocarrier Host to Achieve Enhanced Osteosarcoma Lung Metastatic Anticancer Selectivity. *J. Am. Chem. Soc.* 140 (4), 1438–1446. doi:10.1021/jacs.7b11462

Tan, P., Cai, H., Wei, Q., Tang, X., Zhang, Q., Kopytynski, M., et al. (2021). Enhanced Chemo-Photodynamic Therapy of an Enzyme-Responsive Prodrug in Bladder Cancer Patient-Derived Xenograft Models. *Biomaterials* 277, 121061. doi:10.1016/j.biomaterials.2021.121061

Ulbrich, K., Holá, K., Šubr, V., Bakandritsos, A., Tuček, J., and Zbořil, R. (2016). Targeted Drug Delivery with Polymers and Magnetic Nanoparticles: Covalent and Noncovalent Approaches, Release Control, and Clinical Studies. *Chem. Rev.* 116 (9), 5338–5431. doi:10.1021/acs.chemrev.5b00589

Wang, B., Lv, P., Cai, H., Li, Y., Zhu, H., Lui, S., et al. (2019a). Enzyme-responsive Copolymer as a Theranostic Prodrug for Tumor *In Vivo* Imaging and Efficient Chemotherapy. *J. Biomed. Nanotechnol.* 15 (9), 1897–1908. doi:10.1166/jbn.2019.2833

Wang, J., Pei, Q., Xia, R., Liu, S., Hu, X., Xie, Z., et al. (2020). Comparison of Redox Responsiveness and Antitumor Capability of Paclitaxel Dimeric Nanoparticles with Different Linkers. *Chem. Mater.* 32 (24), 10719–10727. doi:10.1021/acs.chemmater.0c04080

Wang, K., Yang, B., Ye, H., Zhang, X., Song, H., Wang, X., et al. (2019b). Self-strengthened Oxidation-Responsive Bioactivating Prodrug Nanosystem with Sequential and Synergistically Facilitated Drug Release for Treatment of Breast Cancer. *ACS Appl. Mater. Inter.* 11 (21), 18914–18922. doi:10.1021/acsami.9b03056

Xia, J., Pei, Q., Zheng, M., and Xie, Z. (2021). An Activatable Fluorescent Prodrug of Paclitaxel and BODIPY. *J. Mater. Chem. B* 9 (9), 2308–2313. doi:10.1039/d0tb02510k

Xu, C., Song, R., Lu, P., Chen, J., Zhou, Y., Shen, G., et al. (2020). A pH-Responsive Charge-Reversal Drug Delivery System with Tumor-specific Drug Release and ROS Generation for Cancer Therapy. *Ijn* Vol. 15, 65–80. doi:10.2147/IJN.S230237

Yang, G.-G., Zhang, H., Zhang, D.-Y., Cao, Q., Yang, J., Ji, L.-N., et al. (2018). Cancer-specific Chemotherapeutic Strategy Based on the Vitamin K3 Mediated

ROS Regenerative Feedback and Visualized Drug Release *In Vivo*. *Biomaterials* 185, 73–85. doi:10.1016/j.biomaterials.2018.08.065

Yi, X., Dai, J., Han, Y., Xu, M., Zhang, X., Zhen, S., et al. (2018). A High Therapeutic Efficacy of Polymeric Prodrug Nano-Assembly for a Combination of Photodynamic Therapy and Chemotherapy. *Commun. Biol.* 1, 202. doi:10.1038/s42003-018-0204-6

Yi, X., Hu, J.-J., Dai, J., Lou, X., Zhao, Z., Xia, F., et al. (2021). Self-guiding Polymeric Prodrug Micelles with Two Aggregation-Induced Emission Photosensitizers for Enhanced Chemo-Photodynamic Therapy. *Acs Nano* 15 (2), 3026–3037. doi:10.1021/acsnano.0c09407

Yi, X., Zeng, W., Wang, C., Chen, Y., Zheng, L., Zhu, X., et al. (2022). A Step-by-step Multiple Stimuli-Responsive Metal-Phenolic Network Prodrug Nanoparticles for Chemotherapy. *Nano Res.* 15 (2), 1205–1212. doi:10.1007/s12274-021-3626-2

Zeng, S., Ou, H., Gao, Z., Zhang, J., Li, C., Liu, Q., et al. (2021). HCPT-peptide Prodrug with Tumor Microenvironment -responsive Morphology Transformable Characteristic for Boosted Bladder Tumor Chemotherapy. *J. Controlled Release* 330, 715–725. doi:10.1016/j.jconrel.2020.12.042

Zhai, S., Hu, X., Hu, Y., Wu, B., and Xing, D. (2017a). Visible Light-Induced Crosslinking and Physiological Stabilization of Diselenide-Rich Nanoparticles for Redox-Responsive Drug Release and Combination Chemotherapy. *Biomaterials* 121, 41–54. doi:10.1016/j.biomaterials.2017.01.002

Zhai, Y., Zhou, X., Jia, L., Ma, C., Song, R., Deng, Y., et al. (2017b). Acetal-linked Paclitaxel Polymeric Prodrug Based on Functionalized mPEG-PCL Diblock Polymer for pH-Triggered Drug Delivery. *Polymers* 9 (12), 698. doi:10.3390/polym9120698

Zhang, Z., Mei, L., and Feng, S.-S. (2013). Paclitaxel Drug Delivery Systems. *Expert Opin. Drug Deliv.* 10, 325–340. doi:10.1517/17425247.2013.752354

Zhou, S., Fu, S., Wang, H., Deng, Y., Zhou, X., Sun, W., et al. (2020a). Acetal-linked Polymeric Prodrug Micelles Based on Aliphatic Polycarbonates for Paclitaxel Delivery: Preparation, Characterization, In vitro Release and Anti-proliferation Effects. *J. Biomater. Sci. Polym. Ed.* 31 (15), 2007–2023. doi:10.1080/09205063.2020.1792046

Zhou, S., Hu, X., Xia, R., Liu, S., Pei, Q., Chen, G., et al. (2020b). A Paclitaxel Prodrug Activatable by Irradiation in a Hypoxic Microenvironment. *Angew. Chem. Int. Ed.* 59 (51), 23198–23205. doi:10.1002/anie.202008732

Zou, L., Liu, X., Li, J., Li, W., Zhang, L., Fu, C., et al. (2021). Redox-sensitive Carrier-free Nanoparticles Self-Assembled by Disulfide-Linked Paclitaxel-Tetramethylpyrazine Conjugate for Combination Cancer Chemotherapy. *Theranostics* 11 (9), 4171–4186. doi:10.7150/thno.42260

Zuo, S., Sun, B., Yang, Y., Zhou, S., Zhang, Y., Guo, M., et al. (2020). Probing the Superiority of Diselenium Bond on Docetaxel Dimeric Prodrug Nanoassemblies: Small Roles Taking Big Responsibilities. *Small* 16 (45), 2005039. doi:10.1002/smll.202005039

Zuo, S., Wang, Z., An, X., Wang, J., Zheng, X., Shao, D., et al. (2021). Self-assembly Engineering Nanodrugs Composed of Paclitaxel and Curcumin for the Combined Treatment of Triple Negative Breast Cancer. *Front. Bioeng. Biotechnol.* 9, 121061. doi:10.3389/fbioe.2021.747637

Conflict of Interest: The authors declare that the research was conducted in the absence of any commercial or financial relationships that could be construed as a potential conflict of interest.

Publisher's Note: All claims expressed in this article are solely those of the authors and do not necessarily represent those of their affiliated organizations, or those of the publisher, the editors, and the reviewers. Any product that may be evaluated in this article, or claim that may be made by its manufacturer, is not guaranteed or endorsed by the publisher.

frontiers | Frontiers in Bioengineering and Biotechnology

ORIGINAL RESEARCH
published: 12 April 2022
doi: 10.3389/fbioe.2022.876641

Camptothecin Delivery *via* Tumor-Derived Exosome for Radiosensitization by Cell Cycle Regulation on Patient-Derived Xenograft Mice

Yiling Yang[1], Shiqi Ren[2], Wenpeng Huang[3], Jiahan Dong[1], Jiancheng Guo[2], Jie Zhao[4]* and Yonggao Zhang[3]**

[1]Department of Ultrasound, The First Affiliated Hospital of Zhengzhou University, Zhengzhou, China, [2]BGI College and Henan Institute of Medical and Pharmaceutical Sciences, Zhengzhou University, Zhengzhou, China, [3]Department of Radiology, The First Affiliated Hospital of Zhengzhou University, Zhengzhou, China, [4]Internet Medical and System Applications of National Engineering Laboratory, Zhengzhou, China

OPEN ACCESS

Edited by:
Qitong Huang,
Gannan Medical University, China

Reviewed by:
Yongri Jin,
Jilin University, China
Chenhui Wang,
Chongqing University, China

***Correspondence:**
Yiling Yang
fccyangyl@zzu.edu.cn
Jie Zhao
zhaojiezzu@163.com
Yonggao Zhang
zyg01578@126.com

Specialty section:
This article was submitted to Nanobiotechnology, a section of the journal Frontiers in Bioengineering and Biotechnology

Received: 15 February 2022
Accepted: 21 March 2022
Published: 12 April 2022

Citation:
Yang Y, Ren S, Huang W, Dong J, Guo J, Zhao J and Zhang Y (2022) Camptothecin Delivery via Tumor-Derived Exosome for Radiosensitization by Cell Cycle Regulation on Patient-Derived Xenograft Mice. Front. Bioeng. Biotechnol. 10:876641. doi: 10.3389/fbioe.2022.876641

Purpose: While radiotherapy remains the leading clinical treatment for many tumors, its efficacy can be significantly hampered by the insensitivity of cells in the S phase of the cell cycle to such irradiation.

Methods: Here, we designed a highly targeted drug delivery platform in which exosomes were loaded with the FDA-approved anti-tumor drug camptothecin (CPT) which is capable of regulating cell cycle. The utilized exosomes were isolated from patient tumors, enabling the personalized treatment of individuals to ensure better therapeutic outcomes.

Results: This exosome-mediated delivery strategy was exhibited robust targeted to patient-derived tumor cells *in vitro* and in established patient-derived xenograft models. By delivering CPT to tumor cells, this nanoplatform was able to decrease cell cycle arrest in the S phase, increasing the frequency of cells in the G1 and G2/M phases such that they were more radiosensitive.

Conclusion: This therapeutic approach was able to substantially enhance the sensitivity of patient-derived tumors to ionizing radiation, thereby improving the overall efficacy of radiotherapy without the need for a higher radiation dose.

Keywords: cell cycle, exosome, radiotherapy, patient-derived xenograft model, camptothecin

INTRODUCTION

Cervical cancer is among the leading causes of cancer and cancer-associated mortality among women (Sung et al., 2021). In individuals with stage Ib and IIa cervical cancer, radiotherapy and radical surgery can both effectively improve patient outcomes, yielding satisfactory 5-year survival rates (Landoni et al., 1997). However, these approaches are less efficacious in more advanced cervical cancer patients in whom tumors are larger (Rose et al., 1999). To achieve the desired outcome, the utilized ionizing radiation dosage may exceed maximum normal tissue tolerance thresholds, resulting in severe adverse events (Sasieni and Sawyer 2021). To overcome this risk, other therapeutic methods including chemotherapy, afterloading therapy, and radioactive particle implantation have been explored (Flay and Matthews 1995).

Nanomedicine-based therapeutic radiosensitization strategies represent a novel emerging approach to enhancing the efficacy of radiotherapy while minimizing normal tissue damage (Zhang et al., 2019; G.; Song et al., 2017). Nano-radiosensitizers have been developed that are capable of increasing ionizing energy deposition in target tumor tissues by enhancing the photoelectric effect. These radiosensitizers are generally composed of high-Z elements including silver (Khochaiche et al., 2021), gold (Yi et al., 2016; Laprise-Pelletier et al., 2018; Xu et al., 2019), tantalum (Song et al., 2016; Lyu et al., 2021), and hafnium (Chen et al., 2019). While promising, however, these nano-radiosensitizers exhibit intrinsic cytotoxicity, and their metabolic processing remains uncertain (Yoon et al., 2018). Other approaches have sought to leverage the tumor microenvironment (TME) to increase radiosensitivity (Jarosz-Biej et al., 2019; Chen et al., 2021). For example, catalytic agents capable of converting H_2O_2 to O_2 within cells have been used to alleviate intratumoral hypoxia as a means of improving radiotherapeutic outcomes (Zhu et al., 2016; Lin et al., 2018; Lyu et al., 2020a). Researchers have also sought to combine radiotherapy with chemotherapy, photothermal therapy, and sonodynamic therapy in an effort to achieve synergistic benefits superior to those of either treatment in isolation (Lyu et al., 2020b; Suo et al., 2020; Yang et al., 2020). Chemotherapeutic drugs can be broadly classified into cell cycle-specific and -nonspecific agents, with the former of these inducing apoptotic cell death at a particular point in the cell cycle and the latter resulting in indiscriminate target cell death (Zhu et al., 2020; Luo et al., 2020). Chemotherapy is a systemic treatment, in contrast to radiotherapy, which is targeted. Severe off-target side effects of chemotherapy can include nausea, malaise, and alopecia (Rose et al., 1999; Bosset et al., 2006; Abraham et al., 2013; Gao et al., 2020; Khochaiche et al., 2021; Zhu et al., 2022). Careful consideration of the most appropriate drug delivery strategy must thus be considered to maximize benefit and minimize discomfort in treated cancer patients (Peeters et al., 2005).

In recent years, personalized therapeutic medicine-based approaches have emerged for the treatment of cancers (Wang et al., 2021). In most *in vivo* preclinical assays, researchers rely on cell-line-derived xenograft (CDX) murine models derived from purified cell lines. While informative to some extent, these models differ substantially from natural tumors. Patient-derived xenograft (PDX) models, in contrast, utilize tumor tissues derived directly from patients and thus more closely recapitulate the heterogeneity, structure, and metastatic potential of true human tumors (Sun et al., 2021). In the present study, we utilized tumor-specific patient-derived exosomes as an approach to delivering camptothecin (CPT) to tumors in PDX model mice (Bhimani et al., 2020). As shown in **Scheme 1** CPT is a chemotherapeutic drug capable of reducing the frequency of cells in the S phase of the cell cycle during which DNA replicates and cells are largely resistant to ionizing radiation (Park et al., 1997). Owing to their robust tumor-targeting capabilities, patient-derived exosomes from a cervical cancer patient were utilized as a vehicle to mediate CPT delivery to the target tumor, thereby enhancing radiosensitization while minimizing normal adjacent tissue damage (Duo et al., 2021). In addition, exosomes derived from HeLa cells were used to deliver CPT, and the relative feasibility of both patient-derived exosome/CPT (EC) hybrid and HeLa cells exosome CPT (ECC) hybrid nanoplatforms were analyzed in a PDX model system using tumor tissues from the same cervical cancer patient. Remarkable, the developed EC hybrid nanoplatform strategy exhibited efficient tumor targeting together with robust radiosensitization, thus underscoring its promising biocompatibility and translational potential.

EXPERIMENTAL SECTION

Animals

Six-week-old female nude BALB/c mice were purchased from Vital River Company (China). The protocols of the Institutional Animal Care and Use Committee were used to guide all animal studies discussed herein.

PATIENT TUMOR SAMPLES

Tumor tissue samples were collected from a 55-year old female patient with advanced stage IIIc cervical cancer within 1 h of surgery as per the protocols of the Institutional Review and Ethics Boards of Zhengzhou University. The patient provided informed consent for the present study.

Patient-Derived Cancer Cell Isolation

Initially, tumor tissues were minced into small ~1 mm^3 cubes, after which they were digested for 1 h using 0.1 mg/ml collagenase IV and filtered through 70 um strainers (Becton Dickinson, United States) to yield patient-derived cancer cells.

EC and ECC Synthesis

Patient-derived exosomes were prepared as per a previously described ultraviolet (UV) stimulation method (Tang et al., 2012; Wang et al., 2019). Briefly, patient-derived cancer cells were plated and exposed to UV irradiation (300 J/m^2) for 1 h. Then, after 12 h, cells were centrifuged at 140,000 g for 2 min to remove any cellular debris, and supernatants were again centrifuged for 1 h at 140,000 g to pellet patient-derived exosomes. Pellets were then washed thrice and resuspended in culture media for subsequent experimental use. EC preparation was conducted by mixing patient-derived exosomes (0.5 mg) and CPT (10 μg in 10 μL DMSO) in 250 μL of PBS in a 0.4 cm cuvette (Bio-Rad), with electroporation (250 V and 350 μF) then being conducted using a Bio-Rad Gene Pulser Xcell Electroporation System. Membrane integrity was then allowed to recovery through a 30 min incubation at 37°C, after which samples were spun for 1 h at 140,000 g to remove unincorporated CPT. EC samples were then stored at 4 °C. ECC preparation was conducted *via* an identical approach, instead using exosomes derived from HeLa cells. Drug loading efficiency (DLE) was calculated as follows: DLE = (weight of input drug—weight of remaining drug)/ weight of input drug.

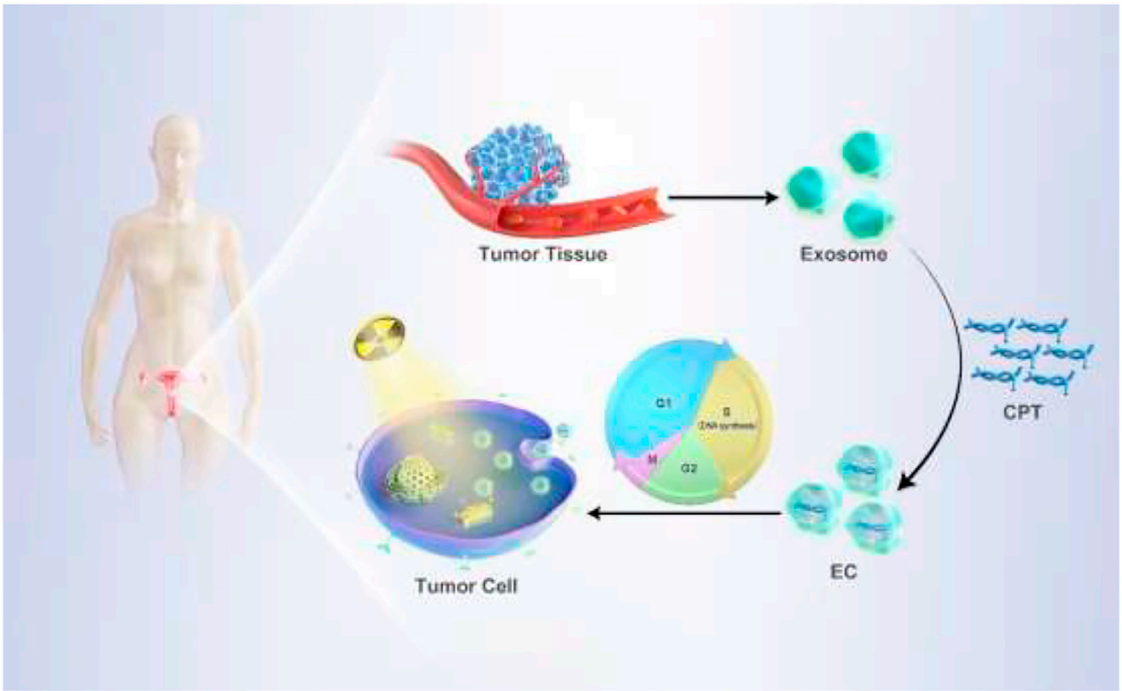

SCHEME 1 | Personalized treatment procedure on PDX model using EC.

Animal Model

A PDX model was established using previously reported methods. Briefly, harvested patient tumor tissues were minced into ~5 mm^3 pieces within 1 h of surgery, after which they were subcutaneously implanted in nude BALB/c mice with a trochar (termed P0). At 2–3 months post-implantation, tumors began to visibly grow. When tumors were 800–1,000 mm^3 in size, mice were euthanized and tumors were collected, respected, and implanted as above to yield a subsequent generation (P1). This process was repeated two more times, with P3 mice being used for all *in vivo* analyses.

Antitumor Efficacy

When tumors in P3 mice were 200 mm^3 in size, mice were randomized into six groups subjected to the following treatments: 1) PBS; 2) RT (6 Gy); 3) CPT (5 mg/kg, 50 μL); 4) EC (equivalent CPT dose: 5 mg/kg, 50 μL); 5) ECC (equivalent CPT dose: 5 mg/kg, 50 μL) + RT (6 Gy); 6) EC (equivalent CPT dose: 5 mg/kg, 50 μL) + RT (6 Gy). Tumor volumes and weight were then monitored every third day, with mice being sacrificed on day 19. Tumors were then collected for immunofluorescent and hematoxylin and eosin (H&E) staining.

RESULTS AND DISCUSSION

Patient- and HeLa cell-derived exosomes were initially prepared *via* UV stimulation and were then loaded with CPT *via* an electroporation approach. EC and ECC particles exhibited an expected round morphology with a visible lipid layer and a diameter of ~115 nm (**Figures 1A,B**). Confocal microscopy analyses were conducted to confirm successful CPT loading into these exosomes using 3, 3-dioctadecyloxacarbocyanine perchlorate (DiO) as a fluorescent membrane probe together, with CPT also being visualized as it releases bright blue fluorescence at an excitation wavelength of 365 nm, with both of these fluorescent signals being visible in prepared revealing both blue CPT and bright green DiO fluorescence confirming the coupling reaction (**Figure 1C**). CLSM imaging further confirmed the loading of CPT into HeLa cell-derived exosomes (**Supplementary Figure S1**). Moreover, the DLE of EC and ECC were 23.5 and 21.5% respectively (**Supplementary Figure S2**). DLS was used to calculate zeta potential values for EC and ECC preparations in PBS (**Figure 1D**). Stability in response to irradiation is a key clinical concern when exploring the potential biomedical application of nano-radiosensitizing agents. To assess EC and ECC stability following radiotherapy treatment, Z-average diameter values were measured for these particles before and after treatment (**Figure 1E**), with the observed absence of any apparent treatment-related change being indicative of satisfactory stability. Western blotting was additionally conducted for patient-derived exosomes and ECC samples to confirm their composition. Both of the patient-derived exosomes and ECC samples exhibited high levels of expression of the exosomal marker proteins CD9 and CD63, indicating the existence of exosomes in ECC samples (**Figure 1F**). As such, these results confirmed the successful production of patient- and tumor cell-derived exosomes loaded with CPT.

EC and ECC biocompatibility were next assessed using the Ect1/E6E7, End1/E6E7, Vk2/E6E7 and HUCEC cervical epithelial cell line, revealing that both of these preparations

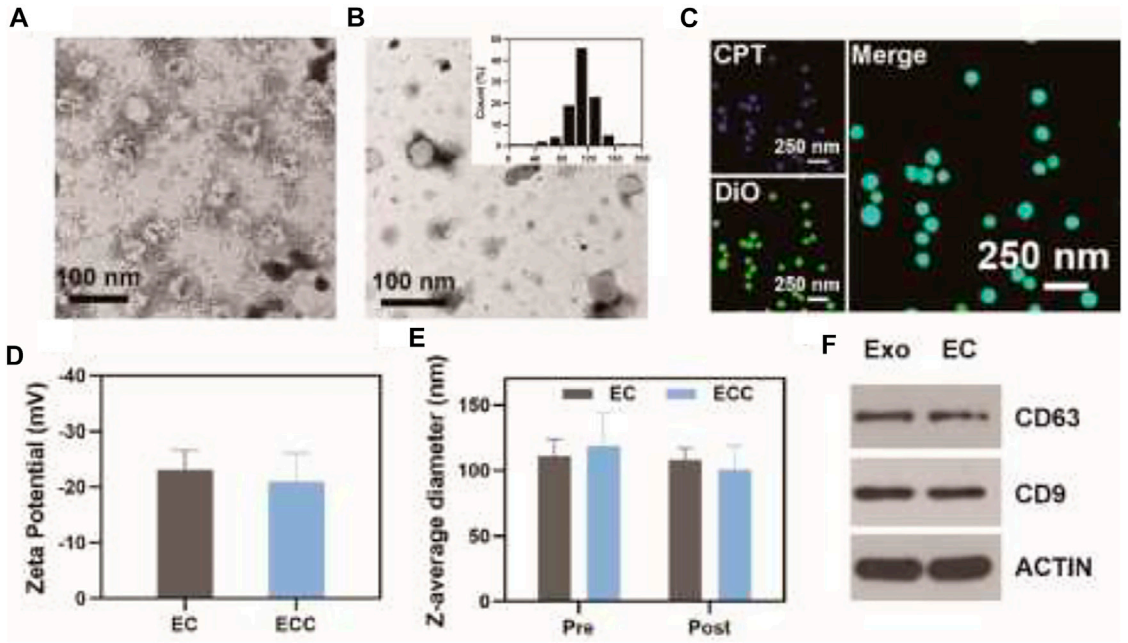

FIGURE 1 | Exosome characterization. **(A)** ECC and **(B)** EC exosomes were imaged *via* transmission electron microscopy, with the inset graph showing EC diameter distributions. **(C)** Confocal microscopic analysis of the colocalization of CPT (blue) and DiO (green) within the EC. **(D)** EC and ECC Zeta potential values; **(E)** EC and ECC Z-average diameter values before and after irradiation (6 Gy); **(F)** Western blotting analysis of patient-derived exosomes and EC.

were associated with negligible cytotoxicity even at high concentrations (**Supplementary Figure S3**). To evaluate EC- and ECC-associated radiotherapy-induced apoptosis, a CCK-8 assay was used to evaluate cell death for both HeLa and patient-derived cells treated with these preparations. While cells treated with RT or CPT alone exhibited >85% viability (**Figure 2A**), consistent with poor efficacy, and EC or ECC treatment alone had limited inhibitor effect, combined ECC + RT and EC + RT treatment were associated with reductions in cell viability to 54.2 and 41.2%, respectively, consistent with robust combination therapeutic efficacy. This efficacy may be attributable to the specific targeting capabilities of patient-derived exosomes. Similar results were also obtained for HeLa cells (**Figure 2B**), with ECC + RT treatment yielding more robust tumor inhibition than EC + RT treatment in this assay system, likely owing to the share homology between HeLa cells and exosomes derived therefrom. Even so, these results suggest that EC and ECC preparations both exhibit some degree of cross-reactive homology that is beneficial to cervical tumor targeting.

Colony formation assays were next conducted to assess the ability of ECC and EC preparations to sensitize patient-derived cells to radiotherapy, revealing clear differences in the ability of EC- and ECC-treated cells following irradiation (**Figure 2C**), consistent with more robust radiosensitization activity. Specifically, EC and ECC exhibited sensitivity enhancement ratio values of 1.13 and 1.35 respectively.

CPT is a cell cycle-regulating antitumor drug. As such, flow cytometry was next used to assess cell cycle progression in patient-derived cells exposed to PBS, ECC, and EC (**Figures 2D–F**). ECC treatment was associated with a decrease in the frequency of cells in S-phase as compared to the control group, and this difference was even more significant for EC-treated cells. Indeed, quantification of these results revealed that the percentages of cells in the S phase in the EC, ECC, and control groups were 8.1, 11.0, and 22.9%, respectively (**Figure 2G**). As such, these results confirmed the ability of EC treatment to enhance radiosensitivity owing to the ability of patient-derived exosomes to efficiently deliver CPT to target tumor cells in which it was able to modulate cell cycle progression. Moreover, as shown in **Supplementary Figure S4**, Cdk2 expression exhibited an pbvious decrease after treatment with EC while a slight decrease of Cdk2 in group treated with ECC, which indicated that EC is capable of regulating cell cycle since the content of Cdk2 raises in the S phase however decreases in G2/M phase. Both of ECC and EC group exhibite great improvement in p-H3 expression, which reflects mitotic abnormalities. It could also be found that p21 and cyclin B1 expression significantly increased in both group treated with ECC and EC, the latter of which demonstrated a more obvious enhancement, suggesting ECC and EC inhibite the activity of Cdk in G2/M.

Given the above results and to further confirm the ability of ECC to facilitate specific tumor targeting, patient-derived tumor cells were treated for 1 h with CPT, ECC, or EC preparations. CLSM was then performed, with mitochondria being stained using the MitoTracker green probe, to assess CPT uptake. EC-treated cells exhibited greater fluorescence intensity as compared to cells in the ECC group, while both of these treatments were associated with superior CPT internalization as compared to direct CPT treatment (**Figure 3A**),

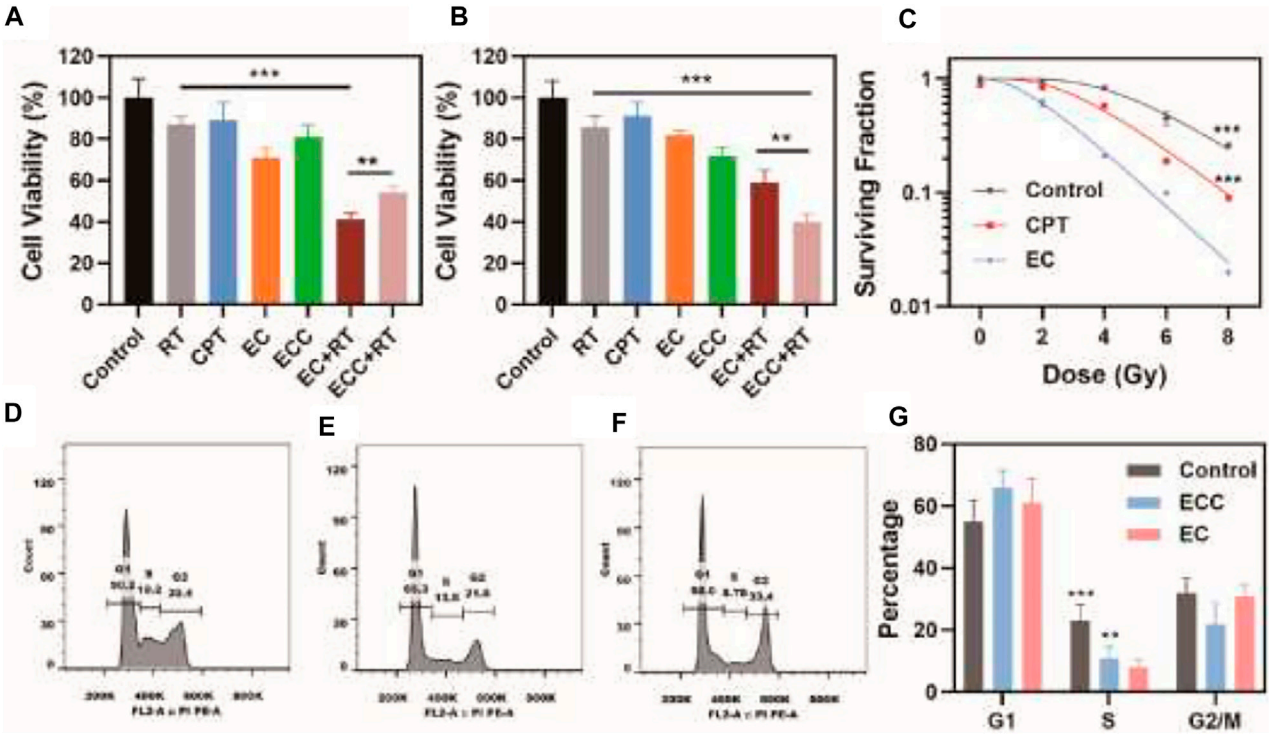

FIGURE 2 | Assessment of *in vitro* therapeutic efficacy. **(A)** Patient-derived cell and **(B)** HeLa cell viability following the indicated treatments. **(C)** Colony formation assay. **(D–G)** Flow cytometry was used to assess cell cycle progression in patient-derived cells treated with **(D)** PBS, **(E)** ECC, and **(F)** EC, with a **(G)** corresponding quantitative cell cycle analysis. *$p < 0.05$, **$p < 0.01$, ***$p < 0.005$; Student's t-test.

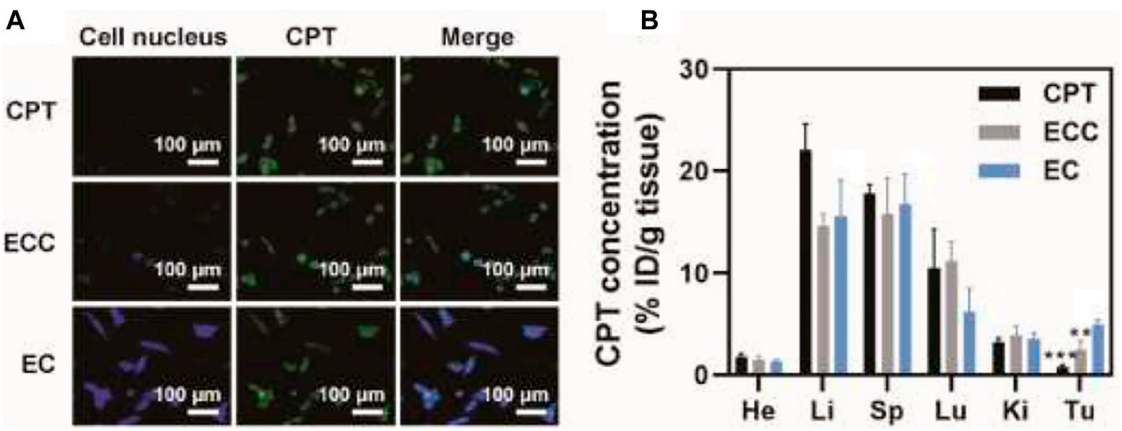

FIGURE 3 | Assessment of tumor-targeting capabilities. **(A)** CLSM images of patient-derived cells following CPT, ECC, and EC treatment, with CPT and mitochondria respectively shown in blue and green. **(B)** CPT biodistribution in mice intravenously administered with CPT, EC, and ECC. *$p < 0.05$, **$p < 0.01$, ***$p < 0.005$; Student's t-test.

consistent with the ability of exosomal preparations to mediate drug internalization and mitochondrial accumulation. Then, a PDX mouse model was used to assess the *in vivo* targeting characteristics of EC preparations, with CPT biodistribution characteristics in major organs being quantified *via* high-performance liquid chromatography (HPLC). At 6 h post-injection, drug levels in the tumor reached ~4.9% ID/g in the EC group (**Figure 3B**), with these levels being 6.1- and 1.9-fold higher than in the CPT (~ 0.8% ID/g) and ECC (~ 2.5% ID/g) groups, respectively. Higher tumor-to-normal tissue distribution ratios were observed for EC as compared to ECC and CPT, indicating the robust tumor selectivity of EC preparations. As such, these results

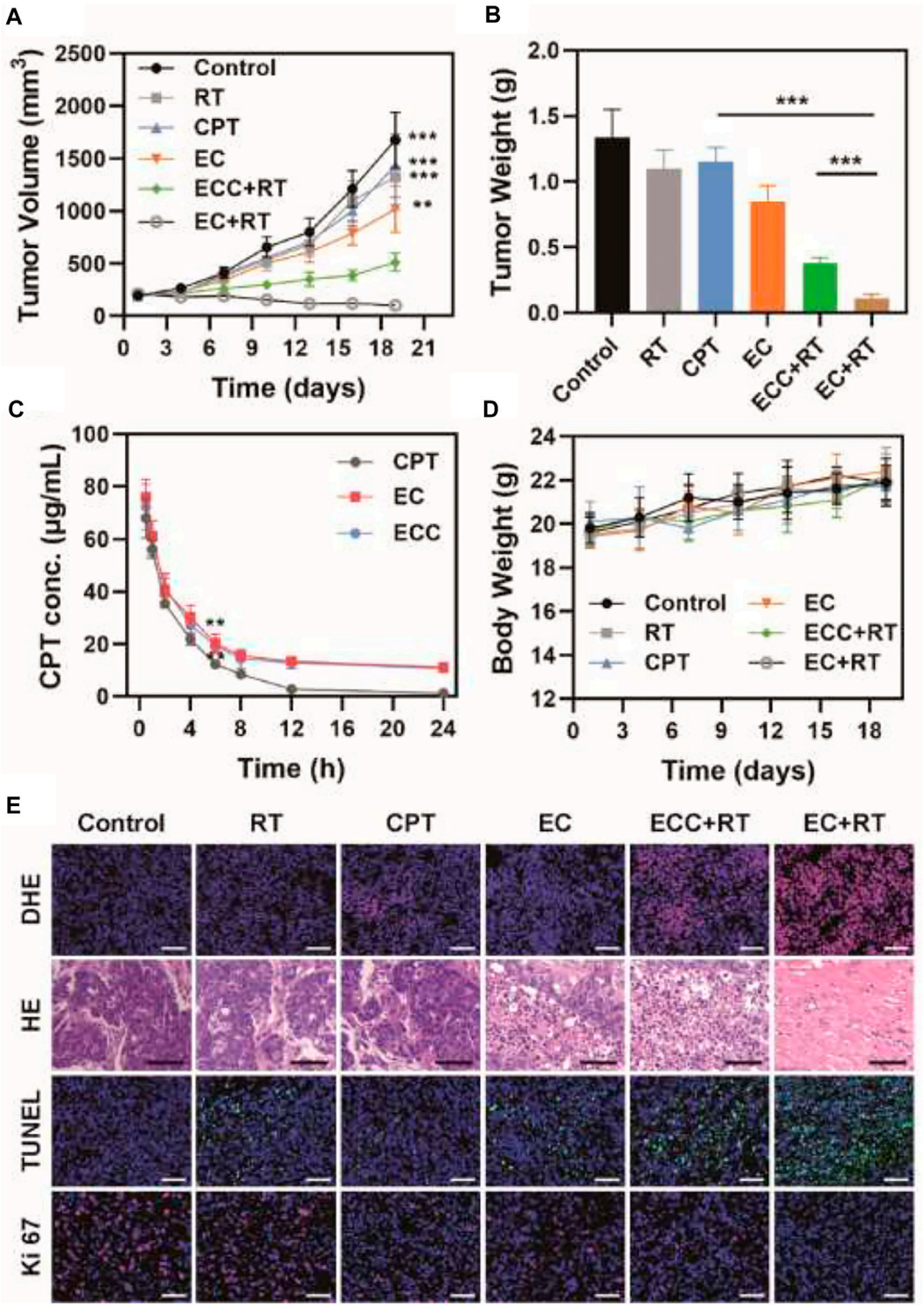

FIGURE 4 | Analysis of antitumor efficacy. **(A)** Tumor volumes and **(B)** tumor weight values for mice in the indicated treatment groups. **(C)** Pharmacokinetics curves for mice injected with CPT, EC, and ECC. **(D)** Changes in murine body weight over the study period. **(E)** DHE, H&E, TUNEL, and Ki 67 staining were conducted after treatment in the indicated groups (Scale bar: 100 μm). $^{*}p < 0.05$, $^{**}p < 0.01$, $^{***}p < 0.005$; Student's t-test.

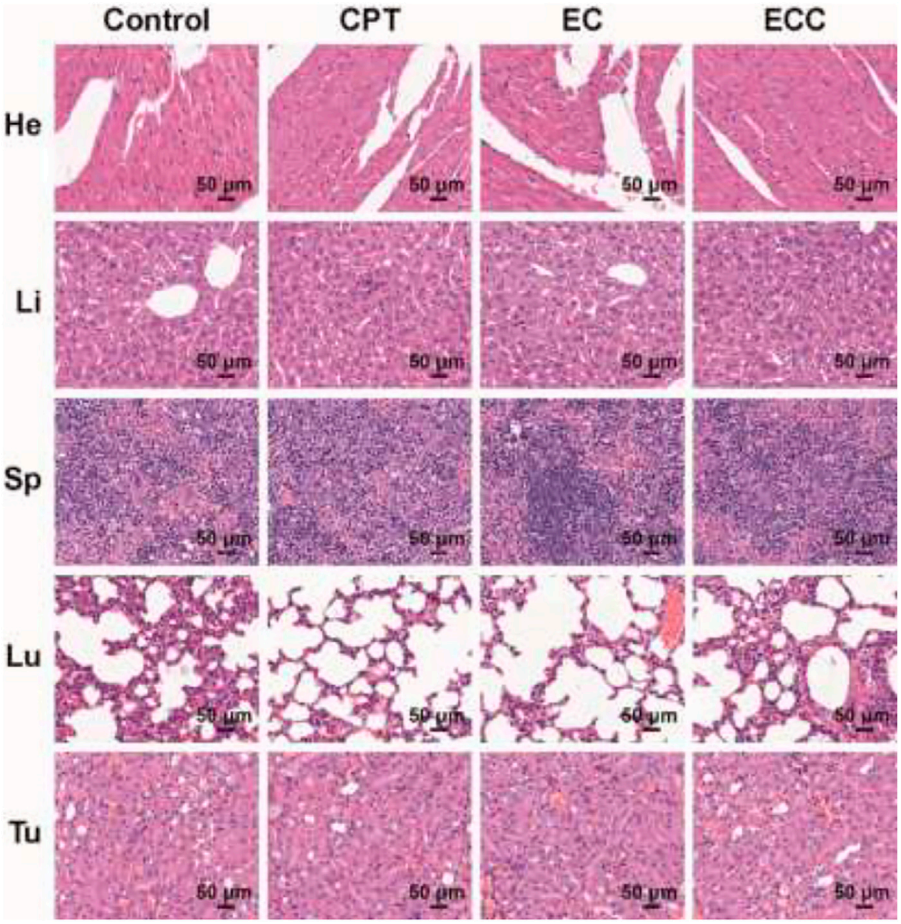

FIGURE 5 | H&E staining of tumor samples from mice injected with PBS, CPT, ECC, and EC.

confirmed that patient-derived exosomes can readily deliver CPT to target tumors *in vivo*.

Given the excellent *in vitro* cytotoxicity, cell cycle regulatory activity, and tumor cell accumulation observed for the EC nanoplatform in the above studies, we next assessed its ability to mediate *in vivo* therapeutic efficacy in nude mice bearing PDX tumors. To that end, mice were intravenously injected with different formulations (CPT, EC, ECC; CPT dose: 5 mg/kg) prior to irradiation (6 Gy). Tumor growth and tumor weight values in these treated animals were then monitored (**Figures 4A,B**). While tumors grew rapidly in PBS-treated mice, weak suppression of tumor growth was evident in mice treated with RT, CPT, or EC alone. In contrast, combination EC + RT treatment resulted in significant antitumor activity, with a 94.0 and 91.8% reduction in tumor volume and tumor weight, respectively, relative to the PBS group. This suppression was also superior to that observed in the ECC + RT group, and the overall tumor inhibition rate in the EC + RT group was 3.43-, 5.48-, and 1.32-fold higher than that observed in the RT, CPT, and EC groups, respectively. While ECC + RT treatment was also effective, its efficacy was less robust than that of EC + RT owing to reductions in tumor targeting efficiency and intratumoral exosome accumulation. Both EC and ECC exhibited prolonged systemic circulation as compared to CPT. At 6 h post-injection, CPT concentrations in the ECC and EC groups were 19.3 μg/ml and 20.3 μg/ml, respectively, owing to the ability of the exosomes to protect this drug from immune system-mediated clearance (**Figure 4C**). Notably, none of the tested treatments were associated with any significant systemic toxicity in these PDX tumor-bearing mice as determined by measuring murine body weight (**Figure 4D**).

Tumor tissue sections from mice in each treatment group were isolated to evaluate tumor tissue histopathological characteristics *via* immunofluorescent and H&E staining (**Figure 4E**). H&E staining revealed that PDX tumors exhibited a larger extracellular matrix component and more disordered cell distributions, thus more closely recapitulating findings observed in cervical cancer patients. Relative to the PBS, RT, and CPT groups, tumor cells in the other treatment groups (EC, ECC + RT, EC + RT) exhibited varying degrees of cellular shrinkage and nuclear pyknosis that was particularly pronounced in the EC + RT group. The reactive oxygen species (ROS) production, proliferation, and apoptosis of these cells were also assessed *via* DHE, Ki-67, and TUNEL, respectively. ROS levels were higher following EC + RT

treatment relative to other treatments. Similarly, EC + RT treatment was associated with the greatest suppression of cellular proliferation (Ki-67 positive cells, red) and the greatest percentage of apoptosis cells (green fluorescence) relative to other tested treatments, consistent with the robust radiosensitization activity of EC.

Systemic toxicity in treated mice was assessed on day 19 post-treatment by collecting the primary organs from animals intravenously injected with PBS, CPT, ECC, and EC for H&E staining. These analyses did not reveal any serious off-target toxicity in normal organs for mice in any of the tested treatment groups (**Figure 5**).

CONCLUSION

In summary, we herein developed a patient-derived exosome CPT (EC) delivery platform as a personalized therapeutic modality for cervical cancer treatment. The prepared EC nanoplatform exhibited specific tumor targeting capabilities and consequent internalization owing to homology with the target cells. Hereby, the accumulation of antitumor drug CPT within these cells was enhanced. Therefore, it was able to modulate the cell cycle and thereby increase tumor cell sensitivity to radiotherapy. Through this approach, EC treatment was able to achieve marked antitumor efficacy both *in vitro* and *in vivo* when combined with radiotherapy without any concomitant systemic toxicity. As such, this therapeutic modality may offer promise as a personalized treatment for patients with a range of cancer types.

DATA AVAILABILITY STATEMENT

The raw data supporting the conclusion of this article will be made available by the authors, without undue reservation.

ETHICS STATEMENT

The animal study was reviewed and approved by Institutional Animal Care and Use Committee.

AUTHOR CONTRIBUTIONS

YY:Conceptualization, Methodology, Writing—Original draft preparation. JZ: Data curation, Methodology. WH: Visualization, Investigation. JD: Methodology, Data curation. JG: Writing—Reviewing and Editing. YZ: Software, Validation, Writing—Reviewing and Editing, Supervision.

FUNDING

We greatly acknowledge the National Key R&D Program of China (2017YFC0909900), and the financial support from Key science and technology project of Education Department of Henan Province (162102310127).

ACKNOWLEDGMENTS

The authors would like to thank all the reviewers who participated in the review and MJEditor (www.mjeditor.com) for its linguistic assistance during the preparation of this manuscript.

SUPPLEMENTARY MATERIAL

The Supplementary Material for this article can be found online at: https://www.frontiersin.org/articles/10.3389/fbioe.2022.876641/full#supplementary-material

REFERENCES

Abraham, A., Habermann, E. B., Rothenberger, D. A., Kwaan, M., Weinberg, A. D., Parsons, H. M., et al. (2013). Adjuvant Chemotherapy for Stage III colon Cancer in the Oldest Old. *Cancer* 119 (2), 395–403. doi:10.1002/cncr.27755

Bhimani, J., Ball, K., and Stebbing, J. (2020). Patient-derived Xenograft Models-The Future of Personalised Cancer Treatment. *Br. J. Cancer* 122 (5), 601–602. doi:10.1038/s41416-019-0678-010.1038/s41416-019-0678-0

Bosset, J.-F., Collette, L., Calais, G., Mineur, L., Maingon, P., Radosevic-Jelic, L., et al. (2006). Chemotherapy with Preoperative Radiotherapy in Rectal Cancer. *N. Engl. J. Med.* 355 (11), 1114–1123. doi:10.1056/nejmoa060829

Chen, D., Suo, M., Guo, J., Tang, W., Jiang, W., Liu, Y., et al. (2021). Development of MOF "Armor-Plated" Phycocyanin and Synergistic Inhibition of Cellular Respiration for Hypoxic Photodynamic Therapy in Patient-Derived Xenograft Models. *Adv. Healthc. Mater.* 10 (3), 2001577. doi:10.1002/adhm.202001577

Chen, Y., Zhong, H., Wang, J., Wan, X., Li, Y., Pan, W., et al. (2019). Catalase-like Metal-Organic Framework Nanoparticles to Enhance Radiotherapy in Hypoxic Cancer and Prevent Cancer Recurrence. *Chem. Sci.* 10 (22), 5773–5778. doi:10.1039/c9sc00747d

Duo, Y., Zhu, D., Sun, X., Suo, M., Zheng, Z., Jiang, W., et al. (2021). Patient-derived Microvesicles/AIE Luminogen Hybrid System for Personalized Sonodynamic Cancer Therapy in Patient-Derived Xenograft Models. *Biomaterials* 272, 120755. Available at: https://www.sciencedirect.com/science/article/pii/S0142961221001113. doi:10.1016/j.biomaterials.2021.120755

Flay, L. D., and Matthews, J. H. L. (1995). The Effects of Radiotherapy and Surgery on the Sexual Function of Women Treated for Cervical Cancer. *Int. J. Radiat. Oncology*Biology*Physics* 31 (2), 399–404. Available at: http://europepmc.org/abstract/MED/7836095. doi:10.1016/0360-3016(94)e0139-b

Gao, S., Li, T., Guo, Y., Sun, C., Xianyu, B., and Xu, H. (2020). Selenium-Containing Nanoparticles Combine the NK Cells Mediated Immunotherapy with Radiotherapy and Chemotherapy. *Adv. Mater.* 32 (12), 1907568. doi:10.1002/adma.201907568

Jarosz-Biej, M., Smolarczyk, R., Cichoń, T., and Kułach, N. (2019). Tumor Microenvironment as A "Game Changer" in Cancer Radiotherapy. *Ijms* 20 (13), 3212. doi:10.3390/ijms20133212

Khochaiche, A., Westlake, M., O'Keefe, A., Engels, E., Vogel, S., Valceski, M., et al. (2021). Rule, Josip Horvat, Konstantin Konstantinov, Anatoly Rosenfeld, Michael Lerch, Stéphanie Corde, and Moeava TeheiFirst Extensive Study of Silver-Doped Lanthanum Manganite Nanoparticles for Inducing Selective Chemotherapy and Radio-Toxicity Enhancement. *Mater. Sci. Eng. C* 123, 111970. doi:10.1016/j.msec.2021.111970

Landoni, F., Maneo, A., Colombo, A., Placa, F., Milani, R., Perego, P., et al. (1997). Randomised Study of Radical Surgery versus Radiotherapy for Stage Ib-IIa Cervical Cancer. *The Lancet* 350 (9077), 535–540. doi:10.1016/S0140-6736(97)02250-2

Laprise-Pelletier, M., Simão, T., and Fortin, M.-A. (2018). Gold Nanoparticles in Radiotherapy and Recent Progress in Nanobrachytherapy. *Adv. Healthc. Mater.* 7 (16), 1701460. doi:10.1002/adhm.201701460

Lin, L.-S., Song, J., Song, L., Ke, K., Liu, Y., Zhou, Z., et al. (2018). Simultaneous Fenton-like Ion Delivery and Glutathione Depletion by MnO2 -Based Nanoagent to Enhance Chemodynamic Therapy. *Angew. Chem. Int. Ed.* 57 (18), 4902–4906. doi:10.1002/anie.201712027

Luo, K., Guo, W., Yu, Y., Xu, S., Zhou, M., Xiang, K., et al. (2020). Reduction-sensitive Platinum (IV)-prodrug Nano-Sensitizer with an Ultra-high Drug Loading for Efficient Chemo-Radiotherapy of Pt-Resistant Cervical Cancer *In Vivo*. *J. Controlled Release* 326, 25–37. doi:10.1016/j.jconrel.2020.06.005

Lyu, M., Chen, M., Liu, L., Zhu, D., Wu, X., Li, Y., et al. (2021). A Platelet-Mimicking Theranostic Platform for Cancer Interstitial Brachytherapy. *Theranostics* 11 (15), 7589–7599. Available at: https://pubmed.ncbi.nlm.nih.gov/34158868 https://www.ncbi.nlm.nih.gov/pmc/articles/PMC8210607/. doi:10.7150/thno.61259

Lyu, M., Zhu, D., Duo, Y., Li, Y., and Quan, H. (2020a). Bimetallic Nanodots for Tri-modal CT/MRI/PA Imaging and Hypoxia-Resistant Thermoradiotherapy in the NIR-II Biological Windows. *Biomaterials* 233, 119656. doi:10.1016/j.biomaterials.2019.119656

Lyu, M., Zhu, D., Kong, X., Yang, Y., Ding, S., Zhou, Y., et al. (2020b). Glutathione-Depleting Nanoenzyme and Glucose Oxidase Combination for Hypoxia Modulation and Radiotherapy Enhancement. *Adv. Healthc. Mater.* 9 (11), 1901819. doi:10.1002/adhm.201901819

Park, D. S., Morris, E. J., Greene, L. A., and Geller, H. M. (1997). G1/S Cell Cycle Blockers and Inhibitors of Cyclin-dependent Kinases Suppress Camptothecin-Induced Neuronal Apoptosis. *J. Neurosci.* 17 (4), 1256–1270. Available at: http://www.jneurosci.org/content/17/4/1256.abstract. doi:10.1523/JNEUROSCI.17-04-01256.1997

Peeters, K. C. M. J., van de Velde, C. J. H., Leer, J. W. H., Martijn, H., Junggeburt, J. M. C., Kranenbarg, E. K., et al. (2005). Late Side Effects of Short-Course Preoperative Radiotherapy Combined with Total Mesorectal Excision for Rectal Cancer: Increased Bowel Dysfunction in Irradiated Patients-A Dutch Colorectal Cancer Group Study. *Jco* 23 (25), 6199–6206. Available at: https://www.ncbi.nlm.nih.gov/pubmed/16135487. doi:10.1200/JCO.2005.14.779

Rose, P. G., Bundy, B. N., Watkins, E. B., Thigpen, J. T., Deppe, G., Maiman, M. A., et al. (1999). Concurrent Cisplatin-Based Radiotherapy and Chemotherapy for Locally Advanced Cervical Cancer. *N. Engl. J. Med.* 340 (15), 1144–1153. doi:10.1056/NEJM199904153401502

Sasieni, P. D., and Sawyer, E. J. (2021). Reply to 'Intraoperative Radiotherapy for Breast Cancer: Powerful Evidence to Change Practice'. *Nat. Rev. Clin. Oncol.* 18 (3), 188–189. Available at: https://www.ncbi.nlm.nih.gov/pubmed/33495551. doi:10.1038/s41571-021-00472-6

Song, G., Chen, Y., Liang, C., Yi, X., Liu, J., Sun, X., et al. (2016). Catalase-Loaded TaOx Nanoshells as Bio-Nanoreactors Combining High-Z Element and Enzyme Delivery for Enhancing Radiotherapy. *Adv. Mater.* 28 (33), 7143–7148. doi:10.1002/adma.201602111

Song, G., Cheng, L., Chao, Y., Yang, K., and Liu, Z. (2017). Emerging Nanotechnology and Advanced Materials for Cancer Radiation Therapy. *Adv. Mater.* 29 (32), 1700996. Available at: https://www.ncbi.nlm.nih.gov/pubmed/28643452. doi:10.1002/adma.201700996

Sun, H., Cao, S., Mashl, R. J., Mo, C.-K., Zaccaria, S., Wendl, M. C., et al. (2021). Comprehensive Characterization of 536 Patient-Derived Xenograft Models Prioritizes Candidates for Targeted Treatment. *Nat. Commun.* 12 (1), 5086. doi:10.1038/s41467-021-25177-3

Sung, H., Ferlay, J., Siegel, R. L., Laversanne, M., Soerjomataram, I., Jemal, A., et al. (2021). Global Cancer Statistics 2020: GLOBOCAN Estimates of Incidence and Mortality Worldwide for 36 Cancers in 185 Countries. *CA: A Cancer J. Clinicians* 71, 209. Available at: https://acsjournals.onlinelibrary.wiley.com/doi/abs/10.3322/caac.21660. doi:10.3322/caac.21660

Suo, M., Liu, Z., Tang, W., Guo, J., Jiang, W., Liu, Y., et al. (2020). Development of a Novel Oxidative Stress-Amplifying Nanocomposite Capable of Supplying Intratumoral H2O2 and O2 for Enhanced Chemodynamic Therapy and Radiotherapy in Patient-Derived Xenograft (PDX) Models. *Nanoscale* 12 (45), 23259–23265. doi:10.1039/D0NR06594C

Tang, K., Zhang, Y., Zhang, H., Xu, P., Liu, J., Ma, J., et al. (2012). Delivery of Chemotherapeutic Drugs in Tumour Cell-Derived Microparticles. *Nat. Commun.* 3 (1), 1282. doi:10.1038/ncomms2282

Wang, D., Yao, Y., He, J., Zhong, X., Li, B., Rao, S., et al. (2019). Engineered Cell-Derived Microparticles Bi 2 Se 3/DOX@MPs for Imaging Guided Synergistic Photothermal/Low-Dose Chemotherapy of Cancer. *Adv. Sci.* 7, 1901293. doi:10.1002/advs.201901293

Wang, H., Zhang, Y., Liang, X., and Zhang, Y. (2021). Smart Fibers and Textiles for Personal Health Management. *ACS Nano* 15 (8), 12497–12508. doi:10.1021/acsnano.1c06230

Xu, X., Chong, Y., Liu, X., Fu, H., Yu, C., Huang, J., et al. (2019). Multifunctional Nanotheranostic Gold Nanocages for Photoacoustic Imaging Guided Radio/photodynamic/photothermal Synergistic Therapy. *Acta Biomater.* 84, 328–338. Available at: https://www.sciencedirect.com/science/article/pii/S1742706118307062. doi:10.1016/j.actbio.2018.11.043

Yang, Y., Zhu, D., Liu, Y., Jiang, B., Jiang, W., Yan, X., et al. (2020). Platinum-carbon-integrated Nanozymes for Enhanced Tumor Photodynamic and Photothermal Therapy. *Nanoscale* 12 (25), 13548–13557. doi:10.1039/D0NR02800B

Yi, X., Chen, L., Zhong, X., Gao, R., Qian, Y., Wu, F., et al. (2016). Core-shell Au@MnO2 Nanoparticles for Enhanced Radiotherapy via Improving the Tumor Oxygenation. *Nano Res.* 9 (11), 3267–3278. doi:10.1007/s12274-016-1205-8

Yoon, H. Y., Selvan, S. T., Yang, Y., Kim, M. J., Yi, D. K., Kwon, I. C., et al. (2018). Engineering Nanoparticle Strategies for Effective Cancer Immunotherapy. *Biomaterials* 178, 597–607. Available at: https://www.sciencedirect.com/science/article/pii/S0142961218302096. doi:10.1016/j.biomaterials.2018.03.036

Zhang, C., Yan, L., Gu, Z., and Zhao, Y. (2019). Strategies Based on Metal-Based Nanoparticles for Hypoxic-Tumor Radiotherapy. *Chem. Sci.* 10 (29), 6932–6943. Available at: https://www.ncbi.nlm.nih.gov/pubmed/31588260. doi:10.1039/c9sc02107h

Zhu, D., Chen, H., Huang, C., Li, G., Wang, X., Jiang, W., et al. (2022). H 2 O 2 Self-Producing Single-Atom Nanozyme Hydrogels as Light-Controlled Oxidative Stress Amplifier for Enhanced Synergistic Therapy by Transforming "Cold" Tumors. *Adv. Funct. Mater.*, 2110268. doi:10.1002/adfm.202110268

Zhu, D., Lyu, M., Jiang, W., Suo, M., Huang, Q., and Li, K. (2020). A Biomimetic Nanozyme/camptothecin Hybrid System for Synergistically Enhanced Radiotherapy. *J. Mater. Chem. B* 8 (24), 5312–5319. Available at: https://www.ncbi.nlm.nih.gov/pubmed/32453333. doi:10.1039/d0tb00676a

Zhu, W., Dong, Z., Fu, T., Liu, J., Chen, Q., Li, Y., et al. (2016). Modulation of Hypoxia in Solid Tumor Microenvironment with MnO2Nanoparticles to Enhance Photodynamic Therapy. *Adv. Funct. Mater.* 26 (30), 5490–5498. doi:10.1002/adfm.201600676

Conflict of Interest: The authors declare that the research was conducted in the absence of any commercial or financial relationships that could be construed as a potential conflict of interest.

Publisher's Note: All claims expressed in this article are solely those of the authors and do not necessarily represent those of their affiliated organizations, or those of the publisher, the editors and the reviewers. Any product that may be evaluated in this article, or claim that may be made by its manufacturer, is not guaranteed or endorsed by the publisher.

frontiers | Frontiers in Bioengineering and Biotechnology

ORIGINAL RESEARCH
published: 13 April 2022
doi: 10.3389/fbioe.2022.889364

Coaxial Spring-Like Stretchable Triboelectric Nanogenerator Toward Personal Healthcare Monitoring

*Jinmei Liu, Saixuan Li, Maosen Yang, Yuxin Wang, Nuanyang Cui and Long Gu**

School of Advanced Materials and Nanotechnology, Xidian University, Xi'an, China

Stretchable triboelectric nanogenerators have attracted increasing interests in the field of Internet of Things and sensor network. Therefore, great efforts have been made to realize the stretchability of electronic devices *via* elaborated material configurations and ingenious device designs. In this work, a flexible and stretchable TENG is developed with a coaxial spring-like structure. The unique structure allows it to generate electrical energy for different degrees of stretching deformations. Its output demonstrates good response to the strain and frequency of the mechanical deformation. At the same time, it exhibits excellent stability and washability. The TENG can be worn on the human fingers, elbow, and knee to monitor the body activities. Furthermore, a self-powered temperature sensor system is fabricated by integrating the TENG with a temperature sensor to identify the operating ambient temperature in real time. A combination of this flexible and stretchable TENG with body motions and a temperature sensor brings a novel insight into wearable functional electronics and user-friendly health monitoring, which has an important basic research significance and practical application value in biometric systems.

Keywords: stretchable triboelectric nanogenerator, biomechanical energy harvesting, coaxial fiber structure, gesture monitoring, self-powered temperature sensor

OPEN ACCESS

Edited by:
Qitong Huang,
Gannan Medical University, China

Reviewed by:
Guangqin Gu,
Henan University, China
Ruoxing Wang,
University of Wisconsin-Madison, United States

****Correspondence:***
Long Gu
lgu@xidian.edu.cn

Specialty section:
This article was submitted to Nanobiotechnology, a section of the journal Frontiers in Bioengineering and Biotechnology

Received: *04 March 2022*
Accepted: *21 March 2022*
Published: *13 April 2022*

Citation:
Liu J, Li S, Yang M, Wang Y, Cui N and Gu L (2022) Coaxial Spring-Like Stretchable Triboelectric Nanogenerator Toward Personal Healthcare Monitoring. Front. Bioeng. Biotechnol. 10:889364. doi: 10.3389/fbioe.2022.889364

INTRODUCTION

Due to the rapid advances in electronics, computing, and integration technologies over the past decade, electronic devices have been trending toward becoming lighter, thinner, smaller, and softer. Since 2012, triboelectric nanogenerators (TENGs) have been developing with the ability of harvesting mechanical energies from the working environment and converting them into electrical energy based on coupling between triboelectrification and electrostatic induction effect (Fan et al., 2012; Zhu et al., 2012; Wang and Wang, 2019; Zhang et al., 2020a; Zhang et al., 2021). With both excellent energy conversion efficiency and possibility of using diverse materials, TENGs have been utilized in a wide range of applications such as wearable electronics, human–machine interfaces, and self-powered sensors (Lai et al., 2016; Li et al., 2016; Park et al., 2016; Bai et al., 2018; Wu et al., 2019; Zhang et al., 2020b; Li et al., 2021). The wearable TENGs can be attached or even wore on the human body to implement the biomedical health monitoring and human motions sensing through harvesting energy generated by human motions, such as walking, running, jumping, tapping, and swinging or bending the arm (Cui et al., 2015; Niu et al., 2015; Pu et al., 2016; Liu et al., 2019; Qi et al., 2020; Cheng et al., 2021). However, intimately involved in the human-body movement response, the wearable TENGs lack high-performance elasticity to properly self-expand and self-loosen. Therefore, flexible and stretchable TENGs are being one of the research hotpots to develop their potential applications in healthcare, energy, and military purposes (Lin et al., 2017; Parida et al., 2019a; Sheng et al., 2021).

Generally, a TENG is composed of three parts: the triboelectric layers to generate triboelectric charges, electrodes to extract charges, and the spacer to separate the triboelectric layers. So, to prepare the stretchable TENGs, a lot of work focused on embedding electronic conductors, such as conductive polymers, silver nanowires, carbon black/nanotubes, graphite spray, and liquid metals, into extendible matrixes to provide the elasticity as the electrode materials and electrification materials (Wang et al., 2016; Dickey, 2017; Yang et al., 2018; Parida et al., 2019b; Han et al., 2020). Under local deformation and stretching condition, these soft conductive composite materials could effectively respond to the external force, but it seems to be powerless under large deformation with irreversible damage due to uneven mixing and poor compatibility (Fang et al., 2016; Mu et al., 2016; Guo et al., 2017). Relatively speaking, the ionic conductor transfers charges through ions, which can be transported using deformable soft polymeric materials. Consequently, the stretchable and conductive hydrogel electrolyte attracted a lot of attentions with its capacity of high flexibility and high elasticity (Fang et al., 2016; Pu et al., 2017; Wang et al., 2018; Sun et al., 2019; Wang et al., 2020a; Wang et al., 2020b; Kim et al., 2020). However, in most of the reported hydrogel-based TENGs, excellent stretching, mechanical toughness, and electrical conductivity cannot be achieved at the same time due to the dehydration or evaporation of the liquid solvent, which largely limits their applications (Niu et al., 2013; Xu et al., 2013; Shuai et al., 2020). In addition to thinking from the materials' point of view, researchers also worked hard to develop new manufacturing processes to design stretchable and deformable TENGs that integrate the structure and function simultaneously. With innate tensile properties, traditional origami and kirigami patterns have been used to fabricate the stretchable TENG, which has provided a structure design strategy using a simple and mature processing technology to make the essentially inelastic material to be available for TENGs. However, their stretchability was quite limited compared with other methods, and Young's modulus of the paper is quite high and easily damaged by reciprocating stretching, resulting in unstable output performance (Yang et al., 2015; Guo et al., 2016; Wu et al., 2016; Lu et al., 2018).In addition, traditional sewing technologies based on textiles and fabrics, such as weaving, knitting, serpentine sewing, and spiral winding, also have advantages in texturing the stretchable structures. Thus, many kinds of two-dimensional (2D) and three-dimensional (3D) orthogonally woven TENGs have been developed to be flexible, stretchable, and comfortable using fabric fibers and conductive fibers (Kim et al., 2015; Zhao et al., 2016; Dong et al., 2017; Gong et al., 2019; Zhu et al., 2019; Cong et al., 2020). Although these TENGs are flexible and stretchable to some extent, the inherent strain constraints between the electrode materials and the electrification materials prevent them from achieving the maximum stretchability. To investigate the fundamental problems, the difficulty lies in the stretchable TENG's working requirements to endure deformation not only in each component but also in the entire TENGs. Therefore, to design a geometric structural with high stretchability, structural integrity, and conformability plays an important role in flexible and stretchable TENGs research imposed by the increasing application requirements.

Here, we introduce a stretchable TENG with a coaxial spring-like structure *via* a simple and effective route, which could be utilized in personal healthcare monitoring. This TENG has excellent flexibility and stretchability and can be folded and bended into different shapes and stretched to different lengths, while it has good stability and washability. It can generate electrical energy under different external mechanical deformation. When worn on the four fingers, it could identify the finger motions. Furthermore, when worn on the elbow and knee, it could respond to the arm and leg activities. At the same time, an output voltage of 0.6 and 1.7 V, and an output current of 10.6 and 25.0 nA can be detected, respectively. Moreover, a temperature sensor is employed to build a self-powered system with the TENG, which could successfully identify the temperature under the working condition. This work may not only promote human biomechanical energy harvesting but also provide a novel design concept of the fiber-based TENG and expand their scope for wearable electronics application in the era of IoT.

RESULTS AND DISCUSSION

Figure 1A is the structural diagram of the TENG in a multi-dimensional core–shell structure. At first, an inner core is designed using four rubber fibers, which is made up of many fine fibers as shown in **Figure 1B**. Then, two kinds of composite fibers in the core–shell structure are enwound around the rubber fibers side by side. As for the two composite fibers, one is a nylon-coated copper wire, and another is a PTFE-coated enameled copper wire, whose detailed experimental process can be referred to our previous work (Liu et al., 2019). The two copper wires in the two composite fibers act as the positive and negative electrodes, respectively. The surface topography of the nylon fiber and the PTFE fiber that we used are observed by SEM as shown in **Figures 1C**,**D**. In this way, the elastic core substrate structure and the helical surrounding triboelectric layers structure together form the spring-like coaxial energy fiber. As demonstrated in **Figures 1E–G**, it can be bent into various shapes, knotted, and stretched, exhibiting excellent flexibility and stretchability, which makes it adaptable to irregular surfaces and appropriate in different human body motion situations. The operating principle of the TENG is briefly described in **Figure 1H**. As we all know, the electron affinity of the PTFE is higher than that of the rubber. Meanwhile, the electron affinity of the rubber is higher than that of the nylon. Under tensile force, the inner rubber fiber and the helical surrounding triboelectric layers structure are stretched, in which the surface of the PTFE and nylon fiber will be closely in contact with the rubber surface, and the electrons will transfer from rubber to PTFE on the interface of these two materials, while the electrons transfer from nylon to rubber on their interface. Therefore, the PTFE surface will become negatively charged, and the nylon surface will become positively charged eventually. Then, when the tensile force is removed, the inner rubber fiber and the helical surrounding triboelectric layers structure will shrink, in which the surface of the PTFE and nylon fibers will separate from the rubber surface, and the electron will transfer from the electrode of PTFE to the electrode of nylon to balance the electric potential. Therefore, the TENG generates electricity under this working cycle. Furthermore,

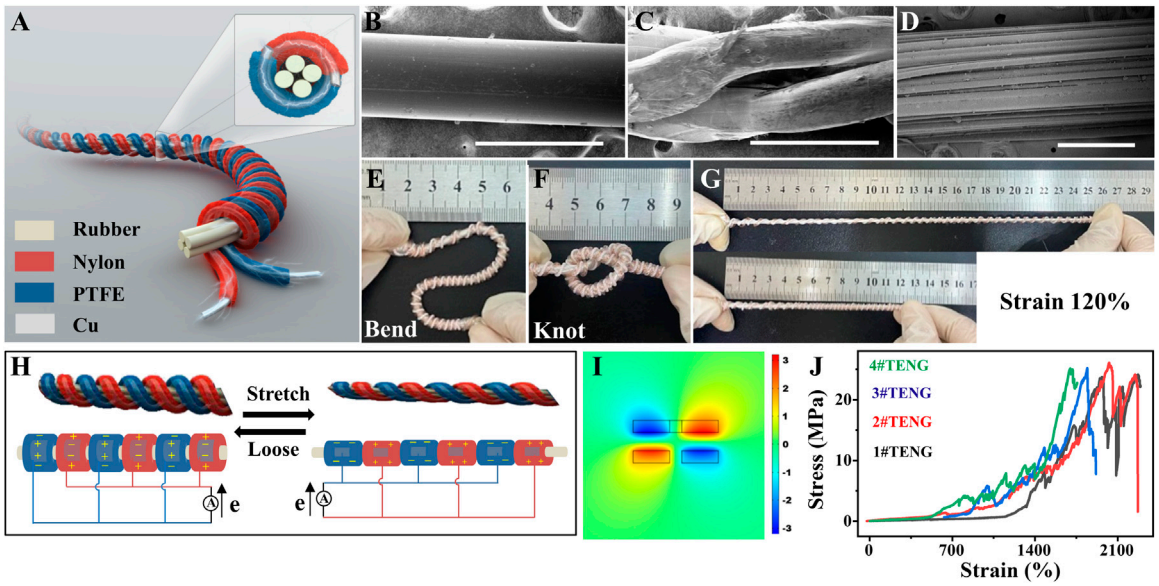

FIGURE 1 | Structure and working mechanism of the TENG. **(A)** Structural diagram of the TENG. **(B–D)** SEM images of the rubber fiber, the nylon fiber, and the PTFE fiber, respectively. Scalebar in **(B–D)** is 500 μm. **(E–G)** Photograph of the flexible and stretchable TENG in different shapes. **(H)** Working principle of the TENG. **(I)** Numerical calculation of the corresponding electrical potential distribution by COMSOL software. **(J)** Stress–strain curve of the four identical TENGs.

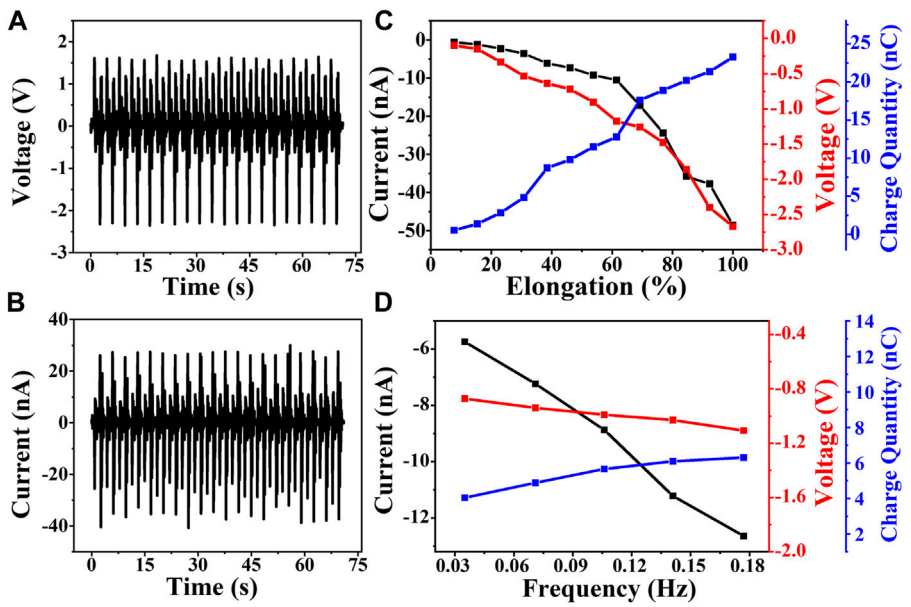

FIGURE 2 | Output performance of the TENG under different conditions. **(A,B)** Voltage and current curves at 90% strain and 0.28 Hz. **(C)** Current, voltage, and charge quantity value with different strains at 0.28 Hz. **(D)** Current, voltage, and charge quantity value with different frequencies at 60% strain.

COMSOL software is used to simulate the electric potential on the PTFE and the nylon fibers (**Figure 1I**), which is consistent with the mechanism description for electricity generation. To work steadily over time, the TENG should have high mechanical strength. Thus, the tensile strength of the TENG is studied, and the stress–strain curves of the four identical TENGs are collected in the tensile-loading test. As shown in **Figure 1J**, the TENG exhibits a strength of 25 MPa with a tension strain of more than 1700%, which effectively proved that the TENG has good tensile properties and great capacity to maintain long-term reliability.

To test the output performance of the TENG, its one end is fixed at the measurement platform, and the other end is connected with the

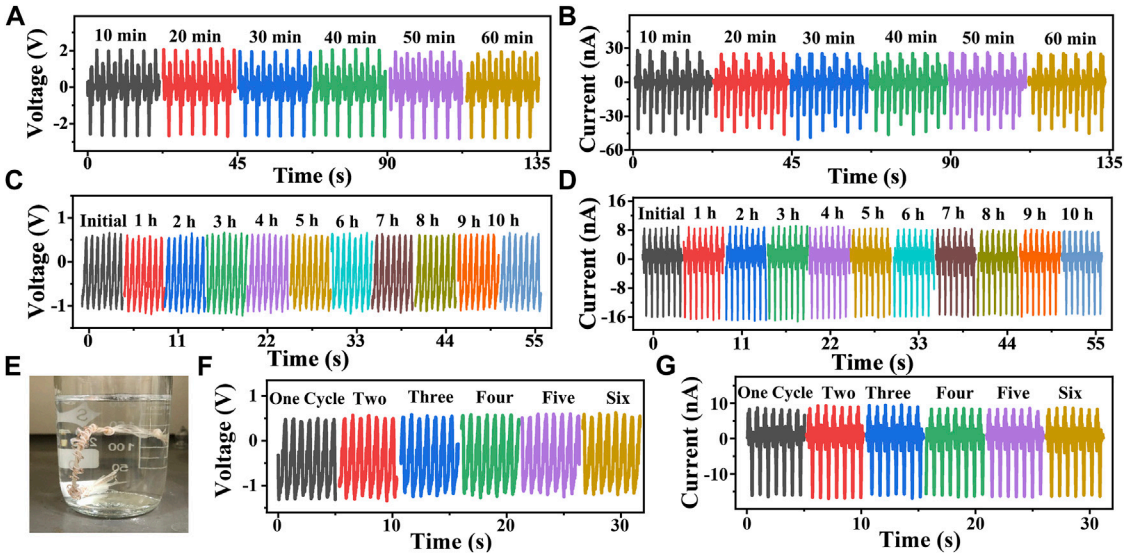

FIGURE 3 | Mechanical endurance of the TENG. **(A,B)** Voltage and current curves measured at 90% strain and 0.28 Hz after holding the TENG stretching at 90% strain for different time periods. **(C,D)** Voltage and current curves measured with the TENG that was kept working at 70% strain and 0.14 Hz for 10 h. **(E)** Photograph of the TENG while washing. **(F–G)** Voltage and current curves measured at 70% strain and 0.14 Hz after washing the TENG for different cycles.

linear motor. When starting the linear motor to move back and forth at a working frequency of 0.28 Hz and displacement of 6 cm, the TENG will be stretched and loosened regularly, which generates an output voltage of 2.4 V and output current of 40.1 nA as shown in **Figures 2A**,**B**. In order to analyze the energy conversion ability toward the tensile force, the TENG is tested at a stretching frequency of 0.28 Hz. At the same time, the displacement of the TENG is adjusted to stretch the TENG to different strain lengths. As shown in **Figure 2C**, it can be found that under the tensile force of the linear motor, the TENG is persistently stretched. Also, when the strain increases from 10 to 100%, the current raises from −1 nA to −49 nA, the voltage raises from −0.11 V to −2.67 V, and the charge quantity raises from 0.9 to 23.3 nC, which can be attributed by the enhancement of an effective triboelectric effect. Also, when the strain increases from 10 to 60%, the output signals increase quite slowly. Further increasing the strain from 60 to 100%, the output signals increase by a greater margin, which can be attributed to a stronger triboelectric effect in a closer contact under larger strain. The tension–relaxation frequency may make a great effect on the output performance of the TENG, so we adjust the working parameters of the linear motor to stretch and release the TENG under different frequencies with a fixed tensile strain of 60%. As displayed in **Figure 2D**, when the tension–relaxation frequency increases from 0.035 to 0.177 Hz, the current raises from −5.8 nA to −12.6 nA due to the increase of the triboelectric charge separation rate. The voltage and the charge quantity raise quite slowly, which is mainly determined by the structure and materials of the TENG.

Mechanical endurance is very important for the supplication of the TENG, so we conducted three groups of experiments. At first, the TENG is stretched to 90% strain and then kept for a certain time (10, 20, 30, 40, 50, and 60 min). When the designed time is up, the TENG starts to work in loosing and stretching at 90% strain and 0.28 Hz driven by the linear motor. The voltage and current curves corresponding to different time periods in the 90% strain stretching state are measured and demonstrated in **Figures 3A**,**B**, which shows good resistance to mechanical tensile loading. Then, the TENG is continuously driven by the linear motor at 70% strain and 0.14 Hz for 10 h to measure if it is in a good condition. The voltage and current curves are measured every hour and displayed in **Figures 3C**,**D**, in which negligible attenuation is found and exhibits a highly stable working performance. As shown in **Figure 3E**, the TENG is immersed into the water, and the glass container is placed in a magnetic stirring apparatus after adding into a magneton. In this way, the TENG can be well washed. After washing and drying, the working performance of the TENG is also measured. **Figures 3F**,**G** show the voltage and current curves measured at 70% strain and 0.14 Hz after washing for six cycles. We can find that there is no reduction in the output performance after each washing, thus displaying good washing durability.

As can be seen from the aforementioned experimental results, the TENG possesses good mechanical properties, especially tensile properties. Therefore, the TENG can be used to monitor hand finger movements. As shown in **Figure 4A**, four TENGs are attached to the index finger, middle finger, ring finger, and little finger, respectively. Every time the finger bends and stretches, the TENG fixed on it is also bent and stretched. The corresponding voltage and current signals generated by the four TENGs are detected and collected by bending these four fingers in turn from the index to the little finger as shown in **Figures 4B**,**C**. When each of the middle three fingers (index, middle, and ring fingers) is in the process of bending and straightening, the adjacent two fingers on both sides also follow slight reactions, resulting in a quite wide baseline. But the motion of the designated finger is rather stronger, so the output signals can be clearly distinguished in the real-time voltage and current signals, indicating promising applications in self-powered smart gesture recognition. Furthermore, its application in monitoring

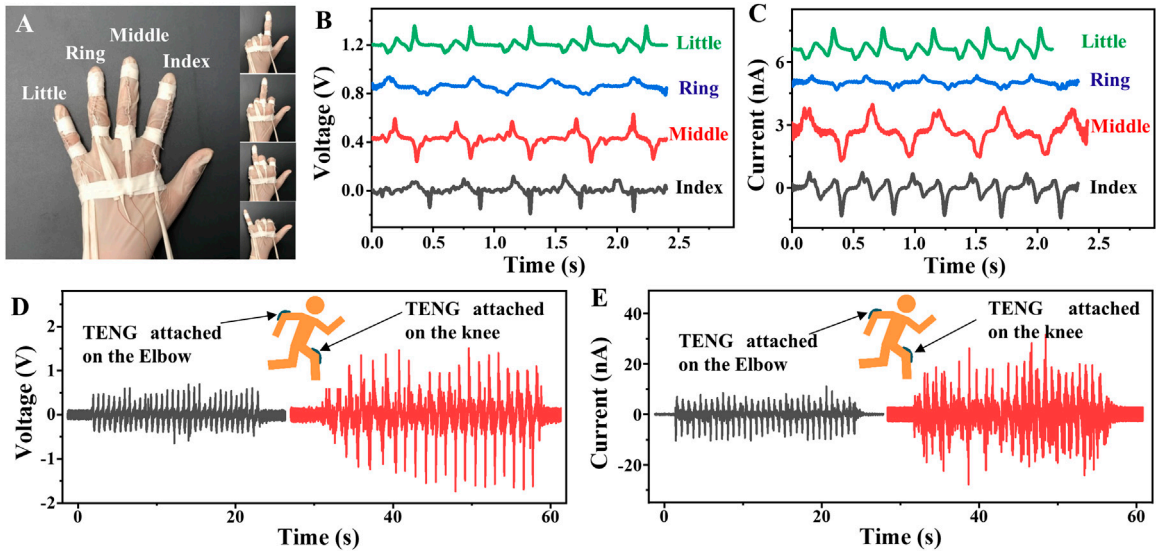

FIGURE 4 | Sensing features to the human-body motions. **(A)** Photograph of a hand with four TENGs fixed on its four fingers from the index finger to the little finger. **(B,C)** Voltage and current curves of the four TENGs fixed on the four fingers. **(D,E)** Voltage and current curves of the TENG fixed on the elbow and knee.

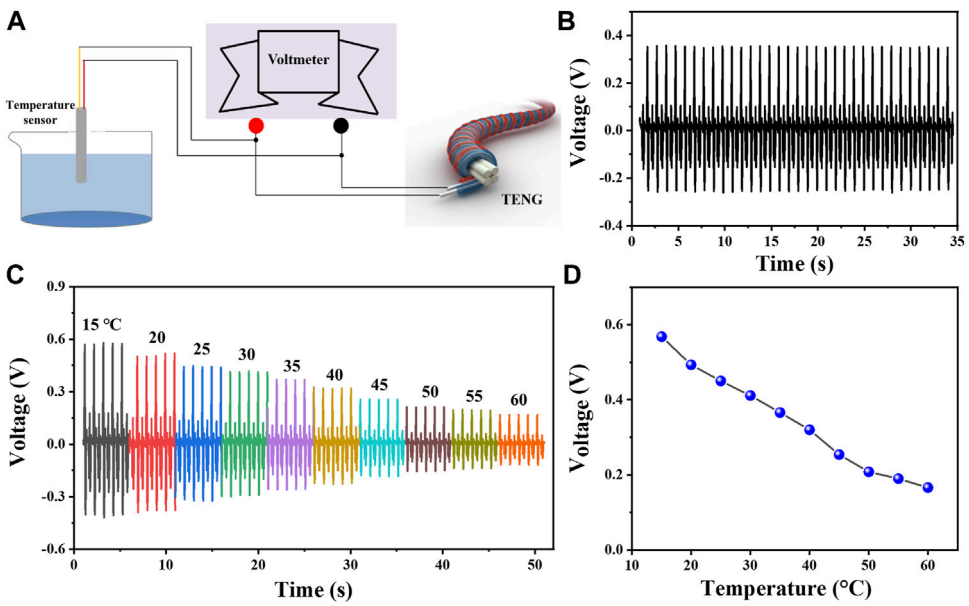

FIGURE 5 | TENG-based self-powered temperature sensor. **(A)** Schematic diagram of the connecting circuit. **(B)** Stable voltage curves of the self-powered temperature sensor system working at 36.5°C. **(C,D)** Stable voltage of the self-powered temperature sensor at different temperatures.

human body motions is achieved by attaching the three TENGs to the elbow and the knee. When people's arms and legs bend, the TENGs are stretched, and electrical signals can be collected. As shown in **Figures 4D,E** (the left), there is one up and one down output peak every time the arm bends up to an angle of about 90°. At the same time, the output voltage and current reach 0.6 V and 10.6 nA, respectively. As for the TENG attached to the knee, it also responds well to the leg activity, and each time the leg bends backward to about 90° an output voltage of 1.7 V and current of 25.0 nA can be generated as demonstrated in **Figures 4D,E** (the right). This result proves that this TENG has great ability in converting human body motion into electrical energy as well as monitoring the human activities.

People may work in different scenes, and the ambient temperature may vary greatly. Taking that into account, we assemble a self-powered temperature sensing system using this TENG and a

temperature sensor. The connection circuit is depicted in **Figure 5A**. In this system, the TENG acts as the power supply for the temperature sensor. Also, when the temperature to be measured varies, the voltage between the two ends of the temperature sensor follows the change. At first, we tested the voltage on the temperature sensor at a temperature of 36.5°C. As shown in **Figure 5B**, it can be found that the voltage and current stay steady at 0.37 V under this condition. Then, to explore its detection range, the working condition is changed continuously from 15 to 60°C. **Figures 5C,D** give the voltage on the temperature sensor at different temperatures. We can find that the voltage signal decreases with the increase of the temperature, which can be attributed to the decrease of the internal resistance of the temperature sensor under higher conditions. It can be seen that this TENG, as a power supply unit, can effectively supply energy to the temperature sensor to ensure that it works properly without other power supplies. Furthermore, this test lays the foundation of this TENG in providing power to more sensors in the future.

CONCLUSION

In summary, we have fabricated a fiber-based TENG with excellent flexibility and stretchability, which can be folded into different shapes and stretched to different lengths. Benefiting from the ingenious structure design composed of the elastic core fiber and helically surrounding triboelectric layers, it responds well to different strains and driven frequencies. Also, its stability and washability are measured to be good. Furthermore, it can be attached to the human body to monitor the finger, arm, and leg activities. At the same time, it can be used as the power supply to drive a temperature sensor in a self-powered sensing system. This work provides great application potential in multifunctional motion sensors and user-friendly health monitoring.

EXPERIMENTAL SECTION

Measurement: a linear motor (LinMot E1100) is used to periodically drive the TENGs, and low-noise preamplifiers (SR570 and SR560) are used to measure the output voltage and current. PCI-6259 (National Instruments) is used for data collection. A software platform based on LabVIEW is used to realize real-time data acquisition and analysis. A strain gauge (Zhiqu, ZQ-990A) is used to test the stress–strain curve.

DATA AVAILABILITY STATEMENT

The original contributions presented in the study are included in the article/Supplementary Material, further inquiries can be directed to the corresponding author.

AUTHOR CONTRIBUTIONS

JL and LG conceived the research. JL, SL, and MY with assistance from LG conducted the experiments, and NC and YW analyzed the results. All authors contributed to the discussion and interpretation of the results.

FUNDING

This research was supported by the Natural Science Basic Research Plan in Shaanxi Province of China (Nos.2021JQ-200 and 2020JM-182) and the Fundamental Research Funds for the Central Universities, China, under Nos. JB211401 and QTZX2183.

REFERENCES

Bai, Y., Han, C. B., He, C., Gu, G. Q., Nie, J. H., Shao, J. J., et al. (2018). Washable Multilayer Triboelectric Air Filter for Efficient Particulate Matter PM2.5 Removal. *Adv. Funct. Mater.* 15 (28), 1706680. doi:10.1002/adfm.201706680

Cheng, R., Dong, K., Chen, P., Ning, C., Peng, X., Zhang, Y., et al. (2021). High Output Direct-Current Power Fabrics Based on the Air Breakdown Effect. *Energy Environ. Sci.* 14, 2460–2471. doi:10.1039/d1ee00059d

Cong, Z., Guo, W., Guo, Z., Chen, Y., Liu, M., Hou, T., et al. (2020). Stretchable Coplanar Self-Charging Power Textile with Resist-Dyeing Triboelectric Nanogenerators and Microsupercapacitors. *ACS Nano* 14, 5590–5599. doi:10.1021/acsnano.9b09994

Cui, N., Liu, J., Gu, L., Bai, S., Chen, X., and Qin, Y. (2015). Wearable Triboelectric Generator for Powering the Portable Electronic Devices. *ACS Appl. Mater. Inter.* 7, 18225–18230. doi:10.1021/am5071688

Dickey, M. D. (2017). Stretchable and Soft Electronics Using Liquid Metals. *Adv. Mater.* 29, 1606425. doi:10.1002/adma.201606425

Dong, K., Deng, J., Zi, Y., Wang, Y.-C., Xu, C., Zou, H., et al. (2017). 3D Orthogonal Woven Triboelectric Nanogenerator for Effective Biomechanical Energy Harvesting and as Self-Powered Active Motion Sensors. *Adv. Mater.* 29, 1702648. doi:10.1002/adma.201702648

Fan, F.-R., Tian, Z.-Q., and Lin Wang, Z. (2012). Flexible Triboelectric Generator. *Nano Energy* 1, 328–334. doi:10.1016/j.nanoen.2012.01.004

Fang, H., Wang, X., Li, Q., Peng, D., Yan, Q., and Pan, C. (2016). A Stretchable Nanogenerator with Electric/Light Dual-Mode Energy Conversion. *Adv. Energ. Mater.* 6, 1600829. doi:10.1002/aenm.201600829

Gong, W., Hou, C., Zhou, J., Guo, Y., Zhang, W., Li, Y., et al. (2019). Continuous and Scalable Manufacture of Amphibious Energy Yarns and Textiles. *Nat. Commun.* 10, 868. doi:10.1038/s41467-019-08846-2

Guo, H., Yeh, M.-H., Lai, Y.-C., Zi, Y., Wu, C., Wen, Z., et al. (2016). All-in-One Shape-Adaptive Self-Charging Power Package for Wearable Electronics. *ACS Nano* 10 (11), 10580–10588. doi:10.1021/acsnano.6b06621

Guo, H., Yeh, M.-H., Zi, Y., Wen, Z., Chen, J., Liu, G., et al. (2017). Ultralight Cut-Paper-Based Self-Charging Power Unit for Self-Powered Portable Electronic and Medical Systems. *ACS Nano* 11, 4475–4482. doi:10.1021/acsnano.7b00866

Han, S., Lee, E. J., Kim, B., Jung, S., Jeong, S., Kim, S.-W., et al. (2020). High-Performance Dual-Mode Triboelectric Nanogenerator Based on Hierarchical Auxetic Structure. *ACS Energ. Lett.* 5, 3507–3513. doi:10.1021/acsenergylett.0c01909

Kim, J. N., Lee, J., Lee, H., and KwonOh, I. (2020). Stretchable and Self-Healable Catechol-Chitosan-Diatom Hydrogel for Triboelectric Generator and Self-Powered Tremor Sensor Targeting at Parkinson Disease. *Nano Energy* 82, 105705. doi:10.1016/j.nanoen.2020.105705

Kim, K. N., Chun, J., Kim, J. W., Lee, K. Y., Park, J.-U., Kim, S.-W., et al. (2015). Highly Stretchable 2D Fabrics for Wearable Triboelectric Nanogenerator under Harsh Environments. *ACS Nano* 9, 6394–6400. doi:10.1021/acsnano.5b02010

Lai, Y. C., Deng, J. N., Zhang, S. L., Niu, S. M., Guo, H. Y., and Wang, Z. L. (2016). Single-Thread-Based Wearable and Highly Stretchable Triboelectric Nanogenerators and Their Applications in Cloth-Based Self-Powered

Human-Interactive and Biomedical Sensing. *Adv. Funct. Mater.* 1 (27), 1604462. doi:10.1002/adfm.201604462

Li, R., Wei, X., Xu, J., Chen, J., Li, B., Wu, Z., et al. (2021). Smart Wearable Sensors Based on Triboelectric Nanogenerator for Personal Healthcare Monitoring. *Micromachines* 12, 352. doi:10.3390/mi12040352

Li, S., Peng, W., Wang, J., Lin, L., Zi, Y., Zhang, G., et al. (2016). All-Elastomer-Based Triboelectric Nanogenerator as a Keyboard Cover to Harvest Typing Energy. *ACS Nano* 10 (8), 7973–7981. doi:10.1021/acsnano.6b03926

Lin, Z., Yang, J., Li, X., Wu, Y., Wei, W., Liu, J., et al. (2017). Large-Scale and Washable Smart Textiles Based on Triboelectric Nanogenerator Arrays for Self-Powered Sleeping Monitoring. *Adv. Funct. Mater.* 28, 1704112. doi:10.1002/adfm.201704112

Liu, J., Gu, L., Cui, N., Bai, S., Liu, S., Xu, Q., et al. (2019). Core-Shell Fiber-Based 2D Woven Triboelectric Nanogenerator for Effective Motion Energy Harvesting. *Nanoscale Res. Lett.* 14, 311. doi:10.1186/s11671-019-3144-2

Lu, C., Chen, J., Jiang, T., Gu, G., Tang, W., and Wang, Z. L. (2018). A Stretchable, Flexible Triboelectric Nanogenerator for Self-Powered Real-Time Motion Monitoring. *Adv. Mater. Technol.* 3, 1800021. doi:10.1002/admt.201800021

Mu, J., Hou, C., Wang, G., Wang, X., Zhang, Q., Li, Y., et al. (2016). An Elastic Transparent Conductor Based on Hierarchically Wrinkled Reduced Graphene Oxide for Artificial Muscles and Sensors. *Adv. Mater.* 28, 9491–9497. doi:10.1002/adma.201603395

Niu, S., Wang, X., Yi, F., Zhou, Y. S., and Wang, Z. L. (2015). A Universal Self-Charging System Driven by Random Biomechanical Energy for Sustainable Operation of mobile Electronics. *Nat. Commun.* 6, 8975. doi:10.1038/ncomms9975

Niu, Z., Dong, H., Zhu, B., Li, J., Hng, H. H., Zhou, W., et al. (2013). Highly Stretchable, Integrated Supercapacitors Based on Single-Walled Carbon Nanotube Films with Continuous Reticulate Architecture. *Adv. Mater.* 25, 1058–1064. doi:10.1002/adma.201204003

Parida, K., Thangavel, G., Cai, G., Zhou, X., Park, S., Xiong, J., et al. (2019). Extremely Stretchable and Self-Healing Conductor Based on Thermoplastic Elastomer for All-Three-Dimensional Printed Triboelectric Nanogenerator. *Nat. Commun.* 10, 2158. doi:10.1038/s41467-019-10061-y

Parida, K., Xiong, J., Zhou, X., and Lee, P. S. (2019). Progress on Triboelectric Nanogenerator with Stretchability, Self-Healability and Bio-Compatibility. *Nano Energy* 59, 237–257. doi:10.1016/j.nanoen.2019.01.077

Park, J., Lee, Y., Ha, M., Cho, S., and Ko, H. (2016). Micro/nanostructured Surfaces for Self-Powered and Multifunctional Electronic Skins. *J. Mater. Chem. B* 4 (18), 2999–3018. doi:10.1039/c5tb02483h

Pu, X., Liu, M., Chen, X., Sun, J., Du, C., Zhang, Y., et al. (2017). Ultra-Stretchable, Transparent Triboelectric Nanogenerator as Electronic Skin for Biomechanical Energy Harvesting and Tactile Sensing. *Sci. Adv.* 3, e1700015. doi:10.1126/sciadv.1700015

Pu, X., Song, W., Liu, M., Sun, C., Du, C., Jiang, C., et al. (2016). Wearable Power-Textiles by Integrating Fabric Triboelectric Nanogenerators and Fiber-Shaped Dye-Sensitized Solar Cells. *Adv. Energ. Mater.* 6 (20), 1601048. doi:10.1002/aenm.201601048

Qi, J., Wang, A. C., Yang, W., Zhang, M., Hou, C., Zhang, Q., et al. (2020). Hydrogel-Based Hierarchically Wrinkled Stretchable Nanofibrous Membrane for High Performance Wearable Triboelectric Nanogenerator. *Nano Energy* 67, 104206. doi:10.1016/j.nanoen.2019.104206

Sheng, F., Yi, J., Shen, S., Cheng, R., Ning, C., Ma, L., et al. (2021). Self-Powered Smart Arm Training Band Sensor Based on Extremely Stretchable Hydrogel Conductors. *ACS Appl. Mater. Inter.* 13 (37), 44868–44877. doi:10.1021/acsami.1c12378

Shuai, L., Guo, Z. H., Zhang, P., Wan, J., Pu, X., and Wang, Z. L. (2020). Stretchable, Self-Healing, Conductive Hydrogel Fibers for Strain Sensing and Triboelectric Energy-Harvesting Smart Textiles. *Nano Energy* 78, 105389. doi:10.1016/j.nanoen.2020.105389

Sun, L., Chen, S., Guo, Y., Song, J., Zhang, L., Xiao, L., et al. (2019). Ionogel-Based, Highly Stretchable, Transparent, Durable Triboelectric Nanogenerators for Energy Harvesting and Motion Sensing over A Wide Temperature Range. *Nano Energy* 63, 103847. doi:10.1016/j.nanoen.2019.06.043

Wang, J., Li, S., Yi, F., Zi, Y., Lin, J., Wang, X., et al. (2016). Sustainably Powering Wearable Electronics Solely by Biomechanical Energy. *Nat. Commun.* 7, 12744. doi:10.1038/ncomms12744

Wang, L., Liu, W., Yan, Z., Wang, F., and Wang, X. (2020). Stretchable and Shape-Adaptable Triboelectric Nanogenerator Based on Biocompatible Liquid Electrolyte for Biomechanical Energy Harvesting and Wearable Human-Machine Interaction. *Adv. Funct. Mater.* 31, 2007221. doi:10.1002/adfm.202007221

Wang, T., Zhang, Y., Liu, Q., Cheng, W., Wang, X., Pan, L., et al. (2018). A Self-Healable, Highly Stretchable, and Solution Processable Conductive Polymer Composite for Ultrasensitive Strain and Pressure Sensing. *Adv. Funct. Mater.* 28, 1705551. doi:10.1002/adfm.201705551

Wang, Y., Zhang, L., and Lu, A. (2020). Highly Stretchable, Transparent Cellulose/PVA Composite Hydrogel for Multiple Sensing and Triboelectric Nanogenerators. *J. Mater. Chem. A.* 8, 13935–13941. doi:10.1039/d0ta02010a

Wang, Z. L., and Wang, A. C. (2019). On the Origin of Contact-Electrification. *Mater. Today* 30, 34–51. doi:10.1016/j.mattod.2019.05.016

Wu, C., Jiang, P., Li, W., Guo, H., Wang, J., Chen, J., et al. (2019). Self-Powered Iontophoretic Transdermal Drug Delivery System Driven and Regulated by Biomechanical Motions. *Adv. Funct. Mater.* 30 (3), 1907378. doi:10.1002/adfm.201907378

Wu, C., Wang, X., Lin, L., Guo, H., and Wang, Z. L. (2016). Paper-Based Triboelectric Nanogenerators Made of Stretchable Interlocking Kirigami Patterns. *ACS Nano* 10 (4), 4652–4659. doi:10.1021/acsnano.6b00949

Xu, S., Zhang, Y., Cho, J., Lee, J., Huang, X., Jia, L., et al. (2013). Stretchable Batteries with Self-Similar Serpentine Interconnects and Integrated Wireless Recharging Systems. *Nat. Commun.* 4, 1543. doi:10.1038/ncomms2553

Yang, P.-K., Lin, L., Yi, F., Li, X., Pradel, K. C., Zi, Y., et al. (2015). A Flexible, Stretchable and Shape-Adaptive Approach for Versatile Energy Conversion and Self-Powered Biomedical Monitoring. *Adv. Mater.* 27, 3817–3824. doi:10.1002/adma.201500652

Yang, Y., Sun, N., Wen, Z., Cheng, P., Zheng, H., Shao, H., et al. (2018). Liquid-Metal-Based Super-stretchable and Structure-Designable Triboelectric Nanogenerator for Wearable Electronics. *ACS Nano* 12, 2027–2034. doi:10.1021/acsnano.8b00147

Zhang, W., Deng, L., Yang, L., Yang, P., Diao, D., Wang, P., et al. (2020). Multilanguage-Handwriting Self-Powered Recognition Based on Triboelectric Nanogenerator Enabled Machine Learning. *Nano Energy* 77, 105174. doi:10.1016/j.nanoen.2020.105174

Zhang, W., Gu, G., Qin, H., Li, S., Shang, W., Wang, T., et al. (2020). Measuring the Actual Voltage of a Triboelectric Nanogenerator Using the Non-grounded Method. *Nano Energy* 77, 105108. doi:10.1016/j.nanoen.2020.105108

Zhang, W., Gu, G., Shang, W., Luo, H., Wang, T., Zhang, B., et al. (2021). A General Charge Compensation Strategy for Calibrating the Voltage of a Triboelectric Nanogenerator Measured by a Capacitive Circuit. *Nano Energy* 86, 106056. doi:10.1016/j.nanoen.2021.106056

Zhao, Z., Yan, C., Liu, Z., Fu, X., Peng, L.-M., Hu, Y., et al. (2016). Machine-Washable Textile Triboelectric Nanogenerators for Effective Human Respiratory Monitoring through Loom Weaving of Metallic Yarns. *Adv. Mater.* 28, 10267–10274. doi:10.1002/adma.201603679

Zhu, G., Pan, C., Guo, W., Chen, C.-Y., Zhou, Y., Yu, R., et al. (2012). Triboelectric-Generator-Driven Pulse Electrodeposition for Micropatterning. *Nano Lett.* 12, 4960–4965. doi:10.1021/nl302560k

Zhu, J., Wang, X., Xing, Y., and Li, J. (2019). Highly Stretchable All-Rubber-Based Thread-Shaped Wearable Electronics for Human Motion Energy-Harvesting and Self-Powered Biomechanical Tracking. *Nanoscale Res. Lett.* 14, 247. doi:10.1186/s11671-019-3085-9

Conflict of Interest: The authors declare that the research was conducted in the absence of any commercial or financial relationships that could be construed as a potential conflict of interest.

Publisher's Note: All claims expressed in this article are solely those of the authors and do not necessarily represent those of their affiliated organizations, or those of the publisher, the editors, and the reviewers. Any product that may be evaluated in this article, or claim that may be made by its manufacturer, is not guaranteed or endorsed by the publisher.

frontiers | Frontiers in Bioengineering and Biotechnology

REVIEW
published: 14 April 2022
doi: 10.3389/fbioe.2022.878524

Triggering Immune System With Nanomaterials for Cancer Immunotherapy

Qiyan Li†, Yulin Liu†, Zihua Huang, Yajie Guo and Qingjiao Li**

The Eighth Affiliated Hospital, Sun Yat-sen University, Shenzhen, China

Cancer is a major cause of incidence rate and mortality worldwide. In recent years, cancer immunotherapy has made great progress in the preclinical and clinical treatment of advanced malignant tumors. However, cancer patients will have transient cancer suppression reaction and serious immune related adverse reactions when receiving immunotherapy. In recent years, nanoparticle-based immunotherapy, which can accurately deliver immunogens, activate antigen presenting cells (APCs) and effector cells, provides a new insight to solve the above problems. In this review, we discuss the research progress of nanomaterials in immunotherapy including nanoparticle-based delivery systems, nanoparticle-based photothermal and photodynamic immunotherapy, nanovaccines, nanoparticle-based T cell cancer immunotherapy and nanoparticle-based bacteria cancer immunotherapy. We also put forward the current challenges and prospects of immunomodulatory therapy.

Keywords: nanomaterials, cancer immunotherapy, delivery system, photothermal immunotherapy, photodynamic immunotherapy, nanovaccines

OPEN ACCESS

Edited by:
Youbin Zheng,
Technion Israel Institute of Technology, Israel

Reviewed by:
Shi-Ying Li,
Guangzhou Medical University, China
Jingjin He,
Shenzhen International Institute for Biomedical Research (SIIBR), China
Zichao Luo,
National University of Singapore, Singapore

****Correspondence:***
Yajie Guo
guoyj36@mail.sysu.edu.cn
Qingjiao Li
liqj23@mail.sysu.edu.cn

†These authors have contributed equally to this work and share first authorship

Specialty section:
This article was submitted to Nanobiotechnology, a section of the journal Frontiers in Bioengineering and Biotechnology

Received: *18 February 2022*
Accepted: *30 March 2022*
Published: *14 April 2022*

Citation:
Li Q, Liu Y, Huang Z, Guo Y and Li Q (2022) Triggering Immune System With Nanomaterials for Cancer Immunotherapy. Front. Bioeng. Biotechnol. 10:878524. doi: 10.3389/fbioe.2022.878524

INTRODUCTION

An Overview of Cancer Immunotherapy

Cancer is a major cause of incidence rate and death in the world. In 2020, there were an estimated 19.3 million new cancer cases and 10 million deaths worldwide (Sung et al., 2021). In view of its high risk and mortality, efforts have been made to develop effective treatments to combat cancer (Li Z. et al., 2017). The conventional anti-tumor treatment methods including surgery, radiotherapy, chemotherapy and molecular targeted therapy, have certain disadvantages, such as low response rate, high side effects and high recurrence rate (Gao et al., 2020). In recent years, cancer immunotherapy has achieved significant successes through the enormous number clinical trials approved by the US Food and Drug Administration (FDA). In immunotherapy, the agents are designed to trigger (activate or boost) the immune system to attack cancer cells, which is a natural mechanism in human body. These therapies can provide potent and prolonged anti-cancer responses for a subset of patients who are resistant to conventional therapy, ultimately considering as a promising strategy to cancer.

The main classes of immunotherapies are immune checkpoint inhibitors (ICIs) (Sharma and Allison, 2015; Ribas and Wolchok, 2018), chimeric antigen receptor (CAR) T cell therapies (June et al., 2018; Schultz and Mackall, 2019), lymphocyte-activating cytokines, agonistic antibodies against co-stimulatory receptors, and cancer vaccines (Schumacher et al., 2019). Since the approval of the first immune checkpoint inhibitor, Ipilimumab (CTLA-4), by the FDA in 2011, cancer immunotherapy has

experienced rapid development (Rosenberg, 2005). Between 2014 and 2018, the field of immunotherapies has witnessed the approval of eight new anticancer drugs by FDA, including programmed death/ligand 1 (PD-1/PD-L1) blockade and CAR T-cell therapy (Sun et al., 2019). In the past decade, the number of cancer immunotherapy has been massively increased, many of which are in clinical trials. These breakthrough advances in immunotherapy for cancer treatment have been recognized by the world, creating a new milestone in immunotherapy. Despite the great success of immunotherapy, its clinical application in cancer treatment still faces challenges in terms of efficacy and safety.

An Overview of Nanomedicine

Nanomedicine which is referred to the application of nanotechnology in medicine has become extensively widespread because of its advantages in diagnosis and therapy (Peer et al., 2007). In biology system, nanomedicines are formulation of therapeutics with lipids, polymers or inorganic materials, and can act as carrier of pharmaceuticals to direct the particles to a specific organ or cell type (Fokong et al., 2012; Lammers et al., 2012; Beech et al., 2013; Li et al., 2013; Shin et al., 2013; Woodman et al., 2021). Nanoscale dimension typically refers to particulate described to 1–100 nm in size in drug delivery systems. Therapeutic agents can selectively accumulate in pathological regions and specifically release pharmacological effects in the site, avoid undesired off-target effects, and overcome the danger of severe immune toxicities, which occur in the case of other systemic administration (Peer et al., 2007; Morachis et al., 2012).

Tumor targeting by nanomedicines is typically mediated via two main mechanisms, including passive targeting and active targeting (Matsumura and Maeda, 1986; Mi et al., 2020). The uncover of mechanism for passive targeting dates back to the year 1986, when Matsumura and Maeda (Matsumura and Maeda, 1986) started to reveal Enhanced Permeability, as well as Jain and colleagues (Gerlowski and Jain, 1986) started to explore Retention (EPR) effect. Active targeting relies on the functionalized nanoparticles (NPs) with targeting molecules, such as antibodies or peptides, which can increase internalization of drugs at the pathological site. In this case, drug-to-antibody ratios can greatly exceed the ratio of conventional antibody-drug conjugates (Kulkarni et al., 2018). Discuss include the fact recently indicates that both strategies have difference in several perspectives, including overall targeting efficiency, specific cell delivery, formulation complexity and translational potential (Lammers et al., 2012; Lammers et al., 2016).

The field has witnessed the success of approximately 50 nanomedicine therapies approved by the FDA for cancer and other diseases (Bobo et al., 2016). Among the main future ways forward is the combination of nanomedicines with immunotherapy, a therapeutic strategy that has been extensively studied preclinically (Wang et al., 2018; Saeed et al., 2019; Sang et al., 2019; Sun et al., 2019) and is also already being explored in the clinic (Yu et al., 2021).

Opportunities of Nanomedicine in Immunotherapy

Although immunotherapy has achieved excellent results in clinical practice, there are still many problems that need to be solved. In terms of safety, immunotherapy can induce transient suppression of cancer response and severe immune-related adverse effects in patients treated with immune checkpoint inhibitors (Bowyer et al., 2016; Milling et al., 2017). As observed with chimeric antigen receptor-T cell therapy, the immune status of patients has been significantly improved. However, the large number of injected immune cells affect the homeostasis of the immune environment and overproduce cytokines, which trigger cytokine storm (Predina et al., 2013). In addition, drugs of immunotherapy are usually administered clinically by intravenous injection. This approach shortens the time of drug delivery to the tumor tissue but loses the precise control of drug distribution *in vivo*. As a result, utilization of the drug is significantly reduced, and meanwhile it may cause systemic random activation of the immune system and induce severe immunotoxicity (Predina et al., 2013).

The emergence of nanocarrier-based delivery systems has provided new perspectives for cancer immunotherapy. The loading of immune agents into nanocarriers, considering its promising biocompatibility and stability, can effectively improve the solubility and bioavailability of hydrophobic drugs, prolong the time of drug circulation in the body, and avoid the recognition and clearance by the immune system. It also significantly increases the utilization of immune agents in the body, achieves precise targeting of immune cells or tumor tissues, and reduces toxic side effects, etc., (Gao et al., 2019; Martin et al., 2020). Meanwhile, through the surface modification of target molecules or enhancing EPR, nanocarriers can effectively deliver drugs, antibodies, immunodulators or functional molecules to tumor tissues (Sindhwani et al., 2020). This method can achieve enrichment of drugs and antibodies, regulation of local immunity, improvement of immunosuppressive microenvironment, enhancing the effect of tumor immunotherapy (Sindhwani et al., 2020).

NP-BASED DELIVERY SYSTEMS FOR CANCER IMMUNOTHERAPY

An increasing number of nanomedicine agents have been used synergistically with immunotherapeutic agents to complement the previously singular cancer therapeutic approaches. The impact of nanoparticle-based delivery systems on tumor immunity is currently being explored (**Figure 1**).

NPs Delivery System of Immunogenic Cell Death Inducing Cytotoxic Drugs

It is reported that low doses of chemotherapeutic agents can activate apoptotic pathways and trigger immunogenic cell death (ICD), which is a specific mode of cell death, as well as an important trigger and enhancer of anticancer immunity (Gupta et al., 2021). ICD in tumors induced with cytotoxic drugs produces a large number of tumor-associated antigens *in situ*, which active the immune system against tumors, conducting to a safe and efficient novel tumor immunotherapy (Bracci et al., 2014; Brown et al., 2018). ICD inducers identified in current

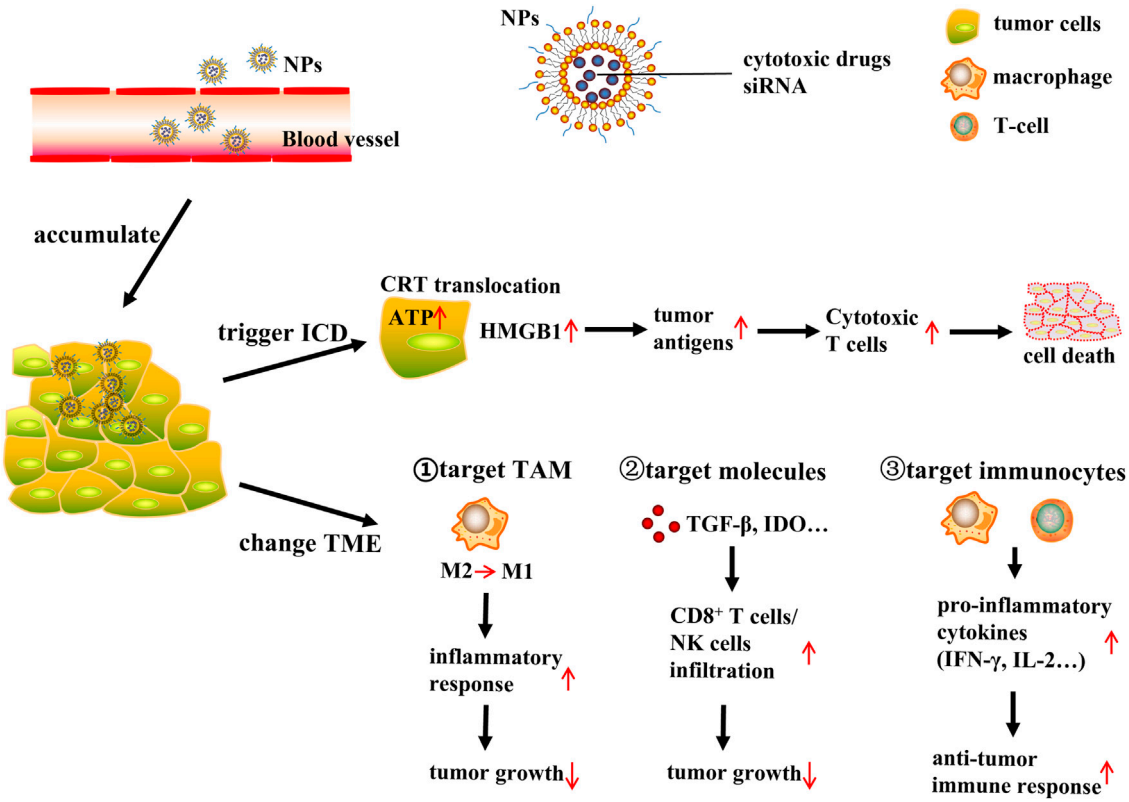

FIGURE 1 | NP-based delivery systems for cancer immunotherapy. NP (nanoparticles); ICD (immunogenic cell death); CRT (calreticulin); ATP (adenosine triphosphate); HMGB1 (high mobility group protein B1); TME (tumor microenvironment); TAM (tumor-associated macrophages). NP-based tumor targeted delivery systems deliver ICD inducing cytotoxic drugs or siRNA to tumor site, then NPs accumulate in the tumor interstitial space, further trigger ICD or change TME to induce immune response and finally lead to tumor cells death. NPs release ICD inducing cytotoxic drugs, inducing CRT translocate to cell surface, ATP release, and HMGB1 expression increase. This triggers tumor antigens process and produce cytotoxic T cells to induce tumor cells death. On the other hand, NPs delivery system could change TME through targeting TAM, immunosuppressive molecules and immunocytes respectively. Target TAM: NPs deliver drugs or siRNA to tumor cells, polarizing macrophages from M2 phenotype to M1 phenotype, and then stimulating inflammatory response, finally suppressing tumor growth. Target immunosuppressive molecules: NPs could act on TME related immunosuppressive molecules such as TGF-β and IDO, this will increase infiltration of $CD8^+$ T cells and NK cells, resulting in tumor growth inhibition. Target immunocytes: NPs could directly act on immune cells such as macrophages and cytotoxic T cells and these cells will produce pro-inflammatory cytokines including IFN-γ and IL-2, leading to antitumor immune response increase to suppress tumor growth.

studies include doxorubicin, 5-fluorouracil, gemcitabine, paclitaxel, mitoxantrone, and oxaliplatin (Bezu et al., 2015).

Classical features of ICD are damage-associated molecular patterns (DAMPs), including the translocation of calreticulin (CRT) to the cell surface, the release of adenosine triphosphate (ATP), and overexpression of high mobility group protein B1 (HMGB1) into the extracellular environment (Krysko et al., 2012; Kadiyala et al., 2019). Alerted by these features, natural antigen presenting cells (APCs) in the immune system ingest and process tumor antigens, and produce cytotoxic T cells, and then migrate to eradicate tumors and metastases. Therefore, the efficacy of immune checkpoint blockade therapies can be effectively improved by potentiating the ICD (Binnewies et al., 2018).

In general, anticancer chemotherapy frequently entails the challenge of resulting in high off-target toxicity in normal and immune cells due to its ability to simultaneously kill malignant cancer cells and other normal cells. As a result, unwanted systemic toxicity and immunosuppression can be observed in patients who have given combination therapy with cytotoxic drugs. The NP-based tumor-targeted delivery systems deliver macromolecules including NPs and nanocomplexes into the tumor interstitial space to accumulate within the tumor tissue, which effectively increases the duration of drug's retention at the tumor site and boosts the EPR effect, yielding a maximum therapeutic effect with low toxicity (Maeda et al., 2000; Gu et al., 2018; Pusuluri et al., 2019). On the other hand, the rapid and enhanced cellular uptake of NPs enhances the tumor-specific immune response (Dai et al., 2017; Golombek et al., 2018). The NP-based drug delivery system for ICD-induced anticancer drugs achieves tumor-specific delivery of cytotoxic agents and suppresses immunosuppression in tumor tissues (Zhang B. et al., 2017).

Recent studies also show that ICD-inducing nanomedicines can be combined with immunotherapy to enhance ICD to potentiate the cancer-immunity cycle (Kuai et al., 2018). For example, Rios-Doria's group recently showed that the combination therapy consisting of doxorubicin-loaded liposomes (Caelyx/Doxil®) and other clinically relevant

immunotherapeutics substantially enhanced antitumor immune response by promoting (*via* ICD) the proliferation of dendritic cells (DCs) and $CD8^+$ T cells. Frequently used immunotherapeutic agents include anti-PD-1, -PD-L1 and -CTLA4 antibodies, as well as tumor necrosis factor receptor alpha agonists. It is reported that Doxil was less potent in immunodeficient mice than in immunocompetent mice, and the experiment *in vivo* provided preliminary evidence of the immune potentiation effects of Doxil (Rios-Doria et al., 2015). Zhao et al. encapsulated ICD-inducing agent oxaliplatin (OXA) into nanoparticles. Compared with free OXA treatment, tumor cells treated with OXA-loaded nanoparticles released more DAMPs, inducing more antitumor immune responses produced by DC and T lymphocytes (Zhao et al., 2016). An exemplary study in this regard was published by Zhang et al., who combined doxorubicin, matrix metalloproteinase (MMP)-cleavable peptide and hyaluronic acid (HA) to a nano-sized prodrugs. The nanomedicines intensified antitumor immune response by upregulating interferon-γ (IFN-γ) and PD-L1 (Gao et al., 2018). Similar beneficial effects were reported by Zan et al. as well, who encapsulated a new type of ICD-inducing agent into nanoparticles. The nanoinducer was generated by packing curcumin (CUR) and iron oxide nanoparticles (IONPs) into disulfide-bond-incorporated dendritic mesoporous organosilica nanoparticles (DDMON) and abbreviated as DDMON-CUR-IONP. DDMON-CUR-IONP significantly amplified the oxidative stress pharmacological properties in the tumor immune microenvironment through complementary pharmacological activities, eventually triggering an effective systemic immune response and ICD. It avoids serious adverse effects compared to conventional nanoinducer (Dai et al., 2020). These improvements stemmed from that the NP-based drug delivery system can more effectively target chemotherapeutic agents to cancer tissues and overcome the lymphotoxicity effectively induced by free chemotherapeutic agents. It is anticipated that in the next couple of years, researchers will synthesize a significant number of novel nanopharmaceutical agents specifically designed to induce ICD in tumor cells without toxic effects on normal cells.

NPs Delivery System for Tumor Immune Microenvironment

The tumor microenvironment (TME) is a heterogeneous environment composed of extracellular matrix (ECM), tumor-infiltrating lymphocytes, cancer-associated fibroblasts (CAF), myeloid suppressor cells, regulatory T cells, and tumor-associated macrophages (TAM). In addition, the TME is filled with soluble proteins such as transforming growth factor beta (TGF-β), cyclooxygenase 2 (COX-2) and epidermal growth factor (EGF) (Lindau et al., 2013; Emon et al., 2018). The synergistic relationship of these components leaves the TME in an immunosuppressed state, consequently supporting the development, progression and metastasis of tumor and limiting the function of APCs and T cells (Joyce and Fearon, 2015). The utilization of nanomedicines that modulate the TME is another important strategy of promoting the efficacy of anticancer immunotherapy, especially for the "cold" solid tumor with low immunogenicity.

NPs Delivery System Targeting Tumor-Associated Macrophages

Tumor-Associated Macrophages (TAMs) are major population of immunomodulatory cells in tumors, accounting for approximately 50% of solid tumor tissues. TAM are implicated in regulating immune processes in the TME by releasing immunosuppressive cytokines, participating in tumor angiogenesis, inhibiting proliferation and activation of T cells, as well as promoting tumor cell growth, invasion and metastasis (Franklin et al., 2014). During the process from the early stage of tumor formation to tumor metastasis, TAM with M2-like phenotype (M2) typically take the dominant position to enhance the invasive and metastatic ability of tumor cells and promote the stocking and continuous growth of tumor cells, and ultimately achieve the purpose of suppressing anti-tumor immune activity (Ruffell et al., 2012; Colegio et al., 2014). In addition, TAM are generally dominated by cells with an M2-like phenotype associated with Th2 immune response, whereas the M2-like phenotype can still be repolarized into the M1-like phenotype which promotes inflammatory response and suppresses neoplasia. Accumulating evidence has confirmed that the potential of macrophage recruitment chemokines (CCL2, CCL3, CCL4, and CCL5), CSF-1 and VEGF as a clinical therapeutic target to prevent malignancy progression by interrupting the recruitment of TAMs (Halama et al., 2016; Argyle and Kitamura, 2018). To inhibit CCL2 and its cognate receptor CCR2 axis, Shen et al. synthesized siCCR2-encapsulated cationic nanoparticle (CNP/siCCR2) to inhibit primary tumor progression and further metastasis by reducing the abundance of TAMs and altering the immunosuppressive tumor microenvironment (Shen et al., 2018). In another recent study, Trac et al. designed KLAK-MCP-1 micelles, consisting of a CCR2-targeting peptide sequence and apoptotic KLAK peptide, which were effective in inhibiting tumor growth by blocking infiltration of TAMs in a subcutaneous B16F10 murine melanoma model (Trac et al., 2021). Zhang et al. loaded gemcitabine onto ultrasmall copper nanoparticles (Cu@CuO x) for PET-guided drug delivery, which could specifically target CCR2 and synergize the therapeutic effects of gemcitabine, ultimately slowing the growth of pancreatic ductal carcinoma (Zhang X. et al., 2021). Analogously, Chen et al. developed a nano-spray gel, and achieved effective clearance of residual carcinoma cells after tumor surgery via polarizing macrophages towards an M1 phenotype (Chen et al., 2019). In this regard, targeting TAM in the TME is a promising strategy for improving cancer therapy.

NPs Delivery System Targeting Immunosuppressive Molecules

Nanomedicines can also act on molecules in the TME, such as TGF-β and Indoleamine 2,3-dioxygenase (IDO), which have immunosuppressive effects. TGF-β is an important

immunosuppressive factor in tumors, which contributes to the formation of promotion of tumor inflammatory microenvironment, and diminishes the efficacy of checkpoint inhibition immunotherapy (Mariathasan et al., 2018; Tauriello et al., 2018). To address the drawbacks of TGF-β inhibitors in clinical trials with poor pharmacokinetic behavior and high systemic toxicity with insufficient tumor permeability, Park and co-workers developed a novel nanoparticle for the co-delivery of TGF-β inhibitor and interleukin-2. They revealed the significant increase in infiltration of $CD8^+$ T cells and NK cells, resulting in the significant inhibition of tumor growth and alleviation of immunosuppression (Park et al., 2012). Huang et al. developed a TGF-β siRNA-containing nanoformulation that synergized with cancer vaccination, which achieved silence of TGF-β expression, to significantly enhance its therapeutic effect on advanced tumors (Xu et al., 2014). As one of the key factors contributing to tumor immune tolerance, IDO promotes the conversion of tryptophan to kynurenine, while the former one is essential for T cell proliferation and killing and the latter one is a potent T cell suppressing metabolite (Yuan et al., 2017). A variety of small molecule IDO inhibitors have been extensively applied in (pre-)clinical trials for adjuvant cancer immunotherapy to improve outcomes of immunotherapeutic interventions. Recently, Lu and colleagues combined an IDO inhibitor indocimod with the ICD inducer OXA in lipid-coated mesoporous silica nanoparticles, achieving the inhibition of tumor growth in a mouse model of pancreatic ductal adenocarcinoma and significantly prolonging the survival period of mice with tumors (Lu et al., 2017). Han et al. developed a nanoparticle NLG-RGD NI, consisting of a peptide backbone and a targeting motif, as a carrier for the IDO inhibitor NLG919. After NLG-RGD NI was targeted to tumor tissue and taken up, it consistently inhibited IDO activity and reduced systemic toxicity caused by the non-specific distribution of NLG919 (Han et al., 2020).

NPs Delivery System Targeting Immunocytes

In addition, nanomedicines can also be used to influence the function of immune cells directly and positively such as macrophages and cytotoxic T cells in TME. To improve selective and immune-mediated eradication of cancer cells, Yuan et al. constructed a multivalent bi-specific nanobioconjugate engager (mBiNE), which could target HER2 expressed by cancer cells and pro-phagocytosis signals at the same time. In mice implanted HER2high E0771/E2 tumors treated with mBiNE, they found that the infiltration of macrophages and T cells, production of pro-inflammatory cytokines such as IFN-γ and IL-2 were substantially increased. Ultimately mBiNE elicited systemic, durable antitumour immune responses by promoting targeted phagocytosis of tumors by macrophages and enhancing T cells activation (Yuan et al., 2017). Recently, Shae et al. designed stimulator of interferon genes (STING)-activating nanoparticles (STING-NPs) that effectively encapsulated 2'3' cyclic guanosine monophosphate-adenosine monophosphate (cGAMP), and acted as a delivery of cGAMP. Through triggering innate immune response derived by IFN-I, cGAMP could inhibit tumor growth, enhance tumor immunogenicity, and increase rates of long-term survival of patients. Treatment with STING-NPs triggers systemic antitumor immunity and enhances the efficacy of checkpoint blockade therapies (Shae et al., 2019). Li et al. constructed a novel cancer-derived magnetosome with Fe_3O_4 magnetic nanoclusters (MNCs) as the core, wrapped around anti-CD205-modified cancer cell membranes. Magnetic resonance imaging (MRI) enabled the magnetic nanoclusters to remain in the lymph nodes, inducing massive proliferation of cytotoxic T cells and triggering antitumor immunity (Li F. et al., 2019).

In conclusion, NP-based delivery systems can generally enhance anticancer immunity by modulating TME in two different approaches, i.e., by alleviating immunosuppression or by promoting immune activation. Depending on the target site, the delivery system will operate with different strategies to enhance the effect of tumor immunity.

NP-BASED PHOTOTHERMAL AND PHOTODYNAMIC IMMUNOTHERAPY

In recent years, phototherapy based on nanoparticles, such as photothermal therapy (PTT) and photodynamic therapy (PDT), has attracted extensive attention for tumor treatment because of its strong efficacy, minimal invasion and negligible side effects. PTT and PDT can not only kill tumor cells directly through heat and reactive oxygen species (ROS), but also induce a variety of antitumor effects. In particular, PTT and PDT lead to a large number of tumor cell deaths and trigger immune responses, including redistribution and activation of immune effector cells, expression and secretion of cytokines, and transformation of memory T lymphocytes (**Figure 2**).

NP-Based Photothermal Therapy With Immunotherapy

The application principle of PTT is to use the performance of photothermal conversion nanomaterials to convert light energy into heat energy at a specific light wavelength, thereby killing cancer cells (**Figure 3**). Compared with the existing tumor treatment methods, PTT has the following advantages: 1) Near-infrared (NIR) can penetrate deeper tissues with minimal damage to healthy tissues (Saneja et al., 2018). 2) In addition to superficial tumors, PTT combined with interventional technology has the potential to treat deep tumors (Hu et al., 2017). 3) Targeted molecular modified nanoparticles are used to drug or nucleic acid delivery, and tumor-specific killing can be achieved after intravenous injection (Zhu H. et al., 2017; Zhu X. et al., 2017). At present, PTT has attracted increasing attention as a non-invasive treatment.

Yan et al. achieved a combination of PTT and PD-L1 blockade by utilizing polyethylene glycol (PEG) and FA functionalized reduced graphene oxide (rGO) -based nanosheets loaded with IDO inhibitor (IDOi) (Yan et al., 2019). Cancer cells could be destroyed significantly by the hyperthermia produced by PTT.

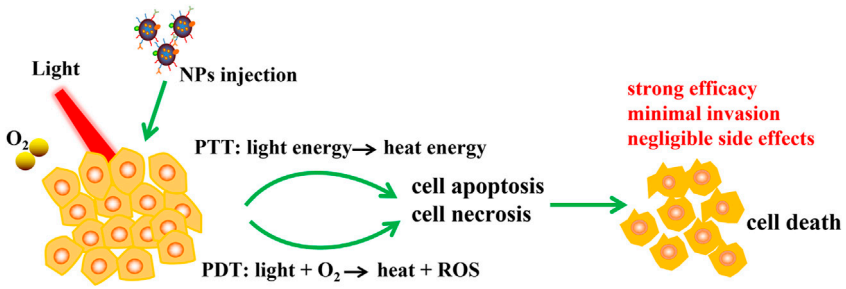

FIGURE 2 | Schematic illustration of NPs based PTT and PDT therapy. NPs was injected to tumor, PTT and PDT convert light energy into heat energy and induce ROS with the help of excitation light and oxygen, then cell apoptosis and necrosis were occurred and finally leading to cell death. PTT and PDT have advantages including strong efficacy, minimal invasion and negligible side effects.

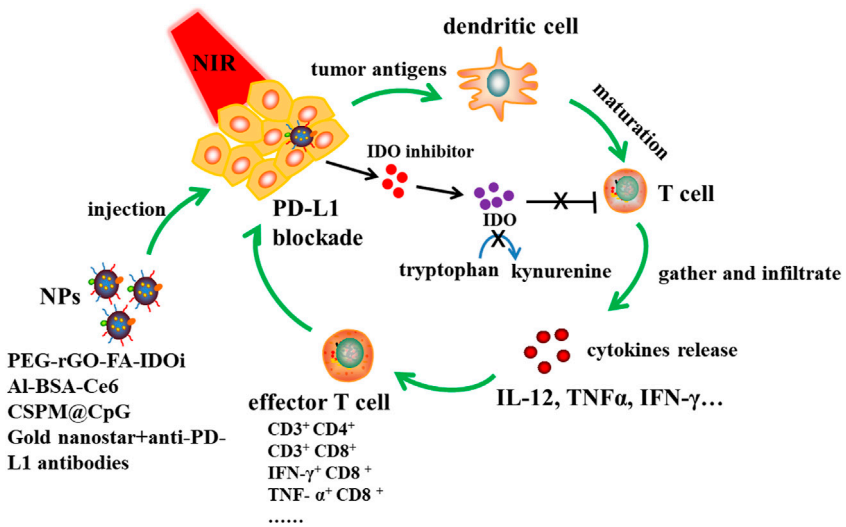

FIGURE 3 | NPs based PTT immunotherapy together with IDO inhibition and PD-L1 blockade. Designed NPs such as PEG-rGO-FA-IDOi, Al-BSA-Ce6, CSPM@CpG, Gold nanostar-anti-PD-L1 antibodies were injected to tumor site, and then immune responses were triggered at a specific light wavelength. Tumor antigens are produced, dendritic cells are maturated into T cells, then T cells gather and infiltrate tumor site, promoting cytokines release like IL-12, TNFα and IFN-γ to increase effctor T cells proportion. NPs release IDO inhibitor, which could inhibit IDO converting tryptophan to kynurenine. This was beneficial to T cell proliferation. What's more, NPs combined with anti-PD-L1 antibodies could induce PD-L1 blockade and then enhance immune response to kill tumor cells.

After treating with PEG-rGO-FA-IDOi nanosheets, $CD45^+$ leukocytes, $CD3^+$ $CD4^+$ T cells and $CD3^+$ $CD8^+$ T cells in the distant tumor would increase. Zhu et al. prepared bovine serum albumin nanosystems (Al-BSA-Ce6 NPs) by albumin-based biomineralization with photosensitizer E6 (Ce6) chloride and immune adjuvant aluminum hydroxide (Zhu et al., 2020). When injected intravenously, nanoparticles not only effectively destroyed tumor cells, but also protected animals from tumor re-invasion and metastasis by strongly inducing an anti-tumor immune response. After photoablation, Al-BSA - Ce6 NPs triggered a systemic anti-tumor immune response that T cells gathered in lymph nodes and infiltrated the tumor sites, increasing the levels of serum antibodies and cytokines, and the proportion of IFN-γ^+ $CD8^+$ T cells, TNF- α^+ $CD8^+$ T cells and IFN- γ^+ $CD4^+$ Th1 cells. Zhou et al. constructed a multifunctional tumor treatment platform by successively coating the surface of Cu_9S_5 nanocrystals with mesoporous silica shell and manganese dioxide shell, and then adsorbing immune adjuvant (CpG) for synergistic phototherapy and immunotherapy (Zhou et al., 2020a). Under 650 nm laser irradiation and 808 nm NIR laser irradiation, CSPM@CpG nanocomposites could effectively produce ROS and a large amount of heat, leading to cancer cell deaths. In addition, it was found that the nanocomposites can promote the uptake of CpG, and promote the generation of IL-12, TNF- α and IFN- γ. Liu et al. revealed a synergistic immuno-PTT combined therapy strategy (SYMPHONY) that completely eliminated primary tumor and distant untreated tumors in mice carrying MB49 bladder cancer cells, which combined immunosuppression point suppression, anti PD — L1 antibodies and gold nanostar (Liu et al., 2017). Gold nanostar provided mild hyperthermia under NIR radiation, which triggered local and systemic immune

responses. Wang et al. combined indocyanine green (ICG)–loaded magnetic silica NIR sensitive nanoparticles (NSNP) to develop temperature activated engineered neutrophils (NE) (Wang et al., 2021). The combination of neutrophil targeting and magnetic targeting increased the accumulation of photothermal agent (PTA) in tumor sites. Under NIR irradiation, NSNP can cause local temperature rise and NE thermal stimulation at the tumor site. High temperature can directly kill tumor cells and also lead to the death of neutrophils. In the case of neutrophil death, it will release active substances with tumor killing effect and kill residual tumor cells, so as to reduce tumor recurrence. Moreover, the composite can significantly enhance the killing effect of photothermal therapy and has no recurrence in animal models with pancreatic tumors.

Heat shock proteins (HSPs) are protective proteins which will be over expressed when cells are stressed by heat, ischemia, heavy metals and toxins. They can repair protein damage and prevent cell apoptosis (Horowitz and Robinson, 2007; Calderwood and Gong, 2016). HSP70 and HSP90 are members of HSP family, participating in the folding and function of a variety of proteins. By regulating the expression of carcinogenic client proteins such as Ras, p53 and Akt, HSP70 and HSP90 are very important for the survival of tumor cells (Cavanaugh et al., 2015). In addition, due to the tolerance of tumor cells to heat stress, overexpression of HSP at tumor sites would lead to low efficiency of PTT (Chen et al., 2017). Therefore, reducing HSP70 and HSP90 in tumor cells not only promotes apoptosis, but also improves the thermal sensitivity of tumor cells (Jego et al., 2013; Ali et al., 2016; Lin et al., 2016). Tang et al. constructed a treatment system (MPEG-AuNR@VER-M) composed of methoxy-polyethylene-glycol-coated-gold-nanorods (MPEG-AuNR) and ver-155008 micelles (VER-M). VER-M promoted tumor cell apoptosis by specifically reducing the expression of HSP70 and HSP90 (Chatterjee et al., 2013; Li H. et al., 2017; Zhang H. et al., 2017; Fan et al., 2017). It is found that *in vitro* study increasing the concentration of VER-M and elevating the temperature of MPEG-AuNR@VER-M can improve the effect of growth inhibitors on human colon cancer (HCT116) cells (Tang et al., 2018). Yang et al. designed a simple strategy to prepare PEG-modified one-dimensional nano coordination polymer (1D-NCPs), and then loaded with gambogic acid (GA), a natural inhibitor of HSP90, which could effectively induce tumor cell apoptosis and achieve low-temperature PTT under mild near-infrared trigger heating (Yang Y. et al., 2017). Wu et al. designed a hollow mesoporous organosilicon nanocapsule (HMONs) nano platform which had an excellent tumor destruction effect after loading indocyanine green (ICG), HSP90 inhibitor and 17AAG were modified with polyethylene glycol (NH2-PEG) (Wu et al., 2018). Zhong et al. designed QE-PEG-Ag_2S by self-assembly of hydrophobic Ag_2S nanodots (Ag_2S NDs), amphiphilic pH-reactive PEG_{5k}-PAE_{10k} polymer, and an HSP70 inhibitor quercetin (QE) (Zhong et al., 2020). QE-PEG-Ag_2S achieved complete tumor ablation without recurrence when irradiated with NIR light for 10 min. It provides a new way for the therapeutic application of Ag_2S NDs. Wu et al. designed nano catalyst (G/A@CaCO3-PEG) which is composed of calcium carbonate ($CaCO_3$) — supported glucose oxidase (GOD) and 2D antimonene quantum dots (AQDS), and further surface modified by lipid bilayer and PEG (Wu et al., 2022). The integrated GOD effectively catalyzes the consumption of glucose, thereby reducing the supply of ATP and subsequently downregulating the expression of HSP. Under the irradiation of NIR light, this effect enhances the efficacy of photothermal hyperthermia induced by 2D AQDS by reversing the heat resistance of cancer cells.

Small interfering RNA (siRNA), as an effective carrier of RNA interference, suppressed the heat shock response and made cancer cells more sensitive to PTT by inhibiting the expression of specific genes and silencing the expression of heat shock proteins. Liu et al. successfully synthesized flower-like gold nanoparticles (GNFs) using CTAC as a soft template, and then loaded siRNA, which was called GNFs-siRNA (Liu Y. et al., 2019). *In vivo* studies showed that due to the synergistic effect of GNF mediated PTT and siRNA triggered inhibition of heat shock response, GNFs-siRNA showed a significant anti-tumor effect in the irradiated HepG2 tumor model. Gold nanorods (GNRs)-siRNA platform with gene silencing ability was fabricated by Wang et al. to improve the efficiency of PTT (Wang et al., 2016). After surface modification, GNRs could deliver siRNA oligomers targeting BAG3, a gene that effectively blocked heat shock response. *In vitro* and *in vivo* experiments showed that GNRs-siRNA nanocomposites increased and promoted apoptosis by down-regulating BAG3 expression under moderate laser irradiation, making cancer cells sensitive to PTT. A folate (FA)-modified polydopamine (PDA) nanodrug for photothermal therapy was designed by Zhang et al. for siRNA delivery to knock down the ROC1 oncogene (Zhang Z. et al., 2021). *In vitro* and *in vivo* experiments show that gene nano drugs combined with PTT can effectively inhibit the proliferation and promote the apoptosis of liver cancer cells. Liu et al. developed a novel multifunctional nanostructure GAL-GNR-siGPC-3, which uses galactose (GAL) as the targeting part of hepatocellular carcinoma (HCC) and gold nanorods (GNR) as the framework to destroy tumor cells under laser irradiation, and the siRNA of Glypican-3 (siGPC-3) which induces specific GPC-3 gene silencing in HCC (Liu Y. et al., 2021). GAL and siGPC-3 can induce targeted silencing of GPC-3 gene in hepatoma cells. The results *in vivo* and *in vitro* showed that GAL-GNR-siGPC-3 could significantly induce the downregulation of GPC-3 gene and inhibit the progression of HCC.

NP-Based Photodynamic Therapy With Immunotherapy

The anti-tumor principle of PDT is that in the presence of molecular oxygen and activated by specific wavelength excitation light, photosensitizers (PSs) are selectively retained in tumor tissues to produce singlet oxygen and other ROS, leading to tumor cell apoptosis and necrosis (Zhang et al., 2018). PDT has the advantages of small trauma, low toxic and side effects, good selectivity and good reproducibility (Park et al., 2017). It is an effective method for clinical treatment of various diseases (**Figure 4**).

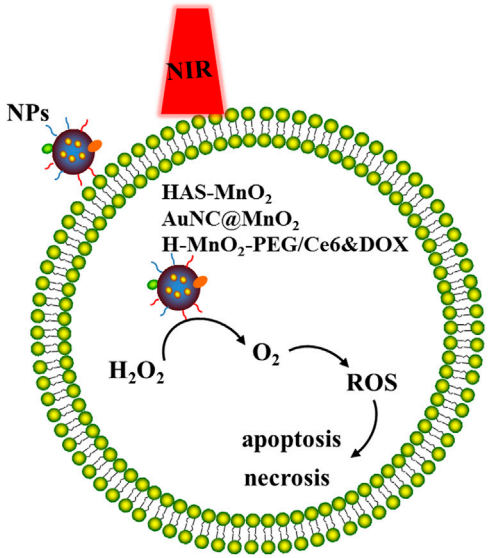

FIGURE 4 | NPs based PDT immunotherapy. In the presence of specific wavelength excitation light, designed nanoparticles like HAS-MnO_2, AuNC@MnO_2 and H-MnO_2-PEG/Ce6&DOX transport oxygen into tumor or *in situ* generation of O_2 inside the tumor from endogenous H_2O_2 with catalysts, which improves tumor oxygenation level and changes tumor microenvironment, increases ROS levels, leading to tumor cell apoptosis and necrosis.

Wu et al. developed an immunotherapy method composed of natural immune activator Astragaloside III (AS) and photodynamic therapy (PDT) reagent chloroe6 (Ce6) [(As + Ce6) @ MSNs-PEG] for colon cancer (Wu et al., 2021). The results showed that *in vitro* (As + Ce6) @ MSNs-PEG could effectively activate NK cells and inhibit the proliferation of tumor cells. Furthermore, it can effectively reach the tumor site *in vivo*, induce immune cells to infiltrate into the tumor, and enhance the cytotoxicity of natural killer cells and $CD8^+$ T cells. In Liu's recent work, they designed a nanocomposite called CE6/MLT@SAB, after light treatment, and the ability of CE6/MLT@SAB-treated cells to activate DCs were significantly increased (Liu H. et al., 2019). Xing et al. constructed a multifunctional nano platform reasonably by pre saturating oxygen fluorinated polymer nanoparticles and encapsulating PS (Ce6) and indoleamine 2,3-dioxygenase (IDO) inhibitor (NLG919) (Xing et al., 2019). The combination of PDT and NLG919 can enhance IFN- γ positive $CD8^+$ T cells significantly, producing effective synergistic antitumor immunity. Liang et al. developed a AuNC@MnO_2 (AM) nanoparticles for oxygen enhanced PDT combined with immunotherapy in the treatment of metastatic triple-negative breast cancer (mTNBC) (Liang et al., 2018). The oxygen enhanced PDT effect of AM can not only effectively destroy the primary tumor, but also induce immunogenic cell death (ICD), release damage related molecular patterns (DAMPs), and then induce DC maturation and effector cell activation, thus effectively stimulating the systematic antitumor immune response against mTNBC.

Tumors are usually exposed to hypoxia. After PDT damages blood vessels, it will cut off the blood supply, further worsen the hypoxic environment, and seriously affect the therapeutic effect, especially in deep tumors (Ma et al., 2019; Zhang Y. et al., 2020). Therefore, it is very important to slow the rapid deterioration of hypoxic environment. pH/H_2O_2 dual-responsive nanoparticles were designed by Chen et al. using albumin-coated MnO_2 (Chen et al., 2016). When MnO_2 penetrated the tumor, it reacted with H_2O_2 and H^+ to produce oxygen. By alleviating hypoxia, the effect of PDT was enhanced. Yang et al. synthesized MnO_2 nano-platform which can regulate the hypoxic TME to and enhance the therapeutic effect of PDT (Yang G. et al., 2017). A carbon nitride (C_3N_4)-based multifunctional nanocomposite (PCCN) was used by Zheng et al. to improve hypoxia (Zheng et al., 2016). *In vitro* studies showed that the obtained PCCN could increase the intracellular oxygen concentration and improve the production of reactive oxygen species in hypoxic and normoxic environments. *In vivo* experiments also show that PCCN had good anti-tumor hypoxia ability. Xiong et al. designed a nano platform (IR775@Met@Lip) whose structure is that the liposome is loaded with metformin (MET) and IR775 (Xiong et al., 2021). It can reverse tumor hypoxia, enhance the production of ROS, reduce the expression of PD-L1 and reduce T cell failure. Furthermore, reversing tumor hypoxia successfully inhibited the growth of primary and distal tumors of bladder and colon cancer, respectively.

Combination Therapy of NP-Based Photothermal Therapy and Photodynamic Therapy Immunotherapy

In the previous discussion, we introduced the research progress of PTT/PDT immunotherapy mediated by different nanomaterials in tumor treatment. The combination of the two methods can not only kill tumor cells through high heat, but also promote the transformation of free radical initiators to toxic free radicals, which further kill tumor cells (Chen et al., 2013). Li et al. designed a nano system composed of ER-targeting pardaxin (FAL) peptides modified-, indocyanine green (ICG) conjugated-hollow gold nanospheres (FAL-ICG-HAuNS) and oxygen-delivering hemoglobin (Hb) liposome (FAL-Hb lipo) to realize PTT and PDT immunotherapy (Li W. et al., 2019). ER-targeted nanosystems induced endoplasmic reticulum stress and calreticulin (CRT) exposure on the cell surface under NIR light irradiation. As a marker of immunogenic cell death (ICD), CRT stimulated the antigen-presenting function of DCs. This activated a series of immune responses, including the proliferation of $CD8^+$ T cells and the secretion of cytotoxic cytokines. Chang et al. deposited plasma gold nanoparticles on CMS nanosheets to construct Cu_2MoS_4 (CMS)/Au heterostructure (Chang et al., 2020). CMS and CMS/Au can be used as catalase to effectively alleviate tumor hypoxia and enhance the therapeutic effect of O_2 dependent PDT. It was found that CMS/Au-induced PTT-PDT can induce a strong immune response by promoting dendritic cell maturation, cytokine secretion and activating the response of anti-tumor effector T cells, thereby eliminating primary and metastatic

TABLE 1 | Nanovaccines for cancer therapy.

Type	Delivery platform	Immunological effects	References
Neoantigen vaccines	HDL nanodisk	Inducing high levels of antigen-specific CTL responses.	Kuai et al. (2017)
	Acid-activatable micellar nanoparticle	Inducing interferon- β secrete and promoting the activation of T cells and neoantigens.	Zhou et al. (2020b)
	α-melittin-NP	Inducing increased activation of APCs and increased antigen-specific $CD8^+$ T cell response.	Yu et al. (2020)
	AC-NPs	Resulting in stronger activation of CD8 + T cells.	Min et al. (2017)
	NPs	Inducing DC maturation, presenting new antigens to $CD8^+$ T cells, and enhancing the effect of $CD8^+$ CTL activation.	Luo et al. (2021)
mRNA-based vaccines	RNA-LPX	Triggering plasma like DCS and macrophages to release interferon-α (IFN-α).	Kranz et al. (2016)
	LNPs	Activating CD8 T cells after single immunization.	Oberli et al. (2017)
	A2-LNPs	Inducing tumor-infiltrating antigen-specific T cells and IFN-γ strong secretion.	Miao et al. (2019)
	RNA-NPs	Activating high levels of $PDL1^+$ $CD86^+$ myeloid cells.	Sayour et al. (2018)
	C1 LNP	Inducing the expression of inflammatory cytokines by stimulating the TLR4 signaling pathway of DCs.	Zhang et al. (2021a)
Biomimetic nanobiomaterials-based nanovaccines	CPG-CCNP	Triggering T cell proliferation.	Kroll et al. (2017)
	MOF@FM	Inducing IL-6 and IFN-γ secretion.	Liu et al. (2019b)
	PLGA	Enhancing the uptake and maturation of bone marrow derived DCs.	Xiao et al. (2021)
	PEI modified macrophage membrane	Promoting antigen uptake and proliferation, and finally triggering the effective activation of T cells and strong T cell specific immune response.	Zhang et al. (2020b)
	APC-MS	Promoting the polyclonal expansion of human T cells.	Cheung et al. (2018)
	R-aAPC-IL2	Promoting the proliferation of antigen-specific CD8 + T cells and increasing the secretion of Inflammatory cytokines.	Sun et al. (2017)

tumors. Yan et al. coated the PDA nanoparticles with UCN and found that in the process of synergy, phototherapy can trigger mature DCs and then activate cytotoxic T lymphocytes cells (CTL) and T memory cells, thus inhibiting tumor metastasis and recurrence. These studies showed that the combination of PTT and PDT can obtain an ideal synergistic effect and start a strong immune response. Liu et al. reported a core shell nanoplatform for enhanced PTT/PDT in the treatment of metastatic breast cancer. The nano system is composed of photosensitizer E6 chloride (Ce6) and rapamycin (RAP) pure drug core and polydopamine (PDA) shell, with the surface is PEGylated (Liu P. et al., 2021). Both *in vitro* and *in vivo* studies showed that coloaded can sensitize PDA based PTT and Ce6 based PDT by inhibiting HSP70 and hypoxia inducible factor-1α (HIF-1α) respectively. In addition, mainly because RAP inhibits matrix metalloproteinases-2 (MMP-2), tumor metastasis is also inhibited.

Although PTT and PDT immunotherapy based on nanoparticles have been widely studied, these studies are still in the laboratory stage and face multiple challenges. For example, there are individual differences in the therapeutic effect of nanomedicines. Furthermore, *in vivo*, the immune responses induced by PTT and PDT are complicated, and their specific manifestations and mechanisms have not been fully understood.

NANOVACCINES FOR CANCER THERAPY

Cancer therapeutic vaccine is a promising class of cancer immunotherapy. However, the effect of cancer vaccines in clinical performance have not been good so far. Nanomaterials provide a unique opportunity to improve the therapeutic effect of cancer vaccines. *In vivo*, nanovaccines have the unique characteristics of improving vaccine efficiency and regulating immune responses (Irvine et al., 2013; Smith et al., 2013). Compared with traditional nano platforms, nanovaccines have some basic advantages. First, coating antigen with nano-carrier can prevent antigen degradation and improve antigen stability. Second, the co-embedding of antigen and adjuvant in nanovaccine can make the antigen and adjuvant co-deliver, thereby enhancing the immunogenicity and therapeutic effect of the vaccine. Furthermore, the multivalent presentation of surface antigens of nanovaccines allow B-cell receptor cross-linking to enhance humoral immune response (Cai et al., 2019). Nanovaccines are usually composed of antigens, molecules or nano adjuvants and/or nano carriers. At present, various nanovaccines based on nanomaterials have been studied, such as those based on cancer neoantigens, mRNA vaccines and biomimetic nanobiomaterials vaccines (**Table 1**).

Neoantigen Vaccines

Neoantigens are expressed only in tumor cells and not in any normal cells. So, these new antigens provide an opportunity to use cancer new antigen vaccine to produce a tumor-selective antitumor immune response. Kuai et al. proved that HDL simulated nanodisk binding antigen (Ag) polypeptide and adjuvant can significantly improve the codelivery of Ag/adjuvant to lymphoid organs and maintain the presentation of Ag on DCs (Kuai et al., 2017). Nanodisk-based neoantigen vaccines can induce high levels (~30%) of antigen-specific

CTL responses, especially when combined with immune checkpoint blockade, showing significant tumor therapeutic effects in mouse tumor models. STING pathway is an endogenous mechanism produced by the innate immune system, which can activate and mobilize neoantigen-specific T cells. Because of its key role in tumor immune monitoring, Zhou et al. demonstrated an acid reactive polymeric nanovaccine that activated the STING pathway and improved cancer immunotherapy (Zhou et al., 2020b). Nanovaccines effectively aggregated in lymph nodes, promoted the uptake of DCs and facilitated the release of neoantigens from the cytosol. At the same time, STING agonists activated the STING pathway in DCs and induced interferon-β secretion and promoted the activation of T cells and neoantigens. The study indicated that the development of neoantigen vaccines is particularly useful for enhancing immunity in tumor treatment. Yu et al. demonstrated a self-assembled melittin lipid nanoparticle without additional tumor antigen (α-melittin-NP) can promote the release of tumor antigen *in situ* and lead to the activation of APCs in lymph nodes (LNs) (Yu et al., 2020). Compared with free melittin, α-melittin-NPs significantly increased the activation of APCs, resulting in a 3.6-fold increase in antigen-specific $CD8^+$ T cell response. In addition, in the bilateral B16F10 tumor model, α-Melittin-NPs significantly inhibited the growth of primary and distant tumors. Min et al. found that antigen-capturing nanoparticles (AC-NPs) enhanced the presentation of tumor-derived protein antigens (TDPA) by APCs, resulting in stronger activation of $CD8^+$ T cells (Min et al., 2017). Luo et al. designed self-assembled polymer NPs with the functions of new antigen capture and self adjuvant. They found that these NPs obtain new antigens from dead cells to form self-adjuvanted molecular activator (SeaMac) nanovaccines, which finally can induce DC maturation, efficiently present new antigens to $CD8^+$ T cells, and enhance the effect of $CD8^+$ CTL activation (Luo et al., 2017).

mRNA-Based Vaccines

Combined with the ideal immune stimulation characteristics, mRNA vaccines have outstanding safety and flexibility of gene vaccine. mRNA has been investigated as an attractive vector for the delivery of tumor antigens to DCs. Kranz et al. used liposomes and mRNA to form RNA liposomes (RNA-LPX) complex (Kranz et al., 2016). LPX protected RNA from the influence of extracellular ribonuclease and triggered plasmacytoid DCs and macrophages to release interferon-α (IFN-α). A lipid nanoparticles library (LNPs) was developed by Oberli et al. for the delivery of mRNA vaccines (Oberli et al., 2017). The effectiveness of the vaccine was tested in the invasive B16F10 melanoma model. It was found that $CD8^+$ T cells were strongly activated after a single immunization. Miao et al. developed a combinatorial library of ionizable lipid-like materials to facilitate mRNA transmission *in vivo* and to provide an effective and specific immune activation (Miao et al., 2019). These results suggested that in these RNA-loaded ionizable lipid nanovaccines (LNPs), A2-LNPs induced approximately 20-fold stronger secretion of tumor-infiltrating antigen-specific T cells and IFN-γ in a B16F10 mouse melanoma model. Sayour et al. found that the non-targeted tumor RNA encapsulated in lipid NPs are derived from the whole transcriptome and carried excess positive charge, which could initiate the response of peripheral and intratumoral environment to immunotherapy (Sayour et al., 2018). In the immune-resistant tumor model, these RNA NPs activated high levels of $PDL1^+$ $CD86^+$ myeloid cells, indicating that extensive immune activation of tumor-loaded RNA-NPs, accompanied by inducible PD-L1 expression, could be used for treatment. These studies showed that mRNA nanovaccines have prospective applications in cancer immunotherapy. Zhang et al. developed a minimalist nanovaccine C1 LNP, which can effectively deliver mRNA to APCs, activate toll like receptor 4 (TLR4) and induce strong T cell activation (Zhang H. et al., 2021). In addition, C1 lipid nanoparticle itself induced the expression of inflammatory cytokines such as IL-12 by stimulating the TLR4 signaling pathway of DCs.

Biomimetic Nanobiomaterials-Based Nanovaccines

As mentioned above, the development of nanotechnology offers a unique approach to facilitate the development of nanovaccines for cancer immunotherapy. To improve the safety and effectiveness of nanovaccines, the use of biomaterials to fabricate multifunctional nanomaterials is emerging (Kang et al., 2018; Li X. et al., 2020).

In recent years, nanocarriers based on cell membrane camouflage have become a biomimetic platform for drug delivery (Guo et al., 2015). Kroll et al. encapsulated CpG adjuvant into poly (lactic-co-glycolic acid) (PLGA) nanoparticles, and then integrated with melanoma cell-derived membrane materials to develop personalized cancer nano vaccine (CpG-CCNP) (Kroll et al., 2017). After vaccination, the T cell proliferation level in the treatment group was the highest. Liu et al. demonstrated a concept of using the biological reprogramming cell membrane of fusion cells (FM) as a tumor vaccine, which was extracted from DCS and cancer cells (Liu W.-L. et al., 2019). In addition, due to the strong passive targeting ability and long cycle profile of metal-organic framework (MOF), they developed a nanovaccine (MOF@FM) using MOF as the carrier of FM. Compared with untreated control group, inoculation MOF@FM can induce increased IL-6 and IFN-γ secretion in experimental groups. Xiao et al. proposed a method for preparing biomimetic cytomembrane nanovaccines (named CCMP@R837) is encapsulated by antigenic cancer cell membrane (CCM)-capped PLGA nanoparticles loaded with imiquimod (R@837) (Xiao et al., 2021). It was found that CCMP@R837 enhanced the uptake and maturation of bone marrow derived DCs and increased the antitumor response to breast cancer 4T1 cells *in vitro*. Zhang et al. have developed a new nano vaccine, which is made by polyethyleneimine (PEI) modified macrophage membrane for co-delivery the antigen (ovalbumin, OVA) and immunostimulant (dendrobium polysaccharides, DP) (Zhang Z. et al., 2020). They found that vaccine can promote antigen uptake and proliferation, and finally trigger the effective activation of T cells and strong T cell specific immune response.

Artificial antigen-presenting cells (aAPCs) are considered as a new bionic nanovaccine which mimics the cellular function of natural APCs to induce tumor-specific immune responses, but does not need to deliver specific antigens and adjuvants required for the activation of natural APCs (Kosmides et al., 2018; Cheng et al., 2020). Cheung et al. described a system simulating natural APCs composed of liquid lipid bilayers supported by mesoporous silica micro rods (Cheung et al., 2018). It was found that APC-simulated scaffolds (APC-MS) could promote the polyclonal expansion of mouse and human T cells. In Kosmides's group, they found that aAPC can also be directly used for T cell activation *in vivo* during tumor immunotherapy (Kosmides et al., 2017). Sun et al. designed a unique aAPC system based on red blood cell (RBC) by engineering antigen polypeptide loaded main histocompatibility complex -I (MCH- I) and CD28 activated antibody on the surface of RBC, combined with interleukin-2 (IL2) as proliferation and differentiation signal (Sun et al., 2017). The RBC-based aAPC-IL2 (R-aAPC-IL2) can not only provide a flexible cell surface with appropriate biophysical parameters, but also simulate cytokine paracrine. Similar to the function of mature DCs, R-aAPC-IL2 cells can promote the proliferation of antigen-specific $CD8^+$ T cells and increase the secretion of inflammatory cytokines to kill tumor cells.

Although many encouraging achievements have been made in the field of cancer nanovaccines in recent years, there are still many challenges to be solved before their clinical transformation and application. As a key step in the development of personalized vaccines, it is still difficult to identify patient specific antigens efficiently and accurately.

NP-BASED T CELL CANCER IMMUNOTHERAPY

Adoptive cell transfer (ACT) therapy, the infusion of T cells into patients after *in vitro* amplification, has achieved remarkable success in clinical cancer treatment. In particular, chimeric antigen receptor (CAR) T cell therapy, which uses genetically engineered T cells to express tumor antigen recognition receptors, has shown impressive therapeutic effects in patients with hematological malignancies (Neelapu et al., 2017; Brudno and Kochenderfer, 2018; Shah and Fry, 2019). Adoptively transferred T cells recognize cancer cells and kill cancer cells by releasing effective cytotoxic molecules. However, T-cell therapy, including CAR T-cell therapy, has many challenges to be solved in wide application. The key challenges include: 1) Due to insufficient stimulation signals, therapeutic T cells cannot expand *in vivo* to produce a sufficient number of effector cells (Gilham et al., 2012). 2) Due to physical barriers (Caruana et al., 2015) and immunosuppressive environment (Motz et al., 2014), the transport efficiency of T cells to tumor sites is low. 3) Malignant TME leads to therapeutic T cell failure and death (Ren et al., 2017; Bollard et al., 2018). 4) Target gene mutation caused the loss of antigen expression (Hamieh et al., 2019). Among these challenges, the use of nanomaterials may be particularly beneficial to solve the shortage of T cell trafficking and overcome the inhibitory tumor microenvironment.

Schmid et al. designed a PLGA and PEG (PLGA–PEG) nanomaterial modified with antibody for programmed cell death protein 1 (anti-PD-1) to target exhausted T cells (Schmid et al., 2017). This nanomaterial loaded with TGF- β receptor inhibitor compound SD-208 successfully reversed the depletion of T cells *in vivo*. Furthermore, TGF-β delivery of signal inhibitors to PD-1 expressing cells can prolong the survival time of tumor bearing mice. Ou et al. describe the combined delivery of tLyp1 peptide modified regulatory T (Treg) cell-targeted hybrid NPs (tLyp1-hNPs) for targeting neuropilin-1 (Nrp1) receptors on Treg cells and well-known anti CTLA4 immune checkpoint inhibitors (Ou et al., 2018). The Treg cell inhibitory drug IMT was encapsulated in tLyp1-hNPs. *In vivo* studies have shown that the synergistic antibody of tLyp1-hNPs loaded with IMT and anti CTLA4 can activate the strong immune response against tumor by down regulating immunosuppressive Treg cells and activating $CD8^+$ T cells. Huang et al. reported a dual-mechanism based cytotoxic T cells (CTL) infiltration enhancer Nano-sapper, which can simultaneously reduce physical obstacles in TME and recruit CTL to enhance immunotherapy of immune-excluded tumor (IET) (Huang et al., 2020). Nano-sapper can reverse the abnormally activated fibroblasts, reduce collagen deposition, normalize the blood vessels in the tumor, and stimulate the expression of chemical attractants of recruited lymphocytes *in situ*, so as to reshape the TME.

Although T-cell cancer immunotherapy based on nanomaterials has made great progress in recent years, how to control the behavior of adoptive transfer T cells *in vivo* needs to be solved urgently.

NP-BASED BACTERIA CANCER IMMUNOTHERAPY

Bacteria based tumor immunotherapy has attracted academic attention because of its unique mechanism and rich application in triggering host anti-tumor immunity. Furthermore, it is considered that the integration of bacteria and nanomaterials for multifunctional synergistic therapy is a promising treatment (Toussaint et al., 2013). Due to the different synthetic methods and encapsulated drugs, nanomaterials can achieve a variety of functions in cancer treatment (Xu et al., 2020; Yang et al., 2020). Therefore, it seems more direct to integrate nanomaterials and other functions on the outer membrane of bacteria.

Liu et al. integrated photosensitizer-encapsulated nanoparticles on the bacterial surface through amide bonds to engineer photosynthetic bacteria (Synechococcus 7942, Syne) (Liu et al., 2020). Under 660 nm laser irradiation, Syne can continuously produce oxygen through photosynthesis, which greatly improves tumor hypoxia and produces more ROS. PDT promoted by photosynthesis not only can inhibit the growth of primary tumors, but also can reverse the TME of immune suppression to immune response, and prevent tumor recurrence even in the triple-negative breast cancer (TNBC) mouse model. Li et al. designed pathogen mimicking nano-

pathogenoids (NPNs) containing pathogen-associated molecular patterns (PAMPs) through cloaking NPs with outer-membrane vesicles (OMVs), which can be recognized by pattern recognition receptors (PRRs) on neutrophils (Li M. et al., 2020). Neutrophils move to the inflamed tumor, exude through blood vessels and penetrate the tumor. After inflammatory stimulation, neutrophils rapidly release NPN, which is then absorbed by tumor cells to exert anticancer effects. Chen et al. designed a eukaryotic–prokaryotic vesicle (EPV) nanoplatform by fusing melanoma cytomembrane vesicles (CMVs) and attenuated Salmonella OMVs (Chen et al., 2020). *In vivo* prophylactic trials have shown that EPV nanoparticles can act as a prophylactic vaccine, stimulating the immune system and triggering an anti-tumor immune response against tumorigenesis.

The biggest advantage of integrating nanomaterials on the surface of bacterial outer membrane is easy preparation and low cost, but there are also some shortcomings. First of all, if a dense and continuous shell is formed when nanomaterials are integrated on the outer membrane of bacteria, the bacteria will be completely surrounded, so as to weaken the targeting ability of bacteria. Furthermore, appropriate functions should be selected in combination with the bacterial body to produce synergistic rather than antagonistic effects.

CONCLUSION AND OUTLOOK

Over the past decades, cancer immunotherapy has achieved tremendous clinical success and become a potential mainstay therapy for cancer treatment. However, due to the low responsiveness of tumor antigens and numerous escape mechanisms in the immunosuppressive microenvironment, the clinical application of immunotherapy is frequently accompanied by low response rates, short durations, and the induction of severe immunotoxicity. The emergence of nanomedicine offers a new way of thinking for cancer immunotherapy, and plays an important role in modulating tumor immune responses. Nanomaterials can be used to modulate the tumor suppressive microenvironment by targeting immunosuppressive cells, immunosuppressive factors or effector T cells. Nanomaterials usually involve in the following roles: 1) activating cellular immunity by enhancing tumor immunogenicity and promoting antigen presentation, and 2) promoting the activation of tumor-infiltrating NK cells to achieve local activation of the immune system. NP-based PTT and PDT can lead to a large number of tumor cell deaths and trigger immune responses, including redistribution and activation of immune effector cells, expression and secretion of cytokines, and transformation of memory T lymphocytes. Furthermore, the combination of two methods can obtain ideal synergistic effect and start a strong immune response. But *in vivo*, the immune responses induced by PTT and PDT are complex, and the specific performance and mechanisms are not fully understood. Nanovaccine is another application based on NPs, which recognizes and attacks tumor cells by activating adaptive immune system, thereby triggering anti-tumor immune response. Compared with traditional nano platforms, nanovaccines have some basic advantages, such as coating antigen with nano-carrier to prevent antigen degradation, co-embedding of antigen and adjuvant to enhance the immunogenicity and therapeutic effect of the vaccine. However, there are still many challenges that need to be solved before their clinical transformation and application. As a key step of personalized vaccine development, it is still difficult to identify patient specific antigens efficiently and accurately. T-cell cancer immunotherapy based on nanomaterials has made great progress in recent years. However, how to control the behavior of adoptive transfer T cells *in vivo* needs to be solved urgently in the future. Integrating nanomaterials on the surface of bacterial outer membrane is easy preparation and low cost, but there are also some shortcomings that need to be overcome.

In summary, most nanomaterials for cancer immunotherapy are still in the experimental stage and are still far from clinical application on account of safety, reproducibility, and individual differences. In order to achieve the clinical applications of nanomaterials, it is essential to further develop nanoparticles. First, optimize the carrier materials to achieve good biodegradable and biocompatibility to provide safe drugs for clinical patients; then optimize the production process of nanomedicines to achieve high-volume production and stable quality control to provide stable drug pathways for clinical patients; third, optimize the different ratios of various drugs in combination to achieve the best therapeutic effect; optimize the targeting effect of drugs to achieve precise control of drug release and clarify the timing of activating immunotherapy. It is believed that with the development of nanotechnology and the continuous research on the mechanism of tumor immunotherapy, nanomaterials will play a powerful role in promoting tumor immunotherapy in clinical.

AUTHOR CONTRIBUTIONS

QL and YG conceived and supervised the study. QL, YL, and ZH searched the literatures, wrote the article and prepared the table. YG prepared the figures. QL revised the article. All authors are involved in the revision and approved the submitted manuscript.

FUNDING

This work was supported by the National Natural Science Foundation of China (No. 32000466) the Natural Science Foundation of Guangdong Province (No. 2019A1515111174), the Shenzhen Science and Technology Program (No. JCYJ20190808100817047, No. RCBS20200714114909234 and No. JCYJ20210324115208024), and the Basic Research Start-up Project of the Eighth Affiliated Hospital of Sun Yat-sen University (No. GCCRCYJ022).

REFERENCES

Ali, M. R. K., Ali, H. R., Rankin, C. R., and El-Sayed, M. A. (2016). Targeting Heat Shock Protein 70 Using Gold Nanorods Enhances Cancer Cell Apoptosis in Low Dose Plasmonic Photothermal Therapy. *Biomaterials* 102, 1–8. doi:10.1016/j.biomaterials.2016.06.017

Argyle, D., and Kitamura, T. (2018). Targeting Macrophage-Recruiting Chemokines as a Novel Therapeutic Strategy to Prevent the Progression of Solid Tumors. *Front. Immunol.* 9, 2629. doi:10.3389/fimmu.2018.02629

Beech, J., Shin, S., Smith, J., and Kelly, K. (2013). Mechanisms for Targeted Delivery of Nanoparticles in Cancer. *Cpd* 19 (37), 6560–6574. doi:10.2174/1381612811319370002

Bezu, L., Gomes-de-Silva, L. C., Dewitte, H., Breckpot, K., Fucikova, J., Spisek, R., et al. (2015). Combinatorial Strategies for the Induction of Immunogenic Cell Death. *Front. Immunol.* 6, 187. doi:10.3389/fimmu.2015.00187

Binnewies, M., Roberts, E. W., Kersten, K., Chan, V., Fearon, D. F., Merad, M., et al. (2018). Understanding the Tumor Immune Microenvironment (TIME) for Effective Therapy. *Nat. Med.* 24 (5), 541–550. doi:10.1038/s41591-018-0014-x

Bobo, D., Robinson, K. J., Islam, J., Thurecht, K. J., and Corrie, S. R. (2016). Nanoparticle-Based Medicines: A Review of FDA-Approved Materials and Clinical Trials to Date. *Pharm. Res.* 33 (10), 2373–2387. doi:10.1007/s11095-016-1958-5

Bollard, C. M., Tripic, T., Cruz, C. R., Dotti, G., Gottschalk, S., Torrano, V., et al. (2018). Tumor-Specific T-Cells Engineered to Overcome Tumor Immune Evasion Induce Clinical Responses in Patients with Relapsed Hodgkin Lymphoma. *Jco* 36 (11), 1128–1139. doi:10.1200/JCO.2017.74.3179

Bowyer, S., Prithviraj, P., Lorigan, P., Larkin, J., McArthur, G., Atkinson, V., et al. (2016). Efficacy and Toxicity of Treatment with the Anti-CTLA-4 Antibody Ipilimumab in Patients with Metastatic Melanoma after Prior Anti-PD-1 Therapy. *Br. J. Cancer* 114 (10), 1084–1089. doi:10.1038/bjc.2016.107

Bracci, L., Schiavoni, G., Sistigu, A., and Belardelli, F. (2014). Immune-based Mechanisms of Cytotoxic Chemotherapy: Implications for the Design of Novel and Rationale-Based Combined Treatments against Cancer. *Cell Death Differ* 21 (1), 15–25. doi:10.1038/cdd.2013.67

Brown, J. S., Sundar, R., and Lopez, J. (2018). Combining DNA Damaging Therapeutics with Immunotherapy: More Haste, Less Speed. *Br. J. Cancer* 118 (3), 312–324. doi:10.1038/bjc.2017.376

Brudno, J. N., and Kochenderfer, J. N. (2018). Chimeric Antigen Receptor T-Cell Therapies for Lymphoma. *Nat. Rev. Clin. Oncol.* 15 (1), 31–46. doi:10.1038/nrclinonc.2017.128

Cai, J., Wang, H., Wang, D., and Li, Y. (2019). Improving Cancer Vaccine Efficiency by Nanomedicine. *Adv. Biosys.* 3 (3), 1800287. doi:10.1002/adbi.201800287

Calderwood, S. K., and Gong, J. (2016). Heat Shock Proteins Promote Cancer: It's a Protection Racket. *Trends Biochem. Sci.* 41 (4), 311–323. doi:10.1016/j.tibs.2016.01.003

Caruana, I., Savoldo, B., Hoyos, V., Weber, G., Liu, H., Kim, E. S., et al. (2015). Heparanase Promotes Tumor Infiltration and Antitumor Activity of CAR-Redirected T Lymphocytes. *Nat. Med.* 21 (5), 524–529. doi:10.1038/nm.3833

Cavanaugh, A., Juengst, B., Sheridan, K., Danella, J. F., and Williams, H. (2015). Combined Inhibition of Heat Shock Proteins 90 and 70 Leads to Simultaneous Degradation of the Oncogenic Signaling Proteins Involved in Muscle Invasive Bladder Cancer. *Oncotarget* 6 (37), 39821–39838. doi:10.18632/oncotarget.5496

Chang, M., Hou, Z., Wang, M., Wang, M., Dang, P., Liu, J., et al. (2020). Cu 2 MoS 4/Au Heterostructures with Enhanced Catalase-Like Activity and Photoconversion Efficiency for Primary/Metastatic Tumors Eradication by Phototherapy-Induced Immunotherapy. *Small* 16 (14), 1907146. doi:10.1002/smll.201907146

Chatterjee, M., Andrulis, M., Stuhmer, T., Muller, E., Hofmann, C., Steinbrunn, T., et al. (2013). The PI3K/Akt Signaling Pathway Regulates the Expression of Hsp70, Which Critically Contributes to Hsp90-Chaperone Function and Tumor Cell Survival in Multiple Myeloma. *Haematologica* 98 (7), 1132–1141. doi:10.3324/haematol.2012.066175

Chen, Q., Feng, L., Liu, J., Zhu, W., Dong, Z., Wu, Y., et al. (2016). Intelligent Albumin-MnO2Nanoparticles as pH-/h2o2-Responsive Dissociable Nanocarriers to Modulate Tumor Hypoxia for Effective Combination Therapy. *Adv. Mater.* 28 (33), 7129–7136. doi:10.1002/adma.201601902

Chen, Q., Huang, G., Wu, W., Wang, J., Hu, J., Mao, J., et al. (2020). A Hybrid Eukaryotic-Prokaryotic Nanoplatform with Photothermal Modality for Enhanced Antitumor Vaccination. *Adv. Mater.* 32 (16), 1908185. doi:10.1002/adma.201908185

Chen, Q., Wang, C., Zhang, X., Chen, G., Hu, Q., Li, H., et al. (2019). *In Situ* sprayed Bioresponsive Immunotherapeutic Gel for post-surgical Cancer Treatment. *Nat. Nanotech* 14 (1), 89–97. doi:10.1038/s41565-018-0319-4

Chen, R., Wang, X., Yao, X., Zheng, X., Wang, J., and Jiang, X. (2013). Near-IR-triggered Photothermal/photodynamic Dual-Modality Therapy System via Chitosan Hybrid Nanospheres. *Biomaterials* 34 (33), 8314–8322. doi:10.1016/j.biomaterials.2013.07.034

Chen, W.-H., Luo, G.-F., Lei, Q., Hong, S., Qiu, W.-X., Liu, L.-H., et al. (2017). Overcoming the Heat Endurance of Tumor Cells by Interfering with the Anaerobic Glycolysis Metabolism for Improved Photothermal Therapy. *ACS Nano* 11 (2), 1419–1431. doi:10.1021/acsnano.6b06658

Cheng, S., Xu, C., Jin, Y., Li, Y., Zhong, C., Ma, J., et al. (2020). Artificial Mini Dendritic Cells Boost T Cell-Based Immunotherapy for Ovarian Cancer. *Adv. Sci.* 7 (7), 1903301. doi:10.1002/advs.201903301

Cheung, A. S., Zhang, D. K. Y., Koshy, S. T., and Mooney, D. J. (2018). Scaffolds that Mimic Antigen-Presenting Cells Enable *Ex Vivo* Expansion of Primary T Cells. *Nat. Biotechnol.* 36 (2), 160–169. doi:10.1038/nbt.4047

Colegio, O. R., Chu, N.-Q., Szabo, A. L., Chu, T., Rhebergen, A. M., Jairam, V., et al. (2014). Functional Polarization of Tumour-Associated Macrophages by Tumour-Derived Lactic Acid. *Nature* 513 (7519), 559–563. doi:10.1038/nature13490

Dai, Y., Xu, C., Sun, X., and Chen, X. (2017). Nanoparticle Design Strategies for Enhanced Anticancer Therapy by Exploiting the Tumour Microenvironment. *Chem. Soc. Rev.* 46 (12), 3830–3852. doi:10.1039/c6cs00592f

Dai, Z., Tang, J., Gu, Z., Wang, Y., Yang, Y., Yang, Y., et al. (2020). Eliciting Immunogenic Cell Death via a Unitized Nanoinducer. *Nano Lett.* 20 (9), 6246–6254. doi:10.1021/acs.nanolett.0c00713

Emon, B., Bauer, J., Jain, Y., Jung, B., and Saif, T. (2018). Biophysics of Tumor Microenvironment and Cancer Metastasis - A Mini Review. *Comput. Struct. Biotechnol. J.* 16, 279–287. doi:10.1016/j.csbj.2018.07.003

Fan, Y., Liu, Y., Zhang, L., Cai, F., Zhu, L., and Xu, J. (2017). C0818, a Novel Curcumin Derivative, Interacts with Hsp90 and Inhibits Hsp90 ATPase Activity. *Acta Pharmaceutica Sinica B* 7 (1), 91–96. doi:10.1016/j.apsb.2016.05.014

Fokong, S., Theek, B., Wu, Z., Koczera, P., Appold, L., Jorge, S., et al. (2012). Image-guided, Targeted and Triggered Drug Delivery to Tumors Using Polymer-Based Microbubbles. *J. Controlled Release* 163 (1), 75–81. doi:10.1016/j.jconrel.2012.05.007

Franklin, R. A., Liao, W., Sarkar, A., Kim, M. V., Bivona, M. R., Liu, K., et al. (2014). The Cellular and Molecular Origin of Tumor-Associated Macrophages. *Science* 344 (6186), 921–925. doi:10.1126/science.1252510

Gao, A., Hu, X.-l., Saeed, M., Chen, B.-f., Li, Y.-p., and Yu, H.-j. (2019). Overview of Recent Advances in Liposomal Nanoparticle-Based Cancer Immunotherapy. *Acta Pharmacol. Sin* 40 (9), 1129–1137. doi:10.1038/s41401-019-0281-1

Gao, D., Guo, X., Zhang, X., Chen, S., Wang, Y., Chen, T., et al. (2020). Multifunctional Phototheranostic Nanomedicine for Cancer Imaging and Treatment. *Mater. Today Bio* 5, 100035. doi:10.1016/j.mtbio.2019.100035

Gao, F., Zhang, C., Qiu, W.-X., Dong, X., Zheng, D.-W., Wu, W., et al. (2018). PD-1 Blockade for Improving the Antitumor Efficiency of Polymer-Doxorubicin Nanoprodrug. *Small* 14 (37), 1802403. doi:10.1002/smll.201802403

Gerlowski, L. E., and Jain, R. K. (1986). Microvascular Permeability of normal and Neoplastic Tissues. *Microvasc. Res.* 31 (3), 288–305. doi:10.1016/0026-2862(86)90018-x

Gilham, D. E., Debets, R., Pule, M., Hawkins, R. E., and Abken, H. (2012). CAR-T Cells and Solid Tumors: Tuning T Cells to challenge an Inveterate Foe. *Trends Mol. Med.* 18 (7), 377–384. doi:10.1016/j.molmed.2012.04.009

Golombek, S. K., May, J.-N., Theek, B., Appold, L., Drude, N., Kiessling, F., et al. (2018). Tumor Targeting via EPR: Strategies to Enhance Patient Responses. *Adv. Drug Deliv. Rev.* 130, 17–38. doi:10.1016/j.addr.2018.07.007

Gu, Z., Wang, Q., Shi, Y., Huang, Y., Zhang, J., Zhang, X., et al. (2018). Nanotechnology-mediated Immunochemotherapy Combined with Docetaxel and PD-L1 Antibody Increase Therapeutic Effects and Decrease Systemic Toxicity. *J. Controlled Release* 286, 369–380. doi:10.1016/j.jconrel.2018.08.011

Guo, Y., Wang, D., Song, Q., Wu, T., Zhuang, X., Bao, Y., et al. (2015). Erythrocyte Membrane-Enveloped Polymeric Nanoparticles as Nanovaccine for Induction of Antitumor Immunity against Melanoma. *ACS Nano* 9 (7), 6918–6933. doi:10.1021/acsnano.5b01042

Gupta, G., Borglum, K., and Chen, H. (2021). Immunogenic Cell Death: A Step Ahead of Autophagy in Cancer Therapy. *J. Cancer Immunol.* 3 (1), 47–59. doi:10.33696/cancerimmunol.3.041

Halama, N., Zoernig, I., Berthel, A., Kahlert, C., Klupp, F., Suarez-Carmona, M., et al. (2016). Tumoral Immune Cell Exploitation in Colorectal Cancer Metastases Can Be Targeted Effectively by Anti-CCR5 Therapy in Cancer Patients. *Cancer Cell* 29 (4), 587–601. doi:10.1016/j.ccell.2016.03.005

Hamieh, M., Dobrin, A., Cabriolu, A., van der Stegen, S. J. C., Giavridis, T., Mansilla-Soto, J., et al. (2019). CAR T Cell Trogocytosis and Cooperative Killing Regulate Tumour Antigen Escape. *Nature* 568 (7750), 112–116. doi:10.1038/s41586-019-1054-1

Han, X., Cheng, K., Xu, Y., Wang, Y., Min, H., Zhang, Y., et al. (2020). Modularly Designed Peptide Nanoprodrug Augments Antitumor Immunity of PD-L1 Checkpoint Blockade by Targeting Indoleamine 2,3-Dioxygenase. *J. Am. Chem. Soc.* 142 (5), 2490–2496. doi:10.1021/jacs.9b12232

Horowitz, M., and Robinson, S. D. M. (2007). Heat Shock Proteins and the Heat Shock Response during Hyperthermia and its Modulation by Altered Physiological Conditions. *Prog. Brain Res.* 162, 433–446. doi:10.1016/S0079-6123(06)62021-9

Hu, Y., Chi, C., Wang, S., Wang, L., Liang, P., Liu, F., et al. (2017). A Comparative Study of Clinical Intervention and Interventional Photothermal Therapy for Pancreatic Cancer. *Adv. Mater.* 29 (33), 1700448. doi:10.1002/adma.201700448

Huang, Y., Chen, Y., Zhou, S., Chen, L., Wang, J., Pei, Y., et al. (2020). Dual-mechanism Based CTLs Infiltration Enhancement Initiated by Nano-Sapper Potentiates Immunotherapy against Immune-Excluded Tumors. *Nat. Commun.* 11 (1), 622. doi:10.1038/s41467-020-14425-7

Irvine, D. J., Swartz, M. A., and Szeto, G. L. (2013). Engineering Synthetic Vaccines Using Cues from Natural Immunity. *Nat. Mater* 12 (11), 978–990. doi:10.1038/nmat3775

Jego, G., Hazoumé, A., Seigneuric, R., and Garrido, C. (2013). Targeting Heat Shock Proteins in Cancer. *Cancer Lett.* 332 (2), 275–285. doi:10.1016/j.canlet.2010.10.014

Joyce, J. A., and Fearon, D. T. (2015). T Cell Exclusion, Immune Privilege, and the Tumor Microenvironment. *Science* 348 (6230), 74–80. doi:10.1126/science.aaa6204

June, C. H., Kawalekar, O. U., Ghassemi, S., and Milone, M. C. (2018). CAR T Cell Immunotherapy for Human Cancer. *Science* 359 (6382), 1361–1365. doi:10.1126/science.aar6711,

Kadiyala, P., Li, D., Nuñez, F. M., Altshuler, D., Doherty, R., Kuai, R., et al. (2019). High-Density Lipoprotein-Mimicking Nanodiscs for Chemo-Immunotherapy against Glioblastoma Multiforme. *ACS Nano* 13 (2), 1365–1384. doi:10.1021/acsnano.8b06842

Kang, T., Huang, Y., Zhu, Q., Cheng, H., Pei, Y., Feng, J., et al. (2018). Necroptotic Cancer Cells-Mimicry Nanovaccine Boosts Anti-tumor Immunity with Tailored Immune-Stimulatory Modality. *Biomaterials* 164, 80–97. doi:10.1016/j.biomaterials.2018.02.033

Kosmides, A. K., Meyer, R. A., Hickey, J. W., Aje, K., Cheung, K. N., Green, J. J., et al. (2017). Biomimetic Biodegradable Artificial Antigen Presenting Cells Synergize with PD-1 Blockade to Treat Melanoma. *Biomaterials* 118, 16–26. doi:10.1016/j.biomaterials.2016.11.038

Kosmides, A. K., Necochea, K., Hickey, J. W., and Schneck, J. P. (2018). Separating T Cell Targeting Components onto Magnetically Clustered Nanoparticles Boosts Activation. *Nano Lett.* 18 (3), 1916–1924. doi:10.1021/acs.nanolett.7b05284

Kranz, L. M., Diken, M., Haas, H., Kreiter, S., Loquai, C., Reuter, K. C., et al. (2016). Systemic RNA Delivery to Dendritic Cells Exploits Antiviral Defence for Cancer Immunotherapy. *Nature* 534 (7607), 396–401. doi:10.1038/nature18300

Kroll, A. V., Fang, R. H., Jiang, Y., Zhou, J., Wei, X., Yu, C. L., et al. (2017). Nanoparticulate Delivery of Cancer Cell Membrane Elicits Multiantigenic Antitumor Immunity. *Adv. Mater.* 29 (47), 1703969. doi:10.1002/adma.201703969

Krysko, D. V., Garg, A. D., Kaczmarek, A., Krysko, O., Agostinis, P., and Vandenabeele, P. (2012). Immunogenic Cell Death and DAMPs in Cancer Therapy. *Nat. Rev. Cancer* 12 (12), 860–875. doi:10.1038/nrc3380

Kuai, R., Ochyl, L. J., Bahjat, K. S., Schwendeman, A., and Moon, J. J. (2017). Designer Vaccine Nanodiscs for Personalized Cancer Immunotherapy. *Nat. Mater* 16 (4), 489–496. doi:10.1038/nmat4822

Kuai, R., Yuan, W., Son, S., Nam, J., Xu, Y., Fan, Y., et al. (2018). Elimination of Established Tumors with Nanodisc-Based Combination Chemoimmunotherapy. *Sci. Adv.* 4 (4), eaao1736. doi:10.1126/sciadv.aao1736

Kulkarni, A., Chandrasekar, V., Natarajan, S. K., Ramesh, A., Pandey, P., Nirgud, J., et al. (2018). A Designer Self-Assembled Supramolecule Amplifies Macrophage Immune Responses against Aggressive Cancer. *Nat. Biomed. Eng.* 2 (8), 589–599. doi:10.1038/s41551-018-0254-6

Lammers, T., Kiessling, F., Ashford, M., Hennink, W., Crommelin, D., and Storm, G. (2016). Cancer Nanomedicine: Is Targeting Our Target? *Nat. Rev. Mater.* 1 (9), 16069. doi:10.1038/natrevmats.2016.69

Lammers, T., Kiessling, F., Hennink, W. E., and Storm, G. (2012). Drug Targeting to Tumors: Principles, Pitfalls and (Pre-) Clinical Progress. *J. Controlled Release* 161 (2), 175–187. doi:10.1016/j.jconrel.2011.09.063

Li, F., Nie, W., Zhang, F., Lu, G., Lv, C., Lv, Y., et al. (2019a). Engineering Magnetosomes for High-Performance Cancer Vaccination. *ACS Cent. Sci.* 5 (5), 796–807. doi:10.1021/acscentsci.9b00060

Li, H., Guo, S., Cai, L., Ma, W., and Shi, Z. (2017a). Lipopolysaccharide and Heat Stress Impair the Estradiol Biosynthesis in Granulosa Cells via Increase of HSP70 and Inhibition of Smad3 Phosphorylation and Nuclear Translocation. *Cell Signal.* 30, 130–141. doi:10.1016/j.cellsig.2016.12.004

Li, M., Li, S., Zhou, H., Tang, X., Wu, Y., Jiang, W., et al. (2020a). Chemotaxis-driven Delivery of Nano-Pathogenoids for Complete Eradication of Tumors post-phototherapy. *Nat. Commun.* 11 (1), 1126. doi:10.1038/s41467-020-14963-0

Li, W., Yang, J., Luo, L., Jiang, M., Qin, B., Yin, H., et al. (2019b). Targeting Photodynamic and Photothermal Therapy to the Endoplasmic Reticulum Enhances Immunogenic Cancer Cell Death. *Nat. Commun.* 10 (1), 3349. doi:10.1038/s41467-019-11269-8

Li, X., Cai, X., Zhang, Z., Ding, Y., Ma, R., Huang, F., et al. (2020b). Mimetic Heat Shock Protein Mediated Immune Process to Enhance Cancer Immunotherapy. *Nano Lett.* 20 (6), 4454–4463. doi:10.1021/acs.nanolett.0c01230

Li, X., Zhao, Q., and Qiu, L. (2013). Smart Ligand: Aptamer-Mediated Targeted Delivery of Chemotherapeutic Drugs and siRNA for Cancer Therapy. *J. Controlled Release* 171 (2), 152–162. doi:10.1016/j.jconrel.2013.06.006

Li, Z., Tan, S., Li, S., Shen, Q., and Wang, K. (2017b). Cancer Drug Delivery in the Nano Era: An Overview and Perspectives. *Oncol. Rep.* 38 (2), 611–624. doi:10.3892/or.2017.5718

Liang, R., Liu, L., He, H., Chen, Z., Han, Z., Luo, Z., et al. (2018). Oxygen-boosted Immunogenic Photodynamic Therapy with Gold Nanocages@manganese Dioxide to Inhibit Tumor Growth and Metastases. *Biomaterials* 177, 149–160. doi:10.1016/j.biomaterials.2018.05.051

Lin, T.-y., Guo, W., Long, Q., Ma, A., Liu, Q., Zhang, H., et al. (2016). HSP90 Inhibitor Encapsulated Photo-Theranostic Nanoparticles for Synergistic Combination Cancer Therapy. *Theranostics* 6 (9), 1324–1335. doi:10.7150/thno.14882

Lindau, D., Gielen, P., Kroesen, M., Wesseling, P., and Adema, G. J. (2013). The Immunosuppressive Tumour Network: Myeloid-Derived Suppressor Cells, Regulatory T Cells and Natural Killer T Cells. *Immunology* 138 (2), 105–115. doi:10.1111/imm.12036

Liu, H., Hu, Y., Sun, Y., Wan, C., Zhang, Z., Dai, X., et al. (2019a). Co-delivery of Bee Venom Melittin and a Photosensitizer with an Organic-Inorganic Hybrid Nanocarrier for Photodynamic Therapy and Immunotherapy. *ACS Nano* 13 (11), 12638–12652. doi:10.1021/acsnano.9b04181

Liu, L., He, H., Luo, Z., Zhou, H., Liang, R., Pan, H., et al. (2020). *In Situ* Photocatalyzed Oxygen Generation with Photosynthetic Bacteria to Enable Robust Immunogenic Photodynamic Therapy in Triple-Negative Breast Cancer. *Adv. Funct. Mater.* 30 (10), 1910176. doi:10.1002/adfm.201910176

Liu, P., Peng, Y., Zhou, Y., Shi, X., Li, Q., Ding, J., et al. (2021a). Rapamycin as a "One-Stone-Three-Birds" Agent for Cooperatively Enhanced Phototherapies against Metastatic Breast Cancer. *ACS Appl. Mater. Inter.* 13 (22), 25674–25684. doi:10.1021/acsami.1c03312

Liu, W.-L., Zou, M.-Z., Liu, T., Zeng, J.-Y., Li, X., Yu, W.-Y., et al. (2019b). Cytomembrane Nanovaccines Show Therapeutic Effects by Mimicking Tumor Cells and Antigen Presenting Cells. *Nat. Commun.* 10 (1), 3199. doi:10.1038/s41467-019-11157-1

Liu, Y., Maccarini, P., Palmer, G. M., Etienne, W., Zhao, Y., Lee, C.-T., et al. (2017). Synergistic Immuno Photothermal Nanotherapy (SYMPHONY) for the Treatment of Unresectable and Metastatic Cancers. *Sci. Rep.* 7 (1), 8606. doi:10.1038/s41598-017-09116-1

Liu, Y., Tan, M., Fang, C., Chen, X., Liu, H., Feng, Y., et al. (2021b). A Novel Multifunctional Gold Nanorod-Mediated and Tumor-Targeted Gene Silencing of GPC-3 Synergizes Photothermal Therapy for Liver Cancer. *Nanotechnology* 32 (17), 175101. doi:10.1088/1361-6528/abdbed

Liu, Y., Xu, M., Zhao, Y., Chen, X., Zhu, X., Wei, C., et al. (2019c). Flower-like Gold Nanoparticles for Enhanced Photothermal Anticancer Therapy by the Delivery of Pooled siRNA to Inhibit Heat Shock Stress Response. *J. Mater. Chem. B* 7 (4), 586–597. doi:10.1039/c8tb02418a

Lu, J., Liu, X., Liao, Y.-P., Salazar, F., Sun, B., Jiang, W., et al. (2017). Nano-enabled Pancreas Cancer Immunotherapy Using Immunogenic Cell Death and Reversing Immunosuppression. *Nat. Commun.* 8 (1), 1811. doi:10.1038/s41467-017-01651-9

Luo, M., Wang, H., Wang, Z., Cai, H., Lu, Z., Li, Y., et al. (2017). A STING-Activating Nanovaccine for Cancer Immunotherapy. *Nat. Nanotech* 12 (7), 648–654. doi:10.1038/nnano.2017.52

Luo, Z., He, T., Liu, P., Yi, Z., Zhu, S., Liang, X., et al. (2021). Self-Adjuvanted Molecular Activator (SeaMac) Nanovaccines Promote Cancer Immunotherapy. *Adv. Healthc. Mater.* 10 (7), 2002080. doi:10.1002/adhm.202002080

Ma, S., Zhou, J., Zhang, Y., Yang, B., He, Y., Tian, C., et al. (2019). An Oxygen Self-Sufficient Fluorinated Nanoplatform for Relieved Tumor Hypoxia and Enhanced Photodynamic Therapy of Cancers. *ACS Appl. Mater. Inter.* 11 (8), 7731–7742. doi:10.1021/acsami.8b19840

Maeda, H., Wu, J., Sawa, T., Matsumura, Y., and Hori, K. (2000). Tumor Vascular Permeability and the EPR Effect in Macromolecular Therapeutics: a Review. *J. Control. Release* 65 (1-2), 271–284. doi:10.1016/s0168-3659(99)00248-5

Mariathasan, S., Turley, S. J., Nickles, D., Castiglioni, A., Yuen, K., Wang, Y., et al. (2018). TGFβ Attenuates Tumour Response to PD-L1 Blockade by Contributing to Exclusion of T Cells. *Nature* 554 (7693), 544–548. doi:10.1038/nature25501

Martin, J. D., Cabral, H., Stylianopoulos, T., and Jain, R. K. (2020). Improving Cancer Immunotherapy Using Nanomedicines: Progress, Opportunities and Challenges. *Nat. Rev. Clin. Oncol.* 17 (4), 251–266. doi:10.1038/s41571-019-0308-z

Matsumura, Y., and Maeda, H. (1986). A New Concept for Macromolecular Therapeutics in Cancer Chemotherapy: Mechanism of Tumoritropic Accumulation of Proteins and the Antitumor Agent Smancs. *Cancer Res.* 46 (12 Pt 1), 6387–6392.

Mi, P., Cabral, H., and Kataoka, K. (2020). Ligand-Installed Nanocarriers toward Precision Therapy. *Adv. Mater.* 32 (13), 1902604. doi:10.1002/adma.201902604

Miao, L., Li, L., Huang, Y., Delcassian, D., Chahal, J., Han, J., et al. (2019). Delivery of mRNA Vaccines with Heterocyclic Lipids Increases Anti-tumor Efficacy by STING-Mediated Immune Cell Activation. *Nat. Biotechnol.* 37 (10), 1174–1185. doi:10.1038/s41587-019-0247-3

Milling, L., Zhang, Y., and Irvine, D. J. (2017). Delivering Safer Immunotherapies for Cancer. *Adv. Drug Deliv. Rev.* 114, 79–101. doi:10.1016/j.addr.2017.05.011

Min, Y., Roche, K. C., Tian, S., Eblan, M. J., McKinnon, K. P., Caster, J. M., et al. (2017). Antigen-capturing Nanoparticles Improve the Abscopal Effect and Cancer Immunotherapy. *Nat. Nanotech* 12 (9), 877–882. doi:10.1038/nnano.2017.113

Morachis, J. M., Mahmoud, E. A., Sankaranarayanan, J., and Almutairi, A. (2012). Triggered Rapid Degradation of Nanoparticles for Gene Delivery. *J. Drug Deliv.* 2012, 1–7. doi:10.1155/2012/291219

Motz, G. T., Santoro, S. P., Wang, L.-P., Garrabrant, T., Lastra, R. R., Hagemann, I. S., et al. (2014). Tumor Endothelium FasL Establishes a Selective Immune Barrier Promoting Tolerance in Tumors. *Nat. Med.* 20 (6), 607–615. doi:10.1038/nm.3541

Neelapu, S. S., Locke, F. L., Bartlett, N. L., Lekakis, L. J., Miklos, D. B., Jacobson, C. A., et al. (2017). Axicabtagene Ciloleucel CAR T-Cell Therapy in Refractory Large B-Cell Lymphoma. *N. Engl. J. Med.* 377 (26), 2531–2544. doi:10.1056/NEJMoa1707447

Oberli, M. A., Reichmuth, A. M., Dorkin, J. R., Mitchell, M. J., Fenton, O. S., Jaklenec, A., et al. (2017). Lipid Nanoparticle Assisted mRNA Delivery for Potent Cancer Immunotherapy. *Nano Lett.* 17 (3), 1326–1335. doi:10.1021/acs.nanolett.6b03329

Ou, W., Thapa, R. K., Jiang, L., Soe, Z. C., Gautam, M., Chang, J.-H., et al. (2018). Regulatory T Cell-Targeted Hybrid Nanoparticles Combined with Immuno-Checkpoint Blockage for Cancer Immunotherapy. *J. Controlled Release* 281, 84–96. doi:10.1016/j.jconrel.2018.05.018

Park, J., Wrzesinski, S. H., Stern, E., Look, M., Criscione, J., Ragheb, R., et al. (2012). Combination Delivery of TGF-β Inhibitor and IL-2 by Nanoscale Liposomal Polymeric Gels Enhances Tumour Immunotherapy. *Nat. Mater* 11 (10), 895–905. doi:10.1038/nmat3355

Park, W., Cho, S., Han, J., Shin, H., Na, K., Lee, B., et al. (2017). Advanced Smart-Photosensitizers for More Effective Cancer Treatment. *Biomater. Sci.* 6 (1), 79–90. doi:10.1039/c7bm00872d

Peer, D., Karp, J. M., Hong, S., Farokhzad, O. C., Margalit, R., and Langer, R. (2007). Nanocarriers as an Emerging Platform for Cancer Therapy. *Nat. Nanotech* 2 (12), 751–760. doi:10.1038/nnano.2007.387

Predina, J., Eruslanov, E., Judy, B., Kapoor, V., Cheng, G., Wang, L.-C., et al. (2013). Changes in the Local Tumor Microenvironment in Recurrent Cancers May Explain the Failure of Vaccines after Surgery. *Proc. Natl. Acad. Sci. U.S.A.* 110 (5), E415–E424. doi:10.1073/pnas.1211850110

Pusuluri, A., Wu, D., and Mitragotri, S. (2019). Immunological Consequences of Chemotherapy: Single Drugs, Combination Therapies and Nanoparticle-Based Treatments. *J. Controlled Release* 305, 130–154. doi:10.1016/j.jconrel.2019.04.020

Ren, J., Liu, X., Fang, C., Jiang, S., June, C. H., and Zhao, Y. (2017). Multiplex Genome Editing to Generate Universal CAR T Cells Resistant to PD1 Inhibition. *Clin. Cancer Res.* 23 (9), 2255–2266. doi:10.1158/1078-0432.CCR-16-1300

Ribas, A., and Wolchok, J. D. (2018). Cancer Immunotherapy Using Checkpoint Blockade. *Science* 359 (6382), 1350–1355. doi:10.1126/science.aar4060

Rios-Doria, J., Durham, N., Wetzel, L., Rothstein, R., Chesebrough, J., Holoweckyj, N., et al. (2015). Doxil Synergizes with Cancer Immunotherapies to Enhance Antitumor Responses in Syngeneic Mouse Models. *Neoplasia* 17 (8), 661–670. doi:10.1016/j.neo.2015.08.004

Rosenberg, S. A. (2005). Cancer Immunotherapy Comes of Age. *Nat. Rev. Clin. Oncol.* 2 (3), 115. doi:10.1038/ncponc0101

Ruffell, B., Affara, N. I., and Coussens, L. M. (2012). Differential Macrophage Programming in the Tumor Microenvironment. *Trends Immunol.* 33 (3), 119–126. doi:10.1016/j.it.2011.12.001

Saeed, M., Gao, J., Shi, Y., Lammers, T., and Yu, H. (2019). Engineering Nanoparticles to Reprogram the Tumor Immune Microenvironment for Improved Cancer Immunotherapy. *Theranostics* 9 (26), 7981–8000. doi:10.7150/thno.37568

Saneja, A., Kumar, R., Arora, D., Kumar, S., Panda, A. K., and Jaglan, S. (2018). Recent Advances in Near-Infrared Light-Responsive Nanocarriers for Cancer Therapy. *Drug Discov. Today* 23 (5), 1115–1125. doi:10.1016/j.drudis.2018.02.005

Sang, W., Zhang, Z., Dai, Y., and Chen, X. (2019). Recent Advances in Nanomaterial-Based Synergistic Combination Cancer Immunotherapy. *Chem. Soc. Rev.* 48 (14), 3771–3810. doi:10.1039/c8cs00896e

Sayour, E. J., Grippin, A., De Leon, G., Stover, B., Rahman, M., Karachi, A., et al. (2018). Personalized Tumor RNA Loaded Lipid-Nanoparticles Prime the Systemic and Intratumoral Milieu for Response to Cancer Immunotherapy. *Nano Lett.* 18 (10), 6195–6206. doi:10.1021/acs.nanolett.8b02179

Schmid, D., Park, C. G., Hartl, C. A., Subedi, N., Cartwright, A. N., Puerto, R. B., et al. (2017). T Cell-Targeting Nanoparticles Focus Delivery of Immunotherapy to Improve Antitumor Immunity. *Nat. Commun.* 8 (1), 1747. doi:10.1038/s41467-017-01830-8

Schultz, L., and Mackall, C. (2019). Driving CAR T Cell Translation Forward. *Sci. Transl. Med.* 11 (481), eaaw2127. doi:10.1126/scitranslmed.aaw2127

Schumacher, T. N., Scheper, W., and Kvistborg, P. (2019). Cancer Neoantigens. *Annu. Rev. Immunol.* 37, 173–200. doi:10.1146/annurev-immunol-042617-053402

Shae, D., Becker, K. W., Christov, P., Yun, D. S., Lytton-Jean, A. K. R., Sevimli, S., et al. (2019). Endosomolytic Polymersomes Increase the Activity of Cyclic Dinucleotide STING Agonists to Enhance Cancer Immunotherapy. *Nat. Nanotechnol.* 14 (3), 269–278. doi:10.1038/s41565-018-0342-5

Shah, N. N., and Fry, T. J. (2019). Mechanisms of Resistance to CAR T Cell Therapy. *Nat. Rev. Clin. Oncol.* 16 (6), 372–385. doi:10.1038/s41571-019-0184-6

Sharma, P., and Allison, J. P. (2015). The Future of Immune Checkpoint Therapy. *Science* 348 (6230), 56–61. doi:10.1126/science.aaa8172

Shen, S., Zhang, Y., Chen, K.-G., Luo, Y.-L., and Wang, J. (2018). Cationic Polymeric Nanoparticle Delivering CCR2 siRNA to Inflammatory Monocytes for Tumor Microenvironment Modification and Cancer Therapy. *Mol. Pharmaceutics* 15 (9), 3642–3653. doi:10.1021/acs.molpharmaceut.7b00997

Shin, S. J., Beech, J. R., and Kelly, K. A. (2013). Targeted Nanoparticles in Imaging: Paving the Way for Personalized Medicine in the Battle against Cancer. *Integr. Biol. (Camb)* 5 (1), 29–42. doi:10.1039/c2ib20047c

Sindhwani, S., Syed, A. M., Ngai, J., Kingston, B. R., Maiorino, L., Rothschild, J., et al. (2020). The Entry of Nanoparticles into Solid Tumours. *Nat. Mater.* 19 (5), 566–575. doi:10.1038/s41563-019-0566-2

Smith, D. M., Simon, J. K., and Baker Jr, J. R., Jr. (2013). Applications of Nanotechnology for Immunology. *Nat. Rev. Immunol.* 13 (8), 592–605. doi:10.1038/nri3488

Sun, Q., Barz, M., De Geest, B. G., Diken, M., Hennink, W. E., Kiessling, F., et al. (2019). Nanomedicine and Macroscale Materials in Immuno-Oncology. *Chem. Soc. Rev.* 48 (1), 351–381. doi:10.1039/c8cs00473k

Sun, X., Han, X., Xu, L., Gao, M., Xu, J., Yang, R., et al. (2017). Surface-Engineering of Red Blood Cells as Artificial Antigen Presenting Cells Promising for Cancer Immunotherapy. *Small* 13 (40), 1701864. doi:10.1002/smll.201701864

Sung, H., Ferlay, J., Siegel, R. L., Laversanne, M., Soerjomataram, I., Jemal, A., et al. (2021). Global Cancer Statistics 2020: GLOBOCAN Estimates of Incidence and Mortality Worldwide for 36 Cancers in 185 Countries. *CA A. Cancer J. Clin.* 71 (3), 209–249. doi:10.3322/caac.21660

Tang, X., Tan, L., Shi, K., Peng, J., Xiao, Y., Li, W., et al. (2018). Gold Nanorods Together with HSP Inhibitor-VER-155008 Micelles for colon Cancer Mild-Temperature Photothermal Therapy. *Acta Pharmaceutica Sinica B* 8 (4), 587–601. doi:10.1016/j.apsb.2018.05.011

Tauriello, D. V. F., Palomo-Ponce, S., Stork, D., Berenguer-Llergo, A., Badia-Ramentol, J., Iglesias, M., et al. (2018). TGFβ Drives Immune Evasion in Genetically Reconstituted colon Cancer Metastasis. *Nature* 554 (7693), 538–543. doi:10.1038/nature25492

Toussaint, B., Chauchet, X., Wang, Y., Polack, B., and Gouëllec, A. L. (2013). Live-attenuated Bacteria as a Cancer Vaccine Vector. *Expert Rev. Vaccin.* 12 (10), 1139–1154. doi:10.1586/14760584.2013.836914

Trac, N., Chen, L.-Y., Zhang, A., Liao, C.-P., Poon, C., Wang, J., et al. (2021). CCR2-targeted Micelles for Anti-cancer Peptide Delivery and Immune Stimulation. *J. Controlled Release* 329, 614–623. doi:10.1016/j.jconrel.2020.09.054

Wang, B.-K., Yu, X.-F., Wang, J.-H., Li, Z.-B., Li, P.-H., Wang, H., et al. (2016). Gold-nanorods-siRNA Nanoplex for Improved Photothermal Therapy by Gene Silencing. *Biomaterials* 78, 27–39. doi:10.1016/j.biomaterials.2015.11.025

Wang, C., Wen, D., and Gu, Z. (2018). Cellular Bioparticulates with Therapeutics for Cancer Immunotherapy. *Bioconjug. Chem.* 29 (3), 702–708. doi:10.1021/acs.bioconjchem.7b00619

Wang, J., Mei, T., Liu, Y., Zhang, Y., Zhang, Z., Hu, Y., et al. (2021). Dual-targeted and MRI-Guided Photothermal Therapy via Iron-Based Nanoparticles-Incorporated Neutrophils. *Biomater. Sci.* 9 (11), 3968–3978. doi:10.1039/d1bm00127b

Woodman, C., Vundu, G., George, A., and Wilson, C. M. (2021). Applications and Strategies in Nanodiagnosis and Nanotherapy in Lung Cancer. *Semin. Cancer Biol.* 69, 349–364. doi:10.1016/j.semcancer.2020.02.009

Wu, J., Bremner, D. H., Niu, S., Shi, M., Wang, H., Tang, R., et al. (2018). Chemodrug-Gated Biodegradable Hollow Mesoporous Organosilica Nanotheranostics for Multimodal Imaging-Guided Low-Temperature Photothermal Therapy/Chemotherapy of Cancer. *ACS Appl. Mater. Inter.* 10 (49), 42115–42126. doi:10.1021/acsami.8b16448

Wu, J., Cai, X., Williams, G. R., Meng, Z., Zou, W., Yao, L., et al. (2022). 2D Antimonene-Integrated Composite Nanomedicine for Augmented Low-Temperature Photonic Tumor Hyperthermia by Reversing Cell Thermoresistance. *Bioactive Mater.* 10, 295–305. doi:10.1016/j.bioactmat.2021.08.018

Wu, X., Yang, H., Chen, X., Gao, J., Duan, Y., Wei, D., et al. (2021). Nano-herb Medicine and PDT Induced Synergistic Immunotherapy for colon Cancer Treatment. *Biomaterials* 269, 120654. doi:10.1016/j.biomaterials.2021.120654

Xiao, L., Huang, Y., Yang, Y., Miao, Z., Zhu, J., Zhong, M., et al. (2021). Biomimetic Cytomembrane Nanovaccines Prevent Breast Cancer Development in the Long Term. *Nanoscale* 13 (6), 3594–3601. doi:10.1039/d0nr08978h

Xing, L., Gong, J.-H., Wang, Y., Zhu, Y., Huang, Z.-J., Zhao, J., et al. (2019). Hypoxia Alleviation-Triggered Enhanced Photodynamic Therapy in Combination with Ido Inhibitor for Preferable Cancer Therapy. *Biomaterials* 206, 170–182. doi:10.1016/j.biomaterials.2019.03.027

Xiong, W., Qi, L., Jiang, N., Zhao, Q., Chen, L., Jiang, X., et al. (2021). Metformin Liposome-Mediated PD-L1 Downregulation for Amplifying the Photodynamic Immunotherapy Efficacy. *ACS Appl. Mater. Inter.* 13 (7), 8026–8041. doi:10.1021/acsami.0c21743

Xu, F., Li, X., Huang, X., Pan, J., Wang, Y., and Zhou, S. (2020). Development of a pH-Responsive Polymersome Inducing Endoplasmic Reticulum Stress and Autophagy Blockade. *Sci. Adv.* 6 (31), eabb8725. doi:10.1126/sciadv.abb8725

Xu, Z., Wang, Y., Zhang, L., and Huang, L. (2014). Nanoparticle-Delivered Transforming Growth Factor-β siRNA Enhances Vaccination against Advanced Melanoma by Modifying Tumor Microenvironment. *ACS Nano* 8 (4), 3636–3645. doi:10.1021/nn500216y

Yan, M., Liu, Y., Zhu, X., Wang, X., Liu, L., Sun, H., et al. (2019). Nanoscale Reduced Graphene Oxide-Mediated Photothermal Therapy Together with Ido Inhibition and PD-L1 Blockade Synergistically Promote Antitumor Immunity. *ACS Appl. Mater. Inter.* 11 (2), 1876–1885. doi:10.1021/acsami.8b18751

Yang, G., Xu, L., Chao, Y., Xu, J., Sun, X., Wu, Y., et al. (2017a). Hollow MnO2 as a Tumor-Microenvironment-Responsive Biodegradable Nano-Platform for Combination Therapy Favoring Antitumor Immune Responses. *Nat. Commun.* 8 (1), 902. doi:10.1038/s41467-017-01050-0

Yang, W., Lyu, Q., Zhao, J., Cao, L., Hao, Y., and Zhang, H. (2020). Recent advance in Near-Infrared/ultrasound-Sensitive 2D-Nanomaterials for Cancer Therapeutics. *Sci. China Mater.* 63 (12), 2397–2428. doi:10.1007/s40843-020-1387-7

Yang, Y., Zhu, W., Dong, Z., Chao, Y., Xu, L., Chen, M., et al. (2017b). 1D Coordination Polymer Nanofibers for Low-Temperature Photothermal Therapy. *Adv. Mater.* 29 (40), 1703588. doi:10.1002/adma.201703588

Yu, N., Ding, M., and Li, J. (2021). Near-Infrared Photoactivatable Immunomodulatory Nanoparticles for Combinational Immunotherapy of Cancer. *Front. Chem.* 9, 701427. doi:10.3389/fchem.2021.701427

Yu, X., Dai, Y., Zhao, Y., Qi, S., Liu, L., Lu, L., et al. (2020). Melittin-lipid Nanoparticles Target to Lymph Nodes and Elicit a Systemic Anti-tumor Immune Response. *Nat. Commun.* 11 (1), 1110. doi:10.1038/s41467-020-14906-9

Yuan, H., Jiang, W., von Roemeling, C. A., Qie, Y., Liu, X., Chen, Y., et al. (2017). Multivalent Bi-specific Nanobioconjugate Engager for Targeted Cancer Immunotherapy. *Nat. Nanotech* 12 (8), 763–769. doi:10.1038/nnano.2017.69

Zhang, B., Hu, Y., and Pang, Z. (2017a). Modulating the Tumor Microenvironment to Enhance Tumor Nanomedicine Delivery. *Front. Pharmacol.* 8, 952. doi:10.3389/fphar.2017.00952

Zhang, H., Jiang, W., Liu, R., Zhang, J., Zhang, D., Li, Z., et al. (2017b). Rational Design of Metal Organic Framework Nanocarrier-Based Codelivery System of Doxorubicin Hydrochloride/Verapamil Hydrochloride for Overcoming Multidrug Resistance with Efficient Targeted Cancer Therapy. *ACS Appl. Mater. Inter.* 9 (23), 19687–19697. doi:10.1021/acsami.7b05142

Zhang, H., You, X., Wang, X., Cui, L., Wang, Z., Xu, F., et al. (2021a). Delivery of mRNA Vaccine with a Lipid-like Material Potentiates Antitumor Efficacy through Toll-like Receptor 4 Signaling. *Proc. Natl. Acad. Sci. U.S.A.* 118 (6), e2005191118. doi:10.1073/pnas.2005191118

Zhang, X., Detering, L., Sultan, D., Luehmann, H., Li, L., Heo, G. S., et al. (2021b). CC Chemokine Receptor 2-Targeting Copper Nanoparticles for Positron Emission Tomography-Guided Delivery of Gemcitabine for Pancreatic Ductal Adenocarcinoma. *ACS Nano* 15 (1), 1186–1198. doi:10.1021/acsnano.0c08185

Zhang, Y., Lv, F., Cheng, Y., Yuan, Z., Yang, F., Liu, C., et al. (2020a). Pd@Au Bimetallic Nanoplates Decorated Mesoporous MnO 2 for Synergistic Nucleus-Targeted NIR-II Photothermal and Hypoxia-Relieved Photodynamic Therapy. *Adv. Healthc. Mater.* 9 (2), 1901528. doi:10.1002/adhm.201901528

Zhang, Y., Wang, F., Liu, C., Wang, Z., Kang, L., Huang, Y., et al. (2018). Nanozyme Decorated Metal-Organic Frameworks for Enhanced Photodynamic Therapy. *ACS Nano* 12 (1), 651–661. doi:10.1021/acsnano.7b07746

Zhang, Z., Li, D., Li, X., Guo, Z., Liu, Y., Ma, X., et al. (2020b). PEI-modified Macrophage Cell Membrane-Coated PLGA Nanoparticles Encapsulating Dendrobium Polysaccharides as a Vaccine Delivery System for Ovalbumin to Improve Immune Responses. *Int. J. Biol. Macromolecules* 165 (Pt A), 239–248. doi:10.1016/j.ijbiomac.2020.09.187

Zhang, Z., Zhang, J., Tian, J., and Li, H. (2021c). A Polydopamine Nanomedicine Used in Photothermal Therapy for Liver Cancer Knocks Down the Anti-cancer Target NEDD8-E3 Ligase ROC1 (RBX1). *J. Nanobiotechnol* 19 (1), 323. doi:10.1186/s12951-021-01063-4

Zhao, X., Yang, K., Zhao, R., Ji, T., Wang, X., Yang, X., et al. (2016). Inducing Enhanced Immunogenic Cell Death with Nanocarrier-Based Drug Delivery Systems for Pancreatic Cancer Therapy. *Biomaterials* 102, 187–197. doi:10.1016/j.biomaterials.2016.06.032

Zheng, D.-W., Li, B., Li, C.-X., Fan, J.-X., Lei, Q., Li, C., et al. (2016). Carbon-Dot-Decorated Carbon Nitride Nanoparticles for Enhanced Photodynamic Therapy against Hypoxic Tumor via Water Splitting. *ACS Nano* 10 (9), 8715–8722. doi:10.1021/acsnano.6b04156

Zhong, Y., Zou, Y., Liu, L., Li, R., Xue, F., and Yi, T. (2020). pH-responsive Ag2S Nanodots Loaded with Heat Shock Protein 70 Inhibitor for Photoacoustic Imaging-Guided Photothermal Cancer Therapy. *Acta Biomater.* 115, 358–370. doi:10.1016/j.actbio.2020.08.007

Zhou, L., Chen, L., Hu, X., Lu, Y., Liu, W., Sun, Y., et al. (2020a). A Cu9S5 Nanoparticle-Based CpG Delivery System for Synergistic Photothermal-, Photodynamic- and Immunotherapy. *Commun. Biol.* 3 (1), 343. doi:10.1038/s42003-020-1070-6

Zhou, L., Hou, B., Wang, D., Sun, F., Song, R., Shao, Q., et al. (2020b). Engineering Polymeric Prodrug Nanoplatform for Vaccination Immunotherapy of Cancer. *Nano Lett.* 20 (6), 4393–4402. doi:10.1021/acs.nanolett.0c01140

Zhu, H., Liu, W., Cheng, Z., Yao, K., Yang, Y., Xu, B., et al. (2017a). Targeted Delivery of siRNA with pH-Responsive Hybrid Gold Nanostars for Cancer Treatment. *Ijms* 18 (10), 2029. doi:10.3390/ijms18102029

Zhu, X., Zhang, Y., Huang, H., Zhang, H., Hou, L., and Zhang, Z. (2017b). Folic Acid-Modified and Functionalized CuS Nanocrystal-Based Nanoparticles for Combined Tumor Chemo- and Photothermal Therapy. *J. Drug Target.* 25 (5), 425–435. doi:10.1080/1061186X.2016.1266651

Zhu, Y., Xue, J., Chen, W., Bai, S., Zheng, T., He, C., et al. (2020). Albumin-biomineralized Nanoparticles to Synergize Phototherapy and Immunotherapy against Melanoma. *J. Controlled Release* 322, 300–311. doi:10.1016/j.jconrel.2020.03.045

Conflict of Interest: The authors declare that the research was conducted in the absence of any commercial or financial relationships that could be construed as a potential conflict of interest.

Publisher's Note: All claims expressed in this article are solely those of the authors and do not necessarily represent those of their affiliated organizations, or those of the publisher, the editors and the reviewers. Any product that may be evaluated in this article, or claim that may be made by its manufacturer, is not guaranteed or endorsed by the publisher.

frontiers | Frontiers in Bioengineering and Biotechnology

ORIGINAL RESEARCH
published: 25 April 2022
doi: 10.3389/fbioe.2022.890668

Superior Fluorescent Nanoemulsion Illuminates Hepatocellular Carcinoma for Surgical Navigation

Jing Zhu[1,2†], Chengchao Chu[2†], Dongsheng Li[2], Yang Zhang[2], Yi Cheng[2], Huirong Lin[2], Xiaoyong Wang[2], Junxian Liu[2], Xin Pang[1,2], Jingliang Cheng[1*] and Gang Liu[2*]*

[1]Department of Magnetic Resonance Imaging, The First Affiliated Hospital of Zhengzhou University, Zhengzhou, China, [2]Center for Molecular Imaging and Translational Medicine, School of Public Health, Xiamen University, Xiamen, China

Hepatocellular carcinoma (HCC), the fifth most common cancer worldwide, poses a severe threat to public health. Intraoperative fluorescence imaging provides a golden opportunity for surgeons to visualize tumor-involved margins, thereby implementing precise HCC resection with minimal damage to normal tissues. Here, a novel-acting contrast agent, which facilely bridges indocyanine green (ICG) and lipiodol using self-emulsifying nanotechnology, was developed for optical surgical navigation. Compared to clinically available ICG probe, our prepared nanoemulsion showed obviously red-shifted optical absorption and enhanced fluorescence intensity. Further benefiting from the shielding effect of lipiodol, the fluorescence stability and anti-photobleaching ability of nanoemulsion were highly improved, indicating a great capacity for long-lasting *in vivo* intraoperative imaging. Under the fluorescence guidance of nanoemulsion, the tumor tissues were clearly delineated with a signal-to-noise ratio above 5-fold, and then underwent a complete surgical resection from orthotopic HCC-bearing mice. Such superior fluorescence performances, ultrahigh tumor-to-liver contrast, as well as great bio-safety, warrants the great translational potential of nanoemulsion in precise HCC imaging and intraoperative navigation.

Keywords: Hepatocellular Carcinoma, fluorescence imaging, nanoemulsion, indocyanine green, surgical navigation

OPEN ACCESS

Edited by:
Miaomiao Yuan,
Sun Yat-sen University, China

Reviewed by:
Bingxia Zhao,
Southern Medical University, China
Yanhong Duo,
Karolinska Institutet (KI), Sweden

***Correspondence:**
Xin Pang
pangxin116@163.com
Jingliang Cheng
fccchengjl@zzu.edu.cn
Gang Liu
gangliu.cmitm@xmu.edu.cn

†These authors have contributed equally to this work.

Specialty section:
This article was submitted to Nanobiotechnology, a section of the journal Frontiers in Bioengineering and Biotechnology

Received: *06 March 2022*
Accepted: *08 April 2022*
Published: *25 April 2022*

Citation:
Zhu J, Chu C, Li D, Zhang Y, Cheng Y, Lin H, Wang X, Liu J, Pang X, Cheng J and Liu G (2022) Superior Fluorescent Nanoemulsion Illuminates Hepatocellular Carcinoma for Surgical Navigation. Front. Bioeng. Biotechnol. 10:890668. doi: 10.3389/fbioe.2022.890668

INTRODUCTION

Surgical resection remains the paramount treatment option for liver tumor, such as hepatocellular carcinoma (HCC), and metastases of gastroenterological cancers (Siegel et al., 2019). Successful oncologic surgery is predicated on accurate visualization of the neoplastic tissue so as to precise removal with minimal damage to normal tissues (Hasegawa and Kokudo, 2009). However, in clinical practice, surgeons usually cannot discriminate the intraparenchymal tumor accurately only by visual inspection and tactile feedback. Their failure to pinpoint the tumor margins results in positive surgical margins, which are correlated with poor prognosis, locoregional recurrence and low patient survival. Promisingly, intraoperative fluorescence imaging provides a golden opportunity for surgery guided due to its high contrast, low cost, real-time feedback, and good availability of imaging whole organs with the potential to zoom in from macroscopic scale to microcosmic structures (Verbeek et al., 2012; Gao et al., 2018; Ren et al., 2020). More importantly, it is easily integrated into the workflow of intraoperative surgery and endoscopy, significantly augmenting the visualization ability of surgeons in identifying tumor-involved margins (Mochida et al., 2018; Wang et al., 2018). As the only near-infrared (NIR) fluorophore approved for surgery intraoperative guidance, indocyanine

green (ICG), which emits at ~800 nm, effectively minimizes photo scattering, absorption and tissue autofluorescence while maximizing tissue penetration depths to several centimeters (Zhang et al., 2017). With the aid of ICG-guided intraoperative imaging, a fluorescent edge of the cancerous tissue can be observed during surgery for margin delineation between cancer and adjacent healthy tissue (Gotoh et al., 2009; Hirche et al., 2010; Xu et al., 2020). Although it holds great promise in improving intraoperative decision-making, this untargeted small-molecule dye still suffers from non-specific binding and usually high background noise. Moreover, fast clearance from tumor site further limits the time window of ICG for surgical applications, and the severe photobleaching and degradation issues also frequently reduce its detectability or observation time (Mindt et al., 2018; Sakka, 2018; Chen et al., 2020a). Consequently, a more efficacious fluorophore that allows tumor-targeted imaging, long-lasting HCC retention, and stable fluorescence signal, is urgently desired.

In the fluorescence-guided surgical navigation, the signal to noise ratio (SNR) of ICG relies on its accumulation and retention in liver cancerous tissues (Ai et al., 2018). Lipiodol (Andre Guerbet, Aulnay-sous-Bois, France), an iodized poppyseed oil, has been most commonly used as an embolic material for transcatheter arterial chemoembolization against HCC in clinic (Lencioni et al., 2016; Chen et al., 2020b). It demonstrates a preferential uptake by hypervascular tumor compared to surrounding liver tissue, which can be used as a vehicle for the targeted delivery of cytotoxic drug or contrast agent (Kawaoka et al., 2009; Jeon et al., 2016; Gruber-Rouh et al., 2018). When combination with these functional agents, the lipiodol is expected to act as a shelter to protect internal agents from dilution and degradation by adverse external environment. Moreover, the high viscosity of lipiodol makes it prone to deposit in the anomalous vessel of HCC, which is a great help for internal agents resist blood flow clearance (Cheng et al., 2020). Further benefiting from the reduced molecular movement, the functional agents inside highly viscous lipiodol expectantly possess increased stability. Some potential problems such as fluorescence quenching of ICG is therefore promisingly relieved (Chen et al., 2020c). However, the task to integrate lipiodol with ICG using a safe and facile platform remains a major challenge. Ideally, the functional agents should be "loaded" inside the droplets of lipiodol (water-in-oil emulsion) for an optimal tumor uptake (De Baere et al., 1996). Stabilization of the emulsion is also a key for lipiodol to serve as a vehicle to carry and localize the ICG inside the cancerous tissue. Thus, solutions for ICG-guided surgical navigation, in the long-run, require a multipronged cooperation.

Nanotechnology has revolutionized medicine including fluorescence-guided intraoperative imaging (Ai et al., 2018). Unlike small molecular designs, the cooperative behaviors of nanosystems, which take advantage of well-developed material engineering and the enhanced permeability and retention (EPR) effect, can be exploited for the development of highly efficient nanoemulsion to amplify pathological signals, and further improve the accuracy of intraoperative imaging (Li et al., 2018; Li et al., 2019). Here, a facile route to bridge lipiodol and ICG was proposed using self-emulsifying nanotechnology **(Scheme 1)**. As a proof-of-principle, Tween-80 and lecithin, the clinically available surfactants, were introduced to emulsify the

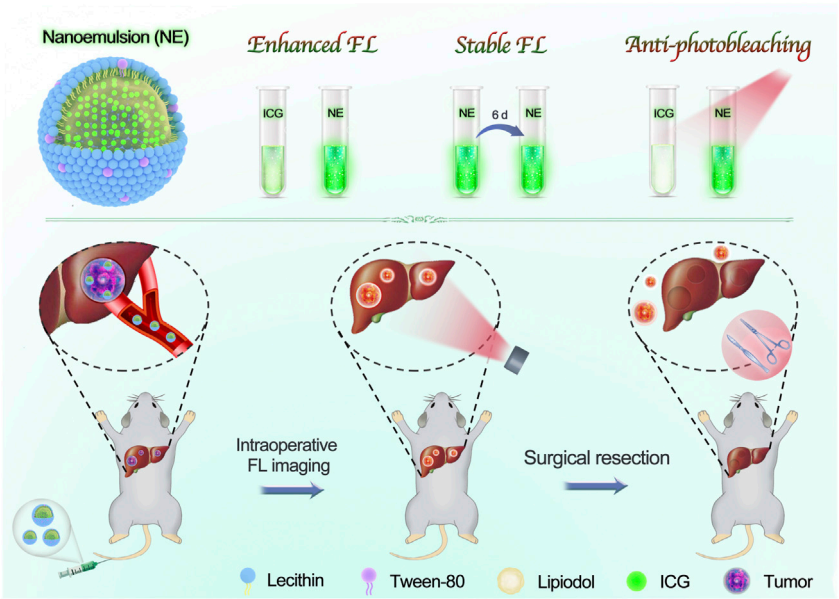

SCHEME 1 | Scheme illustration of our developed nanoemulsion for FL imaging-guided surgical resection of HCC. The nanoemulsion was facilely prepared with clinically approved materials, including ICG, lipiodol, lecithin, and tween-80. By taking advantage of superior FL performances and ultrahigh tumor accumulation, the tumor tissues were clearly delineated, and then underwent a complete surgical resection from orthotopic HCC-bearing mice.

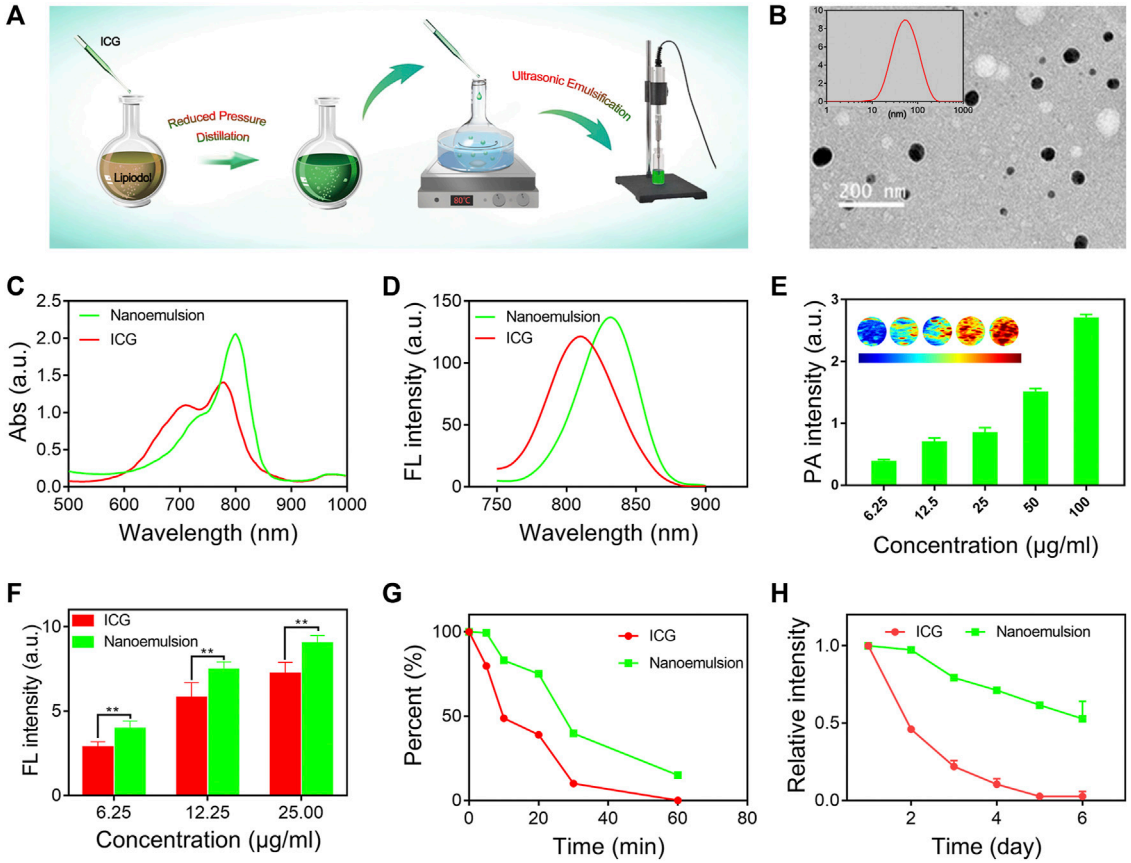

FIGURE 1 | (A) Schematic illustration of the preparation process of nanoemulsion. **(B)** TEM image and size distribution of nanoemulsion. **(C)** NIR-UV–vis spectra and **(D)** FL spectra of free ICG solution and nanoemulsion. **(E)** PA imaging signals of nanoemulsion with different ICG concentrations. **(F)** FL intensity comparison of free ICG solution and nanoemulsion at different concentrations. **(G)** FL intensity change of ICG and nanoemulsion after laser (2 W/cm^2, 808 nm) irradiation. **(H)** FL intensity change of ICG and nanoemulsion after different storage times.

mixture of lipiodol and ICG. Strikingly, the developed nanoemulsion obviously shifted excitation and emission peaks and produced enhanced fluorescence intensity compared with free ICG, which suggests superior potential for NIR intraoperative imaging. With the aid of shielding effect by lipiodol, the fluorescence stability and anti-photobleaching ability of nanoemulsion was greatly improved, indicating the capacity for real-time *in vivo* imaging continuously for long periods. Moreover, this nanoemulsion could successfully localize to neoplastic tissue with excellent tumor-to-normal contrast. Under the fluorescence guidance of ICG-lipiodol nanoemulsion, the tumor tissues from orthotopic HCC-bearing mice were clearly visualized, accurately delineated and then effectively resected.

EXPERIMENTAL SECTION

Materials

ICG, Lipoid and Tween-80 were obtained from Aladdin (China). 4′,6-Diamidino-2-phenylindole (DAPI) and 3-[4,5-dimethylthiazol-2-yl]-2,5-diphenyl tetrazolium bromide (MTT) were obtained from Sigma-Aldrich. Fetal bovine serum (FBS) and high glucose DMEM were purchased from Hyclone (United States). Penicillin and streptomycin were obtained from GIBCO BRL (United States).

Preparation of Nanoemulsion

5 mg ICG was dissolved in 5 ml chloroform, and then mixed with 500 μL iodinated oil. The mixture was removed chloroform by rotary evaporation. 100 mg Lipoid was dissolved in 300 μL ethanol. 400 μL Tween-80 was dispersed in 20 ml distilled water and brought to a boil. Subsequently, the Lipoid solution and the mixture were added into the above-mentioned boiling liquid dropwise under continuous stirring (700 rpm). The preparation was concentrated to 10 ml. Finally, the crude emulsion was homogenized for 15 min using a sonicator tip (Sonics, United States) to form uniform nanoemulsion. The final nanoemulsion was obtained by using dialysis (30 KDa) and stored in dark at 4°C.

Characterization of Nanoemulsion

The morphology of nanoemulsion was observed by transmission electron microscopy (TEM). The dynamic light scattering (DLS)

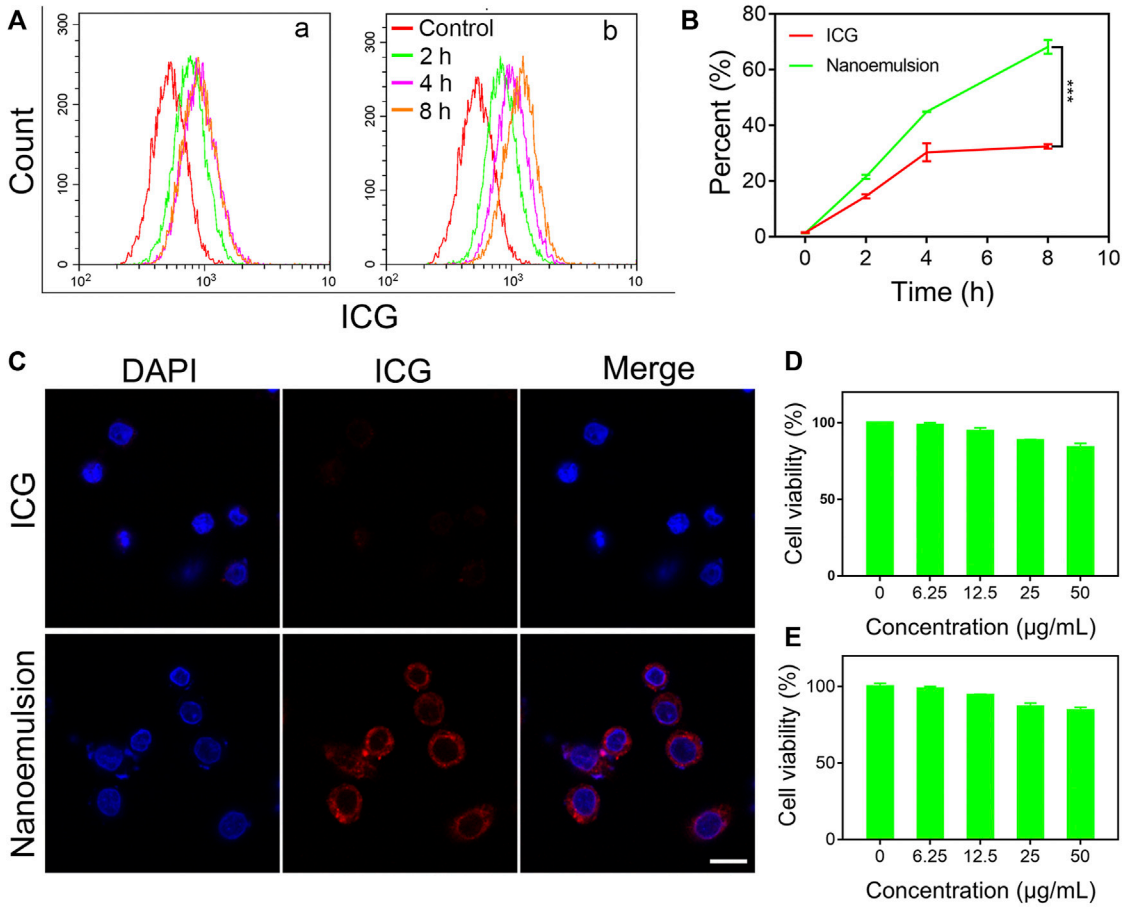

FIGURE 2 | (A) Flow cytometry profiles, **(B)** quantitative analysis, and **(C)** CLSM images of ICG and nanoemulsion internalization by HepG2 cells. Cell viability of **(D)** LO2 cells and **(E)** HepG2 cells treated with nanoemulsion at different ICG concentrations.

and surface zeta potential of nanoemulsion were captured using a Nano Particle analyzer (SZ-100, Horiba Scientific). UV–vis–NIR absorbance spectra of ICG and nanoemulsion were recorded using a microplate reader (Thermo). Fluorescence emission spectrum of ICG and nanoemulsion were recorded using fluorescence spectrometer (LS55, Perkin Elmer), the excitation wavelength was 780 nm. The FL images of ICG and nanoemulsion (gradient concentration) were acquired using a IVIS Lumina imaging system (Caliper, United States) (Ex/Em = 740 nm/ICG). The fluorescence intensity of nanoemulsion and ICG solution (10 μg/ml) were measured after different laser irradiating time (808nm, 2 W/cm^2) or at different storage time. The nanoemulsion with different iodine concentration were scanned by a micro-CT imaging system. The PA images of nanoemulsion were acquired using a preclinical PA imaging system (Endra Nexus 128, Ann Arbor, MI) under 808 nm laser. The stability of nanoemulsion in PBS solution and DMEM were evaluated at different time points by DLS.

In vitro Cell Uptake and Cytotoxicity Study

HepG2 and normal hepatocytes (LO2) were purchased from the cell bank of the Chinese Academy of Sciences in Shanghai. Cells were cultured in DMEM containing with 10% (v/v) FBS and 100 μg/ml of penicillin/streptomycin at 37°C under 5% CO2. The HepG2 cells were seeded into 6-well microplates at a density of 5 × 10^5 cells per plate, and incubated for 12 h. Then, the culture media was replaced by fresh media containing ICG or nanoemulsion (1 ml, at the equivalent ICG dose of 10 μg/ml in DMEM), respectively. After co-incubation for different time points, the cellular uptake was analyzed by fiow cytometry equipment. Furthermore, the CLSM was applied to study the cell uptake of nanoemulsion. Briefiy, HepG2 cells were seeded into a CLSM-specifc dish at a density of 1 × 10^5 cells per dish, and incubated for 12 h for adherence. Then, the culture media were replaced by fresh media containing nanoemulsion or ICG (1 ml, at the equivalent ICG dose of 10 μg/ml in DMEM) and incubated for 12 h. For locating the cell, 10 μL of DAPI was added into each dish to stain the cell nuclei for 15 min followed by observation with CLSM.

The cytotoxicity of the ICG and nanoemulsion was assessed by 3-(4,5-dimethylthiazol-2-yl)-2,5-diphenyltetrazolium bromide (MTT) assay. The HepG2 and LO2 cells were seeded into 96-well microplates and cultured overnight. Then, the culture media were replaced by fresh media containing ICG and nanoemulsion with gradient

concentrations of ICG and cultured for 24 h. Finally, the cell viability was detected by MTT assay.

Animal Model Establishment

All animal experiments were performed according to the protocol approved by the Animal Care and Use Committee of Xiamen University, China. For the establishment of tumor model, the female Balb/c nude mice (5–6 weeks, 22 ± 2 g) were supplied by the Center for Experimental Animals, Xiamen University, China. Orthotopic liver tumor models were established by inoculation of suspended HepG2 cells (25 μl, 1×10^7 cells/ml) at the left lobe of liver. The models were used for further experiments when the tumor grown up.

Orthotopic Liver Tumor PA and Fluorescence Imaging

After the model of tumor-bearing mice was established, the mice were randomly divided into two groups: ICG and nanoemulsion. The dose of ICG (2 mg/kg) was administrated by intravenously injection in each group. PA signals in the liver and tumor were observed using Endra Nexus. The FL images were acquired before and at different time points (1, 3, 6, 9, 12, and 24 h) after administration using IVIS Lumina imaging system (Caliper, United States) (Ex/Em = 740 nm/ICG). At 24 h post injection, the mice were sacrificed and their major organs (heart, liver, spleen, lung, and kidney) and the tumor were harvested for *ex vivo* FL imaging. The fluorescence signal intensity was quantified by analyzing the signals at the region of interests.

The mice were randomly divided into two groups, After i.v. administration of nanoemulsion and ICG (2 mg/kg), the mice were sacrificed at scheduled time (0, 1, 3, 6, 12, 24, and 36 h) and were taken for *in vitro* FL imaging. The fluorescence signal intensity of liver and tumor were quantified, and the signal-to-noise ratio (SNR) of FL imaging was calculated:

$$SNR = FL\,intensity_{Tumor} / FL\ intensity_{Liver}$$

Surgical Resection of Orthotopic Liver Tumor

Orthotopic liver tumor mice were performed surgical excision at 24 h with i.v. administration of nanoemulsion (2 mg/kg). Surgeons were asked to remove tumor tissues with maximum protection of the normal tissue based on real-time fluorescent surgical navigation. If tumor tissue remained, the surgeons continued the resection with FL imaging guidance until removing all tumor tissues. The resected tissues were also analyzed by H&E staining.

In vivo Biocompatibility Assessment

Healthy BALB/c nude mice (20–22 g) were intravenously injected with PBS, ICG or nanoemulsion at a ICG identical dose of 2 mg/kg, respectively. At 24 h post-injection, the blood samples were collected and followed by sacrificing the mice. The blood samples were used to detect the RBC, PLT, WBC, HGB, ALT, AST, BUN, and CREA parameters. The major organs, including heart, liver, spleen, lung, kidney, were dissected for H&E staining.

RESULTS AND DISCUSSION

The ICG-lipiodol nanoemulsion was prepared *via* a self-emulsifying method with proper modification (**Figure 1A**), and further characterized with morphology, optical performances, and stability. As observed from the transmission electron microscopy (TEM) image shown in **Figure 1B**, the developed nanoemulsion had a well-defined spherical structure with a narrow size distribution. The hydrodynamic diameter and ζ-potential of nanoemulsion was about 60 nm and -5 mV by the dynamic light scattering (DLS) analysis (**Figure 1B** insertion). Compared to free ICG solution, the nanoemulsion showed obvious enhanced and red-shifted absorption with a maximum absorption peak of 805 nm (**Figure 1C**). Similarly, a significant red-shift of fluorescence emission spectra between ICG (810 nm) and nanoemulsion (840 nm) was also observed (**Figure 1D**). Such shifted absorption and emission peaks may be attributed to the different external mediums of ICG that the nanoemulsion disperses ICG molecules in oily lipiodol instead of direct dispersion in water like free ICG solution. When imaging *in vivo*, the red-shifted optical performances of nanoemulsion are conducive to overcome the tissue absorption and scattering, implementing accurate intraoperative navigation. In addition to fluorescence imaging, the potential ability of nanoemulsion as a photoacoustic (PA) imaging and computed tomography (CT) imaging contrast agent was also evaluated. As expected, the PA and CT signals steadily enhanced with the concentration of nanoemulsion increasing, which can be clearly visualized in photographs (**Figures 1E**, **Supplementary Figure S1**).

Fluorescence performance of contrast agent is an important factor governing the outcomes of intraoperative imaging. Successful surgical resection of HCC closely relies on strong FL intensity, great anti-photobleaching ability, and excellent FL stability (Nagaya et al., 2017). In this study, we systemically investigated the FL performance of prepared nanoemulsion. It was found that nano-emulsification did not disrupt the FL characteristics of ICG (**Figure 1F**). On the contrary, the FL intensity of ICG from nanoemulsion was remarkably higher than that from free ICG solution, which suggests great potential in improving SNR of intraoperative imaging. Upon laser irradiation (808 nm, 2 W/cm^2, 10 min), the ICG solution reduced its FL intensity to almost 50%, while 80% of FL intensity was remained in the group of nanoemulsion (**Figure 1G**). Moreover, after 60 min light exposure, the nanoemulsion still exhibited FL imaging performance, but the ICG solution has completely photobleached without any FL signal. Such potent anti-photobleaching ability is expected to prolong the working period of ICG-mediated FL imaging, as a result, the time window of surgical navigation promisingly extends. In clinical practice, the ICG solution should be freshly prepared when using due to its self-quenching phenomenon. However, in our study, the ICG

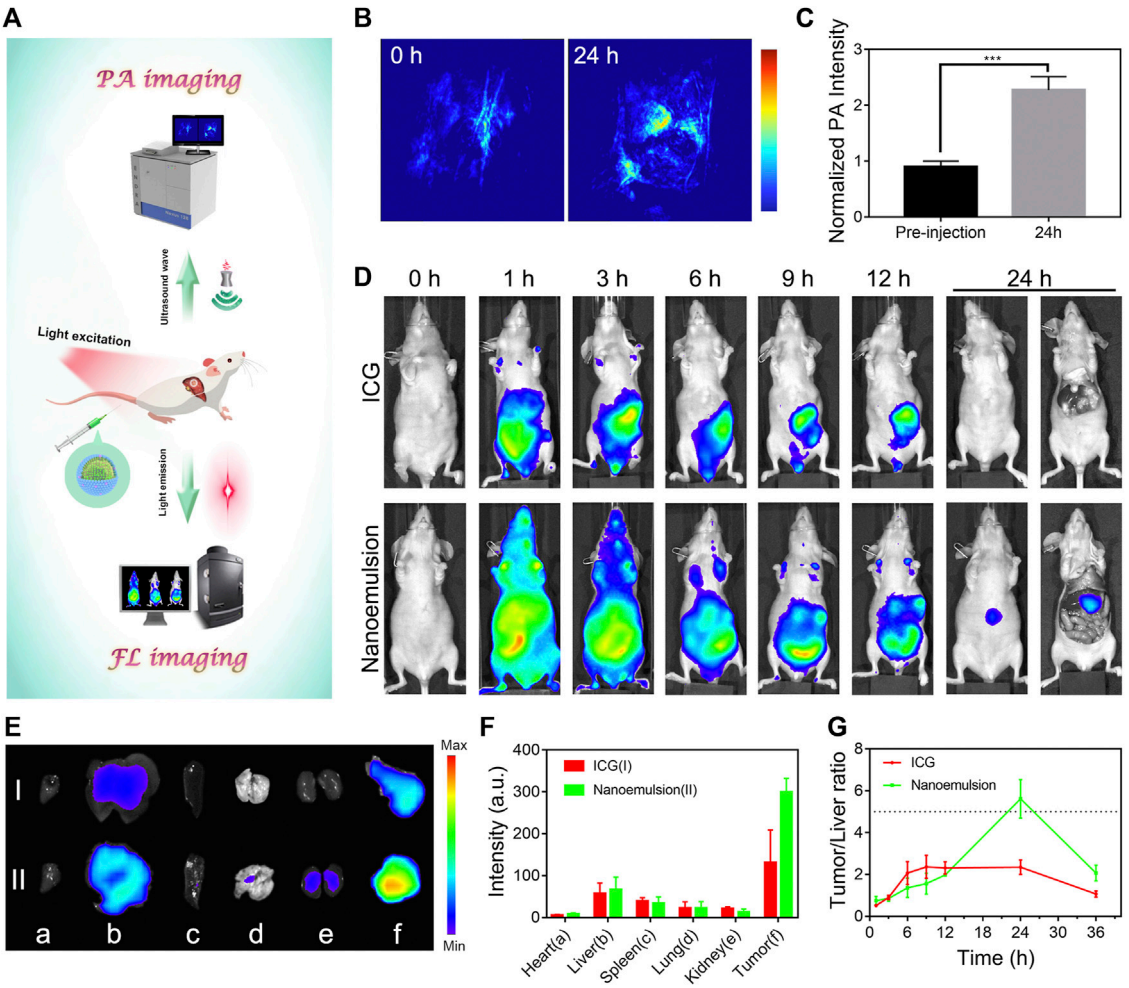

FIGURE 3 | (A) Schematic illustration of the optical diagnosis of nanoemulsion in orthotopic HCC-bearing mice. **(B)** PA images and **(C)** intensity analysis of tumor sites from nanoemulsion-treated mice. **(D)** FL images of orthotopic HCC-bearing mice model after tail vein injection of ICG solution or nanoemulsion. **(E)** *Ex vivo* tissue FL image and **(F)** FL intensity (I: ICG group; II: nanoemulsion group) of HCC-bearing mice after different treatments at 24 h post-injection. The a, b, c, d, e, and f represent heart, liver, spleen, lung, kidney, and tumor. **(G)** FL signal ratio of tumor-to normal liver tissue at various time points.

molecules after nano-emulsification showed highly enhanced FL stability (**Figure 1H**). Different from ICG solution whose FL signal rapidly declined to zero on the fifth day, the FL intensity of nanoemulsion stored for 6 days was still more than 50%. The great FL stability can be explained by the strong viscosity of lipiodol, which significantly restricts the movement of ICG molecules and therefore reduces molecular packing-induced FL quenching (Zweck and Penzkofer, 2001). Further morphology stability evaluation also demonstrated the great stability of nanoemulsion (**Supplementary Figure S2**). Its diameter stayed pretty constant during 2 months. Benefiting from the red-shifted optical spectra, superior fluorescence performances, and enhanced stability, the nanoemulsion could serve as a novel-acting contrast agent for FL-guided intraoperative imaging.

Efficient uptake by tumor cells is the fundamental step for contrast agent in the optical surgical navigation and can lead to a more precise and effective HCC resection. To validate the internalization ability of nanoemulsion in the cellular environment, the human hepatoma cell line (HepG2) was selected. As shown in **Figures 2A,B**, both ICG solution and nanoemulsion exhibited a time-dependent internalization by HepG2 cells. With increasing co-incubation time, the cellular uptake of ICG became enhanced. Comparatively, the ICG after nano-emulsification performed dramatically higher cellular internalization efficiency than its free state. After 8 h co-incubation, the uptake rate of nanoemulsion was 68.23%, more than twice that of pristine ICG solution (32.44%). This result was also supported by confocal laser scanning microscopy (CLSM) assay in which the nanoemulsion-treated HepG2 cells presented bright red fluorescence in cytoplasm, but the red ICG signal was almost invisible in the cells incubated with ICG solution (**Figure 2C**). Such efficient cellular uptake of nanoemulsion may be attributed to the combination of good cell membrane affinity provided by lecithin carrier and deposition effect of lipiodol. For future biomedical applications, toxicity

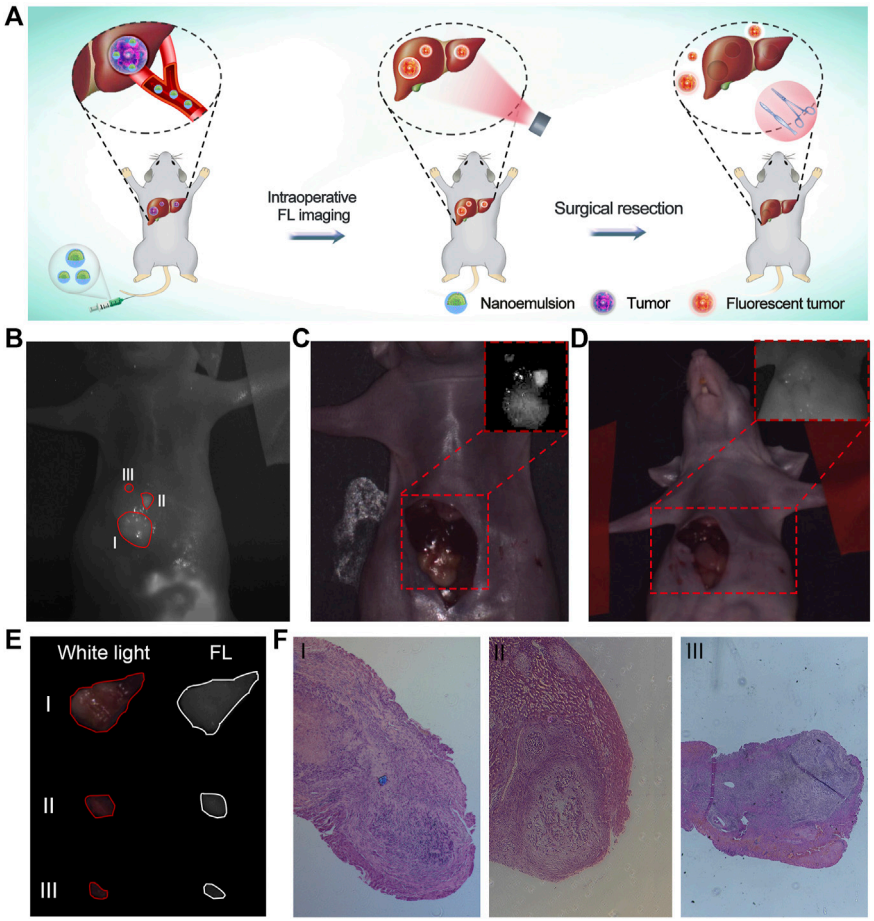

FIGURE 4 | (A) Schematic illustration of nanoemulsion for FL imaging-guided surgical resection of HCC. **(B)** Post-mortem FL images of orthotopic HCC-bearing mice under surgical navigation imaging system. Image was taken 24 h after injection of nanoemulsion. I, II, and III represent tumors with different sizes. **(C)** Pre-operative and **(D)** Post-operative white light images of orthotopic HCC-bearing mice. Insertions are the FL images of liver region under surgical navigation imaging system. **(E)** White light and FL images of resected tissues under the nanoemulsion-mediated FL guidance. **(F)** Histological analysis of tumor specimens from the resected tissues.

testing of nanoemulsion is a critical requirement. Its cytotoxicity was studied in a human hepatic cell line (LO2) and HCC line (HepG2). MTT assays showed no significant toxic effect on the two cell lines after incubation with nanoemulsion for 24 h (**Figures 2D,E**). When the ICG concentration from nanoemulsion is up to 50 μg/ml, the viability of both cell lines still maintained higher than 80%. This good cellular safety, coupled with efficient tumor cell uptake, greatly supports the bio-application of nanoemulsion for intraoperative imaging of HCC.

Accurate diagnosis of HCC is imperative to guide surgical resection and control the metastasis of this disease (Alam et al., 2018; Pang et al., 2020). Considering the unique imaging properties of ICG (Chu et al., 2020), the nanoemulsion is expected as a powerful contrast agent to reveal the tumor margins. We evaluated multi-modality cancer visualization by prepared nanoemulsion in orthotopic HCC-bearing mice (**Figure 3A**). The PA images were acquired before and after intravenous injection of nanoemulsion for 24 h. As shown in **Figures 3B,C**, the PA signal was notably stronger in the tumor than in healthy hepatic tissue, indicating the great potential of nanoemulsion in HCC PA imaging *in vivo*. To verify the *in vivo* targeting ability of nanoemulsion and the optimum time point for intraoperative imaging, we then compared and analyzed the FL imaging results at different time points after administration. **Figure 3D** shows that free ICG was rapidly accumulated to the abdomen within 1 h. No obvious FL signal from liver region was detected during the entire monitoring period. However, after being packaged into nanoemulsion, the ICG showed a different biodistribution behavior, with gradual FL attenuation in normal sites but a time-dependent FL enhancement at the liver tissue. At 24 h post-injection, the FL signal was completely cleared from abdomen, only concentrating to the liver area. Subsequently, the main organs and tumor of mice were isolated for distribution analysis (**Figures 3E,F**). Obviously, mice treated with free ICG solution exhibited weak FL signal intensity, suggesting the fast metabolism and clearance of ICG from body. By contrast, the FL signal from nanoemulsion-

treated mice was only weak in the organs, but was rather strong in the tumor tissue. The higher FL signal of nanoemulsion can be explained by the enhanced FL intensity and stability of ICG after nano-emulsification, and the efficient tumor accumulation is attributed to the tumor-associated EPR effect. **Figure 3G** shows the tumor-to-normal liver tissue ratio of the FL signal at different time points. It can be seen that the maximal tumor signal over liver contrast was only 2-fold at 6 h post-injection of free ICG solution, which is nearly one-third of that from nanoemulsion-treated mice (5.7-fold at 24 h post-injection). Such significant positive contrast enhancement in the tumor site, but gradually reduced signal in healthy liver tissue, greatly ensures a clear visualization of tumor margin. Observed by the FL and bioluminescence imaging (**Supplementary Figure S3**), the resected tumor by nanoemulsion-mediated FL guidance was exactly coincident with the tumor formed by luciferase-transfected HepG2 cells, revealing the potent ability of nanoemulsion in pinpointing tumor margin.

After verifying the maximal tumor-to-liver tissue ratio of nanoemulsion, orthotopic hepatic tumor-bearing mice ($n = 3$) were subjected to laparotomy with general anesthesia and subsequent luminescence imaging liver-resection guidance at 24 h post-injection of nanoemulsion (**Figure 4A**). With the guidance of nanoemulsion-mediated FL imaging, some tissues in the liver region showed bright fluorescence signal and then were removed (**Figures 4B–D**). Strikingly, the FL signal at the resection area disappeared after the surgery (**Figure 4D**), which could provide a timely feedback to the surgeon regarding the surgical outcome. Under the guidance of nanoemulsion-mediated FL imaging, the delineated tissues were resected (**Figure 4E**). Postoperative histological analysis of the excised tissues showed disordered structure and mass tumor cell infiltrating (**Figure 4F**), suggesting that the tumor tissues, even small volumes, could be illuminated and removed completely. Further safety examination revealed that the nanoemulsion was nontoxic to organs (**Supplementary Figure S4**), and showed negligible changes in peripheral blood (**Supplementary Figure S5**), liver functions (alanine transaminase and aspartate transaminase), and renal functions (creatinine and blood urea nitrogen) (**Supplementary Figure S6**). All of these demonstrated that the developed nanoemulsion could be competent for an effective and safe platform to accurately highlight tumor lesions, guiding HCC intraoperative resection.

CONCLUSION

In this study, we reported a novel-acting nanoemulsion for NIR FL imaging-guided HCC surgery. This highly potent nanoemulsion was prepared using self-emulsifying nanotechnology to facilely bridge ICG and lipiodol, and shows three primary advantages as follows: 1) superior FL performances, including red-shifted optical spectra, enhanced FL intensity, great anti-photobleaching ability and excellent FL stability; 2) distinguished HCC targeting and accumulation, achieving an ultrahigh tumor-to-liver FL signal ratio of 5.7 for precise surgical navigation; 3) great biosafety that all of the materials prepared for nanoemulsion are clinically approved. Under the guidance of nanoemulsion-mediated NIR FL imaging, the tumor margins were clearly delineated and resected from orthotopic HCC-bearing mice. Such fluorescent nanoemulsion could represent a promising real-time imaging platform to improve clinical intraoperative quality, reduce the risk of postoperative complications, and even potentially shift the current paradigm of optical surgical navigation.

DATA AVAILABILITY STATEMENT

The original contributions presented in the study are included in the article/**Supplementary Material**, further inquiries can be directed to the corresponding authors.

ETHICS STATEMENT

The animal study was reviewed and approved by The Animal Management and Ethics Committee of Xiamen University.

AUTHOR CONTRIBUTIONS

JZ performed most of the experiments shown in this work, with the help of CCC and DSL. YZ and YC analyzed and discussed the data. XP and JZ wrote the paper. HRL, XYW and JXL revised critically the study. XP, JLC and GL provided financial support.

FUNDING

This work was supported by the Major State Basic Research Development Program of China (2017YFA0205201), the National Natural Science Foundation of China (81901876, 81925019, 81801817, and U1705281), the Fundamental Research Funds for the Central Universities (20720190088 and 20720200019), and the Program for New Century Excellent Talents in University, China (NCET-13-0502). The Joint Construction Project of Henan Medical Science and Technology Research Program (LHGJ20210345 and LHGJ20200201).

SUPPLEMENTARY MATERIAL

The Supplementary Material for this article can be found online at: https://www.frontiersin.org/articles/10.3389/fbioe.2022.890668/full#supplementary-material

REFERENCES

Ai, T., Shang, W., Yan, H., Zeng, C., Wang, K., Gao, Y., et al. (2018). Near Infrared-Emitting Persistent Luminescent Nanoparticles for Hepatocellular Carcinoma Imaging and Luminescence-Guided Surgery. *Biomaterials* 167, 216–225. doi:10.1016/j.biomaterials.2018.01.031

Alam, I. S., Steinberg, I., Vermesh, O., van den Berg, N. S., Rosenthal, E. L., van Dam, G. M., et al. (2018). Emerging Intraoperative Imaging Modalities to Improve Surgical Precision. *Mol. Imaging Biol.* 20, 705–715. doi:10.1007/s11307-018-1227-6

Chen, C., Tian, R., Zeng, Y., Chu, C., and Liu, G. (2020). Activatable Fluorescence Probes for "Turn-On" and Ratiometric Biosensing and Bioimaging: From NIR-I to NIR-II. *Bioconjug. Chem.* 31, 276–292. doi:10.1021/acs.bioconjchem.9b00734

Chen, H., Cheng, H., Dai, Q., Cheng, Y., Zhang, Y., Li, D., et al. (2020). A Superstable Homogeneous Lipiodol-ICG Formulation for Locoregional Hepatocellular Carcinoma Treatment. *J. Controlled Release* 323, 635–643. doi:10.1016/j.jconrel.2020.04.021

Chen, H., Cheng, H., Wu, W., Li, D., Mao, J., Chu, C., et al. (2020). The Blooming Intersection of Transcatheter Hepatic Artery Chemoembolization and Nanomedicine. *Chin. Chem. Lett.* 31, 1375–1381. doi:10.1016/j.cclet.2020.03.024

Cheng, H., Yang, X., and Liu, G. (2020). Superstable Homogeneous Iodinated Formulation Technology: Revolutionizing Transcatheter Arterial Chemoembolization. *Sci. Bull.* 65, 1685–1687. doi:10.1016/j.scib.2020.06.029

Chu, C., Yu, J., Ren, E., Ou, S., Zhang, Y., Wu, Y., et al. (2020). Multimodal Photoacoustic Imaging-Guided Regression of Corneal Neovascularization: A Non-Invasive and Safe Strategy. *Adv. Sci.* 7, 2000346. doi:10.1002/advs.202000346

De Baere, T., Zhang, X., Aubert, B., Harry, G., Lagrange, C., Ropers, J., et al. (1996). Quantification of Tumor Uptake of Iodized Oils and Emulsions of Iodized Oils: Experimental Study. *Radiology* 201, 731–735. doi:10.1148/radiology.201.3.8939223

Gao, R. W., Teraphongphom, N. T., van den Berg, N. S., Martin, B. A., Oberhelman, N. J., Divi, V., et al. (2018). Determination of Tumor Margins with Surgical Specimen Mapping Using Near-Infrared Fluorescence. *Cancer Res.* 78, 5144–5154. doi:10.1158/0008-5472.can-18-0878

Gotoh, K., Yamada, T., Ishikawa, O., Takahashi, H., Eguchi, H., Yano, M., et al. (2009). A Novel Image-Guided Surgery of Hepatocellular Carcinoma by Indocyanine green Fluorescence Imaging Navigation. *J. Surg. Oncol.* 100, 75–79. doi:10.1002/jso.21272

Gruber-Rouh, T., Schmitt, C., Naguib, N. N. N., Nour-Eldin, N. A., Eichler, K., Beeres, M., et al. (2018). Transarterial Chemoembolization (TACE) Using Mitomycin and Lipiodol with or without Degradable Starch Microspheres for Hepatocellular Carcinoma: Comparative Study. *BMC Cancer* 18, 188. doi:10.1186/s12885-018-4099-x

Hasegawa, K., and Kokudo, N. (2009). Surgical Treatment of Hepatocellular Carcinoma. *Surg. Today* 39, 833–843. doi:10.1007/s00595-008-4024-z

Hirche, C., Murawa, D., Mohr, Z., Kneif, S., and Hünerbein, M. (2010). ICG Fluorescence-Guided sentinel Node Biopsy for Axillary Nodal Staging in Breast Cancer. *Breast Cancer Res. Treat.* 121, 373–378. doi:10.1007/s10549-010-0760-z

Jeon, M. J., Gordon, A. C., Larson, A. C., Chung, J. W., Kim, Y. I., and Kim, D.-H. (2016). Transcatheter Intra-arterial Infusion of Doxorubicin Loaded Porous Magnetic Nano-Clusters with Iodinated Oil for the Treatment of Liver Cancer. *Biomaterials* 88, 25–33. doi:10.1016/j.biomaterials.2016.02.021

Kawaoka, T., Aikata, H., Takaki, S., Katamura, Y., Hiramatsu, A., Waki, K., et al. (2009). Transarterial Infusion Chemotherapy Using Cisplatin-Lipiodol Suspension with or without Embolization for Unresectable Hepatocellular Carcinoma. *Cardiovasc. Intervent Radiol.* 32, 687–694. doi:10.1007/s00270-009-9570-2

Lencioni, R., de Baere, T., Soulen, M. C., Rilling, W. S., and Geschwind, J.-F. H. (2016). Lipiodol Transarterial Chemoembolization for Hepatocellular Carcinoma: A Systematic Review of Efficacy and Safety Data. *Hepatology* 64, 106–116. doi:10.1002/hep.28453

Li, D., He, S., Wu, Y., Liu, J., Liu, Q., Chang, B., et al. (2019). Excretable Lanthanide Nanoparticle for Biomedical Imaging and Surgical Navigation in the Second Near-Infrared Window. *Adv. Sci.* 6, 1902042. doi:10.1002/advs.201902042

Li, X., Schumann, C., Albarqi, H. A., Lee, C. J., Alani, A. W. G., Bracha, S., et al. (2018). A Tumor-Activatable Theranostic Nanomedicine Platform for NIR Fluorescence-Guided Surgery and Combinatorial Phototherapy. *Theranostics* 8, 767–784. doi:10.7150/thno.21209

Mindt, S., Karampinis, I., John, M., Neumaier, M., and Nowak, K. (2018). Stability and Degradation of Indocyanine green in Plasma, Aqueous Solution and Whole Blood. *Photochem. Photobiol. Sci.* 17, 1189–1196. doi:10.1039/c8pp00064f

Mochida, A., Ogata, F., Nagaya, T., Choyke, P. L., and Kobayashi, H. (2018). Activatable Fluorescent Probes in Fluorescence-Guided Surgery: Practical Considerations. *Bioorg. Med. Chem.* 26, 925–930. doi:10.1016/j.bmc.2017.12.002

Nagaya, T., Nakamura, Y. A., Choyke, P. L., and Kobayashi, H. (2017). Fluorescence-Guided Surgery. *Front. Oncol.* 7, 314. doi:10.3389/fonc.2017.00314

Pang, X., Li, D., Zhu, J., Cheng, J., and Liu, G. (2020). Beyond Antibiotics: Photo/Sonodynamic Approaches for Bacterial Theranostics. *Nano-micro Lett.* 12, 144. doi:10.1007/s40820-020-00485-3

Ren, E., Chu, C., Zhang, Y., Wang, J., Pang, X., Lin, X., et al. (2020). Mimovirus Vesicle-Based Biological Orthogonal Reaction for Cancer Diagnosis. *Small Methods* 4, 2000291. doi:10.1002/smtd.202000291

Sakka, S. G. (2018). Assessment of Liver Perfusion and Function by Indocyanine green in the Perioperative Setting and in Critically Ill Patients. *J. Clin. Monit. Comput.* 32, 787–796. doi:10.1007/s10877-017-0073-4

Siegel, R. L., Miller, K. D., and Jemal, A. (2019). Cancer Statistics, 2019. *CA A. Cancer J. Clin.* 69, 7–34. doi:10.3322/caac.21551

Verbeek, F. P. R., van der Vorst, J. R., Schaafsma, B. E., Hutteman, M., Bonsing, B. A., van Leeuwen, F. W. B., et al. (2012). Image-guided Hepatopancreatobiliary Surgery Using Near-Infrared Fluorescent Light. *J. Hepato-Biliary-Pancreatic Sci.* 19, 626–637. doi:10.1007/s00534-012-0534-6

Wang, C., Wang, Z., Zhao, T., Li, Y., Huang, G., Sumer, B. D., et al. (2018). Optical Molecular Imaging for Tumor Detection and Image-Guided Surgery. *Biomaterials* 157, 62–75. doi:10.1016/j.biomaterials.2017.12.002

Xu, D., Li, L., Chu, C., Zhang, X., and Liu, G. (2020). Advances and Perspectives in Near-infrared Fluorescent Organic Probes for Surgical Oncology. *WIREs Nanomed Nanobiotechnol* 12, 1635. doi:10.1002/wnan.1635

Zhang, R. R., Schroeder, A. B., Grudzinski, J. J., Rosenthal, E. L., Warram, J. M., Pinchuk, A. N., et al. (2017). Beyond the Margins: Real-Time Detection of Cancer Using Targeted Fluorophores. *Nat. Rev. Clin. Oncol.* 14, 347–364. doi:10.1038/nrclinonc.2016.212

Zweck, J., and Penzkofer, A. (2001). Microstructure of Indocyanine green J-Aggregates in Aqueous Solution. *Chem. Phys.* 269, 399–409. doi:10.1016/s0301-0104(01)00368-8

Conflict of Interest: The authors declare that the research was conducted in the absence of any commercial or financial relationships that could be construed as a potential conflict of interest.

frontiers | Frontiers in Bioengineering and Biotechnology

ORIGINAL RESEARCH
published: 28 April 2022
doi: 10.3389/fbioe.2022.893608

RNA-Seq Based Toxicity Analysis of Mesoporous Polydopamine Nanoparticles in Mice Following Different Exposure Routes

Zihua Huang†, Luoyijun Xie†, Jifan Zhang, Qiyan Li, Yulin Liu, Xuemei Fu, Miaomiao Yuan* and Qingjiao Li**

The Eighth Affiliated Hospital, Sun Yat-sen University, Shenzhen, China

OPEN ACCESS

Edited by:
Qitong Huang,
Gannan Medical University, China

Reviewed by:
He Xiaoyan,
Anhui Medical University, China
Xudong Wang,
National Vaccine and Serum Institute, China

***Correspondence:**
Xuemei Fu
fxmzj2004@163.com
Miaomiao Yuan
yuanmm3@mail.sysu.edu.cn
Qingjiao Li
liqj23@mail.sysu.edu.cn

†These authors have contributed equally to this work and share first authorship

Specialty section:
This article was submitted to Nanobiotechnology, a section of the journal Frontiers in Bioengineering and Biotechnology

Received: *10 March 2022*
Accepted: *22 March 2022*
Published: *28 April 2022*

Citation:
Huang Z, Xie L, Zhang J, Li Q, Liu Y, Fu X, Yuan M and Li Q (2022) RNA-Seq Based Toxicity Analysis of Mesoporous Polydopamine Nanoparticles in Mice Following Different Exposure Routes. Front. Bioeng. Biotechnol. 10:893608. doi: 10.3389/fbioe.2022.893608

Mesoporous polydopamine nanoparticles (MPDA NPs) are promising nanomaterials that have the prospect of clinical application for multi-strategy antitumor therapy, while the biosecurity of MPDA NPs remains indistinct. Here, transcriptome sequencing (RNA-Seq) was performed to systematically reveal the toxicity of MPDA NPs to five categories of organs after three different exposure routes, including intravenous injection, intramuscular injection, and intragastric administration. Our results uncovered that MPDA NPs could be deposited in various organs in small amounts after intravenous administration, not for the other two exposure routes. The number of differentially expressed genes (DEGs) identified in the heart, liver, spleen, lung, and kidney from the intragastric administration group was from 22 to 519. Similarly, the corresponding number was from 23 to 64 for the intramuscular injection group and was from 11 to 153 for the intravenous injection group. Functional enrichment analyses showed 6, 39, and 4 GO terms enriched for DEGs in intragastric administration, intramuscular injection, and intravenous injection groups, respectively. One enriched pathway was revealed in intragastric administration group, while no enriched pathway was found in other groups. Our results indicated that MPDA NPs produced only slight changes at the transcriptome level in mice, which provided new insights for further clinical application of MPDA NPs.

Keywords: transcriptome sequencing, MPDA NPs, intravenous injection, intramuscular injection, intragastric administration

1 INTRODUCTION

An increasing number of nanotechnologies are being developed for medical applications, including drug and gene delivery, clinical diagnostics as well as improved imaging agents, and several nanoparticle-based delivery systems have entered clinical trials (English and Aloi, 2015; Verma et al., 2015; Stidl et al., 2016). In parallel, the potential harm to public health and the environment brought by nanotechnologies has caught the attention of researchers. In the past decade, the biosafety of nanomaterials has been one of the major obstacles to the further use of nanoparticles in medical applications (Greish et al., 2018).

It was reported that polydopamine (PDA) had been widely utilized in tumor nanodrug delivery systems (Wang et al., 2018; Zeng et al., 2018; Li et al., 2020), which could significantly improve the drug distribution in the body, enhance the curative benefits as well as reduce toxic and side effects.

However, traditional PDA nanoparticles have a finite specific surface area, and the loaded drugs are easily separated under complex physiological conditions, limiting the drug-loading efficiency and tumor suppression efficiency. To solve these problems, Tang et al. (2015) synthesized mesoporous polydopamine nanoparticles (MPDA NPs) based on a preparation procedure for mesoporous carbon material using high-molecular-weight block copolymers as templates (Tang et al., 2015), which provided new insight into high drug-loading capacity, multimodal anticancer treatment, and visual therapy of nanoparticles. Despite the fascinating applicability of MDPA NPs, the toxicity and safety of MDPA NPs remained unknown, which prevented further clinical application.

The exposure route of the nanomaterials is a key factor in the interaction between nanomaterials and the human body. More specifically, various exposure routes could affect the toxicity, distribution, metabolism as well as their performance as nanomedicine of nanomaterials in the human body. For example, Elbrink et al. (2021) evaluated the impact of drug loading and the administration routes for solid lipid nanoparticles (SLNs) and revealed that the subcutaneous injection performed better than the intramuscular injection and intravenous administration owing to lower blood perfusion in the subcutaneous tissues (Elbrink et al., 2021). In addition, Yu et al. (2017) systematically studied the distribution of polyethyleneimine-modified NaYF4:Yb, Er upconversion nanoparticles (PEI@UCNPs) in mice under different exposure routes and observed that a large number of PEI@UCNPs were deposited in the spleen within 30 days in the intraperitoneal administration group while PEI@UCNPs *via* intragastric administration exhibited an accumulation that decreased with time in various body tissues (Yu et al., 2017). Hence, it was necessary to systematically assess the biosafety of MPAD NPs undergoing various administration routes, which was one of the important steps before clinical application.

To understand and predict the toxicity of a compound at a systems level, global transcriptome sequencing (RNA-Seq) is undoubtedly the most optimal approach. For instance, Yang et al. (2020) revealed the modulation of gene expression in the liver and lungs after treatment with ZnO quantum dots (QDs) by using RNA-Seq, and the changed transcripts were used to infer the potential toxicity of ZnO QDs (Yang et al., 2020). On the one hand, RNA-Seq detects unknown transcripts, while the DNA microarrays could only detect specific transcripts since the probes are designed with specific nucleotide sequences (Kaliyappan et al., 2012; Casamassimi et al., 2017). On the other hand, RNA-Seq enables the quantification of gene expression levels and allele-specific expression in a single experiment, as well as the identification of novel genes, splice isoforms, and fusion transcripts (Casamassimi et al., 2017).

In this study, we systematically examined the toxicity of MPDA NPs with three different exposure routes, including intravenous injection, intramuscular injection, and intragastric administration. After injection of MPDA NPs to female mice for 7 days, histopathology observation was performed to measure the degree of deposition of MPDA NPs and morphological changes at the cell level on five categories of tissues including the heart, liver, lung, kidney, and spleen. Next, with the application of RNA-Seq technology, differentially expressed genes (DEGs) were acquired between the MPDA NP injection group and the control group. At last, the gene ontology (GO) and Kyoto encyclopedia of genes and genomes (KEGG) pathways annotation of DEGs were used to access the possible toxicity of the MPDA NPs at the transcriptome level. This study will be helpful for exploring the possibility of MPDA NPs in further clinical application, and especially for selecting the appropriate exposure routes.

TABLE 1 | Basic administration information of the mice exposed by the intragastric (i.g.) administration, intramuscular (i.m.) injection, and intravenous (i.v.) injection.

Group	Dose (mg)	Day	The number of mice
Control	0	7	3
i.g.	50	7	3
i.m.	40	7	3
i.v.	8	7	3

2 MATERIAL AND METHODS

Materials

Dopamine hydrochloride and 1,3,5-trimethylbenzene (TMB) were purchased from Aladdin Reagent (Shanghai, China). Ammonia aqueous solution ($NH_3{\cdot}H_2O$, 30 wt%) was purchased from Macklin (Shanghai, China). Pluronic F127 was purchased from Sigma-Aldrich (MO, United States). Phosphate buffered saline (PBS) was bought from Gibco (Shanghai, China). Anhydrous ethanol was bought from Aladdin Reagent (Shanghai, China). Chloral hydrate was bought from Xiya (Chengdu, China). Dopamine hydrochloride was bought from Aladdin Reagent (Shanghai, China).

Synthesis and Characterization of MPDA NPs

MPDA NPs were synthesized according to the procedure which had been previously reported (Chen et al., 2016). The structural and elemental distribution of MPDA NPs were detected by transmission electron microscope (TEM). The morphology of MPDA NPs was measured by scanning electron microscope (SEM). The particle size and zeta potential of MPDA NPs were determined by dynamic light scattering (DLS). The crystal structure was analyzed by X-ray powder diffraction (XRD). The surface area and pore diameter were determined by Brunauer–Emmett–Teller (BET).

Animals and Experiments

Twelve BALB/c mice (female, aged 4 weeks old, weight 20 ± 2 g) were supplied by the Guangdong Medical Laboratory Animal Center (Guangdong, China). To get mice to acclimate to the new environment, they were fed in rearing rooms for a week before intervention. The temperature in the rearing room was controlled at 20 ± 3°C and the relative humidity was from 30 to 73%. The

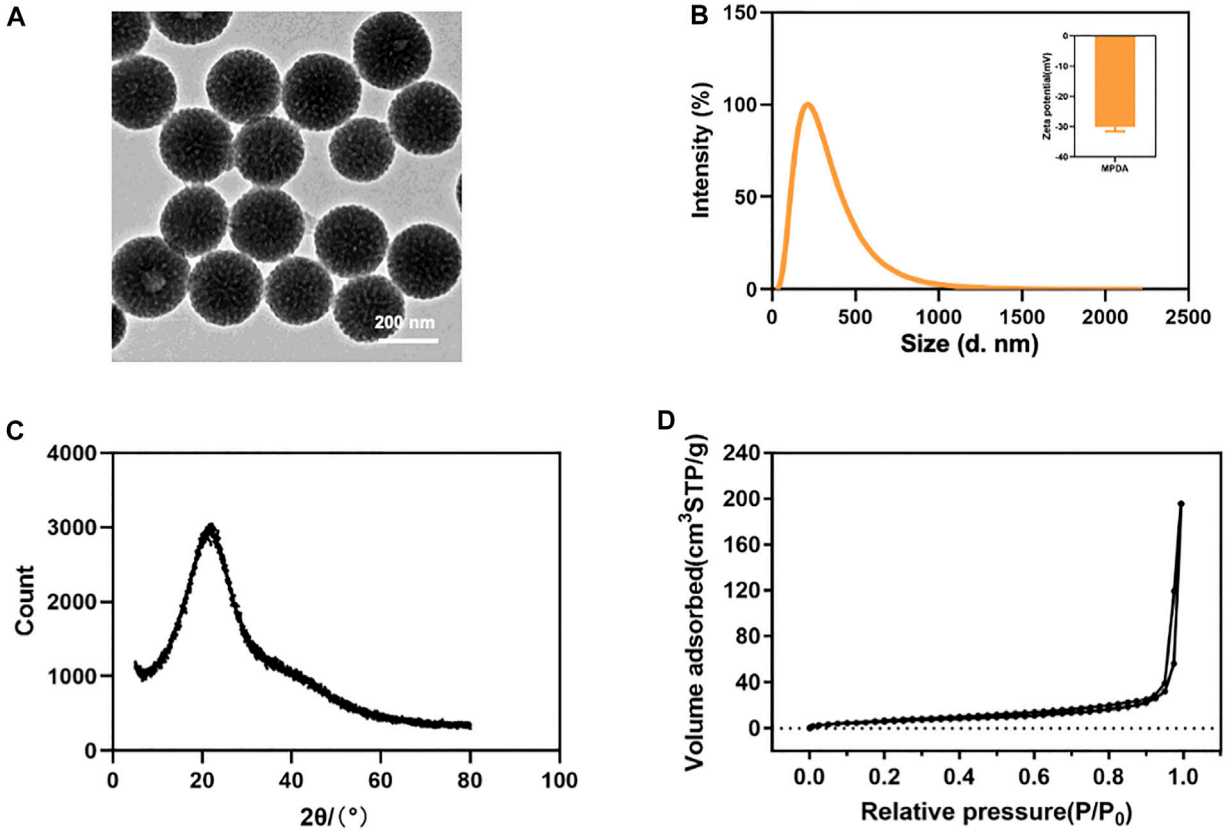

FIGURE 1 | (A) TEM image of MPDA NPs. **(B)** Size distribution and zeta potentials of MPDA NPs. **(C)** XRD spectrum of MPDA NPs. **(D)** N2 adsorption-desorption isotherms of MPDA NPs.

animals were housed (3/cage) and they were allowed to walk around the cage, eat and drink freely. The animal studies were approved by IACUC of The Eighth Affiliated Hospital, Sun Yat-sen University (2022-002-01).

After 1-week acclimation, 12 female BALB/c mice were randomly divided into 4 groups of 3 mice each (**Table 1**), and the mice of experimental groups were accepted MPDA NPs treatment for one time. In the following 7 days, the mice were allowed to walk around the cage, eat and drink freely, and their weight was recorded every day. On day 7, all mice were taken under anesthesia for cervical dislocation, and then organs were weighted and collected, including the heart, liver, spleen, kidney, and lung.

Organ Indexes

After the dissection of mice, the fat and fascia adhered to the exposed organs were carefully removed with surgical forceps, and then the organs were subsequently placed in cold PBS to wash away residual blood. After carefully drying, the organs were weighed immediately with an electronic balance. The following formula was used to calculate the organ indexes.

$$\text{organ indexes}(\%) = (W1)/W2*100\%$$

where W_1 is the weight of the organ and W_2 is the weight of the corresponding mouse.

Histopathological Examinations

After weighting, the needed tissues were immediately fixed in a 10% formalin solution. The fixed tissues were embedded in paraffin blocks and then sectioned into 5 mm sections and mounted on the slides. The slides were observed after hematoxylin and eosin staining (HE). Using a light microscope, the images were observed at a magnification of 100X.

RNA Extraction, cDNA Library Construction, and Sequencing

RNA Extraction

The TRIzol reagent (Invitrogen, Carlsbad, CA, United States) was used to extract total RNA from tissues of mice. First, RNA degradation and contamination were detected by agarose gel electrophoresis. The purity and concentration of RNA were assessed with Nanodrop. Second, to get more accurate information, the concentration and integrity of RNA were measured with a Qubit 2.0 Fluorometer (Life Technologies, Carlsbad, CA, United States) and an Agilent 2100 bioanalyzer (Santa Clara, CA, United States), respectively.

cDNA Library Construction

After RNA extraction, sequencing libraries were generated using the NEBNext® UltraTM RNA Library Prep Kit for Illumina®

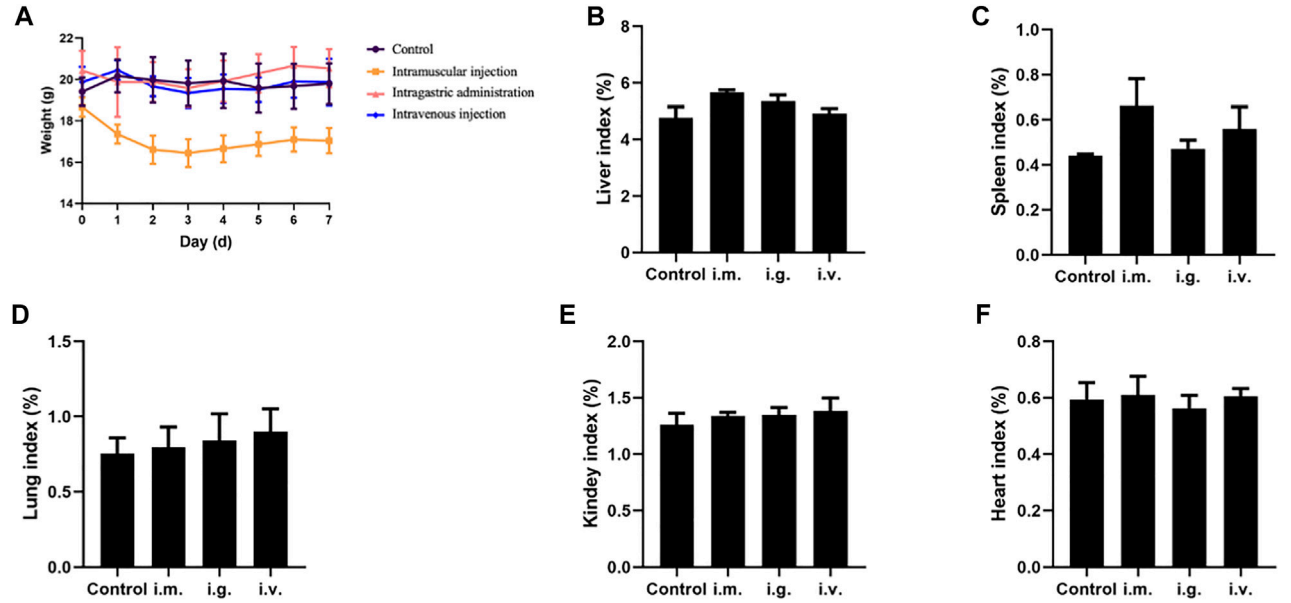

FIGURE 2 | (A) Body weight curve of mice. **(B–F)** Organ indexes of tissues from the mice exposed by intramuscular (i.m.) injection, intragastric (i.g.) administration, and intravenous (i.v.) injection, for the liver, spleen, lung, kidneys, and heart, respectively.

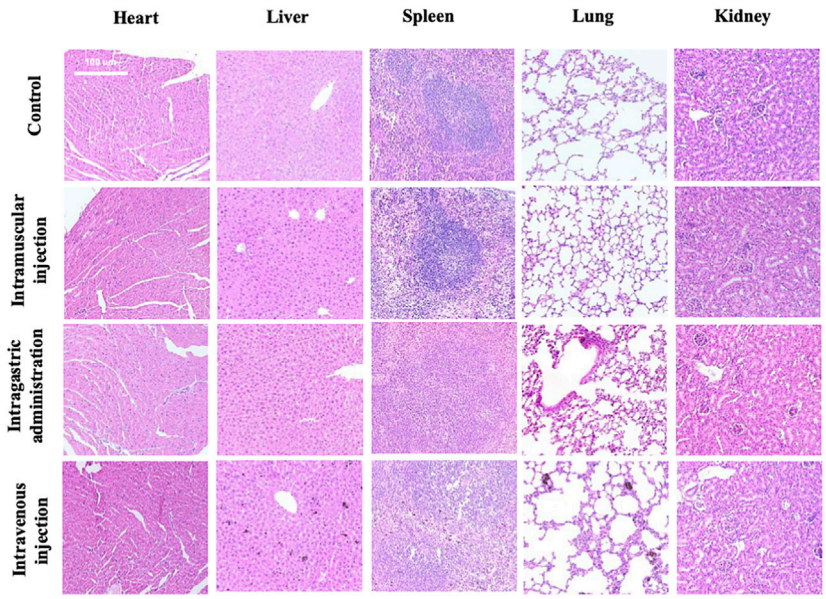

FIGURE 3 | Histological examination of tissues (heart, liver, spleen, lung, and kidneys) from the mice exposed by intramuscular (i.m.) injection, intragastric (i.g.) administration, and intravenous (i.v.) injection at day 7. The scale bar is 100 μm.

(NEB, United States), and each sample was labeled with an index code at the beginning.

First, mRNA was separated from total RNA using poly-T oligo-attached magnetic beads. Next, using divalent cations under elevated temperature, mRNA was fragmented in NEBNext First Strand Synthesis Reaction Buffer (5X). Then, the first-strand of cDNA was synthesized using a random hexamer primer and M-MuLV Reverse Transcriptase (RNase H). The second-strand cDNA was subsequently synthesized using DNA Polymerase I and RNase H. The remaining overhangs were converted into blunt ends via exonuclease/polymerase activities. After adenylation of 3′ ends of DNA fragments, NEBNext Adaptor

TABLE 2 | The number of DEGs of tissues (heart, liver, spleen, lung, and kidneys) from the mice exposed by the intragastric (i.g.) administration, intramuscular (i.m.) injection, and intravenous (i.v.) injection. (|log2 (fold change)| > 1, adjust *p* value <0.05).

Tissue	The number of DEGs		
	i.g.	i.m.	i.v.
Heart	37	58	124
Liver	519	64	52
Spleen	29	32	153
Lung	52	23	11
Kidney	22	34	93

with hairpin loop structures were ligated to prepare for hybridization. Then, the library fragments were purified with the AMPure XP system (Beckman Coulter, Beverly, United States) to select cDNA fragments of specified length interval 250–300 bp. Next, 3 μl USER Enzyme (NEB, United States) was used with size-selected, adaptor-ligated cDNA at 37°C for 15 min, followed by 5 min at 95°C before PCR. Then PCR was performed with Phusion High-Fidelity DNA polymerase, Universal PCR primers, and Index (X) Primer. Finally, PCR products were purified (AMPure XP system), and library quality was assessed on the Agilent Bioanalyzer 2100 system.

Sequencing

The library preparations were sequenced on an Illumina Novaseq 6000 platform (Novogene, Beijing, China) and 150 bp paired-end reads were generated.

Trimming, Transcriptomic Assembly, and Gene Annotation

The raw sequencing data obtained from the Illumina platform contained sequence artifacts, including reads containing adapter contamination, low-quality nucleotides, and unrecognizable nucleotide (N), which would cause errors in the following data analyses steps. Therefore, the downstream analysis was based on clean data which was transformed from raw data using Fastp software (Chen et al., 2018) according to the following standard: 1) Discarding a paired-end reads if either one end contains adapter contamination; 2) discarding a paired-end reads if more than 10% of bases are uncertain in either one end; 3) discarding a paired-end reads if the proportion of low quality (Phred quality <5) bases is over 50% in either one end. Next, the paired-end were mapped to the mouse genome [mm10, Genome Reference Consortium Mouse Build 38 (GCA_000001635.2)] using HISAT2 software (Kim et al., 2019). Counts for each gene were obtained using HTSeq software (Anders et al., 2015). Sequencing statistics for each sample were summarized in **Supplementary Table S1**.

Analyses of Differentially Expressed Genes

The differentially expressed genes between each treated group and the control group (n = 3 per group) were determined by the DESeq2 R package (Love et al., 2014), which is a popular method for differential analysis of count data. The DEGs were determined based on two criteria: 1) |log2 (fold change)| > 1 and 2) adjust *p* value <0.05. FPKM (fragments per kb per million reads) were transformed from count data in R (https://www.r-project.org/). To visualize the overall distribution of the DEGs, the volcano plots based on count data and the heatmaps based on FPKM data were created in R.

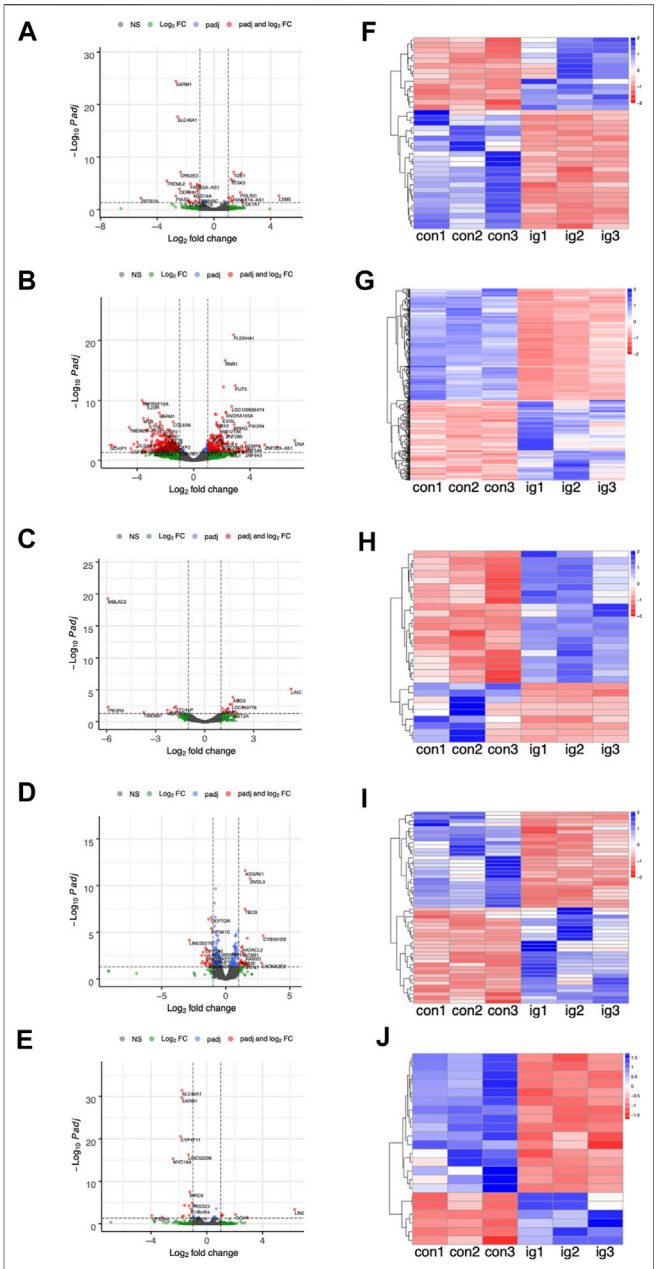

FIGURE 4 | (A–E) The volcano plots of DEGs between the intragastric (i.g.) administration group and control group, for the heart, liver, spleen, lung, and kidneys, respectively. **(F–J)** The heatmap of DEGs.

Functional Annotation of DEGs

To determine the functional annotation, GO enrichment (Harris et al., 2004), and KEGG pathway (Kanehisa and Goto, 2000),

TABLE 3 | The number of enriched GO terms of tissues (heart, liver, spleen, lung, and kidneys) from the mice exposed by the intragastric (i.g.) administration, intramuscular (i.m.) injection, and intravenous (i.v.) injection. (adjust *p* value <0.05, # of unique gene >1).

Tissue	i.g.			i.m.			i.v.		
	BP	MF	CC	BP	MF	CC	BP	MF	CC
Heart	0	4	0	0	0	6	0	0	2
Liver	0	2	0	0	6	0	0	1	0
Spleen	0	0	0	0	21	4	0	0	0
Lung	0	0	0	0	0	0	0	1	0
Kidney	0	0	0	0	2	0	0	0	0

TABLE 4 | The number of KEGG pathway of tissues (heart, liver, spleen, lung, and kidneys) from the mice exposed by the intragastric (i.g.) administration, intramuscular (i.m.) injection, and intravenous (i.v.) injection. (adjust *p* value <0.05, # of unique gene >1).

Group	The number of KEGG pathway		
	i.g.	i.m.	i.v.
Heart	0	0	0
Liver	0	0	0
Spleen	0	0	0
Lung	0	0	0
Kidney	1	0	0

enrichment analyses were performed for the DEGs using the clusterProfiler R package (Yu et al., 2012). Moreover, three categories were included in enriched GO terms, which are biological processes (BP), cellular components (CC), and molecular functions (MF). The enriched GO terms were selected based on two standards: 1) adjust *p* value <0.05 and 2) the number of unique genes in each GO term was more than one. Similarly, the enriched KEGG pathways were selected based on two standards: 1) adjust *p* value <0.05 and 2) the number of unique genes in each KEGG pathway was more than one.

3 RESULTS

Characterization of MPDA

Both TEM and SEM observations displayed spherical morphology and mesoporous structure with a clear arrangement and uniform size distribution of MPDA NPs (**Figure 1A**, **Supplementary Figures S1A, B, C**). As shown in **Figure 1B**, the DLS measurements showed that the average hydrated particle size was roughly 223 nm, and the zeta potential was approximately -30 mV, indicating that the MPDA NPs surface had a negative charge. At the same time, the element mapping of MPDA NPs showed that C, N, and O elements were evenly distributed throughout the nanoparticles, with the C skeleton forming the core structure of MPDA NPs (**Supplementary Figure S2**), which was consistent with the XRD results. As shown in **Figure 1C**, the XRD spectrum of MPDA NPs exhibited a wide peak centered at approximately $2\theta = 22^{\circ}$, and the corresponding crystal plane was (002), which verified that the main composition of MPDA was carbon element (Chen et al., 2016; Peng et al., 2019; Wang et al., 2019). The broad peak also indicated that MPDA NPs did not belong to crystalline materials (Ili Balqis et al., 2017). In addition, the MPDA NPs showed a BET surface area of 28.882 $m^2\ g^{-1}$ (**Figure 1D**), which enabled them to load the drug efficiently. According to the BJH model, the pore diameter of MPDA NPs was about 1.75 nm and its pore volume was 0.311 $cm^3\ g^{-1}$ (**Supplementary Figure S1D**).

Mortality, Body Weight, and Organ Indexes of Mice

In intravenous and intramuscular injection groups, mice were administrated with MPDA NPs suspended in PBS at 40 and 8 mg for a single time, and in the intragastric administration group, mice were administrated with MPDA NPs suspension at 50 mg at two points in time, 6 hours had passed between them. It was noticeable that the maximum tolerated dose (MTD) of intragastric administration was higher than that of other exposure routes. During the 7-day period, no mouse deaths were observed. Furthermore, no abnormal behaviors including vocalizations, labored breathing, difficulties moving, hunching or unusual interactions with cage mates were observed as well.

As shown in **Figure 2A**, the weight of mice in each group was relatively stable, but the weight of mice in the intramuscular injection group saw a slight decrease in the first 3 days. Organ indexes analysis was performed on the hearts, liver, spleen, lung, and kidneys of mice, and it was found that organ indexes did not alter significantly after different exposure routes to MPDA NPs (**Figures 2B–F**).

Histopathological Examinations

MPDA NPs did not induce any changes in both the shape and volume of the organs on day 7 by different exposure routes, while the color of the spleen and liver in the intramuscular injection group and spleen, liver, and lung in the intravenous injection group became darker than the control group (**Supplementary Figure S3**). Furthermore, **Figure 3** depicted the micromorphology of the organs of mice in each group after exposure to MPDA NPs. It could be observed that a small amount of MPDA NPs deposited in the liver, spleen, and lungs in the intravenous injection group, while no nanoparticles were observed in the organs of mice in the other two treated groups. It meant that some MPDA NPs could deposit in tissues passing through biological barriers and could not be excreted within 7 days. In addition, compared to the control group, the organs of mice in each experimental group did not display any histopathological changes.

TABLE 5 | Information of the enriched KEGG pathway.

Group	Tissue	KEGG id	Description	Gene no.	Genes	p.adj
i.g.	Kidney	mmu04020	Calcium signaling pathway	2	Itpkc/Mcoln2	0.0496

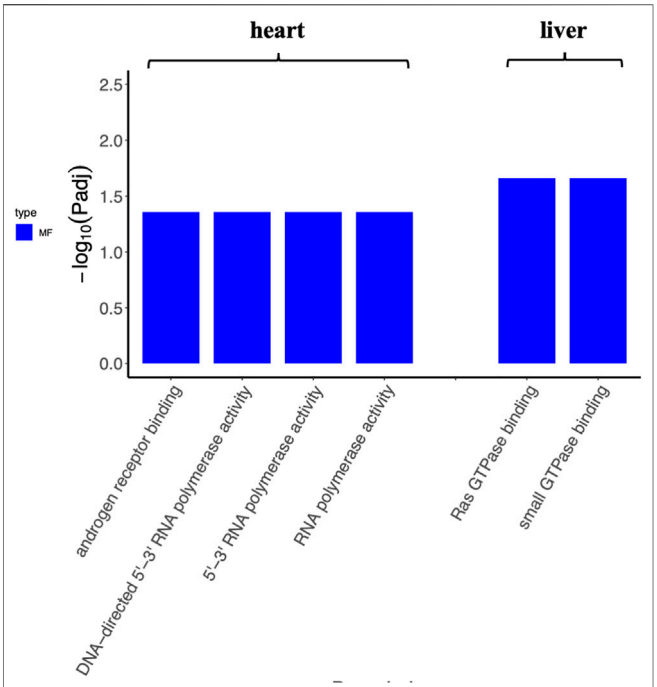

FIGURE 5 | The enriched GO terms of tissues (heart and liver) from the intragastric administration group. No GO term is enriched for the spleen, lung, and kidney.

Analysis of Differentially Expressed Genes

The number of DEGs between the treated groups and control group were list in **Table 2** and **Supplementary Table S2**. Furthermore, **Figure 4** display the heatmaps and volcano plots of DEGs between the intragastric administration group and control group, for the five tissues, including heart, liver, spleen, lung and kidney separately. Also, the DEGs of intramuscular group and intravenous group were shown in **Supplementary Figure S4** and **Supplementary Figure S5**. For the intragastric administration group, the organ with the largest number of DEGs was liver, up to 519. The rest of the organs had close numbers of DEGs, which were 37, 29, 52 and 22 identified in heart, spleen, lung and kidney separately. For the intramuscular injection group, the organ with the least number of DEGs was lung, down to 23. And 58, 64, 32 and 34 DEGs were identified in heart, liver, spleen, and kidney separately. For intravenous group, the organ with the least number of DEGs was lung, down to 11. And 124, 52, 153 and 93 DEGs were identified in heart, liver, spleen and kidney respectively. Furthermore, the number of up-regulated and down-regulated DEGs were close for each comparison (**Supplementary Tables S3–S5**).

Functional Annotation of DEGs

To determine the function of DEGs and metabolic pathway enrichment, GO (**Table 3**) and KEGG pathway analyses (**Table 4**, **Table 5**) were performed on DEGs in each group. For intragastric administration group, we obtained 6 enriched GO terms, including regulation of cellular response to androgen receptor binding (GO:0050681), polymerase activity (GO: 0003899, GO:0034062, GO:0097747), and GTPase binding (GO:0017016, GO:0031267) (**Figure 5**, **Supplementary Table S6**). Only one enriched KEGG pathway was observed, which is calcium signaling pathway (mmu04020). For intramuscular injection group, we obtained 39 enriched GO terms, including transmembrane transporter activity (GO: 0008509, GO:0046943, GO:0051184, GO:0046873, GO: 0072349, GO:0005342, GO:0022803, GO:0015081), channel activity (GO:0015267, GO:0022836, GO:0005217, GO:0005216, GO:0022839, GO:0099094, GO:0022834, GO:0015276, GO: 0022838) and so on (**Supplementary Figure S6**, **Supplementary Table S7**). No enriched KEGG pathway was observed in this group. For intravenous injection group, we obtained 4 enriched GO terms, including catenin complex (GO:0016342), apical junction complex (GO:0043296), mismatch repair complex binding (GO:0032404), and catalytic activity, acting on RNA (GO:0140098) (**Supplementary Figure S7**, **Supplementary Table S8**). No enriched KEGG pathway was found in this group as well.

4 DISCUSSION

In the past few years, researchers mainly focused on the application of MPDA NPs, especially its application in tumor treatment. For example, Zhang et al. (2019) discovered an MPDA-based synthetic for chemo-photothermal therapy, polyethylene glycol-modified MPDA (PEG-MPDA), which had not only photothermal conversion efficiency but also high paclitaxel (PTX) loading content (Zhang et al., 2019). According to their result, the tumor ablation could be observed after MPDA-PEG-PTX treatment combined with 2 Wcm-2 laser irradiations for 5 min. In addition to chemo-photothermal therapy, MPDA could also be applied to immuno-photothermal, a combination of photothermal therapy and photodynamic therapy/chemodynamic therapy, as well as cancer theranostics (Hu et al., 2019; Huang et al., 2021; Wu et al., 2021). However, few studies have illustrated the potential toxicity of MPDA so far, which blocked further clinical application. In this study, we adopted RNA sequencing-based strategy to discover the toxicity of MPDA NPs.

In our pre-experiment, we exposed mice to MPDA for different durations (7 and 30 days) and then stained the heart, liver, spleen, lung, and kidney with HE staining. **Figure 3** displays the tissues examined at day 7, while **Supplementary Figure S8** (**Supplementary Figure S8**) displays the tissues examined on day 30. We did not observe any changes in the tissues with the different time periods of administration. Therefore, we decided to examine the tissues on day 7. As mentioned above, on day 7, the mice from the intramuscular injection group weighed approximately 2 g less than they did on day 1 while the weight of mice from the other two experimental groups did not significantly change. We assumed that the abnormal phenomenon was likely caused by the injection of a large volume of suspension rather than the toxicity of MPDA NPs. It was necessary to point out that the volume of MPDA suspension for this group was up to 1.6 ml, which was a lot for mice around 20 g. However, it was difficult to reduce the volume of suspension

because the solubility of MPDA NPs was limited. Furthermore, we observed some MDPA NPs deposition in several tissues in intravenous group, which indicated the material has not been completely metabolized. In the intravenous injection group, deposited MPDA NPs were not observed in the heart and kidney, but could be observed in the liver, spleen, and lung of the same mouse. This phenomenon supported the different metabolic capacities of different visceral tissues to MPDA. The photographs we presented above just showed the result on day 7 and it might take more time to metabolize.

No enriched KEGG pathway was found in both intramuscular injection and intravenous injection groups. In parallel, only one KEGG pathway was identified in kidneys in the intragastric administration group, which was the calcium signaling pathway. Calcium ions are abundant in the human body, regulating significant physiological activities as an important signaling molecule. It is reported that the concentration of Ca^{2+} plays an important role in the regulation of nervous system excitability, the contraction of muscles, intestinal microbial activity, the activity of enzymes, and the biological clock (Simpson et al., 1995; Kon and Fukada, 2015). As shown in **Table 5**, two down-regulated genes were included in this pathway, suggesting the calcium signaling pathway might be inhibited after MPDA NPs intragastric administration. In other words, calcium concentration in the human body should be of concern when receiving MPDA treatment.

In conclusion, we investigated the toxicity of MPDA NPs on global gene expression of important organs by RNA-Seq. The DEGs detected in each organ were quite a few and only several GO terms, and one KEGG pathway were enriched for these DEGs. The results suggested that MPDA NPs did not cause great or serious changes in mice from three different administration routes, which shed light on the toxicity of MPDA NPs at the molecular mechanism level.

DATA AVAILABILITY STATEMENT

The raw RNA sequencing data are available from Genome Sequence Archive (GSA) at The National Genomics Data Center (https://ngdc.cncb.ac.cn), with the accession number PRJCA008032.

ETHICS STATEMENT

The animal study was reviewed and approved by the IACUC of The Eighth Affiliated Hospital, Sun Yat-sen University (2022-002-01).

AUTHOR CONTRIBUTIONS

ZH: Data curation, writing—original draft, writing—review and editing. LX: Methodology, writing—review and editing. JZ: Methodology. QL: Software. YL: Validation. XF: Conceptualization, funding acquisition, writing—review and editing. MY: Conceptualization, funding acquisition, writing—review and editing. QL: Project administration, conceptualization, funding acquisition, writing—review and editing.

FUNDING

This work was supported by the National Natural Science Foundation of China (grant numbers 32000466, 81972488, 91959204, and 81871197); the Natural Science Foundation of Guangdong Province (grant number 2019A1515111174); the Shenzhen Science and Technology Program (grant numbers JCYJ20190808100817047, JCYJ20210324115209026, and RCBS20200714114909234); and the Shenzhen "Sanming" Project of Medicine (grant number SZSM201602102).

ACKNOWLEDGMENTS

The authors would like to thank the Eighth Affiliated Hospital, Sun Yat-sen University, for providing the experimental platform.

SUPPLEMENTARY MATERIAL

The Supplementary Material for this article can be found online at: https://www.frontiersin.org/articles/10.3389/fbioe.2022.893608/full#supplementary-material

REFERENCES

Anders, S., Pyl, P. T., and Huber, W. (2015). HTSeq--a Python Framework to Work with High-Throughput Sequencing Data. *Bioinformatics* 31 (2), 166–169. doi:10.1093/bioinformatics/btu638

Casamassimi, A., Federico, A., Rienzo, M., Esposito, S., and Ciccodicola, A. (2017). Transcriptome Profiling in Human Diseases: New Advances and Perspectives. *Int. J. Mol. Sci.* 18 (8), 1652. doi:10.3390/ijms18081652

Chen, F., Xing, Y., Wang, Z., Zheng, X., Zhang, J., and Cai, K. (2016). Nanoscale Polydopamine (PDA) Meets π-π Interactions: An Interface-Directed Coassembly Approach for Mesoporous Nanoparticles. *Langmuir* 32 (46), 12119–12128. doi:10.1021/acs.langmuir.6b03294

Chen, S., Zhou, Y., Chen, Y., and Gu, J. (2018). Fastp: An Ultra-Fast All-In-One FASTQ Preprocessor. *Bioinformatics (Oxford, England)* 34 (17), i884–i890. doi:10.1093/bioinformatics/bty560

Elbrink, K., Van Hees, S., Chamanza, R., Roelant, D., Loomans, T., Holm, R., et al. (2021). Application of Solid Lipid Nanoparticles as a Long-Term Drug Delivery Platform for Intramuscular and Subcutaneous Administration: *In Vitro* and *In Vivo* Evaluation. *Eur. J. Pharm. Biopharm.* 163, 158–170. doi:10.1016/j.ejpb.2021.04.004

English, C., and Aloi, J. J. (2015). New FDA-Approved Disease-Modifying Therapies for Multiple Sclerosis. *Clin. Ther.* 37 (4), 691–715. doi:10.1016/j.clinthera.2015.03.001

Greish, K., Mathur, A., Bakhiet, M., and Taurin, S. (2018). Nanomedicine: Is it Lost in Translation? *Ther. Deliv.* 9 (4), 269–285. doi:10.4155/tde-2017-0118

Harris, M. A., Clark, J., Ireland, A., Lomax, J., Ashburner, M., Foulger, R., et al. (2004). The Gene Ontology (GO) Database and Informatics Resource. *Nucleic Acids Res.* 32 (Database issue), 258D–261D. doi:10.1093/nar/gkh036

Hu, X., Lu, Y., Shi, X., Yao, T., Dong, C., and Shi, S. (2019). Integrating *In Situ* Formation of Nanozymes with Mesoporous Polydopamine for Combined Chemo, Photothermal and Hypoxia-Overcoming Photodynamic Therapy. *Chem. Commun.* 55 (98), 14785–14788. doi:10.1039/c9cc07125c

Huang, C., Zhang, L., Guo, Q., Zuo, Y., Wang, N., Wang, H., et al. (2021). Robust Nanovaccine Based on Polydopamine-Coated Mesoporous Silica Nanoparticles for Effective Photothermal-Immunotherapy against Melanoma. *Adv. Funct. Mater.* 31 (18), 2010637. doi:10.1002/adfm.202010637

Ili Balqis, A. M., Nor Khaizura, M. A. R., Russly, A. R., and Nur Hanani, Z. A. (2017). Effects of Plasticizers on the Physicochemical Properties of Kappa-Carrageenan Films Extracted from Eucheuma Cottonii. *Int. J. Biol. macromolecules* 103, 721–732. doi:10.1016/j.ijbiomac.2017.05.105

Kaliyappan, K., Palanisamy, M., Govindarajan, R., and Duraiyan, J. (2012). Microarray and its Applications. *J. Pharm. Bioall Sci.* 4 (Suppl. 2), 310–312. doi:10.4103/0975-7406.100283

Kanehisa, M., and Goto, S. (2000). KEGG: Kyoto Encyclopedia of Genes and Genomes. *Nucleic Acids Res.* 28 (1), 27–30. doi:10.1093/nar/28.1.27

Kim, D., Paggi, J. M., Park, C., Bennett, C., and Salzberg, S. L. (2019). Graph-Based Genome Alignment and Genotyping with HISAT2 and HISAT-Genotype. *Nat. Biotechnol.* 37 (8), 907–915. doi:10.1038/s41587-019-0201-4

Kon, N., and Fukada, Y. (2015). Cognitive Function and Calcium. Ca2+-Dependent Regulatory Mechanism of Circadian Clock Oscillation and its Relevance to Neuronal Function. *Clin. Calcium* 25 (2), 201–208.

Li, Y., Hong, W., Zhang, H., Zhang, T. T., Chen, Z., Yuan, S., et al. (2020). Photothermally Triggered Cytosolic Drug Delivery of Glucose Functionalized Polydopamine Nanoparticles in Response to Tumor Microenvironment for the GLUT1-Targeting Chemo-Phototherapy. *J. Controlled Release* 317, 232–245. doi:10.1016/j.jconrel.2019.11.031

Love, M. I., Huber, W., and Anders, S. (2014). Moderated Estimation of Fold Change and Dispersion for RNA-Seq Data with DESeq2. *Genome Biol.* 15 (12), 550. doi:10.1186/s13059-014-0550-8

Peng, L., Hung, C.-T., Wang, S., Zhang, X., Zhu, X., Zhao, Z., et al. (2019). Versatile Nanoemulsion Assembly Approach to Synthesize Functional Mesoporous Carbon Nanospheres with Tunable Pore Sizes and Architectures. *J. Am. Chem. Soc.* 141 (17), 7073–7080. doi:10.1021/jacs.9b02091

Simpson, P. B., John Challiss, R. A., and Nahorski, S. R. (1995). Neuronal Ca2+ Stores: Activation and Function. *Trends Neurosciences* 18 (7), 299–306. doi:10.1016/0166-2236(95)93919-o

Stidl, R., Fuchs, S., Bossard, M., Siekmann, J., Turecek, P. L., and Putz, M. (2016). Safety of PEGylated Recombinant Human Full-Length Coagulation Factor VIII (BAX 855) in the Overall Context of PEG and PEG Conjugates. *Haemophilia* 22 (1), 54–64. doi:10.1111/hae.12762

Tang, J., Liu, J., Li, C., Li, Y., Tade, M. O., Dai, S., et al. (2015). Synthesis of Nitrogen-Doped Mesoporous Carbon Spheres with Extra-Large Pores through Assembly of Diblock Copolymer Micelles. *Angew. Chem. Int. Ed. Engl.* 54 (2), 588–593. doi:10.1002/anie.201407629

Verma, J., Lal, S., and Noorden, C. J. F. V. (2015). Inorganic Nanoparticles for the Theranostics of Cancer. *J. Eur. J. Nanomedicine* 7 (4), 271–287. doi:10.1515/ejnm-2015-0024

Wang, Z., Duan, Y., and Duan, Y. (2018). Application of Polydopamine in Tumor Targeted Drug Delivery System and its Drug Release Behavior. *J. Controlled Release* 290, 56–74. doi:10.1016/j.jconrel.2018.10.009

Wang, Z., Wang, L., Prabhakar, N., Xing, Y., Rosenholm, J. M., Zhang, J., et al. (2019). CaP Coated Mesoporous Polydopamine Nanoparticles with Responsive Membrane Permeation Ability for Combined Photothermal and siRNA Therapy. *Acta Biomater.* 86, 416–428. doi:10.1016/j.actbio.2019.01.002

Wu, Y., Huang, Y., Tu, C., Wu, F., Tong, G., Su, Y., et al. (2021). A Mesoporous Polydopamine Nanoparticle Enables Highly Efficient Manganese Encapsulation for Enhanced MRI-Guided Photothermal Therapy. *Nanoscale* 13 (13), 6439–6446. doi:10.1039/d1nr00957e

Yang, Y., Li, P., Lin, Y., Li, Z., Cui, T., Song, Z., et al. (2020). Gene Expression Profiling of the Liver and Lung in Mice after Exposure to ZnO Quantum Dots. *Int. J. Nanomedicine* 15, 2947–2955. doi:10.2147/IJN.S246754

Yu, G., Wang, L.-G., Han, Y., and He, Q.-Y. (2012). ClusterProfiler: An R Package for Comparing Biological Themes Among Gene Clusters. *OMICS: A J. Integr. Biol.* 16 (5), 284–287. doi:10.1089/omi.2011.0118

Yu, J., Yin, W., Peng, T., Chang, Y.-N., Zu, Y., Li, J., et al. (2017). Biodistribution, Excretion, and Toxicity of Polyethyleneimine Modified NaYF4:Yb,Er Upconversion Nanoparticles in Mice via Different Administration Routes. *Nanoscale* 9 (13), 4497–4507. doi:10.1039/c7nr00078b

Zeng, X., Luo, M., Liu, G., Wang, X., Tao, W., Lin, Y., et al. (2018). Polydopamine-Modified Black Phosphorous Nanocapsule with Enhanced Stability and Photothermal Performance for Tumor Multimodal Treatments. *Adv. Sci.* 5 (10), 1800510. doi:10.1002/advs.201800510

Zhang, L., Yang, P., Guo, R., Sun, J., Xie, R., and Yang, W. (2019). Multifunctional Mesoporous Polydopamine with Hydrophobic Paclitaxel for Photoacoustic Imaging-Guided Chemo-Photothermal Synergistic Therapy. *Int. J. Nanomedicine* 14, 8647–8663. doi:10.2147/IJN.S218632

Conflict of Interest: The authors declare that the research was conducted in the absence of any commercial or financial relationships that could be construed as a potential conflict of interest.

frontiers | Frontiers in Bioengineering and Biotechnology

ORIGINAL RESEARCH
published: 10 May 2022
doi: 10.3389/fbioe.2022.903424

A New Nano Adjuvant of PF3 Used for an Enhanced Hepatitis B Vaccine

*Pu Shan[1], Zhibiao Wang[1], Jilai Li[1], Duoqian Wei[1], Zhuan Zhang[1], Shaojie Hao[1], Yibo Hou[1], Yunyang Wang[2], Shuxiang Li[1], Xudong Wang[1] and Jing Xu[1]**

[1]National Vaccine and Serum Institute (NVSI), China National Biotech Group (CNBG), Beijing, China, [2]Beijing Institute of Biological Products Co., Beijing, China

Recombinant protein vaccines, with highly pure ingredients and good safety, are gradually replacing some attenuated and inactivated vaccines in clinical practice. However, since their low immunogenicity of the recombinant proteins, adjuvants are often needed to enhance immune response after vaccination. Aluminum adjuvant has been widely used in some vaccines for decades, it can induce strong humoral immunity, but the deficiency of cellular immunity limits its application for some vaccines. Therefore, it is urgently needed to develop novel adjuvant to increase not only humoral but also cellular immune response. To address this, we designed and prepared a new nano adjuvant (PF3) through microfluidization by the combination of saponin (Ginsenoside Rg1) and oil-in-water nano emulsion (NE) in the present study. As compared to aluminum adjuvant, PF3 had stronger humoral and cellular immune induction effect because of high cellular uptake and activization of immune response pathways. Furthermore, PF3 showed better immune enhancement and acceptable biosafety equivalent to that of aluminum adjuvant. In addition, no obvious changes of PF3 were observed in size and zeta potential after 12 weeks storage at 4 and 37°C, demonstrating its high stability *in vitro*. This study provided an adjuvant platform to replace traditional aluminum adjuvant in design of recombinant vaccines.

Keywords: PF3, nano adjuvant, ginsenoside Rg1, aluminum adjuvant, hepatitis B surface antigen

OPEN ACCESS

Edited by:
Qitong Huang,
Gannan Medical University, China

Reviewed by:
Boya Liu,
Harvard Medical School, Boston, United States
Yujing Li,
Beijing Institute of Technology, China

****Correspondence:***
Jing Xu
xj17b@163.com
xujing@sinopharm.com

Specialty section:
This article was submitted to Nanobiotechnology, a section of the journal Frontiers in Bioengineering and Biotechnology

Received: *24 March 2022*
Accepted: *25 April 2022*
Published: *10 May 2022*

Citation:
Shan P, Wang Z, Li J, Wei D, Zhang Z, Hao S, Hou Y, Wang Y, Li S, Wang X and Xu J (2022) A New Nano Adjuvant of PF3 Used for an Enhanced Hepatitis B Vaccine. Front. Bioeng. Biotechnol. 10:903424. doi: 10.3389/fbioe.2022.903424

INTRODUCTION

The importance of adjuvants to vaccines such as recombinant proteins is self-evident. In clinical settings, adjuvants are often incorporated within vaccine formulations through physical or chemical association with antigens (Lee et al., 2020). Aluminum has been on the market for nearly 90 years as a vaccine adjuvant, however, it tends to attach on the membrane rather than entering the dendritic cells (DCs), leading to the absence of intracellular transfer and process of the antigens, and thus limits T-cell-mediated immunity (Peng et al., 2020). The development trend of adjuvants clearly shows that single components, such as aluminium adjuvants, cytokine or chemokine adjuvants and TLR (Toll-like receptor) agonists, often fail to meet the needs of various infectious diseases. Thus, combined adjuvants show great promise in the development of adjuvants in the future. For example, $AS01_B$ is one type of combined adjuvant that is composed of a liposome, MPL and QS21 and $AS01_B$ has been employed in a recombinant herpes zoster vaccine, Shingrix. It reduced the risk of herpes zoster infection by 97.2% in an elderly population aged 50 years and older and by 96.6–97.9% for all age groups (Syed, 2018). However, the efficacy of the marketed live attenuated herpes zoster vaccine Zostavax was only 69.8% in the population aged 50–59 years, and it was even lower in the elderly

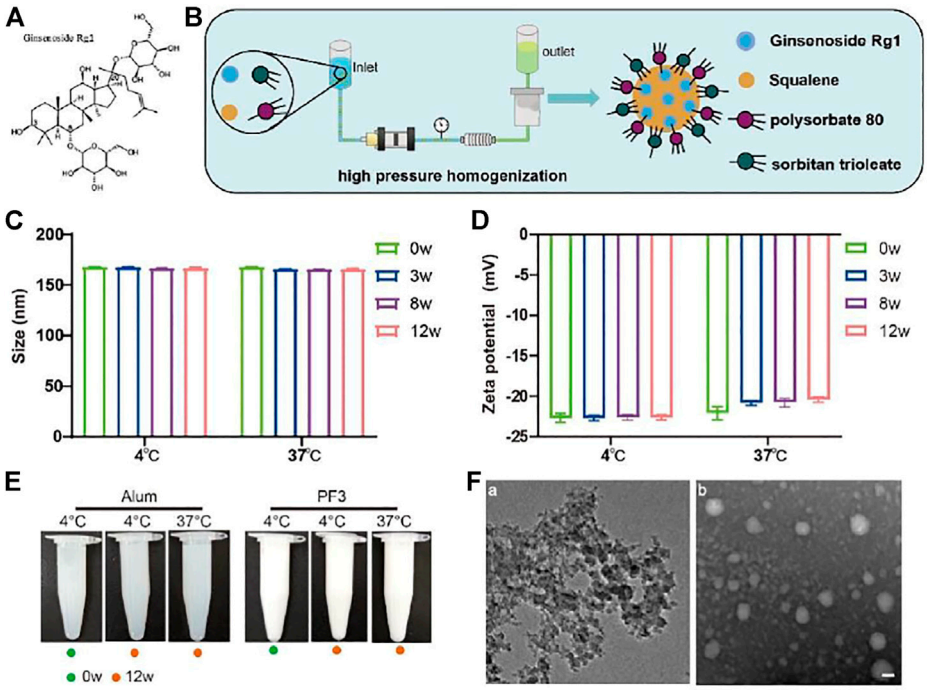

FIGURE 1 | Preparation and characterization of PF3. **(A).** Chemical structure of ginsenoside Rg1. **(B).** Schematic illustration of PF3 preparation process. **(C,D).** Size and Zeta potential of PF3 after 0, 3, 8 and 12 weeks of storge at the indicated temperature. **(E).** Appearance of aluminium hydroxide and PF3 after 0 or 12 weeks of storge at the indicated temperature. **(F).** TEM images of aluminium hydroxide **(a)** and PF3 **(b)**. Scale bar represents 100 nm.

population aged over 60 years (James et al., 2018). Therefore, combined adjuvants showed the tremendous potential in boosting immune response of vaccines.

The safety of combined adjuvants is also very important. However, the saponin QS21 in $AS01_B$ adjuvant can cause injection-site pain and myalgia (Syed, 2018). Saponins are natural glycosides of steroid or triterpene which exhibited many different biological and pharmacological activities (Sun et al., 2009). Panax ginseng is an edible plant with medicinal effects, such as antitumour, anti-fatigue, immune boosting and anti-aging (Lee and Lau, 2011; Patel and Rauf, 2017). Ginsenoside is an important component of Panax ginseng, and it is a type of immunomodulator that has a wide range of pharmacological activities and significant effects on cardiovascular, central nervous system, endocrine and immune systems (Shin et al., 2015; Ni et al., 2016). Ginsenosides are divided into three types according to the chemical structure of their aglycone: 1) ginsenediol saponins, including Ra1, Ra2, Ra3, Rb1, Rb2, Rb3, Rc and Rd; 2) ginsentriol saponins, including Re, Rf, Rg1, Rg2, Rh1 and notoginsenoside; and 3) ginsenoside of oleanolic acid as a glycoside (Li et al., 2019). Rg1 (**Figure 1A**) is the main component of ginseng, and it belongs to the protopanaxatriol type (PPT), which has antitumour and steroid hormone effects and improves the non-specific immune function of mice via an unclear mechanism of action. Rg1 plus oil significantly upregulated TLR2 expression but decreased the level of NF-κB in splenocytes. Rg1-oil adjuvant may increase the levels of IL-2 and IL-4 by upregulating TLR2, thus enhancing the immune effect of B. bronchiseptica vaccine in rabbits (Chenwen et al., 2021).

Although the traditional hepatitis B vaccines with aluminum adjuvants can induce high titers of anti-HBs, they cannot cause an adequate cellular immune response to effectively protect hepatocytes from hepatitis B virus (HBV) invasion (Xu et al., 2015). The immune response initiated by the T-cell response to viral antigens is thought to be fundamental for viral clearance and disease pathogenesis in HBV infection (Jung and Pape, 2002). With the development of nanotechnology, nano adjuvants have more advantages, such as enhancing the ability of helping more antigens to enter lysosomes of innate immune cells, or achieving step-by-step multiple stimulus-responsive drug delivery which is similar to that of nanoparticle development in tumor treatment (Yi et al., 2022). In order to overcome weak cellular immunity of aluminum adjuvant, a new nano adjuvant (PF3) was constructed by dynamic high-pressure microfluidization in the present study (**Figure 1B**). The PF3 is stored at 4°C in solution form as a kind of oil-in-water nano adjuvant. The PF3 consists of ginsenoside Rg1, a natural plant-based immune stimulant, and the MF59-like NE, a nano emulsion which has been marketed and used safely for many years (O'Hagan et al., 2012; O'Hagan et al., 2013; Orsi et al., 2013; Schaffner et al., 2018). Similar to aluminum adjuvant, MF59 induced weak cellular immunity (Del Giudice et al., 2018). The prepared nano adjuvant provided a more comprehensive and balanced humoral and cellular immunologic response and an expected better choice of compound adjuvant for hepatitis B virus than traditional aluminum adjuvant. Moreover, PF3 displayed

synergy with Hepatitis B surface antigen (HBsAg) which enhanced cell-mediated immune response. Additionally, PF3 performed excellent biocompatibility *in vivo* with well-controlled immunogenicity and it has good accessibility, low cost and high purity. We anticipate that the new nano PF3 may serve as a safe, accessible and efficient adjuvant.

MATERIALS AND METHODS

Adjuvants Preparation, Antigen, Reagents and Sample for Immunization

Aluminium hydroxide was purchased from Beijing Institute of Biological Products Co., Ltd. (Beijing, China). PF3 (3.9% squalene, 0.47% polysorbate 80 and 0.47% sorbitan trioleate, 0.01% Rg1) was prepared through dynamic high-pressure microfluidization (Microfludics, USA) with the pressure of 10000psi by 7 cycles. Specifically, the oil phase containing squalene and sorbitan trioleate and the water phase containing polysorbate 80 and Rg1 were prepared respectively, then the two were mixed into coarse emulsion, and then the PF3 was prepared through dynamic high-pressure microfluidization. Each batch of PF3 can be up to 20 L in production scale. Squalene, polysorbate 80 and sorbitan trioleate were purchased from Nanjing Weir Pharmaceutical Co., Ltd. (Nanjing, China) and they are all medicinal grade. Ginsenoside Rg1 (purity 99.44%, HPLC) was purchased from Chengdu MUST Bio-Technology Co., Ltd. (Chengdu, China).

Hepatitis B surface antigen (HBsAg) was purchased from the Beijing Institute of Biological Products Co., Ltd. (Beijing, China). HRP Conjugated Goat anti-Mouse IgG1 and IgG2a were purchased from Bethyl Laboratories, Inc. (Montgomery, TX, USA). Anti-HBs kit was purchased from Beijing WANTAI Biotech CO., Ltd. (Beijing, China). Flow cytometry kit was purchased from BD (BD, USA). All other chemical reagents are products of analytically pure grade.

For the preparation of samples for immunization, PF3 (100 μg/ml target concentration of Rg1) was mixed 1:1 v/v with HBsAg antigen (5 μg/ml target concentration).

Physiochemical Characteristics and Stability of PF3

The particle size, PdI and Zeta potential of PF3 at different time points (weeks 3, 8, and 12) at 4 and 37°C were determined to delineate the physical characteristics and stability. Particle size, PdI and Zeta potential were determined using the ZetaSizer Nano ZS90 dynamic light scattering instrument (Malvern Instruments, United Kingdom). For transmission electron microscopy (TEM,JEOL, Japan) images of PF3 and aluminium hydroxide, first, put a drop of sample (about 30 μl) to the supporting film, stay for about 10min, then put the dried supporting film on the sealing film, put a drop of uranium dioxy acetate dye, stay for 90s, and then dry on the filter paper for 3 h for observation.

Mice and Method of Euthanasia

Eight-week-old, specific pathogen free (SPF) female BALB/c mice were purchased from Beijing Vital River Laboratory Animal Technology Co., Ltd. (Beijing, China) and randomly divided into several different groups, with starting weights between 16 and 18 g. The experiment personnel are blind to each immunized group. The Animal Ethics Committee of the National Vaccines and Serum Institute (AECNVSI) approved the animal experiments and all procedures. Mice were euthanized via an intraperitoneal injection of 80 mg/kg sodium pentobarbital (Serva, Germany) and blood or spleens were collected.

Grouping of Mice and Immunization Procedures

The mice were divided into 3 groups of 10 mice: S(HBsAg), S + $Al(OH)_3$ and S + PF3. Mice were immunized at weeks 0 and 3 via intramuscular injection, 0.5 μg/100 μl HBsAg per mouse for one dose, and blood was collected from 5 mice per group 3 weeks after immunization for the quantitative detection of anti-HB antibodies and IgG1 and IgG2a antibody subclass detection using enzyme-linked immunosorbent assay (ELISA). One week after booster immunization, the spleens of 5 mice per group were collected for enzyme-linked immunospot assay (ELISpot) and intracellular cytokine staining (ICS) testing using fluorescence-activated cell sorting (FACS).

Determination of Serum Anti-HBs and IgG1 and IgG2a Antibody Response

Serum anti-HBs and IgG1 and IgG2a antibody levels were determined using indirect ELISA kits. Serum was collected 3 weeks after immunization. Quantitative detection of anti-HBs (mIU/ml) antibodies was performed using commercially available ELISA kits. For IgG1 and IgG2a (ng/ml) antibody determination, ninety-six well plates were coated with 1 μg/ml HBsAg overnight, and the plate was blocked with 2% bovine serum albumin (BSA) for 1 h then washed 5 times with 1‰ Tween 20-PBS. The initial series of diluted mouse serum was added and incubated at 37°C for 1 h. After washing, HRP-labelled sheep anti-mouse IgG1 or IgG2a antibodies (1:10,000 dilution) were added, and incubated at 37°C for 1 h. A chromogenic solution (containing substrate A hydrogen peroxide and substrate B tetramethylbenzidine (TMB)) was added and incubated at 37°C for 10 min and the termination solution was added. The absorbance value at dual wavelengths of 450/630 nm was read. Four Parameter Logistic (4 PL) Regression was used to calculate the IgG1 and IgG2a antibody concentration (ng/ml).

Determination of Cell-Mediated Immune Response

Specific T-cell responses to HBsAg were measured using ELISpot and ICS. One week after the booster immunization, mice were sacrificed. Splenocytes were isolated from the spleen and stimulated with a specific S peptide (S28-39, *IPQSLDSWWTSL*, H-2d restricted). Briefly, for ELISpot, mice spleen cells were isolated and added into each well with 50,000 cells and 1 μg stimulating peptide per well. ConA was used as positive control. After incubation at 37°C for 20 h, biotin-labeled

antibody (Mabtech, Sweden; IFN-r or IL-2) was added, followed by substrate coloration, water washing terminated, and plate reading counting after drying. For ICS, 250 μl of flow fluid (2% FBS PBS) was added to each well of the 96-well cell plate, and centrifugation was performed at 200 g for 5 min. Then, 50 μl of FITC-CD8 (BD, USA) and PerCP-CD3 (BD, USA) dyes were added to each well for surface dyeing. After centrifugation at 200 *g* for 5 min, 250 μl of flow fluid was added to each well, and 100 μl Fixation/Permeabilization solution (BD, USA) was added each well. The reaction was performed at 4°C for 20 min in the dark. Then, 50 μl of PE-IFN-γ and APC-IL-2 dyes (BD, USA) diluted in Perm/Wash buffer (BD, USA) were added to each well. After washing, 200 μl of flow solution was added to each well, and the results were detected using flow cytometry (BD FACS Canto™ II, USA). PMT voltages are as follows, P2 385V, P3 607V, P4 565V, P5 557V, P7 668V. Data are presented as the means ± SD and are representative of one of two independent experiments with similar results.

Safety

The safety of the new nano adjuvant PF3 was evaluated using changes in body weight and histopathological changes of heart, liver, spleen, lung and kidney by HE staining of sections 7 days after injection. Meanwhile, histopathological changes at the intramuscular injection site were observed at 4 and 72 h. The injection dose for safety was the same as the immunoassay.

Statistical Analysis

GraphPad Prism 8.0 software (GraphPad Software Inc., San Diego, CA, USA) was used for data analyses and statistical tests. The data were measured with mean standard deviation. Means were compared using Student-t test and one-way analysis of variance (ANOVA) followed by a Tukey-Kramer post hoc test using a 95% confidence interval. *p* values of less than 0.05*, 0.01**, 0.001*** and 0.0001**** were considered as statistically significant.

RESULTS

PF3 has Stable Physiochemical Characteristics

In order to evaluate the physicochemical stability of PF3, particle size and Zeta potential were measured at 4 and 37°C, the latter is a destructive condition for acceleration. The tolerance and stability of PF3 formulation were investigated to provide data supporting for long-term storage at 4°C. The particle size of PF3 was 168.1 nm and the Zeta potential was -22.8mV at 4°C. The results of particle size and Zeta potential at 37°C at different time (3, 8 and 12 weeks) showed that PF3 displayed relatively stable physicochemical characteristics (**Figures 1C,D**). There was no obvious change in appearance of aluminium hydroxide and PF3 after 0 or 12 weeks of storge at 4°C or 37°C. These results suggest that PF3 may be stored stably at 4°C for a much longer time. The results of TEM showed that PF3 presented uniform nanoparticles, while the aluminum hydroxide presented irregular particles of uneven size (**Figure 1E**), which is similar to the DLS results (particle size 168.1 ± 2.483nm, PdI 0.128 ± 0.007 for PF3; particle size 12,980 ± 289.9nm, PdI 0.395 ± 0.006 for aluminum hydroxide).

PF3 Enhanced the Antibody Responses to HBsAg

It is well known that the aluminum adjuvant has a strong humoral immunity enhancing effect, and the anti-HBs antibodies play an important role in clearing viral infection. For the immunopotentiation of the PF3 adjuvant to HBsAg, the humoural immunity results 3 weeks after 1 dose showed that the PF3 had a significantly higher mean serum antibody level than aluminium hydroxide (1552.74 vs. 268.35, 5.79 times;$p < 0.01$; **Figure 2A**). IgG1 and IgG2a level in serum showed similar results, the serum IgG1 (1623923.00 vs. 587,830.25, 2.76 times) and IgG2a (209,790.85 vs. 5344.41, 39.25 times) level of the PF3 was significantly higher than aluminium hydroxide ($p < 0.01$ and $p < 0.0001$, respectively; **Figures 2B,C**). Therefore, PF3 showed a higher humoral immune-enhancing effect than aluminium hydroxide for the hepatitis B virus, and the higher IgG2a levels suggested that the Rg1 in the PF3 may play an enhanced cellular immunity role as a stimulus molecule for HBsAg to a much higher extent (**Figure 2C**).

PF3 Enhanced the Cell-Mediated Immune Response to HBsAg

Although aluminum adjuvant has a strong humoral immunity enhancing effect, it has a weak cellular immunity effect. To assess the ability of PF3 to elicit a cellular immune response when administered intramuscularly with HBsAg, PF3-induced IL-2 and IFN-γ (as markers of the Th1 response) secreting cells in the spleen were detected using ELISpot and ICS. As shown in **Figures 2D,E**, mice vaccinated with PF3 produced significantly higher counts of specific IFN-γ and IL-2-expressing cells (SFCs, Spot Forming Cells) than aluminium hydroxide (978.50 vs. 113.75, 8.60 times for IFN-γ; 715.50 vs. 62.00, 11.54 times for IL-2; $p < 0.0001$ and $p < 0.0001$, respectively). The results of ICS were similar to ELISpot. IFN-γ, IL-2 and IFN-γ/IL-2 expression in $CD8^+$ T cells of the PF3 group showed a significantly higher enhancement than the aluminium hydroxide (0.35 vs. 0.05%, 6.87 times for IFN-γ; 0.71 vs. 0.01%, 94.00 times for IL-2; 0.33 vs. 0.05%, 6.89 times for IFN-γ/IL-2; $p < 0.01$, $p < 0.01$ and $p < 0.01$, respectively. **Figures 2F–H**). These results suggest that PF3 can significantly improve the cellular immunity against HBsAg compared with aluminum adjuvant.

PF3 is Safe in Mice

Changes in morphology and inflammatory cell infiltration of the major organs including the heart, liver, spleen, lungs, and kidneys were observed 7 days after injection of the PBS, Alum or PF3. The histopathological results showed that PBS group were normal and almost no inflammatory cell infiltration 72 h after intramuscular injection. No evident pathology was found in the major organs and no significant difference was observed between the PF3 group

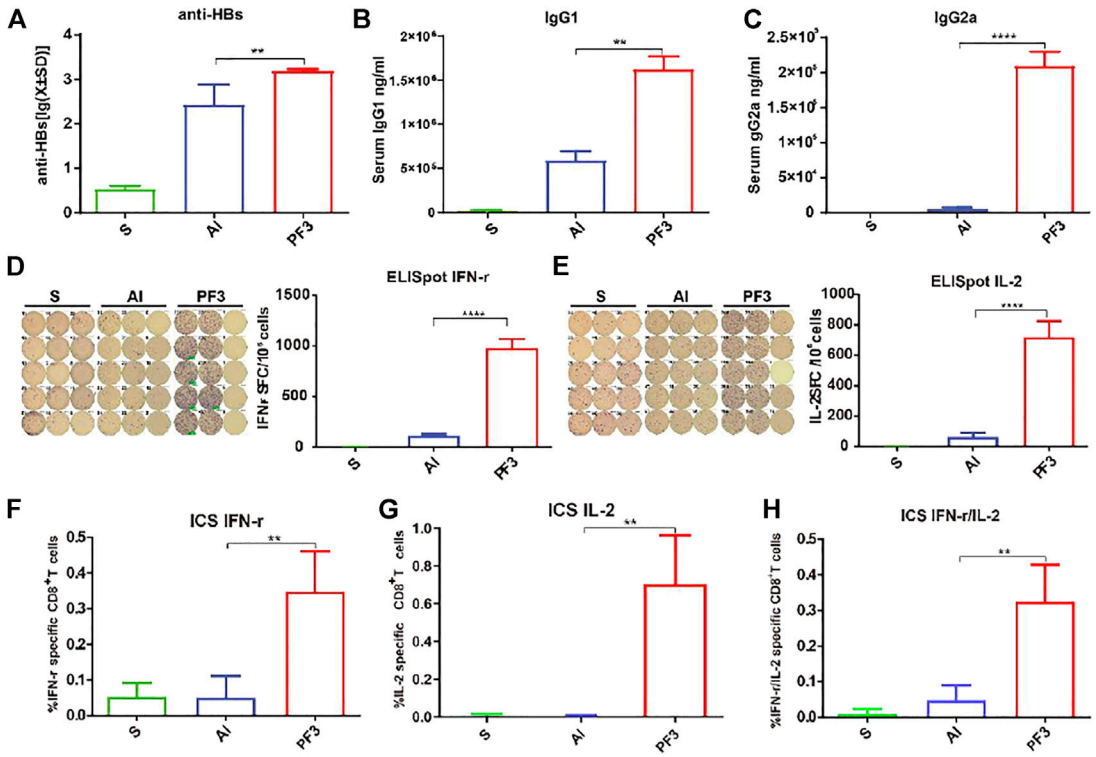

FIGURE 2 | Serum anti-HBs and IgG1 and IgG2a antibody levels of mice and specific T-cell responses measured using ELISpot and ICS immunized with HBsAg combined with different adjuvants. BALB/c mice (n = 5) were immunized intramuscularly with HBsAg (5 μg/ml) combined with Al (500 μg/ml), PF3(50 μg/ml) or Rg1 (50 μg/ml). **(A).** anti-HBs (mIU/ml); **(B,C).** IgG1 and IgG2a (ng/ml); **(D,E).** ELISpot IFN-r and IL-2; **(F–H).** ICS IFN-r and IL-2. Data are presented as the means ± SD and are representative of one of two independent experiments with similar results. Note: $*p < 0.05$, $**p < 0.01$, $***p < 0.001$ and $****p < 0.0001$.

and the aluminum hydroxide group (**Figure 3A**). No significant differences were observed of histopathological change at the intramuscular injection site at 4 and 72 h between the PF3 group and the aluminum hydroxide group (**Figure 3B**). As indicated in **Figure 3C**, the body weight of mice showed a steady increase trend among the three groups, and no significant difference was observed. Therefore, PF3 exhibited well-controlled immunogenicity and acceptable biosafety as a kind of HBV vaccine adjuvant candidate.

DISCUSSION

Hepatitis B is a kind of infectious liver disease caused by hepatitis B virus, mainly including acute hepatitis and chronic hepatitis. While HBV may also cause cirrhosis and primary liver cancer. Hepatitis B has become a major global health problem, infecting nearly 350 million people worldwide and killing about 60,000 of them each year (Rein et al., 2012). Hepatocellular carcinoma (HCC) accounts for 70–90% of primary hepatic carcinoma cases (Yu and Yuan, 2004). It is the third leading cause of cancer-related deaths worldwide and is expected to get worse in the coming years (Venook et al., 2010). So far, hepatitis B Vaccine (HepB) is the most effective way to prevent HBV infection and transmission, with an effective rate of 85–95%. However, there are still 5–10% of the population with no response or low response. The risk groups for poor response include those with immunosuppression or dialysis-dependent or end-stage renal disease. Therefore, immunogenicity enhanced vaccines are needed to protect them from hepatitis B infection (Saco et al., 2018). In addition, the level of anti-HBs decreased with the increase of time after vaccination, with the fastest decline in the first year after immunization and gradually decreased thereafter. The persistence of antibody was positively correlated with the peak response after the initial vaccination (Honorati et al., 1999). Cellular immunity is also important for hepatitis B virus clearance, and one reason for the weak cellular immunity of aluminum adjuvants is that antigens are processed through the lysosomal pathway and presented via major histocompatibility complex II (MHC-II), instead of cross-presentation for MHC-I-mediated cellular immunity (Peng et al., 2020). To achieve the complete clearance of HBV, it is vital to augment strong cellular immunity and cytotoxic T lymphocytes (CTLs) (Hu et al., 2020).

Although there are a variety of new adjuvants developed, they also have some inevitable shortcomings, such as the need to improve the stability of liposomes, some adjuvants have strong adverse reactions, some are poor in water solubility, and some cost too much and are complicated to prepare.

The present study showed that PF3 induced stronger humoral immunity and cellular immune response than aluminium hydroxide

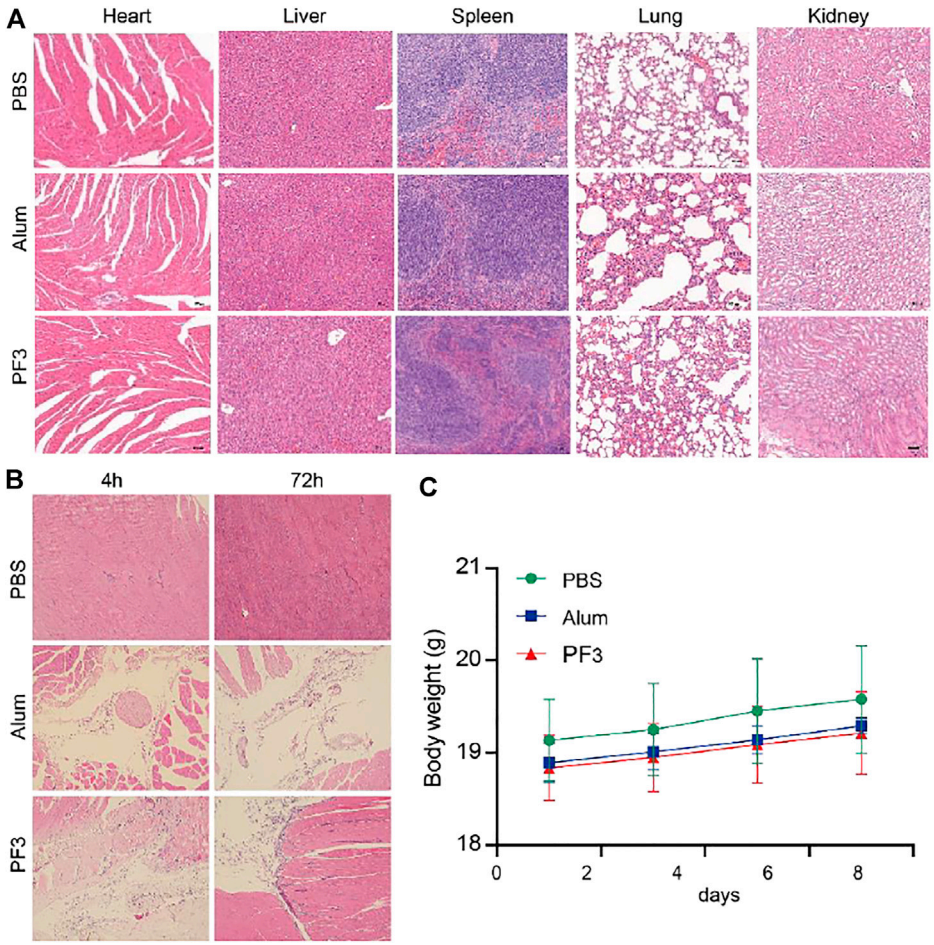

FIGURE 3 | PF3 is Safe in Mice. **(A)** Representative images of biocompatibility evaluations via H&E staining of vital organ sections. Scale bar represents 100 μm. **(B)** HE staining of muscle at different time after intramuscular injection. **(C)** Change of the body weight of BALB/c mice (n = 3).

when combined with the HBsAg antigen. Besides, it induced higher IgG2a, IFN-γ and IL-2 levels, which means that it may induce a more balanced Th1/Th2 response that compensates for the weak Th1-type response induced by aluminium hydroxide. Moreover, PF3 also showed a strong cellular immune enhancement on VZV (varicella zoster virus) recombinant gE antigen, demonstrated by the method ELISpot and flow cytometry ICS (data not shown), which suggest that PF3 can be a potential candidate adjuvant for recombinant herpes zoster vaccine. In addition, PF3 had no obvious inflammation in the major organs, exhibiting comparable safety to aluminium hydroxide. In terms of ginsenosides, they have strong efficacy and good safety in antitumour and other aspects (Huang et al., 2017). Moreover, it is easy to extract and purify with very high purity and lower costs for Rg1. In terms of safety, the PF3 infiltration of inflammatory cells at the intramuscular injection site recovered better at 72 h than at 4 h compared with aluminum hydroxide (**Figure 3B**). These results suggest that PF3 have a faster inflammatory recovery at the site of intramuscular injection than aluminum hydroxide.

In conclusion, our data demonstrated that the new nano adjuvant PF3 produced a range of immunological adjuvant effects in HBsAg immunized mice and better humoral and cellular immunity than aluminum adjuvant. PF3 also showed favourable safety characteristics and acceptable stability. Because of easy preparation, low cost, simple dosage form and water soluble, PF3 could be combined with other antigen to construct novel vaccines to induce strong immune response.

DATA AVAILABILITY STATEMENT

The original contributions presented in the study are included in the article/Supplementary Material, further inquiries can be directed to the corresponding author.

ETHICS STATEMENT

The animal study was reviewed and approved by Animal Ethics Committee of the National Vaccines and Serum

Institute (AECNVSI) of National Vaccines and Serum Institute.

AUTHOR CONTRIBUTIONS

Experiments were conceived by JX, PS and ZW; The experiments were carried out by PS, ZW, JL, DW, ZZ, SH, YH, YW and SL. The writing, statistical analysis and formal analysis were performed by PS, XW and ZW. The manuscript was reviewed by JX. All the authors read and approved the final version manuscript.

FUNDING

This research was completed with the financial support of NVSI (National Vaccine and Serum Institute).

SUPPLEMENTARY MATERIAL

The Supplementary Material for this article can be found online at: https://www.frontiersin.org/articles/10.3389/fbioe.2022.903424/full#supplementary-material

REFERENCES

Chenwen, X., Quanan, J., Yee, H., Yan, L., Jiaoyu, W., Qiang, W., et al. (2021). Efficacy of Rg1-Oil Adjuvant on Inducing Immune Responses against Bordetella Bronchiseptica in Rabbits. *J. Immunol. Res.* 2021, 1–9. doi:10.1155/2021/8835919

Del Giudice, G., Rappuoli, R., and Didierlaurent, A. M. (2018). Correlates of Adjuvanticity: A Review on Adjuvants in Licensed Vaccines. *Seminars Immunol.* 39, 14–21. doi:10.1016/j.smim.2018.05.001

Honorati, M. C., Palareti, A., Dolzani, P., Busachi, C. A., Rizzoli, R., and Facchini, A. (2001). A Mathematical Model Predicting Anti-hepatitis B Virus Surface Antigen (HBs) Decay after Vaccination against Hepatitis B. *Clin. Exp. Immunol.* 116, 121–126. doi:10.1046/j.1365-2249.1999.00866.x

Hu, F., Yue, H., Lu, T., and Ma, G. (2020). Cytosolic Delivery of HBsAg and Enhanced Cellular Immunity by pH-Responsive Liposome. *J. Control. Release* 324, 460–470. doi:10.1016/j.jconrel.2020.05.042

Huang, Y., Zou, Y., Lin, L., and Zheng, R. (2017). Ginsenoside Rg1 Activates Dendritic Cells and Acts as a Vaccine Adjuvant Inducing Protective Cellular Responses against Lymphomas. *DNA Cell Biol.* 36, 1168–1177. doi:10.1089/dna.2017.3923

James, S. F., Chahine, E. B., Sucher, A. J., and Hanna, C. (2018). Shingrix: The New Adjuvanted Recombinant Herpes Zoster Vaccine. *Ann. Pharmacother.* 52, 673–680. doi:10.1177/1060028018758431

Jung, M.-C., and Pape, G. R. (2002). Immunology of Hepatitis B Infection. *Lancet Infect. Dis.* 2, 43–50. doi:10.1016/s1473-3099(01)00172-4

Lee, A. L. Z., Yang, C., Gao, S., Wang, Y., Hedrick, J. L., and Yang, Y. Y. (2020). Biodegradable Cationic Polycarbonates as Vaccine Adjuvants. *ACS Appl. Mat. Interfaces* 12, 52285–52297. doi:10.1021/acsami.0c09649

Lee, D. C., and Lau, A. S. (2011). Effects of Panax Ginseng on Tumor Necrosis Factor-α-Mediated Inflammation: A Mini-Review. *Molecules* 16, 2802–2816. doi:10.3390/molecules16042802

Li, Y., Wang, H., Wang, R., Lu, X., Wang, Y., Duan, M., et al. (2019). Pharmacokinetics, Tissue Distribution and Excretion of Saponins after Intravenous Administration of ShenMai Injection in Rats. *J. Chromatogr. B* 1128, 121777. doi:10.1016/j.jchromb.2019.121777

Ni, J., Bi, S., Xu, W., Zhang, C., Lu, Y., Zhai, L., et al. (2016). Improved Immune Response to an Attenuated Pseudorabies Virus Vaccine by Ginseng Stem-Leaf Saponins (GSLS) in Combination with Thimerosal (TS). *Antivir. Res.* 132, 92–98. doi:10.1016/j.antiviral.2016.05.018

O'hagan, D. T., Ott, G. S., De Gregorio, E., and Seubert, A. (2012). The Mechanism of Action of MF59 - an Innately Attractive Adjuvant Formulation. *Vaccine* 30, 4341–4348. doi:10.1016/j.vaccine.2011.09.061

O'Hagan, D. T., Ott, G. S., Nest, G. V., Rappuoli, R., and Giudice, G. D. (2013). The History of MF59adjuvant: a Phoenix that Arose from the Ashes. *Expert Rev. Vaccines* 12, 13–30. doi:10.1586/erv.12.140

Orsi, A., Ansaldi, F., De Florentiis, D., Ceravolo, A., Parodi, V., Canepa, P., et al. (2013). Cross-protection against Drifted Influenza Viruses. *Hum. Vaccines Immunother.* 9, 582–590. doi:10.4161/hv.23239

Patel, S., and Rauf, A. (2017). Adaptogenic Herb Ginseng (Panax) as Medical Food: Status Quo and Future Prospects. *Biomed. Pharmacother.* 85, 120–127. doi:10.1016/j.biopha.2016.11.112

Peng, S., Cao, F., Xia, Y., Gao, X. D., Dai, L., Yan, J., et al. (2020). Particulate Alum via Pickering Emulsion for an Enhanced COVID-19 Vaccine Adjuvant. *Adv. Mat.* 32, 2004210. doi:10.1002/adma.202004210

Rein, D. B., Stevens, G. A., Theaker, J., Wittenborn, J. S., and Wiersma, S. T. (2012). The Global Burden of Hepatitis E Virus Genotypes 1 and 2 in 2005. *Hepatology* 55, 988–997. doi:10.1002/hep.25505

Saco, T. V., Strauss, A. T., and Ledford, D. K. (2018). Hepatitis B Vaccine Nonresponders. *Ann. Allergy, Asthma & Immunol.* 121, 320–327. doi:10.1016/j.anai.2018.03.017

Schaffner, W., Van Buynder, P., Mcneil, S., and Osterhaus, A. D. M. E. (2018). Seasonal Influenza Immunisation: Strategies for Older Adults. *Int. J. Clin. Pract.* 72, e13249. doi:10.1111/ijcp.13249

Shin, B.-K., Kwon, S. W., and Park, J. H. (2015). Chemical Diversity of Ginseng Saponins from Panax Ginseng. *J. Ginseng Res.* 39, 287–298. doi:10.1016/j.jgr.2014.12.005

Sun, H.-X., Xie, Y., and Ye, Y.-P. (2009). Advances in Saponin-Based Adjuvants. *Vaccine* 27, 1787–1796. doi:10.1016/j.vaccine.2009.01.091

Syed, Y. Y. (2018). Recombinant Zoster Vaccine (Shingrix): A Review in Herpes Zoster. *Drugs Aging* 35, 1031–1040. doi:10.1007/s40266-018-0603-x

Venook, A. P., Papandreou, C., Furuse, J., and Ladrón de Guevara, L. (2010). The Incidence and Epidemiology of Hepatocellular Carcinoma: a Global and Regional Perspective. *Oncologist* 15 (Suppl. 4), 5–13. doi:10.1634/theoncologist.2010-s4-05

Xu, W., He, J., Wu, G., Xiong, F., Du, H., and Wang, G. (2015). Stabilization and Immune Response of HBsAg Encapsulated within Poly(lactic-Co-Glycolic Acid) Microspheres Using HSA as a Stabilizer. *Int. J. Pharm.* 496, 332–341. doi:10.1016/j.ijpharm.2015.10.004

Yi, X., Zeng, W., Wang, C., Chen, Y., Zheng, L., Zhu, X., et al. (2022). A Step-by-step Multiple Stimuli-Responsive Metal-Phenolic Network Prodrug Nanoparticles for Chemotherapy. *Nano Res.* 15, 1205–1212. doi:10.1007/s12274-021-3626-2

Yu, M. C., and Yuan, J.-M. (2004). Environmental Factors and Risk for Hepatocellular Carcinoma. *Gastroenterology* 127, S72–S78. doi:10.1016/j.gastro.2004.09.018

Conflict of Interest: Author YW was employed by Beijing Institute of Biological Products Co.

The remaining authors declare that the research was conducted in the absence of any commercial or financial relationships that could be construed as a potential conflict of interest.

Publisher's Note: All claims expressed in this article are solely those of the authors and do not necessarily represent those of their affiliated organizations, or those of the publisher, the editors and the reviewers. Any product that may be evaluated in this article, or claim that may be made by its manufacturer, is not guaranteed or endorsed by the publisher.

frontiers | Frontiers in Bioengineering and Biotechnology

REVIEW
published: 12 May 2022
doi: 10.3389/fbioe.2022.907232

Application of Microfluidics in Detection of Circulating Tumor Cells

Can Li[1†], Wei He[2†], Nan Wang[1], Zhipeng Xi[1], Rongrong Deng[1], Xiyu Liu[1], Ran Kang[1,3], Lin Xie[1]* and Xin Liu[1]**

[1]Affiliated Hospital of Integrated Traditional Chinese and Western Medicine, School of Artificial Intelligence and Information Technology, Nanjing University of Chinese Medicine, Nanjing, China, [2]Department of Clinical Medical Engineering, The First Affiliated Hospital of Nanjing Medical University, Nanjing, China, [3]Department of Orthopedics, Nanjing Lishui Hospital of Traditional Chinese Medicine, Nanjing, China

Tumor metastasis is one of the main causes of cancer incidence and death worldwide. In the process of tumor metastasis, the isolation and analysis of circulating tumor cells (CTCs) plays a crucial role in the early diagnosis and prognosis of cancer patients. Due to the rarity and inherent heterogeneity of CTCs, there is an urgent need for reliable CTCs separation and detection methods in order to obtain valuable information on tumor metastasis and progression from CTCs. Microfluidic technology is increasingly used in various studies of CTCs separation, identification and characterization because of its unique advantages, such as low cost, simple operation, less reagent consumption, miniaturization of the system, rapid detection and accurate control. This paper reviews the research progress of microfluidic technology in CTCs separation and detection in recent years, as well as the potential clinical application of CTCs, looks forward to the application prospect of microfluidic technology in the treatment of tumor metastasis, and briefly discusses the development prospect of microfluidic biosensor.

Keywords: tumor metastasis, circulating tumor cells, microfluidic, biosensor, cancers

OPEN ACCESS

Edited by:
Qitong Huang,
Gannan Medical University, China

Reviewed by:
Ruipeng Chen,
Institute of Animal Sciences (CAAS), China
Zhuoying Xie,
Southeast University, China

***Correspondence:**
Ran Kang
kangran126@126.com
Lin Xie
xielin6508@163.com
Xin Liu
liuxin@njucm.edu.cn

[†]*These authors have contributed equally to this work*

Specialty section:
This article was submitted to Nanobiotechnology, a section of the journal Frontiers in Bioengineering and Biotechnology

Received: *29 March 2022*
Accepted: *11 April 2022*
Published: *12 May 2022*

Citation:
Li C, He W, Wang N, Xi Z, Deng R, Liu X, Kang R, Xie L and Liu X (2022) Application of Microfluidics in Detection of Circulating Tumor Cells. Front. Bioeng. Biotechnol. 10:907232. doi: 10.3389/fbioe.2022.907232

1 INTRODUCTION

Despite decades of deepening understanding of cancer, cancer is still one of the leading causes of death worldwide. It is estimated that the number of cancer cases may increase by 60% in the next two decades. Among them, the growth rate of low—and middle-income countries may be as high as 81% (Wild et al., 2020). The burden of cancer is increasing in all countries, and the cancer burden in low—and middle—income countries is expected to double in the next decade. Without further action, millions of people will die prematurely from cancer in the next decade. Cancer metastasis refers to cells spreading from the primary focus to the distal organs. It is one of the main causes of cancer death (Suhail et al., 2019). Circulating tumor cells (CTCs) are defined as cancer cells that depart from solid tumor lesions and enter the blood, originally discovered by Ashworth (Shen et al., 2017). CTCs are not the only tumor derivative in the circulation, but they contain many metastatic precursors, which is very important for disease progression (Castro-Giner and Aceto, 2020). Clinical circulating tumor cells mainly refer to diverse tumor cells in peripheral blood. Understanding CTCs is helpful to explore the mechanism of primary tumors and metastatic lesions. Early diagnosis of circulating tumor cells (CTCs) can effectively identify patients who need further systemic treatment after initial tumor resection. CTCs detection mainly detects the content of various tumor cells in peripheral blood through capture to detect the changing tendency of CTCs type and quantity and subsequently monitor the dynamic evaluation of tumor treatment effect in real-time. The circulating tumor cells in peripheral blood can be used to help judge the

cancer complications of patients. However, the content of CTCs in human blood is infrequent. The contents of red blood cells, white blood cells, and platelets can reach 5×10^9/ml, 4×10^6/ml, and 3×10^8/ml, while CTCs are usually only 0–10/ml (Yu M. et al., 2013). Moreover, tumor cells can constantly transform their characteristics through epithelial mesenchymal transformation and interstitial epithelial-transformation in metastasis. Due to its scarcity, heterogeneity and the interference of complex matrix in blood, the precise detection of CTCs has become an enormous issue.

Currently developed CTCs detection methods, including immunofluorescence (Ramirez et al., 2019; Lin and Chang, 2021), fluorescence *in situ* hybridization (Cheng et al., 2019), reverse transcription-polymerase chain reaction (RT-PCR) (Yang et al., 2017; Tong and Wang, 2019), real-time fluorescence quantitative PCR (Guo et al., 2015), flow cytometry (Galanzha and Zharov, 2013; Ruiz-Rodríguez et al., 2021), immunofluorescence *in situ* hybridization and immunohistochemical staining (Yu et al., 2020; Guo et al., 2019; Wu et al., 2020a), are challenging to meet the requirements of direct detection in detection limit and sensitivity. Therefore, some sample pretreatment methods are usually used to separate and enrich CTCs before detecting CTCs in peripheral blood. In the process of sample pretreatment to realize the separation and enrichment of CTCs, as these methods are discontinuous, it is inevitable to cause the loss of cells in adsorption, elution, and transfer. Additionally, the scarcity of CTCs can easily lead to false-negative results. Moreover, most CTCs detection technologies are time-consuming, require skilled operators and high-tech instruments. Moreover, the detection of CTCs is still challenging due to their low concentration and heterogeneity in blood samples. Therefore, there is an urgent need to develop novel technologies to make the separation and detection of CTCs more convenient, accurate, and noninvasive.

In recent years, microfluidic technology has attracted considerable interest in CTCs detection. Microfluidic technology is characterized by a micro-manufacturing structure, which usually manipulates the fluid with high flux and sensitivity on the micron scale (Cao et al., 2021). With the remarkable progress of micro-machining methods, the microfluid platform has significant advantages such as low cost, good micro-structure, reduced sample consumption, rapid fluid processing, good detection sensitivity, and so on, and is applied to the primary and applied research of oncology (Lin et al., 2020; Pei et al., 2020a). Microfluidic technology makes it possible for rapid and reliable sample separation and high selectivity and sensitivity detection of CTCs. This paper looks forward to the microfluidic CTCs detection system, which is significant for biomedicine and its application in early cancer diagnosis.

2 MICROFLUIDIC TECHNOLOGIES FOR CTCS SEPARATION

Microfluidic technology is a new technology used in the primary and applied research of cancer metastasis for decades. A microchannel with a small size is used to accurately control a small volume of liquid or process multiple samples in an integrated bioreactor simultaneously. Compared with traditional methods, it has the advantages of automatic operation, reasonable sensitivity, and throughput, which makes it possible to construct structures on the cell scale. In the past decade, microfluidic platforms based on functional microchannel have been developed to separate CTCs. As a miniaturized analysis, it realizes the one-step process of sample collection, loading, separation, and analysis to significantly reduce the processing time and improve the opportunity to capture CTCs. A microfluidic platform can hinder the interaction between cell and antibody by accurately controlling the direction and speed of fluid flow, which directly impacts the capture efficiency. In addition, it is a simple tool to integrate other technologies/materials (such as ceramics, metals, and polymers) to improve the analysis efficiency of CTCs.

With the growth of solid tumors and specific changes in the surrounding microenvironment, some tumor cells will obtain abnormal activity ability, that is, epithelial-mesenchymal transformation (EMT). These cells shed from the primary tumor and find a new foothold in the body. These tumor cells will be brought to various body parts through the blood system or lymphatic system, and the tumor cells shed through the blood circulation are CTCs. When they reach an appropriate target, they will become malignant reproductive machines. This is the hematogenous metastasis of the tumor from the primary site to the secondary tumor. Therefore, after obtaining the patient's blood, we first need to separate and enrich the CTCs, analyze the characteristics of these CTCs, and then give the appropriate treatment strategy. However, the content of CTCs in the human circulatory system is shallow (Zou and Cui, 2018). There are only 1~10 CTCs per ml of the whole blood in patients with tumor metastasis. Therefore, to realize the detection of CTCs, sorting, and enrichment are crucial steps. CTCs' separation and enrichment will directly affect subsequently detection effect. Therefore, CTCs sorting and enrichment with high purity, high sensitivity (without losing CTCs), fast and high cell activity is the focus and difficulty of CTCs clinical application.

The enrichment of CTCs can be divided into the positive enrichment method of capturing CTCs and the negative enrichment method of removing leukocytes. The positive enrichment method mainly includes affinity and physical enrichment methods. The affinity enrichment method mainly utilizes a specific antibody to combine with tumor cell surface antigen to enrich CTCs specifically. The physical enrichment method mainly screens out CTCs according to their physical characteristics, such as size, density, mechanical and dielectric properties. Due to the slight size difference between leukocytes and CTCs, leukocytes are often the chief interference factor in sorting CTCs in blood. Therefore, leukocytes can be selectively isolated to achieve the purpose of CTCs enrichment, that is, the negative enrichment method.

2.1 Positive Enrichment

2.1.1 Enrichment Based on Biological Affinity

The affinity enrichment method mainly separates target cells through the antigen expression on the cell surface, tissue-

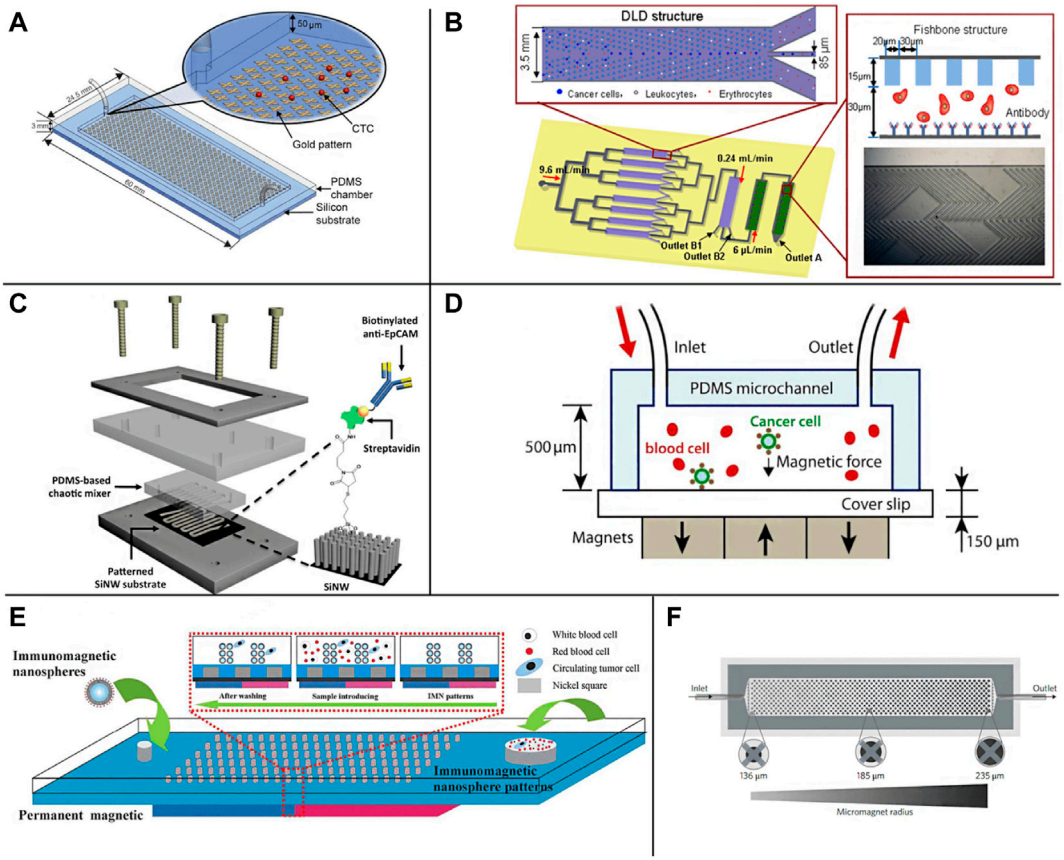

FIGURE 1 | Schematic illustration of the EpCAM specific recognition chips. **(A)** The GO chip (Yoon et al., 2013); **(B)** The deterministic lateral displacement (DLD) chip (Liu et al., 2013); **(C)** The NanoVelcro CTC chip (Lu et al., 2013); **(D)** The microchip designed for immunomagnetic detection of cancer cell (Hoshino et al., 2011); **(E)** The magnetic nanospheres (MNs) based microfluidic device (Tang et al., 2016); **(F)** The wavy-HB microfluidic device (Shi et al., 2017)

specific membrane antigens or peptides, and aptamers to capture CTCs.

2.1.1.1 EpCAM Specific Recognition

CTCs can be divided into epithelial CTCs, mesenchymal CTCs, and mixed phenotype CTCs (Pan et al., 2019), in which epithelial markers are expressed on normal epithelial cells and epithelial tumors but not on interstitial leukocytes. Therefore, they are often distinguished between cancer cells and normal blood cells. Epithelial cell adhesion molecule (EpCAM) is a transmembrane glycoprotein expressed in most solid cancers, so it is one of the most widely used surface markers for CTCs enrichment (Eslami-S et al., 2020; Ahmed et al., 2017; Thege et al., 2014). The EpCAM antibodies can be immobilized on the surface of microchannels, micropores, or other nanostructures to achieve positive capture of CTCs. In 2007, the Toner group reported the first Immunocapture platform CTCs chip, which consists of a series of EpCAM coated micropores and can separate CTCs from whole blood with high sensitivity and high activity. It can be used to capture CTCs from peripheral blood of patients with lung, breast, prostate, pancreatic, and colon cancer metastases (Nagrath et al., 2007). Since then, the microfluidic platform based on EpCAM has developed rapidly. Subsequently, the above group developed a herringbone chip (HB chip), whose unique structure maximizes the collision between cancer cells and the EpCAM coating surface in the microchannel (Stott et al., 2010). Further, Nagrath et al. designed graphene oxide nanosheets on the EpCAM antibody coating for positive CTCs selection (**Figure 1A**). The improved CTCs chip obtained an average of 73% CTCs capture efficiency from whole blood samples of lung, breast, and pancreatic cancer patients (Yoon et al., 2013). However, a technical challenge of the microfluidic platform is that blood cells pass through the platform in a straight-line streamline with a low Reynolds number, resulting in limited interaction between CTCs and antibodies coated on the surface of the microchannel, thus reducing the capture efficiency. Although the microcolumn array in the CTCs chip developed by Nagrath et al. effectively destroys the laminar flow to improve the interaction between CTCs and antibodies, it is still challenging to capture and target CTCs at different heights along the microcolumn. Therefore, geometric enhancement attracted people's attention to increase the contact probability between cells and antibody functionalized surfaces. For example, the Soper group proposed a curved microchannel structure coated with EpCAM antibodies to improve the isolation performance of CTCs (Jackson et al., 2014). In addition, an integrated

microfluidic platform composed of a triangular microcolumn array allows CTCs to be captured with continuous throughput, efficiency, and purity (Liu et al., 2013) (**Figure 1B**). Combining the deterministic lateral displacement (DLD) chamber and the anti-EpCAM based capture method, more than 90% capture rate and 90% purity of live CTCs were observed in the added blood samples.

Due to the high surface area volume ratio, compatible capture and release ability, nanomaterials provide a high collision probability for antibodies and CTCs (Park et al., 2017; Wu C. et al., 2019; Shi et al., 2022; Yi et al., 2022; Liu et al., 2022; Liu J. et al., 2021), which can help improve the sensitivity and specificity of capture, and have attracted extensive attention in the separation of CTCs (Wongkaew et al., 2018; Wu and Qu, 2015; Zhu G. et al., 2021; Naskar et al., 2020; Chandankere et al., 2020). So far, carbon nanotubes (CNTs) (Cho H. et al., 2018; Zhang P. et al., 2019; Poudineh et al., 2017), graphene oxide (GO) (Chen et al., 2012; Yoon et al., 2013; Yu X. et al., 2013; Yoon et al., 2016), gold nanoparticles (AuNP) (Park et al., 2017), nanocolumns (Lin et al., 2014; Shi et al., 2022) and TiO_2 nanofibers (Zhang et al., 2012) have been widely used in affinity group capture methods (Zhao et al., 2016; Cai et al., 2017; Wongkaew et al., 2018). NanoVelcro CTCs chip is a representative nanostructure microfluidic platform. It uses siliceous nanowire substrate (SINS), so that the interaction between SINS and cells can be similar to Velcro (Wang et al., 2011; Jan et al., 2018). The results demonstrate that compared with a planar siliceous substrate, the capture efficiency of anti-EpCAM coated SINS is significantly improved. Fan group has developed a microfluidic platform with gold nanoparticles assembled with multivalent DNA aptamers to efficiently separate CTCs from blood (Sheng et al., 2012). In addition, the Zhao group also developed an antibody functionalized electrospun TiO2 nanofiber (TiNF) matrix for CTCs capture (Zhang et al., 2012). Lu et al. introduced a nanovelcro CTCs chip containing silicon nanowires and a pattern substrate to enumerate CTCs in prostate cancer (Lu et al., 2013) (**Figure 1C**). They proved its clinical utility in continuous CTCs enumeration of prostate cancer patients and the effectiveness of continuous CTCs enumeration in monitoring cancer progression.

Immunomagnetic enrichment is also a widely used CTCs separation method in a microfluidic platform, which enriches CTCs from blood cells using magnetic particles labeled with anti-EpCAM. With the introduction of a microchip based on Polydimethylsiloxane (PDMS), the Hoshino group proposed an immunomagnetic-based microchip to capture CTCs under a magnetic field (**Figure 1D**), which combines the dual advantages of magnetophoresis enrichment and microfluidic technology (Hoshino et al., 2011). Continuous operation and improved throughput make PDMS-based immunomagnetic microchannel promising to capture cells. Zhang group has developed a microfluidic device based on magnetic nanospheres (MNS) to capture tumor cells (**Figure 1E**). The device integrates the functions of the magnetic microfluidic chip and immunomagnetic nanospheres (IMN), forming a new and stable IMN mode (Tang et al., 2016). Liu group has developed a microfluidic device with a wavy HB structure (**Figure 1F**). Under the external magnetic field, the magnetic particles of anti-EpCAM coating are fixed on the wavy HB surface to capture tumor cells (Shi et al., 2017). Poutine et al. used magnetic grading cytometry to analyze CTCs according to the surface expression phenotype of CTCs. Whole blood samples were processed using microfluidic chips, and then CTCs subsets were captured by controlling magnetic field strength and fluid flow rate based on the number of magnetic nanoparticles labeled on a single cell. The higher EpCAM expressing cells are captured in the higher linear velocity region, while the lower EpCAM expressing cells with fewer magnetic nanoparticles are captured in the lower linear velocity region (Poudineh et al., 2017). By using magnetic nanoparticles to separate and release recovered CTCs, the loss of live CTCs can be reduced without adding biotin. At the same time, this technology can reduce the damage to CTCs in the isolation process and maintain the high throughput of capture performance (Qian et al., 2015).

2.1.1.2 Tissue Specific Membrane Antigen Recognition

In addition to the EpCAM specific recognition, other approaches based on tissue-specific membrane antigens, such as prostate-specific membrane antigen (PSMA) of prostate cancer and epidermal growth factor receptor 2 (HER2) of breast cancer, have been designed to uniquely separate tissue-specific tumor cells from blood (Santana et al., 2012). In 2010, the Kirby group developed a geometrically enhanced differential immune capture chip (GEDI), used to separate prostate CTCs using PSMA. Its purity is higher than EpCAM coated CTCs chip and opens up a stage for capturing CTCs using tissue-specific antibodies other than EpCAM (Gleghorn et al., 2010). Subsequently, the group combined EpCAM and mucin 1 (MUC1) in a GEDI (**Figure 2A**), which was shown to be more effective than a single marker (Thege et al., 2014). Different antibodies or antibody mixtures used to capture CTCs can obtain populations that a single capture ligand may miss, so this method is becoming increasing popular. It is reported that another geometrically enhanced differential immune capture (GEDI) microfluidic platform designed by Kirby et al. can promote the collision frequency between CTCs and antibody functionalized microcolumn and reduce nonspecific leukocyte adhesion to enhance the enrichment of CTCs (Kirby et al., 2012) (**Figure 2B**). In this platform, prostate-specific membrane antigen (PSMA) introduces cross barriers to effect size-dependent cell trajectories to increase capture opportunities. The results showed that the capture efficiency of the GEDI microfluidic platform coated with anti PSMA was 97 ± 3%.

2.1.1.3 Aptamer Recognition

Compared to antibodies, the aptamer is a small oligonucleotide (such as DNA, RNA and polypeptide), which is easy to bind to molecular and cellular components (Song et al., 2019). They can also be used to specifically recognize target molecules on the cell surface and further integrate into CTCs capture (Bai et al., 2014; Wu L. et al., 2019; Wu et al., 2020b,). Systematically evolved through the exponential enrichment (SELEX) process, the ligands are easy to synthesize and separate. They have high sensitivity and specificity, which is the key feature of aptamers for separating

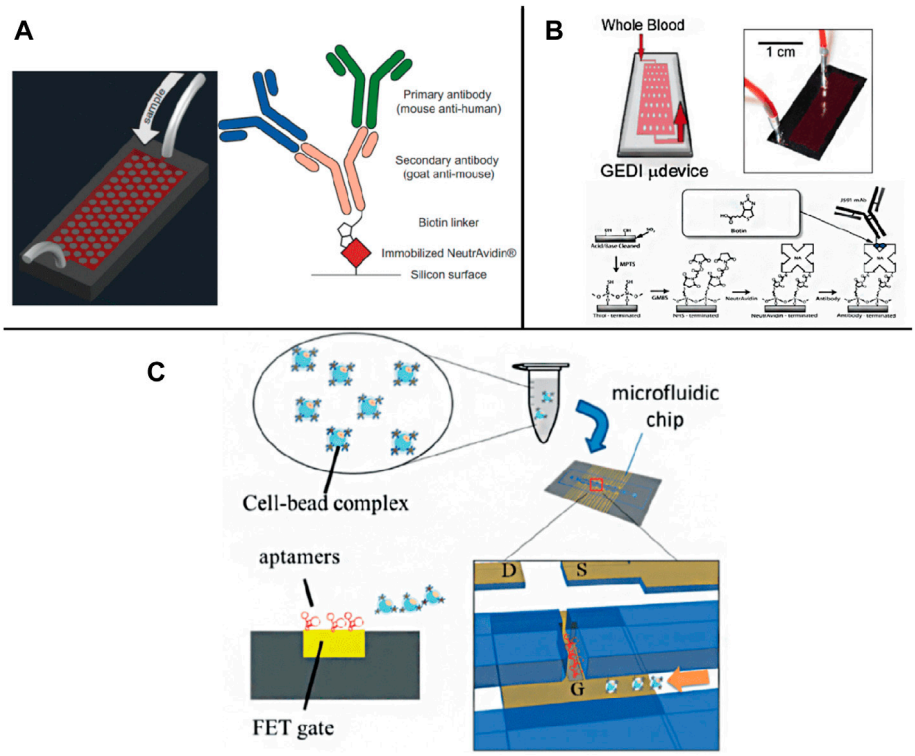

FIGURE 2 | Schematic illustration of membrane antigen and aptamer recognition based chips. **(A)** A GEDI device combined EpCAM and MUC1 detection (Thege et al., 2014); **(B)** A GEDI microfluidic device for whole blood detection (Kirby et al., 2012); **(C)** A FET chip for CTC trapping by bonding CTCs to specific aptamer (Chen et al., 2019).

CTCs (Zamay et al., 2019). For example, Lee Group has developed a new microfluidic platform that integrates field-effect transistors (FETs) and chambers for automatic detection and counting of CTCs (**Figure 2C**). Only target cells bound to a specific aptamer on the FET sensor array can be enumerated (Chen Y. H. et al., 2019). In addition, aptamer functionalized nanostructures were introduced to increase the topographic interaction between targeted CTCs and the surface of specific antibody coating to restore the separation of CTCs. It has satisfactory capture efficiency (Cai et al., 2017; Yu et al., 2019; Fraser et al., 2019).

Although the positive separation method of biological affinity can separate CTCs with a high efficiency and purity, due to the heterogeneous expression of specific surface markers, the ability to target CTCs is limited, and the potentially important CTCs subsets are lost. In addition, affinity-based strategies require sufficient time to prepare samples and sufficient interaction between cells and antibodies, resulting in reduced cell viability and throughput.

2.1.2 Enrichment Based on Physical Screening

According to the differences between CTCs and other blood cells in physical properties such as cell size, density, charge, and deformation ability, CTCs can be screened without biomarkers. Compared with the biological affinity method, the experimental operation of the physical screening method is often simpler without chemical modification and biomarkers; therefore, it has little effect on cell activity. Physical screening methods include active separation methods using external physical fields, such as dielectrophoresis (Augustsson et al., 2012; Alshareef et al., 2013; Aghaamoo et al., 2019), surface acoustic wave (Antfolk et al., 2015; Magnusson et al., 2017), optical tweezers technology (Hu et al., 2019), and passive separation methods with or without external force intervention using inertial effect (Tanaka et al., 2012; Sollier et al., 2014; Warkiani et al., 2014) and viscoelastic effect (Tian et al., 2018; Lim H. et al., 2019) in microscale hydrodynamics.

2.1.2.1 Active Separation Methods

The active separation mainly separates CTCs by imposing an external field source manipulating cells. The interaction between dielectric particles and the electric field (Dielectrophoresis, DEP) can be used for cell separation, sorting, and capture (Kwizera et al., 2021). Due to the difference in dielectric properties, such as polarization constant between different kinds of cells, cells can be distinguished by applying an appropriate electric field. Jahangiri et al. (2020) completed the separation of CTCs and blood cells from different kinds of breast cancer by applying a low-frequency alternating current (AC) electric field on the chip (**Figure 3A**). Gascoyne et al. (2009) separated and screened CTCs in blood under the condition

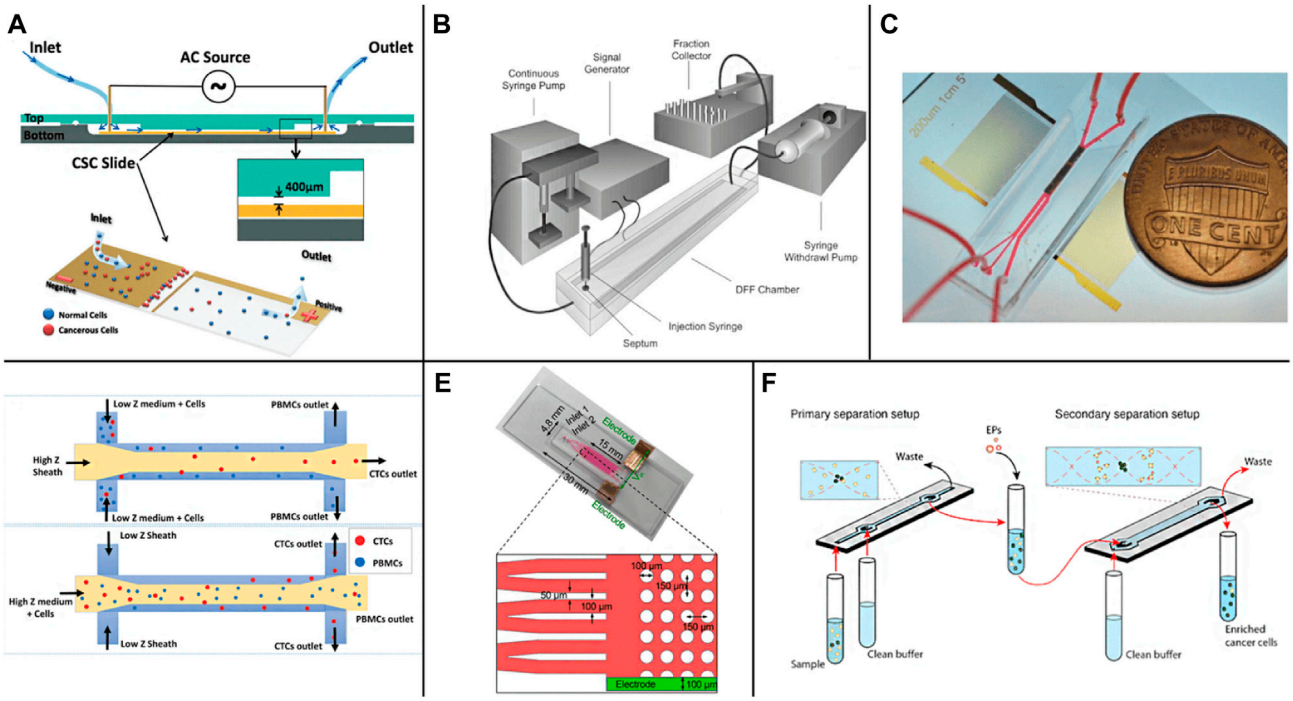

FIGURE 3 | Active enrichment methods based on physical screening **(A)** The CTCs detection chip based on AC electric field (Jahangiri et al., 2020); **(B)** The DEP flow fractionation (depFFF) configuration in CTCs detection (Gascoyne et al., 2009); **(C)** The acoustic CTC separation device (Wu et al., 2018); **(D)** Size insensitive isolation of CTCs from PBMCs (Karthick et al., 2018); **(E)** The microfluidic device on a glass slide with anti-EpCAM modification on the micropost in the device (Sun et al., 2019); **(F)** The two-step acoustophoresis (Undvall Anand et al., 2021).

of an external AC electric field (**Figure 3B**), realized the enrichment of CTCs, and obtained more than 90% cell capture rate with a fast processing time and much higher separation efficiency than biological affinity method. Montoya et al. developed a label-free dielectrophoresis microfluidic platform to promote the enrichment of circulating hybrid cells (CHCs) in a high-throughput and rapid manner by consuming healthy peripheral blood mononuclear cells (PBMC). 75% of the clinical samples were enriched, which proved that this method is a promising non-invasive method for analyzing tumor cells of patients (Montoya Mira et al., 2021).

Manipulating cells, droplets, and particles by sound waves in microfluidic chips is a rapidly developing field that is widely used in cell and particle sorting, blood separation, droplet transportation, and rare or cancer cell enrichment (Yiannacou and Sariola, 2021). Wu et al. (2018) realized the sorting of CTCs in peripheral blood by using surface acoustic waves (**Figure 3C**), adding sound field and surface acoustic wave sensor according to the arrangement of cells with different sizes, densities, and shapes in the standing wave field. The recovery rate of more than 86% CTCs can be obtained at the flux of 7.5 ml/h. Karthick et al. reported a combined sorting method based on acoustic impedance contrast and cell size for separating CTCs from peripheral blood mononuclear cells (PBMC) using acoustic electrophoresis in a microchannel (**Figure 3D**). By controlling the acoustic impedance contrast of the liquid in the channel, the CTCs whose acoustic impedance is higher or lower than PBMC are isolated. Hela and MDA-MB-231 cells were isolated unlabeled from PBMC (collected from 2.0 ml of blood) within 1 h, and >86% recovery and >50 times enrichment was obtained (Karthick et al., 2018). Sun et al. realized the efficient detection of CTCs in human blood by creating a separate capture area and flow area in the microfluidic device (zone chip) (**Figure 3E**) and using the patterned dielectrophoresis force to guide the cells from the flow area to the capture area (Sun et al., 2019). Antfolk et al. Introduced a simple cell separation instrument based on acoustic electrophoresis for continuous flow, unbiased and label-free separation of cancer cells and leukocytes based on acoustic electrophoresis. The cells were acoustically pre-aligned using ultrasound before separation, while the cells were maintained in the initial suspension medium. Even if the transverse displacement of particles in the sound field is less than 50 μm, the platform can still separate cells and particles with high precision. The system can separate the particles directly in the suspension medium without matching the acoustic characteristics of the sample with the system of multiple laminar flows (Antfolk et al., 2015). Undvall et al. presented a new two-step acoustic electrophoresis (A2) method for separating unfixed live cancer cells from whole blood lysed by red blood cells (RBC) (**Figure 3F**). The method uses the initial acoustic flow pre-separation step to separate the cells according to the acoustic mobility of the cells (Undvall Anand et al., 2021). Magnusson et al. used a clinical scale acoustic microfluidic platform to enrich

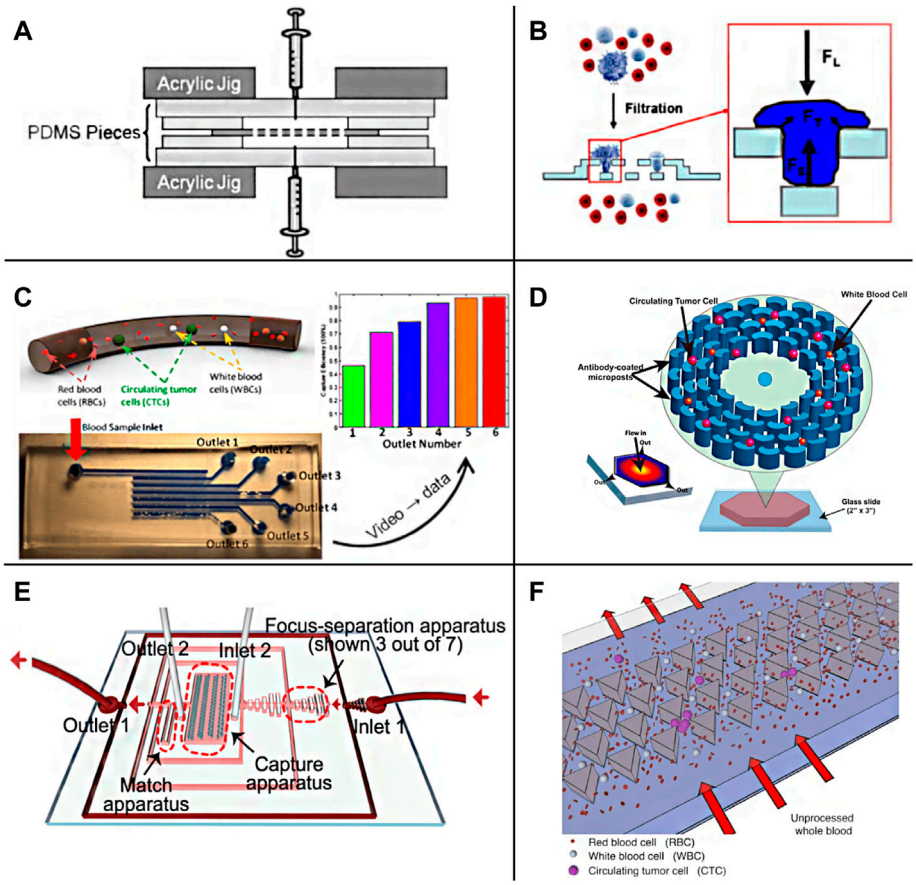

FIGURE 4 | Passive enrichment methods based on physical screening **(A)** A functional microdevice consists of parylene membrane filter (Lin et al., 2010); **(B)** Filtration process and forces on a trapped cell of the three-dimensional microfiltration device (Zheng et al., 2011); **(C)** Sequential Size-Based Microfluidic Chip (Ren et al., 2018); **(D)** The OncoBean Chip (Murlidhar et al., 2014); **(E)** A schematic illustration of the chip combining microscale hydrodynamics and pore sieve principle (Lu et al., 2020); **(F)** Schematic representation of the Cluster-Chip operation (Sarioglu et al., 2015).

paraformaldehyde-fixed or living cancer cells. The platform can be adjusted to meet the requirements of high cancer cell recovery or higher purity and can process 5 ml of blood in about 2 h. It opens up a broader field for the post-separation analysis and characterization of CTCs in patient samples in the future (Magnusson et al., 2017).

Using tumor cell targeting molecules to bind homologous red blood cells (RBC) to tumor cells shows a significant difference in optical constants (size and average refractive index) between red blood cell-bound CTCs and other blood cells. Then, the modified CTCs can be accurately separated under laser irradiation in the optical jet system. Experiments showed that CTCs effectively modified with red blood cells were finally separated from blood with high purity (more than 92%) and high recovery (more than 90%). Throughout the process, CTCs were shown to maintain membrane and functional integrity. This method provides a convenient tool for early diagnosis and treatment monitoring of cancer, which performs well in the non-invasive and accurate separation of CTCs (Hu et al., 2019).

2.1.2.2 Passive Separation Methods

Despite the external field source method having high efficiency in cell separation, it is difficult to integrate it into the chip, so Lin et al. (Lin et al., 2010) designed a straightforward CTCs separation chip according to the principle of pore screen filtration (**Figure 4A**). By adjusting the size of the filter hole, the separation of CTCs can be completed according to the difference in cell size, and the recovery rate is more than 90%. Zheng et al. reported a new three-dimensional microfiltration device (**Figure 4B**), which can enrich living circulating tumor cells from the blood. The device consists of two layers of palling film, and the holes and gaps are accurately defined by lithography technology. The position of the hole moves between the top and bottom membranes. The bottom membrane supports the captured cells, minimizes the stress concentration on the cell membrane, and maintains cell viability during filtration (Zheng et al., 2011). After that, various functional microfluidic platforms have been optimized to enhance the isolation of CTCs. Ren et al. (2018) designed a high-throughput CTCs capture chip according to cell size and deformability (**Figure 4C**). The chip has multiple

channels, and the channels are connected by multiple rows of miniature shrink tubes, in which there is a capture cavity designed according to the size of CTCs. When the blood flows through the intersection of the main channel and the miniature systolic tube, the capillary action generated by the surface tension will drive the fluid through the systolic tube. At this time, CTCs will be trapped in the capture chamber, and other components in the blood can pass smoothly and then enter the adjacent channel. In order to ensure a high capture rate of CTCs, the process can be repeated between multiple channels, and the capture rate of CTCs could exceed 95%. Chen et al. (2021) constructed a pore sieve chip system based on the biomimetic splenic sinus microstructure. The filter hole of the fissure structure has lower flow resistance than the traditional circular structure. Through the optimization of flow velocity and slit width, it can ensure the high cell activity of CTCs while realizing efficient separation. However, because the size of leukocytes and CTCs is the same, the screening accuracy of this method is low, which may produce false-positive results. In addition, setting a filter hole on the cell flow path is easy to increase the negative pressure due to blockage, which affects the separation efficiency. Qin et al. (2015) used the resettable cell trap (RCT) mechanism to separate cells by using an adjustable pore size that can be removed regularly to prevent blockage according to the size and deformability of cells. Inspired by the antifouling membrane, Kim et al. (2017) used an independent onboard laboratory system equipped with fluid-assisted separation technology (fast) to separate live CTCs from whole blood without prior sample processing. Numerical simulation and experiments show that under 1 kPa, this method provides uniform, non-clogging, and ultrafast cell enrichment, and the pressure drop is much lower than the traditional size-based filtration.

There are usually many physical barrier microstructures in the chip screened for CTCs according to the cell size, and the processing of these precise structures is often difficult. With the development of fluid mechanics theory on a micro-scale, based on the study of particle motion law in microfluid, the separation and enrichment of CTCs can be realized just by regulating the fluid without any microstructure. A microfluidic separation device with the asymmetric bifurcation of laminar flow around obstacles is used to separate particles. Particles determine their path based on their size. All particles of a given size follow an equivalent migration path to obtain high resolution (Huang et al., 2004). Murlidhar et al. reported an ultra-high throughput oncogene chip (**Figure 4D**) that can isolate live CTCs even at a high screening rate. The platform uses radial flow to produce different shear on the chip so that CTCs can be effectively captured under a high flow rate (Murlidhar et al., 2014). The results showed that at a high flow rate of 10 ml/h, the recovery rate of rare CTCs (cancer cell lines MCF7 and h1650) was 93%, and the capture efficiency was more than 80%, which increased the chance of CTCs recovery in subsequent downstream analysis. Ahmed et al. (2017) described a new device, a size-controlled immune capture chip, for efficient, sensitive, and spatial resolution CTCs capture and detection. The size-controlled immune capture chip can make CTCs interact selectively, frequently, and widely with the surface of immunocoated microcolumn optimized by fluid dynamics. CTCs with different antigen expression levels can be effectively captured and spatially resolved around the microcolumn. The capture efficiency is greater than 92%, and the purity is 82%. Wu et al. (2020c) designed a fluid multivalent nano interface and decorated the microfluidic chip with aptamer functionalized leukocyte membrane nanovesicles to efficiently separate CTCs. This fluid biomimetic nano interface with an active supplement combination provides significant affinity enhancement of four orders of magnitude and shows seven times the capture efficiency compared with the monovalent aptamer functional chip in blood. At the same time, this soft nano interface inherits the biological advantages of natural biofilm, minimizes the adsorption of background blood cells, and maintains good CTCs activity (97.6%). Kulasinghe et al. (2019) designed a square channel chip with a straightforward structure based on the inertial effect on the micro-scale. Due to the action of the dean and the center point of the square pipe, the vortex will gather preferentially near the center point of the large diameter pipe. Therefore, CTCs will be enriched near the center of the channel while other components are arranged on the outside. There is no microstructure or capture cavity in the chip to increase the negative pressure, so there can be a higher breakthrough in the processing flux. In addition, without the influence of any other external effects, the cells can better retain their physiological activity and morphological characteristics. Lim S. B. et al. (2019) also introduced tangential flow at the T-shaped channel to screen the blood cells close to the tube wall according to the inertial effect to realize the separation of CTCs. Zhang et al. (2018) and Tian et al. (2018) used the viscoelastic effect to complete the separation of CTCs. Using the fluid with low viscosity and no shear thinning can achieve an effect similar to the inertial effect. Moreover, the theoretical convergence model of this method is relatively simple, which is convenient for more accurate numerical simulation analysis. Zhu Z. et al. (2021) used a polymer film as material and constructed spiral microfluidic chips of trapezoidal channels through jigsaw puzzle technology. Using the combined action of inertial force and Dean eddy current in trapezoidal channel, the separation of CTCs can be realized at a high flux of 3 ml/min, and the experimental recovery rate is 90%–94%. The microfluidic chip system designed by Lu et al. (2020) combines microscale hydrodynamics and the pore sieve principle (**Figure 4E**). First, the preliminary separation of blood cells is completed through the inertial effect, and then the capture of CTCs is realized by the triangular microcolumn array. Ensuring a high capture rate of 94.8%, the flux can reach 40 ml/h. Liu Z. et al. (2021) combined filtration with deterministic lateral displacement (DLD) and designed a cascaded DLD microcolumn array chip to achieve 96% recovery of CTCs at a high throughput of 1 ml/min and eliminate 99.99% white blood cells. Cancer cells metastasize in the blood in single migrating circulating tumor cells (CTC) or multicellular clusters (CTC clusters). Sarioglu et al. Designed a chip with a triangular micro column structure to sort CTCs clusters with high precision (**Figure 4F**). When the CTCs cluster flows through the triangular microcolumn, it will be captured at its apex due to the intercellular connection, and a single cell will pass directly along the side waist surface of the microcolumn.

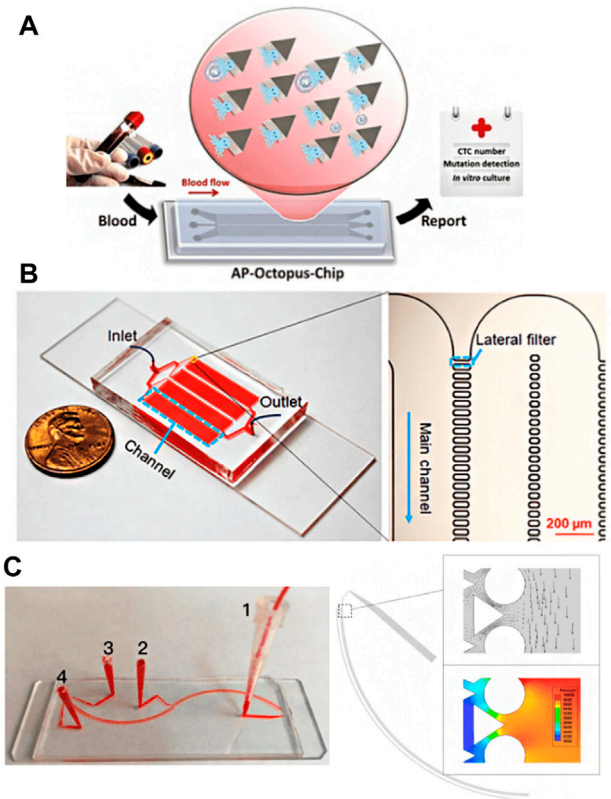

FIGURE 5 | CTCs Enrichment by combining biological affinity with physical screening **(A)** The Octopus chip for cell capture (Song et al., 2019); **(B)** The LFAM device consisting of four serpentine main channels (Chen et al., 2019); **(C)** The antibody functional microsphere integrated filter chip (Su et al., 2019).

This method requires that the flow rate should not be too high; otherwise, the large shear force will destroy the structure of the CTCs cluster, resulting in capture failure. The chip was used to separate the actual samples, determine the heterogeneity of CTCs clusters, and find that they may contain tumor-associated macrophages (TAMs), which is of great significance for the study of the interaction between TAMs and CTCs (Sarioglu et al., 2015).The label-free physical screening strategy is characterized by the CTCs integrity and fast sample processing. However, due to the heterogeneity of CTCs and the overlapping of CTCs and background cells, the observed recovery and purity of targeted CTCs are not satisfactory.

2.1.3 Enrichment by Combining Biological Affinity With Physical Screening

CTCs separation chips based on biological affinity and physical screening methods have advantages. The former is more specific, while the latter has higher separation efficiency. However, both of them also have shortcomings. For example, the biological affinity method depends on exogenous markers, which often affect the cell activity of CTCs, while the physical screening method has low separation accuracy and is easy to produce false-positive results. Therefore, the researchers tried to combine the two methods (Pei et al 2019; Lee, et al., 2017), effectively remove leukocytes using a label-free method, and then separate CTCs with high efficiency and purity using an affinity-based method. Song et al. (2019) designed a deterministic lateral displacement (DLD) pattern microfluidic chip modified with multivalent aptamer functionalized nanospheres (AuNP-syl3c) based on the principle of deterministic lateral displacement (**Figure 5A**). When cells with different sizes and elasticity flow through the angular triangular microcolumn array area, they choose different paths due to the collision with the microcolumn. By adjusting the size and spacing of microcolumn, CTCs can produce lateral displacement when colliding with microcolumn, and other blood cells flow out along the original path. In addition, the microcolumn is modified with AuNP-syl3c, the multivalent aptamer antigen-binding efficiency is increased by 100 times, and the capture performance of CTCs is significantly improved. Compared with the monovalent nucleic acid aptamer modified chip, the capture efficiency of this method is increased by more than 3 times. Chen K. et al. (2019) used the chip with lateral microcolumn array structure, modified EpCAM antibody on the microcolumn (**Figure 5B**), combined size based separation with immunoaffinity based separation to improve the capture efficiency of CTCs and reduce the nonspecific geometric capture of normal cells. Using the same principle, Su et al. (2019) developed a functional antibody microsphere integrated microchip (**Figure 5C**) by integrating cell size and tumor cell surface-specific antigen and introducing surface-functionalized modified zinc oxide microsphere, which greatly improved the effective capture area.

2.2 Negative Enrichment

Although high capture purity can be obtained by positive selection of CTCs by affinity methods such as anti-EpCAM, anti PSMA, and aptamer due to the specificity of tumor markers, the main disadvantage of this technology is that it may not be conducive to the integrity and vitality of CTCs recovered in the separation process. Therefore, the negative enrichment or selection of CTCs has been widely used. Due to the small size difference between leukocytes and CTCs, leukocytes are often the most interfering factor in sorting CTCs in blood. Therefore, leukocytes can be selectively isolated to achieve the purpose of CTCs enrichment, that is, reverse enrichment (Jiang et al., 2021). Hematopoietic cells were removed by negative selection targeting antigens (CD45) that do not express CTCs (Sun et al., 2018; Tan et al., 2018). The recovered high-purity CTCs were trapped on the platform surface, while most other blood cells were washed away. The reverse enrichment strategy can not only effectively realize the separation of CTCs; moreover, CTCs whose EpCAM expression is down-regulated due to EMT, even non-epithelial tumor cells, can be enriched. At the same time, it can also avoid the effect of direct labeling on the activity of CTCs cells.

Liu et al. used the commercial easysep system to deplete leukocytes through magnetic nanoparticles and tetramer antibody complexes targeting CD45 and then collected rare CTCs from peripheral blood samples of cancer patients (Liu et al., 2011). According to the results of low cell analysis, capture

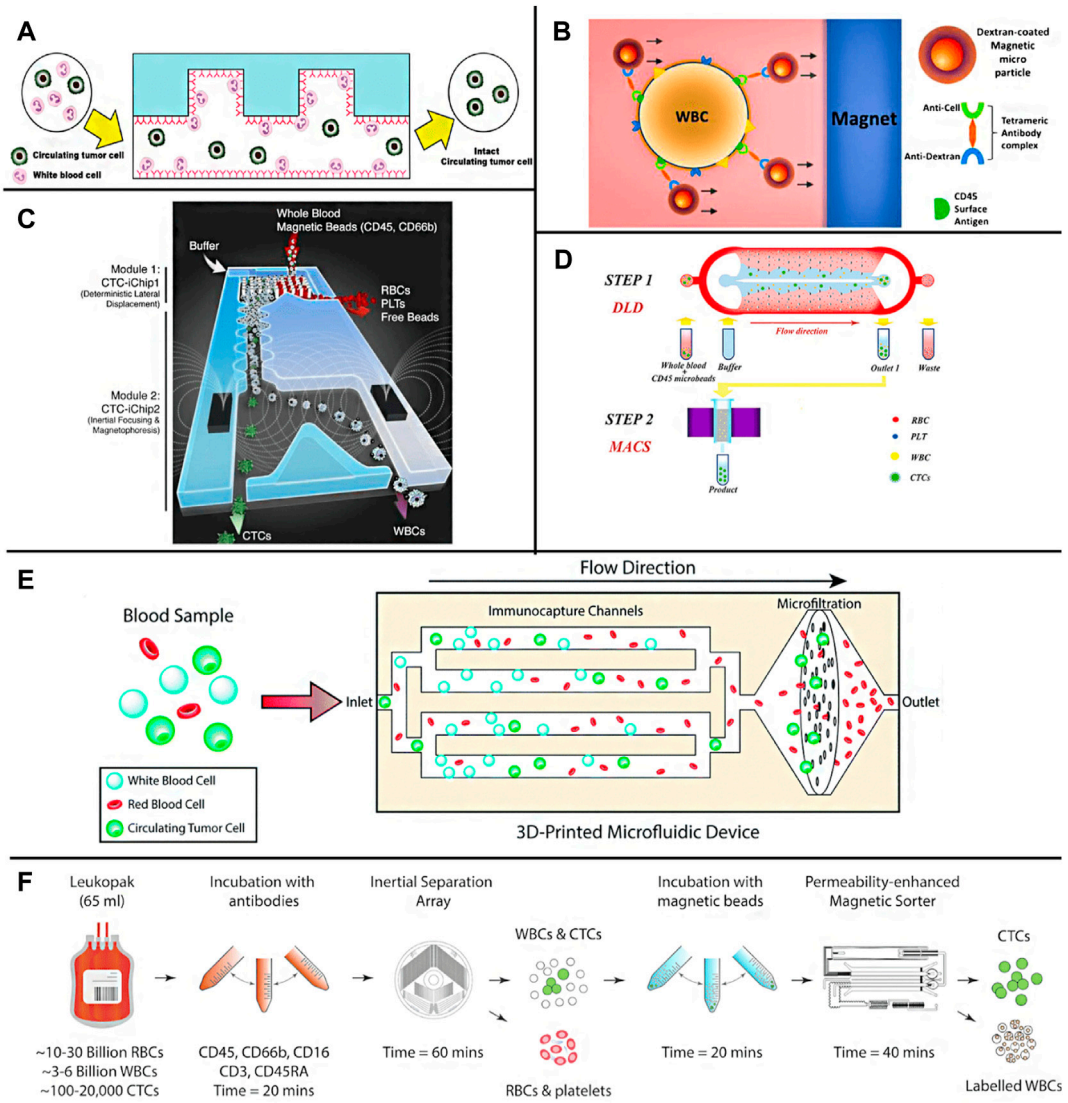

FIGURE 6 | Negative enrichment methods for CTCs **(A)** Pictorial presentation of negative enrichment of the GASI chip (Hyun et al., 2013); **(B)** Illustration of immunomagnetic WBC depletion in which magnetic particles bound to WBC through Tetrameric antibody complex in whole human blood (Sajay et al., 2014); **(C)** The CTC-iChip schematic (Karabacak et al., 2014); **(D)** The capture platform integrating a DLD structure with a MACS separator for inline operation (Wang et al., 2019); **(E)** A schematic showing the tumor cell enrichment process in the 3D-printed microfluidic device (Chu et al., 2019); **(F)** A schematics illustrating the microfluidic approach for untouched CTCs isolation from leukapheresis products (Mishra et al., 2020).

efficiencies of 56% (47 of 84 samples) and 53% (17 of 32 samples) were obtained from patients with cancer and melanoma, respectively. In contrast, flexible microfluidic platforms (e.g., microfluidic magnetically activated cell sorters (MACS) and CTCs-iChip) have been introduced for negative capture (Giordano et al., 2012; Ramirez et al., 2019; Cheng et al., 2019). In addition, the negative selection of the microfluidic platform can isolate CTCs with no or less EpCAM expression, while the recovered CTCs are complete and have relatively good survivability. It is reported that geometrically activated surface interaction chips can improve the capture efficiency of labeled leukocytes by enhancing the interaction between leukocytes and the chip surface (Hyun et al., 2013) (**Figure 6A**). In addition, Sajay et al. Proposed an upstream immunomagnetic removal technology to remove $CD45^{+}$ labeled leukocytes and then use a specially designed micro fabrication filter membrane to remove chemical-free erythrocytes and separate targeted CTCs (Sajay et al., 2014) (**Figure 6B**). The results showed that about 90% of targeting MCF-7 and NCIH 1975 cells could restore blood samples at the peak. Karabacak et al. (2014) designed an integrated dual-chip separation system (**Figure 6C**). Firstly, leukocytes and CTCs were quickly separated from the blood through two physical screening methods of DLD and inertial effect, and then magnetic beads modified with CD45 and CD66b composite antibodies were used to bind leukocytes selectively, and then the accurate screening of leukocytes and CTCs was

realized under the induction of external magnetic field. Ensuring a high capture rate of CTCs, this method can also achieve high flux, and it only takes 2 h for 8 ml blood samples processing. Wang et al. (2019) used a similar DLD-MACS method to analyze the clinical samples of patients with liver cancer (**Figure 6D**). The capture rate of CTCs under the flow rate of 60 μl/min is 85.1% ± 3.2%, and the experiment shows that this method still has a good separation effect for tumor cells with low expression of EpCAM. Chu et al. (2019) developed an integral 3D microfluidic device (**Figure 6E**), which combines immune removal and post-filtration to enrich CTCs directly from whole blood negatively. Blood samples first flow through the immune capture area modified with CD45 antibody, selectively screen out leukocytes, and then pass through 3 μM pore size filter membrane to remove the small volume of red blood cells and platelets to realize the separation of CTCs. The CTCs separation chip designed by Mishra et al. (2020) combines immunomagnetic separation with inertial effect (**Figure 6F**) and uses immunomagnetic beads modified with a variety of antibodies to label leukocytes. Under the external strengthening of the magnetic field and fluid regulation, it can realize the efficient separation of CTCs and leukocytes. The enrichment of CTCs can reach 105 times, and the flux is up to 168 ml/h. Overall, the advantage of the negative enrichment strategy over positive selection is that the rate of recovered CTCs is higher. However, the separation purity is usually lower than that of the positive method, requiring multiple separation processes (Kang et al., 2019; Civelekoglu et al., 2022).

For the negative selection of CTCs (strategy based on biological affinity), it usually has a recovery rate of more than 90%. However, the purity of recovered CTCs is less than 10% because some background cells are not labeled by antibodies against leukocytes surface markers and avoid subsequent depletion.

3 ON-CHIP DETECTION OF CTCS

For the detection of CTCs, cell staining is usually carried out first and then observed by a fluorescence microscope (Qian et al., 2015). However, the sensitivity of this method needs to be improved, and the reproducibility is poor, which requires manual operation and manual counting. In recent years, researchers have optimized and improved the imaging analysis method of CTCs on-chip. Watanabe et al. (2014) developed a cell capture platform using on-chip sorting (on-chip Biotechnology) and used anti-CD45 coated magnetic beads to negatively enrich remove leukocytes, and then fixed and labeled the samples. Then, the enriched and labeled samples were sorted according to the expression of cytokeratin, vimentin, and CD45. The captured cells were immediately subjected to genome-wide amplification, followed by a mutation analysis using deep targeted sequencing and copy number analysis using quantitative polymerase chain reaction (qPCR). Deng et al. (2014) developed an integrated microfluidic system specially used to simplify the separation, purification, and single-cell secretory omics analysis of whole blood CTCs (**Figure 7A**). The first is to capture CTCs through antibody conjugate encoded by photodegradable single-stranded DNA and microfluidic chip producing fretting protein. The captured CTCs are then photochemically released from the chip by brief ultraviolet irradiation and then negatively consume red blood cells (RBC) and white blood cells (WBC). The high-purity CTCs are then delivered to the single-cell barcode chip (SCBC), which integrates the enhanced polylysine (PLL) barcode mode and can capture a very small number of target cells on the chip. A single CTC is isolated in a microchamber and used to analyze a group of functional proteins secreted by a single CTC. The microfluidic system can process 1 ml of whole blood samples in less than 2 h, and the separation efficiency is more than 70%. The platform can also classify CTCs into specific phenotypes through the characteristics of surface markers and conduct single-cell secretory omics analysis on these subsets. Watanabe et al. (2018) successfully stained the CTCs of patients with metastatic non-small cell lung cancer isolated by a chip with a fluorescent-labeled antibody targeting tumor cell markers. The desktop on-chip cell sorter is equipped with disposable microfluidic equipment to detect and isolate rare tumor cells for subsequent molecular analysis. Wang et al. (2020) used immune microspheres modified with CD45 antibody to label leukocytes. After a wedge chip completes the preliminary sorting of blood cells, CTCs can be directly distinguished under bright-field microscopic imaging, and automatic counting can be realized through image processing software. Lee et al. (Lee and Kwak, 2020), through multi-channel fluorescence imaging, simultaneously characterizing the expression of estrogen receptor (ER), progesterone receptor (PR), and human epidermal growth factor receptor 2 (HER2) on CTCs, completes the rapid diagnosis and typing of breast cancer. Wang J. et al. (2021)) introduced a gas driving device into the integrated CTCs separation, immunofluorescence staining, and imaging system, which greatly reduced the time and reagent consumption and was able to capture and recognize CTCs within 90 min. The smart chip developed by Pahattuge et al. (2021) integrates CTCs sorting, cell counting, and immunofluorescence imaging modules, which realizes the fully automatic operation of the separation and detection of CTCs in blood and avoids human interference **(Figure 7B)**.

In addition, some common spectral detection methods, represented by fluorescence spectroscopy, are also widely used in the detection of on-chip CTCs. Shen et al. (2018) designed a chip based on the gold film, sorted CTCs by immunomagnetic separation, and then observed and detected CTCs by near-infrared fluorescence method based on surface plasmon resonance. Because the light absorption and spontaneous fluorescence intensity of the biological sample matrix in the near-infrared region are very small, and the fluorescence signal intensity is greatly enhanced by the surface plasmon resonance effect, the detection sensitivity of this method is nearly 10 times higher than that of ordinary fluorescence analysis method. Cho H. et al. (2018); Cho H. Y. et al. (2018) used gold nanoparticles modified with antibodies and Raman signal molecules to label CTCs (**Figure 7C**). The CTCs captured on the chip can be characterized and detected *in situ* by surface-enhanced Raman technology. This method has high sensitivity and can distinguish

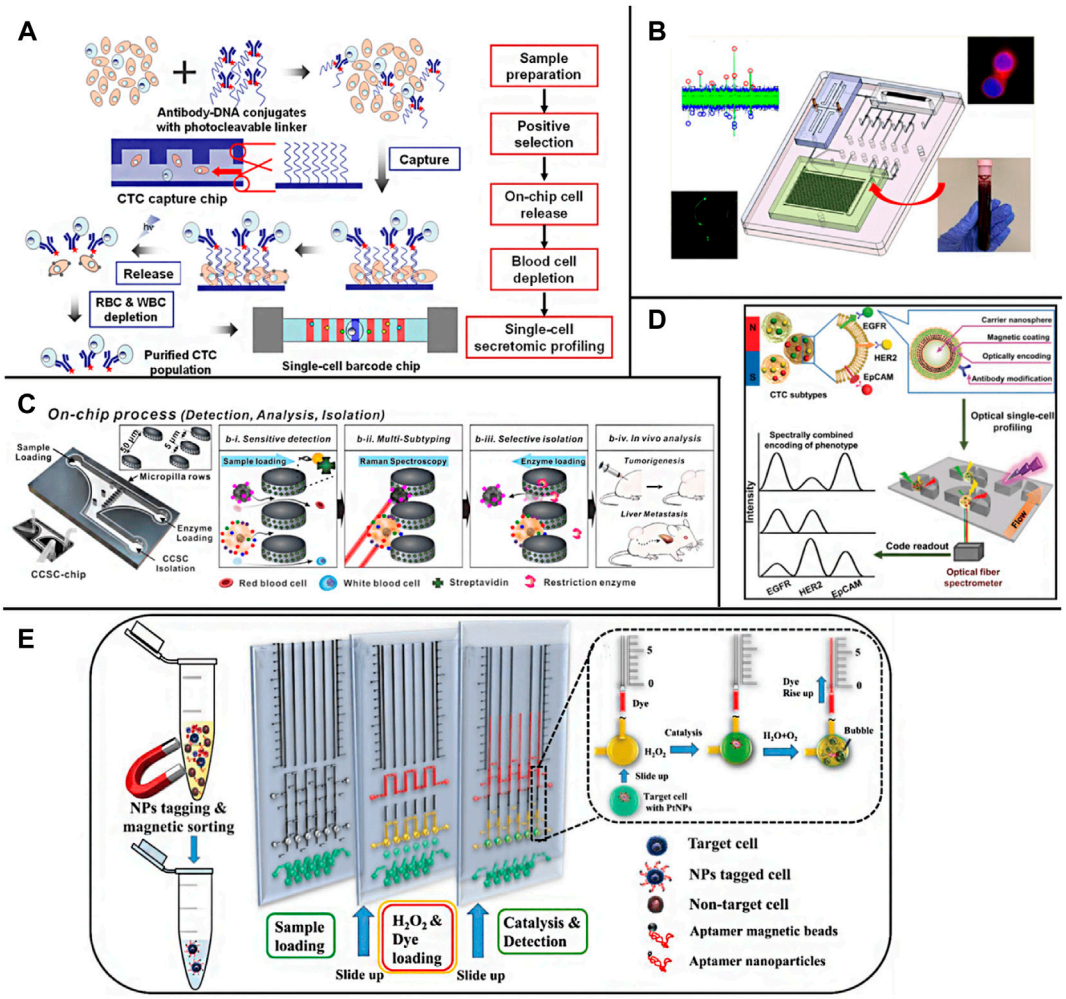

FIGURE 7 | On-chip detection of CTCs **(A)** Overall strategy for CTC isolation and single-cell secretome analysis (Deng et al., 2014); **(B)** A system modularity chip for the analysis of rare targets (SMART-Chip) (Pahattuge et al., 2021); **(C)** A 3-step process for blood sample solutions with RANs labeled CCSCs and CTCs (Cho et al., 2018); **(D)** A multifunctional nanosphere-mediated microfluidic platform for multiplex biomarker profiling of heterogeneous CTCs (Wu et al., 2020); **(E)** The working principle of the aptamer-conjugated PtNPs with volumetric bar-chart chip readout for quantifiable visual detection of CTCs (Abate et al., 2019).

common CTCs and circulating tumor stem cells (CTSCs) according to the difference in Raman signal peaks. Dhar et al. (2018) wrapped the CTCs obtained after inertial vortex separation in the droplets containing matrix metalloproteinase (MMP) reaction system through droplet microfluidic technology. Due to the high MMP reaction activity of the target CTCs, the detection and counting of CTCs can be realized by the resonance fluorescence transfer phenomenon generated by the enzymatic reaction system. Wu et al. (2020d) labeled the target protein on CTCs with magnetic nanoparticles loaded with antibody and fluorescence coding at the same time, captured CTCs with a chip under an external magnetic field (**Figure 7D**), and characterized the contents of epidermal growth factor receptor (EGFR), HER2 and EP-CAM on a single CTC through fluorescence intensity.

In addition to optical analysis methods, researchers also realized the direct digital reading or visual analysis of CTCs chip detection results by using sensing elements. Chen Y. H. et al. (2019) used Al-GaN/GaN with high electron mobility as the material to make field-effect transistors (FETs), set the FETs sensor array on the chip, and modify the specifically recognized nucleic acid aptamer of EpCAM on its surface, to realize the continuous capture and counting of CTCs. The high transconductance gain of FETs makes the bioelectronic sensor have high detection sensitivity. Experiments show that this method can realize the rapid and automatic detection of CTCs in a wide dynamic range and provide accurate cell count data. Niitsu et al. (2018) first proposed a fully integrated CMOS circuit based on a vector network analyzer and transmission line for CTCs and exosome analysis and detection. A fully integrated architecture is introduced to eliminate unwanted parasitic components and achieve high sensitivity to analyze very low concentrations of CTCs in blood. Kim et al. (2021) introduced a one-time intelligent microfluidic platform called "DIS-μ Chip", in which microfluidic flow sensors are integrated. Due to

integration, the flow between the flow sensor and the microfluidic function is significantly reduced without a pipeline connection. Isolated CTCs from the blood of patients with pancreatic cancer using the DIS-μ chip can further be extracted the cancer-specific gene information by the digital droplet PCR, proving that the DIS-μ chip is effective. Chang et al. (2015) isolated and detected CTCs from blood samples using a microchip system integrating immunomagnetic, high-throughput fluidics, and size-based filtration. Magnetic beads with antibody functionalization were used to target CTCs in samples. Then, the mixture passes through a micro-machined chip fluid chamber containing an 8 μM-diameter aperture array. The fluid runs parallel to the microchip and generates a magnetic field below it, pulling the beads and cells bound to it to the surface of the chip to detect CTCs larger than pore diameter and remove free beads and other smaller particles bound to it. The system allows high volumetric flow rate detection and allows the sample fluid to circulate multiple times through the system in a short time. An average of 89% MCF-7 of breast cancer cells was detected. Gao et al. (Gao et al., 2018) combined CTCs chip screened by composite immunomagnetic beads with droplet digital PCR chip to improve the detection sensitivity through PCR amplification. Abate et al. (2019) added Pt nanoparticles (Pt NPs) modified with nucleic acid aptamer to the blood sample to be tested, obtained the target CTCs bound with Pt NPs through immunomagnetic separation, and introduced them into the detection chip pre-loaded with H_2O_2 and dye. Because Pt can catalyze the decomposition of H_2O_2, the generated oxygen gas will lead to the rise of the dye liquid column, to the content of CTCs in the blood can be judged according to the height of the liquid column (**Figure 7E**). Jian et al. (2020) labeled CTCs with magnetic metal-organic frameworks (MOF) nanoparticles modified with glucose oxidase. After the TiO_2 nanotube array on the chip captured CTCs by magnetic force, Fe^{2+}/Fe^{3+} in MOF was reduced to FeO through the photocatalytic action of TiO_2 and the electrochemical signal was obtained by differential pulse voltammetry to realize the quantitative detection of CTCs.

4 CLINICAL APPLICATION PROSPECT AND CHALLENGE OF CTCS MICROFLUIDIC BIOSENSOR

CTCs have attracted extensive attention in tumor research as a new tumor biomarker, and their clinical application is also being widely studied. The emerging microfluidic technology has become a general tool for basic and applied tumor metastasis research because of its relatively low cost, simple operation, small volume, and accurate fluid control. With the progress of micromachining technology, the microfluidic platform is thriving. The functional microfluidic platform will contribute to an in-depth understanding of cancer biology and multiple drug screening. Based on the large amount of information provided by CTCs, the use of CTCs includes early screening and cancer diagnosis, treatment and drug resistance monitoring, drug evaluation, disease progression, and prognosis. It is reported that a detectable tumor lesion contains at least 109 tumor cells (Steeg, 2006; Lawson et al., 2015). Although high-resolution imaging techniques such as CT, PET and MRI (Wang Q. et al., 2021) have been widely used in the clinical detection of tumor lesions, their ability to detect early tumor formation is limited. The detection of non-invasive CTCs has been explored for early tumor screening and diagnosis (Ilie et al., 2014). It can detect early events before the formation of primary tumors (Pantel and Alix-Panabières, 2010; Alix-Panabières and Pantel, 2016; Zhang et al., 2016; Austin et al., 2018; Moon et al., 2018; Poudineh et al., 2018), which provides a basis for early cancer detection (Nagrath et al., 2007; Zahirović et al., 2022).In addition, CTCs count is helpful to predict tumor progression and overall survival (Gorin et al., 2017). The level of CTCs in many cancer patients is highly correlated with tumor progression. CTCs Count is helpful to identify tumor progression. For patients with breast cancer who had a CTCs count below 5 CTCs/mL in blood, the overall survival rate of patients with a CTCs count over 5 CTCs/mL was lower (Krebs et al., 2010; Krebs et al., 2011). In addition, the phenotype of CTCs is related to the tumor stage (Jordan et al., 2016), which can be used as a good indicator to evaluate tumor progression. CTCs can provide information about tumor progression before and during treatment and provide information about the molecular evolution of tumor cells during treatment (Kidess-Sigal et al., 2016). For example, as cancer patients develop resistance to treatment, CTCs show more mesenchymal-like CTCs (Yu et al., 2013). CTCs analysis was used to determine the maximum tolerated dose and guide the optimal dose selection of anticancer drugs (An et al., 2021; Guo et al., 2021). Through the simultaneous monitoring of EMT biomarkers and apoptosis of CTCs, the results show that even if they act on the same tumor type, there are significant differences in the optimal drug dose, indicating that tumor heterogeneity has an impact on the drug use of patients (Pei et al., 2020b). CTCs counts can monitor treatment and help clinicians make the best chemotherapy decisions. CTCs count decreases with the continuation of effective treatment. CTCs count may become an effective tool to monitor the early effect of cancer treatment (Sheng et al., 2014). Tracking and detecting the CTCs of patients in real-time during the treatment can predict the treatment results faster and more accurately, which can be used to evaluate the efficacy of clinical drugs (Bruna et al., 2016; Stevens et al., 2016; Praharaj et al., 2018), and customize the treatment scheme for individual patients (Weinstein et al., 2018; Kozminsky et al., 2019).

At the same time, in the transformation and application of clinical tumor diagnosis and treatment, the detection of tumor biomarkers of CTCs still faces many challenges: first, the content of tumor biomarkers in the blood is rare, and there is tumor heterogeneity, which makes it very difficult to isolate and purify them. To overcome this challenge, it is necessary to develop a microfluidic platform that fully uses the physical and biological characteristics of tumor biomarkers. Secondly, the high-precision and fully automated systems based on microfluidic separation and purification of tumor biomarkers are mostly in the scientific research stage and have not been widely used in the clinic. Moreover, the integration between circulating tumor biomarkers and the microfluidic platform needs to be

improved. In order to further promote the development of the microfluidic system with high sensitivity and good repeatability, a large number of clinical trials need to be carried out on a variety of cancer patients. In addition, our understanding of tumor biology is still in its infancy. With the in-depth study of the role of various circulating tumor biomarkers in tumor formation and development, more powerful and effective commercial microfluidic systems will emerge as the times require.

5 CONCLUSION

In this paper, we reviewed the separation strategy, technical principle, and research progress of microfluidic chip separation of CTCs. The separation strategy can be divided into positive enrichment and negative enrichment. The technical principle is also mainly divided into biological affinity and physical screening. At the same time, the main technical methods and optimization strategies of CTCs on-chip detection are introduced. The application prospect of microfluidic chips in tumor diagnosis and treatment and the development direction of microfluidic chips in tumor detection are analyzed. With the rapid development of microfluidic chip technology, its ability for microscale fluid manipulation, microstructure processing, and integrated sensing and detection has been greatly improved, which further promotes the development of CTCs separation microfluidic chip technology. Using a microfluidic chip as a platform to separate and detect CTCs in peripheral blood can give full play to the advantages of micro, high efficiency, easy automation, and integration of the chip itself, and finally realize the rapid and accurate analysis of CTCs in clinical blood. It has important application space in many fields such as early tumor diagnosis, recurrence, metastasis monitoring, and anti-tumor drug evaluation (Ankeny et al., 2016; Pei et al., 2020; Sun et al., 2021; Kelley et al., 2014; Farshchi and Hasanzadeh, 2021; Dong et al., 2019).

Although microfluidic devices have successfully achieved the capture performance of CTCs through various affinity-based or label-free methods, no method has satisfactory separation results of high efficiency through porosity, purity, recovery, and throughput at the same time. At this stage, the CTCs chip still has great room for improvement in screening accuracy and screening efficiency. In response to this challenge, because it is difficult to have both accuracy and efficiency, future chip design should focus more on realizing a single goal. On the one hand, we should focus on improving the cell purity and the cell activity of CTCs screening for basic research. Firstly, separate the blood roughly using the inertia effect and screen out the larger white blood cells and CTCs. Then, screen CTCs accurately adopting droplet sorting (Joensson and Andersson Svahn, 2012; Dong and Fang, 2020) through immunomagnetic separation (Chen et al., 2013). Droplet sorting technology can achieve the accuracy of single-cell analysis, which has been reported for tumor cell screening (Popova et al., 2019). On the other hand, in clinical testing, the researchers focus to realize the high-throughput analysis of clinical samples. The electrical analysis method can be used to set the appropriate threshold according to the difference in specific membrane capacitance and cytoplasmic conductivity of different kinds of cells to realize the rapid analysis of CTCs passing through the detection window (Lannin et al., 2016; Chiu et al., 2017; Zhao et al., 2018; Zhang Y. et al., 2019). In addition, microfluidic chip technology belongs to an interdisciplinary field. The development of CTCs chips also benefits from technological breakthroughs in fields such as microelectromechanical systems (MEMS), materials science, hydrodynamics, and biomedicine. In the future, the microfluidic platform designed for multi-step CTCs separation will be integrated with advanced functions to minimize the shortcomings of the complex sample preparation process. With the development of related technologies, the CTCs chip is expected to become an important platform for basic tumor research and early clinical diagnosis of cancer in the future.

AUTHOR CONTRIBUTIONS

CL and WH: Conceptualization, Methodology, Investigation, Writing-original draft. NW: Conceptualization, Datum analysis. ZX: Writing-review and editing. RD and XL: Writing-review and editing. RK, LX, and XL: Writing and Revising, Supervision.

FUNDING

This work was supported by the National Natural Science Foundation of China (81772356).

REFERENCES

Abate, M. F., Jia, S., Ahmed, M. G., Li, X., Lin, L., Chen, X., et al. (2019). Visual Quantitative Detection of Circulating Tumor Cells with Single-Cell Sensitivity Using a Portable Microfluidic Device. *Small* 15 (14), 1804890–1804897. doi:10.1002/smll.201804890

Aghaamoo, M., Aghilinejad, A., Chen, X., and Xu, J. (2019). On the Design of Deterministic Dielectrophoresis for Continuous Separation of Circulating Tumor Cells from Peripheral Blood Cells. *Electrophoresis* 40 (10), 1486–1493. doi:10.1002/elps.201800459

Ahmed, M. G., Abate, M. F., Song, Y., Zhu, Z., Yan, F., Xu, Y., et al. (2017). Isolation, Detection, and Antigen-Based Profiling of Circulating Tumor Cells Using a Size-Dictated Immunocapture Chip. *Angew. Chem. Int. Ed.* 56 (36), 10681–10685. doi:10.1002/anie.201702675

Alix-Panabières, C., and Pantel, K. (2016). Clinical Applications of Circulating Tumor Cells and Circulating Tumor DNA as Liquid Biopsy. *Cancer Discov.* 6 (5), 479–491. doi:10.1158/2159-8290.CD-15-1483

Alshareef, M., Metrakos, N., Juarez Perez, E., Azer, F., Yang, F., Yang, X., et al. (2013). Separation of Tumor Cells with Dielectrophoresis-Based Microfluidic Chip. *Biomicrofluidics* 7 (1), 011803–011814. doi:10.1063/1.4774312

An, H. W., Mamuti, M., Wang, X., Yao, H., Wang, M. D., Zhao, L., et al. (2021). Rationally Designed Modular Drug Delivery Platform Based on Intracellular Peptide Self-assembly. *Exploration* 1 (2), 20210153–20210163. doi:10.1002/EXP.20210153

Ankeny, J. S., Court, C. M., Hou, S., Li, Q., Song, M., Wu, D., et al. (2016). Circulating Tumour Cells as a Biomarker for Diagnosis and Staging in Pancreatic Cancer. *Br. J. Cancer* 114 (12), 1367–1375. doi:10.1038/bjc.2016.121

Antfolk, M., Antfolk, C., Lilja, H., Laurell, T., and Augustsson, P. (2015). A Single Inlet Two-Stage Acoustophoresis Chip Enabling Tumor Cell Enrichment from white Blood Cells. *Lab. Chip* 15 (9), 2102–2109. doi:10.1039/c5lc00078e

Augustsson, P., Magnusson, C., Nordin, M., Lilja, H., and Laurell, T. (2012). Microfluidic, Label-free Enrichment of Prostate Cancer Cells in Blood Based on Acoustophoresis. *Anal. Chem.* 84 (18), 7954–7962. doi:10.1021/ac301723s

Austin, R. G., Huang, T. J., Wu, M., Armstrong, A. J., and Zhang, T. (2018). Clinical Utility of Non-EpCAM Based Circulating Tumor Cell Assays. *Adv. Drug Deliv. Rev.* 125, 132–142. doi:10.1016/j.addr.2018.01.013

Bai, L., Du, Y., Peng, J., Liu, Y., Wang, Y., Yang, Y., et al. (2014). Peptide-based Isolation of Circulating Tumor Cells by Magnetic Nanoparticles. *J. Mater. Chem. B* 2 (26), 4080–4088. doi:10.1039/c4tb00456f

Bruna, A., Rueda, O. M., Greenwood, W., Batra, A. S., Callari, M., Batra, R. N., et al. (2016). A Biobank of Breast Cancer Explants with Preserved Intra-tumor Heterogeneity to Screen Anticancer Compounds. *Cell* 167 (1), 260–274. doi:10.1016/j.cell.2016.08.041

Cai, P., Leow, W. R., Wang, X., Wu, Y.-L., and Chen, X. (2017). Programmable Nano-Bio Interfaces for Functional Biointegrated Devices. *Adv. Mater.* 29 (26), 1605529. doi:10.1002/adma.201605529

Cao, Y., Zhang, B., Zhu, Z., Xin, X., Wu, H., and Chen, B. (2021). Microfluidic Based Whole-Cell Biosensors for Simultaneously On-Site Monitoring of Multiple Environmental Contaminants. *Front. Bioeng. Biotechnol.* 9 (178), 622108–622113. doi:10.3389/fbioe.2021.622108

Castro-Giner, F., and Aceto, N. (2020). Tracking Cancer Progression: from Circulating Tumor Cells to Metastasis. *Genome Med.* 12 (1), 1–12. doi:10.1186/s13073-020-00728-3

Chandankere, R., Chelliah, J., Subban, K., Shanadrahalli, V. C., Parvez, A., Zabed, H. M., et al. (2020). Pleiotropic Functions and Biological Potentials of Silver Nanoparticles Synthesized by an Endophytic Fungus. *Front. Bioeng. Biotechnol.* 8, 95–108. doi:10.3389/fbioe.2020.00095

Chang, C.-L., Huang, W., Jalal, S. I., Chan, B.-D., Mahmood, A., Shahda, S., et al. (2015). Circulating Tumor Cell Detection Using a Parallel Flow Micro-aperture Chip System. *Lab. Chip* 15 (7), 1677–1688. doi:10.1039/c5lc00100e

Chen, A., Byvank, T., Chang, W.-J., Bharde, A., Vieira, G., Miller, B. L., et al. (2013). On-chip Magnetic Separation and Encapsulation of Cells in Droplets. *Lab. Chip* 13 (6), 1172–1181. doi:10.1039/c2lc41201b

Chen, J., Yang, Z., Xu, W., Yi, M., Zhong, M., Li, X., et al. (2021). Sorting of Circulating Tumor Cells Based on the Microfluidic Device of a Biomimetic Splenic Interendothelial Slit Array. *Microfluid Nanofluid* 25 (7), 1–13. doi:10.1007/s10404-021-02459-2

Chen K, K., Dopico, P., Varillas, J., Zhang, J., George, T. J., and Fan, Z. H. (2019). Integration of Lateral Filter Arrays with Immunoaffinity for Circulating-Tumor-Cell Isolation. *Angew. Chem.* 131 (23), 7688–7692. doi:10.1002/anie.201901412 10.1002/ange.201901412

Chen Yh, Y.-H., Pulikkathodi, A. K., Ma, Y.-D., Wang, Y.-L., and Lee, G.-B. (2019). A Microfluidic Platform Integrated with Field-Effect Transistors for Enumeration of Circulating Tumor Cells. *Lab. Chip* 19 (4), 618–625. doi:10.1039/c8lc01072b

Chen, Z., Hong, G., Wang, H., Welsher, K., Tabakman, S. M., Sherlock, S. P., et al. (2012). Graphite-coated Magnetic Nanoparticle Microarray for Few-Cells Enrichment and Detection. *ACS nano* 6 (2), 1094–1101. doi:10.1021/nn2034692

Cheng, Y.-H., Chen, Y.-C., Lin, E., Brien, R., Jung, S., Chen, Y.-T., et al. (2019). Hydro-Seq Enables Contamination-free High-Throughput Single-Cell RNA-Sequencing for Circulating Tumor Cells. *Nat. Commun.* 10 (1), 1–11. doi:10.1038/s41467-019-10122-2

Chiu, T.-K., Zhao, Y., Chen, D., Hsieh, C.-H., Wang, K., Chou, W.-P., et al. (2017). A Low-Sample-Loss Microfluidic System for the Quantification of Size-independent Cellular Electrical Property-Its Demonstration for the Identification and Characterization of Circulating Tumour Cells (CTCs). *Sensors Actuators B: Chem.* 246, 29–37. doi:10.1016/j.snb.2017.02.048

Cho H, H., Kim, J., Song, H., Sohn, K. Y., Jeon, M., and Han, K.-H. (2018). Microfluidic Technologies for Circulating Tumor Cell Isolation. *Analyst* 143 (13), 2936–2970. doi:10.1039/c7an01979c

Cho Hy, H.-Y., Hossain, M. K., Lee, J.-H., Han, J., Lee, H. J., Kim, K.-J., et al. (2018). Selective Isolation and Noninvasive Analysis of Circulating Cancer Stem Cells through Raman Imaging. *Biosens. Bioelectron.* 102, 372–382. doi:10.1016/j.bios.2017.11.049

Chu, C.-H., Liu, R., Ozkaya-Ahmadov, T., Boya, M., Swain, B. E., Owens, J. M., et al. (2019). Hybrid Negative Enrichment of Circulating Tumor Cells from Whole Blood in a 3D-Printed Monolithic Device. *Lab. Chip* 19 (20), 3427–3437. doi:10.1039/c9lc00575g

Civelekoglu, O., Frazier, A. B., and Sarioglu, A. F. (2022). The Origins and the Current Applications of Microfluidics-Based Magnetic Cell Separation Technologies. *Magnetochemistry* 8 (1), 10–28. doi:10.3390/magnetochemistry8010010

C. Wild, E. Weiderpass, and B. W. Stewart (Editors) (2020). *World Cancer Report: Cancer Research for Cancer Prevention* (France: IARC Press).

Dan, Z., and Daxiang, C. (2018). Advances in Isolation and Detection of Circulating Tumor Cells Based on Microfluidics. *Cancer Biol. Med.* 15 (4), 335–353. doi:10.20892/j.issn.2095-3941.2018.0256

Deng, Y., Zhang, Y., Sun, S., Wang, Z., Wang, M., Yu, B., et al. (2014). An Integrated Microfluidic Chip System for Single-Cell Secretion Profiling of Rare Circulating Tumor Cells. *Sci. Rep.* 4 (1), 1–8. doi:10.1038/srep07499

Dhar, M., Lam, J. N., Walser, T., Dubinett, S. M., Rettig, M. B., and Di, Carlo, D. (2018). Functional Profiling of Circulating Tumor Cells with an Integrated Vortex Capture and Single-Cell Protease Activity Assay. *Proc. Natl. Acad. Sci. U.S.A.* 115 (40), 9986–9991. doi:10.1073/pnas.1803884115

Dong, R., Liu, Y., Mou, L., Deng, J., and Jiang, X. (2019). Microfluidics-Based Biomaterials and Biodevices. *Adv. Mater.* 31 (45), 1805033–1805050. doi:10.1002/adma.201805033

Dong, Z., and Fang, Q. (2020). Automated, Flexible and Versatile Manipulation of Nanoliter-To-Picoliter Droplets Based on Sequential Operation Droplet Array Technique. *Trac Trends Anal. Chem.* 124, 115812–115867. doi:10.1016/j.trac.2020.115812

Eslami-S, Z., Cortés-Hernández, L. E., and Alix-Panabières, C. (2020). Epithelial Cell Adhesion Molecule: an Anchor to Isolate Clinically Relevant Circulating Tumor Cells. *Cells* 9 (8), 1836–1852. doi:10.3390/cells9081836

Farshchi, F., and Hasanzadeh, M. (2021). Microfluidic Biosensing of Circulating Tumor Cells (CTCs): Recent Progress and Challenges in Efficient Diagnosis of Cancer. *Biomed. Pharmacother.* 134, 111153–111170. doi:10.1016/j.biopha.2020.111153

Fraser, L. A., Cheung, Y. W., Kinghorn, A. B., Guo, W., Shiu, S. C. C., Jinata, C., et al. (2019). Microfluidic Technology for Nucleic Acid Aptamer Evolution and Application. *Adv. Biosys.* 3 (5), 1900012–e1900027. doi:10.1002/adbi.201900012

Galanzha, E., and Zharov, V. (2013). Circulating Tumor Cell Detection and Capture by Photoacoustic Flow Cytometry *In Vivo* and *Ex Vivo*. *Cancers* 5 (4), 1691–1738. doi:10.3390/cancers5041691

Gao, W., Huang, T., Yuan, H., Yang, J., Jin, Q., Jia, C., et al. (2018). Highly Sensitive Detection and Mutational Analysis of Lung Cancer Circulating Tumor Cells Using Integrated Combined Immunomagnetic Beads with a Droplet Digital PCR Chip. *Talanta* 185, 229–236. doi:10.1016/j.talanta.2018.03.083

Gascoyne, P. R. C., Noshari, J., Anderson, T. J., and Becker, F. F. (2009). Isolation of Rare Cells from Cell Mixtures by Dielectrophoresis. *Electrophoresis* 30 (8), 1388–1398. doi:10.1002/elps.200800373

Giordano, A., Gao, H., Anfossi, S., Cohen, E., Mego, M., Lee, B.-N., et al. (2012). Epithelial-Mesenchymal Transition and Stem Cell Markers in Patients with HER2-Positive Metastatic Breast Cancer. *Mol. Cancer Ther.* 11 (11), 2526–2534. doi:10.1158/1535-7163.MCT-12-0460

Gleghorn, J. P., Pratt, E. D., Denning, D., Liu, H., Bander, N. H., Tagawa, S. T., et al. (2010). Capture of Circulating Tumor Cells from Whole Blood of Prostate Cancer Patients Using Geometrically Enhanced Differential Immunocapture (GEDI) and a Prostate-specific Antibody. *Lab. Chip* 10 (1), 27–29. doi:10.1039/b917959c

Gorin, M. A., Verdone, J. E., Van Der Toom, E., Bivalacqua, T. J., Allaf, M. E., and Pienta, K. J. (2017). Circulating Tumour Cells as Biomarkers of Prostate, Bladder, and Kidney Cancer. *Nat. Rev. Urol.* 14 (2), 90–97. doi:10.1038/nrurol.2016.224

Guo, M., Li, X., Zhang, S., Song, H., Zhang, W., Shang, X., et al. (2015). Real-time Quantitative RT-PCR Detection of Circulating Tumor Cells from Breast Cancer Patients. *Int. J. Oncol.* 46 (1), 281–289. doi:10.3892/ijo.2014.2732

Guo, S., Li, K., Hu, B., Li, C., Zhang, M., Hussain, A., et al. (2021). Membrane-destabilizing Ionizable Lipid Empowered Imaging-guided siRNA Delivery and Cancer Treatment. *Exploration* 1 (1), 35–49. doi:10.1002/EXP.20210008

Guo, T., Stankiewicz, E., Mao, X., and Lu, Y.-J. (2019). The Isolation and Analysis of Circulating Tumor Cells. *Methods Mol. Biol.* 2054, 115–128. doi:10.1007/978-1-4939-9769-5_7

Hoshino, K., Huang, Y.-Y., Lane, N., Huebschman, M., Uhr, J. W., Frenkel, E. P., et al. (2011). Microchip-based Immunomagnetic Detection of Circulating Tumor Cells. *Lab. Chip* 11 (20), 3449–3457. doi:10.1039/c1lc20270g

Hu, X., Zhu, D., Chen, M., Chen, K., Liu, H., Liu, W., et al. (2019). Precise and Non-invasive Circulating Tumor Cell Isolation Based on Optical Force Using Homologous Erythrocyte Binding. *Lab. Chip* 19 (15), 2549–2556. doi:10.1039/c9lc00361d

Huang, L. R., Cox, E. C., Austin, R. H., and Sturm, J. C. (2004). Continuous Particle Separation through Deterministic Lateral Displacement. *Science* 304 (5673), 987–990. doi:10.1126/science.1094567

Hyun, K.-A., Lee, T. Y., and Jung, H.-I. (2013). Negative Enrichment of Circulating Tumor Cells Using a Geometrically Activated Surface Interaction Chip. *Anal. Chem.* 85 (9), 4439–4445. doi:10.1021/ac3037766

Ilie, M., Hofman, V., Long-Mira, E., Selva, E., Vignaud, J.-M., Padovani, B., et al. (2014). "Sentinel" Circulating Tumor Cells Allow Early Diagnosis of Lung Cancer in Patients with Chronic Obstructive Pulmonary Disease. *PloS one* 9 (10), e111597–e111603. doi:10.1371/journal.pone.0111597

Jackson, J. M., Witek, M. A., Hupert, M. L., Brady, C., Pullagurla, S., Kamande, J., et al. (2014). UV Activation of Polymeric High Aspect Ratio Microstructures: Ramifications in Antibody Surface Loading for Circulating Tumor Cell Selection. *Lab. Chip* 14 (1), 106–117. doi:10.1039/c3lc50618e

Jahangiri, M., Ranjbar-Torkamani, M., Abadijoo, H., Ghaderinia, M., Ghafari, H., Mamdouh, A., et al. (2020). Low Frequency Stimulation Induces Polarization-Based Capturing of normal, Cancerous and white Blood Cells: a New Separation Method for Circulating Tumor Cell Enrichment or Phenotypic Cell Sorting. *Analyst* 145 (23), 7636–7645. doi:10.1039/D0AN01033B

Jan, Y. J., Chen, J.-F., Zhu, Y., Lu, Y.-T., Chen, S. H., Chung, H., et al. (2018). NanoVelcro Rare-Cell Assays for Detection and Characterization of Circulating Tumor Cells. *Adv. Drug Deliv. Rev.* 125, 78–93. doi:10.1016/j.addr.2018.03.006

Jian, X., Xu, J., Yang, L., Zhao, C., Xu, J., Gao, Z., et al. (2020). Intracellular Metal-Organic Frameworks: Integrating an All-In-One Semiconductor Electrode Chip for Therapy, Capture, and Quantification of Circulating Tumor Cells. *Anal. Chem.* 92 (19), 13319–13326. doi:10.1021/acs.analchem.0c02618

Jiang, R., Agrawal, S., Aghaamoo, M., Parajuli, R., Agrawal, A., and Lee, A. P. (2021). Rapid Isolation of Circulating Cancer Associated Fibroblasts by Acoustic Microstreaming for Assessing Metastatic Propensity of Breast Cancer Patients. *Lab. Chip* 21 (5), 875–887. doi:10.1039/d0lc00969e

Joensson, H. N., and Andersson Svahn, H. (2012). Droplet Microfluidics-A Tool for Single-Cell Analysis. *Angew. Chem. Int. Ed.* 51 (49), 12176–12192. doi:10.1002/anie.201200460

Jordan, N. V., Bardia, A., Wittner, B. S., Benes, C., Ligorio, M., Zheng, Y., et al. (2016). HER2 Expression Identifies Dynamic Functional States within Circulating Breast Cancer Cells. *Nature* 537 (7618), 102–106. doi:10.1038/nature19328

Kang, H., Kim, J., Cho, H., and Han, K.-H. (2019). Evaluation of Positive and Negative Methods for Isolation of Circulating Tumor Cells by Lateral Magnetophoresis. *Micromachines* 10 (6), 386–395. doi:10.3390/mi10060386

Karabacak, N. M., Spuhler, P. S., Fachin, F., Lim, E. J., Pai, V., Ozkumur, E., et al. (2014). Microfluidic, Marker-free Isolation of Circulating Tumor Cells from Blood Samples. *Nat. Protoc.* 9 (3), 694–710. doi:10.1038/nprot.2014.044

Karthick, S., Pradeep, P. N., Kanchana, P., and Sen, A. K. (2018). Acoustic Impedance-Based Size-independent Isolation of Circulating Tumour Cells from Blood Using Acoustophoresis. *Lab. Chip* 18 (24), 3802–3813. doi:10.1039/c8lc00921j

Kelley, S. O., Mirkin, C. A., Walt, D. R., Ismagilov, R. F., Toner, M., and Sargent, E. H. (2014). Advancing the Speed, Sensitivity and Accuracy of Biomolecular Detection Using Multi-Length-Scale Engineering. *Nat. Nanotech* 9 (12), 969–980. doi:10.1038/nnano.2014.261

Kidess-Sigal, E., Liu, H. E., Triboulet, M. M., Che, J., Ramani, V. C., Visser, B. C., et al. (2016). Enumeration and Targeted Analysis of KRAS, BRAF and PIK3CA Mutations in CTCs Captured by a Label-free Platform: Comparison to ctDNA and Tissue in Metastatic Colorectal Cancer. *Oncotarget* 7 (51), 85349–85364. doi:10.18632/oncotarget.13350

Kim, J., Cho, H., Kim, J., Park, J. S., and Han, K.-H. (2021). A Disposable Smart Microfluidic Platform Integrated with On-Chip Flow Sensors. *Biosens. Bioelectron.* 176, 112897–112927. doi:10.1016/j.bios.2020.112897

Kim, T.-H., Lim, M., Park, J., Oh, J. M., Kim, H., Jeong, H., et al. (2017). FAST: Size-Selective, Clog-free Isolation of Rare Cancer Cells from Whole Blood at a Liquid-Liquid Interface. *Anal. Chem.* 89 (2), 1155–1162. doi:10.1021/acs.analchem.6b03534

Kirby, B. J., Jodari, M., Loftus, M. S., Gakhar, G., Pratt, E. D., Chanel-Vos, C., et al. (2012). Functional Characterization of Circulating Tumor Cells with a Prostate-cancer-specific Microfluidic Device. *PloS one* 7 (4), e35976–e35985. doi:10.1371/journal.pone.0035976

Kozminsky, M., Fouladdel, S., Chung, J. S., Wang, Y., Smith, D. C., Alva, A., et al. (2019). Detection of CTC Clusters and a Dedifferentiated RNA-Expression Survival Signature in Prostate Cancer. *Adv. Sci.* 6 (2), 1801254–1801262. doi:10.1002/advs.201801254

Krebs, M. G., Hou, J.-M., Ward, T. H., Blackhall, F. H., and Dive, C. (2010). Circulating Tumour Cells: Their Utility in Cancer Management and Predicting Outcomes. *Ther. Adv. Med. Oncol.* 2 (6), 351–365. doi:10.1177/1758834010378414

Krebs, M. G., Sloane, R., Priest, L., Lancashire, L., Hou, J.-M., Greystoke, A., et al. (2011). Evaluation and Prognostic Significance of Circulating Tumor Cells in Patients with Non-small-cell Lung Cancer. *Jco* 29 (12), 1556–1563. doi:10.1200/JCO.2010.28.7045

Kulasinghe, A., Zhou, J., Kenny, L., Papautsky, I., and Punyadeera, C. (2019). Capture of Circulating Tumour Cell Clusters Using Straight Microfluidic Chips. *Cancers* 11 (1), 89–99. doi:10.3390/cancers11010089

Kwizera, E. A., Sun, M., White, A. M., Li, J., and He, X. (2021). Methods of Generating Dielectrophoretic Force for Microfluidic Manipulation of Bioparticles. *ACS Biomater. Sci. Eng.* 7 (6), 2043–2063. doi:10.1021/acsbiomaterials.1c00083

Lannin, T., Su, W.-W., Gruber, C., Cardle, I., Huang, C., Thege, F., et al. (2016). Automated Electrorotation Shows Electrokinetic Separation of Pancreatic Cancer Cells Is Robust to Acquired Chemotherapy Resistance, Serum Starvation, and EMT. *Biomicrofluidics* 10 (6), 064109–064124. doi:10.1063/1.4964929

Lawson, D. A., Bhakta, N. R., Kessenbrock, K., Prummel, K. D., Yu, Y., Takai, K., et al. (2015). Single-cell Analysis Reveals a Stem-Cell Program in Human Metastatic Breast Cancer Cells. *Nature* 526 (7571), 131–135. doi:10.1038/nature15260

Lee, J., and Kwak, B. (2020). Simultaneous On-Chip Isolation and Characterization of Circulating Tumor Cell Sub-populations. *Biosens. Bioelectron.* 168, 112564–112569. doi:10.1016/j.bios.2020.112564

Lee, T. Y., Hyun, K.-A., Kim, S.-I., and Jung, H.-I. (2017). An Integrated Microfluidic Chip for One-step Isolation of Circulating Tumor Cells. *Sensors Actuators B: Chem.* 238, 1144–1150. doi:10.1016/j.snb.2016.05.163

Lim H, H., Back, S. M., Hwang, M. H., Lee, D.-H., Choi, H., and Nam, J. (2019). Sheathless High-Throughput Circulating Tumor Cell Separation Using Viscoelastic Non-newtonian Fluid. *Micromachines* 10 (7), 462–463. doi:10.3390/mi10070462

Lim Sb, S. B., Yeo, T., Lee, W. D., Bhagat, A. A. S., Tan, S. J., Tan, D. S. W., et al. (2019). Addressing Cellular Heterogeneity in Tumor and Circulation for Refined Prognostication. *Proc. Natl. Acad. Sci. U S A.* 116 (36), 17957–17962. doi:10.1073/pnas.1907904116

Lin, H.-I., and Chang, Y.-C. (2021). Colorectal Cancer Detection by Immunofluorescence Images of Circulating Tumor Cells. *Ain Shams Eng. J.* 12 (3), 2673–2683. doi:10.1016/j.asej.2021.01.013

Lin, H. K., Zheng, S., Williams, A. J., Balic, M., Groshen, S., Scher, H. I., et al. (2010). Portable Filter-Based Microdevice for Detection and Characterization of Circulating Tumor Cells. *Clin. Cancer Res.* 16 (20), 5011–5018. doi:10.1158/1078-0432.CCR-10-1105

Lin, M., Chen, J.-F., Lu, Y.-T., Zhang, Y., Song, J., Hou, S., et al. (2014). Nanostructure Embedded Microchips for Detection, Isolation, and Characterization of Circulating Tumor Cells. *Acc. Chem. Res.* 47 (10), 2941–2950. doi:10.1021/ar5001617

Lin, Z., Luo, G., Du, W., Kong, T., Liu, C., and Liu, Z. (2020). Recent Advances in Microfluidic Platforms Applied in Cancer Metastasis: Circulating Tumor Cells'

(CTCs) Isolation and Tumor-On-A-Chip. *Small* 16 (9), 1903899–e1903919. doi:10.1002/smll.201903899

Liu J, J., Chen, C., Wei, T., Gayet, O., Loncle, C., Borge, L., et al. (2021). Dendrimeric Nanosystem Consistently Circumvents Heterogeneous Drug Response and Resistance in Pancreatic Cancer. *Exploration* 1 (1), 21–34. doi:10.1002/EXP.20210003

Liu, X., Sun, Y., Chen, B., Li, Y., Zhu, P., Wang, P., et al. (2022). Novel Magnetic Silk Fibroin Scaffolds with Delayed Degradation for Potential Long-Distance Vascular Repair. *Bioactive Mater.* 7, 126–143. doi:10.1016/j.bioactmat.2021.04.036

Liu Z, Z., Huang, Y., Liang, W., Bai, J., Feng, H., Fang, Z., et al. (2021). Cascaded Filter Deterministic Lateral Displacement Microchips for Isolation and Molecular Analysis of Circulating Tumor Cells and Fusion Cells. *Lab. Chip* 21 (15), 2881–2891. doi:10.1039/d1lc00360g

Liu, Z., Fusi, A., Klopocki, E., Schmittel, A., Tinhofer, I., Nonnenmacher, A., et al. (2011). Negative Enrichment by Immunomagnetic Nanobeads for Unbiased Characterization of Circulating Tumor Cells from Peripheral Blood of Cancer Patients. *J. Transl Med.* 9 (1), 1–8. doi:10.1186/1479-5876-9-70

Liu, Z., Zhang, W., Huang, F., Feng, H., Shu, W., Xu, X., et al. (2013). High Throughput Capture of Circulating Tumor Cells Using an Integrated Microfluidic System. *Biosens. Bioelectron.* 47, 113–119. doi:10.1016/j.bios.2013.03.017

Lu, C., Xu, J., Han, J., Li, X., Xue, N., Li, J., et al. (2020). A Novel Microfluidic Device Integrating Focus-Separation Speed Reduction Design and Trap Arrays for High-Throughput Capture of Circulating Tumor Cells. *Lab. Chip* 20 (22), 4094–4105. doi:10.1039/d0lc00631a

Lu, Y.-T., Zhao, L., Shen, Q., Garcia, M. A., Wu, D., Hou, S., et al. (2013). NanoVelcro Chip for CTC Enumeration in Prostate Cancer Patients. *Methods* 64 (2), 144–152. doi:10.1016/j.ymeth.2013.06.019

Magnusson, C., Augustsson, P., Lenshof, A., Ceder, Y., Laurell, T., and Lilja, H. (2017). Clinical-scale Cell-Surface-Marker Independent Acoustic Microfluidic Enrichment of Tumor Cells from Blood. *Anal. Chem.* 89 (22), 11954–11961. doi:10.1021/acs.analchem.7b01458

Mishra, A., Dubash, T. D., Edd, J. F., Jewett, M. K., Garre, S. G., Karabacak, N. M., et al. (2020). Ultrahigh-throughput Magnetic Sorting of Large Blood Volumes for Epitope-Agnostic Isolation of Circulating Tumor Cells. *Proc. Natl. Acad. Sci. U.S.A.* 117 (29), 16839–16847. doi:10.1073/pnas.2006388117

Montoya Mira, J., Sapre, A. A., Walker, B. S., Alvarez, J. B., Gustafson, K. T., Tu, E., et al. (2021). Label-free Enrichment of Rare Unconventional Circulating Neoplastic Cells Using a Microfluidic Dielectrophoretic Sorting Device. *Commun. Biol.* 4 (1), 1–9. doi:10.1038/s42003-021-02651-8

Moon, D. H., Lindsay, D. P., Hong, S., and Wang, A. Z. (2018). Clinical Indications for, and the Future of, Circulating Tumor Cells. *Adv. Drug Deliv. Rev.* 125, 143–150. doi:10.1016/j.addr.2018.04.002

Murlidhar, V., Zeinali, M., Grabauskiene, S., Ghannad-Rezaie, M., Wicha, M. S., Simeone, D. M., et al. (2014). A Radial Flow Microfluidic Device for Ultra-high-throughput Affinity-Based Isolation of Circulating Tumor Cells. *Small* 10 (23), 4895–4904. doi:10.1002/smll.201400719

Nagrath, S., Sequist, L. V., Maheswaran, S., Bell, D. W., Irimia, D., Ulkus, L., et al. (2007). Isolation of Rare Circulating Tumour Cells in Cancer Patients by Microchip Technology. *Nature* 450 (7173), 1235–1239. doi:10.1038/nature06385

Naskar, A., Lee, S., and Kim, K.-s. (2020). Easy One-Pot Low-Temperature Synthesized Ag-ZnO Nanoparticles and Their Activity against Clinical Isolates of Methicillin-Resistant *Staphylococcus aureus*. *Front. Bioeng. Biotechnol.* 8, 216–223. doi:10.3389/fbioe.2020.00216

Niitsu, K., Nakanishi, T., Murakami, S., Matsunaga, M., Kobayashi, A., Karim, N. M., et al. (2019). A 65-nm CMOS Fully Integrated Analysis Platform Using an On-Chip Vector Network Analyzer and a Transmission-Line-Based Detection Window for Analyzing Circulating Tumor Cell and Exosome. *IEEE Trans. Biomed. Circuits Syst.* 13 (2), 470–479. doi:10.1109/TBCAS.2018.2882472

Pahattuge, T. N., Freed, I. M., Hupert, M. L., Vaidyanathan, S., Childers, K., Witek, M. A., et al. (2021). System Modularity Chip for Analysis of Rare Targets (SMART-Chip): Liquid Biopsy Samples. *ACS Sens.* 6 (5), 1831–1839. doi:10.1021/acssensors.0c02728

Pan, L., Yan, G., Chen, W., Sun, L., Wang, J., and Yang, J. (2019). Distribution of Circulating Tumor Cell Phenotype in Early Cervical Cancer. *Cmar* 11, 5531–5536. doi:10.2147/CMAR.S198391

Pantel, K., and Alix-Panabières, C. (2010). Circulating Tumour Cells in Cancer Patients: Challenges and Perspectives. *Trends Mol. Med.* 16 (9), 398–406. doi:10.1016/j.molmed.2010.07.001

Park, M.-H., Reátegui, E., Li, W., Tessier, S. N., Wong, K. H. K., Jensen, A. E., et al. (2017). Enhanced Isolation and Release of Circulating Tumor Cells Using Nanoparticle Binding and Ligand Exchange in a Microfluidic Chip. *J. Am. Chem. Soc.* 139 (7), 2741–2749. doi:10.1021/jacs.6b12236

Pei, H., Li, L., Han, Z., Wang, Y., and Tang, B. (2020a). Recent Advances in Microfluidic Technologies for Circulating Tumor Cells: Enrichment, Single-Cell Analysis, and Liquid Biopsy for Clinical Applications. *Lab. Chip* 20 (21), 3854–3875. doi:10.1039/d0lc00577k

Pei, H., Li, L., Wang, Y., Sheng, R., Wang, Y., Xie, S., et al. (2019). Single-cell Phenotypic Profiling of CTCs in Whole Blood Using an Integrated Microfluidic Device. *Anal. Chem.* 91 (17), 11078–11084. doi:10.1021/acs.analchem.9b01647

Pei, H., Yu, M., Dong, D., Wang, Y., Li, Q., Li, L., et al. (2020b). Phenotype-related Drug Sensitivity Analysis of Single CTCs for Medicine Evaluation. *Chem. Sci.* 11 (33), 8895–8900. doi:10.1039/c9sc05566e

Popova, A. A., Tronser, T., Demir, K., Haitz, P., Kuodyte, K., Starkuviene, V., et al. (2019). Facile One Step Formation and Screening of Tumor Spheroids Using Droplet-Microarray Platform. *Small* 15 (25), 1901299–1901307. doi:10.1002/smll.201901299

Poudineh, M., Aldridge, P. M., Ahmed, S., Green, B. J., Kermanshah, L., Nguyen, V., et al. (2017). Tracking the Dynamics of Circulating Tumour Cell Phenotypes Using Nanoparticle-Mediated Magnetic Ranking. *Nat. Nanotech* 12 (3), 274–281. doi:10.1038/nnano.2016.239

Poudineh, M., Sargent, E. H., Pantel, K., and Kelley, S. O. (2018). Profiling Circulating Tumour Cells and Other Biomarkers of Invasive Cancers. *Nat. Biomed. Eng.* 2 (2), 72–84. doi:10.1038/s41551-018-0190-5

Praharaj, P. P., Bhutia, S. K., Nagrath, S., Bitting, R. L., and Deep, G. (2018). Circulating Tumor Cell-Derived Organoids: Current Challenges and Promises in Medical Research and Precision Medicine. *Biochim. Biophys. Acta (Bba) - Rev. Cancer* 1869 (2), 117–127. doi:10.1016/j.bbcan.2017.12.005

Qian, W., Zhang, Y., and Chen, W. (2015). Capturing Cancer: Emerging Microfluidic Technologies for the Capture and Characterization of Circulating Tumor Cells. *Small* 11 (32), 3850–3872. doi:10.1002/smll.201403658

Qin, X., Park, S., Duffy, S. P., Matthews, K., Ang, R. R., Todenhöfer, T., et al. (2015). Size and Deformability Based Separation of Circulating Tumor Cells from Castrate Resistant Prostate Cancer Patients Using Resettable Cell Traps. *Lab. Chip* 15 (10), 2278–2286. doi:10.1039/c5lc00226e

Ramirez, A. B., Bhat, R., Sahay, D., De Angelis, C., Thangavel, H., Hedayatpour, S., et al. (2019). Circulating Tumor Cell Investigation in Breast Cancer Patient-Derived Xenograft Models by Automated Immunofluorescence Staining, Image Acquisition, and Single Cell Retrieval and Analysis. *BMC Cancer* 19 (1), 1–10. doi:10.1186/s12885-019-5382-1

Ren, X., Foster, B. M., Ghassemi, P., Strobl, J. S., Kerr, B. A., and Agah, M. (2018). Entrapment of Prostate Cancer Circulating Tumor Cells with a Sequential Size-Based Microfluidic Chip. *Anal. Chem.* 90 (12), 7526–7534. doi:10.1021/acs.analchem.8b01134

Ruiz-Rodríguez, A. J., Molina-Vallejo, M. P., Aznar-Peralta, I., González Puga, C., Cañas García, I., González, E., et al. (2021). Deep Phenotypic Characterisation of CTCs by Combination of Microfluidic Isolation (IsoFlux) and Imaging Flow Cytometry (ImageStream). *Cancers* 13 (24), 6386–6400. doi:10.3390/cancers13246386

Sajay, B. N. G., Chang, C.-P., Ahmad, H., Khuntontong, P., Wong, C. C., Wang, Z., et al. (2014). Microfluidic Platform for Negative Enrichment of Circulating Tumor Cells. *Biomed. Microdevices.* 16 (4), 537–548. doi:10.1007/s10544-014-9856-2

Santana, S. M., Liu, H., Bander, N. H., Gleghorn, J. P., and Kirby, B. J. (2012). Immunocapture of Prostate Cancer Cells by Use of Anti-PSMA Antibodies in Microdevices. *Biomed. Microdevices* 14 (2), 401–407. doi:10.1007/s10544-011-9616-5

Sarioglu, A. F., Aceto, N., Kojic, N., Donaldson, M. C., Zeinali, M., Hamza, B., et al. (2015). A Microfluidic Device for Label-free, Physical Capture of Circulating Tumor Cell Clusters. *Nat. Methods* 12 (7), 685–691. doi:10.1038/nmeth.3404

Shen, W., Song, Y., Burklund, A., Le, B., Zhang, R., Wang, L., et al. (2018). Combined Immunomagnetic Capture Coupled with Ultrasensitive Plasmonic Detection of Circulating Tumor Cells in Blood. *Biomed. Microdevices* 20 (4), 1–9. doi:10.1007/s10544-018-0333-1

Shen, Z., Wu, A., and Chen, X. (2017). Current Detection Technologies for Circulating Tumor Cells. *Chem. Soc. Rev.* 46 (8), 2038–2056. doi:10.1039/c6cs00803h

Sheng, W., Chen, T., Kamath, R., Xiong, X., Tan, W., and Fan, Z. H. (2012). Aptamer-enabled Efficient Isolation of Cancer Cells from Whole Blood Using a Microfluidic Device. *Anal. Chem.* 84 (9), 4199–4206. doi:10.1021/ac3005633

Sheng, W., Ogunwobi, O. O., Chen, T., Zhang, J., George, T. J., Liu, C., et al. (2014). Capture, Release and Culture of Circulating Tumor Cells from Pancreatic Cancer Patients Using an Enhanced Mixing Chip. *Lab. Chip* 14 (1), 89–98. doi:10.1039/c3lc51017d

Shi, J., Zhao, C., Shen, M., Chen, Z., Liu, J., Zhang, S., et al. (2022). Combination of Microfluidic Chips and Biosensing for the Enrichment of Circulating Tumor Cells. *Biosens. Bioelectron.* 202, 114025–114033. doi:10.1016/j.bios.2022.114025

Shi, W., Wang, S., Maarouf, A., Uhl, C. G., He, R., Yunus, D., et al. (2017). Magnetic Particles Assisted Capture and Release of Rare Circulating Tumor Cells Using Wavy-Herringbone Structured Microfluidic Devices. *Lab. Chip* 17 (19), 3291–3299. doi:10.1039/c7lc00333a

Sollier, E., Go, D. E., Che, J., Gossett, D. R., O'Byrne, S., Weaver, W. M., et al. (2014). Size-selective Collection of Circulating Tumor Cells Using Vortex Technology. *Lab. Chip* 14 (1), 63–77. doi:10.1039/c3lc50689d

Song, Y., Shi, Y., Huang, M., Wang, W., Wang, Y., Cheng, J., et al. (2019). Bioinspired Engineering of a Multivalent Aptamer-Functionalized Nanointerface to Enhance the Capture and Release of Circulating Tumor Cells. *Angew. Chem. Int. Ed.* 58 (8), 2236–2240. doi:10.1002/anie.201809337

Steeg, P. S. (2006). Tumor Metastasis: Mechanistic Insights and Clinical Challenges. *Nat. Med.* 12 (8), 895–904. doi:10.1038/nm1469

Stevens, M. M., Maire, C. L., Chou, N., Murakami, M. A., Knoff, D. S., Kikuchi, Y., et al. (2016). Drug Sensitivity of Single Cancer Cells Is Predicted by Changes in Mass Accumulation Rate. *Nat. Biotechnol.* 34 (11), 1161–1167. doi:10.1038/nbt.3697

Stott, S. L., Hsu, C.-H., Tsukrov, D. I., Yu, M., Miyamoto, D. T., Waltman, B. A., et al. (2010). Isolation of Circulating Tumor Cells Using a Microvortex-Generating Herringbone-Chip. *Proc. Natl. Acad. Sci. U.S.A.* 107 (43), 18392–18397. doi:10.1073/pnas.1012539107

Su, Y., Tian, Q., Pan, D., Hui, L., Chen, Y., Zhang, Q., et al. (2019). Antibody-Functional Microsphere-Integrated Filter Chip with Inertial Microflow for Size-Immune-Capturing and Digital Detection of Circulating Tumor Cells. *ACS Appl. Mater. Inter.* 11 (33), 29569–29578. doi:10.1021/acsami.9b09655

Suhail, Y., Cain, M. P., Vanaja, K., Kurywchak, P. A., Levchenko, A., Kalluri, R., et al. (2019). Systems Biology of Cancer Metastasis. *Cell Syst.* 9 (2), 109–127. doi:10.1016/j.cels.2019.07.003

Sun, M., Xu, J., Shamul, J. G., Lu, X., Husain, S., and He, X. (2019). Creating a Capture Zone in Microfluidic Flow Greatly Enhances the Throughput and Efficiency of Cancer Detection. *Biomaterials* 197, 161–170. doi:10.1016/j.biomaterials.2019.01.014

Sun, N., Li, X., Wang, Z., Li, Y., and Pei, R. (2018). High-purity Capture of CTCs Based on Micro-beads Enhanced Isolation by Size of Epithelial Tumor Cells (ISET) Method. *Biosens. Bioelectron.* 102, 157–163. doi:10.1016/j.bios.2017.11.026

Sun, Y.-F., Wu, L., Liu, S.-P., Jiang, M.-M., Hu, B., Zhou, K.-Q., et al. (2021). Dissecting Spatial Heterogeneity and the Immune-Evasion Mechanism of CTCs by Single-Cell RNA-Seq in Hepatocellular Carcinoma. *Nat. Commun.* 12 (1), 1–14. doi:10.1038/s41467-021-24386-0

Tan, K., Leong, S. M., Kee, Z., Caramat, P. V., Teo, J., Blanco, M. V. M., et al. (2018). Longitudinal Monitoring Reveals Dynamic Changes in Circulating Tumor Cells (CTCs) and CTC-Associated miRNAs in Response to Chemotherapy in Metastatic Colorectal Cancer Patients. *Cancer Lett.* 423, 1–8. doi:10.1016/j.canlet.2018.02.039

Tanaka, T., Ishikawa, T., Numayama-Tsuruta, K., Imai, Y., Ueno, H., Matsuki, N., et al. (2012). Separation of Cancer Cells from a Red Blood Cell Suspension Using Inertial Force. *Lab. Chip* 12 (21), 4336–4343. doi:10.1039/c2lc40354d

Tang, M., Wen, C.-Y., Wu, L.-L., Hong, S.-L., Hu, J., Xu, C.-M., et al. (2016). A Chip Assisted Immunomagnetic Separation System for the Efficient Capture and *In Situ* Identification of Circulating Tumor Cells. *Lab. Chip* 16 (7), 1214–1223. doi:10.1039/c5lc01555c

Thege, F. I., Lannin, T. B., Saha, T. N., Tsai, S., Kochman, M. L., Hollingsworth, M. A., et al. (2014). Microfluidic Immunocapture of Circulating Pancreatic Cells Using Parallel EpCAM and MUC1 Capture: Characterization, Optimization and Downstream Analysis. *Lab. Chip* 14 (10), 1775–1784. doi:10.1039/c4lc00041b

Tian, F., Cai, L., Chang, J., Li, S., Liu, C., Li, T., et al. (2018). Label-free Isolation of Rare Tumor Cells from Untreated Whole Blood by Interfacial Viscoelastic Microfluidics. *Lab. Chip* 18 (22), 3436–3445. doi:10.1039/c8lc00700d

Tong, B., and Wang, M. (2019). Circulating Tumor Cells in Patients with Lung Cancer: Developments and Applications for Precision Medicine. *Future Oncol.* 15 (21), 2531–2542. doi:10.2217/fon-2018-0548

Undvall Anand, E., Magnusson, C., Lenshof, A., Ceder, Y., Lilja, H., and Laurell, T. (2021). Two-Step Acoustophoresis Separation of Live Tumor Cells from Whole Blood. *Anal. Chem.* 93 (51), 17076–17085. doi:10.1021/acs.analchem.1c04050

Wang J, J., Li, Y., Wang, R., Han, C., Xu, S., You, T., et al. (2021). A Fully Automated and Integrated Microfluidic System for Efficient CTC Detection and its Application in Hepatocellular Carcinoma Screening and Prognosis. *ACS Appl. Mater. Inter.* 13 (25), 30174–30186. doi:10.1021/acsami.1c06337

Wang Q, Q., Liang, Z., Li, F., Lee, J., Low, L. E., and Ling, D. (2021). Dynamically Switchable Magnetic Resonance Imaging Contrast Agents. *Exploration* 1 (2), 20210009–20210016. doi:10.1002/EXP.20210009

Wang, S., Hong, S., Cai, S., Lei, J., Chen, J., Zhang, N., et al. (2020). Negative Depletion Mediated Brightfield Circulating Tumour Cell Identification Strategy on Microparticle-Based Microfluidic Chip. *J. Nanobiotechnol* 18 (1), 70–78. doi:10.1186/s12951-020-00623-4

Wang, S., Liu, K., Liu, J., Yu, Z. T.-F., Xu, X., Zhao, L., et al. (2011). Highly Efficient Capture of Circulating Tumor Cells by Using Nanostructured Silicon Substrates with Integrated Chaotic Micromixers. *Angew. Chem. Int. Ed.* 50 (13), 3084–3088. doi:10.1002/anie.201005853

Wang, X., Sun, L., Zhang, H., Wei, L., Qu, W., Zeng, Z., et al. (2019). Microfluidic Chip Combined with Magnetic-Activated Cell Sorting Technology for Tumor Antigen-independent Sorting of Circulating Hepatocellular Carcinoma Cells. *Peer J.* 7, e6681–e6697. doi:10.7717/peerj.6681

Warkiani, M. E., Guan, G., Luan, K. B., Lee, W. C., Bhagat, A. A. S., Kant Chaudhuri, P., et al. (2014). Slanted Spiral Microfluidics for the Ultra-fast, Label-free Isolation of Circulating Tumor Cells. *Lab. Chip* 14 (1), 128–137. doi:10.1039/c9lc00361d10.1039/c3lc50617g

Watanabe, M., Kenmotsu, H., Ko, R., Wakuda, K., Ono, A., Imai, H., et al. (2018). Isolation and Molecular Analysis of Circulating Tumor Cells from Lung Cancer Patients Using a Microfluidic Chip Type Cell Sorter. *Cancer Sci.* 109 (8), 2539–2548. doi:10.1111/cas.13692

Watanabe, M., Serizawa, M., Sawada, T., Takeda, K., Takahashi, T., Yamamoto, N., et al. (2014). A Novel Flow Cytometry-Based Cell Capture Platform for the Detection, Capture and Molecular Characterization of Rare Tumor Cells in Blood. *J. Transl. Med.* 12 (1), 1–12. doi:10.1186/1479-5876-12-143

Weinstein, Z. B., Kuru, N., Kiriakov, S., Palmer, A. C., Khalil, A. S., Clemons, P. A., et al. (2018). Modeling the Impact of Drug Interactions on Therapeutic Selectivity. *Nat. Commun.* 9 (1), 1–9. doi:10.1038/s41467-018-05954-3

Wongkaew, N., Simsek, M., Griesche, C., and Baeumner, A. J. (2018). Functional Nanomaterials and Nanostructures Enhancing Electrochemical Biosensors and Lab-On-A-Chip Performances: Recent Progress, Applications, and Future Perspective. *Chem. Rev.* 119 (1), 120–194. doi:10.1021/acs.chemrev.8b00172

Wu C, C., Li, P., Fan, N., Han, J., Zhang, W., Zhang, W., et al. (2019). A Dual-Targeting Functionalized Graphene Film for Rapid and Highly Sensitive Fluorescence Imaging Detection of Hepatocellular Carcinoma Circulating Tumor Cells. *ACS Appl. Mater. Inter.* 11 (48), 44999–45006. doi:10.1021/acsami.9b18410

Wu L, L., Zhu, L., Huang, M., Song, J., Zhang, H., Song, Y., et al. (2019). Aptamer-based Microfluidics for Isolation, Release and Analysis of Circulating Tumor Cells. *Trac Trends Anal. Chem.* 117, 69–77. doi:10.1016/j.trac.2019.05.003

Wu, L., Ding, H., Qu, X., Shi, X., Yang, J., Huang, M., et al. (2020c). Fluidic Multivalent Membrane Nanointerface Enables Synergetic Enrichment of Circulating Tumor Cells with High Efficiency and Viability. *J. Am. Chem. Soc.* 142 (10), 4800–4806. doi:10.1021/jacs.9b13782

Wu, L. L., Zhang, Z. L., Tang, M., Zhu, D. L., Dong, X. J., Hu, J., et al. (2020d). Spectrally Combined Encoding for Profiling Heterogeneous Circulating Tumor

Cells Using a Multifunctional Nanosphere-Mediated Microfluidic Platform. *Angew. Chem. Int. Ed.* 59 (28), 11240–11244. doi:10.1002/anie.201914468

Wu, L., and Qu, X. (2015). Cancer Biomarker Detection: Recent Achievements and Challenges. *Chem. Soc. Rev.* 44 (10), 2963–2997. doi:10.1039/c4cs00370e

Wu, L., Wang, Y., Zhu, L., Liu, Y., Wang, T., Liu, D., et al. (2020b). Aptamer-Based Liquid Biopsy. *ACS Appl. Bio Mater.* 3 (5), 2743–2764. doi:10.1021/acsabm.9b01194

Wu, M., Huang, P. H., Zhang, R., Mao, Z., Chen, C., Kemeny, G., et al. (2018). Circulating Tumor Cell Phenotyping via High-Throughput Acoustic Separation. *Small* 14 (32), 1801131–1801162. doi:10.1002/smll.20200443810.1002/smll.201801131

Wu, S., Gu, L., Qin, J., Zhang, L., Sun, F., Liu, Z., et al. (2020a). Rapid Label-free Isolation of Circulating Tumor Cells from Patients' Peripheral Blood Using Electrically Charged Fe3O4 Nanoparticles. *ACS Appl. Mater. Inter.* 12 (4), 4193–4203. doi:10.1021/acsami.9b16385

Yang, C., Zou, K., Zheng, L., and Xiong, B. (2017). Prognostic and Clinicopathological Significance of Circulating Tumor Cells Detected by RT-PCR in Non-metastatic Colorectal Cancer: a Meta-Analysis and Systematic Review. *BMC Cancer* 17 (1), 1–13. doi:10.1186/s12885-017-3704-8

Yi, X., Zeng, W., Wang, C., Chen, Y., Zheng, L., Zhu, X., et al. (2022). A Step-by-step Multiple Stimuli-Responsive Metal-Phenolic Network Prodrug Nanoparticles for Chemotherapy. *Nano Res.* 15 (2), 1205–1212. doi:10.1007/s12274-021-3626-2

Yiannacou, K., and Sariola, V. (2021). Controlled Manipulation and Active Sorting of Particles inside Microfluidic Chips Using Bulk Acoustic Waves and Machine Learning. *Langmuir* 37 (14), 4192–4199. doi:10.1021/acs.langmuir.1c00063

Yoon, H. J., Kim, T. H., Zhang, Z., Azizi, E., Pham, T. M., Paoletti, C., et al. (2013). Sensitive Capture of Circulating Tumour Cells by Functionalized Graphene Oxide Nanosheets. *Nat. Nanotech* 8 (10), 735–741. doi:10.1038/nnano.2013.194

Yoon, H. J., Shanker, A., Wang, Y., Kozminsky, M., Jin, Q., Palanisamy, N., et al. (2016). Tunable Thermal-Sensitive Polymer-Graphene Oxide Composite for Efficient Capture and Release of Viable Circulating Tumor Cells. *Adv. Mater.* 28 (24), 4891–4897. doi:10.1002/adma.201600658

Yu, H., Ma, L., Zhu, Y., Li, W., Ding, L., and Gao, H. (2020). Significant Diagnostic Value of Circulating Tumour Cells in Colorectal Cancer. *Oncol. Lett.* 20 (1), 317–325. doi:10.3892/ol.2020.11537

Yu M, M., Bardia, A., Wittner, B. S., Stott, S. L., Smas, M. E., Ting, D. T., et al. (2013). Circulating Breast Tumor Cells Exhibit Dynamic Changes in Epithelial and Mesenchymal Composition. *Science* 339 (6119), 580–584. doi:10.1126/science.1228522

Yu X, X., He, R., Li, S., Cai, B., Zhao, L., Liao, L., et al. (2013). Magneto-Controllable Capture and Release of Cancer Cells by Using a Micropillar Device Decorated with Graphite Oxide-Coated Magnetic Nanoparticles. *Small* 9 (22), 3895–3901. doi:10.1002/smll.201300169

Yu, X., Wu, N., Chen, F., Wei, J., and Zhao, Y. (2019). Engineering Microfluidic Chip for Circulating Tumor Cells: from Enrichment, Release to Single Cell Analysis. *Trac Trends Anal. Chem.* 117, 27–38. doi:10.1016/j.trac.2019.03.027

Zahirović, A., Plavec, T. V., and Berlec, A. (2022). Dual Functionalized Lactococcus Lactis Shows Tumor Antigen Targeting and Cytokine Binding *In Vitro*. *Front. Bioeng. Biotechnol.* 10, 822823–822833. doi:10.3389/fbioe.2022.822823

Zamay, G., Kolovskaya, O., Ivanchenko, T., Zamay, T., Veprintsev, D., Grigorieva, V., et al. (2019). Development of DNA Aptamers to Native EpCAM for Isolation of Lung Circulating Tumor Cells from Human Blood. *Cancers* 11 (3), 351–354. doi:10.3390/cancers11030351

Zhang, J., Chen, K., and Fan, Z. H. (2016). Circulating Tumor Cell Isolation and Analysis. *Adv. Clin. Chem.* 75, 1–31. doi:10.1016/bs.acc.2016.03.003

Zhang, N., Deng, Y., Tai, Q., Cheng, B., Zhao, L., Shen, Q., et al. (2012). Electrospun TiO2 Nanofiber-Based Cell Capture Assay for Detecting Circulating Tumor Cells from Colorectal and Gastric Cancer Patients. *Adv. Mater.* 24 (20), 2756–2760. doi:10.1002/adma.201200155

Zhang P, P., Zhou, X., He, M., Shang, Y., Tetlow, A. L., Godwin, A. K., et al. (2019). Ultrasensitive Detection of Circulating Exosomes with a 3D-Nanopatterned Microfluidic Chip. *Nat. Biomed. Eng.* 3 (6), 438–451. doi:10.1038/s41551-019-0356-9

Zhang, X., Hashem, M. A., Chen, X., and Tan, H. (2018). On Passing a Non-newtonian Circulating Tumor Cell (CTC) through a Deformation-Based Microfluidic Chip. *Theor. Comput. Fluid Dyn.* 32 (6), 753–764. doi:10.1007/s00162-018-0475-z

Zhang Y, Y., Zhao, Y., Chen, D., Wang, K., Wei, Y., Xu, Y., et al. (2019). Crossing Constriction Channel-Based Microfluidic Cytometry Capable of Electrically Phenotyping Large Populations of Single Cells. *Analyst* 144 (3), 1008–1015. doi:10.1039/c8an02100g

Zhao, L., Tang, C., Xu, L., Zhang, Z., Li, X., Hu, H., et al. (2016). Enhanced and Differential Capture of Circulating Tumor Cells from Lung Cancer Patients by Microfluidic Assays Using Aptamer Cocktail. *Small* 12 (8), 1072–1081. doi:10.1002/smll.201503188

Zhao, Y., Wang, K., Chen, D., Fan, B., Xu, Y., Ye, Y., et al. (2018). Development of Microfluidic Impedance Cytometry Enabling the Quantification of Specific Membrane Capacitance and Cytoplasm Conductivity from 100,000 Single Cells. *Biosens. Bioelectron.* 111, 138–143. doi:10.1016/j.bios.2018.04.015

Zheng, S., Lin, H. K., Lu, B., Williams, A., Datar, R., Cote, R. J., et al. (2011). 3D Microfilter Device for Viable Circulating Tumor Cell (CTC) Enrichment from Blood. *Biomed. Microdevices* 13 (1), 203–213. doi:10.1007/s10544-010-9485-3

Zhu G, G., Song, P., Wu, J., Luo, M., Chen, Z., and Chen, T. (2021). Application of Nucleic Acid Frameworks in the Construction of Nanostructures and Cascade Biocatalysts: Recent Progress and Perspective. *Front. Bioeng. Biotechnol.* 9, 792489–792515. doi:10.3389/fbioe.2021.792489

Zhu Z, Z., Wu, D., Li, S., Han, Y., Xiang, N., Wang, C., et al. (2021). A Polymer-Film Inertial Microfluidic Sorter Fabricated by Jigsaw Puzzle Method for Precise Size-Based Cell Separation. *Analytica Chim. Acta* 1143, 306–314. doi:10.1016/j.aca.2020.11.001

Conflict of Interest: The authors declare that the research was conducted in the absence of any commercial or financial relationships that could be construed as a potential conflict of interest.

Publisher's Note: All claims expressed in this article are solely those of the authors and do not necessarily represent those of their affiliated organizations, or those of the publisher, the editors and the reviewers. Any product that may be evaluated in this article, or claim that may be made by its manufacturer, is not guaranteed or endorsed by the publisher.

frontiers | Frontiers in Bioengineering and Biotechnology

ORIGINAL RESEARCH
published: 13 May 2022
doi: 10.3389/fbioe.2022.902312

A Strategy to Design Cu_2MoS_4@MXene Composite With High Photothermal Conversion Efficiency Based on Electron Transfer Regulatory Effect

Lihua Li[1†], Jifan Zhang[2†], Yang Lin[1], Yongfeng Zhang[3], Shujie Li[1], Yanzhen Liu[1], Yingxu Zhang[1], Leilei Shi[2], Shouzhang Yuan[1]* and Lihao Guo[3]**

[1]NORINCO Kunming Institute of Physics, Kunming, China, [2]The Eighth Affiliated Hospital, Sun Yat-Sen University, Shenzhen, China, [3]School of Advanced Materials and Nanotechnology, Interdisciplinary Research Center of Smart Sensors, Xidian University, Xi'an, China

OPEN ACCESS

Edited by:
Zhe Wang,
Nanyang Technological University, Singapore

Reviewed by:
Xin Yu,
University of Jinan, China
Ning Tang,
Shanghai Jiao Tong University, China

***Correspondence:**
Leilei Shi
shillei@mail.sysu.edu.cn
Shouzhang Yuan
phelix@126.com
Lihao Guo
20141213346@stu.xidian.edu.cn

[†]These authors have contributed equally to this work and share first authorship

Specialty section:
This article was submitted to Nanobiotechnology, a section of the journal Frontiers in Bioengineering and Biotechnology

Received: 23 March 2022
Accepted: 04 April 2022
Published: 13 May 2022

Citation:
Li L, Zhang J, Lin Y, Zhang Y, Li S, Liu Y, Zhang Y, Shi L, Yuan S and Guo L (2022) A Strategy to Design Cu_2MoS_4@MXene Composite With High Photothermal Conversion Efficiency Based on Electron Transfer Regulatory Effect. Front. Bioeng. Biotechnol. 10:902312. doi: 10.3389/fbioe.2022.902312

Using photothermal therapy to treat cancer has become an effective method, and the design of photothermal agents determines their performance. However, due to the major radiative recombination of a photogenerated electron in photothermal materials, the photothermal performance is weak which hinders their applications. In order to solve this issue, preventing radiative recombination and accelerating nonradiative recombination, which can generate heat, has been proved as a reasonable way. We demonstrated a Cu_2MoS_4@MXene nanocomposite with an obviously enhanced photothermal conversion efficiency (η = 87.98%), and this improvement can be attributed to the electron migration. Then, a mechanism is proposed based on the electron transfer regulatory effect and the localized surface plasmon resonance effect, which synergistically promote nonradiative recombination and generate more heat. Overall, our design strategy shows a way to improve the photothermal performance of Cu_2MoS_4, and this method can be extended to other photothermal agents to let them be more efficient in treating cancer.

Keywords: photothermal conversion, MXene, heterostructure, nanocomposite, electron migration

INTRODUCTION

In the 21st century, the cancer problem has become more dominant and malignant, which is one of the most threatening public health questions and causes over 9.6 million deaths annually in the world (Massagué and Obenauf, 2016; Steeg, 2016). However, there is still a method that can rapidly and completely treat cancer because of metastasis; meanwhile, the traditional treatments, for e.g., radiotherapy and chemotherapy, may induce severe side effects which are traumatic for patients (Yilmaz et al., 2007). In recent decades, the optical treatment has been considered an efficient and less traumatic approach to treat primary and metastatic tumors, and the photothermal therapy (PTT) has been synergistically used with traditional methods and has shown a satisfied treatment effect (Chang et al., 2019; Yuan et al., 2020). In brief, under optical irradiation, photothermal reagents can generate localized hyperthermia and treat cancer. However, most of the existing photothermal materials lack photothermal performance due to the minority nonradiative recombination of the photogenerated

electron. The low photothermal conversion determines that more materials or higher laser power will be used to achieve the heat temperature, which can easily cause damage to patients (Zhou et al., 2018; Xi et al., 2020). So, the suitable photothermal materials with high photothermal performance are urgently needed.

Ternary chalcogenide, Cu_2MoS_4, is a representative material that has been exploited in photothermal therapy (Chen et al., 2014; Chang et al., 2019). However, the photothermal performance of Cu_2MoS_4 is weak which is common for simplex phototherapy reagents and can be explained by the band theory that the photothermal effect of Cu_2MoS_4 is mainly induced by the nonradiative recombination (producing phonon) of photogenerated electron–hole pairs, but this recombination is low compared with the radiative recombination (Zhang et al., 2015; Cheng et al., 2018; Zhang et al., 2018; Lv et al., 2021). Hence, it is highly desirable to improve the photothermal performance of Cu_2MoS_4 to make it a suitable photothermal reagent that achieves better anticancer outcomes.

In order to accelerate the probability of nonradiative recombination in the electron transfer process and prevent radiative recombination, which can efficiently enhance the photothermal effect of Cu_2MoS_4, constructing a heterostructure of noble metal or graphene and Cu_2MoS_4 has been proved as a reasonable method (Zhang et al., 2016; Chang et al., 2020). The high conductivity can lead the electron to migrate from Cu_2MoS_4 to noble metal or graphene when they come into contact with Cu_2MoS_4, and then the radiative recombination can be prevented while the probability of nonradiative recombination increases, thus enhancing photothermal performance (Rameshbabu et al., 2017). Nevertheless, the composite process of Cu_2MoS_4 and noble metal (usually nanoparticles) or graphene is difficult, and the interface resistance of metal nanoparticles may hinder the transfer of electrons, weakening the migration. Hence, MXene, a new member of 2D materials considered 2D transition metal carbides or nitrides with metallic conductivity, has become a substitute for noble metal and graphene, and the abundant surface termination groups on MXene's surface provide a large number of sites for Cu_2MoS_4 to anchor on (Guo et al., 2021; Mohammadi et al., 2021; Qiu et al., 2021). Meanwhile, owing to the high work function, superior electron conductivity, and lower interface resistance (compared with noble metal nanoparticles) of MXene, the caused electron transfer regulatory effect can enhance the photothermal performance of composites, which is similar to the aforementioned noble metal (Mariano et al., 2016; Chang et al., 2020; Li et al., 2021). More interestingly, under visible light radiation at 800 nm (1.5 eV), the MXene can produce the localized surface plasmon resonance (LSPR) effect which is a novel method to assist the separation of electrons and further stimulate the generation of heat (Mariano et al., 2016; Demellawi et al., 2018; Lioi et al., 2019).

We introduced $Ti_3C_2T_x$ MXene nanosheets to improve the photothermal performance of Cu_2MoS_4, and a Cu_2MoS_4@MXene nanocomposite was synthesized (**Scheme 1**). The results of the photothermal conversion experience confirmed our hypothesis, and the best performance of the nanocomposite obtained can increase the temperature by more than 55 °C under NIR radiation (1.0 W/cm^{-2} at 808 nm) with an obviously enhanced photothermal conversion efficiency (87.98%) compared with pure Cu_2MoS_4 (72.07%). Using the absorption spectrum and photoluminescence (PL) spectrum, the electron transfer process can be verified, and the obvious quenching phenomenon, i.e., weakened radiative recombination, reflects the rapid separation and transfer of photogenerated electrons. Based on the experimental results and band theory, we proposed a mechanism of enhanced photothermal performance that is mainly caused by promoted separation and transfer of electron and nonradiative recombination, owing to the electron transfer regulatory effect and LSPR effect. Therefore, these results suggest that the Cu_2MoS_4@MXene nanocomposite with enhanced photothermal performance could be used to treat cancers.

EXPERIMENTAL SECTION

Preparation of $Ti_3C_2T_x$ MXene Nanosheets

Using a minimally intensive layer delamination (MILD) method as previously reported (Halim et al., 2014), the $Ti_3C_2T_x$ MXene nanosheets were prepared from commercial Ti_3AlC_2 MAX purchased from Forsman Scientific Co. In detail, first, the etching agent was prepared by gently adding 1.5 g LiF into 20 ml of 9 M HCl with continuous stirring. After LiF was totally dissolved, 1 g Ti_3AlC_2 MAX powder was slowly added to the etching agent, and the mixture was continuously stirred at 35°C for 30 h. Afterward, the product was washed several times with deionized water (DI water), and when the pH of the supernatant reached 6, the supernatant was ultrasonicated for 1.5 h with N_2 atmosphere protection in an ice bath. Then, the $Ti_3C_2T_x$ MXene nanosheets were obtained after centrifugation (3,500 rpm for 1 h).

Preparation of Cu_2O Precursor

The Cu_2O precursor was synthesized by reducing copper hydroxide. NaOH (30 ml 3.75 M) solution was added dropwise in $CuSO_4$ (30 ml 0.5 M) solution with continuous stirring to prepare $Cu(OH)_2$ colloid; meanwhile, glucose ($C_6H_{12}O_6$, 30 ml 0.75 M) solution was prepared and kept at 60°C. Then, the $Cu(OH)_2$ colloid was heated to 60°C and added into glucose solution drop by drop at 60°C by placing in a water bath. Then, the mixture color gradually turned brick-red which indicates the successful preparation of Cu_2O. After allowing the colloid to react at 60°C for 30 min, the precursor was obtained through filtrating colloid and vacuum drying.

Synthesis of Cu_2MoS_4@MXene Nanocomposites

To synthesize Cu_2MoS_4@MXene nanocomposites, 0.02 g MXene was first dissolved in 30 ml DI water, and (0 g, 0.14 g, 0.42 g, 0.70 g, 0.98 g, and 1.3 g) thioacetamide (TAA) was added into MXene colloidal solution. Meanwhile, (0 g, 0.17 g, 0.51 g, 0.85 g, 1.2 g, and 1.6 g) MoO_3 and (0 g, 0.12 g, 0.36 g, 0.60 g, 0.84 g, and 1.1 g) Cu_2O were

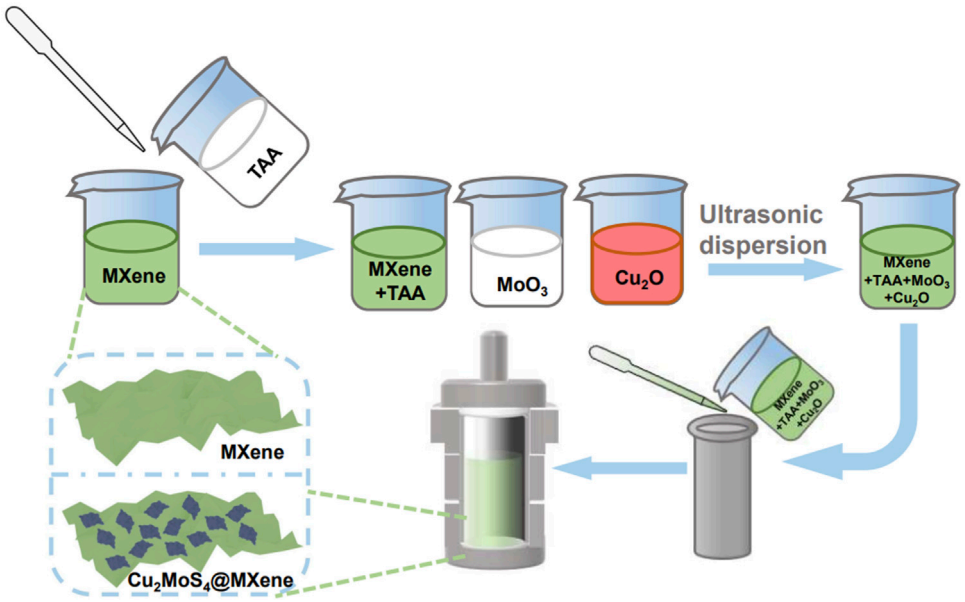

SCHEME 1 | Process of synthesizing Cu_2MoS_4@MXene nanocomposites.

ultrasonically dispersed into 5 ml DI water, respectively. Then, three dispersion solutions were transferred into a 100-ml tailor-made Teflon reactor, and using a microwave, the reaction temperature could be rapidly elevated to 150°C within 3 min. Afterward, the reaction temperature was maintained at 150°C for 2 h, and the Cu_2MoS_4@MXene nanocomposite (marked Cu_2MoS_4, Cu_2MoS_4@MXene-1, Cu_2MoS_4@MXene-3, Cu_2MoS_4@MXene-5, Cu_2MoS_4@MXene-7, and Cu_2MoS_4@MXene-9 for different ratios) products were obtained after washing and drying.

Photothermal Effect of Cu_2MoS_4@MXene Nanocomposites

In the following photothermal performance experiment, a series of concentration (0, 50, 100, 200, 500, and 1,000 μg/ml) solutions (1 ml) of six samples were prepared in an Eppendorf tube, respectively, and a NIR laser (1.0 W/cm^2) at 808 nm was used to irradiate the samples (Zhang et al., 2021). Then, during 600 s of irradiation, the temperature change of samples was monitored using an infrared thermal imaging camera and recorded on a computer connected to the camera in real-time. The photostability was tested (500 μg/ml) by repeating the heating (laser on for 600 s)/cooling (laser off for 600 s) processes three times (power density is 1.0 W/cm^2). Furthermore, the laser was modulated for 0.5 W/cm^2, 1.0 W/cm^2, and 1.5 W/cm^2 to evaluate the influence of power density.

Calculation of Photothermal Conversion Efficiency

Based on the results of the photothermal experiment, the photothermal conversion efficiency can be calculated according to **Equation 1**:

$$\eta = \frac{hS(T_{max} - T_0) - Q_{dis}}{W(1 - 10^{-A_{808}})}, \quad (1)$$

where η is the photothermal conversion efficiency, h (Wcm^{-2} K^{-1}) is the heat transfer coefficient, S (cm^2) is the surface area of quartz cuvette, T_{max} (K) is the highest equilibrium temperature, T_0 (K) is the surrounding temperature, Q_{dis} (W) is the heat loss which is approximate to 0, W is the power density of the laser, and A_{808} is the absorbance of samples at 808 nm. Moreover, the T_{max}, T_0, and A_{808} can be measured, while the hS is calculated through **Equation 2**:

$$hS = \frac{m_W C_W}{\tau_s}, \quad (2)$$

where m_W and C_W represent the total mass and the specific heat capacity of solvent and water, respectively, and τ_s is the time constant which can be obtained through **Equation 3**:

$$t = -\tau_s \times ln\theta = -\tau_s ln\frac{T - T_0}{T_{max} - T_0}, \quad (3)$$

Using the recording temperature T, the τ_s can be calculated, and then the photothermal conversion efficiency is calculated (Chen et al., 2019).

Characterization and Measurement

The morphologies and compositions of precursors and composites were characterized using the transmission electron microscope (TEM, JEOL-2100F), the X-ray diffraction spectrometer (XRD, Bruker D8 Advance), Raman and photoluminescence (PL) spectroscopy (Renishaw inVia), and UV-vis-NIR spectra (JASCO V-570). Infrared thermal imaging was monitored using an IR thermal camera (TELEDYNE FLIR Exx) and recorded using a computed connected to the camera.

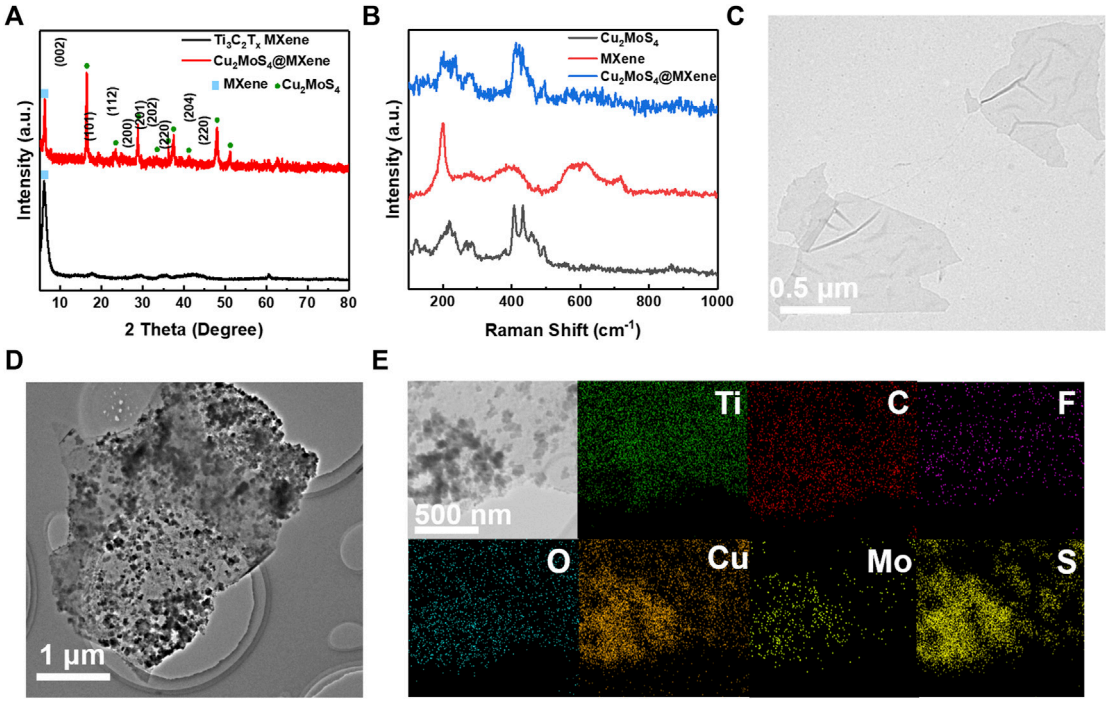

FIGURE 1 | Characterization of precursor and Cu_2MoS_4@MXene nanocomposites. **(A)** XRD pattern of $Ti_3C_2T_x$ MXene and Cu_2MoS_4@MXene. **(B)** Raman spectra of Cu_2MoS_4, MXene, and Cu_2MoS_4@MXene. TEM images of **(C)** MXene nanosheets and **(D)** Cu_2MoS_4@MXene. **(E)** EDS mapping of Ti, C, F, O, Cu, Mo, and S of Cu_2MoS_4@MXene.

RESULT AND DISCUSSION

Characterization of Precursors and Cu_2MoS_4@MXene Nanocomposites

As illustrated in **Scheme 1**, we have prepared Cu_2MoS_4@MXene nanocomposites through the *in situ* hydrothermal method (see details in Experimental Section). In brief, the prepared MXene nanosheets were first mixed with thioacetamide (TAA) in water; meanwhile, the MoO_3 and Cu_2O were ultrasonically dispersed in water. Then, the reaction fluid prepared by mixing three dispersions was poured into a microwave hydrothermal reactor and allowed to react using a microwave. After washing with DI water, the Cu_2MoS_4@MXene nanocomposites can be obtained. More importantly, this process allows Cu_2MoS_4 nanoplates to uniformly grow on MXene nanosheets which cannot be reached by the physical mixing method. Furthermore, due to the high quality of Cu_2MoS_4@MXene nanocomposites and the unique effect caused by composite processes, such as band engineering and high electron conductivity of MXene, a more excellent photothermal conversion performance can be achieved than than that of pure Cu_2MoS_4 nanoplates.

As for the basics of nanocomposites, the MXene nanosheets were first prepared using the MILD method (Halim et al., 2014). The Ti_3AlC_2 (MAX) precursor was etched with LiF and HCl. During the etching process, the Al layer in the MAX phase was selectively etched and $Ti_3C_2T_x$ nanosheets remained. As shown in the XRD pattern (**Figure 1A**), both the diffraction peaks at 39°, which can be indexed to the (104) plane of Ti_3AlC_2 MAX, disappear, and the (002) peak left shifts to 6.5°, indicating successful preparation of $Ti_3C_2T_x$ nanosheets (Lipatov et al., 2016). According to the pattern of the Raman spectrum (**Figure 1B**), the vibration modes of MXene nanosheets can be divided into two types: out-of-plane mode (A_{1g}) and in-plane mode (E_g), and the vibration peak at 198 cm^{-1}, 715 cm^{-1} and 253 cm^{-1}, and 502 cm^{-1} can be well assigned to these two modes, respectively (Hu et al., 2015). Using TEM, the monolayer $Ti_3C_2T_x$ nanosheets can be seen with a size of approximately 1 μm, as shown in **Figure 1C**. The results of these characterization methods show that the high-quality MXene nanosheets have been successfully produced and can be used in the next composite process.

Because of many hydrophilic terminations planted on the surface of MXene nanosheets during the liquid etching process, the MXene can be well dispersed in water, as shown in **Supplementary Figure S1**, which ensures the stability of MXene solution in the hydrothermal process. After the hydrothermal process, the morphology of MXene nanosheets has undergone an obvious change (**Figure 1D**), and there are many nanoplates anchored on the surface of unimpaired MXene nanosheets. In **Figure 1E**, the distribution of elements reflected by EDS shows that the MXene is still intact, and the Cu_2MoS_4 nanoplates are only synthesized on the surface of MXene nanosheets which meets our expectations. Interestingly, it can be seen that the size of Cu_2MoS_4@MXene nanocomposites appears bigger than that of pure MXene nanosheets, and this phenomenon may be a combination of

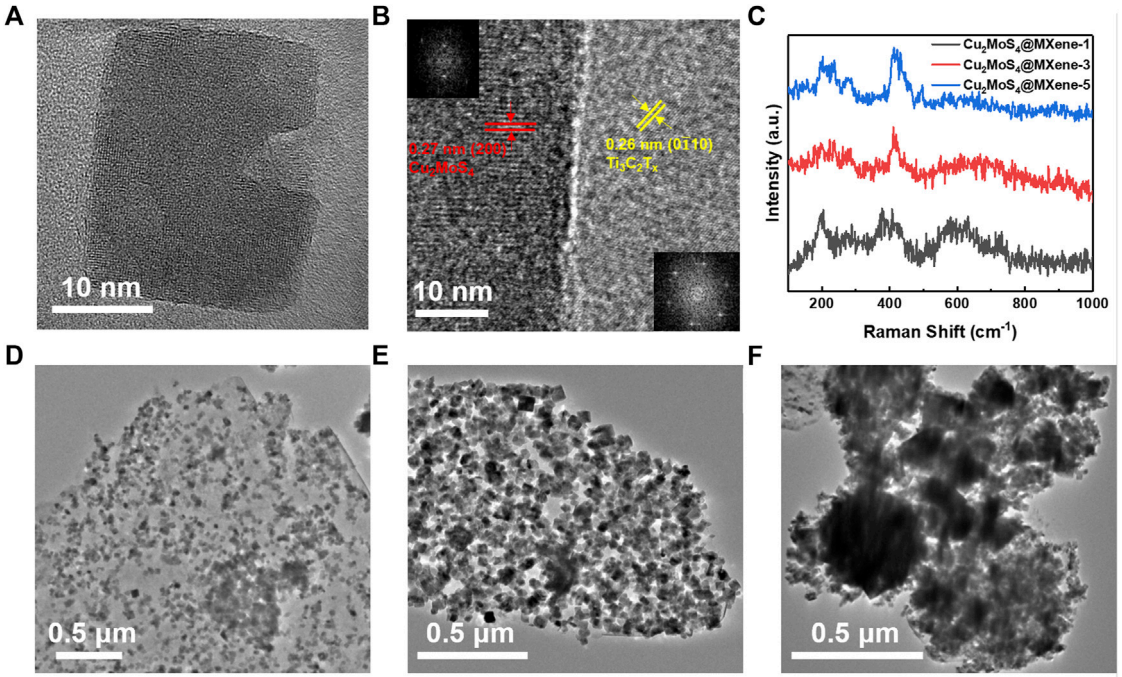

FIGURE 2 | Characterization of different Cu_2MoS_4@MXene nanocomposites. **(A,B)** HRTEM of Cu_2MoS_4@MXene (inset in B is the FFT of Cu_2MoS_4 and MXene, respectively). **(C)** Raman spectra of Cu_2MoS_4@MXene-1, Cu_2MoS_4@MXene-3, and Cu_2MoS_4@MXene-5. **(D–F)** TEM images of Cu_2MoS_4@MXene-1, Cu_2MoS_4@MXene-5, and Cu_2MoS_4@MXene-9, respectively.

several nanosheets, which is caused by some anchored Cu_2MoS_4 that can connect adjacent MXene nanosheets. In order to further confirm the successful synthesis of Cu_2MoS_4@MXene nanocomposites, the XRD and Raman spectra were used. In **Figure 1A**, the XRD result of Cu_2MoS_4@MXene nanocomposites illustrates that the Cu_2MoS_4 on the MXene nanosheets has good crystallinity, and the major peaks at 6.1°, 16.3°, 28.8° , 37.4°, and 47.9° are well indexed to the MXene and tetragonal-phase of Cu_2MoS_4 ($P\bar{4}2m$, JCPDS 81–1,159) (Lipatov et al., 2016; Zhang K. et al., 2017). Moreover, no evident diffraction peak of TiO_2 is consistent with the aforementioned verdict that the MXene nanosheets are unimpaired during the hydrothermal process which is because of a reductive environment made by the hydrolytic process of TAA. This conclusion can also be proved by the Raman spectrum in **Figure 1B**, where there is no peak at 150 cm^{-1} assigned to TiO_2 (Zhang C. J. et al., 2017). In addition to this, the peaks of Cu_2MoS_4@MXene nanocomposites at 200 cm^{-1}, 233 cm^{-1}, and 415 cm^{-1} represent the coexistence of Cu_2MoS_4 and MXene (Kim et al., 2017). In the microscopic image, the size of tetragonal Cu_2MoS_4 nanoplates that anchored on the MXene surface is about 20 nm (**Figure 2A**). Furthermore, the high-resolution TEM image in **Figure 2B** shows the crystal lattice spacing between 0.27 and 0.26 nm, which can be ascribed to the (200) plane of Cu_2MoS_4 and the (0,110) plane of MXene, and the FFT images (inset of **Figure 2B**) illustrate the tetragonal and hexagonal structure of Cu_2MoS_4 and MXene, respectively (Zhang K. et al., 2017; Agresti et al., 2019). Thus, according to the spectrum analysis and microscopic analysis, it can be confirmed that the Cu_2MoS_4@MXene nanocomposites have been successfully prepared with high quality.

Considering the ratio of Cu_2MoS_4 and MXene in Cu_2MoS_4@MXene nanocomposites may affect their performance, we prepared a series of nanocomposite samples with a gradient ratio. There is a regular variation in the Raman spectrum (**Figure 2C** and **Supplementary Figure S2**), and with the increased ratio of Cu_2MoS_4, the vibration peak of MXene becomes decrescent and that of Cu_2MoS_4 becomes stronger. Moreover, the microscopic morphology of Cu_2MoS_4@MXene-1, Cu_2MoS_4@MXene-5, and Cu_2MoS_4@MXene-9 prove the result of the Raman spectrum, which shows that the observed coverage ratio of anchored Cu_2MoS_4 nanoplates on MXene nanosheets increases, but when the ratio of Cu_2MoS_4 is too high (Cu_2MoS_4@MXene-9), the excessive aggregation occurs which is unfavorable in application (Fang et al., 2020). In addition, when the ratio of Cu_2MoS_4 becomes high, there are more evident signals of Cu and Mo elements in EDS mapping (**Supplementary Figure S3**) compared with the low ratio sample. Also, an evident aggregation of Cu_2MoS_4 can be seen, which further verified the aforementioned point. However, even if the ratio is excessively increased, there are still no Cu_2MoS_4 nanoplates lying outside the MXene nanosheets because of the anchoring effect mentioned earlier, which ensures the contact of Cu_2MoS_4 with high conductivity MXene and the electron transfer regulatory effect.

Optical Properties of Cu_2MoS_4@MXene Nanocomposites

As introduced earlier, the MXene can affect the photothermal performance of nanocomposites through band engineering and regulatory effect, so to make clear the role of MXene in this

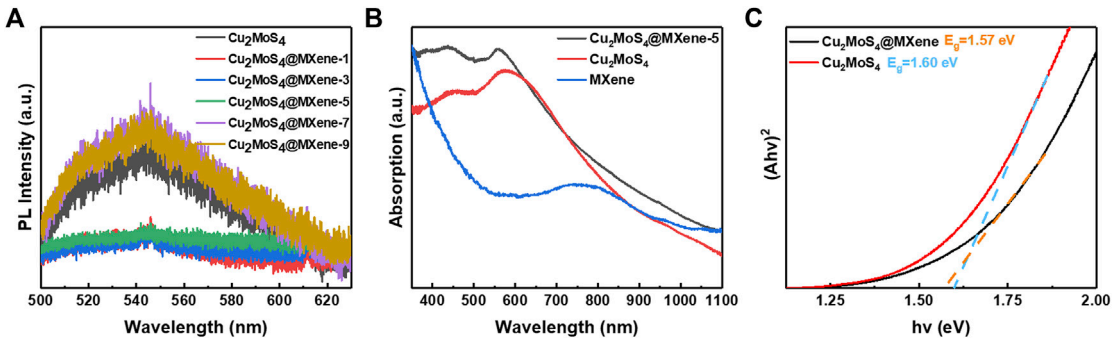

FIGURE 3 | Optical properties of Cu_2MoS_4@MXene nanocomposites. **(A)** PL spectra (excited by a 325-nm laser from 500 to 630 nm) of Cu_2MoS_4 and Cu_2MoS_4@MXene nanocomposites. **(B)** UV-vis-NIR absorption spectra of Cu_2MoS_4, Cu_2MoS_4@MXene, and MXene. **(C)** Tauc plots of Cu_2MoS_4 and Cu_2MoS_4@MXene.

process and whether the nanocomposite will gather an improved performance, the following optical properties of nanocomposites are enumerated: the result of the PL spectrum suggests that the nanocomposites' PL intensity is different from pure Cu_2MoS_4, and the samples marked as Cu_2MoS_4@MXene-1, Cu_2MoS_4@MXene-3, and Cu_2MoS_4@MXene-5 have a lower intensity. According to the band theory, the PL intensity is associated with the recombination of photogenerated electron–hole pairs, and the more radiative recombination occurs, and the higher PL intensity will be received (Feng et al., 2021; Li et al., 2021). Thus, it is obvious that the radiative recombination rate of samples with lower PL intensity is slower than that of pure Cu_2MoS_4 because the MXene with high electron conductivity can separate and transfer electrons from photogenerated exciton which prevents the radiative recombination and increases the concentration of carriers. Moreover, the separated carriers can efficiently facilitate crystal lattice vibrations after interacting with hot carriers produced by MXene because of the NIR-induced LSPR effect, thus leading to elevated temperatures (Zhou et al., 2020; Wang et al., 2021). However, when the ratio of Cu_2MoS_4 is excessive, the PL intensity becomes stronger and more radiative recombination occurs, which could be caused by aggregation issues and may weaken the photothermal performance.

Figure 3B is the UV-vis-NIR absorption spectrum of Cu_2MoS_4 and Cu_2MoS_4@MXene nanocomposites, and the pattern illustrates that the nanocomposites exhibit a stronger absorption than the pure Cu_2MoS_4 in a nearly full band spectrum, which is another cause of high photothermal performance. As shown in **Figure 3B**, the absorption spectra of pure MXene shows a weak absorption intensity in visible and near-infrared region compared with Cu_2MoS_4@MXene nanocomposite. Furthermore, according to Tauc's formulation (Wood and Tauc, 1972; Tauc, 1974), the optical band gaps can be calculated as around 1.60 and 1.57 eV for pure Cu_2MoS_4 and Cu_2MoS_4@MXene nanocomposites, respectively (**Figure 3C**). The narrowing band gap can be explained by the band theory that when the high work function MXene nanosheets come in contact with Cu_2MoS_4, the electrons will be drawn from a higher Fermi level of Cu_2MoS_4 to MXene, and when this process achieves a balance, the Fermi level of Cu_2MoS_4 will be brought down. So the band gap of nanocomposites is narrower than that of pure Cu_2MoS_4. In addition, this band gap engineering can promote the separation of photogenerated exciton and improve the photothermal performance, thus conforming to the result of the PL spectrum mentioned previously.

Photothermal Performance

On account of the previously mentioned results, we forecast that the high-quality Cu_2MoS_4@MXene nanocomposites possess better photothermal performance than pure Cu_2MoS_4 due to the novel effects caused by the composite process, e.g., band engineering, electron transfer regulatory effect, and anchored effect. Thus, the NIR thermal conversion performance of Cu_2MoS_4 and Cu_2MoS_4@MXene nanocomposites was tested to verify this forecast. As shown in **Figure 4A**, under NIR light (1.0 W/cm^2 at 808 nm) for 10 min, the temperature of each sample (500 μg/ml) has an obvious increase, and the highest ΔT can reach more than 55°C with two samples, i.e., Cu_2MoS_4@MXene-1 and Cu_2MoS_4@MXene-5, which is higher than pure Cu_2MoS_4 (50°C). However, the photothermal performance of samples marked as Cu_2MoS_4@MXene-7 and Cu_2MoS_4@MXene-9 is worse, which may be caused by the aggregation issue mentioned earlier. In addition, the temperature change is also dependent on concentration and laser power density which further demonstrates the distinguished photothermal conversion property of Cu_2MoS_4@MXene nanocomposites (**Figure 4B** and **Supplementary Figure S4**) (Hao et al., 2021). Taking into account the photostability of Cu2MoS4@MXene-1 and Cu2MoS4@MXene-5 (**Supplementary Figure S5**), Cu2MoS4@MXene-5 has the best performance, which matches the microscopic morphology and optical properties. When compared with the corresponding NIR thermal time constants (τ_s) and conversion efficiency (η) of pure Cu_2MoS_4 (292.12 s and 72.07%), the better τ_s and η of Cu_2MoS_4@MXene-5 are calculated as 242.44 s and 87.98%, respectively (**Figure 4C** and **Figure 4D**) (Chang et al., 2019; Chen et al., 2019; Li et al., 2021). Therefore, based on all of these experimental data, it is evident that the composite process efficiently promoted the photothermal conversion ability.

Mechanism of Photothermal Performance

To reveal the reasons for the enhanced performance of Cu_2MoS_4@MXene nanocomposites, their photothermal

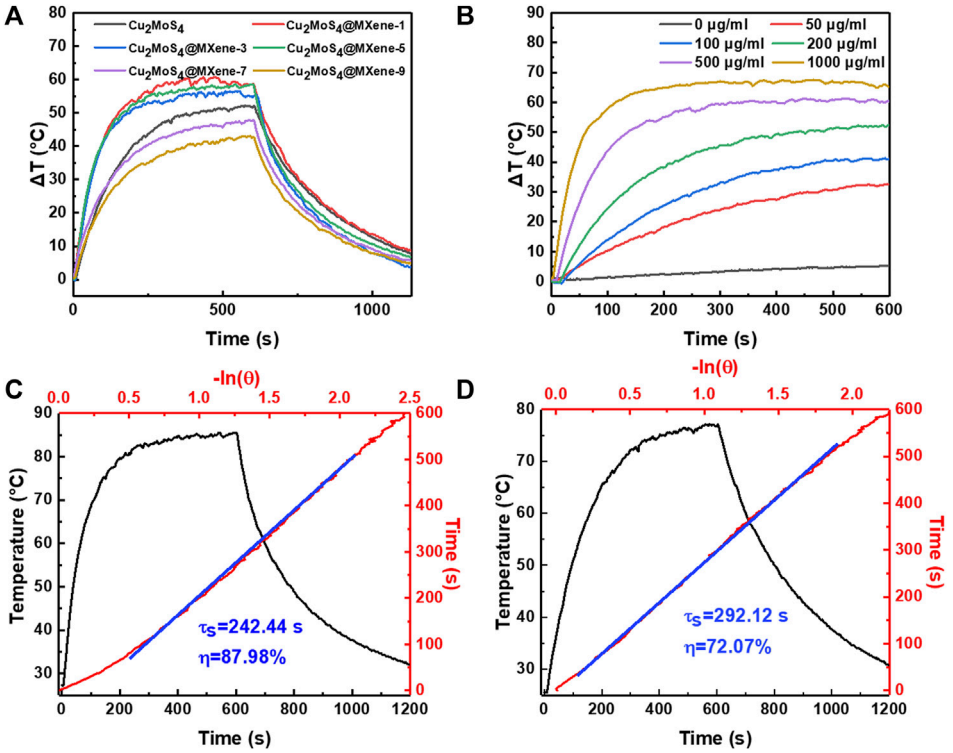

FIGURE 4 | Photothermal performance of Cu_2MoS_4 and Cu_2MoS_4@MXene. **(A)** Photothermal activity of Cu_2MoS_4 and Cu_2MoS_4@MXene nanocomposites. **(B)** Concentration-dependent temperature change curves of Cu_2MoS_4@MXene-5. **(C,D)** Heating–cooling curves and linear time constant curves of Cu_2MoS_4@MXene and Cu_2MoS_4.

mechanism is proposed based on the previously analyzed experimental data. As reported in other previous work, under NIR irradiation, the electron in the photogenerated exciton will transit to the conduction band; then, the major electron in the excited state will recombine with the hole through radiating fluorescence; meanwhile, only a minority of electron–hole pairs have a photothermal effect due to nonradiative recombination, which can be described as the photothermal mechanism (Li et al., 2021). However, when the high work function (5.28 ± 0.03 eV) MXene is introduced, the heterojunction formed between Cu_2MoS_4 and MXene should be regarded as the transfer barrier (Regulacio et al., 2018; Lin et al., 2019; Yang et al., 2019; Prabaswara et al., 2020; Li et al., 2021). Referring to the band theory, the excited electron will irreversibly migrate from the Cu_2MoS_4 to MXene until their Fermi level reaches equilibrium; then, this migration can be accelerated because of the high-electron conductivity of MXene, and this process is defined as the band engineering caused by electron transfer regulatory effect. Obviously, the major excited electron of Cu_2MoS_4 in Cu_2MoS_4@MXene nanocomposites will migrate to MXene instead of radiatively recombining with the hole, so the probability of nonradiative recombination can multiply which improves the photothermal performance (Li et al., 2021).

Meanwhile, the UV-vis spectrum and Raman spectrum indicate an LSPR effect of MXene at 800 nm (1.5 eV) which can be attributed to an out-of-plane transverse plasmonic resonance, and owing to the LSPR effect, the MXene can generate the hot carriers under vis-NIR irradiation. Then, the injected hot carriers can further assist the separation and transfer of electrons and prevent the radiative recombination which is another crucial reason for improved photothermal performance.

In brief, after the hydrothermal process, Cu_2MoS_4 was anchored on the surface of MXene nanosheets, and the electron spontaneously migrates across the transfer barrier (electron transfer regulatory effect and band engineering). Then, with the synergy of MXene's LSPR effect, the nonradiative recombination, i.e., the performance of photothermal conversion, can be efficiently accelerated.

CONCLUSION

In summary, in order to improve the photothermal performance of Cu_2MoS_4, the MXene nanosheets were introduced, and the Cu_2MoS_4@MXene nanocomposite was successfully synthesized. Due to the superior electron conductivity and high work function of MXene, the motion of the electron was changed at the heterostructure of Cu_2MoS_4 and MXene, and the electron can migrate from Cu_2MoS_4 to MXene which promotes the nonradiative

recombination and generates heat. Also, the experimental results show that the radiative combination was evidently prevented, indicating an accelerated nonradiative combination, and the enhanced photothermal conversion efficiency of Cu_2MoS_4@MXene nanocomposite can reach 87.98% compared with the pure Cu_2MoS_4 (η = 72.07%). Then, a mechanism was proposed based on the electron transfer regulatory effect and LSPR effect. Finally, this work provides an efficient method to enhance the photothermal performance of phototherapy reagents and make them play a great role in cancer treatment.

DATA AVAILABILITY STATEMENT

The original contributions presented in the study are included in the article/**Supplementary Material,** further inquiries can be directed to the corresponding authors.

AUTHOR CONTRIBUTIONS

LL, JZ, LS, and LG designed the project and analyzed the data. YL, YoZ, SL, YZL, and YiZ performed the experiments. LG wrote the manuscript. LS, SY, and LG revised the manuscript. All authors commented on the manuscript.

FUNDING

This work was supported by the National Natural Science Foundation of China (No. 22105229).

SUPPLEMENTARY MATERIAL

The Supplementary Material for this article can be found online at: https://www.frontiersin.org/articles/10.3389/fbioe.2022.902312/full#supplementary-material

REFERENCES

Agresti, A., Pazniak, A., Pescetelli, S., Di Vito, A., Rossi, D., Pecchia, A., et al. (2019). Titanium-carbide MXenes for Work Function and Interface Engineering in Perovskite Solar Cells. *Nat. Mater.* 18, 1264. doi:10.1038/s41563-019-0527-9

Chang, M., Wang, M., Wang, M., Shu, M., Ding, B., Li, C., et al. (2019). A Multifunctional Cascade Bioreactor Based on Hollow-Structured Cu 2 MoS 4 for Synergetic Cancer Chemo-Dynamic Therapy/Starvation Therapy/Phototherapy/Immunotherapy with Remarkably Enhanced Efficacy. *Adv. Mater.* 31, 1905271. doi:10.1002/adma.201905271

Chang, M. Y., Hou, Z. Y., Wang, M., Wang, M. F., Dang, P. P., Liu, J. H., et al. (2020). Cu_2MoS_4/Au Heterostructures with Enhanced Catalase-like Activity and Photoconversion Efficiency for Primary/Metastatic Tumors Eradication by Phototherapy-Induced Immunotherapy. *Small* 16, 14. doi:10.1002/smll.201907146

Chen, W. C., Wang, X. F., Zhao, B. X., Zhang, R. J., Xie, Z., He, Y., et al. (2019). CuS-MnS_2 Nano-Flowers for Magnetic Resonance Imaging Guided Photothermal/photodynamic Therapy of Ovarian Cancer through Necroptosis. *Nanoscale* 11, 12983–12989. doi:10.1039/c9nr03114f

Chen, W. X., Chen, H. P., Zhu, H. T., Gao, Q. Q., Luo, J., Wang, Y., et al. (2014). Solvothermal Synthesis of Ternary Cu_2MoS_4 Nanosheets: Structural Characterization at the Atomic Level. *Small* 10, 4637–4644. doi:10.1002/smll.201400752

Cheng, Y., Chang, Y., Feng, Y. L., Jian, H., Tang, Z. H., and Zhang, H. Y. (2018). Deep-Level Defect Enhanced Photothermal Performance of Bismuth Sulfide-Gold Heterojunction Nanorods for Photothermal Therapy of Cancer Guided by Computed Tomography Imaging. *Angew. Chem. Int. Ed.* 57, 246–251. doi:10.1002/anie.201710399

Demellawi, J. K., Lopatin, S., Yin, J., Mohammed, O. F., and Alshareef, H. N. (2018). Tunable Multipolar Surface Plasmons in 2D $Ti_3C_2T_X$ MXene Flakes. *ACS Nano* 12, 8485–8493. doi:10.1021/acsnano.8b04029

Fang, Y. Z., Hu, R., Zhu, K., Ye, K., Yan, J., Wang, G. L., et al. (2020). Aggregation-Resistant 3D $Ti_3C_2T_x$ MXene with Enhanced Kinetics for Potassium Ion Hybrid Capacitors. *Adv. Funct. Mater.* 30, 10. doi:10.1002/adfm.202005663

Feng, H., Dai, Y., Guo, L., Wang, D., Dong, H., Liu, Z., et al. (2021). Exploring Ternary Organic Photovoltaics for the Reduced Nonradiative Recombination and Improved Efficiency Over 17.23% With a Simple Large-Bandgap Small Molecular Third Component. *Nano Res.* 15, 3222–3229. doi:10.1007/s12274-021-3945-3

Guo, L. H., Li, Z. K., Hu, W. W., Liu, T. P., Zheng, Y. B., Yuan, M. M., et al. (2021). A Flexible Dual-Structured MXene for Ultra-sensitive and Ultra-wide Monitoring of Anatomical and Physiological Movements. *J. Mater. Chem. A.* 9, 26867–26874. doi:10.1039/d1ta08727d

Halim, J., Lukatskaya, M. R., Cook, K. M., Lu, J., Smith, C. R., Näslund, L.-Å., et al. (2014). Transparent Conductive Two-Dimensional Titanium Carbide Epitaxial Thin Films. *Chem. Mater.* 26, 2374–2381. doi:10.1021/cm500641a

Hao, Y., Mao, L., Zhang, R., Liao, X., Yuan, M., and Liao, W. (2021). Multifunctional Biodegradable Prussian Blue Analogue for Synergetic Photothermal/Photodynamic/Chemodynamic Therapy and Intrinsic Tumor Metastasis Inhibition. *ACS Appl. Bio. Mater.* 4, 7081–7093. doi:10.1021/acsabm.1c00694

Hu, T., Wang, J. M., Zhang, H., Li, Z. J., Hu, M. M., and Wang, X. H. (2015). Vibrational Properties of Ti_3C_2 and $Ti_3C_2T_2$ (T = O, F, OH) Monosheets by First-Principles Calculations: a Comparative Study. *Phy. Chem. Chem. Phy.* 17, 9997–10003. doi:10.1039/c4cp05666c

Kim, Y., Tiwari, A. P., Prakash, O., and Lee, H. (2017). Activation of Ternary Transition Metal Chalcogenide Basal Planes through Chemical Strain for the Hydrogen Evolution Reaction. *Chempluschem* 82, 785–791. doi:10.1002/cplu.201700164

Li, J., Li, Z., Liu, X., Li, C., Zheng, Y., Yeung, K. W. K., et al. (2021). Interfacial Engineering of Bi_2S_3/$Ti_3C_2T_x$ MXene Based on Work Function for Rapid Photo-Excited Bacteria-Killing. *Nat. Commun.* 12, 1224. doi:10.1038/s41467-021-21435-6

Lin, Y. X., Chen, S. M., Zhang, K., and Song, L. (2019). Recent Advances of Ternary Layered Cu_2MX_4 (M = Mo, W; X = S, Se) Nanomaterials for Photocatalysis. *Solar, Rrl* 3, 13. doi:10.1002/solr.201800320

Lioi, D. B., Neher, G., Heckler, J. E., Back, T., Mehmood, F., Nepal, D., et al. (2019). Electron-Withdrawing Effect of Native Terminal Groups on the Lattice Structure of $Ti_3C_2T_X$ MXenes Studied by Resonance Raman Scattering: Implications for Embedding MXenes in Electronic Composites. *ACS Appl. Nano Mater.* 2, 6087–6091. doi:10.1021/acsanm.9b01194

Lipatov, A., Alhabeb, M., Lukatskaya, M. R., Boson, A., Gogotsi, Y., and Sinitskii, A. (2016). Effect of Synthesis on Quality, Electronic Properties and Environmental Stability of Individual Monolayer Ti3C2 MXene Flakes. *Adv. Electro. Mater.* 2, 9. doi:10.1002/aelm.201600255

Lv, R., Liang, Y.-Q., Li, Z.-Y., Zhu, S.-L., Cui, Z.-D., and Wu, S.-L. (2021). Flower-like CuS/graphene Oxide with Photothermal and Enhanced Photocatalytic Effect for Rapid Bacteria-Killing Using Visible Light. *Rare Met.* 41, 639–649. doi:10.1007/s12598-021-01759-4

Mariano, M., Mashtalir, O., Antonio, F. Q., Ryu, W. H., Deng, B. C., Xia, F. N., et al. (2016). Solution-processed Titanium Carbide MXene Films Examined as Highly Transparent Conductors. *Nanoscale* 8, 16371–16378. doi:10.1039/c6nr03682a

Massagué, J., and Obenauf, A. C. (2016). Metastatic Colonization by Circulating Tumour Cells. *Nature* 529, 298–306. doi:10.1038/nature17038

Mohammadi, A. V., Rosen, J., and Gogotsi, Y. (2021). The World of Two-Dimensional Carbides and Nitrides (MXenes). *Science* 372, 1165. doi:10.1126/science.abf1581

Prabaswara, A., Kim, H., Min, J.-W., Subedi, R. C., Anjum, D. H., Davaasuren, B., et al. (2020). Titanium Carbide MXene Nucleation Layer for Epitaxial Growth of High-Quality GaN Nanowires on Amorphous Substrates. *ACS Nano* 14, 2202–2211. doi:10.1021/acsnano.9b09126

Qiu, Z. M., Bai, Y., Gao, Y. D., Liu, C. L., Ru, Y., Pi, Y, C., et al. (2021). MXenes Nanocomposites for Energy Storage and Conversion. *Rare Met.* 41 1101–1128. doi:10.1007/s12598-021-01876-0

Rameshbabu, R., Vinoth, R., Navaneethan, M., Hayakawa, Y., and Neppolian, B. (2017). Fabrication of Cu2MoS4 Hollow Nanotubes with rGO Sheets for Enhanced Visible Light Photocatalytic Performance. *Crystengcomm* 19, 2475–2486. doi:10.1039/c6ce02337a

Regulacio, M. D., Wang, Y., Seh, Z. W., and Han, M.-Y. (2018). Tailoring Porosity in Copper-Based Multinary Sulfide Nanostructures for Energy, Biomedical, Catalytic, and Sensing Applications. *ACS Appl. Nano Mater.* 1, 3042–3062. doi:10.1021/acsanm.8b00639

Steeg, P. S. (2016). Targeting Metastasis. *Nat. Rev. Cancer* 16, 201–218. doi:10.1038/nrc.2016.25

Tauc, J. (1974). *Amorphous and Liquid Semiconductors*. London: Plenum Press.

Wang, D. B., Fang, Y. X., Yu, W., Wang, L. L., Xie, H. Q., and Yue, Y. A. (2021). Significant Solar Energy Absorption of MXene $Ti_3C_2T_x$ Nanofluids via Localized Surface Plasmon Resonance. *Sol. Energ. Mat. Sol. C.* 220, 12. doi:10.1016/j.solmat.2020.110850

Wood, D. L., and Tauc, J. (1972). *Phys. Rev. B* 5, 3144–2151. doi:10.1103/physrevb.5.3144

Xi, D. M., Xiao, M., Cao, J. F., Zhao, L. Y., Xu, N., and Long, S. R. (2020). NIR Light-Driving Barrier-free Group Rotation in Nanoparticles with an 88.3% Photothermal Conversion Efficiency for Photothermal Therapy. *Adv. Mater.* 32, 8. doi:10.1002/adma.201907855

Yang, Y., Jeon, J., Park, J.-H., Jeong, M. S., Lee, B. H., Hwang, E., et al. (2019). Plasmonic Transition Metal Carbide Electrodes for High-Performance InSe Photodetectors. *ACS Nano* 13, 8804–8810. doi:10.1021/acsnano.9b01941

Yilmaz, M., Christofori, G., and Lehembre, F. (2007). Distinct Mechanisms of Tumor Invasion and Metastasis. *Trends Mol. Med.* 13, 535–541. doi:10.1016/j.molmed.2007.10.004

Yuan, M., Xu, S., Zhang, Q., Zhao, B., Feng, B., Ji, K., et al. (2020). Bicompatible Porous Co3O4 Nanoplates with Intrinsic Tumor Metastasis Inhibition for Multimodal Imaging and DNA Damage-Mediated Tumor Synergetic Photothermal/photodynamic Therapy. *Chem. Eng. J.* 394, 124874. doi:10.1016/j.cej.2020.124874

Zhang, C. J., Pinilla, S., McEvoy, N., Cullen, C. P., Anasori, B., Long, E., et al. (2017b). Oxidation Stability of Colloidal Two-Dimensional Titanium Carbides (MXenes). *Chem. Mater.* 29, 4848–4856. doi:10.1021/acs.chemmater.7b00745

Zhang, K., Chen, W. X., Wang, Y., Li, J., Chen, H. P., Gong, Z. Y., et al. (2015). Cube-like Cu_2MoS_4 Photocatalysts for Visible Light-Driven Degradation of Methyl orange. *Aip Adv.* 5, 5. doi:10.1063/1.4926923

Zhang, K., Lin, Y., Muhammad, Z., Wu, C., Yang, S., He, Q., et al. (2017a). Active {010} Facet-Exposed Cu_2MoS_4 Nanotube as High-Efficiency Photocatalyst. *Nano Res.* 10, 3817–3825. doi:10.1007/s12274-017-1594-3

Zhang, K., Lin, Y. X., Wang, C. D., Yang, B., Chen, S. M., Yang, S., et al. (2016). Facile Synthesis of Hierarchical Cu_2MoS_4 Hollow Sphere/Reduced Graphene Oxide Composites with Enhanced Photocatalytic Performance. *J. Phys. Chem. C* 120, 13120–13125. doi:10.1021/acs.jpcc.6b03767

Zhang, Q., Song, Q. C., Wang, X. Y., Sun, J. Y., Zhu, Q., Dahal, K., et al. (2018). Deep Defect Level Engineering: a Strategy of Optimizing the Carrier Concentration for High Thermoelectric Performance. *Energy Environ. Sci.* 11, 933–940. doi:10.1039/c8ee00112j

Zhang, R., Zheng, Y., Liu, T., Tang, N., Mao, L., Lin, L., et al. (2021). The Marriage of Sealant Agent between Structure Transformable Silk Fibroin and Traditional Chinese Medicine for Faster Skin Repair. *Chin. Chem. Lett.* 33 1599–1603. doi:10.1016/j.cclet.2021.09.018

Zhou, B., Su, M., Yang, D., Han, G., Feng, Y., Wang, B., et al. (2020). Flexible MXene/Silver Nanowire-Based Transparent Conductive Film with Electromagnetic Interference Shielding and Electro-Photo-Thermal Performance. *ACS Appl. Mater. Interf.* 12, 40859–40869. doi:10.1021/acsami.0c09020

Zhou, J., Jiang, Y., Hou, S., Upputuri, P. K., Wu, D., Li, J., et al. (2018). Compact Plasmonic Blackbody for Cancer Theranosis in the Near-Infrared II Window. *ACS Nano* 12, 2643–2651. doi:10.1021/acsnano.7b08725

Conflict of Interest: The authors declare that the research was conducted in the absence of any commercial or financial relationships that could be construed as a potential conflict of interest.

Publisher's Note: All claims expressed in this article are solely those of the authors and do not necessarily represent those of their affiliated organizations, or those of the publisher, the editors, and the reviewers. Any product that may be evaluated in this article, or claim that may be made by its manufacturer, is not guaranteed or endorsed by the publisher.

frontiers | Frontiers in Bioengineering and Biotechnology

REVIEW
published: 23 May 2022
doi: 10.3389/fbioe.2022.865682

Biomimetic Exosomes: A New Generation of Drug Delivery System

*Xudong Wang, Xian Zhao, Youxiu Zhong, Jiuheng Shen and Wenlin An**

National Vaccine & Serum Institute (NVSI), China National Biotech Group (CNBG), Beijing, China

Most of the naked drugs, including small molecules, inorganic agents, and biomacromolecule agents, cannot be used directly for disease treatment because of their poor stability and undesirable pharmacokinetic behavior. Their shortcomings might seriously affect the exertion of their therapeutic effects. Recently, a variety of exogenous and endogenous nanomaterials have been developed as carriers for drug delivery. Among them, exosomes have attracted great attention due to their excellent biocompatibility, low immunogenicity, low toxicity, and ability to overcome biological barriers. However, exosomes used as drug delivery carriers have significant challenges, such as low yields, complex contents, and poor homogeneity, which limit their application. Engineered exosomes or biomimetic exosomes have been fabricated through a variety of approaches to tackle these drawbacks. We summarized recent advances in biomimetic exosomes over the past decades and addressed the opportunities and challenges of the next-generation drug delivery system.

Keywords: exosomes, drug delivery system, biomimetic exosomes, smart, large scale production

OPEN ACCESS

Edited by:
Qitong Huang,
Gannan Medical University, China

Reviewed by:
Ruoning Wang,
Nanjing University of Chinese Medicine, China
Lang Rao,
Shenzhen Bay Laboratory, China

****Correspondence:***
Wenlin An
anwlin@163.com

Specialty section:
This article was submitted to Nanobiotechnology, a section of the journal Frontiers in Bioengineering and Biotechnology

Received: *30 January 2022*
Accepted: *21 March 2022*
Published: *23 May 2022*

Citation:
Wang X, Zhao X, Zhong Y, Shen J and An W (2022) Biomimetic Exosomes: A New Generation of Drug Delivery System. Front. Bioeng. Biotechnol. 10:865682. doi: 10.3389/fbioe.2022.865682

1 INTRODUCTION

During the past several decades, naked therapeutic agents, including small molecule drugs and biomacromolecule drugs, were used to prevent, diagnose, or treat different diseases. However, some limitations such as low solubility, poor stability, short circulating half-life, and poor biodistribution of these drugs contributed to limited efficiency (Zhao et al., 2021). In order to solve the aforementioned problems, a wide variety of delivery systems have been constructed in recent years to enhance the therapeutic effect and reduce side effects (Wang et al., 2021; Yi et al., 2022). Among them, nanotechnology was introduced into medicine and, therefore, improved treatment. Various synthetic nanoparticles, such as liposomes (Sur et al., 2014; Dammes et al., 2021), micelles (Gong et al., 2012; Kataoka et al., 2012), and self-assembled peptides (Cully, 2015; Worthington et al., 2017), and inorganic materials, such as graphene (Xiaoming et al., 2008; Panwar et al., 2019) and graphene-like 2D materials (Huang et al., 2021), are used to carry different cargo (Kuang et al., 2020; Zhou et al., 2021). Over the past few decades, nanocarriers for drug delivery have found applications in clinical use (Wicki et al., 2015; Min et al., 2015). The approved nano-drugs Doxil, Lipusu, and Abraxane mainly utilized liposomes as carriers. With the outbreak of COVID-19, liposome-based mRNA vaccines (Flemming, 2021; Gebre et al., 2021) were applied against COVID-19 (Flemming, 2021; Gebre et al., 2021); liposomes have drawn wide concern. However, these exogenous nanomaterials encountered several biological barriers and were quickly cleared from the blood upon delivering drugs to targeted locations (Peng et al., 2013). Studies have shown that less than 1% of nanomedicine reaches the target tissue (Huang et al., 2020). The failure of clinical trials of synthetic nanomedicine is mainly due to the difference in the biological barrier and immune system of humans and animals (Foulkes et al., 2020). By coupling with PEG to nanoparticles to prolong the

circulation time of nanomedicine in the blood (Tam et al., 2013; Suk et al., 2016), antibodies (Sun et al., 2014), peptides (David, 2017), and aptamers (Subjakova et al., 2021) were modified at the surface of nanocarriers to increase the targeting ability and improve biodistribution. Nevertheless, the delivery efficiency of modified nanoparticles to targeted locations was still limited. This was because repeated injections of PEGylated nanomedicine caused faster blood clearance and a significant increase in the amount of aggregation in the liver and spleen (Ishihara et al., 2009). The long cycle capability of nanomedicine was therefore dramatically decreased, which was endowed by introduction of PEG onto nanoparticles. In addition, serious toxic and side effects in the body were caused for the encapsulated drug on account of the change of its pharmacokinetic behavior.

In order to tackle these issues, numerous biological carriers have recently been applied to achieve intracellular delivery of nanomedicine. Biological sources of carriers have received widespread attention due to their ability to alter biological distribution, uptake, and cause controllable responses (Bu et al., 2019). These vectors included membrane fragments (Park et al., 2021), exosomes (Liang et al., 2021), and viruses (Sokullu et al., 2019), while further applications of these virus were restricted due to strong immunogenicity (Bulcha et al., 2021). Exosomes were one kind of vesicles which were secreted from the cell membrane by cells with a particle size in the range of 40–160 nanometers. Since vesicles were derived from cells, exosomes have similar structures and properties to those of cells (Antimisiaris et al., 2018). Exosomes contained phospholipid bilayers and cytoplasmic proteins, membrane proteins, RNA, DNA, and other components similar to parent cells, but exosomes have no organelles. Exosomes played key roles in many biological processes under a variety of physiological and pathological conditions, and were considered to be a new mechanism for cell-to-cell communication (EL Andaloussi et al., 2013). Exogenous materials, including proteins, lipids, and genetic materials, could be delivered into recipient cells through exosomes. As a consequence, exosomes can be used as biomarkers for disease diagnosis (Ge et al., 2020) and prognosis (De Rubis et al., 2019). In addition, the large capacity and efficient ability of exosomes to exchange protein genes with cells give them the potential to be used clinically as a carrier for gene and drug delivery (Jie et al., 2021). Exosomes showed higher biocompatibility and lower toxicity in comparison to synthetic vehicles (Li et al., 2019). The surface of the exosome membrane contains all sorts of proteins that interact with integrins, allowing exosomes to overcome various biological barriers in the body, including clear monocytes, cell adhesion, permeation of tissues, spreading into the blood, and even passing through the blood–brain barrier. Thus, exosomes were regarded as natural vehicles to transport not only RNA but also DNA toward cells.

Although exosomes show great potential in treatment, their targeting capability of natural exosomes was relatively low, limiting further clinical applications (Liang et al., 2021). Over the years, a series of engineered exosomes have been developed to increase drug loading rates and improve the ability to target sites (Sterzenbach et al., 2017). By means of chemical modification, genetic engineering, and physical method, the exosomes were endowed with more functions and improved the targeting efficiency.

There were some major drawbacks of exosomes before clinical applications. For exosomes, it was virtually impossible for the preparation of vesicles with the exact duplicate for biomedical applications owing to the complex structures (De La Peña et al., 2009). In addition, the exact working mechanism was hard to elucidate due to its intricately pathophysiological functions. As a consequence, their development of extracellular vesicles may be hampered by their short- and long-term side effects caused by the unknown components for clinical practice. Furthermore, no standard methodologies existed to produce pure exosomes which met clinical applications to date. On account of different methods of preparation, the characteristics and functions of generated extracellular vesicles were also alike (Yong-Jiang Li et al., 2021). Thus, there is an urgent need to develop a common strategy to fabricate exosomes by researchers in the near future. Furthermore, extracellular vesicles which originated from organisms comprised of a mixture of a variety of extracellular vesicles derived from cell types of sorts, causing difficulty for the isolation of a single vesicle population to determine the dominant inducer of a particular function. Furthermore, they were not sufficient to generate at a large scale because of the low production yield in naturally secreted extracellular vesicles, which limited their further application (Antimisiaris et al., 2018).

In an attempt to overcome the shortcoming of exosomes which acted as cargo, artificial exosomes have been developed as vehicles to different delivery agents. In this review, the progress of biomimetic exosomes for drug delivery over the past decades was reviewed (**Scheme 1**). First, we introduced the preparation methods of biomimetic exosomes including chemical methods and genetic engineering methods. Second, we introduced the application scenarios of biomimetic exosomes. Finally, we summarized the advantages and challenges of biomimetic exosomes, aiming to provide inspiration in developing delivery systems for cell-free therapy.

2 PREPARATION OF BIOMIMETIC EXOSOMES

2.1 Strategies for Biomimetic Exosome Preparation

Compared to exosomes, biomimetic exosomes with high-titer production were used to import therapeutic agents into cells. With the rapid development of nanotechnology, a great deal of research efforts has been made to develop strategies of preparation methods for constructing novel functional materials. For the fabrication of materials at nanoscale, the materials were prepared with minimum dimensions with particle size ranging from 1 to 100 nm. A series of approaches have been used to fabricate nanoscale biomimetic exosomes with different functions from cells and small molecules. Currently, the method for artificial exosome preparation could be divided into three categories: top-down, bottom-up, and biological strategies.

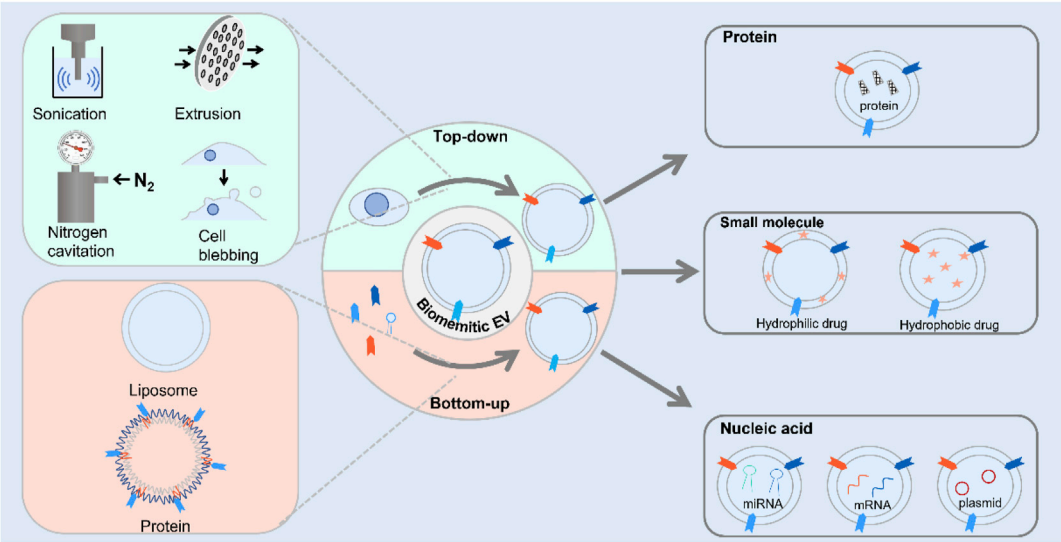

SCHEME 1 | Scheme illustration of the route for the preparation of biomimetic exosomes and its application to deliver therapeutic agents.

2.1.1 Top-Down Approach

The top-down approach for the preparation of materials at nanometer scale was that larger materials were broken into nanoscale structures. The exosome was secreted by various kinds of cells, with similar components to cells such as proteins and lipids. Therefore, cells were usually used as bulk materials for the preparation of artificial exosome *via* the aforementioned strategy. Cell membrane sheets were obtained by breaking cells to form vesicles. The composition of the fabricated nanovesicle membrane showed high similarity with natural exosomes because both of them were produced from cells. The generated artificial exosomes contained proteins, nucleic acids, and lipids. These artificial exosomes possessed the same biological complexity of exosome, whereas little heterogeneity was observed. On the basis of this approach, several strategies have been used to produce nanovesicles, including extrusion, filtration, microfluidic device, sonication nitrogen cavitation, and chemical-induced cell blebbing.

2.1.1.1 Extrusion-Based Strategies

Filter extrusion (using polycarbonate membrane filters) was extensively applied with dimension reduction. This method was ready to operate and produced nanomaterials with controllable size. For the preparation of nanovesicles, cells at the micron level were extruded by polycarbonate membranes of defined pore size with sequential extrusion, obtaining homogeneous nanovesicles with nanoscale size. Generally, a commercial liposome extruder was used to accomplish the extrusion process. In addition, several devices have been used for preparing artificial exosomes at large scale.

In 2014, nanosized vesicles loaded with chemotherapeutic drugs were developed by the GHO Group utilizing sequential extrusion through polycarbonate membrane filters with a decrease in pore sizes, starting at monocytes or macrophages in the presence of doxorubicin (**Figure 1A**) (Jang et al., 2014). As compared with the yield of natural exosomes from an identical number of cells, the bioinspired nanovesicle yield was increased 100-fold. The obtained nanovesicles ranged in size from 120–130 nm, and exosome marker proteins such as moesine, CD63, and TSG101 also existed in nanovesicles. These nanovesicles were similar to natural exosomes in particle size, morphology, and protein contents. Owing to endothelial CAMs as raw materials, the generated nanovesicles which maintained the topology of plasma membrane protein showed the targeting ability toward tumor site. By means of the obtained nanovesicles, chemotherapeutic drugs could be efficiently delivered to the site of the tumor with less adverse effects. Importantly, the curative effect of nanosystems reduced obviously as plasma membrane proteins were removed. Importantly, the plasma membrane proteins of the nanovesicles were removed by trypsin to reduce their therapeutic effects. Taken together, the bioengineered nanovesicles as novel exosome-mimetics were successfully transferred chemo drugs toward malignant tumors.

Although extruding cell *via* microchannel was successfully employed to generate nanovesicles, the critical challenge for clinical applications was both the delivery efficiency and the scale-up production. The fabrication processes should be well controlled in large-scale nanovesicle preparation with uniform quality. Recently, the Park group developed a method to prepare a massive range of artificial exosome with culture cells through utilizing a common centrifuge (**Figure 1B**) (Jo et al., 2014). Compared with hand extruder, the extrusion force by centrifugation could be controllable to extrude cells. Once the centrifuge worked, cells were directly broken into nanovesicles by hydrophilic micro-size pores. Two much of the intracellular contents in the generated nanovesicles were observed when compared with natural exosomes. In addition, the nanovesicles could be selected to deliver their contents, including Oct3/4 and

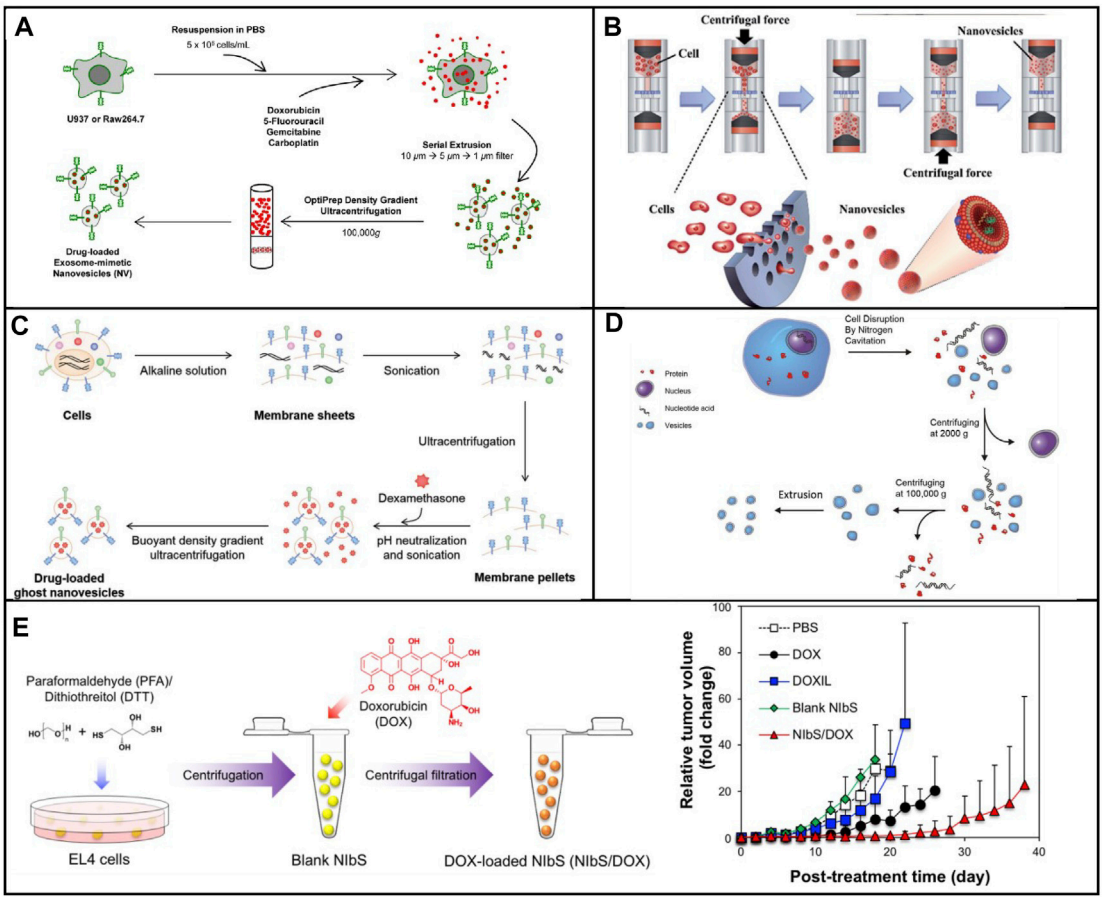

FIGURE 1 | (A) Schematic illustration of the procedure for the generation of NV and chemotherapeutics-loaded NV (Jang et al., 2014). **(B)** Schematic process of nanovesicle generation (Jo et al., 2014). **(C)** Schematic illustration of the procedure for generation of ghost nanovesicles (ghost NVs) and dexamethasone-loaded ghost NVs (Go et al., 2019). **(D)** Schematic shows a process to generate a uniform size of nanovesicles including cell disruption, differential centrifugation, and extrusion (Gao et al., 2016). **(E)** Production and drug loading of NIbS derived from cancer cells and efficient therapeutic efficacy against murine EL4 tumors by EL4-derived NIbS/DOX (Ingato et al., 2018).

Nanog, to recipient cells and used for activation of the signaling pathway. A huge amount of nanovesicles, which were produced by using a centrifuge and polycarbonate structure with the filter, could be utilized for practical applications including drug delivery. The source cell which expressed specific targeting molecules endowed the produced nanovesicles with a targeting capability.

In addition to cells being raw materials, the lysed cell membrane could be used to form nanovesicles, which has the capability to replicate the functionalities of cell. With the development of the cell membrane coating technology, nanovesicles were prepared by coating various types of cell membranes onto nanoparticles. The generated nanovesicles have been demonstrated to efficiently deliver the drug because of their abilities to prolong circulation time. In addition, proteins on the cells endow that biomimetic nanovesicles could interact with a series of disease substrates, leading to the home capability toward disease. Additional functions were provided by nanoparticles in the nanovesicles to enhance their effect in nanomedicine. A series of nanovesicles based on cell membrane–coated nanoparticles have been constructed to treat multiple diseases (Rao et al., 2017; Rao et al., 2018; Ai et al., 2021; Meng et al., 2021). For example, Rao et al. (2020a) developed hybrid cell membrane nanovesicles from cancer cells and macrophages to restrain tumor recurrence and metastasis after surgery. Cancer cell membranes with high-affinity SIRPα variant overexpression, platelet, and M1 macrophage–derived nanovesicles were sonicated and extruded through 100-nm pores. SαV-C-NVs, M1-NVs, and P-NVs have endowed the hybrid nanovesicles with long systemic circulation time, specific targeting, and activation to combat cancer. The hybrid nanovesicle could act as a platform to deliver bioactive molecules. In addition, a biomimetic exosome as nanodecoy for COVID-19 was produced by the extrusion of both 293 T-cell membranes with overexpressed ACE2 and human monocytes (Rao et al., 2020b). ACE2 on the surface of biomimetic exosomes was capable of hijacking the S protein–mediated viral infection. Meanwhile, biomimetic exosomes showed that the neutralization capability toward inflammatory cytokines significantly suppressed immune disorder and lung injury against COVID-19.

2.1.1.2 Sonication-Based Strategies

Sonication was a widely spread method that used a strong bath sonicator or ultrasonic probe to reduce particle size to yield nanosized particles. Sonication was another common approach for making liposome. Cells could be broken into cellular fragments in the preparation of artificial exosomes at the beginning. Then, the cell fragments were subjected to sonication to assemble into nanosized vesicles. In 2019, Go et al. (2019) constructed a novel approach to synthesize artificial exosomes by removing the unwanted cellular content. First, the cells were treated with alkaline solution, fragmented, and disassembled into membrane sheets (**Figure 1C**). Meanwhile, cellular contents including cytoplasm protein, nucleoprotein, and nucleic acids were completely released into an aqueous solution. Second, the cell membrane fragments in aqueous media were harvested by ultracentrifugation. Finally, membrane sheets were subjected to sonication with or without the addition of dexamethasone. These vesicles showed high efficiency in the treatment and production yield. In addition, undesired luminal cargos were separated, resulting in the reduction of potential adverse effects and facilitating drug loading. Moreover, artificial exosomes could be generated from various types of cells loading other drugs for the treatment of other diseases, expanding its practical application in clinical environment.

2.1.1.3 Nitrogen Cavitation-Based Strategies

Membrane proteins play significant roles in selectively delivering therapeutic agents into the site of lesion. A series of membrane proteins was involved in signal pathways to trigger the pathway activation or inhibition. The activity of membrane proteins should be retained in the process of generating nanovesicles. The nitrogen cavitation method was an effective approach for the disruption of cells and maintained the biological function of membrane proteins. Nitrogen cavitation referred that nitrogen could be dissolved in the cytoplasm of the cells under high pressure. Subsequently, nitrogen bubbles were formed in the cytoplasm cell suspension, which was abruptly exposed to atmospheric pressure such that nitrogen bubbles were formed in the cytoplasm, leading to fragmentation of cells. Gao et al. (2016) proposed a general approach to prepare cell-derived vesicles by employing nitrogen cavitation (**Figure 1D**). To generate nanovesicles with the capability of reducing acute lung inflammation and injury, active neutrophils were used as source cells. In comparison with extracellular vesicles, 100-fold was achieved in the production yield of nanosized vesicles loaded with dexamethasone. This proposed strategy showed great potential for the development of personalized nanomedicine to treat the given disease.

2.1.1.4 Cellular Blebbing–Based Strategies

Cellular blebbing was a large and spherical outgrowth of cell membrane, which occurred throughout the lifecycle of different cell types. Cell blebbing was observed in the presence of chemical or multiple mechanical stimulations. Although giant plasma membrane vesicles had been used, a wide size range caused a barrier for the practical application. To address the aforementioned drawback, the chemical stimulation method was used by Ingato et al. (2018) to efficiently produce nanovesicles induced by sulfhydryl-blocking (NIbS) (**Figure 1E**). Intracellular and extracellular osmotic pressure was used to control the blebbing process. The resulting nanovesicles could deliver chemotherapeutic agents to the tumor, improving cellular uptake and facilitating drug release in the cells. Furthermore, the accumulation in major organs was avoided by employing the nanosystem as compared to commercial liposomal formulation. The drug-loaded nanosystem obviously reduced the growth rate of tumor, resulting in the increase of the survival of tumor-bearing mice. Nanosized chemical-induced vesicles could be considered for mass production of nanovesicles with efficient, quick, and simple harvest and purification. In addition, NIbS were utilized in various therapeutic scenarios such as immunotherapy, gene therapy, and cell therapy.

2.1.2 Bottom-Up Approach

To date, the bottom-up approach was that small molecules were dissolved in an organic solvent and then precipitated on addition of an anti-solvent in the presence of a stabilizer. There are a variety of strategies of this approach including liposome conjugated with specific peptide, liposome coupled with antibody, NPs embedded with specific protein, liposomes modified with membrane proteins, and fully synthetic nanovesicles.

2.1.2.1 Liposomes Coupled With Peptides

Peptides could perform a lot of functions such as the targeting capability, the ability to penetrate cellular membrane, the stimuli responsive ability, and the therapeutic ability because of these specific sequences. Thus, the function of exosomes could be mimicked by liposomes after modification by peptides with specific sequences. It was an easy way to construct biomimetic exosomes with various functions owing to its highly modular design. Liposomes modified with MHC Class I/peptide complexes served as biomimetic exosomes to activate and expand functional antigen-specific T cells at sufficient cells (De La Peña et al., 2009). As shown in **Figure 2A**, the peptide was conjugated on the maleimide group in the liposome and sulfhydryl group, which was introduced to peptides with Tarut's reagent. Interestingly, the sulfhydryl group was introduced *via* the reaction between Tarut's reagent and primary amines without altering charge characteristics. The fabricated biomimetic exosomes have a similar size as that of exosomes as well as similar functions for activation and expansion toward T cells. Moreover, the fluorescent and magnetic elements were introduced into biomimetic exosomes, which endow the targeting and traceable capability. In addition to covalent modification of liposome with peptides, peptides could be inserted into liposomes at 60°C. Moreira et al., 2002 inserted a peptide (antagonist G) into a liposome through the postinsertion technique. Compared with antagonist G-liposome using the conventional coupled technique, the generated antagonist

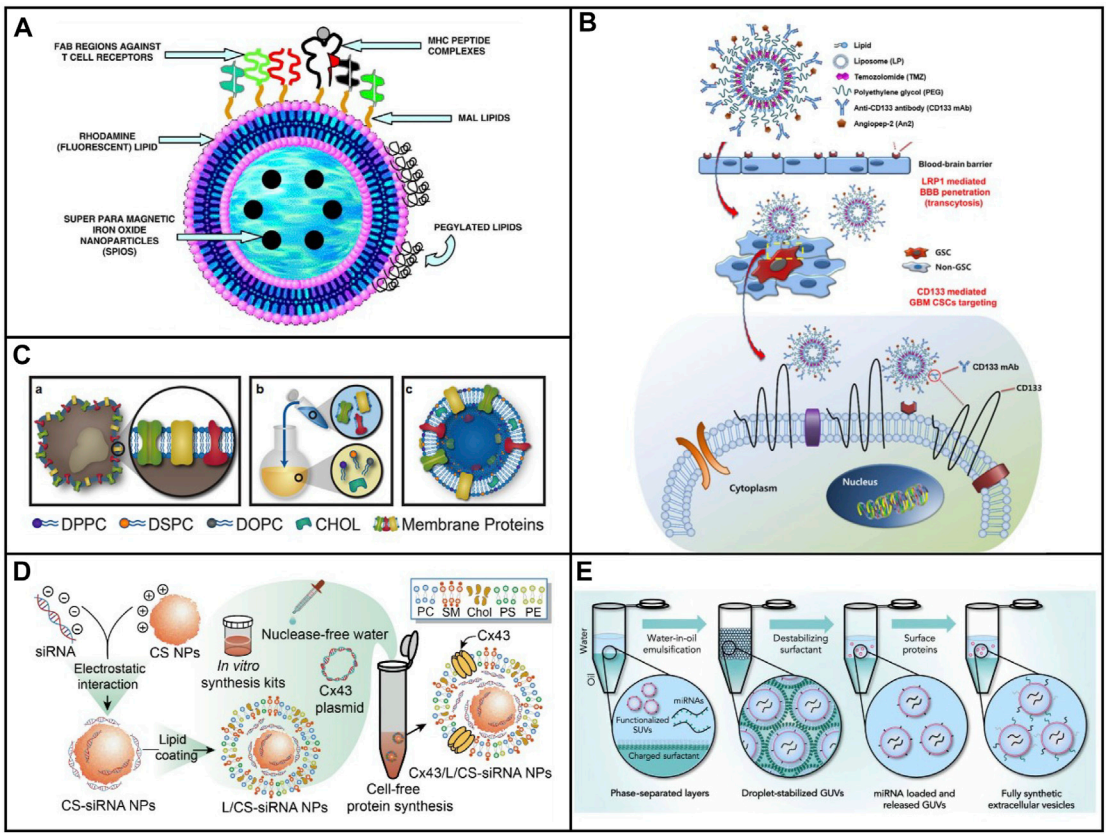

FIGURE 2 | (A) Schematic of immuno-magnetoliposomes as artificial exosomes. **(B)** Scheme of a dual-targeting immunoliposome encapsulating TMZ and mechanism for the delivery of TMZ to GSCs in dual-targeting immunoliposome formulation (Moreira et al., 2002). **(C)** Scheme of leukosome synthesis and formulation (Molinaro et al., 2016). **(D)** Schematic illustration of the preparation procedure for the construction of exosome mimetic Cx43/L/CS-siRNA NPs (Lu et al., 2019). **(E)** Schematic illustration of the fsEV formation process inside w/o droplet compartments produced by mechanical emulsification (Staufer et al., 2021).

G-liposome exhibited high binding under the same number of peptides, resulting in higher cytotoxicity toward H69 cell line.

2.1.2.2 Liposomes Coupled With Antibody

In addition to peptides, antibodies and proteins were composed of a variety of amine acids, which could also be covalently modified through different groups. As a consequence, both antibodies and proteins could be modified onto the surface of liposome *via* coupling and the postinsertion technique. Kim et al. (2018) developed angiopep-2 (An2) and anti-CD133 monoclonal antibody (CD133 mAb) conjugated liposomes, which could be used to deliver temozolomide for the treatment of glioblastoma multiforme (**Figure 2B**) (Moreira et al., 2002). An2 showed high targeting to low-density lipoprotein receptor-related protein on the blood–brain barrier (BBB), while anti-CD133 was capable of targeting toward CD133, which was highly expressed on the cancer stem cells of glioblastoma multiforme. Dual targeting liposomes endowed them to deliver drugs across BBB and reach the cancer stem cells. Much better therapeutic efficacy and fewer side effects were observed after treatment with dual targeting liposome. The system provided a convenient approach to fabricate biomimetic exosomes with dual function.

2.1.2.3 Liposome Embedded With Membrane Proteins

The bottom-up strategy has offered a novel solution to mimic the function of natural nanoparticles. Nevertheless, the complexity of membranes which was on the surface of liposomes was still not reproduced. In order to mimic the function of natural NPs, the complex synthetic route was required to add multiple elements onto the surface of liposome. Although the top-down strategy has provided a simple way to endow NPs with several bioactive functions, several limitations still existed by utilizing these approaches in the control of physical parameters, various kinds of cargo loading, and standardized preparation and storage approaches. In view of this, Molinaro et al. (2016) developed a biomimetic vesicle for the first time which incorporated membrane proteins into a lipid bilayer. As can be seen in **Figure 2C**, the nanovesicle could be fabricated by using the thin layer evaporation approach and integrating proteins derived from the leukocytes' plasmalemma into a synthetic phospholipid bilayer. Not only primary but also immortalized immune cells were used to extract the membrane proteins, which were utilized onto the surface of biomimetic vesicle. Subsequently, a mixture of cholesterol, synthetic choline-based phospholipids, and purified membrane proteins was assembled

through thin layer evaporation methods. The generated nanovesicles called leukosomes showed the well-targeting property of inflamed endothelia. The proposed route offered a universally synthetic method to produce biomimetic exosomes, which maintained the multiple functions of natural membranes.

2.1.2.4 Liposome-Coated Polysaccharides

Polysaccharides are biological polymers which consist of a lot of small monosaccharides. Polysaccharides include glycogen, inulin, hyaluronic acid, heparin, chondroitin 4 sulfate, gamma globulin, chitosan, alginate, dextran, cellulose, gelatin, and starch, and are widely used in biomedical applications. Chitosan was a positively charged polysaccharide which could bind polyanionic molecules, for example, nucleic acids. Liposome-based artificial exosomes could be used as cargo to carry drug or gene delivery. Lu et al. (2019) developed liposome-coated chitosan NPs to biomimetic exosomes for the delivery of siRNA. A plasmid that encoded, transcribed, translated, and integrated a transmembrane protein called connexin 43 (Cx43), transcription, translation, and integration was introduced into liposomes in the lipid layers in biomimetic exosomes (**Figure 2D**) (Lu et al., 2019). Integrated Cx43 worked functionally in cellular transport and facilitated the delivery of siRNA in EM to Cx43-expressing U87 MG cells. The EM exhibited high siRNA delivery efficiency and biocompatibility. Despite limited delivery efficiency than commercial transfection Lipo 2000 reagent, the strategy formulated EM using a cell-free protein synthetic approach and advanced the development of artificial exosomes as biomimetic nanocarriers.

Hyaluronic acid (HA) is a natural negatively charged hydrophilic polysaccharide with appreciable water solubility. Owing to the specific interaction of HA to CD44, a cell surface receptor, HA, could be served as a targeting moiety in nanomedicine for cancer therapy. Ravar et al. (2016) developed a HA-coated liposome to deliver paclitaxel through electrostatic interaction. The prepared biomimetic exosomes demonstrated high uptake efficiency in CD44 overexpressed cells, resulting in the improved cytotoxic activity compared to free drug and PTX liposomes without HA. Furthermore, HA-coated PTX liposomes showed high accumulation in the tumor area because of a high level of CD44 in tumors, and promising results on antitumors have been achieved in 4T1 tumor-bearing mice. Therefore, modifying liposomes with polysaccharides was an effective strategy to construct the biomimetic exosomes with specific functions.

2.1.2.5 Protein Vesicles

Generally, vesicles were prepared from lipids (liposomes) or polymers (polymersomes). In order to construct membrane-bound compartments, proteins were considered ideal building blocks. A vesicle to mimic the properties of cells has been developed by Huang and his colleagues through self-assembly of conjugated protein-polymers. In this design, a protein was covalently linked with a polymer *via* chemical reaction between mercaptothiazoline-activated amide and primary amine groups. The vesicle was formed through self-assembly at a constant aqueous/oil interface. The vesicles possessed the properties including molecule encapsulation, semipermeable nature, and protein synthesis guided by gene and enzyme catalysis. However, the function of proteins has been lost after chemical modification (Huang et al., 2013). To retain the biological activity of proteins on the surface of vesicles, a novel method has been used by Dautel and Champion (2021). Two recombinant fusion proteins, elastin-like polypeptide and globule-Z_E, were utilized to form vesicles. A glutamate-rich leucine zipper (Z_E) that could bind arginine-rich leucine zipper (ZR) was genetically fused with globules. The hydrophilic globule-ZE domain and the hydrophobic domain, Z_R-ELP, were connected *via* the leucine zipper pair to form an amphiphilic complex. Hydrophobic conformational changes of ELPs were induced upon heating, leading to lower critical solution temperature (LCST) behavior. During the heating from 4°C to room temperature, the vesicle occurred *via* a transient coacervate phase owing to the LCST behavior. The aforementioned approach showed advantages such as tunability *via* genetic engineering and the incorporation functional proteins with maintained activity.

2.1.2.6 Fully Synthetic Exosomes

To precisely mimic the functions of natural exosomes, Staufer et al. (2021) constructed a complementary synthetic biology method to generate biomimetic exosomes with full function of natural exosomes (**Figure 2E**). The fully synthetic exosomes were composed of proteins, RNA, and lipids, which contained the most abundant lipid composition in natural exosomes. The ratio of various lipid components was cholesterol: SM: DOPC: DOPS: DOPE: DOPG: PA: DAG: DOPI = 43:16:15:11:6:5:2:1:1. Thereafter, lipids were assembled through the charge-mediated vesicle assembly technology (**Figure 2E**). Abundant encapsulation efficiencies were achieved for diverse kinds of biomolecules. Furthermore, it offers precise quantitative control over vesicle composition and, therefore, over the biochemical and biophysical phenotype of the vesicles. Lastly, the resulting synthetically assembled vesicles in many parts closely resemble naturally occurring lipid carriers such as EVs.

2.1.3 Biological Approaches

2.1.3.1 Assembly Mechanism of Virus

Viruses consist of nucleic acids and proteins, having a particle size in the range of 20–400 nm. A protein called capsid could package their nucleic acid including DNA or RNA with single strand or double strand, thus protecting them from damage by external factors. In some cases, the lipid bilayer membrane of host cells coats viruses such as HIV and influenza. During the formation of viruses, capsid was assembled, and subsequently nucleic acid genome was packaged into capsid. Finally, the cell membrane was coated on the surface of capsid if enveloped. Generally, a large number of viruses whose genomes were single strand assembled spontaneously around their capsid. Nucleic acids with double strands having high charge density prevented spontaneous encapsulation. Consequently, an empty protein capsid was formed in numerous dsDNA virus assemblies (procapsid), and thereafter, DNA was pumped into capsid with the help of a molecular motor.

Viruses could act as vehicles to deliver nucleic acids for gene therapy. Gene therapy utilized genetic materials to replace a defective gene for the treatment of genetic diseases. Significant

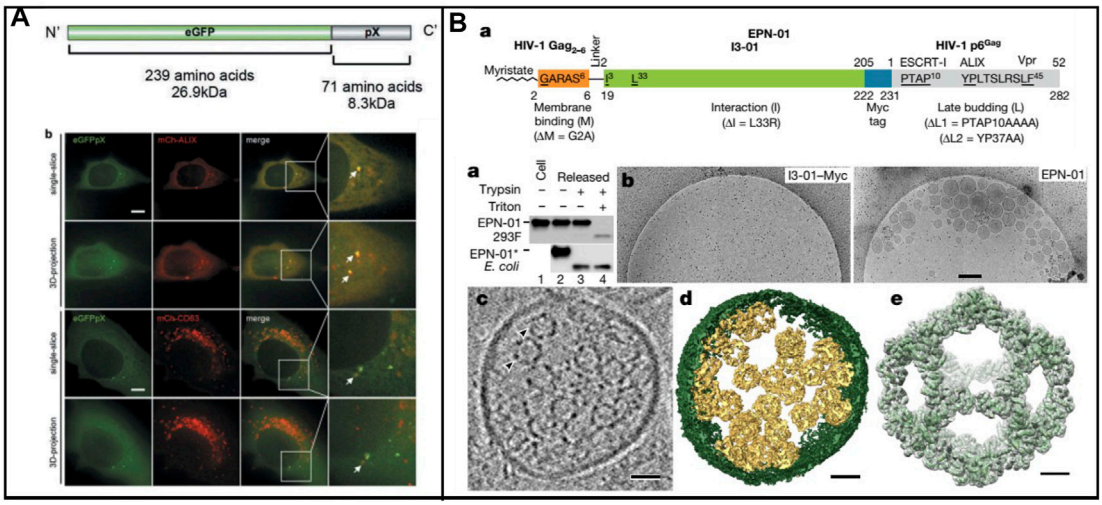

FIGURE 3 | (A) Schematic representation of the enveloped nanocages and representative cryo-EM images showing exosome/EPNs (Jiang et al., 2020). **(B)** Scheme of the recombinant eGFPpX protein and eGFPpX co-localized with the ALIX and CD63 in live cells. mCh-ALIX and mCh-CD63 were stably expressed in Huh7-eGFP and Huh7-eGFPpX cells (Votteler et al., 2016).

progress has been achieved in the field of treatment of diseases, which was incurable previously. The common genetic materials included mRNA and plasmid DNA in gene therapy. Gene-delivery vectors were needed for gene therapy due to their easy degradation. Adeno-associated virus (AAV) and retroviruses were widely used to transfer genes across the cell membrane. Nevertheless, the biggest challenge *via* AAV as gene vector was the limited efficiency because AAV could be degraded or neutralized rapidly owing to host immune response. The delivery efficiency could be enhanced after the envelopment of AAV to protect them from the immune system. Recently, a virus could evade neutralizing antibodies after envelopment with cell membranes from host cells. Endosomal-sorting complexes required for transport (ESCRT) involved the process to envelop the virus. Interestingly, ESCRT was also involved in the formation of exosomes. Thus, exosomes produced from virus-infected cells contained virus-derived nucleic acids, viral proteins, and even viruses. During the process of viral invasion, exosomes played several roles such as the transportation of virus into target cells and changing the physiology of target cells to facilitate infection. There were two mechanisms for exosomes to promote viral infection. One was that exosomes could interact with the ligand on the surface of the cell membrane to elicit down signaling events, and another was to promote cell uptake and intracellular release through membrane fusion or receptor-mediated endocytosis. In addition, the reduction systemic toxicity was achieved by employing engineering exosome with targeting element to improve the targeting ability.

2.1.3.2 Biomimetic Exosomes Derived From Virus

A lot of enveloped RNA viruses were released from host cells through ESCRT, which displayed unique characteristics. In many biological events, including the biogenesis of multivesicular bodies (MVBs), cytokinesis, and retrovirus budding, ESCRT is essential (Vietri et al., 2020). Significantly, the host cell membrane could be hijacked by the nonenveloped RNA virus in nonlytic release. Recently, a classic nonenveloped virus (Hepatitis A virus, HAV) was reported its release in the form of quasi-enveloped HAV. Furthermore, the Long group found that the exosome markers such as CD9, CD81, and CD63 existed in an enveloped HAV particle (**Figure 3A**) (Jiang et al., 2020). ALIX, a protein associated with ESCRT, was also found in enveloped HAV, demonstrating that ESCRT involved the formation of enveloped virus. In addition, pX, which existed on the surface of the virus capsid, could direct the virus into exosome-like EVs. In the meantime, ALIX was involved in the aforementioned process. This study provides a fresh insight into large proteins packaged into vesicle-derived cells.

In addition, nonenveloped viruses were loaded into exosomes to form biomimetic exosomes; protein nanocages could be enveloped into exosome-like vesicles *via* ESCRT. Votteler et al. (2016) developed the design of self-assembling protein nanocages that direct their own release from human cells inside small vesicles in a manner that resembles some viruses (**Figure 3B**). Three distinct functions of protein sequence that served as membrane binding, self-assembly, and recruitment of ESCRT were required in the biogenesis enveloped protein nanocages (EPNs). Fused peptide sequences (EPN-01) with the ability of membrane binding and ESCRT were constructed. To promote membrane binding, N-myristoylation signal corresponding to the first six amino acids of the HIV-1 structural Gag protein was added to I3-01. To promote ESCRT recruitment, the 52-residue HIV-1 Gag p6 peptide (p6Gag) was added to the C terminus. EPN-01 could be detected in the culture supernatant, whereas no peptides without membrane-binding element were released, demonstrating its necessity of binding-membrane for the release of nanocages. In addition, a nanocage with a size of about 25 nm was observed owing to the presence of the designed self-assembly unit. Moreover, many different

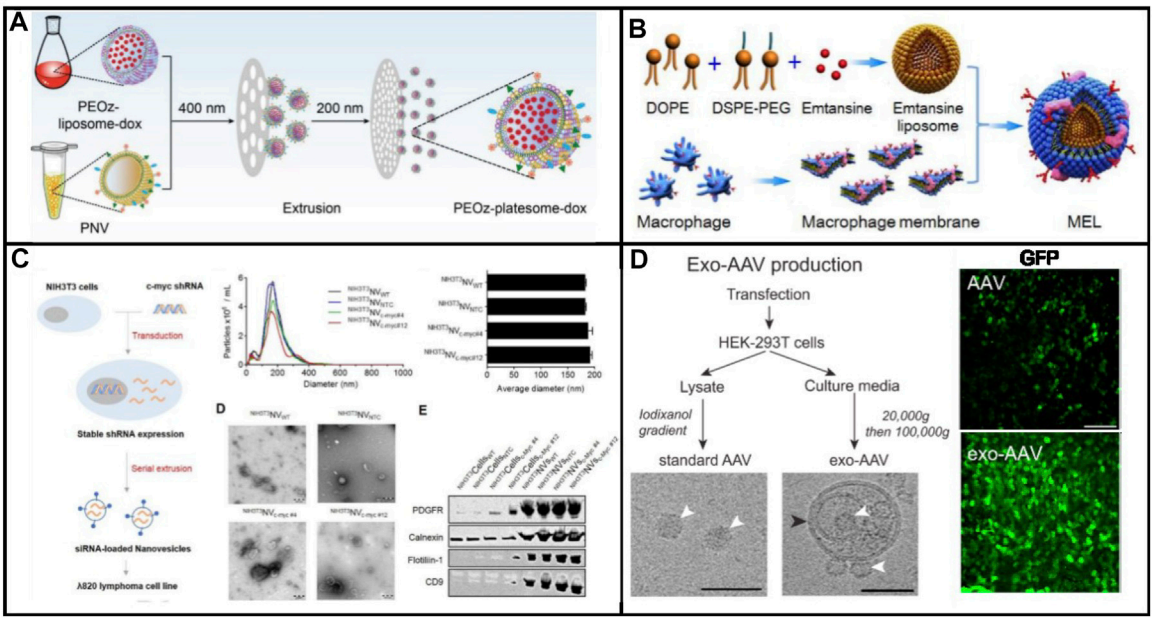

FIGURE 4 | (A) Schematic illustration of biomimetic exosomes to deliver small molecule (Dox) (Liu et al., 2019). **(B)** Biomimetic exosomes to deliver protein (emtansine) for suppressing lung metastasis of breast cancer (Cao et al., 2016). **(C)** Scheme illustration of endogenous siRNA loading into nanovesicles (Lunavat et al., 2016). **(D)** Scheme of the preparation of standard (conventional) AAV and exo-AAV production workflow (Ramakrishnaiah et al., 2013).

membrane-binding, self-assembly, and ESCRT-recruiting units were carried out to ensure the formation of nanocages, coated with host cell membrane and released from cells. A key feature of the proposed strategy is that it enables control over the biogenesis and contents of the materials through modification of EPN protein sequences. Enveloped nanocages are highly modular and tolerant to substantial alterations, demonstrating that they could be engineered to incorporate a series of properties and functions tailored to desired applications. Proteins which work within cells could be efficiently delivered across the cell membrane *via* the aforementioned strategy. In addition, the protein was packaged into nanoscaled vesicles to mimic the virus; the association of AAV with exosomes have been developed for gene therapy. Moreover, the biosynthesis strategy to construct biomimetic exosomes was utilized to improve the delivering efficiency.

2.2 Cargo Packaging

Until now, the drug loading approaches of exosomes and biomimetic exosomes have been divided into two main groups, the pre-loading methods and the post-loading methods.

In pre-loading approaches, the drug is first generated or loaded in the parental cells. Subsequently, these vesicles which were obtained by isolation or generation from cells have been preloaded into the desired drugs. By utilizing cell engineering techniques, the cells could be used to generate exosomes or biomimetic exosomes. It was a useful strategy for loading cargo including protein and nucleic acids into vesicles which could be produced in cells.

In post-loading approaches, the cargo was packaged into exosomes after isolation by different methods. Cargo packages with high yields have been developed by liposome engineering. A high ratio of cargo loading was successfully achieved in comparison to electroporation, which was utilized earlier. Generally, most drugs were loaded by passive loading with low loading rate. Active loading was an effective method to improve the encapsulation efficiency of drugs with amphiphilic properties. The loading approach of amphiphilic drugs such as DOX and camptothecin was passive, which included gradient ammonium sulfate and pH strategies. The cargo was loaded into vesicles derived from red blood cells through the active loading method, which was proposed by Zhang and his colleagues (Krishnan et al., 2021). To retain a fluorescent dye, the content of cholesterol in the membrane should be increased. The fluorescence intensity gradually increased with the increase in cholesterol content. When the percentage composition for cholesterol, the fluoresce signal reached its maximum. Using similar strategies, Vogelstein and coworkers have constructed an active method to load hydrophobic drugs, which was at a low drug loading rate *via* passive loading (Sur et al., 2014; Wang et al., 2022). Hydrophobic drugs were first packaged into modified β-cyclodextrins with weak basic groups, which facilitate to load drugs. By utilizing pH gradients, these cyclodextrins could subsequently carry drugs to pass through the lipid bilayer of liposomes. These strategies could be expanded to the package drugs into biomimetic exosomes.

2.3 Advantage and Disadvantage of Synthetic Strategies for Biomimetic Exosomes

Although the techniques to generate exosomes have made great progress, several drawbacks such as scalable production, isolation,

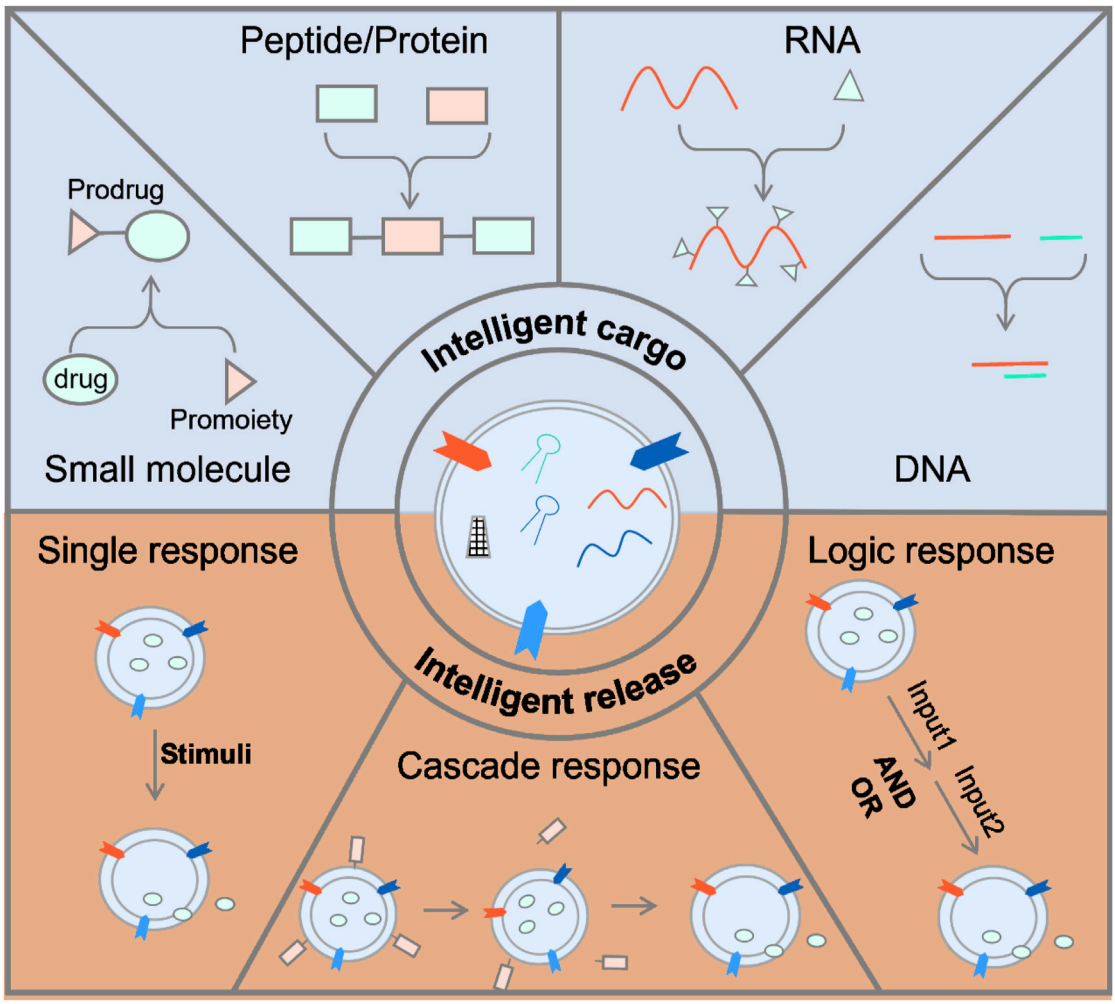

FIGURE 5 | Strategies for smart nanomedicine based on biomimetic exosome.

purification, and cargo loading should be circumvented for their clinical application. In view of this, artificial exosomes have been carried out through bio-nanotechnology, particularly the development of fully synthetic exosomes. Currently, some problems remain to fabricate biomimetic exosomes, which include low output, time-consumption, and characterization (**Table 1**).

Through top-down fabrication, cell membranes used as raw materials endowed the biomimetic exosomes with wide applicability because these vesicles showed a high similarity in physiochemical and biological characteristics to exosomes. Extrusion was the most widely applied strategy to produce a large number of exosome-mimetic vesicles. By applying this technology to cells, as much as 100-fold on the amount of biomimetic exosomes has been achieved in comparison to that of natural exosomes. Furthermore, conventional laboratory centrifuges were applied for the scale-up generation of biomimetic exosomes. However, ultracentrifugation was indispensable during isolation and purification after serial extrusion by using the top-down strategy. The fabrication of final vesicles was time-consuming. In addition, lack of selectivity in cargo sorting in the preparation of biomimetic exosomes was presented because the surrounding medium was packaged into biomimetic exosomes in the self-assembly of membrane debris. Nevertheless, the production sustainability was limited in the generation of biomimetic exosomes owing to cells as raw materials.

The bottom-up fabrication was capable of large-scale production of these vesicles with various forms, which was similar to the liposome generation. Since synthetic materials were easily available for large-scale processing, biomimetic exosomes could be obtained with a mass of vesicles. In order to mimic the function of natural exosomes, liposomes were modified with multiple components, leading to poor stability of liposomes and complex preparation processes. Even so, it was hard to mimic the component of natural exosomes. As a result, the function of exosomes was difficult to be completely reproduced by biomimetic exosomes on the basis of the bottom-up fabrication.

3 APPLICATION OF BIOMIMETIC EXOSOMES

In recent years, nano-delivery systems have received extensive attention due to their ability to deliver drugs to targeting lesions (Geranpayehvaghei et al., 2021). Therapeutic agents included small molecules and macromolecules such as proteins and nucleic acids. Nucleic acid drugs were composed of siRNA, shRNA, miRNA, antisense oligonucleotide (ASO), CRISPR/Cas 9 system, plasmid DNA, and mRNA. Similar to natural exosomes, biomimetic exosomes could transport these therapeutic agents into cells. Compared with other carriers, biomimetic exosomes showed good biocompatibility and possessed a targeting ability due to the presence of proteins or peptides on the surface of these nanovesicles. According to the types of molecules, the cargo delivered by biomimetic exosomes could be divided into four groups: small molecules, proteins, RNA, and DNA.

3.1 Small Molecule Delivery

Hydrophobic drugs could be loaded into phospholipid bilayers through hydrophobic interaction, while hydrophilic drugs were encapsulated into the core of artificial exosome. A pH responsive artificial exosome was constructed by Liu et al. (2019) *via* a convenient way for targeting delivery toward tumors. As can be seen in **Figure 4A**, platelet membranes and liposomes, which were functionalized with a pH responsive unit, were merged to construct the proposed nanocarrier. The platelet membranes of the vector endow the ability to escape from the immune system; pH responsive liposome endows the vehicle to release cargo selectively in the acidic microenvironment in lysosomal. Furthermore, the therapeutic effect toward tumors was better than that of plateletsome without a pH responsive unit or pH-sensitive liposome. Recently, biomimetic exosomes were designed for the delivery of various therapeutic drugs to meet treatment needs (Jang et al., 2013; Bozhao Li et al., 2021; Liao et al., 2021). The constructed nanocarriers were expected to treat a variety of diseases through chemotherapy, immune therapy, and phototherapy.

3.2 Protein Delivery

Compared with small drugs, protein drugs have the advantages of high activity, high specificity, and low toxicity. So far, more than 130 drugs have been approved by the FDA for the treatment of various diseases (Sanchez-Moreno et al., 2018). However, delivering proteins across cell membranes is a challenge, and as such, most protein drugs are developed with membranes as targets. Intracellular protein delivery is a huge obstacle to its development as a universal treatment. The progress of intracellular protein delivery will promote the development of protein drugs. The impermeability of cells is a major obstacle to the intracellular delivery of recombinant proteins. Endosomal escape is an effective way to overcome the cell barrier, but this strategy still presents a very big challenge. Therefore, there is an urgent need to develop a universal method for protein delivery. Natural exosomes themselves carry proteins, which are excellent carriers and deliver a variety of proteins. The biomimetic exosome delivery protein has the advantages of easy availability, easy functionalization, and large-scale production. Cao et al. (2016) developed a nanovesicle to deliver emtansine to metastatic sites for the treatment of cancer metastasis of breast cancer. As shown in **Figure 4B**, the nanomedicine was composed of macrophage membranes, liposomes, and emtansine. For the first time, a pH-responsive liposome was used to load emtansine, which was toxic to cancer cells. Subsequently, an isolated macrophage membrane was used to coat the liposome, ensuring the ability of nanomedicine toward metastases foci in the lung. The mixing between the liposome and macrophage membrane was conducted through extrusion. High expression of α4 and β1 integrins contributed to the enhancement of the cellular uptake of emtansine, where a 25% reduction in the cellular uptake of emtansine-loaded liposome is compared with that of macrophage membrane functionalized liposome. This was due to the interaction between α4β1 integrin and VCAM-1 in cancer cells that contributed to specific metastasis-targeting toward cancer metastasis. In particular, the specific metastasis targeting ability and anti-metastatic activity of MEL were evaluated in a lung metastatic breast cancer model.

3.3 RNA Delivery

Owing to its intrinsic capacity, various kinds of RNA species could be transferred by exosomes and other extracellular vesicles from one cell to another. As a consequence, these vesicles have been utilized as carriers for the delivery of therapeutic RNA molecules. Nevertheless, the rare production of exosomes limited its practical application field. Alternatively, biomimetic exosomes could serve as carriers to deliver RNA and DNA into cells. Lunavat et al. (2016) prepared artificial exosomes derived from cells *via* multiple extrusion, and thereafter these vesicles were loaded with a specific siRNA *via* electroporation (**Figure 4C**). These nanomedicines were taken up by cells effectively. The proteins in the generated nanovesicle were similar to those of the plasma membrane of parent cells. Subsequently, a decreased level of GFP was observed in the nanovesicle, which loaded GFP siRNA, indicating the reduction of target genes. In addition, the expression of C-myc was decreased after treatment with siRNA, which was loaded into biomimetic exosomes, demonstrating that these biomimetic exosomes could be served as nanomedicine to treat diseases which were caused by the overexpression of C-myc.

In general, biomimetic exosomes can efficiently protect their payload against degradation, although the active targeting efficiency is currently debated for both systems. Similar to exosomes, biomimetic exosomes can deliver small molecules and large biological molecules (RNA and proteins). Genetic materials are fragile in the human body, so they must be protected to take effect. mRNAs and viral or nonviral plasmid DNAs are the common genetic materials used in gene therapy. Encapsulation in nanostructures protects the AAV vectors from the host immune system and delivers them into cells across the plasma membrane. Recently, Ramakrishnaiah et al. (2013) reported that hepatocyte-derived exosomes containing hepatitis C virus (HCV) RNA can activate innate immune cells (**Figure 4D**). In the presence of neutralizing antibodies, the virus could be transferred by exosomes. Exosomes from HCV-

TABLE 1 | Advantages and disadvantage of synthetic strategies for biomimetic exosomes.

	Method	Yield	Cargo loading	Stability	Reference
Top-down	Extrusion	High	Lack selectivity	Good	Jang et al. (2014)
	Sonication	High	Lack selectivity	Good	Go et al. (2019)
	Nitrogen cavitation	High	Lack selectivity	Good	Gao et al. (2016)
	Cellular blebbing	High	Lack selectivity	Good	Ingato et al. (2018)
Bottom-up	Liposome-based	High	Selectivity	Poor	Kim et al. (2018)
	Protein-based	High	Selectivity	Good	Dautel and Champion (2021)
	Fully synthetic exosomes	High	Selectivity	Good	Staufer et al. (2021)
Biological approaches	Derived from virus	Low	Selectivity	Good	Votteler et al. (2016)

infected cells were capable of transmitting infection to naive human hepatoma Huh7.5.1 cells and establishing a productive infection. Even with sub-genomic replicons, lacking structural virus proteins, exosome-mediated transmission of HCV RNA was observed. Treatment with patient-derived IgGs showed a variable degree of neutralization of exosome-mediated infection compared with free virus. Therefore, biomimetic exosomes can be used as vectors to deliver plasmids, mRNA, etc., for gene therapy. Furthermore, exosome-AAV hybrid biomimetic exosomes combined the advantages of viral vectors and nonviral vectors, which can escape from the immune system and significantly reduce the immunogenicity of the vector. The Maguire group has developed an artificial exosome as a vector to deliver genes toward all inner hair cells (Gyorgy et al., 2017). Compared with the adeno-associated virus, the GFP expression delivered by artificial exosomes was significantly higher than that of AAV. Exo-AAV shows no toxicity *in vivo* as assayed by tests of auditory and vestibular function. Finally, exo-AAV1 gene therapy partially rescues hearing in a mouse model of hereditary deafness.

3.4 DNA Delivery

Nucleic acid drugs contain siRNA, shRNA, miRNA, antisense oligonucleotide (ASO), CRISPR/Cas 9 system, plasmid DNA, and mRNA, which have captured much attention for therapeutic treatment of a variety of diseases and disorders. In order to prevent degradation *in vitro* and *in vivo*, different vehicles such as virus and non-virus have been developed to deliver these nucleic acids. In addition to the aforementioned delivery of RNA-based drugs, biomimetic exosomes have also been used to transfer DNA including plasmid and antisense oligonucletide to targeting cells. In 2021, the Lee group utilized biomimetic exosomes to efficiently deliver plasmid against glioblastoma with low toxicity (Han et al., 2021). The biomimetic exosomes consist of three units including cell membrane, PEI25k, and plasmid DNA. The cell membrane which was extracted from C6 rat glioblastoma cells could prolong circulation time by reducing the clearance of the reticuloendothelial system. Meanwhile, cell membranes in nanoparticles decrease their toxicity before reaching the target location *via* preventing drug leakage. PEI25k was a positively charged polymer, which could act as a vehicle by the formation of polymer/pDNA complex. The biomimetic exosomes were stable with a size of around 120 nm owing to the surface charge of approximately −32mV. Interestingly, no significant change was observed in the size of nanovesicles compared with nanoparticles without cell membranes, indicating a high stability of biomimetic exosomes. Furthermore, the biomimetic exosomes showed high transfection efficiency in a serum containing medium as compared to nanoparticles without cell membranes. After treatment with the prepared nanoparticle in glioblastoma-bearing mice, obvious reduction in tumor size was observed, demonstrating that biomimetic exosomes could be served as carriers for gene therapy.

Similar to the delivery of plasmid, ASO, which was a negatively charged DNA, could be transported by biomimetic exosomes to treat various diseases. Due to their strong anionic nature of ASOs, it was difficult to package the ASOs into nanovesicles. When using biomimetic exosomes for delivery of ASO, electroporation was a general approach to load these therapeutics into vesicles. Electroporation could increase the permeability of nanovesicles, therefore facilitating cargo into vesicles. In addition, electroporation could transfer more than two different ASOs into the same vesicles. Oieni et al. (2021) reported a scalable preparation strategy to generate gene vehicle for delivery of ASOs targeted to miRNA-221. Under low voltage conditions (700V), about 30% ASOs was encapsulated in biomimetic exosomes. To improve the targeting of biomimetic exosomes toward target tissue, cell membranes from human mesenchymal stem cells were employed to act as coating of nanoparticles. These nanovesicles could efficiently uptake by MSCs without endo-lysosomal degradation at 24 h after treatment with biomimetic exosomes. Subsequently, the miR-221 expression was dramatically decreased in MSCs on subjecting these nanomedicines. The proposed method could be extended to deliver different payloads toward various tissues with high specificity.

3.5 Smart Nanomedicine

However, due to the nonspecific release of the delivery system and rapid clearance in the blood, the therapeutic effect was limited, which required an increase in the dose of the drug and caused side effects (Meng et al., 2019). Nonspecific release referred that the drug is not delivered to the target location in advance before release (Tiwari et al., 2012). Another reason is that the drug is not released at the target location, so that it recirculates in the blood, and the drug is released in the process. Mu et al. (2020) Therefore, it is necessary to develop smart nanomedicine by using biomimetic exosomes so that it can only be released in a specific lesion site. As shown in **Figure 4**, there are two types of smart nanomedicine based on biomimetic exosomes: the smart

drug and the smart drug delivery system. As shown in **Figure 5**, there are two types of smart nanomedicines based on biomimetic exosomes: the smart drug and the smart drug delivery system.

3.5.1 Smart Drugs

Intelligence drug is a drug, which is inactive during the delivery process, and decomposes to release the original drug after reaching the target location to exert its therapeutic effect. The aforementioned strategies could improve the metabolic stability of the drug (Rautio et al., 2008; Walther et al., 2017; Rautio et al., 2018). Drugs have been classified into two types: small molecules and macromolecules (peptide, proteins, antibodies, and nucleic acids). Small molecule drugs could enhance their metabolic stability and reduce the toxicity caused by off-target *via* modifying functional groups (Rautio et al., 2008). Peptides were amino acids linked through peptide bonds. Biomacromolecule drugs could be incorporated with caging groups. The initial functions of biomacromolecules were restored upon removal of these caging groups (Diemer et al., 2020). Peptides could also constitute a variety of biological macromolecule-proteins that are essential for cell life activities (Lian and Ji, 2020). Peptides can increase their accumulation in specific tissues by adding targeting groups, adding transmembrane peptides to improve membrane penetration efficiency and endosome escape efficiency, adding self-assembly modules to increase drug stability, increasing response groups, and promoting drug release at the targeted location (Newman and Benoit, 2018). Stimulus-responsive groups can be roughly classified into enzyme-responsive (He et al., 2016), pH-responsive (Dharmayanti et al., 2021), and redox-responsive. By taking advantage of biotransformations, nucleic acids which were modified with specific groups were capable of transferring to bioactive nucleic acids in living cells.

3.5.2 Smart Release

The smart drug carrier with a unique stimulate-response mechanism can make response adjustments to changes in related physical and chemical properties under the stimulation of exogenous or endogenous factors, control the release of the drug to the target site, and automatically adjust the rate of drug release Li et al. (2019). Smart deliveries have shown great promise in the field of material science and pharmacy (Huang et al., 2019). Due to the advantages of improving the bioavailability of drugs in the body and reducing their toxic and side effects, intelligent drug carriers will play an increasingly important role in future clinical treatments (Pan et al., 2021). The main potential mechanism of nanomedicine design is the enhanced permeability and retention effect (EPR) (Duan et al., 2021). Nevertheless, a number of recent studies have shown that less accumulation of nanomedicine was observed on account of poor therapeutic effect. Therefore, researchers have tried to improve the EPR effect or reduce the characteristics of the anti-EPR effect and found that strategies to improve the delivery of multifunctional nano-drugs such as regulating the abnormal tumor microenvironment and stimulus-responsive nano-drugs can enhance the anti-cancer drug delivery system.

4 CHALLENGES AND PERSPECTIVE

On account of multiple drawbacks including low stability and unsatisfactory pharmacokinetic behavior, the naked therapeutic agents showed limited curative effect during clinical application. To address this issue, a series of delivery systems have been constructed to improve the therapeutic effect and reduce side effects over the past decades. Biomimetic exosomes are composed of reasonably designed lipids, proteins, and RNA, which have similar structures to liposome or exosome. Considering the disadvantages of lipid nanoparticles and liposomes, biomimetic exosomes may be the basis of personalized nanomedicine in terms of drug delivery system in the future, which is characterized by a wide range of sources, low price, stable physical and chemical properties, and good biocompatibility. In comparison with natural exosomes, biomimetic exosomes are much easier to be synthesized on a large scale. However, clinical trials of biomimetic exosomes have just begun, and biomimetic materials produced through synthetic strategies have not yet been used for clinical transformation. The main challenge is that there are no standard methods in preparation, characterization, and biocompatibility. In addition, a fully automated purification method is required for the preparation of biomimetic exosomes. To achieve large-scale production, the bottom-up method to produce biomimetic exosomes can be synthesized by a method similar to the synthesis of liposome-microfluidics. The fully synthesized biomimetic exosomes are easier to modify, and the modification of antibodies and other functional groups can help to control the release of biomimetic exosomes under a controllable spatiotemporal manner. In the future, new and multifunctional biomimetic exosomes will be developed through biotechnology, nanotechnology, and chemical technology as personalized nanomedicine.

AUTHOR CONTRIBUTIONS

XW, XZ and WA developed the review outline, drafted and wrote the manuscript, and developed the figures. XW conceived the idea and supervised the content and writing. YZ and JS critically contributed to the content and reviewed the manuscript to ensure accuracy and completeness. All authors contributed to the article and approved the submitted version.

REFERENCES

Ai, X., Wang, S., Duan, Y., Zhang, Q., Chen, M. S., Gao, W., et al. (2021). Emerging Approaches to Functionalizing Cell Membrane-Coated Nanoparticles. *Biochem.* 60, 941–955. doi:10.1021/acs.biochem.0c00343

Antimisiaris, S., Mourtas, S., and Marazioti, A. (2018). Exosomes and Exosome-Inspired Vesicles for Targeted Drug Delivery. *Pharmaceutics* 10, 218. doi:10.3390/pharmaceutics10040218

Li, B., Chu, T., Wei, J., Zhang, Y., Qi, F., Lu, Z., et al. (2021). Platelet-Membrane-Coated Nanoparticles Enable Vascular Disrupting Agent Combining Anti-angiogenic Drug for Improved Tumor Vessel Impairment. *Nano Lett.* 21, 2588–2595. doi:10.1021/acs.nanolett.1c00168

Bu, L. L., Rao, L., Yu, G. T., Chen, L., Deng, W. W., Liu, J. F., et al. (2019). Cancer Stem Cell-Platelet Hybrid Membrane-Coated Magnetic Nanoparticles for Enhanced Photothermal Therapy of Head and Neck Squamous Cell Carcinoma. *Adv. Funct. Mater.* 29, 1807733. doi:10.1002/adfm.201807733

Bulcha, J. T., Wang, Y., Ma, H., Tai, P. W. L., and Gao, G. (2021). Viral Vector Platforms within the Gene Therapy Landscape. *Sig Transduct Target. Ther.* 6, 53. doi:10.1038/s41392-021-00487-6

Cao, H., Dan, Z., He, X., Zhang, Z., Yu, H., Yin, Q., et al. (2016). Liposomes Coated with Isolated Macrophage Membrane Can Target Lung Metastasis of Breast Cancer. *Acs Nano* 10, 7738–7748. doi:10.1021/acsnano.6b03148

Cully, M. (2015). Long Live the Peptides. *Nat. Rev. Drug Discov.* 14, 750. doi:10.1038/nrd4766

Dammes, N., Goldsmith, M., Ramishetti, S., Dearling, J. L. J., Veiga, N., Packard, A. B., et al. (2021). Conformation-sensitive Targeting of Lipid Nanoparticles for RNA Therapeutics. *Nat. Nanotechnol.* 16, 1030–1038. doi:10.1038/s41565-021-00928-x

Dautel, D., and Champion, J. (2021). Protein Vesicles Self-Assembled from Functional Globular Proteins with Different Charge and Size. *Biomacromolecules* 22, 116–125. doi:10.1021/acs.biomac.0c00671

David, A. (2017). Peptide Ligand-Modified Nanomedicines for Targeting Cells at the Tumor Microenvironment. *Adv. Drug Deliv. Rev.* 119, 120–142. doi:10.1016/j.addr.2017.05.006

De La Peña, H., Madrigal, J. A., Rusakiewicz, S., Bencsik, M., Cave, G. W. V., Selman, A., et al. (2009). Artificial Exosomes as Tools for Basic and Clinical Immunology. *J. Immunol. Methods* 344, 121–132. doi:10.1016/j.jim.2009.03.011

De Rubis, G., Rajeev Krishnan, S., and Bebawy, M. (2019). Liquid Biopsies in Cancer Diagnosis, Monitoring, and Prognosis. *Trends Pharmacol. Sci.* 40, 172–186. doi:10.1016/j.tips.2019.01.006

Dharmayanti, C., Gillam, T. A., Klingler-Hoffmann, M., Albrecht, H., and Blencowe, A. (2021). Strategies for the Development of pH-Responsive Synthetic Polypeptides and Polymer-Peptide Hybrids: Recent Advancements. *Polymers* 13, 624. doi:10.3390/polym13040624

Diemer, V., Ollivier, N., Leclercq, B., Drobecq, H., Vicogne, J., Agouridas, V., et al. (2020). A Cysteine Selenosulfide Redox Switch for Protein Chemical Synthesis. *Nat. Commun.* 11, 2558. doi:10.1038/s41467-020-16359-6

Duan, R., Xu, Y., Zeng, X., Xu, J., Liang, L., Zhang, Z., et al. (2021). Uncovering the Metabolic Origin of Aspartate for Tumor Growth Using an Integrated Molecular Deactivator. *Nano Lett.* 21, 778–784. doi:10.1021/acs.nanolett.0c04520

EL Andaloussi, S., Mager, I., Breakefield, X. O., and Wood, M. J. (2013). Extracellular Vesicles: Biology and Emerging Therapeutic Opportunities. *Nat. Rev. Drug Discov.* 12, 347–357. doi:10.1038/nrd3978

Flemming, A. (2021). mRNA Vaccine Shows Promise in Autoimmunity. *Nat. Rev. Immunol.* 21, 72. doi:10.1038/s41577-021-00504-3

Foulkes, R., Man, E., Thind, J., Yeung, S., Joy, A., and Hoskins, C. (2020). The Regulation of Nanomaterials and Nanomedicines for Clinical Application: Current and Future Perspectives. *Biomater. Sci.* 8, 4653–4664. doi:10.1039/d0bm00558d

Gao, J., Chu, D., and Wang, Z. (2016). Cell Membrane-Formed Nanovesicles for Disease-Targeted Delivery. *J. Controlled Release* 224, 208–216. doi:10.1016/j.jconrel.2016.01.024

Ge, Y., Mu, W., Ba, Q., Li, J., Jiang, Y., Xia, Q., et al. (2020). Hepatocellular Carcinoma-Derived Exosomes in Organotropic Metastasis, Recurrence and Early Diagnosis Application. *Cancer Lett.* 477, 41–48. doi:10.1016/j.canlet.2020.02.003

Gebre, M. S., Brito, L. A., Tostanoski, L. H., Edwards, D. K., Carfi, A., and Barouch, D. H. (2021). Novel Approaches for Vaccine Development. *Cell* 184, 1589–1603. doi:10.1016/j.cell.2021.02.030

Geranpayehvaghei, M., Dabirmanesh, B., Khaledi, M., Atabakhshi-Kashi, M., Gao, C., Taleb, M., et al. (2021). Cancer-associated-platelet-inspired Nanomedicines for Cancer Therapy. *Wires. Nanomed. Nanobio.* 13, e1702. doi:10.1002/wnan.1702

Go, G., Lee, J., Choi, D. S., Kim, S. S., and Gho, Y. S. (2019). Extracellular Vesicle-Mimetic Ghost Nanovesicles for Delivering Anti-inflammatory Drugs to Mitigate Gram-Negative Bacterial Outer Membrane Vesicle-Induced Systemic Inflammatory Response Syndrome. *Adv. Healthc. Mater.* 8, e1801082. doi:10.1002/adhm.201801082

Gong, J., Chen, M., Zheng, Y., Wang, S., and Wang, Y. (2012). Polymeric Micelles Drug Delivery System in Oncology. *J. Controlled Release* 159, 312–323. doi:10.1016/j.jconrel.2011.12.012

György, B., Sage, C., Indzhykulian, A. A., Scheffer, D. I., Brisson, A. R., Tan, S., et al. (2017). Rescue of Hearing by Gene Delivery to Inner-Ear Hair Cells Using Exosome-Associated AAV. *Mol. Ther.* 25, 379–391. doi:10.1016/j.ymthe.2016.12.010

Han, S., Lee, Y., and Lee, M. (2021). Biomimetic Cell Membrane-Coated DNA Nanoparticles for Gene Delivery to Glioblastoma. *J. Controlled Release* 338, 22–32. doi:10.1016/j.jconrel.2021.08.021

He, H., Sun, L., Ye, J., Liu, E., Chen, S., Liang, Q., et al. (2016). Enzyme-triggered, Cell Penetrating Peptide-Mediated Delivery of Anti-tumor Agents. *J. Controlled Release* 240, 67–76. doi:10.1016/j.jconrel.2015.10.040

Huang, X., Li, M., Green, D. C., Williams, D. S., Patil, A. J., and Mann, S. (2013). Interfacial Assembly of Protein-Polymer Nano-Conjugates into Stimulus-Responsive Biomimetic Protocells. *Nat. Commun.* 4, 2239. doi:10.1038/ncomms3239

Huang, Q., Wang, L., Yu, H., and Ur-Rahman, K. (2019). Advances in Phenylboronic Acid-Based Closed-Loop Smart Drug Delivery System for Diabetic Therapy. *J. Controlled Release* 305, 50–64. doi:10.1016/j.jconrel.2019.05.029

Huang, H., Yang, X., Li, H., Lu, H., Oswald, J., Liu, Y., et al. (2020). iRGD Decorated Liposomes: A Novel Actively Penetrating Topical Ocular Drug Delivery Strategy. *Nano Res.* 13, 3105–3109. doi:10.1007/s12274-020-2980-9

Huang, H., Feng, W., and Chen, Y. (2021). Two-Dimensional Biomaterials: Material Science, Biological Effect and Biomedical Engineering Applications. *Chem. Soc. Rev.* 50, 11381–11485. doi:10.1039/d0cs01138j

Ingato, D., Edson, J. A., Zakharian, M., and Kwon, Y. J. (2018). Cancer Cell-Derived, Drug-Loaded Nanovesicles Induced by Sulfhydryl-Blocking for Effective and Safe Cancer Therapy. *Acs Nano* 12, 9568–9577. doi:10.1021/acsnano.8b05377

Ishihara, T., Takeda, M., Sakamoto, H., Kimoto, A., Kobayashi, C., Takasaki, N., et al. (2009). Accelerated Blood Clearance Phenomenon upon Repeated Injection of PEG-Modified PLA-Nanoparticles. *Pharm. Res.* 26, 2270–2279. doi:10.1007/s11095-009-9943-x

Jang, S. C., Kim, O. Y., Yoon, C. M., Choi, D.-S., Roh, T.-Y., Park, J., et al. (2013). Bioinspired Exosome-Mimetic Nanovesicles for Targeted Delivery of Chemotherapeutics to Malignant Tumors. *Acs Nano* 7, 7698–7710. doi:10.1021/nn402232g

Jang, S. C., Kim, O. Y., Yoon, C. M., Choi, D. S., Roh, T. Y., Park, J., et al. (2014). Bioinspired Exosome-Mimetic Nanovesicles for Targeted Delivery of Chemotherapeutics to Malignant Tumors. *Acs Nano.* 7, 7698–7710. doi:10.1021/nn402232g

Jiang, W., Ma, P., Deng, L., Liu, Z., Wang, X., Liu, X., et al. (2020). Hepatitis A Virus Structural Protein pX Interacts with ALIX and Promotes the Secretion of Virions and Foreign Proteins through Exosome-like Vesicles. *J. Extracell. Vesicles* 9, 1716513. doi:10.1080/20013078.2020.1716513

Jie, Z., Bxa, B., Ssc, D., Az, E., Sz, F., Jcc, D., et al. (2021). High-quality Milk Exosomes as Oral Drug Delivery System. *Biomaterials* 277, 121126.

Jo, W., Kim, J., Yoon, J., Jeong, D., Cho, S., Jeong, H., et al. (2014). Large-scale Generation of Cell-Derived Nanovesicles. *Nanoscale* 6, 12056–12064. doi:10.1039/c4nr02391a

Kataoka, K., Harada, A., and Nagasaki, Y. (2012). Block Copolymer Micelles for Drug Delivery: Design, Characterization and Biological Significance. *Adv. Drug Deliv. Rev.* 64, 37–48. doi:10.1016/j.addr.2012.09.013

Kim, J. S., Shin, D. H., and Kim, J.-S. (2018). Dual-Targeting Immunoliposomes Using Angiopep-2 and CD133 Antibody for Glioblastoma Stem Cells. *J. Controlled Release* 269, 245–257. doi:10.1016/j.jconrel.2017.11.026

Krishnan, N., Fang, R. H., and Zhang, L. (2021). Engineering of Stimuli-Responsive Self-Assembled Biomimetic Nanoparticles. *Adv. Drug Deliv. Rev.* 179, 114006. doi:10.1016/j.addr.2021.114006

Kuang, Y., Zhang, J., Xiong, M., Zeng, W., Lin, X., Yi, X., et al. (2020). A Novel Nanosystem Realizing Curcumin Delivery Based on Fe3O4@Carbon Dots Nanocomposite for Alzheimer's Disease Therapy. *Front. Bioeng. Biotechnol.* 8, 614906. doi:10.3389/fbioe.2020.614906

Li, Y., Zhang, Y., Li, Z., Zhou, K., and Feng, N. (2019). Exosomes as Carriers for Antitumor Therapy. *ACS Biomater. Sci. Eng.* 5, 4870–4881. doi:10.1021/acsbiomaterials.9b00417

Lian, Z., and Ji, T. (2020). Functional Peptide-Based Drug Delivery Systems. *J. Mater. Chem. B* 8, 6517–6529. doi:10.1039/d0tb00713g

Liang, Y., Duan, L., Lu, J., and Xia, J. (2021). Engineering Exosomes for Targeted Drug Delivery. *Theranostics* 11, 3183–3195. doi:10.7150/thno.52570

Liao, Z., Li, S., Lu, S., Liu, H., Li, G., Ma, L., et al. (2021). Metformin Facilitates Mesenchymal Stem Cell-Derived Extracellular Nanovesicles Release and Optimizes Therapeutic Efficacy in Intervertebral Disc Degeneration. *Biomaterials* 274, 120850. doi:10.1016/j.biomaterials.2021.120850

Liu, G., Zhao, X., Zhang, Y., Xu, J., Xu, J., Li, Y., et al. (2019). Engineering Biomimetic Platesomes for pH-Responsive Drug Delivery and Enhanced Antitumor Activity. *Adv. Mater.* 31, e1900795. doi:10.1002/adma.201900795

Lu, M., Zhao, X., Xing, H., Liu, H., Lang, L., Yang, T., et al. (2019). Cell-free Synthesis of Connexin 43-integrated Exosome-Mimetic Nanoparticles for siRNA Delivery. *Acta Biomater.* 96, 517–536. doi:10.1016/j.actbio.2019.07.006

Lunavat, T. R., Jang, S. C., Nilsson, L., Park, H. T., Repiska, G., Lässer, C., et al. (2016). RNAi Delivery by Exosome-Mimetic Nanovesicles - Implications for Targeting C-Myc in Cancer. *Biomaterials* 102, 231–238. doi:10.1016/j.biomaterials.2016.06.024

Meng, Q., Zhao, Y., Dong, C., Liu, L., Pan, Y., Lai, J., et al. (2021). Genetically Programmable Fusion Cellular Vesicles for Cancer Immunotherapy Angew. *Chem. Int. Ed.* 60, 26320. doi:10.1002/anie.202108342

Meng, T., Kulkarni, V., Simmers, R., Brar, V., and Xu, Q. (2019). Therapeutic Implications of Nanomedicine for Ocular Drug Delivery. *Drug Discov. Today* 24, 1524–1538. doi:10.1016/j.drudis.2019.05.006

Min, Y., Caster, J. M., Eblan, M. J., and Wang, A. Z. (2015). Clinical Translation of Nanomedicine. *Chem. Rev.* 115, 11147–11190. doi:10.1021/acs.chemrev.5b00116

Molinaro, R., Corbo, C., Martinez, J. O., Taraballi, F., Evangelopoulos, M., Minardi, S., et al. (2016). Biomimetic Proteolipid Vesicles for Targeting Inflamed Tissues. *Nat. Mater* 15, 1037–1046. doi:10.1038/nmat4644

Moreira, J. N., Ishida, T., Gaspar, R., and Allen, T. M. (2002). Use of the post-insertion Technique to Insert Peptide Ligands into Pre-formed Stealth Liposomes with Retention of Binding Activity and Cytotoxicity. *Pharm. Res.* 19, 265–269. doi:10.1023/a:1014434732752

Mu, W., Chu, Q., Liu, Y., and Zhang, N. (2020). A Review on Nano-Based Drug Delivery System for Cancer Chemoimmunotherapy. *Nano-micro Lett.* 12, 142. doi:10.1007/s40820-020-00482-6

Newman, M. R., and Benoit, D. S. W. (2018). *In Vivo* Translation of Peptide-Targeted Drug Delivery Systems Discovered by Phage Display. *Bioconjug. Chem.* 29, 2161–2169. doi:10.1021/acs.bioconjchem.8b00285

Oieni, J., Lolli, A., D'atri, D., Kops, N., Yayon, A., Van Osch, G. J. V. M., et al. (2021). Nano-ghosts: Novel Biomimetic Nano-Vesicles for the Delivery of Antisense Oligonucleotides. *J. Controlled Release* 333, 28–40. doi:10.1016/j.jconrel.2021.03.018

Pan, P., Yue, Q., Li, J., Gao, M., Yang, X., Ren, Y., et al. (2021). Smart Cargo Delivery System Based on Mesoporous Nanoparticles for Bone Disease Diagnosis and Treatment. *Adv. Sci.* 8, e2004586. doi:10.1002/advs.202004586

Panwar, N., Soehartono, A. M., Chan, K. K., Zeng, S., Xu, G., Qu, J., et al. (2019). Nanocarbons for Biology and Medicine: Sensing, Imaging, and Drug Delivery. *Chem. Rev.* 119, 9559–9656. doi:10.1021/acs.chemrev.9b00099

Park, J. H., Mohapatra, A., Zhou, J., Holay, M., Krishnan, N., Gao, W., et al. (2021). Virus-Mimicking Cell Membrane-Coated Nanoparticles for Cytosolic Delivery of mRNA. *Angew. Chem. Int. Ed.* 61, e202113671. doi:10.1002/anie.202113671

Peng, Q., Zhang, S., Yang, Q., Zhang, T., Wei, X.-Q., Jiang, L., et al. (2013). Preformed Albumin corona, a Protective Coating for Nanoparticles Based Drug Delivery System. *Biomaterials.* 34, 8521–8530. doi:10.1016/j.biomaterials.2013.07.102

Ramakrishnaiah, V., Thumann, C., Fofana, I., Habersetzer, F., Pan, Q., De Ruiter, P. E., et al. (2013). Exosome-mediated Transmission of Hepatitis C Virus between Human Hepatoma Huh7.5 Cells. *Proc. Natl. Acad. Sci. U S A.* 110, 13109–13113. doi:10.1073/pnas.1221899110

Rao, L., Cai, B., Bu, L. L., Liao, Q. Q., Guo, S. S., Zhao, X. Z., et al. (2017). Microfluidic Electroporation-Facilitated Synthesis of Erythrocyte Membrane-Coated Magnetic Nanoparticles for Enhanced Imaging-Guided Cancer Therapy. *ACS Nano* 11, 3496–3505. doi:10.1021/acsnano.7b00133

Rao, L., Bu, L. L., Ma, L., Wang, W., Liu, H., Wan, D., et al. (2018). Platelet-Facilitated Photothermal Therapy of Head and Neck Squamous Cell Carcinoma. *Angew. Chem. Int. Ed.* 57, 986–991. doi:10.1002/anie.201709457

Rao, L., Wu, L., Liu, Z., Tian, R., Yu, G., Zhou, Z., et al. (2020a). Hybrid Cellular Membrane Nanovesicles Amplify Macrophage Immune Responses against Cancer Recurrence and Metastasis. *Nat. Commun.* 11, 4909. doi:10.1038/s41467-020-18626-y

Rao, L., Xia, S., Xu, W., Tian, R., Yu, G., Gu, C., et al. (2020b). Decoy Nanoparticles Protect against COVID-19 by Concurrently Adsorbing Viruses and Inflammatory Cytokines. *Proc. Natl. Acad. Sci. U S A.* 117, 27141–27147. doi:10.1073/pnas.2014352117

Rautio, J., Kumpulainen, H., Heimbach, T., Oliyai, R., Oh, D., Järvinen, T., et al. (2008). Prodrugs: Design and Clinical Applications. *Nat. Rev. Drug Discov.* 7, 255–270. doi:10.1038/nrd2468

Rautio, J., Meanwell, N. A., Di, L., and Hageman, M. J. (2018). The Expanding Role of Prodrugs in Contemporary Drug Design and Development. *Nat. Rev. Drug Discov.* 17, 559–587. doi:10.1038/nrd.2018.46

Ravar, F., Saadat, E., Gholami, M., Dehghankelishadi, P., Mahdavi, M., Azami, S., et al. (2016). Hyaluronic Acid-Coated Liposomes for Targeted Delivery of Paclitaxel, In-Vitro Characterization and In-Vivo Evaluation. *J. Control Release* 229, 10–22. doi:10.1016/j.jconrel.2016.03.012

Sanchez-Moreno, P., Ortega-Vinuesa, J. L., Peula-Garcia, J. M., Marchal, J. A., and Boulaiz, H. (2018). Smart Drug-Delivery Systems for Cancer Nanotherapy. *Curr. Drug Targets* 19, 339–359. doi:10.2174/1389450117666160527142544

Sokullu, E., Soleymani Abyaneh, H., and Gauthier, M. A. (2019). Plant/Bacterial Virus-Based Drug Discovery, Drug Delivery, and Therapeutics. *Pharmaceutics* 11, 211. doi:10.3390/pharmaceutics11050211

Staufer, O., Dietrich, F., Rimal, R., Schroter, M., Fabritz, S., Boehm, H., et al. (2021). Bottom-up Assembly of Biomedical Relevant Fully Synthetic Extracellular Vesicles. *Sci. Adv.* 7, eabg6666. doi:10.1126/sciadv.abg6666

Sterzenbach, U., Putz, U., Low, L. H., Silke, J., Tan, S. S., and Howitt, J. (2017). Engineered Exosomes as Vehicles for Biologically Active Proteins. *Mol.* 25, 1269–1278. doi:10.1016/j.ymthe.2017.03.030

Subjakova, V., Oravczova, V., and Hianik, T. (2021). Polymer Nanoparticles and Nanomotors Modified by DNA/RNA Aptamers and Antibodies in Targeted Therapy of Cancer. *Polymers (Basel)* 13, 341. doi:10.3390/polym13030341

Suk, J. S., Xu, Q., Kim, N., Hanes, J., and Ensign, L. M. (2016). PEGylation as a Strategy for Improving Nanoparticle-Based Drug and Gene Delivery. *Adv. Drug Deliv. Rev.* 99, 28–51. doi:10.1016/j.addr.2015.09.012

Sun, T., Zhang, Y. S., Pang, B., Hyun, D. C., Yang, M., and Xia, Y. (2014). Engineered Nanoparticles for Drug Delivery in Cancer Therapy. *Angew. Chem. Int. Ed. Engl.* 53, 12320–12364. doi:10.1002/anie.201403036

Sur, S., Fries, A. C., Kinzler, K. W., Zhou, S., and Vogelstein, B. (2014). Remote Loading of Preencapsulated Drugs into Stealth Liposomes. *Proc. Natl. Acad. Sci. U S A.* 111, 2283–2288. doi:10.1073/pnas.1324135111

Tam, Y., Chen, S., Zaifman, J., Tam, Y. K., Lin, P., Ansell, S., et al. (2013). Small Molecule Ligands for Enhanced Intracellular Delivery of Lipid Nanoparticle Formulations of siRNA. *Nanomedicine* 9, 665–674. doi:10.1016/j.nano.2012.11.006

Tiwari, G., Tiwari, R., Sriwastawa, B., Bhati, L., Pandey, S., Pandey, P., et al. (2012). Drug Delivery Systems: An Updated Review. *Int. J. Pharm. Investing.* 2, 2–11. doi:10.4103/2230-973x.96920

Vietri, M., Radulovic, M., and Stenmark, H. (2020). The many Functions of ESCRTs. *Nat. Rev. Mol. Cel Biol.* 21, 25–42. doi:10.1038/s41580-019-0177-4

Votteler, J., Ogohara, C., Yi, S., Hsia, Y., Nattermann, U., Belnap, D. M., et al. (2016). Designed Proteins Induce the Formation of Nanocage-Containing Extracellular Vesicles. *Nature* 540, 292–295. doi:10.1038/nature20607

Walther, R., Rautio, J., and Zelikin, A. N. (2017). Prodrugs in Medicinal Chemistry and Enzyme Prodrug Therapies. *Adv. Drug Deliv. Rev.* 118, 65–77. doi:10.1016/j.addr.2017.06.013

Wang, D., Wang, S., Zhou, Z., Bai, D., Zhang, Q., Gao, W., et al. (2022). White Blood Cell Membrane-Coated Nanoparticles: Recent Development and Medical Applications. *Adv. Healthc. Mater.* 11, 2101349.

Wang, J., Li, Y., and Nie, G. (2021). Multifunctional Biomolecule Nanostructures for Cancer Therapy. *Nat. Rev. Mater.* 19, 1–18. doi:10.1038/s41578-021-00315-x

Wicki, A., Witzigmann, D., Balasubramanian, V., and Huwyler, J. (2015). Nanomedicine in Cancer Therapy: Challenges, Opportunities, and Clinical Applications. *J. Controlled Release* 200, 138–157. doi:10.1016/j.jconrel.2014.12.030

Worthington, P., Langhans, S., and Pochan, D. (2017). β-Hairpin Peptide Hydrogels for Package Delivery. *Adv. Drug Deliv. Rev.* 110-111, 127–136. doi:10.1016/j.addr.2017.02.002

Xiaoming, S., Zhuang, L., Kevin, W., Joshua, T. R., Andrew, G., Sasa, Z., et al. (2008). Nano-graphene Oxide for Cellular Imaging and Drug Delivery. *Nano Res.* 1, 203–212. doi:10.1007/s12274-008-8021-8

Yi, X., Zeng, W., Wang, C., Chen, Y., Zheng, L., Zhu, X., et al. (2022). A Step-by-step Multiple Stimuli-Responsive Metal-Phenolic Network Prodrug Nanoparticles for Chemotherapy. *Nano Res.* 15, 1205–1212. doi:10.1007/s12274-021-3626-2

Li, Y.-J., Wu, J.-Y., Liu, J., Xu, W., Qiu, X., Huang, S., et al. (2021). Artificial Exosomes for Translational Nanomedicine. *J. Nanobiotechnol.* 19, 242. doi:10.1186/s12951-021-00986-2

Zhao, X., Yang, X., Wang, X., Zhao, X., Zhang, Y., Liu, S., et al. (2021). Penetration Cascade of Size Switchable Nanosystem in Desmoplastic Stroma for Improved Pancreatic Cancer Therapy. *Acs Nano* 15, 14149–14161. doi:10.1021/acsnano.0c08860

Zhou, M., Luo, Y., Zeng, W., Yang, X., Chen, T., Zhang, L., et al. (2021). A Co-delivery System Based on a Dimeric Prodrug and Star-Shaped Polymeric Prodrug Micelles for Drug Delivery. *Front. Chem.* 9, 765021. doi:10.3389/fchem.2021.765021

Conflict of Interest: The authors declare that the research was conducted in the absence of any commercial or financial relationships that could be construed as a potential conflict of interest.

Publisher's Note: All claims expressed in this article are solely those of the authors and do not necessarily represent those of their affiliated organizations, or those of the publisher, the editors, and the reviewers. Any product that may be evaluated in this article, or claim that may be made by its manufacturer, is not guaranteed or endorsed by the publisher.

frontiers | Frontiers in Bioengineering and Biotechnology

REVIEW
published: 31 May 2022
doi: 10.3389/fbioe.2022.920162

Progress of Nanomaterials in Photodynamic Therapy Against Tumor

*Lei Chen[1†], Jiahui Huang[2†], Xiaotong Li[3], Miaoting Huang[3], Shaoting Zeng[3], Jiayi Zheng[3], Shuyi Peng[3] and Shiying Li[4]**

[1]Department of Anesthesiology, The First Affiliated Hospital of Guangzhou Medical University, Guangzhou, China, [2]Department of Anesthesiology, Huizhou Central People's Hospital, Huizhou, China, [3]Guangzhou Medical University, Guangzhou, China, [4]Key Laboratory of Molecular Target and Clinical Pharmacology and The State Key Laboratory of Respiratory Disease, School of Pharmaceutical Sciences and The Fifth Affiliated Hospital, Guangzhou Medical University, Guangzhou, China

Photodynamic therapy (PDT) is an advanced therapeutic strategy with light-triggered, minimally invasive, high spatiotemporal selective and low systemic toxicity properties, which has been widely used in the clinical treatment of many solid tumors in recent years. Any strategies that improve the three elements of PDT (light, oxygen, and photosensitizers) can improve the efficacy of PDT. However, traditional PDT is confronted some challenges of poor solubility of photosensitizers and tumor suppressive microenvironment. To overcome the related obstacles of PDT, various strategies have been investigated in terms of improving photosensitizers (PSs) delivery, penetration of excitation light sources, and hypoxic tumor microenvironment. In addition, compared with a single treatment mode, the synergistic treatment of multiple treatment modalities such as photothermal therapy, chemotherapy, and radiation therapy can improve the efficacy of PDT. This review summarizes recent advances in nanomaterials, including metal nanoparticles, liposomes, hydrogels and polymers, to enhance the efficiency of PDT against malignant tumor.

Keywords: photodynamic therapy, tumor microenvironment, nanomaterials, tumor-targeting, photosensitizers

OPEN ACCESS

Edited by:
Qitong Huang,
Gannan Medical University, China

Reviewed by:
Zhong Feng Gao,
Linyi University, China
Xiaofeng Lin,
Gannan Medical University, China

****Correspondence:***
Shiying Li
lisy-sci@gzhmu.edu.cn

†These authors have contributed equally to this work and share first authorship

Specialty section:
This article was submitted to Nanobiotechnology, a section of the journal Frontiers in Bioengineering and Biotechnology

Received: *14 April 2022*
Accepted: *02 May 2022*
Published: *31 May 2022*

Citation:
Chen L, Huang J, Li X, Huang M, Zeng S, Zheng J, Peng S and Li S (2022) Progress of Nanomaterials in Photodynamic Therapy Against Tumor. Front. Bioeng. Biotechnol. 10:920162. doi: 10.3389/fbioe.2022.920162

1 INTRODUCTION

PDT mainly relies on PSs to generate $^1O_2$ from O_2 under the induction of specific wavelengths of light, causing oxidative damage to tumor cells and killing them, and even triggering immunogenic cell death (ICD). However, the insufficient supply of key factors such as PSs, light, and O_2 in tumor tissue greatly reduces the therapeutic effect of PDT (Lee et al., 2022). Nanoparticles (NPs) as drug carriers have received extensive attention in the field of tumor therapy. They can achieve high-efficiency delivery of PSs to tumor tissues through physicochemically optimized passive targeting, ligand-modified active targeting, and stimulus-responsive release (Zhao et al., 2021). Attempts have been made to overcome the unfavorable tumor microenvironment through photocatalytic oxygen production, Fenton reaction, and combination with other chemical drugs (Wan et al., 2021). In this review, we first describe the composition and tumor-promoting mechanisms of the tumor microenvironment, and then introduce metal NPs, nanoliposomes, mesoporous silica NPs, dendrimers, hydrogels, polymer micelles and these creative methods to solve the problems faced by tumor PDT. In particular, in this review, we focus on recent advances in diverse metal NPs including metal-organic frameworks (MOF), which provide a promising approach for the design of integrative therapeutics in clinical treatments.

2 TUMOR MICROENVIRONMENT

TME refers to the non-cancerous cells and components presented in the tumor, including blood vessels, extracellular matrix (ECM), fibroblasts, the surrounding immune cells, molecules produced and released by them (**Figure 1**) (Chang et al., 2021). Hypoxic and acidic microenvironment, caused by tumor vascular tissue distribution disorder and structural abnormality, is the most important supporting component in TME and immunosuppressive microenvironment and has offered a favorable niche for tumor growth, proliferation and invasion (Yuan X. et al., 2022). The immune cells, including granulocytes, lymphocytes, and macrophages, are involved in various immune responses and activities orchestrated by the tumor to promote tumor survival. Among them, the macrophages abundantly infiltrating TME are called tumor-associated macrophages (tumor-associated macrophages, TAMs), which are the most prominent immune cell type in the TME. According to the difference of phenotype and function, activated macrophages can be divided into M1 and M2, and their polarization direction is regulated by microenvironment (Wang et al., 2021a). For example, tissue microenvironment, external factors and inflammatory response factors can activate macrophages in different forms (Cenowicz et al., 2021). The macrophages that promote tumor growth are M2 phenotype and have the function of repairing injury and inhibiting inflammatory response in normal tissues. The macrophages that inhibit tumor growth are M1 phenotype, which can induce inflammatory response and activate immune response to kill tumor cells (Chen J. et al., 2021). In the process of tumorigenesis, TAMs can often stimulate angiogenesis, promote tumor cell migration and invasion, and mediate tumor immune escape (De Lerma et al., 2021). In the site of tumor metastasis, TAMs promote tumor cell exosmosis, survival and follow-up activity. At the same time, TAMs affect the clinical therapeutic effect of tumors by enhancing the genetic instability of tumor cells, nourishing tumor stem cells, and promoting infiltration and metastasis, and they are the key driving force for tumor growth. The degree of macrophage infiltration in tumor tissues is related to the poor prognosis of patients, and the number of TAMs is negatively related to the survival time of patients (Munir et al., 2021). In addition, an increase in neutrophils in blood also accounts for a sign of poor prognosis for cancer. Imitating the naming method used to define macrophages (M1-like and M2-like/TAM), tumor-associated neutrophils (TANs) can obtain at least two different phenotypes: N1 neutrophils, endowed with anti-tumor activities, and N2 neutrophils endowed with immunosuppressive and pro-angiogenic properties to support tumor progression (Li et al., 2020). The tumor-promoting activity of TAN can cover a variety of mechanisms (Taucher et al., 2021). TAN can't only promote tumor angiogenesis by secreting matrix metalloproteinase-9 (MMP-9) and vascular endothelial growth factor (VEGF) from the extracellular matrix (ECM), but also inhibit CD8T cells and produce immunosuppressive environment by secreting arginase 1 (Xiao et al., 2021).

Cancer cells harbor a different metabolic profile with respect to healthy cells (Chou and Yang, 2021). Cancer cells can maintain a high rate of glycolysis even in the presence of O_2, consume large amounts of glucose and significant areas in tumors exhibit lactic acidosis. This phenomenon known as "aerobic glycolysis" or the "Warburg effect" (Yuan et al., 2021). The tumor-promoting mechanisms of TME include: 1) HIF-1α nuclear transport pathway: Hypoxia inducible factor-1 (HIF-1) is a key transcriptional activator responsible for regulating target genes that contribute to survival and growth of cells in hypoxia condition (You et al., 2021). It consists of two subunits (HIF-1β and HIF-1α) and HIF-1α is sensitive to hypoxia. Under hypoxic conditions, HIF-1 becomes a stable and transcriptionally active dimer and then induces transcriptional and post-transcriptional regulation of target genes. In addition, overexpression of HIF-1α also promotes the transcription and activation of angiogenic factors, such as angiogenin, platelet-derived growth factors, plasminogen activator inhibitors and VEGF (Sun et al., 2022). 2) STAT3 phosphorylation pathway: Acidic TME inhibits T cell activation and cytotoxicity by inducing STAT3 phosphorylation (Liang et al., 2021). 3) mTOR signaling pathway: The persistent stress of hypoxic TME leads to excessive activation of mTOR signaling in NK cells, mitochondrial fission, and impaired metabolism, ultimately leading to NK cell depletion and reduced anti-tumor ability (Liang et al., 2021). 4) VEGF pathway and nuclear transcription factor (NF-κB) pathway: Enriching cytokines such as VEGF and eosinophil chemokine (Eotaxin) in tumor tissue, inducing macrophage polarization into M2 type. M2 TAMs further produce factors such as CC motif chemokine 2 (CCL2), CC motif chemokine 5 (CCL5) or macrophage colony stimulating factor 1 (CSF-1) to participate in immunosuppression (Huang et al., 2021). 5) Promote the production of factors such as hyaluronic acid (HA) and VEGF, thereby maintaining tumor growth and migration (Niu et al., 2021).

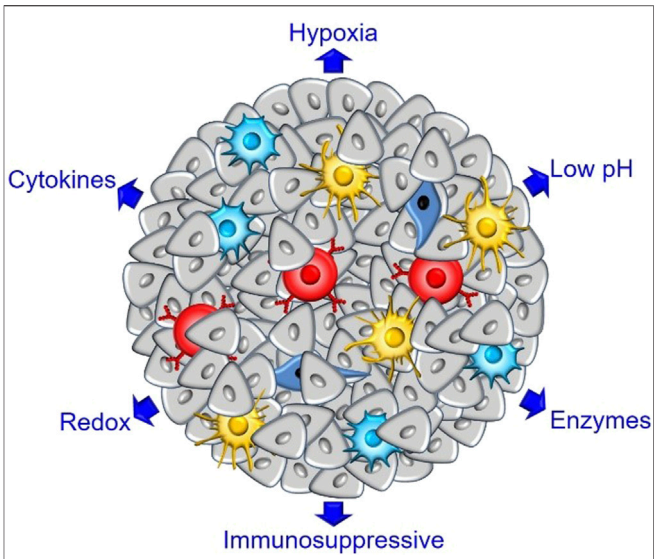

FIGURE 1 | Schematic representation of the tumor microenvironment in solid tumors.

3 PHOTODYNAMIC THERAPY

Taking advantage of the fact that PSs can't generate ROS in the dark environment, and is not toxic to cells and tissues. By finely controlling the illumination area, the PDT process can be confined within the tumor tissue, achieving highly selective killing of tumor cells and reducing the side effects of normal cell death (Lee et al., 2020). According to the different types and production methods of ROS, PDT can be divided into two mechanisms, type I and type II (Algorri et al., 2021). Type I reactions can directly react with biomolecules to produce radicals by transferring protons or electrons. In Type II reactions, the excited PS transfers energy to oxygen molecules to produce singlet oxygen ($^1O_2$). Both oxygen-containing free radicals and $^1O_2$ have extremely high reactivity, which can damage a variety of biomolecules and kill tumor cells. Type II PDT requires PSs to generate ROS. However, PSs are often excited by visible light, which limits the efficacy of PDT for deep tumors. Furthermore, due to the short intracellular half-life of ROS (≈10–320 ns), the light penetration depth and the distribution of PSs in tumor tissue limit the efficacy of PDT (Lee et al., 2022). Nanomaterials provide a powerful tool to overcome many drawbacks of PSs in cancer PDT, such as hydrophobicity, short blood circulation time after intravenous injection, which lead to insufficient accumulation, retention and internalization in tumor tissues (Silva et al., 2021). Furthermore, some multifunctional nanomaterials can increase the levels of O_2 and ROS in tissues by mediating photocatalytic oxygen production and Fenton reaction. In addition, upconverting NPs can enhance light delivery in tumor tissues by converting more penetrating NIR to visible light or preparing them as persistent luminescent NPs (Liu B. et al., 2021). In addition to enhancing PSs in tumor tissues through physicochemically optimized passive targeting, ligand-modified active targeting, and stimulus-responsive release. Nanomaterials can also be combined with chemotherapy, gene therapy, immunotherapy, photothermal therapy, hyperthermia/magnetothermal therapy, radiotherapy, sonodynamic therapy to overcome the limitations of PDT (Yang G. et al., 2021; Zhang P. et al., 2022). This study focuses on the commonly used PSs nanomodification techniques and the application of different types of novel nanomaterials for cancer treatment and diagnosis, such as nanoparticles, liposomes, hydrogels, polymers, etc.

4 STRATEGIES FOR NANOPARTICLE-BASED PHOTOCONTROLLED DELIVERY

4.1 Metal Nanoparticles

Among the NPs, metal NPs have the advantages of high biocompatibility and stability, adjustable size, good optical properties, easy surface functionalization, and a long activity period (Desai et al., 2021). They can be used as PSs, delivery carriers and up-conversion tools to improve the delivery of chemotherapy, radionuclides and antibody drugs to tumor cells.

4.1.1 Metal Based Nanoparticles

4.1.1.1 Au Based Nanoparticles

Au NPs have surface plasmon resonance (SPR), chemical inertness and excellent biocompatibility, which are mainly used as passivation agents, drug delivery agents, imaging agents, and photothermal agents, which have different characteristic shapes, such as particles, rod-shaped, cluster-shaped, shell-shaped, spike-shaped and star, etc., (Younis et al., 2021). In PDT, gold nanoparticles can be used alone or as part of a multifunctional nanomaterial hybrid system for PSs delivery.

DNA is considered to be one of the best components for building nanomaterials due to its excellent sequence specificity and programmable supramolecular self-assembly. Among them, functional modification of nanomaterials can significantly improve the cellular stability of DNA nanomaterials. Based on this, Yu et al. utilized doxorubicin (Dox), antisense DNA (target Survivin mRNA) that could inhibit Survivin expression, photosensitizer (ZnPc), and Au NPs with excellent plasmonic properties, to develop a multifunctional nanotherapeutic platform with both diagnostic and therapeutic functions, termed Apt-DNA-Au nanomachines, for *in situ* imaging and targeted PDT/PTT/CDT synergistic therapy of breast cancer (**Figure 2**) Yu et al. (2021). Moreover, the tightly packed DNA sequences on the surface of nanomaterials were used as highly specific aptamers, which not only resisted the enzymatic hydrolysis of DNA sequences, but also improved the tumor targeting of PDT (Lv et al., 2021). Su et al. took persistent luminescent nanoparticles (PLNPs) as the core, and formed a novel nanoprobe TCPP-gDNA-Au/PLNP for persistent luminescence imaging-guided photodynamic therapy by coupling DNA sequences containing AS1411 aptamers through AuNPs Su et al. (2021). PLNPs could emit long-term fluorescence under near-infrared light irradiation. The AS1411 aptamer could specifically recognize the overexpressed nucleolin in cancer cells and improve the tumor targeting of the photosensitizer TCPP. Furthermore, increasing the types of DNA modified on the surface of NPs can improve the accuracy of PDT tumor identification. Cai et al. designed and synthesized a nano-therapeutic platform for fully automatic diagnosis and treatment of Au/Pd nanomachines with the main marker miRNA-21 and two auxiliary markers miRNA-224 and TK-1 mRNA as the targeted detection unit (Au/Pd ONP-DNA nanomachine) Cai X. et al. (2021). Using ONPs as a carrier, when all specified targets were detected [logic system input was (1, 1, 1), output was (1, 1)], the 808 nm laser could be programmed to automatically irradiate the tumor and perform PDT and PTT. However, the stability of the Au-S bond is poor, and the DNA is non-specifically detached from the surface of AuNPs, resulting in false positive signals and severe side effects. Zhang et al. used a simple and highly stable amide bond (-CO-NH-) instead of the Au-S bond and combined the DNA probe on Au@graphene (AuG) to prepare Label-rcDNA-AuG Zhang J. et al. (2021). Label-rcDNA-AuG could improve the anti-interference ability of nanoprobes against nucleases, GSH and other biological agents. By accurately monitoring the level of intracellular miR-21, Label-rcDNA-AuG could identify positive

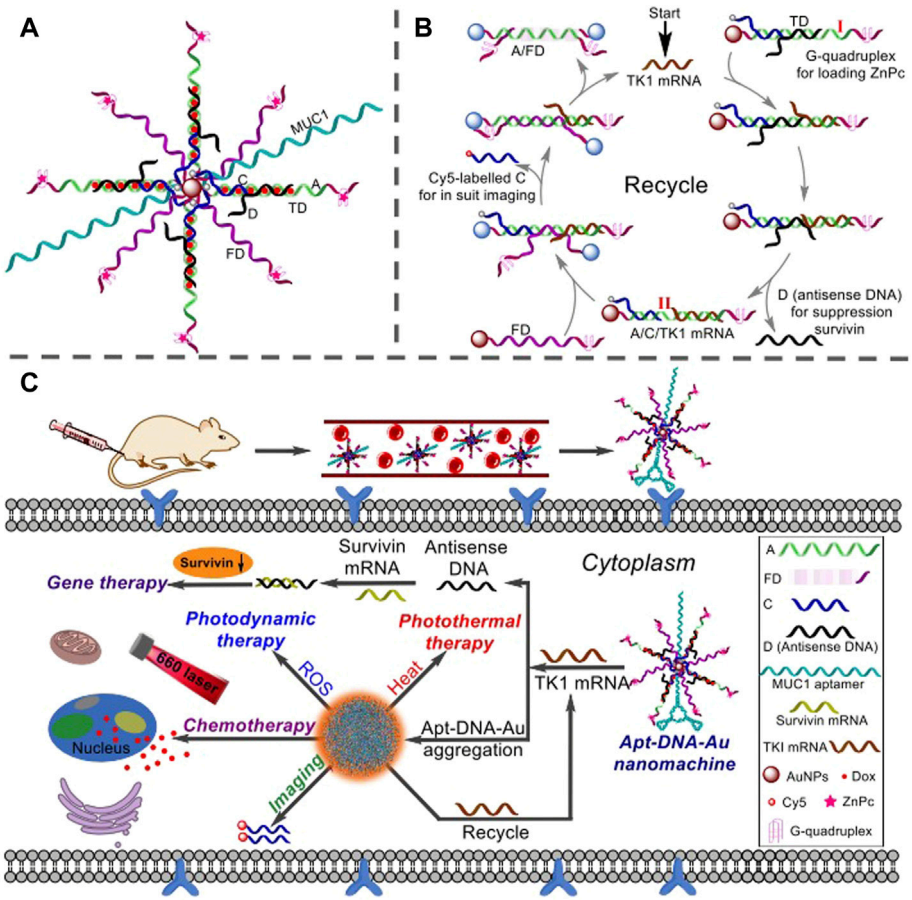

FIGURE 2 | Multifunctional Apt-DNA-Au nanomachines for *in situ* imaging and targeted multimodal synergistic cancer therapy. **(A)** Schematic diagram of the structure of the Apt-DNA-Au nanomachine. MUC1 segment is an aptamer that specifically recognizes MCF-7 cells; A segment and Fd segment contain G-quadruplex structure for loading photosensitizer (ZnPc); C segment is labeled with Cy5 for *in situ* fluorescence imaging; D segment is incorporated into antisense DNA that inhibits Survivin expression for inhibiting tumor cell proliferation; TD segment is an A/C/D mixture loaded with Dox. **(B)** Working principle of the Apt-DNA-Au nanomachine. **(C)** Apt-DNA-Au nanomachines specifically recognize and internalize to target cancer cells, and monitor tumor therapeutic effects in real time through *in situ* fluorescence imaging and multimodal anticancer therapy (combined with chemotherapy, gene therapy, PDT, and PTT). Reproduced with permission from (Yu et al., 2021).

cancer cells even in a mixture of cancer cells and normal cells, improving the precision of PDT treatment and reducing damage to normal cells.

Besides DNA modification, surface modification of biotin (Bt) is also an effective way to improve the tumor targeting of NPs (Li J. et al., 2021). The targeting of Bt-modified Au-NPs (BT@Au-NPs) to C6 glioma cells was more than 2 times that of Au-NPs (He F. et al., 2021). Modification of arginine (R)-glycine (G)-aspartic acid (D) (RGD) on the surface of NPs, which could bind to integrin $\alpha_v\beta_3$ integrin with high affinity, could not only improve the anticancer ability of NPs, but also reduced tumor migration rate. The HB-AuNRs@cRGD prepared by Liu et al. had a tumor inhibition rate of up to 77.04% in the ECA109 esophageal cancer model, and significantly reduced the migration and invasion of cancer cells in ECA109 cells Liu D. et al. (2021).

Besides improving the PDT efficiency of Au-NPs in combination with other nanomaterials, oxygen production can also be optimized by changing the physical structure of Au-NPs. By adjusting the ratio of silicon core radius and gold shell thickness, Sajid et al. enhanced the field strength of Au nanoshells with 40/20 core radius/shell thickness by 35 times and increased $^1O_2$ yield by 320% compared to before optimization (Farooq and de Araujo, 2021). Furthermore, the introduction of ionic complexes assembled by heterometallic colloids (Mo_6-Au_2) can affect the cytotoxicity, cellular internalization and PDT activity of NPs by regulating the order of their supramolecular stacking (Kirakci et al., 2021). For example, through the 1:1 binding of $[Mo_6I_8(L')_6]^{2-}$ (L′ = I-, CH_3COO-) with $[Au_2L_2]^{2+}$ (L was the ligand of cyclic double amines and phosphine), Faizullin et al. synthesized a heterometallic colloids composed of positively and negatively charged metal-organic complexes Faizullin et al. (2021). Among them, the cellular internalization of Mo_6-Au_2 (L′ = CH_3COO-) assembled with poly-DL-lysine (PL) exhibited a three-fold enhancement when L′ = CH_3COO- and could accumulates in the cytoplasm by fast endo-lysosomal escape. In addition, the

photodynamic effect of $[Mo_6I_8 (L')_6]^{2-}$ clusters was much higher at L′ = CH_3COO- than at L′ = I-. In recent years, bimetallic NPs are also improving the therapeutic efficiency of PSs due to the inherent properties of the introduced metal elements and the interaction between two metal atoms (Park et al., 2021). He et al. synthesized Au_1Bi_1-SR NPs by introducing Bi into captopril-coated Au NPs (Au-SR NPs) by utilizing the X-ray CT signal enhancement effect of Bi He G. et al. (2021). Au_1Bi_1-SR NPs not only exhibited higher ROS yield than Au-SR NPs, but also enabled CT imaging-guided and light-mediated PDT for synergistic tumor therapy. In addition, Jia et al. further modified Au-Bi bimetallic nanoparticles with IR808 fuel and prepared Au-BiGSH@IR808 to obtain higher NIR photon capture ability, which effectively solved the problem of low absorption rate of Au-Bi nanoparticles in the near-infrared region Jia et al. (2021). Noble metal Pt nanozymes have catalase-like activity (Cao et al., 2021). Truncated octahedral Au (ToHAu) can enhance LSPR by increasing the spatial separation and realizing the simultaneous participation of holes and electrons in the reaction due to the special structure of twin planes and stacking faults (Yoon et al., 2017). Accordingly, Bu and his team designed and synthesized a comprehensive phototherapy nanomodulator (ToHAu@Pt-PEG-Ce6/HA) based on the enhanced LSPR effect Bu et al. (2021). Pt was deposited on ToHAu to form a spatially separated structure, which enabled the reactive molecules to freely enter the hot holes and electron fluxes, and had strong photothermal and photodynamic properties. The antitumor effect of NPs is also closely related to their size. For example, large NPs (>100 nm), despite their enhanced permeability and penetration (EPR) effect, cannot fully infiltrate into tumor tissue due to dense extracellular matrix and elevated interstitial fluid pressure (Zmerli et al., 2021). In contrast, small NPs (<20 nm) exhibited better tumor penetration but were easily cleared by the blood circulation. Therefore, it is particularly important to design a TME-responsive size-tunable NPs. To this end, Liu et al. designed and prepared Au-MB-PEG NPs by exploiting the efficient polymerization ability of AuNPs and the excellent performance of TME ROS-triggered HOCl-responsive platform Liu H. et al. (2021). Small-sized Au-MB-PEG NPs responded to highly expressed HOCl in the tumor region through a HOCl-sensitive molecule (FDOCl-24). After reaching the tumor tissue, Au-MB-PEG NPs were cleaved by HOCI to release Au NPs that rapidly aggregated into larger aggregates in the tumor through electrostatic interactions, and simultaneously released methylene blue as a photosensitizer for photodynamic therapy (PDT). The aggregated AuNPs red-shifted the light absorption to the NIR region, resulting in enhanced photoacoustic imaging (PAI) and PTT under laser irradiation.

4.1.1.2 Ag Based Nanoparticles

Ag NPs have higher $^1O_2$ yield than Au NPs and Pt NPs due to stronger SPR (Younis et al., 2021). Inspired by the ability of ICD to transform tumors from cold to heat by inducing tumor cells to release tumor antigens and damage-associated molecular patterns (DAMPs) and then enhance T cell proliferation and infiltration (Xu et al., 2022). Jin et al. developed a corn-like Au/Ag nanorod (Au/Ag NR) that could induce ICD in tumor cells under NIR-II (1064 nm) light irradiation (**Figure 3**) Jin F. et al. (2021). They covered the Ag shell on Au NRs, and by changing the amount of Ag^+, the SPR band in the vertical region with higher $^1O_2$ yield was red-shifted to the NIR-II window. In addition, Au/Ag NRs could maintain the immune memory effect for up to 40 days in animal experiments by enhancing the therapeutic effect of immune checkpoint blocking (ICB). Wang and his team further used DNA probe technology to prepare the DNA-functionalized nanoprobe Au-AgNP-Ag-HM loaded with the photosensitizer hematoporphyrin monomethyl ether (HMME) Wang et al. (2021b). Au-AgNP-Ag-HM not only had the ROS production mediated by the LSPR signal change of Au-Ag-HM and photosensitizer HMME, but also had fluorescent probe technology mediated by caspase-3 specific recognition sequence (DEVD), which effectively integrate the functions of pro-apoptosis and detection, and can be used for the treatment and efficacy evaluation of tumor cells.

4.1.1.3 Cu Based Nanoparticles

Cu-based Fenton reagents have superior ROS yields to Fe-based systems (Zhu F. et al., 2021). In addition, Cu-doped layered double hydroxide (Cu-LDH) nanosheets can not only further enhance the yield of ROS, but also take advantage of the small size and positive charge to actively infiltrate cancer cells for deep tumor therapy (Wu et al., 2021). But positively charged NPs have a shorter residence time in the blood circulation than negatively charged NPs (Smith et al., 2019). To this end, Wu and his team used negatively charged liposomes to encapsulate Cu-LDH (Cu-LDH@Lips) and embedded HMME into the bilayer of CuLDH@Lips, forming a dual size/charge switchable reactive oxygen species generator (Cu-LDH/HMME@Lips) (**Figure 4**) Wu et al. (2021). Liposomes could prolong the residence time in the circulatory system by reducing the clearance of Cu-LDH/HMME@Lips by immune cells, and HMME could disintegrate Cu-LDH/HMME@Lips in response to ultrasound to release positively charged Cu-LDH, which could penetrate deep into tumor cells and then caused oxidative stress damage to tumor cells through Fenton-like reaction. Similarly, Wang et al. prepared ICG/CAC-LDH nanosheets by intercalating indocyanine green (ICG) into a hydrophobic bilayer of Ce-doped Cu-Al layered double hydroxide (CAC-LDH) Wang X. et al. (2021). ICG/CAC-LDH could not only induce the depletion of intracellular GSH, but also decompose to generate Cu^+ and Ce^{3+} to stimulate the Fenton-like reaction to generate OH.

4.1.1.4 Ruthenium Based Nanoparticles

Ru complexes are commonly used as PDT PSs due to their high water solubility, photostability, and high ROS yield (Smithen et al., 2020). However, it has the disadvantages of dark toxicity, DNA mutation and being excited only by short-wave visible light, which limit its clinical application (Chen M. et al., 2021). To this end, He et al. synthesized a new red light-responsive Ru complex PSs (Ru-I) without two-photon activation, by using large conjugated indolepyridine benzopyrans as ligands He Y. et al. (2021). Positively charged Ru-I could effectively target cancer cell

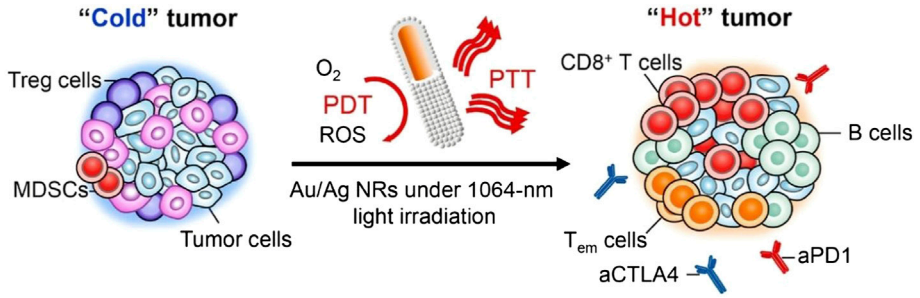

FIGURE 3 | Illustration of Corn-like Au/AgNR-mediated antitumor immune responses. Corn-like Au/Ag NR-mediated NIR-II PTT/PDT significantly increased the expression of calreticulin, high-mobility group box 1, and adenosine triphosphate in tumor cells, reprogramming the immunosuppressive cold tumor microenvironment to immunogenic heat tumor, which achieve the combined anti-cancer activity with the ICB antibody and effectively inhibit the growth of distant tumors and prevent tumor recurrence. Reproduced with permission from (Jin L. et al., 2021).

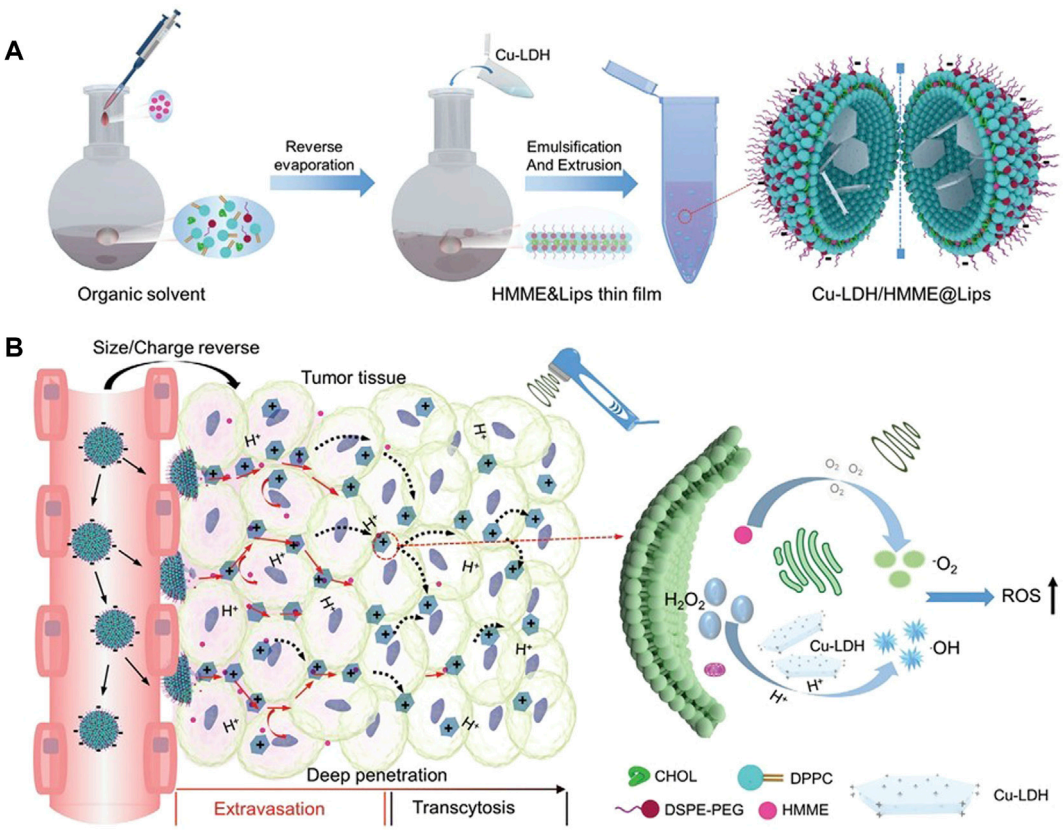

FIGURE 4 | Schematic diagram of the synthesis and working principle of Cu-LDH/HMME@Lips. **(A)** Schematic diagram of the synthesis of Cu-LDH/HMME@Lips. **(B)** Schematic diagram of the working principle of Cu-LDH/HMME@Lips. Dual-size/charge-switchable Cu-LDH/HMME@Lips utilizes negatively charged liposomes to prolong circulation residence time in low-permeability solid tumor models, and then HMME decompose Cu-LDH/HMME@Lips in response to ultrasound to release positively charged Cu-LDH, which can penetrate deep into tumor cells. HMM generates $^1O_2$ under ultrasound irradiation, while Cu-LDH infiltrates deep in tumor generates ROS through a Fenton-like reaction. Reproduced with permission from (Wu et al., 2021).

lysosomes and activate PSs under 660 nm red light to induce apoptosis. In addition, Karges et al. proposed to wrap Ru (II) polypyridine complexes with amphiphilic polymer DSPE-PEG_{2000}-folate to prepare nanoparticles without dark toxicity, which could target cancer cells overexpressing the folate receptor Karges et al. (2021). It exhibited significant phototoxicity under irradiation at 480 or 595 nm and induced tumor cell apoptosis through the caspase3/7 pathway. Furthermore, this complex not only shown the highest 1- and 2-photon absorption to date, but also exhibited properties of inhibiting multidrug-resistant tumors

in a rat model. In addition to the introduction of folate groups, bio-orthogonal labels such as copper-catalyzed azide-alkyne cycloaddition (CuAAC) are also effective methods to improve tumor cell recognition (Kappenberg et al., 2022). Lin et al. prepared the first bio-orthogonal two-photon PSs based on Ru (II) complexes by bio-orthogonally labeling Ru-alkynyl-2 Lin C.-C. et al. (2021). In addition to generating ROS to exert cytotoxic effects, it could also exert anti-tumor effects by specifically binding to cancer cell membranes and inducing membrane damage.

4.1.1.5 Iridium Based Nanoparticles

In recent years, new photoredox catalyst systems based on Ir compounds have been widely used in catalysis and PDT, and can also be used to prepare new PSs (Raza et al., 2021). Liu and his team prepared two Ir (III) complex dimers that could self-assemble into NPs in aqueous media, named Ir1 and Ir2 Liu J. et al. (2021). Ir1 and Ir2 not only enhance cancer cell uptake through positive charges on the surface, but also exhibit type I and type II PDT activity in the 350–500 nm (UV-Vis spectrum) range, even in hypoxic microenvironments. Ir NPs might be promising alternatives to traditional organic PSs. Ir (III) complexes show great potential in the construction of oxygen-sensitive sensing probes due to their unique oxygen quenching pathway (Yasukagawa et al., 2021). Xiao et al. designed and synthesized a red light-excited Ir (III) complex encapsulated in the hydrophobic pocket of Cyanine7-modified β-cyclodextrin (β-CD) Xiao and Yu (2021). Ir (III) complexes achieved different degrees of oxygen quenching according to the change of oxygen concentration in the environment. β-CD could not only be used to improve the water solubility of Ir (III) complexes, but also be used to carry Cyanine7 to establish a proportional oxygen fluorescent probe. The results of *in vitro* and *in vivo* experiments shown that the prepared probe had remarkable oxygen sensitivity and could be used for quantitative determination of the oxygen level in the hypoxic microenvironment of solid tumors. Mitochondria are not only the decisive regulators of cellular metabolic function and apoptosis, but also the organelles with the highest intracellular oxygen concentration (Tabish and Narayan, 2021). Therefore, the preparation of PSs that target the mitochondria of cancer cells will be the key to maximize the therapeutic potential of PDT. Recently, Redrado et al. prepared four novel mitochondria-selective trackable PSs, which are called bifunctional Ir (III) complexes of the type [Ir $(CN)_2$ (NN-R)]+, where NC is either phenylpyridine (PPY) or benzoquinoline (BZQ), NN is 2,20-dipyridylamine (Dpa), and R either anthracene (1 and 3) or acridine (2 and 4) (Redrado et al., 2021). Only complex 4 ([Ir $(Bzq)_2$ (dpa-acr)]+) clearly shown a dual emission mode. The organic luminescent chromophore (acridine) could display the cellular localization of the complexes under irradiation at 407–450 nm. Ir (III) had more than 110-fold higher photosensitivity values under 521–547 nm irradiation than under dark conditions, and promoted apoptotic cell death and a possible apoptotic pathway by generating ROS. Although two-photon near-infrared photoactivation can partially overcome the lack of absorption or weak absorption of Ir (III) complexes in the red to near-infrared region, the requirements of ultrafast femtosecond laser source and small irradiation area limits its application in solid tumor therapy. To this end, Liu and his team designed and synthesized bifunctional micelles (Micelle-Ir) for synergistic PDT and PTT therapy *in vivo* (**Figure 5**) Liu N. et al. (2021). They were prepared by micellization of a neutral Ir (III) complex (BODIPY-Ir) containing a distyryl boron-dipyrrole methylene group (BODIPY-Ir). BODIPY enabled BODIPY-Ir to acquire the ability to absorb in the far-red/near-infrared region, and micellization enabled BODIPY-Ir to acquire the ability to synergize PDT and PTT therapy, not only destroying primary 4T1-Luc tumors, but also preventing lung metastases.

4.1.2 Metal Oxide-Based Nanoparticles

Metal oxide nanomaterials have found promising biomedical applications for fluorescent labeling due to the advantages of high photostability, large extinction coefficient, high emission quantum yield and easy surface modification (Younis et al., 2021). In view of the fact that nano-heterostructures can promote photo-induced electron-hole separation and the generation of ROS, 2D nano-heterostructure-based PSs can provide a major advancement in PDT. Qiu et al. designed and synthesized a bismuthene/bismuth oxide (Bi/BiO_x)-based lateral nano-heterostructure synthesized by a regioselective oxidation process Qiu et al. (2021). Upon irradiation at 660 nm, the heterostructure could effectively generates $^1O_2$ under normal oxygen conditions but produces cytotoxicity OH and H_2 under hypoxic conditions, which synergistically improves the intensity of PDT. In addition, this Bi/biox nano-heterostructure had biocompatibility and biodegradability, with the surface molecular engineering used here, it improved the penetrability of tumor tissue and increased the cellar uptake, and then produced an excellent oxygen-independent tumor ablation effect. Iridium dioxide (IrO_2) with semiconductor behavior has high catalytic activity for oxygen release reaction (OER) in a wide pH range, and also has excellent photocatalytic efficiency (Arias-Egido et al., 2021). For this, Yuan et al. synthesized IrO_2-Gox@ HA NPs that could target TME by combining glucose oxidase (GOx) and IrO_2 NPs on hyaluronic acid (HA) Yuan Y. et al. (2022). First, Gox converted the high levels of glucose in tumors to H_2O_2, and then IrO_2 NPs converted H_2O_2 to O_2, thereby enhancing type II PDT, which could effectively alleviate hypoxia in tumor tissues.

Relevant literature points out that the larger the specific surface area of the sheet-like structure, the higher the zeta potential, and the greater the drug-carrying capacity of nanomaterials (Duo et al., 2021). Dai et al. synthesized a radiosensitizer based on 4-layer O-Ti_7O_{13} nanosheets by using two-dimensional titanium peroxide nanomaterials with mesoporous structure to support DOX Dai Y. et al. (2021). O-Ti_7O_{13} could quickly load the drug within 5 min while other nanomaterials need 24 h and release the drug continuously in an acidic microenvironment. In addition, under the action of high-energy X-rays, titanium dioxide could absorb radiation energy to synthesize ROS and kill tumor cells.

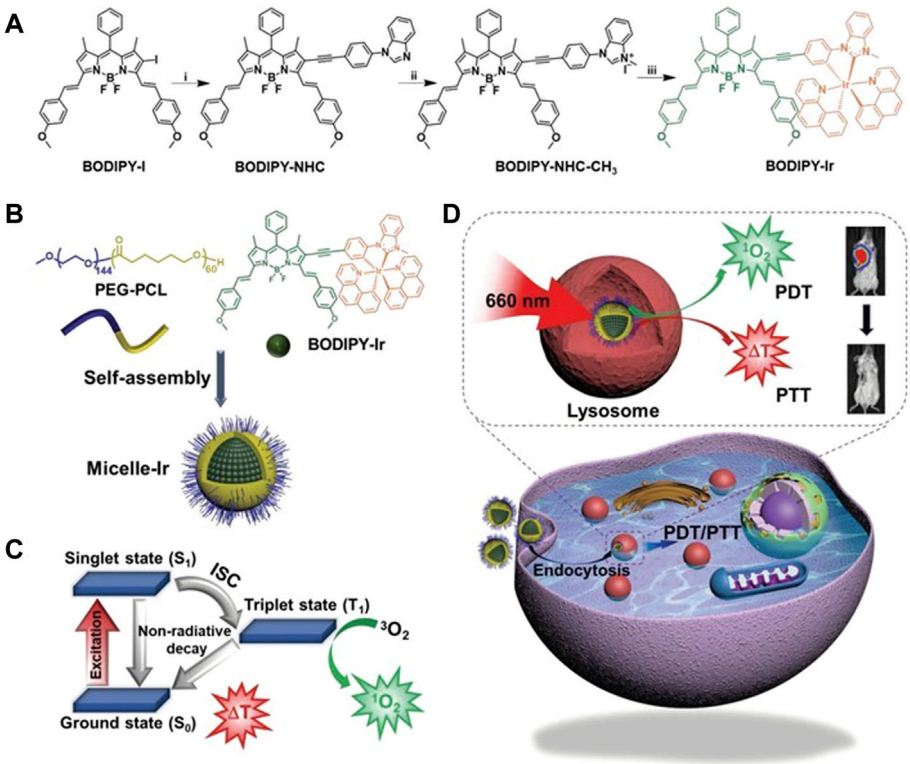

FIGURE 5 | Schematic diagram of synthesis of BODIPY-IR and schematic diagram of PDT/PTT synergistic therapy mechanism. **(A)** Schematic synthesis of BODIPY-IR: Reagents and conditions: 1) 1-(4-ethynylphenyl)-1H-benzo [d]imidazole, CuI, Pd (PPh3)4, THF, TEA, 50°C, 16 h; 2) MeI, THF, 100°C, 24 h; 3) [Ir (benzo [h] quinoline)2 (μ-Cl)]2, Ag2O, 1,2-dichloroethane, reflux, 24 h. **(B–D)** Schematic representations of Encapsulation of BODIPY-Ir into micelles for constructing Micelle-Ir. **(B)** PEG-PCL-encapsulated BODIPY-Ir self-assembles into Micelle-Ir. **(C)** Photophysical processes of PDT and PTT. **(D)** Michelle-Ir-mediated PDT/PTT synergistic therapy *in vivo*. Reproduced with permission from (Liu S. et al., 2021).

O-Ti_7O_{13} could reduce the X-ray dose and irradiation frequency, and reduce damage to normal tissues while ensuring the therapeutic effect. Mn^{3+}-rich oxides (MnO_x) can be decomposed into catalytically competent Mn^{3+} and Mn^{2+} in TME, accelerating the conversion of endogenous O_2 into highly toxic $^1O_2$ and OH. Meanwhile, the released Mn^{2+} can be used as a magnetic resonance imaging agent with higher spatial resolution. Studies have shown that Zinc gallogermanate (ZGGO) persistent luminescent NPs can be loaded with therapeutic drugs to achieve long-term imaging tracking of drugs and significant tumor treatment effects. To improve the poor resolution of ZGGO, Ding et al. used MnO_x to coat chromium-doped ZGGO NPs (Mn-ZGGO) Ding D. et al. (2021). Mn-ZGGO could not only generate $^1O_2$ and OH without light, but also serve as a diagnostic tool for MR, US, and sustained luminescence to guide precise cancer therapy. Similarly, Li and his team used MnO_2 and IrO_2 to prepare nanozymes (MnO_2/IrO_2-PVP, MIP NPs) to combine photothermal effect, catalytic effect and magnetic resonance imaging function Li R. et al. (2021). IrO_2 enabled the photothermal conversion efficiency of MIP NPs to reach 27.57%. Polyvinylpyrrolidone (PVP) enabled the Ce6 loading efficiency of MIP NPs to be as high as 76.07 ± 0.52%, and could shed PVP from the surface of MIP NPs in an acidic microenvironment, realizing the local enrichment of MIP NPs at tumor. Besides MnO_2, CeO_2 also has similar functions to catalase (CAT) and superoxide dismutase (Yang Y.-L. et al., 2021). Zeng et al. prepared a dual-targeted tumor drug delivery system (ICG@PEI–PBA–HA/CeO_2) by using ICG, inorganic nanozyme (HA/CeO_2) and pH-sensitive cationic polymer carrier phenylboronic acid-modified polyethyleneimine-4-carboxyphenylboronate (PEI-PBA) Zeng et al. (2021). After ICG@PEI–PBA–HA/CeO_2 targeted cancer cells with HA, the CeO_2 released from the pH cleavage reaction of phenylboronic acid catalyzeed H_2O_2 to generate O_2 through the cerium valence cycle of Ce^{3+}/Ce^{4+}. The regenerable CAT-like nanozyme activity of CeO_2 increased the bioavailability of ICG and promoted tumor cell apoptosis by improving the tumor hypoxic microenvironment.

The efficacy of PDT/PTT combination therapy was better than that of PDT or PTT monotherapy. Traditional PDT/PTT synergistic therapy requires two light sources to excite the PSs of PDT and the thermosensitive agent of PTT respectively, which increases the difficulty of nanoparticle preparation. Guo and his team used B-TiO_2 with oxygen vacancies and narrow band gaps to prepare a nanothermosensitive system (B-TiO_2@SiO_2-HA) with full-spectrum response to light stimulation Guo et al. (2021). Under NIR-II laser irradiation, B-TiO_2@SiO_2-HA

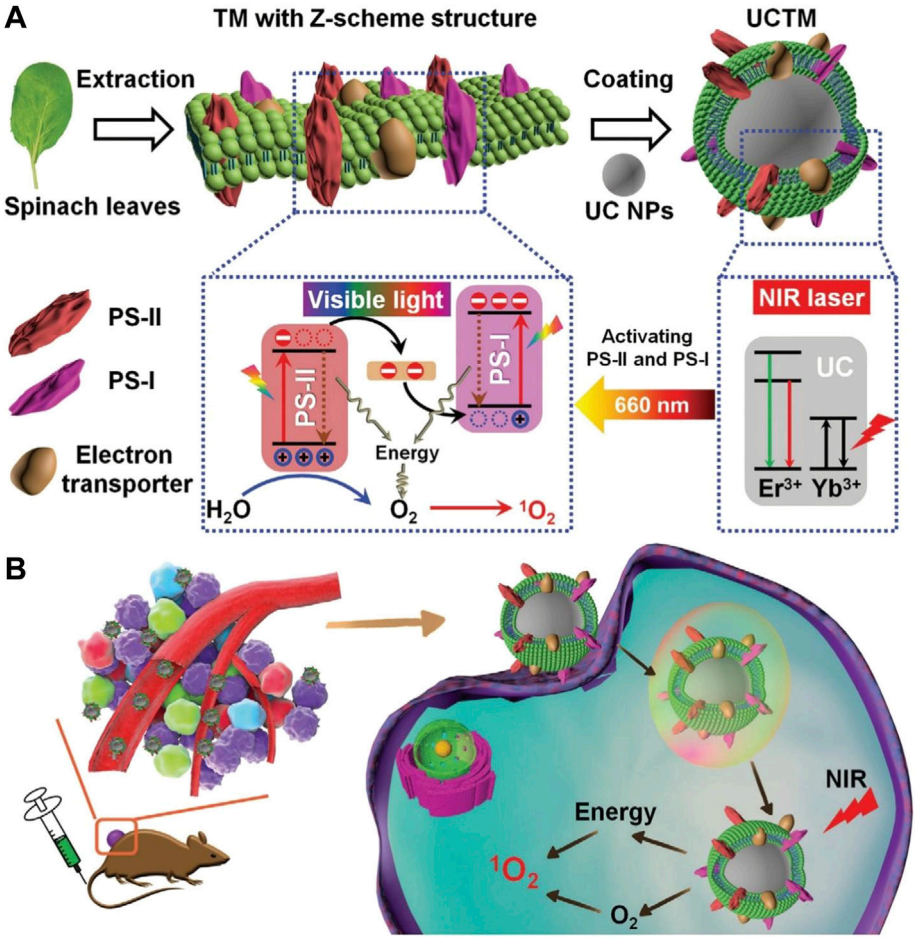

FIGURE 6 | Schematic illustration of the PDT effect of UCTM NPs on hypoxic TME. **(A)** The fabrication process of UCTM NPs. The corresponding electron transfer of UCTM NPs under NIR laser irradiation and the mechanism for realizing spatiotemporally synchronized O_2 self-supply and ROS production. **(B)** The therapeutic process of oxygen supply and ROS generation by UCTM NPs under NIR laser irradiation. Reproduced with permission from (Cheng Y. et al., 2021).

could not only provide PDT/PTT synergistic therapy for tumors, but also perform high-resolution photoacoustic imaging (PAI) to achieve precise nanothermothermal effects. Similarly, Gao and his team used SnO_{2-x} with oxygen vacancies to prepare a multifunctional nano-thermosensitive material (SnO_{2-x}@SiO_2-HA) with a target-specific synergistic PDT/PTT with full spectrum response Gao et al. (2021a). In addition to exerting precise PDT/PTT synergistic antitumor therapeutic effect through PAI, SnO_{2-x}@SiO_2-HA also had antibacterial effect, which effectively promotes the healing of skin wounds. But most metal or carbon NPs are toxic to normal cells or tissues. Sengupta et al. used the biosafety and magnetic properties of magnetite (Fe_3O_4) nanoparticles to synthesize a new PS E-NP with anti-inflammatory and immunoprotective effects Sengupta et al. (2022). E-NP could not only upregulate the expression of cyclin kinase inhibitory protein p21, but also inhibit cancer cell cycle arrest in sub-G0G1 phase. It also acted as an anti-inflammatory by reducing macrophage myeloperoxidase (MPO) and nitric oxide (NO) release, thereby minimizing collateral damage to healthy cells.

4.1.3 Upconversion Nanoparticles

UCNPs have nonlinear anti-Stokes properties and can emit high-energy photons under low-energy NIR light excitation through lanthanide ion doping. UCNPs also have the advantages of low toxicity, narrow emission bandwidth, large decay time, resistance to photobleaching, and no autofluorescence background (Liu et al., 2022). The emission wavelength of UCNPs can be controllably adjusted from ultraviolet light to near-infrared light to match PSs with different absorption wavelengths, which provides a new method to solve the problem of PDT light penetration depth (Zhang L. et al., 2021). The photosystem-I/photosystem-II (PS-I/PS-II) PDT system can only be excited by red light to generate O_2, so that it can quickly supply its own O_2 consumption in $^1O_2$ production, showing a spatiotemporal synchronous system of O_2 self-supply and ROS production. However, the tissue penetration ability of red light is unsatisfactory, so it is unsuitable for the removal of deep tissue tumors (Fakurnejad et al., 2019). Recently, Cheng et al. used the ability of UCNPs can emit red light to activate PS-I and PS-II under NIR light, decorated thylakoid membrane of

chloroplasts on UCNPs to form UCTM NPs, and developed a new photosynthesis-based PDT strategy for realizing spatiotemporally synchronous O_2 self-supply and ROS production (**Figure 6**) Cheng X. et al. (2021). Both *in vitro* and *in vivo* assessments prove that UCTM NPs can effectively relieve hypoxia, induce cell apoptosis, and eliminate tumors with NIR light irradiation. A large amount of APT produced during the ICD process can be hydrolyzed by the extracellular enzyme CD73 into ADO (immunosuppressant), which prevents the cytotoxic T-cell immune response (Workenhe et al., 2021). To this end, Jin and his team prepared cancer-cell-biomimetic UCNPs (CM@UCNP-Rb/PTD) by exploiting the properties of anti-CD73 antibody to block the adenosine pathway Jin F. et al. (2021). CM@UCNP-Rb/PTD utilized the cancer cell membrane (CM) to target cancer cells and avoid macrophage uptake. After reaching the tumor tissue, UCNPs converted NIR into visible light to generate ROS, and released DOX to achieve a Chemo-PDT synergistic combination therapy. CD73-blocked CM@UCNP-Rb/PTD enhanced spontaneous antitumor immunity through the combined effect of chemotherapeutic drugs, PDT-triggered ICD and CD73 blockade. In immunotherapy, ligands that block PD-L1 can also directly prevent PD-1/PD-L1 immune blockade (Lee et al., 2021). Liu and his team modified UCNPs with MIPs formed by Pd-L1 peptide phase transfer imprinting, and prepared MC540/MNPs@MIPs/UCNP composite imprinted particles Lin M. et al. (2021). MC540/MNPs@MIPs/UCNP utilized MIPs to target tumor cells, which improved the binding rate to tumor cells and achieved targeted PDT. The nucleus is the control center of cellular biological activities, and targeting PDT to the nucleus can lead to severe DNA damage and inactivation of nuclear enzymes (Teng et al., 2021). Base on this, Chen and his team proposed a PDT strategy of "one treatment, multiple irradiation" Chen X. et al. (2021). They modified hollow mesoporous silica nanoparticles with amine group with acidification effect and loaded RB and UCNPs to synthesize UCNP/RB@mSiO_2-NH based on the lysosome-nucleus pathway. After UCNP/RB@mSiO_2-NH entered the lysosome, it entered the nucleus through the nuclear pore by generating ROS and destroying the lysosome under the first 980 nm (3 min) NIR irradiation. Subsequently, efficient nuclear-targeted PDT was achieved under a second 980 nm NIR irradiation. Dual PSs PDT is also one of the effective strategies to improve ROS yield. Pham and his team utilized SiO_2-coated core-shell UCNPs to support two PSs (Rb and Ce6) to form UCNP/RB, Ce6 Pham et al. (2021). UCNP/RB, Ce6 produced a large amount of $^1O_2$ under 1550 nm NIR-IIb irradiation, which had higher PDT efficiency than single PS. However, the application of UCNPs in the biomedical field still faces challenges due to the low quantum yield and superheating effect of the 980 nm light source, and the low drug loading capacity (Lee et al., 2020).

4.1.4 Carbon-Based Nanoparticles

However, g-C_3N_4NSs have poor PDT efficacy due to wide band gap and low utilization of visible light (He F. et al., 2021). Graphitic carbon nitride nanosheets (g-C_3N_4NSs) are a recently reported promising carbon-based nanomaterial with the advantages of high biocompatibility, high photoluminescence quantum yield and surface modifiability. However, g-C_3N_4NSs have poor PDT efficacy due to wide band gap and low utilization of visible light (Younis et al., 2021). It has been proposed that the PDT efficiency of g-C_3N_4NSs can be enhanced by doping metal ions or UCNPs.

Although Ru (II) polypyridine complexes have high $^1O_2$ generation and stability, the hypoxic microenvironment limits their PDT efficacy (Karges et al., 2020). Therefore, Wei's group synthesized a novel oxygen self-sufficient PS (Ru-g-C_3N_4) by grafting $[Ru\ (Bpy)_2]^{2+}$ onto g-C_3N_4 nanosheets through Ru-N bonds Wei et al. (2021). The incorporation of $[Ru\ (Bpy)_2]^{2+}$ enabled Ru-g-C_3N_4 to obtain high loading capacity, narrow bandgap and high stability, thereby greatly improving the PDT efficiency. In addition, Ru-g-C_3N_4 not only had catalase-like activity in hypoxic environment, but also could effectively react with H_2O_2 to generate free radicals, causing oxidative stress damage to tumor cells. Molybdenum carbide (MoxC) has an electronic structure similar to that of noble metals, among which, Mo_2C nanospheres can simultaneously induce PTT and PDT under illumination in the entire near-infrared radiation region due to their metallic properties and interband/intraband transitions, exhibiting highly efficient redox capacity (Zhang et al., 2019). Based on this, Hou and his team prepared a novel nanocomposite, Mo_2C@N-Carbon-3@PEG, by combining Mo_2C nanospheres with N-carbon. N-carbon could improve the photogenerated charge separation of Mo_2C@N-Carbon-3@PEG, which doubles its photocatalytic performance Hou et al. (2022). However, the doping of metal ions and integration with other nanomaterials increases the risk of biological toxicity and side effects on the one hand, and increases the complexity of the PSs multistep synthetic protocols on the other hand. Based on this, Liu's group had designed and synthesized a nitrogen-rich graphitic carbon nitride nanomaterial, 3-amino-1,2,4-triazole (3-AT) derived g-C_3N_5NSs Liu X. et al. (2021). The photocatalytic activity of g-C_3N_5NSs was 9.5 times higher than that of g-C_3N_4NSs. Compared with g-C_3N_4, the nitrogen-rich triazole group could achieve low-energy transition by reducing the band gap of g-C3N5NSs conjugation, thereby improving the utilization efficiency of visible light.

4.1.5 Sulfur-Based Nanoparticles

Metal sulfides are often used as photothermal agents for photothermal therapy, among which Ni_3S_2, CuS and Co_3S_4 nanoparticles can be used to synthesize semiconductor PSs, which is an effective way to combine PTT/CDT/PDT (Shukla et al., 2021).

Co_3S_4 NPs will be degraded in the acidic microenvironment and trigger a Fenton-like reaction to generate hydroxyl radicals (·OH), which exerts the efficacy of CDT. Based on this, Jiang and his group prepared a nanocomposite Co_3S_4-ICG, which could responsively release PSs in an acidic microenvironment and realize the synergistic antitumor effect of CDT/PTT/PDT under NIR by loading indocyanine green (ICG) into hollow Co_3S_4 Jiang Y. et al. (2021). The combination of Fenton-like reaction and PDT enhanced ROS production and antitumor effect. Similarly, Feng and his team designed and prepared a nanocomposite FeS_2@SRF@BSA with bovine serum albumin

(BSA) as a carrier to encapsulate FeS_2 NPs and SRF, for combining CDT, PTT and PDT to achieve trimodal synergistic tumor therapy Feng et al. (2021). In addition, the Z-scheme heterostructure possesses both narrow band gap and highly oxidative holes, which are helpful for inducing near-infrared photocatalytic oxygen production (Mafa et al., 2021). Based on this, Sang's group had designed and synthesized a Z-scheme nanoheterostructures, $Ni_3S_2/Cu_{1.8}S$@HA Sang et al. (2021). The doping of Cu improves the near-infrared absorption and photothermal conversion efficiency by 7.7% compared with Ni_3S_2. It not only had catalase/peroxidase-like activity to generate endogenous O_2 to relieve hypoxic internal environment, but also had a targeted recognition effect on cancer cells with high CD44 receptor expression, showing good anti-cancer properties effect.

4.1.6 Phosphorus-Based Nanoparticles

Black phosphorus (BP) is a kind of post-graphene two-dimensional (2D) nanomaterials with special structural in-plane anisotropy, which have better optical and electrical properties than carbon-based metal NPSs and sulfur-based metal NPSs (Younis et al., 2021). In recent years, microorganisms with photosynthetic properties and biocompatibility, such as cyanobacteria, have been rapidly developed and used in cancer therapy and other diseases related to oxygen tension (Dahiya et al., 2021; Qamar et al., 2021). Qi and his team hybridized cyanobacterial cells with 2D BP nanosheets to form a microbe-based nanoplatform, Cyan@BPNSs Qi et al. (2021). *In vivo* experiments, Cyan@BPNSs could effectively increase the oxygenation level in the tumor and maintain a tumor inhibition rate of more than 100%.

Although black phosphorus quantum dots (BPQDs) have larger surface area and higher $^1O_2$ quantum yield than BP (up to 0.91 in oxygen-saturated solution), the instability and poor tumor targeting of BPQDs in physiological environment limit their further research and clinical applications (Ding S. et al., 2021; Liu Y. et al., 2021). To this end, Liu and his team used the cationic polymer polyethyleneimine (PEI) to modify BPQDs, and modified RGD peptides targeting tumor cells on their surfaces to prepare BPQDs@PEI + RGD-PEG + DMMA, which had pH-responsive charge-switching and tumor-targeting properties Liu et al. (2021i). The results shown that BPQDs@PEI + RGD-PEG + DMMA had good stability *in vivo*, and could increase the uptake of BPQDs by tumor cells through charge conversion under light, and achieved tumor target enrichment. Most tumor microenvironment-responsive nanoparticles improve the targeting of nanomaterials by responding to the hypoxic microenvironment, but many tumor tissues do not exhibit hypoxia (Huang C. et al., 2020). The hypoxic sites of tumors are mostly located deep in the core of metabolically active tumor tissues, but traditional nanomaterials have the disadvantage of weak tissue penetration (Chen et al., 2019). To this end, Ding and his team were the first to combine BPQDs and genetically engineered *E. coli* expressing catalase by electrostatic adsorption to form hybrid engineered *E. coli*/BPQDs (EB) Ding D. et al. (2021). EB could dissolve the cell membrane of *E. coli* carrying catalase under light exposure, and then the released catalase could generate oxygen to improve hypoxia in the tumor.

Besides BP, red phosphorus (RP) can also generate reactive oxygen species under visible light irradiation (Zhang P. et al., 2021). Among them, Z-type RP/BP nanosheets prepared by exploiting the high separation efficiency of electron-hole pairs not only have photocatalytic activity, but also ROS can be generated with higher efficiency (Liu et al., 2019). To this end, Kang and his team prepared M-RP/BP@$ZnFe_2O_4$ NSs hybrid nanomaterials with higher stability and tumor targeting by loading Z-type RP/BP nanosheets with $ZnFe_2O_4$ and tumor cell membranes Kang et al. (2022). Among them, $ZnFe_2O_4$ could not only increase the productivity of ROS by catalyzing the Fenton reaction, but also induced apoptosis of MB-231 cells through oxidative stress.

4.1.7 Metal-Organic Frameworks

MOFs are a new class of molecular crystal materials, composed of metal ions or clusters bridged by organic connectors. MOFs can integrate NPs and/or biomolecules into a single framework hierarchically through taking advantage of their synthetic tunability and structural regularity, and can be used as highly active sites for multifunctional therapy (Gao et al., 2021b). Focusing on the key factors of O_2 production, Ren et al. designed and assembled a novel two-stage intelligent oxygen generation nanoplatform based on metal organic framework core modified by Pt and CaO_2 NPs (UIO@Ca-Pt) Ren et al. (2021). It was based on the porphyrin metal-organic framework (UIO), and at the same time loaded by CaO_2 NPs with polydopamine (PDA), and then used Pt to further improve biocompatibility and efficiency. In TME, CaO_2 could react with water to increase the content of H_2O_2. These H_2O_2 were further decomposed into O_2 by Pt NPs, thereby promoting the TCPP in the nanometer parent nucleus to convert the surrounding O_2 into $^1O_2$ under laser irradiation. On the other hand, as the most toxic ROS,·OH has stronger oxidizing property and better therapeutic properties than $^1O_2$ (Manivasagan et al., 2022). Recently, the strategy to induce *in situ* generation of OH has been proposed by introducing Fenton-based agents into tumor cells to induce over-expressed H_2O_2 in tumor cells. Chen et al.'s research focused on designing nanocarriers for the transport of Fenton catalysts or metal ions such as iron ions. They synthesized MIL-101(Fe)@TCPP using nanoscale iron-based metal-organic framework MIL-101(Fe) loaded with 5,10,15,20-tetrakis (4-carboxyphenyl) porphyrin (TCPP) PS Chen et al. (2021d). MIL-101(Fe) catalyzed the conversion of H_2O_2 to OH through Fenton reaction under acidic TME, and served as a nanocarrier to deliver TCPP PS to generate photoactivated $^1O_2$ for tumor-specific therapy without serious side effects, showing antitumor great potential for applications.

Iron-based MOFs have the advantages of high drug loading capacity, adjustable degradability and flexible structure. Porphyrin-based MOFs can be used as PSs for high-efficiency PDT with high stability (Ren et al., 2021). Hypoxic TME and endogenous antioxidant defense (AOD) (such as high expression of glutathione and GSH) can weaken the therapeutic effect of PDT. Therefore, breaking cellular redox balance through ROS enrichment and AOD inactivation may lead to effective tumor suppression with high clinical significance (Zhao et al., 2020). By

combining iron with porphyrin-based MOFs, the maximum anti-tumor efficacy can be exerted by intelligently responding to exogenous and endogenous stimuli. Inspired by all this, Yu et al. first prepared a metal organic framework nanosystem (NMOF) based on coordination between Fe (III) and TCPP by a one-pot method (Fe-TCPP NMOF). Then, after capping the surface of silk fibroin (SF) to form NMOF@SF NPs, this nanoplatform can load a hypoxia-activated precursor tirapazamine (TPZ) to form NMOF@SF/TPZ (NST) Yu et al. (2022). Utilizing Fe (III) in Fe-TCPP, NST could effectively react with tumorous GSH to generate glutathione disulfide (GSSG) and Fe (II), for the ineffectiveness of AOD system. On the other hand, Fenton-like activity of Fe (II) and TCPP-mediated PDT promoted the accumulation of OH and ROS, and aggravated the intracellular oxidative stress under light laser irradiation. The redox metabolism disorder caused by the ineffective AOD and the enrichment of ROS might cause irreversible tumor cell damage. In addition, the deoxygenation of PDT led to an increase in hypoxia and then activated TPZ to transform into cytotoxic benzotriazinyl (BTZ) for tumor-specific chemotherapy. NST could achieve complete tumor elimination *in vitro* and *in vivo*. Similarly, Wang et al. also prepared nano-carrier system Zr-MOF@PPa/AF@PEG based on the consideration that PDT oxygen consumption could activate chemotherapy (CT) drugs to solve the hypoxic challenge and improve anti-tumor effect Wang Y. et al. (2021). Nano-carrier system Zr-MOF@PPa/AF@PEG included zirconium ion metal organic framework (UIO-66, carrier), pyropheophorbide-a (PPa, PS) and 6-amino flavone (AF, hypoxic-sensitive drug). Under ultraviolet light, although Zr-MOF@PPa/AF@PEG accepted part energy of PPa, leading to the $^1O_2$ yield (40%) was lower than that of PPa (60%), it solved the problem of self-agglomeration caused by hydrophobicity of PPa, thereby improving the PDT effect. In addition, Zr-MOF@PPa/AF@PEG produced $^1O_2$ under light stimulation with temporal-spatial selectivity. Therefore, Zr-MOF@PPa/AF@PEG took advantage of the PDT-induced hypoxia to activate HIF-1 inhibitor AF to enhance the anti-tumor effect and achieve the synergistic PDT-chemotherapy (PDT-CT) therapeutic effects. In addition, tuning the PDT efficiency by adjusting the thickness of the MOF shell is also a good approach. The Au@MOF core-shell hybrids prepared by Cai et al. could tune the thickness of the MOF shell by controlling the interlayer coordination reaction Cai Z. et al. (2021). As the MOF shell thickness increased, the percentage of TCPP and the efficiency of PDT also increased.

The use of solar energy to drive the photocatalytic reaction has always been considered an ideal way to obtain O_2 (Liu et al., 2021j). Compared with the previous oxygen-generating substances, water-splitting materials have the unique advantage of the O_2 self-supply and generation of ROS, because there is abundant water in the organism. At present, ultraviolet (UV) light, visible light (Nguyen et al., 2021) and a limited region of the first near-infrared (NIR-I) (650–950 nm) light (Huang L. et al., 2020) can activate water-splitting materials to achieve light-driven endogenous water oxidation (photocatalytic water-splitting reaction) to obtain O_2 and ROS, but water splitting materials with NIR-II light triggered molecular O_2 generators have not been reported for tumor therapeutics, even though NIR-II can provide deeper tissue penetration. For this, Liu et al. synthesized a new type of plasmonic Ag-AgCl@Au core-shell nanomushrooms (NMs) by selectively photodepositing plasmonic Au at the bulge sites of the Ag-AgCl nanocubes (NCs) (**Figure 7**) Liu B. et al. (2021). Under NIR-II light irradiation, the plasma effect of the Au nanostructure could overcome hypoxia to oxidize endogenous H_2O to produce O_2, thereby alleviating the hypoxic microenvironment. Almost at the same time, O_2 could react with the electrons on the AgCl nuclear conduction band to generate superoxide anion radicals (O_2^-) for photodynamic therapy. In addition, the combination index value of PDT for Ag-AgCl@Au NMs was 0.92, indicating that Ag-AgCl@Au NMs with excellent PDT properties toward further and promoting the PDT effect in deep O_2-deprived tumor tissues. It is also a research hotspot in recent years to use the functionalization of NMOFs with stimuli-responsive gating units to develop signal-controlled drug delivery systems for biomedical applications. One important subcategory of gated drug-loaded NMOF includes stimulus-responsive nucleic acid-locked drug-loaded NMOF, gaining from the remarkable versatility of nucleic acid sequences to generate recognition elements and structural elements (Zhao et al., 2020). For this, Zhang et al. designed and synthesized the UIO-66 metal-organic framework nanoparticles (NMOF) modified with aptamer-functionalized DNA tetrahedra functionalized by ATP-aptamer or VEGF-aptamer could be loaded with the DOX, which responded to ATP or VEGF to release the drug Zhang S. et al. (2021). They utilized VEGF-responsive tetrahedral-gated NMOFs to load the photosensitizer Zn (II) protoporphyrin IX (Zn (II)-PPIX) to synthesize Zn (II)-PPIX/G-quadruplex VEGF aptamer-tetrahedral nanostructures. VEGF triggered the release of Zn (II)-PPIX from the complex. Association of the released Zn (II)-PPIX with the G-quadruplex structure yielded a highly fluorescent supramolecular Zn (II)-PPIX/G-quadruplex VEGF aptamer-tetrahedral structure, enabling efficient PDT treatment of malignant cells.

4.2 Nanoliposomes

Nanoliposomes are single-lamellar or multilamellar nano-systems formed spontaneously when phospholipids are dispersed in aqueous medium. Except biocompatibility and biodegradability, liposomes have high structural flexibility, which can combine a variety of hydrophilic and hydrophobic drugs to improv their solubility and pharmacokinetics (Cheng X. et al., 2021). In addition, liposome nanotechnology can also co-package a variety of PSs and/or drugs, provide sufficient binding sites for conjugation with a variety of functional ligands.

Several mechanisms have demonstrated that high concentrations of soluble NKG2DLs derived from tumor cells may inhibit tumor immunity and NK cell-mediated target cell lysis by downregulating the expression of NKG2DL, thereby contributing to tumor immune escape (Curio et al., 2021). Based on this, Wang's group had designed and synthesized a Chlorin-based photoactivable Galectin-3-inhibitor

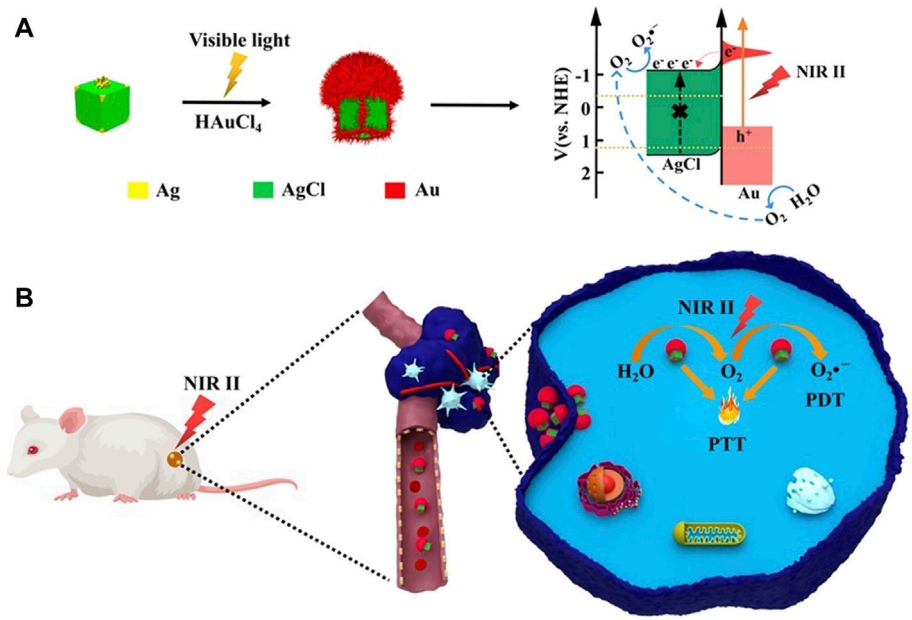

FIGURE 7 | Synthesis of Ag-AgCl@Au NMs and schematic diagram of PDT/PTT synergistic therapy under NIR-II irradiation. **(A)** Schematic diagram of the synthesis of Ag-AgCl@Au NMs. Schematic diagram and electron energy level diagram of O_2 reacting with electrons in AgCl nuclear conduction band to generate superoxide anion radical (O_2^-). **(B)** Schematic diagram of PDT/PTT synergistic therapy under *in vivo* NIR-II light irradiation of Ag-AgCl@Au NMs. Under NIR-II light irradiation, the plasmonic effect of Au nanostructures generates O_2 through photocatalysis and enhances the yield of O_2^-. Reproduced with permission from (Liu D. et al., 2021).

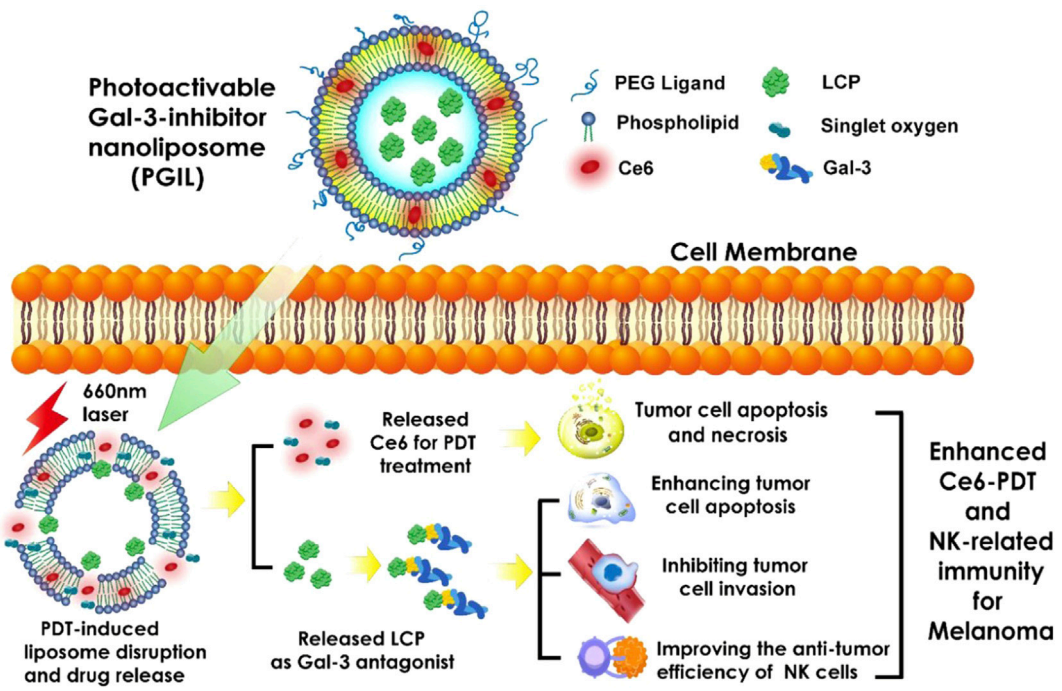

FIGURE 8 | Structure of prostacyclin and its sensitizing effect in tumor cells. After PGIL is taken up by cancer cells, $^1O_2$ generated by Ce6 triggered by NIR causes the liposomes in the outer layer to rupture, releasing Ce6 and LCP. Ce6 mediates PDT, while LCP enhances PDT-induced apoptosis, inhibits cell metastasis, and activates NK cell-mediated immune clearance by inhibiting galectin-3. Abbreviations: Gal-3, galectin-3 protein. Reproduced with permission from (Wang et al., 2019).

nanoliposome (PGIL), which could combine photosensitizer chlorin e6 (Ce6) and low molecular citrus pectin (LCP) (**Figure 8**) Wang et al. (2019). The intracellular release of LCP inhibits the activity of galectin-3, which increases the affinity of major histocompatibility complex (MHC) proteins on tumor cell membrane for NKG2D on NK cell membranand, and then increases the tumor cell apoptosis, inhibits the invade ability, and enhances the recognition ability of NK cells to tumor cells in melanoma cells after PDT. In addition, pharmacological inhibition of MMPs reduce the level of released NKG2DLs, which could increase the tumor cell surface expression of NKG2DLs, reverse their immunosurveillance escape properties, and make them easier to be cleared by immune cells (mainly NK cells) (Tampa et al., 2021). Based on this, Liu's group had designed and synthesized a PS-MMP inhibitor nanoliposome (i.e., Ce6-SB3CT@Liposome [Lip-SC]), which combines the PS, Ce6, and a matrix metalloproteinase (MMP) inhibitor (i.e., SB3CT) Liu H. et al. (2021). Nanoliposomes have significant anti-tumor proliferation and metastasis efficacy after laser irradiation in A375 cells. The relatively fast internalization of Lip-SC could accumulate in the tumor area under 660 nm light irradiation, induce apoptosis in cancer cells, which could trigger an immune response. In addition, it could also induce the expression of NK group 2 member D ligand (NKG2DL), while activate NKG2D, thus, NK cells could better recognize and kill tumor cells. The subsequent release of SB-3CT could further activate NK cells effectively and strengthen the immune system though inhibiting the shedding of soluble NKG2D ligands. As a result, Lip-SC caused induce apoptosis in cancer cells regardless of the presence or absence of irradiation. In the process of PDT agents inducing tumor cell necrosis and apoptosis, local inflammation occur and a variety of tumor cell antigens are exposed, thereby inducing local immune responses. Therefore, by supplementing immunomodulators to enhance immune activity, the anti-tumor effect of PDT can be increased. Dual-ligand-modified NPs increased the number of total liposomes bound to cancer cells through dual-ligand modification, and had higher tumor enrichment capacity and PDT efficiency than single-ligand-modified NPs. For example, Li and his team prepared Fru-Bio-Lip by co-modifying liposomes with fructose (targeting fructose transporter) and biotin (targeting multivitamin transporter) ligands Li J. et al. (2021). Besides targeted aptamer modification, the combination with near-infrared light-activated photon thermodynamic therapy (PTDT), PTT and other phototherapy methods is also an effective strategy to improve the tumor killing effect of PDT. Dai et al. synthesized thiadiazoloquinoxaline semiconductor polymer (PTT), 2, 2′-azobis [2-(2-imidazolin-2-yl) propane] dihydrochloride (AIPH) (PTDT prodrug) and γ-aminoacetic acid (GA, heat shock protein inhibitor) were incorporated into thermosensitive liposomes, which were then modified with targeting aptamers to form Lip(PTQ/GA/AIPH) Dai Z. et al. (2021). Under NIR-II laser irradiation, Lip (PTQ/GA/AIPH) could achieve precise diagnosis and effective suppression of deep triple-negative breast cancer. However, the clinical application of nanoliposomes in PDT still faces challenges due to poor stability *in vivo* and low drug loading (Cheng Y. et al., 2021).

4.3 Mesoporous Silica Nanoparticles

Among various nanomaterials, mesoporous silica nanoparticles (MSNs) have become an important nano-delivery system for PDT and multiple combination therapy due to their unique physical and chemical advantages, such as high loading capacity, controllable pore size and morphology, versatile surface chemistry, satisfying biocompatibility and biodegradability, which can ensure stable and efficient loading of PSs, targeted delivery of PSs, and regulation of drug release and cellular uptake behavior (Wang Z. et al., 2021). Hypoxia is a typical feature of tumor TME, which seriously affects the efficacy of PDT. The development of nano-enzymes with the ability to produce oxygen is a promising strategy to overcome the oxygen-dependent of PDT. In this regard, Chen's group had designed and synthesized a dual-nanozymes based cascade reactor HMSN@Au@MnO_2-Fluorescein Derivative (HAMF), which was composed of hollow mesoporous silica nanoparticles (HMSN), high-efficiency photosensitizer 4-DCF-MPYM (4-FM), ultra-small Au-NPs and MnO_2 Chen et al. (2021e). 4-Fm was a thermally activated delayed fluorescence (TADF) fluorescein derivative with high fluorescence quantum yield, photostability, two-photon excitation and low biological toxicity. Au NPs exhibited glucose oxidase (GOx)-mimic ability that could catalyze glucose into gluconic acid and H_2O_2, simultaneously, the consumption of glucose could cut off the energy supply of tumor cells (Zhang Y. et al., 2021). With the response to the hypoxic microenvironment, MnO_2 could catalyze H_2O_2 into O_2 and accelerate the oxidation of glucose by Au NPs to generate additional H_2O_2, which was used as a substrate for the catalytic reaction of MnO_2, which can be used in light irradiation, thereby constantly producing $^1O_2$ for enhanced PDT upon light irradiation. HAMF could alleviate tumor hypoxia and achieve an effective tumor inhibition *in vitro* and *in vivo* studies. Yin's team had also designed and synthesized a kind of H_2O_2-responsive and oxygen-producing nanozyme by loading a large number of gold nanoclusters (AuNCs) into MSNs to form nanoassembly, and wrapped MnO_2 nanosheets in the form of a switch shielding shell (denoted as AuNCs@mSiO_2@MnO_2) Yin et al. (2021). In a neutral physiological environment, stable MnO_2 shells could switch off PDT by eliminating the generation of $^1O_2$. However, in an acidic TME, the MnO_2 shell reacted with H_2O_2, and simultaneously sufficient O_2 generation guaranteed a 74% high $^1O_2$ yield, which showing strong PDT performance. In addition, multifunctional NPs loading with chemotherapeutic drugs and PSs are also a promising method for effective tumor combination therapy. Zhang's group had designed and synthesized a novel pH-sensitive and bubble-generating mesoporous silica-based drug delivery system (denoted as M (A) D@PI-PEG-RGD) (**Figure 9**) Zhang Z. et al. (2021). DOX and NH_4HCO_3 were loaded into MSNs pores, MSNs was coated with polydopamine (PDA) layer, and then ICG as a photothermal and photodynamic agent was loaded onto the PDA layer surface, finally the nanoparticles were modified with polyethylene glycol (PEG) and RGD. RGD is a ligand for the recognition site of integrins and displays great adhesion capacity between extracellular matrix cells and cells, which can improve the

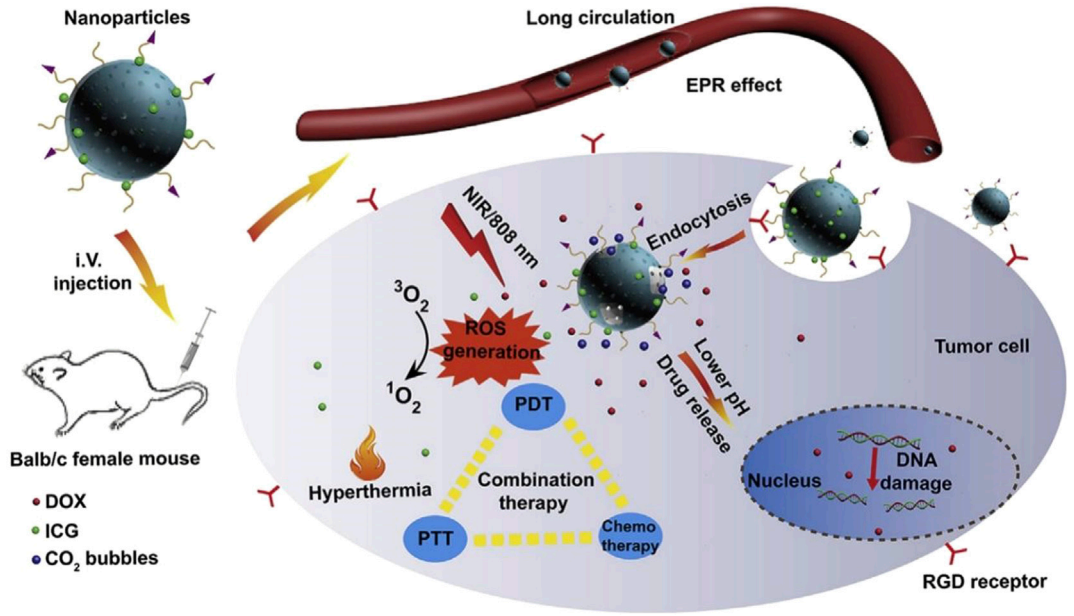

FIGURE 9 | Schematic illustration of M (A)D@PI-PEG-RGD for enhanced tumor combination therapy. M(A)D@PI-PEG-RGD targets tumor cells through RGD, generates ROS and induces temperature increase through ICG under NIR irradiation. In addition, the acidic microenvironment accelerates the release of DOX by breaking down NH_4HCO_3, which combine chemotherapy, PTT and PDT to enhance the therapeutic effect. Reproduced with permission from (Zhang J. et al., 2021).

accuracy of M (A)D@PI-PEG-RGD. Under NIR irradiation, M (A)D@PI-PEG-RGD could generate ROS and induce the temperature rise performed by ICG. In addition, acidic environment and high temperature would also decompose NH_4HCO_3, thereby accelerating the release of DOX. In summary, the multifunctional pH-sensitive and bubble-producing M (A)D@PI-PEG-RGD combines chemotherapy, PTT and PDT to improve the therapeutic effect of tumors.

4.4 Dendrimers

Dendrimers are synthetic high molecular polymers with tree-like and highly branched structure. They are composed of the small initial core, the internal cavity formed by multiple branches, and the peripheral functional groups. Due to their special structure, dendrimers have the advantages of easy surface modification with PSs along with other functional moieties and structural configuration with other components or nanoformulations *via* the hyperbranched units for enhanced tumor accumulation and penetration (Ouyang et al., 2021). The combination of molecular targeted therapy of epidermal growth factor receptor tyrosine kinase inhibitors (EGFR-TKIs) and photodynamic therapy PDT can combat non-small cell lung cancer (NSCLC) with effective synergistic results (Qiao et al., 2021). However, the hypoxic TME not only affects the efficacy of PDT, but also induces EGFR-TKIs resistance. In this regard, Zhu and researchers had designed a nanocomplex APFHG by loading gefitinib (Gef) and PS hematoporphyrin (Hp) into an aptamer modified fluorinated dendrimer (APF) Zhu L. et al. (2021). Due to the targeting effect of EGFR-TKIs and the good oxygen-carrying capacity of APF, APFHG could specifically recognize EGFR-positive NSCLC cells and release Gef and Hp in response to the hypoxic acidic microenvironment. Under laser irradiation, APFHG could significantly increase the production of intracellular ROS, effectively improve the tumor hypoxia microenvironment, and overcome hypoxia-related drug resistance. In other work, X-ray-induced photodynamic therapy (XPDT) is overwhelmingly superior in treating deep-seated cancers (Chuang et al., 2020). However, low energy transfer efficiency of the therapeutic nanoplatform and hypoxic environment presented in the tumor tissue limits the therapeutic effect of XPDT. In order to improve the therapeutic effect of XPDT in deep-seated cancers, it is necessary to develop a delicate architecture to support the organization of nanoscintillator and multiple agents to improve the effectiveness of XPDT (Ahmad et al., 2019). In this regard, Zhao and researchers developed a dual-core-satellite architecture nanosmart system (CCT-DPRS) that the polyamidoamine (PAMAM) dendrimer would be used as an intermediate framework with nanoscintillator, PSs, and sunitinib (SU) (**Figure 10**) (Jiang Z. et al., 2021). It had high XPDT and antiangiogenetic capabilities by systematic optimizing the scintillation efficiency and nanoplatform structure. After exposure to ultralow dose radiation, the codoped CaF_2NPs converted the trapped energy into green emission, which enable further excitation of Rb to produce $^1O_2$ to kill malignant tumor cells. At the same time, the antiangiogenic drug SU effectively blocked tumor vascularization aggravated by XPDT-mediated hypoxia, rendering a pronounced synergy effect. However, PAMAM dendrimer and indocyanine green (ICG) have inevitable interaction with proteins and cells, which induces biological toxicity and reduces therapeutic

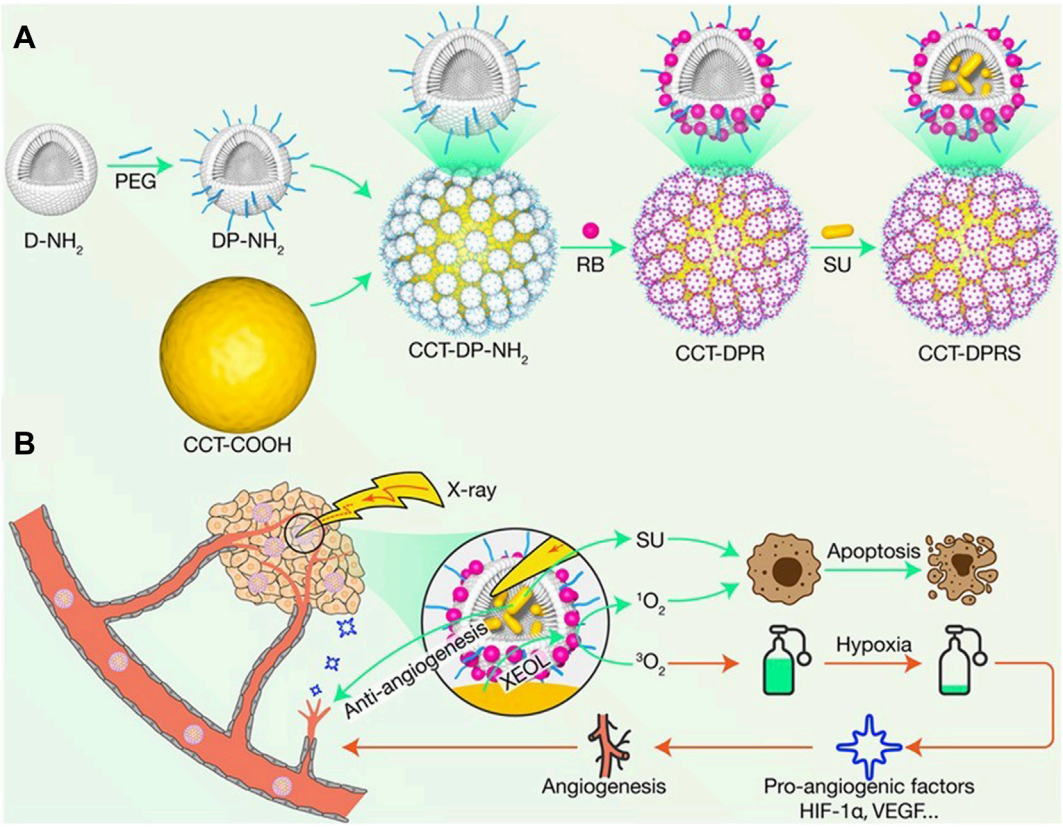

FIGURE 10 | Schematic diagram of the construction and function of CCT-DPRS. **(A)** CCT-DPRS is prepared using PAMAM as an intermediate framework to load nanoscintillator, PSs, and SU. **(B)** Mechanism of combined therapy of XPDT and SU. After exposure to ultra-low dose radiation, Rb produces $^1O_2$ to kill malignant tumor cells. Meanwhile, SU effectively block XPDT-mediated hypoxia-exacerbated tumor angiogenesis, with a clear synergistic effect. Reproduced with permission from (Jiang Y. et al., 2021).

efficacy *in vivo* (Mindt et al., 2018). To overcome these shortcomings, Cui and researchers had designed a new drug delivery system G5MEK7C (n)-ICG with a "stealth" layer Cui et al. (2021). The surface of G5MEK7C (n)-ICG was modified with p (EK) peptide, which was double-layer super hydrophilic zwitterionic material. When the pH was lower than 6.5, the surface of G5MEK7C (n)-ICG showed a positive charge, which made it more likely to interact with the cell membrane in the tumor tissue. Therefore, under laser irradiation *in vitro* and *in vivo*, due to the good targeting effect of G5MEK7C(70)-ICG, G5MEK7C(70)-ICG was more effective in killing tumors than free ICG, while the damage to the liver was less than free ICG. The combination of chemotherapy and other therapeutic modalities can overcome chemoresistance through different mechanisms of action to achieve the purpose of enhancing anti-tumor efficacy. Furthermore, adding chemicals during mitosis to block cell division may be a promising approach to promote nuclear uptake of PSs. Recently, based on dendrimers and phenylboronic acid-sialic acid interactions, Zhong and researchers modified phenylboronic acid (PBA) into the surface of dendrimers, which can selectively recognize the sialic acids, meanwhile, conjugated lipoic acid modified Ps onto the core of dendrimer Zhong D. et al. (2021). In this work, a novel tumor targeting and penetrating, GSH/ROS heterogeneity responsive and PTX-loaded dendrimeric nanoparticles (P-NPs) was developed for mutually synergetic chemo-photodynamic therapy of PTX-resistant tumors. Lentinan was coated on the periphery of dendrimers through boronate bonds, which could avoid non-specific binding of P-NPs with normal cells during blood circulation. P-NPs penetrated into tumor tissues and actively entered into the cells through the PBA-SA interactions, showing enhanced cellular uptake and tumor penetration. Subsequently, P-NPs released PTX in response to high concentrations of glutathione and H_2O_2 in tumor cells, arresting the cells in the G2/M phase and exerting anti-tumor effects. At the same time, the time of nuclear membrane disintegration increased caused the enhanced intranuclear photosensitizer accumulation, thereby increasing the efficiency of PDT by increasing nuclear DNA damage.

4.5 Hydrogels

Hydrogel is a type of nano-delivery carrier system formed by a hydrophilic polymer material with a three-dimensional network structure through chemical cross-linking or physical cross-linking. Hydrogels are biocompatible and have similar physical

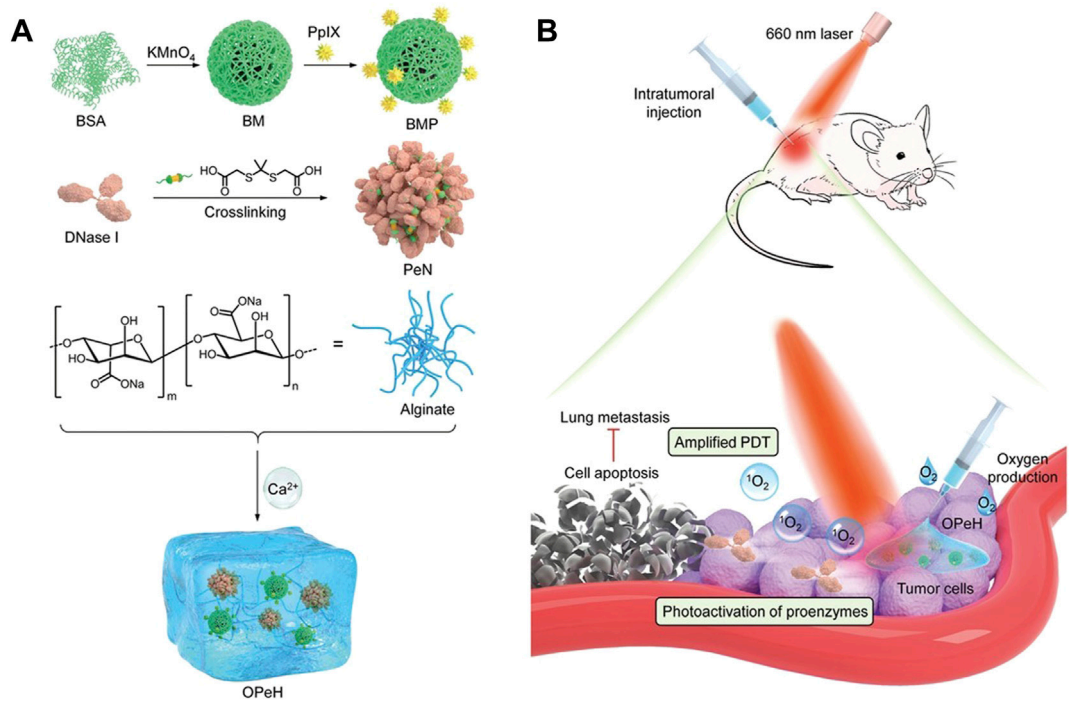

FIGURE 11 | Schematic diagram of the preparation and treatment principle of OPeH. **(A)** Schematic diagram of the preparation of OPeH. **(B)** Mechanism of oxygen production and NIR photoactivation of OPeH. OPeH integrates PDT and NIR light-activated enzymes to achieve the combined therapeutic effect of inhibiting tumor growth and lung metastasis. Reproduced with permission from (Liu N. et al., 2021).

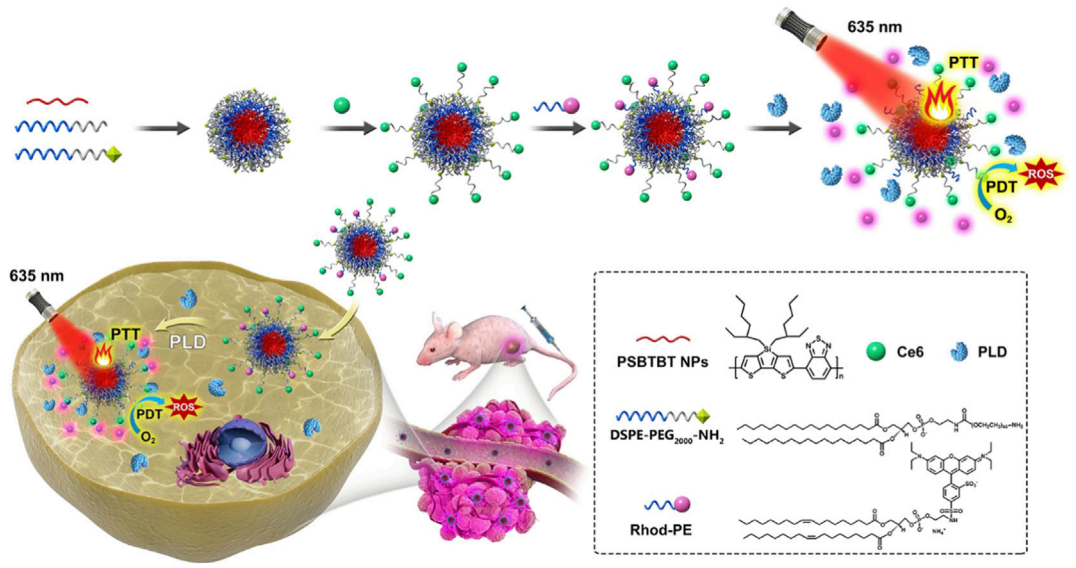

FIGURE 12 | Schematic representation of PSBTBT-Ce6@Rhod NPs-mediated PLD-activatable tumor images and combined PTT/PDT therapy. PSBTBT-Ce6@Rhod NPs can kill MCF-7 cells only under light conditions. Among them, PSBTBT-Ce6 NPs mediate PTT/PDT synergistic therapy, and can also cleave Rhod in response to overexpressed phospholipase D (PLD) in tumor tissue, resulting in the fluorescence recovery of Rhod B, thereby exerting biomarker-triggered fluorescence imaging and targeting PDT. Reproduced with permission from (Bao et al., 2021).

properties like living tissues. Some drugs are easily dispersed in the hydrogel matrix (Hu et al., 2022). Therefore, hydrogels have been widely used for the delivery of hydrophilic drugs. Among them, local injection of hydrogels has received special attention in tumor treatment and prevention of tumor recurrence, because this injection method can achieve desired drug accumulation in

TABLE 1 | Summary of the advantages and disadvantages of Metal NPs.

Metal NPs	Advantages	Disadvantages
Au based NPs	●Utilization for PTT, PAI ●Controllable size and structure and easy surface modification ●Optical quenching ability ●Chemical inertness and excellent biocompatibility	●Limited stability under aqueous conditions
Ag based NPs	●Tuning optoelectronic properties according to size and shape ●High $^1O_2$ yield	●Ag NPs with diameters less than 200 nm are prone to aggregation
Cu based NPs	●High photothermal conversion efficiency ●Low price ●Simple synthesis ●Controllable morphology and size ●Microwaves-induced PDT	●Potential toxicity
Ru based NPs	●Low-lying excitation energy states and high ROS yield ●Good photophysical and photochemical properties ●Controllable photophysical properties ●Low photobleaching rates ●High water solubility	●Dark toxicity ●DNA mutation ●Being excited only by short-wave visible light
Ir based NPs	●Unique oxygen quenching pathway ●Excellent electrocatalytic performance ●Long triplet state lifetime and good photophysical properties ●Significant tumor targeting ability	●Most Ir complexes are water-insoluble
Metal oxide-based NPs	●Utilization for PDT, PTT ●Clinical used MRI contrast agent ●Magnetic hyperthermia and PAI ●Easy surface modification ●High photostability ●Large extinction coefficient ●High emission quantum yield	●Limited stability under aqueous conditions ●Toxicity accumulation of NPs ●Physical damage from magnetic guidance
UCNPs	●Utilization for PDT, PTT, bioimaging, diagnosis, and therapy ●Narrow emission bandwidth, large decay time, resistance to photobleaching, and no autofluorescence background ●Unique optical property and utilization for luminescence imaging ●Easy surface modification and functionalization ●Ability to absorb light in the NIR region	●Potential toxicity ●Limited biodegradability ●Low drug loading capacity ●Low quantum yield and superheating effects under 980 nm light source
Carbon-Based NPs	●Strong optical absorbance and utilization for PTT, PAI ●Unique electrical property ●Easy surface modification ●High surface-to-volume ratio ●Thermal stability ●High photoluminescence quantum yield	●Induce inflammatory reactions and cytotoxicity ●Limited biodegradability ●Low utilization of visible light ●Expensive and complex synthetic method
Sulfur-based NPs	●Utilization for PTT, CDT, PDT ●Good biocompatibility ●High photothermal conversion efficiency ●Cheap and simple manufacturing method ●Biodegradability and rapid metabolism	●The degradation products have potential toxicity ●Killing efficiency on hypoxic tumor cells is limited
Phosphorus-based NPs	●Optical and electrical properties better than carbon-based metal NPSs and sulfur-based metal NPSs ●For making photosensitizers	●Weak absorption in the biowindow and low photo catalytic activity in a TME ●The inherent instability of BP NSs and BP QDs in water–air environments
MOFs	●Facile diffusion of ROSs through their porous structures ●High specific surface area ●Controllable size, shape and function of the pore ●Effectively enhance the ROS generation effect ●High PSs loadings	●Complex design, lengthy preparation steps and high operating costs ●Early clearance by body immune system ●Off-target accumulation ●Untimely drug release ability

tumors. Compared with oxygen-generating nanomaterials, prodrugs that can be activated by external light show the unique advantages of highly consistent responsiveness and high temporal and spatial selectivity (Rapp and DeForest, 2021). Recently, Liu's group constructed a kind of original oxygen-generating hydrogel (OPeH) with photoactivated enzyme activity by loading the oxygen-generating MnO_2 nanoparticles conjugated with protoporphyrin IXpt (PPIX), and the proenzyme nanoparticles (PeN) crosslinked by a $^1O_2$ cleavable linker into alginate hydrogels (**Figure 11**) Liu J. et al. (2021). Under NIR laser irradiation, MnO_2 NPs converted H_2O_2 into O_2, which further promoted the production of $^1O_2$ from PpIX and improved the efficiency of $^1O_2$ generation. In addition, after PEN was cross-linked with the $^1O_2$ cleavable linker, it

TABLE 2 | Advantages and disadvantages of other representative nanomaterials.

Type	Advantages	Disadvantages
Nanoliposomes	● Biocompatibility and biodegradability ● High structural flexibility ● Targeted delivery and triggered release ● Easy and diverse surface modification ● Prolonged tissue penetration and retention of PSs	● Low drug loading capacity ● Limited stability *in vivo* ● Uncontrolled drug leakage ● The inevitable self-quenching effect of water-insoluble PSs
MSNs	● Large specific surface area and huge specific pore volume ● Easy and diverse internal and external surface modification ● High loading efficiency ● High targeting	● The larger the specific surface area, the greater the cytotoxicity
Dendrimers	● Controllable molecular size ● Large number of terminal functional groups ● Large number of cavities in the molecule	● High molecular weight, high-density surface positive charge increases the toxicity of dendrimers
Hydrogels	● Good biocompatibility ● Efficient adhesion to biotic surfaces ● Delivery of hydrophilic drugs	● Low mechanical strength ● Poor repeatability of material properties
Polymers	● The designability and diversity of composition, structure and function ● Diverse surface modification ● High loading efficiency and sustained release ● Good circulation stability ● Improve PSs solubility, permeability, and targeting	● Limited storage stability ● Potential toxicity ● Limited loading capacity for hydrophilic drugs ● Complex synthesis process

induced cell death and suppressed metastasis by inhibiting the extracellular trap (NET) of neutrophils. In animal experiments, it was found that OPeH integrates PDT and NIR light-activated enzymes to achieve the combined therapeutic effect of inhibiting tumor growth and lung metastasis. In addition, phototherapy against deep tumors may greatly limited by the lack of light flux and the chemotherapy drugs against tumor cells may limited by insufficient resident time. Therefore, Zhong's group developed a dual drug carrying system DOX-CA4P@Gel, which achieved the best curative effect, efficacy and safety through local sequential delivery of drugs Zhong Y. et al. (2021). With dextran oxide, chitosan, porphyrin and hollow mesoporous silica (HMSN), DOX-CA4P@Gel was constructed, in which combretastatin A4 phosphate (CA4P) and DOX were both loaded. In weakly acidic condition, the degradation rate of the hydrogels increased significantly. CA4P was released rapidly at the early stage and relatively stable after 48, while DOX released slowly at first and then quickly released after 48 h, showing an obvious sequential release behavior. The porphyrin in hydrogel could trigger the formation of ROS, DOX could kill cancer cells at different stages of proliferation, while CA4P could inhibit the establishment of blood vessels around the tumor and increase the sensitivity of cancer cells to DOX.

4.6 Polymers

Due to the designability and diversity of composition, structure and function, polymers have become one of the preferred carrier materials for nanomedicine. Conjugated polymers can control tissue penetration by adjusting the conjugation length. Among them, the integration of multichromophoric conjugated polymer base NPs into PSs enhanced ROS generation by improving PSs solubility, permeability, and targeting (Jiang and McNeill, 2017). According to the characteristics of carbon-based fluorescent nanomaterials such as carbon dots (CDs) and carbon-based polymer dots (CPDs) with good biocompatibility and high fluorescence yield, Sajjad et al. conjugated green-emitting CPDs to PPa to enhance the photocatalytic performance of PSs through covalent and π-π interactions Sajjad et al. (2022). Semiconducting polymer NPs (PSBTBT NPs) can't only load PSs, but also act as photothermal agents for PDT/PTT synergistic therapy. Inspired by "biomarker-triggered image"-guided therapy, Bao et al. loaded the fluorescence quenchers Rhodamine B (Rhod B) and Ce6 on PSBTBT NPs to prepare a smart "Sensing and Healing" nanoplatform for PTT/PDT combination therapy (PSBTBT-Ce6@Rhod NPs) (**Figure 12**) Bao et al. (2021). Similarly, IR780 iodide can generate heat and oxygen for PDT/PTT synergistic therapy. In addition, it has strong fluorescence intensity and inherent specificity for various tumor cells, which is suitable for near-infrared imaging of tumor cells. In view of this, Potara et al. used temperature-sensitive block copolymer Pluronic F127 to wrap IR780 iodide, and coupled folic acid (FA) to Plu-IR780 micelles through chitosan to designe a thermoresponsive and thermal reversible size distribution and spectral properties of a novel FA-targeted near-infrared phototherapy NPs (Plu-IR780-chit-FA) Potara et al. (2021). Plu-IR780-chit-FA not only retained the PTT, PDT and NIR imaging properties of IR780 iodide, but also adjusted the size of the nanocapsules to the smallest (30 nm) at physiological temperature to ensue cellular uptake, while also had maximum absorption and fluorescence emission intensity.

Polymeric micelles, which constructed by amphiphilic polymers, have been regarded as ideal carriers for nanomedicine due to their good biocompatibility, degradability, easy modification of the structure, and special "core-shell" structure (Tian and Mao, 2012). Using

TABLE 3 | Summary of recently developed NPs to overcome the obstacles of current photodynamic therapy in tumor.

Obstacles to overcome	NP type	Name	Strategy	Year
PSs delivery	DNA-modified NPs	Apt-DNA-Au nanomachines (Yu et al., 2021)	Tumor-associated TK1 mRNA-responsive PSs release and survivin targeting by antisense DNA	2021
	DNA-modified NPs	TCPP-gDNA-Au/PLNP (Su et al., 2021)	Nucleolin targeting by AS1411 aptamer	2021
	DNA-modified NPs	Au/Pd ONP-DNA nanomachine (Cai et al., 2021a)	Using the primary marker miRNA-21 and two auxiliary markers miRNA-224 and TK-1 mRNA to improve the accuracy of tumor identification	2021
	DNA-modified NPs	Label-rcDNA-AuG (Zhang et al., 2021b)	Recognition of cancer cells by miR-21	2021
	Biotin-modified NPs	BT@Au-NPs (He et al., 2021b)	Movement to cellular sites and efficient binding sites in tumor cell lines by biotin	2021
	AuNRs-grafted RGD	HB-AuNRs@cRGD (Liu et al., 2021f)	Binding of RGD to integrin avb3 in tumor cells and tumor neovascular endothelial cells	2021
	Au nanoshells	40/20 core radius/shell thickness optimized gold nanoshell (Farooq and de Araujo, 2021)	Optimization of nanoshells structure (silica core radius and gold shell thickness) to increase the singlet oxygen production	2021
	Heterometallic colloids	(L' = I–, CH_3COO–) Mo_6Au_2 colloids (Faizullin et al., 2021)	Affecting NPs cytotoxicity, cellular internalization, and PDT activity by modulating the order of supramolecular stacking by Mo_6-Au_2	2021
	Polymer-coated AuNRs	Au-MB-PEG NPs (Liu et al., 2021g)	Response to highly expressed HOCl in the tumor region *via* FDOCI-24	2021
	Cu-based Fenton reagents	Cu-LDH/HMME@Lips (Wu et al., 2021)	Active infiltration of cancer cells by Cu-LDH for deep tumor therapy. Extended circulatory residence time by liposome encapsulation	2021
	Hollow mesoporous silica supported UCNPs	UCNP/RB@mSiO2-NH (Chen et al., 2021a)	"One treatment, multiple irradiation" PDT strategy for efficient nuclear-targeted PDT	2021
	Metal-organic frameworks	Zn (II)-PPIX/G-quadruplex VEGF aptamer-tetrahedra structures (Zhang et al., 2021c)	Release of PSs in response to VEGF *via* VEGF-aptamer-functionalized DNA tetrahedra	2021
	Nanoliposomes	Fru-Bio-Lip (Li et al., 2021b)	Increased total number of liposomes bound to cancer cells by dual-ligand modification of fructose and Bt	2021
	Fluorinated dendrimer	APFHG (Zhu et al., 2021a)	EGFR-TKI specifically recognizes EGFR-positive NSCLC cells and releases Gef and Hp in response to a hypoxic acidic microenvironment	2021
	Polyamidoamine Dendrimers	G5MEK7C(n)-ICG (Cui et al., 2021)	p (EK) converts to positive charge in response to acidic TME and interacts more readily with tumor cell membranes	2021
Light delivery	Bimetallic NPs	Au-BiGSH@IR808 (Jia et al., 2021)	Modified by IR808 fuel for higher NIR photon capture capability	2021
	Ultra-thin two-dimensional nanosheets	4-layer O-Ti_7O_{13} nanosheets (Dai et al., 2021a)	X-ray irradiation-induced ROS generation by OTi_7O_{13} nanosheets and chemotherapy mediated by DOX	2021
	Ti-based targeting agent	B-TiO_2@SiO_2-HA (Guo et al., 2021)	Simultaneous generation of ROS and hyperthermia under NIR-II laser irradiation and full spectral response to light stimulation obtained by B-TiO_2	2021
	Semiconductor metal oxide	SnO_{2-x}@SiO_2-HA (Gao et al., 2021a)	SnO_{2-x}-mediated full-spectrum response target-specific synergistic PDT/PTT	2021
	Block copolymer	Plu-IR780-chit-FA (Potara et al., 2021)	PTT/PDT synergistic therapy under NIR *via* IR780	2021
	UCNP	UCNP/RB, Ce6 (Pham et al., 2021)	Dual PSs have higher PDT efficiency than single PS	2021
New PSs	Ru complex	Ru-I (He et al., 2021c)	Red-Light-Responsive Ru Complex PSs for lysosome localization PDT	2021
	Amphiphilic polymer	DSPE-PEG_{2000}-Folic encapsulated Ru (II) polypyridine complex (Karges et al., 2021)	Enhanced tumor cell selectivity by DSPE-PEG_{2000}-Folic	2021
	Ru (II) complex	Ru (II) complex-based bioorthogonal two-photon PSs (Lin et al., 2021a)	Anti-tumor effects by specifically binding to cancer cell membranes and inducing cell membrane damage	2021
	Ir compounds	Ir (III) complexes (Xiao et al., 2021)	Different degrees of oxygen quenching *via* Ir (III) complexes	2021
	Bifunctional Ir (III) complexes	4 ([Ir(Bzq)$_2$ (dpa-acr)]+ (Redrado et al., 2021)	Targeted mitochondrial and cellular imaging *via* organic chromophores and Ir (III) complexes	2021
	Superparamagnetic Fe_3O_4 NPs	E-NP (Sengupta et al., 2022)	E-NP show immunoprotective and anti-inflammatory effects by inhibiting MPO and down-regulating NO	2022
	Ru (II) polypyridine complexes	Ru-g-C_3N_4 (Sengupta et al., 2022)	Oxygen self-sufficient PSs generated by grafting metal complexes onto g-C_3N_4	2021
	Graphitic carbon nitride	g-C_3N_5NSs (Liu et al., 2021h)	Due to the addition of nitrogen-rich triazole groups, the visible light utilization and photocatalytic activity of g-C_3N_5NSs are higher than those of g-C_3N_4NSs	2021
	nanoheterostructures	Ni_3S_2/$Cu_{1.8}$S@HA (Sang et al., 2021)	Production of ROS and O2 by Ni_3S_2/$Cu_{1.8}$S	2021

(Continued on following page)

TABLE 3 | (*Continued*) Summary of recently developed NPs to overcome the obstacles of current photodynamic therapy in tumor.

Obstacles to overcome	NP type	Name	Strategy	Year
	BPQDs	BPQDs@PEI + RGD-PEG + DMMA (Liu et al., 2021i)	Enrichment of tumor targets through pH-responsive charge switching	2021
	2D black phosphorus nanosheets	Cyan@BPNSs (Qi et al., 2021)	Continuous oxygen supply through cyanobacterial photosynthesis	2021
	Red/black phosphorus composite nanosheet	M-RP/BP@$ZnFe_2O_4$ (Kang et al., 2022)	$ZnFe_2O_4$ enhances the productivity of ROS through the Fenton reaction and can also induce apoptosis in MB-231 cells through oxidative stress	2022
	Carbon-based polymer dots	PPa-CPD (Sajjad et al., 2022)	PPa enhances the photocatalytic performance of photosensitizers *via* covalent and π-π interactions	2021
Unfavorable TME	Hyaluronic acid-Bimetallic NPs	ToHAu@Pt-PEG-Ce6/HA (Bu et al., 2021)	Oxygen enrichment in tumor and PDT by Pt	2021
	Bimetallic NPs	Au/Ag NR (Jin et al., 2021b)	Increases heat and ROS production by altering the amount of Ag^+, triggering ICD in tumor cells	2021
	lateral nano-heterostructure	(Bi/BiO_x)-based lateral nano-heterostructure (Qiu et al., 2021)	Oxygen-independent PDT using BiO_x	2021
	Nanozyme	IrO_2-Gox@HA NPs (Yuan et al., 2022a)	Enhancement of type II PDT by GOx and IrO_2 NPs	2022
	ZGGO durable luminescent NPs	Mn-ZGGO (Ding et al., 2021b)	Oxygen-independent PDT using MnO_x shell	2021
	Nanozyme	ICG@PEI-PBA-HA/CeO_2 (Zeng et al., 2021)	CeO_2 catalyzes H_2O_2 to O_2 through Ce^{3+}/Ce^{4+} cerium valence cycling	2021
	UCNPs	UCTM NPs (Cheng et al., 2021a)	Oxygen-enriching role of thylakoid membranes of chloroplasts in tumors and photodynamic therapy	2021
	UCNPs	CM@UCNP-Rb/PTD (Jin et al., 2021a)	PEG-TK-DOX releases DOX in response to ROS and prevention of tumor metastasis by CD73 antibody	2021
	MIPs modify UCNPs	MC540/MNPs@MIPs/UCNP (Lin et al., 2021b)	Using MIPs to target tumor cells and prevent PD-1/PD-L1 immune blockade	2021
	Molybdenum Carbide	Mo_2C@N-Carbon-3@PEG (Hou et al., 2022)	Photocatalytic Oxygen Generation by Mo_2C	2022
	Engineered bacteria	EB (Ding et al., 2021a)	Targeting anoxic TME and catalyzing H_2O_2 to produce O_2 using engineered *Escherichia coli*	2021
	Metal-organic frameworks	UIO@Ca-Pt (Ren et al., 2021)	Increase intracellular oxygen content by endogenous oxygen through CaO_2 and Pt	2021
	Nanoscale iron-based metal organic frameworks	MIL-101(Fe)@TCPP (Chen et al., 2021b)	Fenton reaction increases intracellular oxygen levels	2021
	Metal Organic Framework Nanosystems	NMOF@SF/TPZ (NST) (Yu et al., 2022)	Disturbed redox metabolism in tumor cells caused by GSH depletion and Fenton reaction oxygen enrichment	2021
	Metal-organic frameworks	Ag-AgCl@Au NMs (Liu et al., 2021j)	Au nanorods produces O_2 through a photocatalytic reaction	2021
	Nanoliposomes	Ce6-SB3CT@Liposome (Lip-SC) (Liu et al., 2021a)	The released SB-3CT can effectively activate NK cells and enhance the immune system by inhibiting the shedding of soluble NKG2D ligands	2021
	Double nanozyme modified HMSN	HMSN@Au@MnO_2-Fluorescein Derivative (HAMF) (Chen et al., 2021c)	Enhancement of intracellular oxygen level by catalytic reaction of MnO_2 and Au NPs	2021
	Double nanozyme modified HMSN	AuNCs@mSiO_2@MnO_2 (Yin et al., 2021)	Acid-TME-responsive dual nanozyme-catalyzed reaction to enhance intracellular oxygen level *via* MnO_2 nanosheets	2021
	Polyamidoamine Dendrimers	CCT-DPRS (Mindt et al., 2018)	CaF_2NPs convert low-dose X-radiation to Wei-green light to excite Rb to generate ROS, while releasing SU to inhibit tumor angiogenesis	2021
	Hydrogels	OPeH (Liu et al., 2021b)	MnO_2 NPs convert H_2O_2 to O_2, which further promotes the generation of $^1O_2$ from PpIX and improves the generation efficiency of $^1O_2$	2021
	Fluorinated polymer micelles	(PFFA)-Ce6 (Tseng et al., 2021)	Using perfluorocarbons to increase intracellular oxygen levels	2021
	Amphiphilic polymer micelles	MPEG-S-S-PCL-Por (MSLP) (Xia et al., 2021)	Amplifies oxidative stress in tumor cells by depleting GSH and producing ROS	2021
Synergistic therapy	layered double hydroxides	ICG/CAC-LDH (Wang et al., 2021a)	Induces intracellular GSH depletion through redox reactions, and can also be decomposed to generate Cu+ and Ce3+, which stimulates Fenton-like reactions to generate OH	2021
	Bimetallic NPs	Au_1Bi_1-SR NPs (He et al., 2021a)	The photothermal effect of NPs is enhanced by the introduction of Bi	2021
	Bifunctional micelles	Micelle-Ir (Liu et al., 2021c)	Promotion of singlet oxygen generation and photothermal effect via BODIPY-Ir	2021
	Nanozyme	MIP/Ce6 (Li et al., 2021a)	PTT by IrO_2 and TME-responsive PDT by MnO_2	2021

(Continued on following page)

TABLE 3 | (*Continued*) Summary of recently developed NPs to overcome the obstacles of current photodynamic therapy in tumor.

Obstacles to overcome	NP type	Name	Strategy	Year
	zeolitic imidazole framework-67 NPs	Co_3S_4-ICG (Jiang et al., 2021b)	Promoting Fenton reaction to generate ROS through PTT	2021
	Bovine serum albumin (BSA) NP	FeS_2@SRF@BSA (Feng et al., 2021)	The combination of Fenton-like reaction and PDT enhanced ROS production and antitumor effect	2021
	Metal-Organic Framework	Zr-MOF@PPa/AF@PEG (Wang et al., 2021b)	Zr-MOF@PPA/AF@PEG take advantage of the PDT-induced hypoxia to activate HIF-1 inhibitor AF to enhance the anti-tumor effect and achieve the synergistic PDT-chemotherapy (PDT-CT) therapeutic effects	2021
	Metal-Organic Framework Core-Shell Hybrid Materials	Au@MOF-FA (Cai et al., 2021b)	$Fe_3O(OAc)_6(H2O)^{3+}$-mediated Fenton reaction and Au nanorod-mediated PTT	2021
	Nanoliposomes	Lip(PTQ/GA/AIPH) (Dai et al., 2021b)	PTDT/PTT/PDT synergistic therapy *via* PTT, PTDT prodrug and GA	2021
	PEGylated MSNs	M(A)D@PI-PEG-RGD (Zhang et al., 2021d)	Synergistic treatment of chemotherapy, PTT and PDT by ICG and DOX	2021
	Phenylboronic acid modified dendrimers	P-NPs (Zhong et al., 2021a)	Synergistic chemophotodynamic therapy that releases PTX in response to high concentrations of glutathione and H_2O_2 in tumor cells increases intranuclear PSs through nuclear membrane disassembly	2021
	Hydrogels	DOX-CA4P@Gel (Zhong et al., 2021b)	The gel can be slowly degraded under acidic TME, and DOX and CA4P are released in different time sequences for tumor therapy	2021
	Polymer micelles	IR780/PTX/FHSV micelles (Yang et al., 2021a)	Release of PTX and IR780 in response to GSH for chemophototherapy	2021
" Sensing and Healing" nanoplatform	Bimetallic NPs	Au-AgNP-Ag-HM (Wang et al., 2021c)	The imaging of intracellular caspase-3 and ROS by DEVD and Au-Ag-HM differentiates cancer cells from normal cells	2021
	Semiconducting polymer NPs	PSBTBT-Ce6@Rhod NPs (Bao et al., 2021)	PSBTBT NPs loaded with Rhodamine B and Ce6 for combined PTT/PDT therapy	2021

perfluorocarbons (PFCs) as oxygen carriers to directly deliver oxygen to tumors is a common way to relieve tumor hypoxia and enhance the PDT effect. Recently, Tseng et al. developed a folate-conjugated fluorinated polymeric micelle (PFFA)-Ce6 micellar system, which exhibited a higher ROS production, good long-term stability, higher oxygen carrying capacity and improved PDT efficacy in inhibiting tumor growth as compared to those of non-PFC system Tseng et al. (2021). The fluorinated segment in PFFA-Ce6 could not only maintain the oxygen carrying capacity of polymer micelle without the problem of PFC molecule leakage, but also acted as a reservoir to accommodate the hydrophobic Ce6 to enhance its solubility. The folic moiety in PFFA-Ce6 provided a function as a specific targeting ligand for cancer cells. In the *in vitro* cell study, due to the selective internalization of PFFA-Ce6, the cell growth inhibition of HeLa cells after irradiation was higher. Cancer cells are accustomed to oxidative stress caused by PDT through overexpressing glutathione (GSH) and other antioxidants. Therefore, preferentially amplifying the oxidative stress of tumor cells by consuming GSH or producing ROS is a reasonable treatment strategy to enhance the efficacy of PDT. To this end, Xia et al. designed a GSH-scavenging and ROS- generating polymeric micelle mPEG-S-S-PCL-Por (MSLP), which was composed of methoxy polyethylene glycol (MPEG)-SS-poly (ε-caprolactone)-protoporphyrin (POR) amphiphilic polymer and the anticancer drug DOX, for amplifying oxidative stress and enhanced anticancer therapy of PDT Xia et al. (2021). MSLP combined Chemotherapy-photodynamic therapy (Chemo-PDT)-based synergy therapy exhibited significant antitumor activity both *in vitro* (IC50 = 0.041 μg/ml) and much better antitumor efficacy than that of mPEG- PCL-Por (MLP) micelles *in vivo*. In addition, Yang et al. also designed a GSH-responsive dual receptor targeting nanomicelle system, which could be used for precise fluorescent bioimaging and superior synergistic chemo-phototherapy of tumors Yang Y. et al. (2021). IR780/PTX/FHSV micelles were composed of amphiphilic hyaluronic acid derivative (FHSV), paclitaxel (PTX) and photosensitizer IR780 iodide (IR780). Once they accumulated at the tumor site through enhanced permeability and retention (EPR) effects, IR780/PTX/FHSV micelles could effectively enter tumor cells through receptor-mediated endocytosis, and then rapidly release PTX and IR780 in the GSH-rich tumor microenvironment. Under near-infrared laser irradiation, IR780 generated local high temperature and sufficient reactive oxygen species to promote tumor cell apoptosis and necrosis. The results of *in vivo* and *in vitro* experiments consistently shown that compared with single chemotherapy and phototherapy, IR780/PTX/FHSV micelle-mediated chemo-phototherapy could more effectively synergize anti-tumor effects to kill tumor cells. However, further clinical applications of polymers are limited due to the disadvantages of poor storage stability, potential tissue toxicity, limited loading capacity for hydrophilic drugs, and complicated preparation processes (Deng et al., 2021).

5 THE APPLICATIONS AND THE PHOTOSENSITIZERS FOR CLINICAL TUMOR TREATMENT

PDT has been used to treat a variety of cancers, including lung, head and neck, brain, pancreas, peritoneal cavity, breast, prostate, skin, and liver cancer (Kubrak et al., 2022).

The first-generation PS are hematoporphyrin derivative. They have long plasma half-life and lack of sensitivity. For example, Photofrin® has been licensed for use in the oesophagus, lung, stomach, cervix and bladder. Since the absorption spectrum of Porfimer sodium peaks at 405 nm, its depth of action is limited to 0.5 cm (Ramsay et al., 2021).

The second-generation PSs are single compound synthesized, derived from porphyrin, bacteriochlorophyll, phthalocyanine, chlorin, benzoporphyrin, curcumin, methylene blue derivatives, etc., Compared with the first-generation PSs, the second-generation PSs have longer absorption spectrum (visible-near-infrared region), higher $^1O_2$ yields, and better tumor targeting. For example, 5-aminolevulinic acid (5-ALA) has been successfully used in the treatment of basal cell carcinoma, actinic keratosis and oral premalignant disorder, Meso-tetrahydroxyphenyl chlorin (mTHPC-Foscan®) has been commonly used for advanced head and neck cancers (Zhang S. et al., 2022). Other second-generation PSs that have received clinical approval or are in clinical trials include Temoporfin (Foscan®), Motexafin lutetium, Palladium bacteriopheophorbide, Purlytin®, Verteporfin (Visudyne®), and Talaporfin (Laserphyrin®) (Baskaran et al., 2018).

The third-generation PS are characterized by combining the second-generation PSs with targeting entities or moieties, such as antibodies, amino acids, polypeptides, or by encapsulation into highly biocompatible nanocarriers to improve the ability of PS improve accumulation of PSs at the targeted tumor sites (Baskaran et al., 2018). Now, third-generation PSs that can significantly improve cancer targeting efficiency through chemical modification, nano-delivery systems, or antibody conjugation are widely studied for preclinical studies, and if satisfactory results are obtained, then more third-generation PSs will be promoted to enter the clinical research stage (Mfouo-Tynga et al., 2021).

6 CONCLUSION AND PERSPECTIVE

In summary, we have introduced the advantages and disadvantages (**Tables 1**, **2**)and recent studies (**Table 3**) based on Metal NPs, Nanoliposomes, MSNs, Dendrimers, Hydrogels, Polymers, which overcome the obstacles of PDT in tumor tissues, such as poor biocompatibility and low delivery efficiency of PSs, compromising poor light transmittance of deep tissues, and hypoxia, reactive oxygen species scavenging and immunosuppression in tumor TME (Lee et al., 2022). Insufficient supply of pivotal factors including PSs, light, and O_2 highly reduces the therapeutic efficacy of PDT. Therefore, the primary source of photodynamic therapy should be optimized by setting parameters such as input dose, intratumoral drug level, light source, and tissue oxygen conditions. Based on recent progress in the combination of nano- and biotechnology, various kinds of NPs have been developed for PDT, and they showed promising potential to overcome these obstacles. PSs are an indispensable key ingredient in photodynamic therapy. In most cases, PSs are aggregated inside the nanoparticles, and $^1O_2$ has the disadvantages of short half-life (<40 ns) and short intracellular distance (<20 nm), resulting in $^1O_2$ needing time and space to diffuse out from NPs to attack cells of biomolecules and further impairs the efficiency of PDT (Deng et al., 2021). Therefore, it is very necessary to release free PSs from nanoparticles before irradiating cancer cells or tumor tissue with light. In addition to the optimization of the physical structure and chemical composition of passive targeting of PSs and the modification of active targeting ligands for efficient, safe, and better tissue penetration, improving drug delivery and combination therapy are also effective strategies. In recent years, stimuli-responsive nanomaterials have received increasing attention because they can react to both endogenous stimuli (low pH, enzymes, redox agents, hypoxia) and exogenous stimuli (light, temperature, magnetic field, ultrasonic) and other stimuli to change its physicochemical properties and release PSs (Chang et al., 2021). However, the release of PSs from endogenous stimuli-responsive nanocarriers is slow due to weak stimulation intensity. In contrast, exogenous stimuli are easily modulated remotely in intensity and timing to release drugs on demand in diseased tissues or cells. However, the poor penetration of drugs into deep tumor tissue and the poor penetration of excitation light source into deep tumor tissue are important issues that need to be solved for NPs delivery systems. The use of UCNPs, XPDT, and fluorescence imaging techniques provides clues for efficient light delivery to deep tissues. Among them, the potential toxicity of heavy metals is a serious limitation, and their potential toxicity needs to be carefully considered, and favorable distribution, degradation and excretion should be achieved (Medici et al., 2021). Attempts to overcome hypoxia caused by hypoxia in tumor tissues include artificial oxygen production, Fenton reaction, and the combined application of chemical drugs related to hypoxia. In addition to promising results, combined with the latest methods to normalize tumor blood vessels and reduce hypoxia itself, it is also expected to become an effective method for PDT to treat tumors. Although many of these ideas are at the level of cell experiments and animal experiments, these studies have made significant progress over traditional PDT research. Therefore, we hope that the results of these trials can maximize the clinical efficacy of PDT in the future. In addition, future research and development of new nanomaterials should focus on targeted therapy and personal medicine. In order to improve the specificity and safety of drugs, targeted delivery and on-demand controlled/triggerable release are still the focus of drug delivery platform development.

AUTHOR CONTRIBUTIONS

The manuscript was written through the contributions of all authors. LC, JH, and SL conceived this work. LC and JH mainly wrote the manuscript. All authors have given approval to the final version of the manuscript.

REFERENCES

Ahmad, F., Wang, X., Jiang, Z., Yu, X., Liu, X., Mao, R., et al. (2019). Codoping Enhanced Radioluminescence of Nanoscintillators for X-Ray-Activated Synergistic Cancer Therapy and Prognosis Using Metabolomics. *Acs Nano* 13, 10419–10433. doi:10.1021/acsnano.9b04213

Algorri, J. F., Ochoa, M., Roldán-Varona, P., Rodríguez-Cobo, L., and López-Higuera, J. M. (2021). Photodynamic Therapy: A Compendium of Latest Reviews. *Cancers* 13, 4447. doi:10.3390/cancers13174447

Arias-Egido, E., Laguna-Marco, M. A., Piquer, C., Jiménez-Cavero, P., Lucas, I., Morellón, L., et al. (2021). Dimensionality-driven Metal-Insulator Transition in Spin-Orbit-Coupled IrO2. *Nanoscale* 13, 17125–17135. doi:10.1039/d1nr04207f

Bao, B., Su, P., Song, K., Cui, Y., Zhai, X., Xu, Y., et al. (2021). A Smart "Sense-And-Treat" Nanoplatform Based on Semiconducting Polymer Nanoparticles for Precise Photothermal-Photodynamic Combined Therapy. *Biomacromolecules* 22, 1137–1146. doi:10.1021/acs.biomac.0c01567

Baskaran, R., Lee, J., and Yang, S.-G. (2018). Clinical Development of Photodynamic Agents and Therapeutic Applications. *Biomater. Res.* 22, 25. doi:10.1186/s40824-018-0140-z

Bu, Y., Huang, R., Li, Z., Zhang, P., Zhang, L., Yang, Y., et al. (2021). Anisotropic Truncated Octahedral Au with Pt Deposition on Arris for Localized Surface Plasmon Resonance-Enhanced Photothermal and Photodynamic Therapy of Osteosarcoma. *ACS Appl. Mat. Interfaces* 13, 35328–35341. doi:10.1021/acsami.1c07181

Cai, X., Zhao, Y., Wang, L., Hu, M., Wu, Z., Liu, L., et al. (2021a). Synthesis of Au@MOF Core-Shell Hybrids for Enhanced Photodynamic/photothermal Therapy. *J. Mat. Chem. B* 9, 6646–6657. doi:10.1039/d1tb00800e

Cai, Z., Fu, Y., Qiu, Z., Wang, Y., Wang, W., Gu, W., et al. (2021b). Multitarget Reaction Programmable Automatic Diagnosis and Treatment Logic Device. *Acs Nano* 15, 19150–19164. doi:10.1021/acsnano.1c07307

Cao, H., Yang, Y., Liang, M., Ma, Y., Sun, N., Gao, X., et al. (2021). Pt@polydopamine Nanoparticles as Nanozymes for Enhanced Photodynamic and Photothermal Therapy. *Chem. Commun.* 57, 255–258. doi:10.1039/d0cc07355e

Cendrowicz, E., Sas, Z., Bremer, E., and Rygiel, T. P. (2021). The Role of Macrophages in Cancer Development and Therapy. *Cancers* 13, 1946. doi:10.3390/cancers13081946

Chang, D., Ma, Y., Xu, X., Xie, J., and Ju, S. (2021). Stimuli-Responsive Polymeric Nanoplatforms for Cancer Therapy. *Front. Bioeng. Biotechnol.* 9, 707319. doi:10.3389/fbioe.2021.707319

Chen, C., Ni, X., Jia, S., Liang, Y., Wu, X., Kong, D., et al. (2019). Massively Evoking Immunogenic Cell Death by Focused Mitochondrial Oxidative Stress Using an AIE Luminogen with a Twisted Molecular Structure. *Adv. Mat.* 31, 1904914. doi:10.1002/adma.201904914

Chen, J., Wang, Y., Niu, H., Wang, Y., Wu, A., Shu, C., et al. (2021a). Metal-Organic Framework-Based Nanoagents for Effective Tumor Therapy by Dual Dynamics-Amplified Oxidative Stress. *ACS Appl. Mat. Interfaces* 13, 45201–45213. doi:10.1021/acsami.1c11032

Chen, M., Song, J., Zhu, J., Hong, G., An, J., Feng, E., et al. (2021b). A Dual-Nanozyme-Catalyzed Cascade Reactor for Enhanced Photodynamic Oncotherapy against Tumor Hypoxia. *Adv. Healthc. Mat.* 10, 2101049. doi:10.1002/adhm.202101049

Chen, X., Zhang, Y., Zhang, X., Zhang, Z., and Zhang, Y. (2021c). Rationally Designed Upconversion Nanoparticles for NIR Light-Controlled Lysosomal Escape and Nucleus-Based Photodynamic Therapy. *Microchim. Acta* 188, 349. doi:10.1007/s00604-021-04915-w

Chen, Y., Bai, L., Zhang, P., Zhao, H., and Zhou, Q. (2021d). The Development of Ru(II)-Based Photoactivated Chemotherapy Agents. *Molecules* 26, 5679. doi:10.3390/molecules26185679

Chen, Y., Jin, H., Song, Y., Huang, T., Cao, J., Tang, Q., et al. (2021e). Targeting Tumor-associated Macrophages: A Potential Treatment for Solid Tumors. *J. Cell.Physiol.* 236, 3445–3465. doi:10.1002/jcp.30139

Cheng, X., Gao, J., Ding, Y., Lu, Y., Wei, Q., Cui, D., et al. (2021a). Multi-Functional Liposome: A Powerful Theranostic Nano-Platform Enhancing Photodynamic Therapy. *Adv. Sci.* 8, 2100876. doi:10.1002/advs.202100876

Cheng, Y., Zheng, R., Wu, X., Xu, K., Song, P., Wang, Y., et al. (2021b). Thylakoid Membranes with Unique Photosystems Used to Simultaneously Produce Self-Supplying Oxygen and Singlet Oxygen for Hypoxic Tumor Therapy. *Adv. Healthc. Mat.* 10, 2001666. doi:10.1002/adhm.202001666

Chou, M.-Y., and Yang, M.-H. (2021). Interplay of Immunometabolism and Epithelial-Mesenchymal Transition in the Tumor Microenvironment. *Ijms* 22, 9878. doi:10.3390/ijms22189878

Chuang, Y.-C., Chu, C.-H., Cheng, S.-H., Liao, L.-D., Chu, T.-S., Chen, N.-T., et al. (2020). Annealing-modulated Nanoscintillators for Nonconventional X-Ray Activation of Comprehensive Photodynamic Effects in Deep Cancer Theranostics. *Theranostics* 10, 6758–6773. doi:10.7150/thno.41752

Cui, T., Li, S., Chen, S., Liang, Y., Sun, H., and Wang, L. (2021). "Stealth" Dendrimers with Encapsulation of Indocyanine Green for Photothermal and Photodynamic Therapy of Cancer. *Int. J. Pharm.* 600, 120502. doi:10.1016/j.ijpharm.2021.120502

Curio, S., Jonsson, G., and Marinović, S. (2021). A Summary of Current NKG2D-Based CAR Clinical Trials. *Immunother. Adv.* 1, b18. doi:10.1093/immadv/ltab018

Dahiya, R., Dahiya, S., Fuloria, N. K., Jankie, S., Agarwal, A., Davis, V., et al. (2021). Natural Thiazoline-Based Cyclodepsipeptides from Marine Cyanobacteria: Chemistry, Bioefficiency and Clinical Aspects. *Cmc* 28, 7887–7909. doi:10.2174/0929867328666210526095436

Dai, Y., Zhao, H., He, K., Du, W., Kong, Y., Wang, Z., et al. (2021a). NIR-II Excitation Phototheranostic Nanomedicine for Fluorescence/Photoacoustic Tumor Imaging and Targeted Photothermal-Photonic Thermodynamic Therapy. *Small* 17, 2102527. doi:10.1002/smll.202102527

Dai, Z., Xu, X., Guo, Z., Zheng, K., Song, X.-Z., Qi, X., et al. (2021b). Effect of ROS Generation on Highly Dispersed 4-layer O-Ti7O13 Nanosheets toward Tumor Synergistic Therapy. *Mater. Sci. Eng. C* 120, 111666. doi:10.1016/j.msec.2020.111666

De Lerma Barbaro, A., Palano, M. T., Cucchiara, M., Gallazzi, M., Mortara, L., and Bruno, A. (2021). Metabolic Rewiring in the Tumor Microenvironment to Support Immunotherapy: A Focus on Neutrophils, Polymorphonuclear Myeloid-Derived Suppressor Cells and Natural Killer Cells. *Vaccines* 9, 1178. doi:10.3390/vaccines9101178

Deng, K., Yu, H., Li, J.-M., Li, K.-H., Zhao, H.-Y., Ke, M., et al. (2021). Dual-step Irradiation Strategy to Sequentially Destroy Singlet Oxygen-Responsive Polymeric Micelles and Boost Photodynamic Cancer Therapy. *Biomaterials* 275, 120959. doi:10.1016/j.biomaterials.2021.120959

Ding, D., Feng, Y., Qin, R., Li, S., Chen, L., Jing, J., et al. (2021a). Mn3+-rich Oxide/persistent Luminescence Nanoparticles Achieve Light-free Generation of Singlet Oxygen and Hydroxyl Radicals for Responsive Imaging and Tumor Treatment. *Theranostics* 11, 7439–7449. doi:10.7150/thno.62437

Ding, S., Liu, Z., Huang, C., Zeng, N., Jiang, W., and Li, Q. (2021b). Novel Engineered Bacterium/Black Phosphorus Quantum Dot Hybrid System for Hypoxic Tumor Targeting and Efficient Photodynamic Therapy. *ACS Appl. Mat. Interfaces* 13, 10564–10573. doi:10.1021/acsami.0c20254

Duo, Y., Luo, G., Li, Z., Chen, Z., Li, X., Jiang, Z., et al. (2021). Photothermal and Enhanced Photocatalytic Therapies Conduce to Synergistic Anticancer Phototherapy with Biodegradable Titanium Diselenide Nanosheets. *Small* 17, 2103239. doi:10.1002/smll.202103239

Faizullin, B. A., Strelnik, I. D., Dayanova, I. R., Gerasimova, T. P., Kholin, K. V., Nizameev, I. R., et al. (2021). Structure Impact on Photodynamic Therapy and Cellular Contrasting Functions of Colloids Constructed from Dimeric Au(I) Complex and Hexamolybdenum Clusters. *Mater. Sci. Eng. C* 128, 112355. doi:10.1016/j.msec.2021.112355

Fakurnejad, S., Krishnan, G., van Keulen, S., Nishio, N., Birkeland, A. C., Baik, F. M., et al. (2019). Intraoperative Molecular Imaging for *Ex Vivo* Assessment of Peripheral Margins in Oral Squamous Cell Carcinoma. *Front. Oncol.* 9, 1476. doi:10.3389/fonc.2019.01476

Farooq, S., and de Araujo, R. E. (2021). Identifying High Performance Gold Nanoshells for Singlet Oxygen Generation Enhancement. *Photodiagnosis Photodyn. Ther.* 35, 102466. doi:10.1016/j.pdpdt.2021.102466

Feng, M., Li, M., Dai, R., Xiao, S., Tang, J., Zhang, X., et al. (2021). Multifunctional FeS2 @SRF@BSA Nanoplatform for Chemo-Combined Photothermal Enhanced Photodynamic/chemodynamic Combination Therapy. *Biomater. Sci.-Uk* 10, 258. doi:10.1039/d1bm01597d

Gao, C., Guo, W., Guo, X., Ding, Z., Ding, Y., and Shen, X.-C. (2021a). Black SnO2−x Based Nanotheranostic for Imaging-Guided Photodynamic/photothermal Synergistic Therapy in the Second Near-Infrared Window. *Acta Biomater.* 129, 220–234. doi:10.1016/j.actbio.2021.05.041

Gao, C., Lyu, F., and Yin, Y. (2021b). Encapsulated Metal Nanoparticles for Catalysis. *Chem. Rev.* 121, 834–881. doi:10.1021/acs.chemrev.0c00237

Guo, X., Wen, C., Xu, Q., Ruan, C., Shen, X.-C., and Liang, H. (2021). A Full-Spectrum Responsive B-TiO2@SiO2-HA Nanotheranostic System for NIR-II Photoacoustic Imaging-Guided Cancer Phototherapy. *J. Mat. Chem. B* 9, 2042–2053. doi:10.1039/d0tb02952a

He, F., Ji, H., Feng, L., Wang, Z., Sun, Q., Zhong, C., et al. (2021a). Construction of Thiol-Capped Ultrasmall Au-Bi Bimetallic Nanoparticles for X-Ray CT Imaging and Enhanced Antitumor Therapy Efficiency. *Biomaterials* 264, 120453. doi:10.1016/j.biomaterials.2020.120453

He, G., Xu, N., Ge, H., Lu, Y., Wang, R., Wang, H., et al. (2021b). Red-Light-Responsive Ru Complex Photosensitizer for Lysosome Localization Photodynamic Therapy. *ACS Appl. Mat. Interfaces* 13, 19572–19580. doi:10.1021/acsami.0c22551

He, Y., Gao, Q., Lv, C., and Liu, L. (2021c). Improved Photothermal Therapy of Brain Cancer Cells and Photogeneration of Reactive Oxygen Species by Biotin Conjugated Gold Photoactive Nanoparticles. *J. Photochem. Photobiol. B Biol.* 215, 112102. doi:10.1016/j.jphotobiol.2020.112102

Hou, H., Wang, Z., Ma, Y., Yu, K., Zhao, J., Lin, H., et al. (2022). NIR-driven Intracellular Photocatalytic Oxygen-Supply on Metallic Molybdenum carbide@N-Carbon for Hypoxic Tumor Therapy. *J. Colloid Interface Sci.* 607, 1–15. doi:10.1016/j.jcis.2021.08.177

Hu, S., Zhi, Y., Shan, S., and Ni, Y. (2022). Research Progress of Smart Response Composite Hydrogels Based on Nanocellulose. *Carbohydr. Polym.* 275, 118741. doi:10.1016/j.carbpol.2021.118741

Huang, C., Chen, T., Zhu, D., and Huang, Q. (2020a). Enhanced Tumor Targeting and Radiotherapy by Quercetin Loaded Biomimetic Nanoparticles. *Front. Chem.* 8, 225. doi:10.3389/fchem.2020.00225

Huang, L., Liu, J., Zhu, Y., Zhou, Q., Xiao, B., Sun, Z., et al. (2021). The Role of Nuclear Receptor Transcription Factor NR2F6 in Tumor. *Sheng Wu Gong Cheng Xue Bao* 37, 2595–2602. doi:10.13345/j.cjb.200488

Huang, L., Wu, W., Li, Y., Huang, K., Zeng, L., Lin, W., et al. (2020b). Highly Effective Near-Infrared Activating Triplet-Triplet Annihilation Upconversion for Photoredox Catalysis. *J. Am. Chem. Soc.* 142, 18460–18470. doi:10.1021/jacs.0c06976

Jia, P., Ji, H., Liu, S., Zhang, R., He, F., Zhong, L., et al. (2021). Integration of IR-808 and Thiol-Capped Au-Bi Bimetallic Nanoparticles for NIR Light Mediated Photothermal/photodynamic Therapy and Imaging. *J. Mat. Chem. B* 9, 101–111. doi:10.1039/d0tb02378g

Jiang, Y., Lu, Y., Lei, L., Zhou, S., Yang, L., Yang, X., et al. (2021a). Near-infrared Light-Triggered Synergistic Antitumor Therapy Based on Hollow ZIF-67-Derived Co3S4-Indocyanine Green Nanocomplex as a Superior Reactive Oxygen Species Generator. *Mater. Sci. Eng. C* 130, 112465. doi:10.1016/j.msec.2021.112465

Jiang, Y., and McNeill, J. (2017). Light-Harvesting and Amplified Energy Transfer in Conjugated Polymer Nanoparticles. *Chem. Rev.* 117, 838–859. doi:10.1021/acs.chemrev.6b00419

Jiang, Z., He, L., Yu, X., Yang, Z., Wu, W., Wang, X., et al. (2021b). Antiangiogenesis Combined with Inhibition of the Hypoxia Pathway Facilitates Low-Dose, X-Ray-Induced Photodynamic Therapy. *Acs Nano* 15, 11112–11125. doi:10.1021/acsnano.1c01063

Jin, F., Qi, J., Liu, D., You, Y., Shu, G., Du, Y., et al. (2021a). Cancer-cell-biomimetic Upconversion Nanoparticles Combining Chemo-Photodynamic Therapy and CD73 Blockade for Metastatic Triple-Negative Breast Cancer. *J. Control. Release* 337, 90–104. doi:10.1016/j.jconrel.2021.07.021

Jin, L., Shen, S., Huang, Y., Li, D., and Yang, X. (2021b). Corn-like Au/Ag Nanorod-Mediated NIR-II Photothermal/photodynamic Therapy Potentiates Immune Checkpoint Antibody Efficacy by Reprogramming the Cold Tumor Microenvironment. *Biomaterials* 268, 120582. doi:10.1016/j.biomaterials.2020.120582

Kang, Y., Li, Z., Lu, F., Su, Z., Ji, X., and Zhang, S. (2022). Synthesis of Red/black Phosphorus-Based Composite Nanosheets with a Z-Scheme Heterostructure for High-Performance Cancer Phototherapy. *Nanoscale* 14, 766–779. doi:10.1039/d1nr07553e

Kappenberg, Y. G., Stefanello, F. S., Zanatta, N., Martins, M. A. P., Nogara, P. A., Rocha, J. B. T., et al. (2022). Hybridized 4-Trifluoromethyl-(1,2,3-triazol-1-yl) quinoline System: Synthesis, Photophysics, Selective DNA/HSA Bio-interactions and Molecular Docking. *Chembiochem* 23, e202100649. doi:10.1002/cbic.202100649

Karges, J., Kuang, S., Maschietto, F., Blacque, O., Ciofini, I., Chao, H., et al. (2020). Rationally Designed Ruthenium Complexes for 1- and 2-photon Photodynamic Therapy. *Nat. Commun.* 11, 3262. doi:10.1038/s41467-020-16993-0

Karges, J., Tharaud, M., and Gasser, G. (2021). Polymeric Encapsulation of a Ru(II)-Based Photosensitizer for Folate-Targeted Photodynamic Therapy of Drug Resistant Cancers. *J. Med. Chem.* 64, 4612–4622. doi:10.1021/acs.jmedchem.0c02006

Kirakci, K., Pozmogova, T. N., Protasevich, A. Y., Vavilov, G. D., Stass, D. V., Shestopalov, M. A., et al. (2021). A Water-Soluble Octahedral Molybdenum Cluster Complex as a Potential Agent for X-Ray Induced Photodynamic Therapy. *Biomater. Sci.* 9, 2893–2902. doi:10.1039/d0bm02005b

Kubrak, T., Karakuła, M., Czop, M., Kawczyk-Krupka, A., and Aebisher, D. (2022). Advances in Management of Bladder Cancer-The Role of Photodynamic Therapy. *Molecules* 27, 731. doi:10.3390/molecules27030731

Lee, D., Kwon, S., Jang, S.-y., Park, E., Lee, Y., and Koo, H. (2022). Overcoming the Obstacles of Current Photodynamic Therapy in Tumors Using Nanoparticles. *Bioact. Mater.* 8, 20–34. doi:10.1016/j.bioactmat.2021.06.019

Lee, M.-H., Thomas, J., Li, J.-A., Chen, J.-R., Wang, T.-L., and Lin, H.-Y. (2021). Synthesis of Multifunctional Nanoparticles for the Combination of Photodynamic Therapy and Immunotherapy. *Pharmaceuticals* 14, 508. doi:10.3390/ph14060508

Lee, S. Y., Lee, R., Kim, E., Lee, S., and Park, Y. I. (2020). Near-Infrared Light-Triggered Photodynamic Therapy and Apoptosis Using Upconversion Nanoparticles with Dual Photosensitizers. *Front. Bioeng. Biotechnol.* 8, 275. doi:10.3389/fbioe.2020.00275

Li, J., Zhou, C., Zhang, J., Xu, F., Zheng, Y., Wang, S., et al. (2021a). Photo-induced Tumor Therapy Using MnO2/IrO2-PVP Nano-Enzyme with TME-Responsive Behaviors. *Colloids Surfaces B Biointerfaces* 205, 111852. doi:10.1016/j.colsurfb.2021.111852

Li, P., Lu, M., Shi, J., Hua, L., Gong, Z., Li, Q., et al. (2020). Dual Roles of Neutrophils in Metastatic Colonization Are Governed by the Host NK Cell Status. *Nat. Commun.* 11, 1–14. doi:10.1038/s41467-020-18125-0

Li, R., Peng, Y., Pu, Y., Zhao, Y., Nie, R., Guo, L., et al. (2021b). Fructose and Biotin Co-modified Liposomes for Dual-Targeting Breast Cancer. *J. Liposome Res.*, 1–10. doi:10.1080/08982104.2021.1894171

Li, Y., Zhao, P., Gong, T., Wang, H., Jiang, X., Cheng, H., et al. (2020). Redox Dyshomeostasis Strategy for Hypoxic Tumor Therapy Based on DNAzyme-Loaded Electrophilic ZIFs. *Angew. Chem. Int. Ed.* 59, 22537–22543. doi:10.1002/anie.202003653

Liang, L., Sui, R., Song, Y., and Zhao, Y. (2021). Acidic Microenvironment Enhances MT1-MMP-mediated Cancer Cell Motility through Integrin β1/cofilin/F-actin axis. *Acta Biochim. Biophys. Sin. (Shanghai)* 53, 1558–1566. doi:10.1093/abbs/gmab130

Lin, C.-C., Lin, H.-Y., Thomas, J. L., Yu, J.-X., Lin, C.-Y., Chang, Y.-H., et al. (2021a). Embedded Upconversion Nanoparticles in Magnetic Molecularly Imprinted Polymers for Photodynamic Therapy of Hepatocellular Carcinoma. *Biomedicines* 9, 1923. doi:10.3390/biomedicines9121923

Lin, M., Zou, S., Liao, X., Chen, Y., Luo, D., Ji, L., et al. (2021b). Ruthenium(II) Complexes as Bioorthogonal Two-Photon Photosensitizers for Tumour-specific Photodynamic Therapy against Triple-Negative Breast Cancer Cells. *Chem. Commun.* 57, 4408–4411. doi:10.1039/d1cc00661d

Liu, B., Jiao, J., Xu, W., Zhang, M., Cui, P., Guo, Z., et al. (2021a). Highly Efficient Far-Red/NIR-Absorbing Neutral Ir(III) Complex Micelles for Potent Photodynamic/Photothermal Therapy. *Adv. Mat.* 33, 2100795. doi:10.1002/adma.202100795

Liu, D., Liu, L., Liu, F., Zhang, M., Wei, P., and Yi, T. (2021b). HOCl-Activated Aggregation of Gold Nanoparticles for Multimodality Therapy of Tumors. *Adv. Sci.* 8, 2100074. doi:10.1002/advs.202100074

Liu, F., Shi, R., Wang, Z., Weng, Y., Che, C. M., and Chen, Y. (2019). Direct Z-Scheme Hetero-phase Junction of Black/Red Phosphorus for Photocatalytic Water Splitting. *Angew. Chem. Int. Ed.* 58, 11791–11795. doi:10.1002/anie.201906416

Liu, H., Yao, C., Zhang, L., Xin, J., Zhang, Z., and Wang, S. (2021c). Nanoliposomes Co-encapsulating Ce6 and SB3CT against the Proliferation and Metastasis of Melanoma with the Integration of Photodynamic Therapy and NKG2D-Related Immunotherapy on A375 Cells. *Nanotechnology* 32, 455102. doi:10.1088/1361-6528/ac1afd

Liu, J., Qing, X., Zhang, Q., Yu, N., Ding, M., Li, Z., et al. (2021d). Oxygen-producing Proenzyme Hydrogels for Photodynamic-Mediated Metastasis-Inhibiting Combinational Therapy. *J. Mat. Chem. B* 9, 5255–5263. doi:10.1039/d1tb01009c

Liu, N., Chen, X., Sun, X., Sun, X., and Shi, J. (2021e). Persistent Luminescence Nanoparticles for Cancer Theranostics Application. *J. Nanobiotechnol.* 19, 113–124. doi:10.1186/s12951-021-00862-z

Liu, Q., Wu, B., Li, M., Huang, Y., and Li, L. (2022). Heterostructures Made of Upconversion Nanoparticles and Metal-Organic Frameworks for Biomedical Applications. *Adv. Sci.* 9, 2103911. doi:10.1002/advs.202103911

Liu, S., Chai, J., Sun, S., Zhang, L., Yang, J., Fu, X., et al. (2021f). Site-Selective Photosynthesis of Ag-AgCl@Au Nanomushrooms for NIR-II Light-Driven O2- and O2--Evolving Synergistic Photothermal Therapy against Deep Hypoxic Tumors. *ACS Appl. Mat. Interfaces* 13, 46451–46463. doi:10.1021/acsami.1c16999

Liu, X., Xing, S., Xu, Y., Chen, R., Lin, C., and Guo, L. (2021g). 3-Amino-1,2,4-triazole-derived Graphitic Carbon Nitride for Photodynamic Therapy. *Spectrochimica Acta Part A Mol. Biomol. Spectrosc.* 250, 119363. doi:10.1016/j.saa.2020.119363

Liu, Y., Zhu, D., and Xie, Z. (2021h). Ir(III) Complex Dimer Nanoparticles for Photodynamic Therapy. *Acs Med. Chem. Lett.* 12, 1374–1379. doi:10.1021/acsmedchemlett.1c00362

Liu, Z., Xie, F., Xie, J., Chen, J., Li, Y., Lin, Q., et al. (2021i). New-generation Photosensitizer-Anchored Gold Nanorods for a Single Near-Infrared Light-Triggered Targeted Photodynamic-Photothermal Therapy. *Drug Deliv.* 28, 1769–1784. doi:10.1080/10717544.2021.1960923

Liu, Z., Xie, Z., Wu, X., Chen, Z., Li, W., Jiang, X., et al. (2021j). pH-responsive Black Phosphorus Quantum Dots for Tumor-Targeted Photodynamic Therapy. *Photodiagnosis Photodyn. Ther.* 35, 102429. doi:10.1016/j.pdpdt.2021.102429

Lv, Z., Zhu, Y., and Li, F. (2021). DNA Functional Nanomaterials for Controlled Delivery of Nucleic Acid-Based Drugs. *Front. Bioeng. Biotechnol.* 9, 720291. doi:10.3389/fbioe.2021.720291

Mafa, P. J., Malefane, M. E., Idris, A. O., Mamba, B. B., Liu, D., Gui, J., et al. (2021). Cobalt Oxide/copper Bismuth Oxide/samarium Vanadate (Co3O4/CuBi2O4/SmVO4) Dual Z-Scheme Heterostructured Photocatalyst with High Charge-Transfer Efficiency: Enhanced Carbamazepine Degradation under Visible Light Irradiation. *J. Colloid Interface Sci.* 603, 666–684. doi:10.1016/j.jcis.2021.06.146

Manivasagan, P., Joe, A., Han, H.-W., Thambi, T., Selvaraj, M., Chidambaram, K., et al. (2022). Recent Advances in Multifunctional Nanomaterials for Photothermal-Enhanced Fenton-based Chemodynamic Tumor Therapy. *Mater. Today Bio* 13, 100197. doi:10.1016/j.mtbio.2021.100197

Medici, S., Peana, M., Pelucelli, A., and Zoroddu, M. A. (2021). An Updated Overview on Metal Nanoparticles Toxicity. *Seminars Cancer Biol.* 76, 17–26. doi:10.1016/j.semcancer.2021.06.020

Mfouo-Tynga, I. S., Dias, L. D., Inada, N. M., and Kurachi, C. (2021). Features of Third Generation Photosensitizers Used in Anticancer Photodynamic Therapy: Review. *Photodiagnosis Photodyn. Ther.* 34, 102091. doi:10.1016/j.pdpdt.2020.102091

Mindt, S., Karampinis, I., John, M., Neumaier, M., and Nowak, K. (2018). Stability and Degradation of Indocyanine Green in Plasma, Aqueous Solution and Whole Blood. *Photochem. Photobiol. Sci.* 17, 1189–1196. doi:10.1039/c8pp00064f

Munir, M. T., Kay, M. K., Kang, M. H., Rahman, M. M., Al-Harrasi, A., Choudhury, M., et al. (2021). Tumor-Associated Macrophages as Multifaceted Regulators of Breast Tumor Growth. *Ijms* 22, 6526. doi:10.3390/ijms22126526

Neha Desai, N., Momin, M., Khan, T., Gharat, S., Ningthoujam, R. S., and Omri, A. (2021). Metallic Nanoparticles as Drug Delivery System for the Treatment of Cancer. *Expert Opin. Drug Deliv.* 18, 1261–1290. doi:10.1080/17425247.2021.1912008

Nguyen, N. T., Xia, M., Duchesne, P. N., Wang, L., Mao, C., Jelle, A. A., et al. (2021). Enhanced CO2 Photocatalysis by Indium Oxide Hydroxide Supported on TiN@TiO2 Nanotubes. *Nano Lett.* 21, 1311–1319. doi:10.1021/acs.nanolett.0c04008

Niu, D., Luo, T., Wang, H., Xia, Y., and Xie, Z. (2021). Lactic Acid in Tumor Invasion. *Clin. Chim. Acta* 522, 61–69. doi:10.1016/j.cca.2021.08.011

Ouyang, Z., Gao, Y., Shen, M., and Shi, X. (2021). Dendrimer-based Nanohybrids in Cancer Photomedicine. *Mater. Today Bio* 10, 100111. doi:10.1016/j.mtbio.2021.100111

Park, C., Koo, W. T., Chong, S., Shin, H., Kim, Y. H., Cho, H. J., et al. (2021). Confinement of Ultrasmall Bimetallic Nanoparticles in Conductive Metal-Organic Frameworks via Site-Specific Nucleation. *Adv. Mat.* 33, 2101216. doi:10.1002/adma.202101216

Pham, K.-Y., Wang, L.-C., Hsieh, C.-C., Hsu, Y.-P., Chang, L.-C., Su, W.-P., et al. (2021). 1550 Nm Excitation-Responsive Upconversion Nanoparticles to Establish Dual-Photodynamic Therapy against Pancreatic Tumors. *J. Mat. Chem. B* 9, 694–709. doi:10.1039/d0tb02655g

Potara, M., Nagy-Simon, T., Focsan, M., Licarete, E., Soritau, O., Vulpoi, A., et al. (2021). Folate-targeted Pluronic-Chitosan Nanocapsules Loaded with IR780 for Near-Infrared Fluorescence Imaging and Photothermal-Photodynamic Therapy of Ovarian Cancer. *Colloids Surfaces B Biointerfaces* 203, 111755. doi:10.1016/j.colsurfb.2021.111755

Qamar, H., Hussain, K., Soni, A., Khan, A., Hussain, T., and Chénais, B. (2021). Cyanobacteria as Natural Therapeutics and Pharmaceutical Potential: Role in Antitumor Activity and as Nanovectors. *Molecules* 26, 247. doi:10.3390/molecules26010247

Qi, F., Ji, P., Chen, Z., Wang, L., Yao, H., Huo, M., et al. (2021). Photosynthetic Cyanobacteria-Hybridized Black Phosphorus Nanosheets for Enhanced Tumor Photodynamic Therapy. *Small* 17, 2102113. doi:10.1002/smll.202102113

Qiao, M., Jiang, T., Liu, X., Mao, S., Zhou, F., Li, X., et al. (2021). Immune Checkpoint Inhibitors in EGFR-Mutated NSCLC: Dusk or Dawn? *J. Thorac. Oncol.* 16, 1267–1288. doi:10.1016/j.jtho.2021.04.003

Qiu, M., Wang, D., Huang, H., Yin, T., Bao, W., Zhang, B., et al. (2021). A Regioselectively Oxidized 2D Bi/BiOx Lateral Nano-Heterostructure for Hypoxic Photodynamic Therapy. *Adv. Mat.* 33, 2102562. doi:10.1002/adma.202102562

Ramsay, D., Stevenson, H., and Jerjes, W. (2021). From Basic Mechanisms to Clinical Research: Photodynamic Therapy Applications in Head and Neck Malignancies and Vascular Anomalies. *Jcm* 10, 4404. doi:10.3390/jcm10194404

Rapp, T. L., and DeForest, C. A. (2021). Targeting Drug Delivery with Light: A Highly Focused Approach. *Adv. Drug Deliv. Rev.* 171, 94–107. doi:10.1016/j.addr.2021.01.009

Raza, M. K., Noor, A., and Samantaray, P. K. (2021). Ir(III) and Ru(II) Complexes in Photoredox Catalysis and Photodynamic Therapy: A New Paradigm towards Anticancer Applications. *Chembiochem* 22, 3270–3272. doi:10.1002/cbic.202100469

Redrado, M., Benedi, A., Marzo, I., Gimeno, M. C., and Fernández-Moreira, V. (2021). Dual Emissive Ir(III) Complexes for Photodynamic Therapy and Bioimaging. *Pharmaceutics* 13, 1382. doi:10.3390/pharmaceutics13091382

Ren, S.-Z., Zhu, X.-H., Wang, B., Liu, M., Li, S.-K., Yang, Y.-S., et al. (2021). A Versatile Nanoplatform Based on Multivariate Porphyrinic Metal-Organic Frameworks for Catalytic Cascade-Enhanced Photodynamic Therapy. *J. Mat. Chem. B* 9, 4678–4689. doi:10.1039/d0tb02652b

Sajjad, F., Jin, H., Han, Y., Wang, L., Bao, L., Chen, T., et al. (2022). Incorporation of Green Emission Polymer Dots into Pyropheophorbide-α Enhance the PDT Effect and Biocompatibility. *Photodiagnosis Photodyn. Ther.* 37, 102562. doi:10.1016/j.pdpdt.2021.102562

Sang, D., Wang, K., Sun, X., Wang, Y., Lin, H., Jia, R., et al. (2021). NIR-driven Intracellular Photocatalytic O2 Evolution on Z-Scheme Ni3S2/Cu1.8S@HA for Hypoxic Tumor Therapy. *ACS Appl. Mat. Interfaces* 13, 9604–9619. doi:10.1021/acsami.0c21284

Sengupta, D., Das, S., Sharma, D., Chattopadhyaya, S., Mukherjee, A., Mazumdar, Z. H., et al. (2022). An Anti-inflammatory Fe 3 O 4 -Porphyrin Nanohybrid Capable of Apoptosis through Upregulation of P21 Kinase Inhibitor Having Immunoprotective Properties under Anticancer PDT Conditions. *Chemmedchem* 17, e202100550. doi:10.1002/cmdc.202100550

Shukla, S., Pandey, P. C., and Narayan, R. J. (2021). Tunable Quantum Photoinitiators for Radical Photopolymerization. *Polymers* 13, 2694. doi:10.3390/polym13162694

Silva, L. B., Castro, K. A. D. F., Botteon, C. E. A., Oliveira, C. L. P., Da Silva, R. S., and Marcato, P. D. (2021). Hybrid Nanoparticles as an Efficient Porphyrin Delivery System for Cancer Cells to Enhance Photodynamic Therapy. *Front. Bioeng. Biotechnol.* 9, 679128. doi:10.3389/fbioe.2021.679128

Smith, S. A., Selby, L. I., Johnston, A. P. R., and Such, G. K. (2019). The Endosomal Escape of Nanoparticles: Toward More Efficient Cellular Delivery. *Bioconjugate Chem.* 30, 263–272. doi:10.1021/acs.bioconjchem.8b00732

Smithen, D. A., Monro, S., Pinto, M., Roque, J., Diaz-Rodriguez, R. M., Yin, H., et al. (2020). Bis[pyrrolyl Ru(ii)] Triads: a New Class of Photosensitizers for Metal-Organic Photodynamic Therapy. *Chem. Sci.* 11, 12047–12069. doi:10.1039/d0sc04500d

Su, Y.-B., Zhao, X., Chen, L.-J., Qian, H.-L., and Yan, X.-P. (2021). Fabrication of G-Quadruplex/porphyrin Conjugated Gold/persistent Luminescence Theranostic Nanoprobe for Imaging-Guided Photodynamic Therapy. *Talanta* 233, 122567. doi:10.1016/j.talanta.2021.122567

Sun, Y., Zhou, Z., Yang, S., and Yang, H. (2022). Modulating Hypoxia Inducible Factor-1 by Nanomaterials for Effective Cancer Therapy. *WIREs Nanomed Nanobiotechnol* 14, e1766. doi:10.1002/wnan.1766

Tabish, T. A., and Narayan, R. J. (2021). Mitochondria-targeted Graphene for Advanced Cancer Therapeutics. *Acta Biomater.* 129, 43–56. doi:10.1016/j.actbio.2021.04.054

Tampa, M., Georgescu, S. R., Mitran, M. I., Mitran, C. I., Matei, C., Caruntu, A., et al. (2021). Current Perspectives on the Role of Matrix Metalloproteinases in the Pathogenesis of Basal Cell Carcinoma. *Biomolecules* 11, 903. doi:10.3390/biom11060903

Taucher, E., Taucher, V., Fink-Neuboeck, N., Lindenmann, J., and Smolle-Juettner, F.-M. (2021). Role of Tumor-Associated Neutrophils in the Molecular Carcinogenesis of the Lung. *Cancers* 13, 5972. doi:10.3390/cancers13235972

Teng, F.-Y., Jiang, Z.-Z., Guo, M., Tan, X.-Z., Chen, F., Xi, X.-G., et al. (2021). G-quadruplex DNA: a Novel Target for Drug Design. *Cell. Mol. Life Sci.* 78, 6557–6583. doi:10.1007/s00018-021-03921-8

Tian, Y., and Mao, S. (2012). Amphiphilic Polymeric Micelles as the Nanocarrier for Peroral Delivery of Poorly Soluble Anticancer Drugs. *Expert Opin. Drug Deliv.* 9, 687–700. doi:10.1517/17425247.2012.681299

Tseng, T.-H., Chen, C.-Y., Wu, W.-C., and Chen, C.-Y. (2021). Targeted and Oxygen-Enriched Polymeric Micelles for Enhancing Photodynamic Therapy. *Nanotechnology* 32, 365102. doi:10.1088/1361-6528/ac020d

Wan, Y., Fu, L. H., Li, C., Lin, J., and Huang, P. (2021). Conquering the Hypoxia Limitation for Photodynamic Therapy. *Adv. Mat.* 33, 2103978. doi:10.1002/adma.202103978

Wang, K., Lu, J., Li, J., Gao, Y., Mao, Y., Zhao, Q., et al. (2021a). Current Trends in Smart Mesoporous Silica-Based Nanovehicles for Photoactivated Cancer Therapy. *J. Control. Release* 339, 445–472. doi:10.1016/j.jconrel.2021.10.005

Wang, K., Zhang, F., Wei, Y., Wei, W., Jiang, L., Liu, Z., et al. (2021b). *In Situ* Imaging of Cellular Reactive Oxygen Species and Caspase-3 Activity Using a Multifunctional Theranostic Probe for Cancer Diagnosis and Therapy. *Anal. Chem.* 93, 7870–7878. doi:10.1021/acs.analchem.1c00385

Wang, S., Liu, H., Xin, J., Rahmanzadeh, R., Wang, J., Yao, C., et al. (2019). Chlorin-Based Photoactivable Galectin-3-Inhibitor Nanoliposome for Enhanced Photodynamic Therapy and NK Cell-Related Immunity in Melanoma. *ACS Appl. Mat. Interfaces* 11, 41829–41841. doi:10.1021/acsami.9b09560

Wang, X., Wang, Z., Ma, W., Wu, X., Fang, W., Guo, C., et al. (2021c). Construction of a Nanotheranostic System Zr-MOF@PPa/AF@PEG for Improved Photodynamic Therapy Effects Based on the PDT-oxygen C-onsumption and H-ypoxia S-ensitive C-hemotherapeutic D-rug. *J. Photochem. Photobiol. B Biol.* 222, 112274. doi:10.1016/j.jphotobiol.2021.112274

Wang, Y., Yu, J., Luo, Z., Shi, Q., Liu, G., Wu, F., et al. (2021d). Engineering Endogenous Tumor-Associated Macrophage-Targeted Biomimetic Nano-RBC to Reprogram Tumor Immunosuppressive Microenvironment for Enhanced Chemo-Immunotherapy. *Adv. Mat.* 33, 2103497. doi:10.1002/adma.202103497

Wang, Z., Fu, L., Zhu, Y., Wang, S., Shen, G., Jin, L., et al. (2021e). Chemodynamic/photothermal Synergistic Therapy Based on Ce-Doped Cu-Al Layered Double Hydroxides. *J. Mat. Chem. B* 9, 710–718. doi:10.1039/d0tb02547j

Wei, F., Kuang, S., Rees, T. W., Liao, X., Liu, J., Luo, D., et al. (2021). Ruthenium(II) Complexes Coordinated to Graphitic Carbon Nitride: Oxygen Self-Sufficient Photosensitizers Which Produce Multiple ROS for Photodynamic Therapy in Hypoxia. *Biomaterials* 276, 121064. doi:10.1016/j.biomaterials.2021.121064

Workenhe, S. T., Pol, J., and Kroemer, G. (2021). Tumor-intrinsic Determinants of Immunogenic Cell Death Modalities. *Oncoimmunology* 10, 1893466. doi:10.1080/2162402X.2021.1893466

Wu, W., Pu, Y., and Shi, J. (2021). Dual Size/Charge-Switchable Nanocatalytic Medicine for Deep Tumor Therapy. *Adv. Sci.* 8, 2002816. doi:10.1002/advs.202002816

Xia, H., Liang, Y., Chen, K., Guo, C., Wang, M., Cao, J., et al. (2021). Reduction-sensitive Polymeric Micelles as Amplifying Oxidative Stress Vehicles for Enhanced Antitumor Therapy. *Colloids Surfaces B Biointerfaces* 203, 111733. doi:10.1016/j.colsurfb.2021.111733

Xiao, P., Liu, C., Ma, T., Lu, X., Jing, L., Hou, Y., et al. (2021). A Cyclodextrin-Hosted Ir(III) Complex for Ratiometric Mapping of Tumor Hypoxia *In Vivo*. *Adv. Sci.* 8, 2004044. doi:10.1002/advs.202004044

Xiao, Y., and Yu, D. (2021). Tumor Microenvironment as a Therapeutic Target in Cancer. *Pharmacol. Ther.* 221, 107753. doi:10.1016/j.pharmthera.2020.107753

Xu, Y., Guo, Y., Zhang, C., Zhan, M., Jia, L., Song, S., et al. (2022). Fibronectin-Coated Metal-Phenolic Networks for Cooperative Tumor Chemo-/Chemodynamic/Immune Therapy via Enhanced Ferroptosis-Mediated Immunogenic Cell Death. *Acs Nano* 16, 984–996. doi:10.1021/acsnano.1c08585

Yang, G., Ji, J., and Liu, Z. (2021a). Multifunctional MnO 2 Nanoparticles for Tumor Microenvironment Modulation and Cancer Therapy. *WIREs Nanomed Nanobiotechnol* 13, e1720. doi:10.1002/wnan.1720

Yang, Y.-L., Lin, K., and Yang, L. (2021b). Progress in Nanocarriers Codelivery System to Enhance the Anticancer Effect of Photodynamic Therapy. *Pharmaceutics* 13, 1951. doi:10.3390/pharmaceutics13111951

Yang, Y., Yun, K., Li, Y., Zhang, L., Zhao, W., Zhu, Z., et al. (2021c). Self-assembled Multifunctional Polymeric Micelles for Tumor-specific Bioimaging and Synergistic Chemo-Phototherapy of Cancer. *Int. J. Pharm.* 602, 120651. doi:10.1016/j.ijpharm.2021.120651

Yasukagawa, M., Shimada, A., Shiozaki, S., Tobita, S., and Yoshihara, T. (2021). Phosphorescent Ir(III) Complexes Conjugated with Oligoarginine Peptides Serve as Optical Probes for *In Vivo* Microvascular Imaging. *Sci. Rep.* 11, 4733. doi:10.1038/s41598-021-84115-x

Yin, Z., Ji, Q., Wu, D., Li, Z., Fan, M., Zhang, H., et al. (2021). H2O2-Responsive Gold Nanoclusters @ Mesoporous Silica @ Manganese Dioxide Nanozyme for "Off/On" Modulation and Enhancement of Magnetic Resonance Imaging and Photodynamic Therapy. *ACS Appl. Mat. Interfaces* 13, 14928–14937. doi:10.1021/acsami.1c00430

Yoon, J., Jang, H.-J., Jung, I., and Park, S. (2017). A Close-Packed 3D Plasmonic Superlattice of Truncated Octahedral Gold Nanoframes. *Nanoscale* 9, 7708–7713. doi:10.1039/c7nr02856c

You, L., Wu, W., Wang, X., Fang, L., Adam, V., Nepovimova, E., et al. (2021). The Role of Hypoxia-inducible Factor 1 in Tumor Immune Evasion. *Med. Res. Rev.* 41, 1622–1643. doi:10.1002/med.21771

Younis, M. R., He, G., Qu, J., Lin, J., Huang, P., and Xia, X. H. (2021). Inorganic Nanomaterials with Intrinsic Singlet Oxygen Generation for Photodynamic Therapy. *Adv. Sci.* 8, 2102587. doi:10.1002/advs.202102587

Yu, H., Li, Y., Zhang, Z., Ren, J., Zhang, L., Xu, Z., et al. (2022). Silk Fibroin-Capped Metal-Organic Framework for Tumor-specific Redox Dyshomeostasis Treatment Synergized by Deoxygenation-Driven Chemotherapy. *Acta Biomater.* 138, 545–560. doi:10.1016/j.actbio.2021.11.009

Yu, S., Zhou, Y., Sun, Y., Wu, S., Xu, T., Chang, Y. C., et al. (2021). Endogenous mRNA Triggered DNA-Au Nanomachine for *In Situ* Imaging and Targeted Multimodal Synergistic Cancer Therapy. *Angew. Chem. Int. Ed.* 60, 5948–5958. doi:10.1002/anie.202012801

Yuan, C.-S., Deng, Z.-W., Qin, D., Mu, Y.-Z., Chen, X.-G., and Liu, Y. (2021). Hypoxia-modulatory Nanomaterials to Relieve Tumor Hypoxic Microenvironment and Enhance Immunotherapy: Where Do We Stand? *Acta Biomater.* 125, 1–28. doi:10.1016/j.actbio.2021.02.030

Yuan, X., Cen, J., Chen, X., Jia, Z., Zhu, X., Huang, Y., et al. (2022a). Iridium Oxide Nanoparticles Mediated Enhanced Photodynamic Therapy Combined with Photothermal Therapy in the Treatment of Breast Cancer. *J. Colloid Interface Sci.* 605, 851–862. doi:10.1016/j.jcis.2021.07.136

Yuan, Y., Li, H., Pu, W., Chen, L., Guo, D., Jiang, H., et al. (2022b). Cancer Metabolism and Tumor Microenvironment: Fostering Each Other? *Sci. China Life Sci.* 65, 236–279. doi:10.1007/s11427-021-1999-2

Zeng, L., Cheng, H., Dai, Y., Su, Z., Wang, C., Lei, L., et al. (2021). *In Vivo* Regenerable Cerium Oxide Nanozyme-Loaded pH/H2O2-Responsive

Nanovesicle for Tumor-Targeted Photothermal and Photodynamic Therapies. *ACS Appl. Mat. Interfaces* 13, 233–244. doi:10.1021/acsami.0c19074

Zhang, J., Lu, L., Song, Z.-L., Song, W., Fu, Z., Chao, Q., et al. (2021a). Covalent Amide-Bonded Nanoflares for High-Fidelity Intracellular Sensing and Targeted Therapy: A Superstable Nanosystem Free of Nonspecific Interferences. *Anal. Chem.* 93, 7879–7888. doi:10.1021/acs.analchem.1c00391

Zhang, L., Jin, D., and Stenzel, M. H. (2021b). Polymer-Functionalized Upconversion Nanoparticles for Light/Imaging-Guided Drug Delivery. *Biomacromolecules* 22, 3168–3201. doi:10.1021/acs.biomac.1c00669

Zhang, P., Fischer, A., Ouyang, Y., Wang, J., Sohn, Y. S., Nechushtai, R., et al. (2021c). Aptamer-modified DNA Tetrahedra-Gated Metal-Organic Framework Nanoparticle Carriers for Enhanced Chemotherapy or Photodynamic Therapy. *Chem. Sci.* 12, 14473–14483. doi:10.1039/d1sc04229g

Zhang, P., Han, T., Xia, H., Dong, L., Chen, L., and Lei, L. (2022a). Advances in Photodynamic Therapy Based on Nanotechnology and its Application in Skin Cancer. *Front. Oncol.* 12, 836397. doi:10.3389/fonc.2022.836397

Zhang, Q., Huang, W., Yang, C., Wang, F., Song, C., Gao, Y., et al. (2019). The Theranostic Nanoagent Mo2C for Multi-Modal Imaging-Guided Cancer Synergistic Phototherapy. *Biomater. Sci.* 7, 2729–2739. doi:10.1039/c9bm00239a

Zhang, S., Ma, S., Hao, X., Wang, Y., Cao, B., Han, B., et al. (2021d). Controllable Preparation of Crystalline Red Phosphorus and its Photocatalytic Properties. *Nanoscale* 13, 18955–18960. doi:10.1039/d1nr06530k

Zhang, S., Wang, J., Kong, Z., Sun, X., He, Z., Sun, B., et al. (2022b). Emerging Photodynamic Nanotherapeutics for Inducing Immunogenic Cell Death and Potentiating Cancer Immunotherapy. *Biomaterials* 282, 121433. doi:10.1016/j.biomaterials.2022.121433

Zhang, Y., Elechalawar, C. K., Hossen, M. N., Francek, E. R., Dey, A., Wilhelm, S., et al. (2021e). Gold Nanoparticles Inhibit Activation of Cancer-Associated Fibroblasts by Disrupting Communication from Tumor and Microenvironmental Cells. *Bioact. Mater.* 6, 326–332. doi:10.1016/j.bioactmat.2020.08.009

Zhang, Z., Huang, C., Zhang, L., Guo, Q., Qin, Y., Fan, F., et al. (2021f). pH-Sensitive and Bubble-Generating Mesoporous Silica-Based Nanoparticles for Enhanced Tumor Combination Therapy. *Acta Pharm. Sin. B* 11, 520–533. doi:10.1016/j.apsb.2020.08.013

Zhao, X., Liu, J., Fan, J., Chao, H., and Peng, X. (2021). Recent Progress in Photosensitizers for Overcoming the Challenges of Photodynamic Therapy: from Molecular Design to Application. *Chem. Soc. Rev.* 50, 4185–4219. doi:10.1039/d0cs00173b

Zhong, D., Wu, H., Wu, Y., Li, Y., Yang, J., Gong, Q., et al. (2021a). Redox Dual-Responsive Dendrimeric Nanoparticles for Mutually Synergistic Chemo-Photodynamic Therapy to Overcome Drug Resistance. *J. Control. Release* 329, 1210–1221. doi:10.1016/j.jconrel.2020.10.048

Zhong, Y., Zhang, L., Sun, S., Zhou, Z., Ma, Y., Hong, H., et al. (2021b). Sequential Drug Delivery by Injectable Macroporous Hydrogels for Combined Photodynamic-Chemotherapy. *J. Nanobiotechnol* 19, 333. doi:10.1186/s12951-021-01066-1

Zhu, F., Xu, L., Li, X., Li, Z., Wang, J., Chen, H., et al. (2021a). Co-delivery of Gefitinib and Hematoporphyrin by Aptamer-Modified Fluorinated Dendrimer for Hypoxia Alleviation and Enhanced Synergistic Chemo-Photodynamic Therapy of NSCLC. *Eur. J. Pharm. Sci.* 167, 106004. doi:10.1016/j.ejps.2021.106004

Zhu, L., Dai, Y., Gao, L., and Zhao, Q. (2021b). Tumor Microenvironment-Modulated Nanozymes for NIR-II-Triggered Hyperthermia-Enhanced Photo-Nanocatalytic Therapy via Disrupting ROS Homeostasis. *Ijn* 16, 4559–4577. doi:10.2147/IJN.S309062

Zmerli, I., Ibrahim, N., Cressey, P., Denis, S., and Makky, A. (2021). Design and Synthesis of New PEGylated Polydopamine-Based Nanoconstructs Bearing ROS-Responsive Linkers and a Photosensitizer for Bimodal Photothermal and Photodynamic Therapies against Cancer. *Mol. Pharm.* 18, 3623–3637. doi:10.1021/acs.molpharmaceut.1c00597

Conflict of Interest: The authors declare that the research was conducted in the absence of any commercial or financial relationships that could be construed as a potential conflict of interest.

Publisher's Note: All claims expressed in this article are solely those of the authors and do not necessarily represent those of their affiliated organizations, or those of the publisher, the editors and the reviewers. Any product that may be evaluated in this article, or claim that may be made by its manufacturer, is not guaranteed or endorsed by the publisher.

frontiers | Frontiers in Bioengineering and Biotechnology

ORIGINAL RESEARCH
published: 01 June 2022
doi: 10.3389/fbioe.2022.913648

Mussel-Inspired Microgel Encapsulated NLRP3 Inhibitor as a Synergistic Strategy Against Dry Eye

Zhiwei Zha[1], Qiumeng Chen[1], Decheng Xiao[1], Chengjie Pan[1], Wei Xu[1], Liangliang Shen[1], Jianliang Shen[1,2,3]* and Wei Chen[1]**

[1]Key Laboratory of Ophthalmology, Optometry and Vision Science, School of Ophthalmology and Optometry, Eye Hospital, School of Biomedical Engineering, Wenzhou Medical University, Wenzhou, China, [2]Wenzhou Institute, University of Chinese Academy of Sciences, Wenzhou, China, [3]Oujiang Laboratory (Zhejiang Lab for Regenerative Medicine, Vision and Brain Health), Wenzhou, China

The inflammatory response mediated by oxidative stress is the main pathogenesis of dry eye, but clinical observations have shown that scavenging oxygen-free radicals alone has limited therapeutic effect. Moreover, the unique anatomy and physiology of the ocular surface result in low bioavailability of drugs, and higher concentration is required to achieve the desired efficacy, which, however, may bring systemic side effects. These problems pose a challenge, but the revelation of the ROS-NLRP3-IL-1β signaling axis opens up new possibilities. In this investigation, an NLRP3 inhibitor was successfully encapsulated in polydopamine-based microgels and used for dry eye treatment. It was demonstrated that the well-designed microgels exhibited good biocompatibility, prolonged drug retention time on the ocular surface, and effective inhibition of corneal epithelial damage and cell apoptosis. In addition, due to the synergistic effect, the NLRP3 inhibitor–loaded microgels could exert enhanced oxygen radical scavenging and inflammation-inhibiting effects at a lower dose than monotherapy. These findings suggest that polydopamine-based microgels have advantages as ocular surface drug delivery platforms and have promising applications in oxidative damage–related inflammatory diseases in synergy with anti-inflammatory drugs.

Keywords: ROS, polydopamine, dry eye disease, synergistic strategy, NLRP3

OPEN ACCESS

Edited by:
Qitong Huang,
Gannan Medical University, China

Reviewed by:
Xiaoqing Yi,
Gannan Medical University, China
Chaoliang Tan,
City University of Hong Kong, Hong Kong SAR, China

****Correspondence:***
Liangliang Shen
shenll@wmu.edu.cn
Jianliang Shen
shenjl@wiucas.ac.cn
Wei Chen
chenweimd@wmu.edu.cn

Specialty section:
This article was submitted to Nanobiotechnology, a section of the journal Frontiers in Bioengineering and Biotechnology

Received: *06 April 2022*
Accepted: *18 April 2022*
Published: *01 June 2022*

Citation:
Zha Z, Chen Q, Xiao D, Pan C, Xu W, Shen L, Shen J and Chen W (2022) Mussel-Inspired Microgel Encapsulated NLRP3 Inhibitor as a Synergistic Strategy Against Dry Eye. Front. Bioeng. Biotechnol. 10:913648. doi: 10.3389/fbioe.2022.913648

INTRODUCTION

Dry eye disease (DED), a multifactorial chronic disorder of the ocular surface with a reported prevalence of 5–50%, affects millions of people worldwide, causing a marked impact on individual well-being (Mason et al., 2021). Especially at present, with the high-frequency use of video terminals, the incidence of DED is gradually increasing. DED is characterized by tear film instability and accompanied by hyperosmolarity, ocular surface inflammation, and damage, resulting in a variety of ocular discomforts and visual impairments (Bron et al., 2017). Tear hyperosmolarity can cause damage to the corneal and conjunctiva epithelial cells, leading to large production of inflammatory cytokines, which will further aggravate damage to the ocular surface epithelium and conjunctival goblet cells (Pflugfelder and de Paiva, 2017). These events will cause the release of damage-associated related pattern molecules, insufficient secretion of ocular surface mucins, and decreased tear film stability, with the interplay of these factors eventually leading to apoptosis (Pflugfelder and de Paiva, 2017; Reins et al., 2018; Baudouin et al., 2019). Current pharmacological treatments of DED include

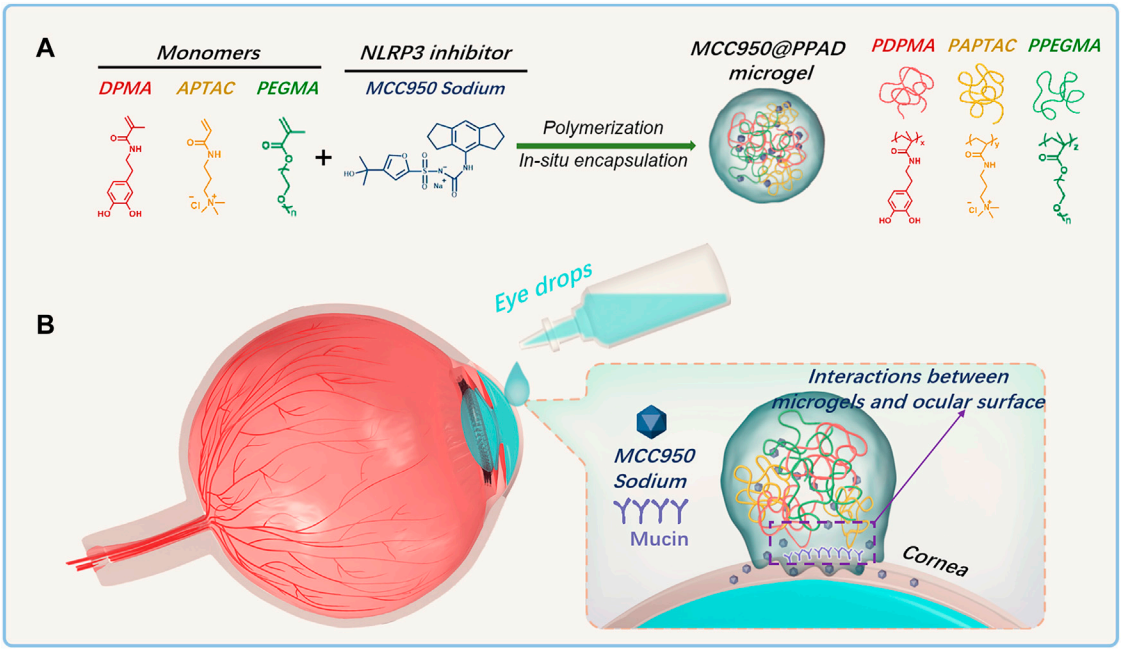

SCHEME 1 | (A) Schematic diagram of the construction of the PPAD microgel and *in situ* encapsulation of MCC950 through radical copolymerization of PEGMA, APTAC, and DPMA; **(B)** Ocular surface retention time of MCC950@PPAD microgels can be enhanced due to the adhesiveness of polydopamines.

artificial tears, autologous serum, glucocorticoids, and non-hormonal immunosuppressants (Jones et al., 2017). Although artificial tears can temporarily relieve mild symptoms of DED patients and stabilize the tear film, the inflammation progression cannot be effectively controlled (Barabino et al., 2020). The application of autologous serum is limited due to the high requirement for preparation, susceptibility to contamination, and difficulty in long-term preservation (Mason et al., 2021). Long-term or improper use of glucocorticoids can cause serious complications such as elevated intraocular pressure and cataract (Roberti et al., 2020). While immunosuppressants can reduce the expression of inflammatory cytokines on the ocular surface, toxicity and side effects still limit their clinical application (Periman et al., 2020). Therefore, new strategies for effective and safe treatment of DED are still urgently required.

Regardless of the inducing mechanisms of DED, the immune inflammation of the ocular surface is regarded as the main cause. High osmotic pressure can trigger intracellular oxidative stress reaction, inducing intracellular outburst of reactive oxygen species (ROS) and irreversible damage to intracellular biological macromolecules (Wang et al., 2016; Favero et al., 2021). Moreover, it was demonstrated that oxidative damage of mitochondria can cause lacrimal gland dysfunction, leading to reduced tear production, increased tear ROS level, and eventually DED (Uchino et al., 2012). In addition, ROS can activate NOD-like receptor pyrin domain– containing protein 3 (NLRP3) in the corneal epithelium and further promote the secretion of interleukin-1β (IL-1β), leading to ocular surface inflammation (Zheng et al., 2014; Zheng et al., 2015). As one of the most prominent inflammasomes, NLRP3 regulates the generation of mature forms of IL-1β and is associated with inflammatory cell death (Zhang et al., 2021). Numerous studies have reported on the critical role of the NLRP3-IL-1β signaling axis mediated by ROS homeostatic imbalance during the inflammatory process with the development and progression of DED (Zheng et al., 2014; Lv et al., 2021; Wang B. et al., 2021). A comparison study indicated that compared with the healthy subjects, the level of ROS, NLRP3, and IL-1β in tears and conjunctival cells of DED patients was significantly improved, suggesting that ROS can further induce IL-1β release by activating NLRP3 expression (Zheng et al., 2015). These findings suggest that the ROS-NLRP3-IL-1β signaling axis may act as a potential therapeutic target for DED treatment. Currently, several NLRP3-related inhibitors have been identified (Jiang et al., 2017; Wong et al., 2018; Yu et al., 2018). Among them, MCC950, a sulfonylurea molecule, exhibits specificity in inhibiting the NLRP3 inflammasome, reducing IL-1β release and apoptosis without affecting other signaling pathways (Coll et al., 2019). Numerous studies have demonstrated that MCC950 has a good anti-inflammatory effect in various inflammatory diseases, such as cryopyrin-related syndrome, lung inflammation, renal fibrosis, hypertension, and myocardial infarction (Gao et al., 2019; Krishnan et al., 2019; Corcoran et al., 2021; Wang L. et al., 2021; Yoon et al., 2021). However, as far as we know, DED treatments using MCC950 have been seldom reported. We envision that the specific inhibition of NLRP3 by MCC950 combined with ROS scavenging will provide a synergistic strategy for DED treatment.

Nevertheless, topically administered ophthalmic solution drugs usually have poor bioavailability due to ocular surface

barriers, such as limited corneal permeability, constant blinking, and rapid nasolacrimal drainage (Park et al., 2015). Accordingly, effective treatments require frequent application of drugs, leading to poor patient compliance and undesirable side effects. It has been well-recognized that drug carriers with high ocular surface adhesion and long retention time can effectively improve the bioavailability of ocular surface medication (Park et al., 2015; Lin et al., 2019). Mussel, a classic example of wet surface adhesion in nature, achieves excellent adhesion by secreting special adhesive proteins containing high levels of catechol amino acid (Yu et al., 2020). Several investigations have demonstrated that polydopamines, the mussel-inspired biomaterials with good biocompatibility and biodegradability (Li et al., 2020), exhibited excellent adhesion properties on almost any surface (Suneetha et al., 2019; Shao et al., 2020). For example, Jia et al. reported on the use of polydopamine microcapsules in prolonging the retention time of pesticides on leaves (Jia et al., 2014). In addition, the catechol moieties of polydopamines have been widely used to scavenge multiple types of ROS (Tang et al., 2019; Hu et al., 2020). It has been demonstrated that polydopamines can protect the brain from ROS-induced brain tissue damage during ischemic stroke injury (Liu et al., 2017), in addition to being applied in chronic inflammatory diseases (e.g., periodontitis) and acute inflammatory injuries (Bao et al., 2018; Zhao et al., 2018). However, to the best of our knowledge, combining the adhesiveness and ROS removal ability of polydopamines for ocular surface drug delivery is rarely reported.

Considering the critical role of the ROS-NLRP3-IL1β signaling axis in the occurrence and development of DED, herein, a synergetic therapeutic strategy for DED treatment was proposed. As demonstrated in **Scheme 1**, a polydopamine-based microgel *in situ* loaded with MCC950 was constructed *via* radical copolymerization of poly (ethylene glycol) methacrylate (PEGMA), 3-acrylamidopropyl trimethylammonium chloride (APTAC), and N-(3,4-dihydroxyphenethyl) methacrylamide (DPMA), which was denoted as $PPAD_{x\text{-}y\text{-}z}$ (x, y, and z referred to the molar ratio of PEGMA, APTAC, and DPMA, respectively). PEGMA was used to improve the biocompatibility of the microgel, while the positively charged APTAC was adopted for *in situ* encapsulation of the negatively charged MCC950 through electrostatic interaction. DPMA was expected to increase the ocular surface retention time and drug bioavailability due to its adhesiveness. Furthermore, DPMA will scavenge excessive ROS on the ocular surface and reduce the activation of the NLRP3 inflammasome, thus contributing to the synergistic treatment of DED combined with MCC950.

EXPERIMENTAL

Materials

MCC950 sodium and dihydroethidium (DHE) were purchased from MedChemExpress (MCE R; China). (3,4-dihydroxyphenethyl) methacrylamide (DPMA) was purchased from Macklin Biochemical Co., Ltd. (Shanghai, China). Poly (ethylene glycol) methacrylate (PEGMA) was purchased from Aladdin Reagent Co., Ltd. and passed through an Al_2O_3 column to remove the inhibitor before use. 3-acrylamidopropyl trimethylammonium chloride (APTAC, 75wt% in H_2O) and lithium phenyl-2,4,6-trimethylbenzoylphosphinate (LAP, 98%) were obtained from Aladdin Reagent Co., Ltd and used without further purification. Fluorescein sodium (FS) was purchased from Abmole Co., Ltd. (United States). Scopolamine (Scop) was purchased from Sigma–Aldrich Co., Ltd. Human corneal epithelial cells (HCECs) were obtained from ATCC (Manassas, VA, United States). Dulbecco's modified Eagle's medium/nutrient mixture F-12 (DMEM/F-12; 1: 1 ratio), FBS, and insulin were purchased from Invitrogen, Gibco Co., Ltd. Triton X-100 was purchased from Sigma Co., Ltd. (Darmstadt, Germany). CM-H2DCFDA (General Oxidative Stress Indicator) was obtained from Invitrogen Molecular Probe Co., Ltd. Cell Counting Kit-8 (CCK-8) was purchased from Beyotime Biotechnology Co. (Shanghai, China). The *In situ* Cell Death Detection kit (TUNEL) was purchased from Roche Co., Ltd. (Germany).

Characterization

Monomer conversions after polymerization were analyzed by ^1H NMR spectroscopy on a QUANTUM-I-400MHz spectrometer using D_2O as the solvent. The hydrodynamic diameter and polydispersity indexes of the microgels were analyzed using dynamic light scattering (DLS) measurements using a Malvern ZS90 with a He–Ne laser (633 nm, 4 mW) at a 90° angle. The morphology of the microgel was observed by using a transmission electron microscope (TEM) on a Jeol 200CX microscope (200 kV). To prepare the TEM samples, a small drop of the microgel solution (1 mg/ml) was carefully deposited onto a carbon-coated copper electron microscopy grid and vacuum-dried overnight. The *in vitro* release of FS from the microgels and the residual FS in rabbit tear samples were analyzed using fluorescence spectroscopy. Human corneal epithelial cells (HCECs) were observed on an inverted fluorescence microscope (Zeiss Axio Vert a3, Germany).

Preparation and Characterization of MCC950@PPAD Microgels

PPAD microgels were prepared *via* photo-induced radical copolymerization of main monomers (PEGMA and APTAC) with the comonomer DPMA in an aqueous solution according to the procedures reported (Xue et al., 2017). Herein, the synthesis of $MCC950@PPAD_{3\text{-}7\text{-}1}$ was described as a representative example. Briefly, PEGMA (0.257 g, 0.714 mmol), MCC950 sodium (2.84 mg, 6.65 μmol), LAP (14 mg, 47.7 μmol), and APTAC (0.345 g, 1.669 mmol) were added into a round-bottomed flask and dissolved in 10 ml of deionized water. After the mixed solution was bubbled with argon at 0°C for 30 min, the flask was sealed and exposed to illumination at 406 nm and stirred at 500 rpm. After 2 h of polymerization, 37 mg of DPMA (0.167 mmol) dissolved in 0.4 ml of ethanol was then injected into the polymerization mixture. After a few minutes, a milky suspension was observed (**Supplementary Figure 1**), indicating the formation of PPAD microgels. The

polymerization continued for 4 h and the resultant microgels were purified by centrifugation. The detailed information of the polymerizations is summarized in **Supplementary Table 1**.

In Vitro Drug Release From the PPAD Microgels

FS, a common fluorescent dye for cornea fluorescein staining, was selected as a model molecule to investigate the *in vitro* release behavior because of its similarity with MCC950, such as molecular weight, water solubility, and being negatively charged. Moreover, the concentration of FS can be conveniently detected by fluorescence spectroscopy. First, the purified FS@PPAD$_{3\text{-}7\text{-}1}$ microgel was obtained and redispersed in a certain volume of ddH_2O. Then, the FS@PPAD$_{3\text{-}7\text{-}1}$ microgel dispersion was added into a dialysis tube with a molecular weight cut-off (MWCO) of 2000 and dialyzed against ddH_2O or PBS with different ionic strengths (50 and 90 mM) at a stirring speed of 200 rpm. A certain volume of the dialyzate outside the dialysis tube was withdrawn at a certain time point and analyzed using fluorescent spectroscopy to monitor the *in vitro* release behavior.

Drug Retention on the Ocular Surface

Herein, FS was also used as the model molecule to assess the ability of the PPAD microgel to improve drug retention on the ocular surface. Briefly, the rabbit eyes were washed with normal saline 1 hour before topical treatment with 50 μL FS solution (1%) or FS@PPAD microgels loaded with the equivalent amount of FS: 5, 15, 30, 45, 60, 90, 120, 150, and 180 min after topical treating, and tear samples were collected by immersing a square piece of filter paper with a size of 1 × 1 cm^2 in the tear fluid for 10 s. Then, the filter paper was immersed in 500 μL of ddH_2O, and FS was extracted from the filter paper using ultrasound. After proper dilution and filtration, the concentrations of FS in tear samples were analyzed by fluorescence spectroscopy.

In Vitro Cytotoxicity and Ocular Histocompatibility Evaluation

The *in vitro* cytotoxicity of free MCC950, PPAD microgels, and MCC950@PPAD microgels on HCECs was evaluated by CCK-8 assay according to the manufacturer's instructions and quantified on a microplate reader. Briefly, HCECs were suspended in DMEM-F12 medium supplemented with fetal bovine serum (10%, v/v) and insulin (5 μg/ml) and then seeded into a 96-well plate at a density of 5000 cells per well. After the HCECs were incubated at 37°C, 90% humidity, and 5% CO_2 for 24 h to allow cell attachment, the original medium was replaced with a fresh medium containing different amounts of PPAD microgels, free MCC950 (0.05, 0.1, 0.2, 0.5, 1, 2, 5, and 10 μM), or MCC950@PPAD microgels loaded with an equal concentration of MCC950. After a further incubation of 24 h, the HCECs were gently washed two times with 100 μL prewarmed PBS, and the medium was replaced with 100 μL medium containing 10 μL CCK-8, followed by further incubation of 2 h. In addition, blank wells with no cells inside were also added with 100 μL of the medium containing 10 μL of CCK-8. The absorbance at 450 nm was recorded using an enzyme marker, and the viability of HCECs was determined based on the percentage of the absorbance of the treated cells compared to that of the untreated control HCECs.

For ocular histocompatibility evaluation, MCC950, PPAD$_{3\text{-}7\text{-}1}$, and MCC950@PPAD$_{3\text{-}7\text{-}1}$ were instilled into the mice's right eye five times a day for 7 days, and an equal volume of physiological saline solution was instilled into the left eye as the negative control. The mice were euthanized by cervical dislocation after 7 days and then the eyeballs were enucleated and fixed in 4% paraformaldehyde (PFA) overnight at 4°C. The samples were subsequently embedded in paraffin. Histological sections of tissues (cornea, conjunctiva, iris, and sclera) were stained with hematoxylin and eosin (HE) staining according to routine protocols and examined using a light microscope (Olympus, Japan).

Evaluation of *In Vivo* and *In vitro* ROS Scavenging Capacity of PPAD$_{3\text{-}7\text{-}1}$ and MCC950@PPAD$_{3\text{-}7\text{-}1}$

To investigate the ability of PPAD$_{3\text{-}7\text{-}1}$ or MCC950@PPAD$_{3\text{-}7\text{-}1}$ to scavenge ROS, stained HCECs cells were treated with hyperosmotic stress by CM-H2DCFDA *in vitro* experiments. Mouse corneal tissues were treated by DHE *in vivo* experiments. For CM-H2DCFDA staining, HCECs were first seeded in a black 96-well plate at a density of 5 × 10^3 cells per well. After the cells were incubated for 24 h, the medium was replaced with DMEM-F12 without FBS containing 90 mM NaCl to create a highly permeable environment (500 mOsm) (Zheng et al., 2018). As the control group, HCECs were also cultured under physiological isotonic conditions. Then, different concentrations of PPAD$_{3\text{-}7\text{-}1}$ microgels were added into the wells so that the final concentrations of the PPAD$_{3\text{-}7\text{-}1}$ microgels were 0.01 mg/ml, 0.1 mg/ml, and 1 mg/ml. After the cells were cultured for 18 h under the hyperosmotic environment, intracellular ROS levels were measured using a reactive oxygen species detection kit (Roche) according to the manufacturer's instructions. Briefly, the cells were gently washed two times using 100 μL of prewarmed PBS, added with 100 uL of CM-H2DCFDA reaction solution diluted by PBS at a concentration of 10 μM and then incubated in an incubator saturated with 5% CO_2 and 90% humidity. After 45 min, the CM-H2DCFDA reaction solution was replaced with PBS, and the HCECs were observed under an inverted phase contrast fluorescence microscope (ZEISS Axio Observer3) after two-time gentle washing with 100 μL PBS. For DHE staining, DED mice were treated with MCC950, PPAD$_{3\text{-}7\text{-}1}$, MCC950/PPAD$_{3\text{-}7\text{-}1}$ (simple mixture of MCC950 and PPAD$_{3\text{-}7\text{-}1}$), and MCC950@PPAD$_{3\text{-}7\text{-}1}$ three times a day for 5 days. The mice were euthanized by cervical dislocation after 5 days and then the eyeballs of the mice were enucleated and embedded with OCT. Subsequently, the embedded samples were cut into 10-μM sections and washed with cold PBS. Then, the cornea sections were incubated with 10 μM fluorescent dye DHE at 37°C for 40 min in a humidified chamber and protected from light. The sections were observed under 20x magnification using a laser confocal microscope (LSM 880 NLO with AiryScan, Zeiss, Germany), and the mean fluorescence intensity was analyzed

by using ImageJ software (ImageJ 1.8; NIH, Bethesda, MD, United States).

Experimental dry eye Disease Animal Model Preparation

C57BL/6j female mice (6–8 weeks, 18–22 g) were obtained from Jiesijie Experimental Animal Co. (Shanghai, China) and maintained in the experimental animal center of Wenzhou Medical University under the regulation of the Code of Conduct for Care and Use of Laboratory Animals. Animal experiments were approved by the Ethical Review Committee for Experimental Animals of Wenzhou Medical University. Before the experiments, the mice were kept in the animal center for 1 week for acclimation and medically examined to exclude unhealthy ones, especially with ocular pathological changes. The immune DED animal model was induced by subcutaneous injection of 200 μL Scop (2.5 mg/ml) three times per day for 5 days (Chen et al., 2013a). Subcutaneous injections were administered at 9:00 a.m., 13:00 p.m., and 19:00 p.m. Afterward, the mice were topically treated with 10 μL MCC950 (10 μM), 10 μL MCC950@PPAD microgel (with 10 μM MCC950), or 10 μL PPAD microgel three times per day for 5 days. As for the animal experiments shown in *Supplementary Material*, dry eye mice were treated with free MCC950 solution (1 μM, 10 μM, 100 μM) four times a day for 5 days. All dry eye mice were kept at 25°C with 13.1 ± 3.5% humidity and 2.2 ± 0.2 m/s airflow.

Corneal Fluorescein Sodium Staining Score

After topical treatment for 5 days, the degree of corneal damage was evaluated using corneal fluorescein staining (CFS). CFS was observed using slit-lamp microscopy 2 min after 2 μL FS solution (2 mg/ml) was instilled into the conjunctiva sac. The scores were calculated according to the National Eye Institute (NEI) scale.[42] Briefly, an experienced ophthalmologist graded them based on the number of positive fluorescein staining points in five areas of the cornea and calculated the total score. Each area was scored according to the following: grade 0 = no significant corneal staining; grade 1 = less than five fluorescent dots; grade 2 = 6–15 fluorescent dots; grade 3 = 16–30 fluorescent dots; and grade 4 = more than 30 fluorescent dots (Lemp, 1995).

Methods for TUNEL Assay

After the mice were euthanized by cervical dislocation, the eye balls were carefully isolated, soaked in Optimum Cutting Temperature (OCT) media, and then frozen in liquid nitrogen. Ten-μm sagittal sections of eye tissues were prepared using a cryostat (HM 500; Micron, Waldorf, Germany) and stored at −80°C before use. Cell apoptosis of these tissue sections was detected by TUNEL (terminal deoxynucleotidyl transferase–mediated dUTP nick-end labeling) staining using an *In Situ* Cell Death Detection Kit (Roche, Mannhein, Germany) according to the manufacturer's instructions. After 20 min of incubation at room temperature, the sections were washed three times with PBS and fixed with 4% paraformaldehyde for 20 min. Then, the sections were transferred into a thermostat at 4°C and permeabilized with 0.5% Triton X-100 for 5 min. Next, the sections were washed three times with PBS to remove Triton X-100. TUNEL staining was performed by adding 50 μL of the staining agent onto the sections, followed by an incubation of 1 h at 37°C. In addition, the sections were counterstained with DAPI for 1 min. The specimens were embedded in a mounting medium (Invitrogen, Oregon, United States), and their fluorescence images were recorded on a Zeiss confocal microscope with a krypton/argon and He–Ne laser (Carl Zeiss Meditec, Sartrouville, Germany) under an excitation wavelength of 405 nm for DAPI and 488 nm for TUNEL. The apoptotic cells were observed under 20x magnification using a laser confocal microscope (LSM 880 NLO with AiryScan, Zeiss, Germany).

In Vivo Expression of Inflammation-Related Factors

The expression of interleukin-6 (IL6), NLRP3, and IL-1β in the ocular surface tissues of C57BL/6j mice at protein level was examined by Western blot. After treatment of DED mice for 5 days, the mice were euthanized and the ocular surface tissue was subsequently cut into small pieces and immediately lysed with 100 μL of PMSF lysis buffer (100 mM), followed by ball milling for 8 min. The proteins in the supernatant were collected following centrifugation at 16,000 g for 10 min at 4°C. Protein concentrations were measured by a BCA assay kit (Pierce). The proteins (20–30 μg) were mixed with 5X SDS sample buffer and loaded onto SDS-PAGE. After electrophoresis, the separated proteins were transferred to PVDF membranes. The membranes were blocked with 5% milk powder in TBST for 2 h at room temperature. After blocking, the membranes were incubated overnight at 4°C with rabbit anti-IL-1β (1:1000, Abcam, #ab234437), mouse-anti-NLRP3 (1:1000, adpiogene, #AG-20B-0014-C100), rabbit anti-IL6 (1:1000, cell signaling technology, #12912S), and rabbit α/β-tubulin Antibody (1: 3000, Cell signaling technology, #2148). Afterward, the membranes were rinsed with TBST and then incubated with HRP-labeled rabbit IgG (1:3000, Biosharp, #BL003A) OR mouse IgG (1:3000, Biosharp, #BL001A) for 2 h. Protein bands were visualized using an enhanced chemiluminescence (ECL) kit and imaged by an AI680 ultra-sensitive multifunctional analyzer. Protein expression was quantified based on the ratio of the target protein and tubulin.

The mRNA expression level of IL-1β, NLRP3, and IL6 in the ocular surface tissue of DED mice was evaluated using the reverse-transcription polymerase chain reaction (RT-PCR). The detailed information on these experiments can be found in our previously published articles.[28] The specific primers for mouse IL-1β, NLRP3, and IL6 genes were designed using the NCBI Primer-Blast (NCBI Web site) and are listed in **Supplementary Table 2**, which had 55–63% GC content. GAPDH was used as the internal reference gene. The expression levels of the target genes were normalized with the expression levels of the internal reference genes according to the manufacturer's instructions.

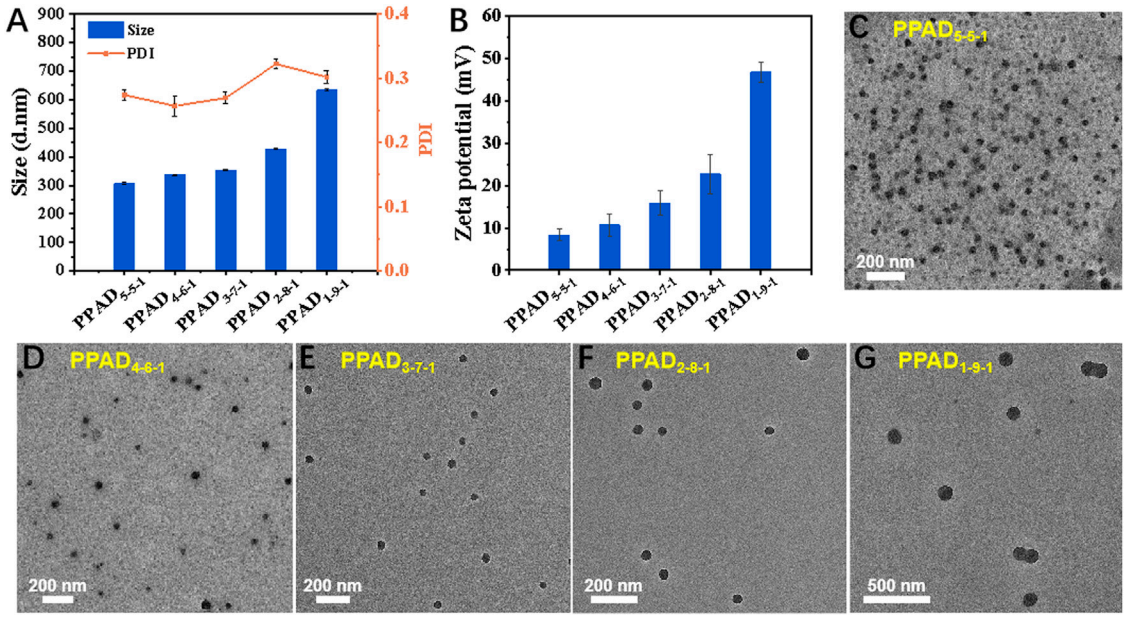

FIGURE 1 | (A) Average value of apparent hydrodynamic diameter (D_h, app), polydispersity index (PDI), **(B)** zeta potential, and morphology of the PPAD microgels, **(C–G)** TEM micrographs of the PPAD microgels.

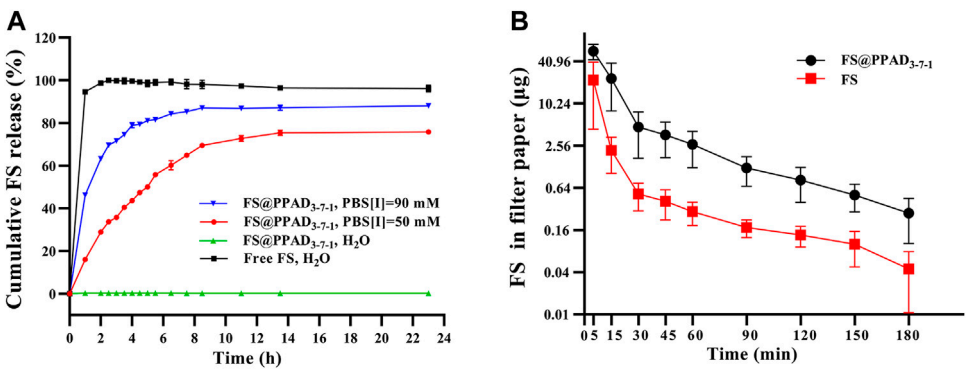

FIGURE 2 | (A) *In vitro* cumulative release of FS from $PPAD_{3\text{-}7\text{-}1}$ microgels under different conditions. **(B)** FS in a filter paper after a single instillation of free FS or FS@ $PPAD_{3\text{-}7\text{-}1}$ microgels.

Statistical Analysis

Each experiment was performed three times, and all data were recorded as means ± standard deviation. Significant differences among groups were determined by one-way analysis of variance (ANOVA) with the level of significance set at $p < 0.05$.

RESULTS AND DISCUSSION

Preparation and Characterization of MCC950@PPAD Microgels

As demonstrated in **Scheme 1**, three kinds of monomers (PEGMA, APTAC, and DPMA) were adopted to prepare PPAD microgels. As well-demonstrated in a previous report (Xue et al., 2017), the comonomer DPMA was needed as a cross-linker for the preparation of microgels. However, increasing the feed ratio of DPMA to the main monomers would cause low colloidal stability and coagulation in aqueous solution. When the feed ratio of DPMA to the main monomers was from 1/20 to 1/8, stable microgels were obtained. Thus, in our study, the molar ratio of DPMA to the main monomers (PEGMA and APTAC) was set to be 1:10. Since the cationic monomer APTAC was responsible for *in situ* encapsulation of MCC950, the content of APTAC is a critical factor. Although the high content of APTAC can contribute to the high encapsulation capacity of MCC950, too many positively charged polymers may lead to cytotoxicity and ocular surface damage. Moreover, the electrostatic repulsion among cationic PAPTAC polymers also influences the size of the microgels.

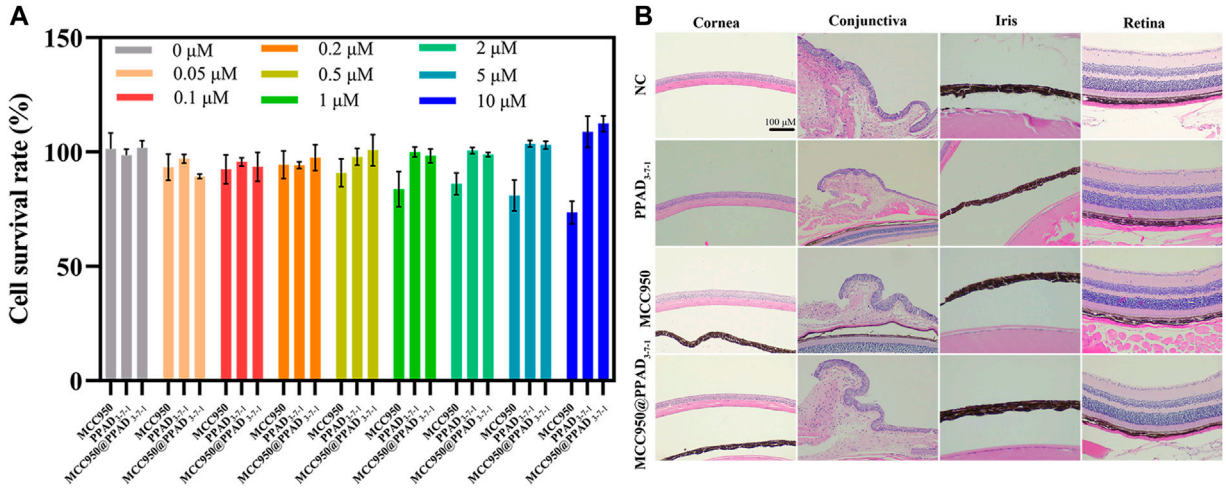

FIGURE 3 | (A) Cytotoxicity of free MCC950, $PPAD_{3\text{-}7\text{-}1}$ microgel, and MCC950@$PPAD_{3\text{-}7\text{-}1}$ microgel. The concentrations of free MCC950 and $PPAD_{3\text{-}7\text{-}1}$ microgel were equal to those of MCC950@$PPAD_{3\text{-}7\text{-}1}$ microgels. The concentration of MCC950 varied from 0 to 10 μM. **(B)** Histopathology microscopy of ocular tissues, including cornea, conjunctiva, iris, and retina, after instilment with 0.9% (w/v) NaCl solution (NC), MCC950, $PPAD_{3\text{-}7\text{-}1}$, and MCC950@$PPAD_{3\text{-}7\text{-}1}$ five times a day for 7 days.

Thus, the impact of APTAC content on the size and zeta potential of the PPAD microgels was first investigated. The feed molar ratio for the synthesis of the PPAD microgels is summarized in **Supplementary Table 1**.^{1}H NMR spectra in **Supplementary Figure 2** revealed near-quantitative monomer conversions. The DLS results in **Figure 1A** indicated that the average hydrodynamic diameter of the PPAD microgels gradually increased with the increase of the APTAC content. This is probably because the increased content of APTAC improved the electrostatic repulsion among PAPTAC polymers, leading to the swelling of the microgels. It is also reasonable that the zeta potential of the microgels gradually increased with the increase of the APTAC content. The morphology of the microgels was observed by TEM and is shown in **Figures 1C–G**. Although the TEM micrographs demonstrated that microgel size increased with the increase of APTAC content, the average diameter revealed by TEM was significantly lower than that determined by DLS, which is also probably due to electrostatic repulsion among PAPTAC polymers. Since the microgels were dispersed in an aqueous solution during DLS characterization, the sufficiently ionized PAPTAC polymer chains resulted in strong electrostatic repulsion and a high degree of swelling. On the contrary, because the microgel samples were dehydrated during TEM analysis, the PAPTAC polymers were not ionized and the strong electrostatic repulsion disappeared, leading to significant shrinkage and size decrease. The drug encapsulation efficiency in PPAD microgels was evaluated by using FS as the model molecule in place of MCC950. After centrifugation of the FS@PPAD microgels, the concentration of FS in the supernatant was analyzed by fluorescence spectroscopy to confirm the encapsulation efficiency. As summarized in **Supplementary Table 1**, high encapsulation efficiency (more than 80%) was achieved for all the PPAD microgel samples. Combining the size, zeta potential, morphology, and drug encapsulation efficiency, the $PPAD_{3\text{-}7\text{-}1}$ microgel with a mean D_h of 356 nm and zeta potential of + 15.9 mV was selected as the optimal sample for the following *in vitro* and *in vivo* experiments.

In Vitro Drug Release From the $PPAD_{3\text{-}7\text{-}1}$ Microgels

Herein, FS was used as the model molecule to evaluate the release behavior of MCC950 from the $PPAD_{3\text{-}7\text{-}1}$ microgel under different conditions. The release of free FS in ddH_2O as a control was also carried out. As shown in **Figure 2A** (the black line), the cumulative release of free FS in ddH_2O rapidly reached more than 90% in the first hour. In contrast, nearly negligible FS release from the $PPAD_{3\text{-}7\text{-}1}$ microgel in ddH_2O was observed because FS was stably encapsulated in $PPAD_{3\text{-}7\text{-}1}$ microgels through electrostatic interaction. Thus, it can be reasonably anticipated that the FS release from the $PPAD_{3\text{-}7\text{-}1}$ microgel can be accelerated by ionic strength. As indicated in **Figure 2A** (the red line), 19.34% of cumulative FS release from the $PPAD_{3\text{-}7\text{-}1}$ microgel under the ionic strength of 50 mM was achieved within 1 h and reached 72.7% after 11 h. Furthermore, FS release from the $PPAD_{3\text{-}7\text{-}1}$ microgel under the ionic strength of 90 mM was significantly improved (the blue line). It has been reported that tear hyperosmolarity is one of the core pathogenesis mechanisms of DED. Moreover, a culture medium containing NaCl (90 mM) was usually utilized to create a highly permeable condition. Thus, based on the abovementioned release results, we envision that efficient drug release can be achieved under hyperosmotic conditions of the ocular surface in the dry eye model.

Ability of $PPAD_{3\text{-}7\text{-}1}$ Microgels to Prolong the Ocular Surface Retention Time of Drugs

Due to sealed anatomical features of the eyes and ocular surface barriers, more than 90% of topically-applied drugs can be rapidly

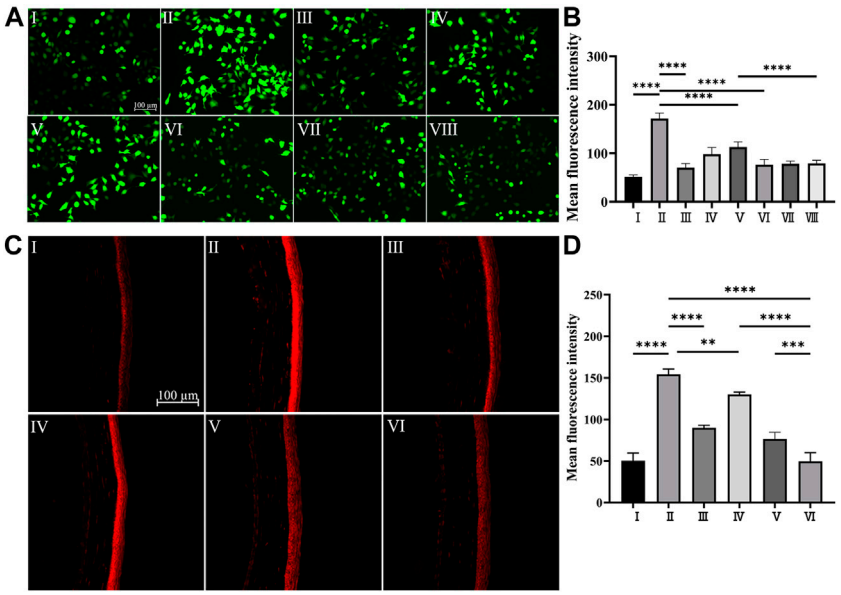

FIGURE 4 | (A,B) *In vitro* ROS scavenging capacity of $PPAD_{3\text{-}7\text{-}1}$ and MCC950@$PPAD_{3\text{-}7\text{-}1}$, Groups I–II are designated as NC and HS, respectively. Groups III–V are designated as HS + $PPAD_{3\text{-}7\text{-}1}$ microgels (the concentrations of $PPAD_{3\text{-}7\text{-}1}$ microgels are 1 mg/ml, 0.1 mg/ml, and 0.01 mg/ml, respectively). Groups III–V are designated as HS + MCC950@$PPAD_{3\text{-}7\text{-}1}$ (the concentrations of $PPAD_{3\text{-}7\text{-}1}$ correspond to III-VIII). **(C,D)** *In vivo* ROS scavenging capacity of MCC950@$PPAD_{3\text{-}7\text{-}1}$. Groups I–VI are designated as NC, Scop, Scop + $PPAD_{3\text{-}7\text{-}1}$, Scop + MCC950, Scop + MCC950/$PPAD_{3\text{-}7\text{-}1}$, and (iv) Scop + MCC950@$PPAD_{3\text{-}7\text{-}1}$. Data are shown as mean ± SD, $n = 4$, $^{**}p < 0.01$, and $^{****}p < 0.0001$.

washed away within minutes, leading to poor bioavailability (Davis et al., 2004; Li et al., 2007). Thus, in this work, the polydopamine-based microgels are expected to improve the drug bioavailability by improving ocular surface adhesion and retention. Accordingly, undesired side effects of MCC950 can be avoided by reducing the dosage (Wang F. et al., 2021). Herein, the ocular surface retention was evaluated by detecting the concentration of FS in tear samples after topical treatment. The tear samples were collected using a filter paper at different time points after topical treatments. As shown in **Figure 2B**, 30 min after the rabbits were topically treated with 50 μL of $PPAD_{3\text{-}7\text{-}1}$ microgels containing 10 mg/ml FS, a significantly ($p < 0.05$) higher amount of FS was detected in tear samples than in the rabbits treated with 50 μL of free FS (10 mg/ml), proving the ability of $PPAD_{3\text{-}7\text{-}1}$ microgels to prolong ocular surface retention time.

Cytotoxicity of MCC950@$PPAD_{3\text{-}7\text{-}1}$ Microgels and Ocular Histocompatibility Evaluation

As MCC950@$PPAD_{3\text{-}7\text{-}1}$ is a novel drug for the treatment of DED, it was necessary to evaluate the ocular histocompatibility of MCC950, $PPAD_{3\text{-}7\text{-}1}$, and MCC950@$PPAD_{3\text{-}7\text{-}1}$. The cytotoxicity of MCC950, $PPAD_{3\text{-}7\text{-}1}$ microgels, and MCC950@$PPAD_{3\text{-}7\text{-}1}$ microgels was evaluated using the CCK-8 assay. As shown in **Figure 3A**, free MCC950 at concentrations less than 0.5 μM was well-tolerated (more than 80% of HCECs survived after 24 h of incubation), while significant cell growth inhibition was observed with the MCC950 concentration up to 10 μM. On the contrary, when treated with the MCC950@$PPAD_{3\text{-}7\text{-}1}$ microgel loaded with 10 μM of MCC950, HCEC survival was approximately 103%, suggesting that loading MCC950 into $PPAD_{3\text{-}7\text{-}1}$ microgels significantly reduced the cytotoxicity of MCC950. Furthermore, when treated with $PPAD_{3\text{-}7\text{-}1}$ microgels, high HCEC survival was also achieved, probably because the abundant dopamine moieties of the $PPAD_{3\text{-}7\text{-}1}$ microgels scavenged excessive ROS, thus providing effective protection of HCECs. As shown in **Figure 3B**, HE stained slides were observed under a light microscope to evaluate the tissue's (cornea, conjunctiva, iris, and retina) structure and integrity for histocompatibility detection. The eyes showed no significant pathologic changes when treated with all formulations. As indicated in **Figure 3A**, 10 μM MCC950 inhibited cell proliferation in the CCK-8 assay. However, when it was applied to the ocular surface, MCC950 could be rapidly cleared from the ocular surface through the lacrimal drainage system and diluted by tear fluid due to its good water-solubility. Therefore, when 10 μM MCC950 was dropped into the ocular surface, the actual concentration of MCC950 was much lower than 10 μM. Moreover, because of the intact morphological structure of the cornea, conjunctiva, iris, and retina, no inflammatory cell infiltration was observed after treatment with $PPAD_{3\text{-}7\text{-}1}$ and MCC950@$PPAD_{3\text{-}7\text{-}1}$. This indicates that $PPAD_{3\text{-}7\text{-}1}$ and MCC950@$PPAD_{3\text{-}7\text{-}1}$ exhibit excellent ocular biocompatibility.

Ability of $PPAD_{3\text{-}7\text{-}1}$ Microgels to Scavenge ROS Produced in Human Corneal Epithelial Cells Under Hyperosmotic Conditions

Under physiological conditions, intracellular ROS levels remain at equilibrium due to the redox system which regulates the

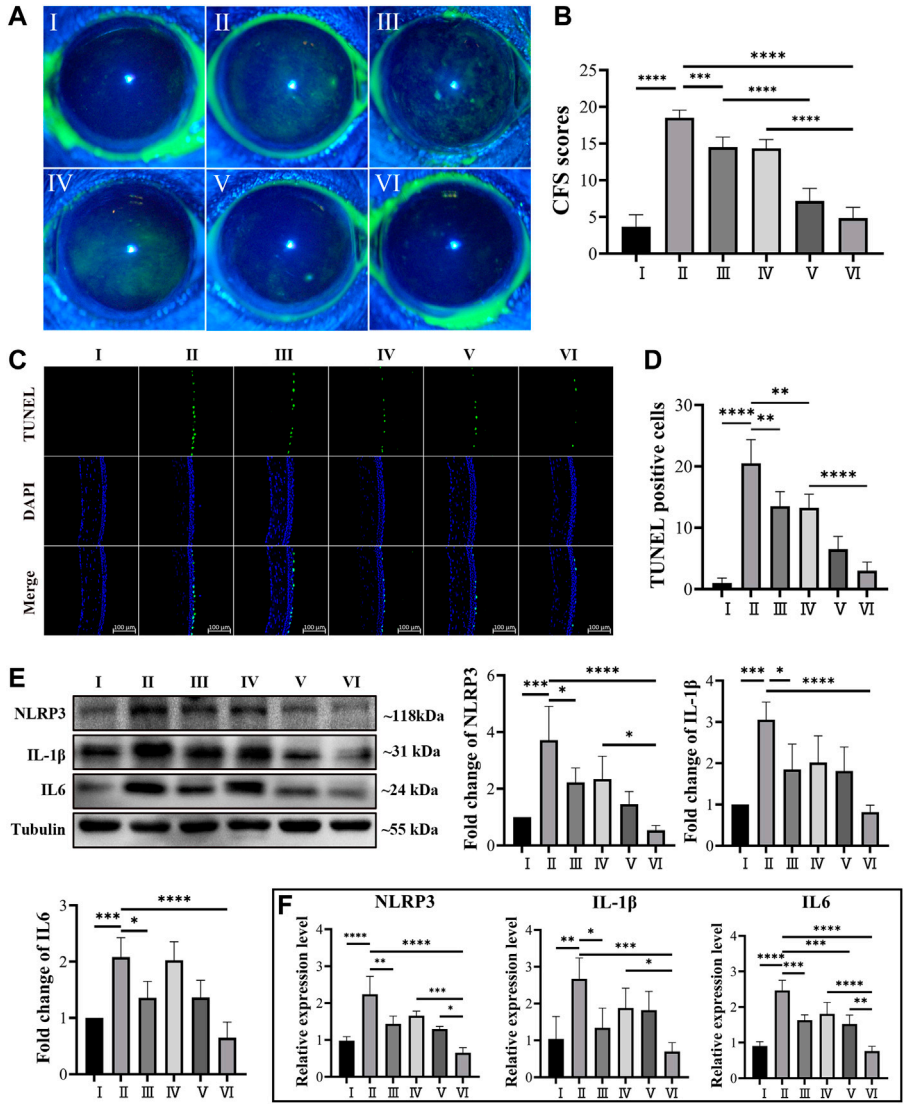

FIGURE 5 | (A,B) Corneal fluorescein sodium staining (CFS) scores in in DED mice. **(C,D)** Representative images of TUNEL staining and number of TUNEL-positive cells in the DED mice corneal epithelium. **(E)** Western blot analysis revealed the protein level of IL-1β, NLRP3, and IL6 using tubulin as the internal control, and **(F)** mRNA expression level of IL-1β, NLRP3, and IL-6 in the ocular surface tissue of DED mice. (Groups I–VI are designated as NC, Scop, Scop + $PPAD_{3\text{-}7\text{-}1}$, Scop + MCC950, Scop + MCC950/$PPAD_{3\text{-}7\text{-}1}$, and Scop + MCC950@$PPAD_{3\text{-}7\text{-}1}$, respectively.) Data are given as the mean ± SD (n = 4), *p < 0.05, **p < 0.01, ***p < 0.001, and ****p < 0.0001.

production and the clearance of ROS through enzymatic or nonenzymatic reactions (Sies, 2015). As one of the main features of DED, tear film hyperosmolarity can cause excessive production of ROS (Chen et al., 2013b), which further triggers the inflammatory cascade effect of DED development (Seen and Tong, 2018). Plenty of research has demonstrated that polydopamine-based biomaterials exhibited a good scavenging effect on a wide range of ROS due to their catechol moiety (Hu et al., 2020). As shown in **Figure 4A** II, when HCECs were exposed to hyperosmotic stress, overproduction of ROS was observed compared with that of HCECs under physiological conditions (**Figure 4A** I). However, as shown in **Figure 4A** III-V, the overexpressed ROS in HCECs induced by hyperosmotic stress can be effectively reduced by $PPAD_{3\text{-}7\text{-}1}$ microgels. The quantitative analysis of the fluorescence intensity shown in **Figure 4B** was well-consistent with the fluorescent images. Moreover, the intracellular ROS can be restored to physiological level when treated with 1 mg/ml $PPAD_{3\text{-}7\text{-}1}$ microgels (**Figure 4A** III), suggesting that $PPAD_{3\text{-}7\text{-}1}$ microgels can act as an excellent ROS scavenger. Interestingly, when MCC950 was loaded in $PPAD_{3\text{-}7\text{-}1}$ microgels, the ability to inhibit ROS production was further enhanced (**Figure 4A** VI-VIII). It is known that inflammatory response and increased ROS production are a mutually reinforcing process; oxidative

stress can lead to increased production of inflammatory factors, while inflammation can also promote ROS production. Polydopamine scavenges overproduced ROS by chemical reactions; thus, the inhibitory effect of $PPAD_{3\text{-}7\text{-}1}$ on ROS shows dose-dependence (**Figure 4B**), while MCC950, an NLRP3 inhibitor, reduces ROS production by inhibiting the inflammatory response (**Supplementary Figure 4**). When $PPAD_{3\text{-}7\text{-}1}$ is loaded with MCC950, inflammation that is not completely inhibited by $PPAD_{3\text{-}7\text{-}1}$ is further suppressed by MCC950, resulting in better ROS scavenging. To further verify the effect of MCC950@$PPAD_{3\text{-}7\text{-}1}$ on ROS production in the corneal tissue of DED mice, DHE staining is used. The DHE staining of mouse corneal tissues showed similar results in **Figures 4C,D**, with MCC950@$PPAD_{3\text{-}7\text{-}1}$ having the best ROS scavenging effect (**Figure 4C** Ⅵ). Collectively, these results suggest that MCC950 can inhibit ROS production in an anti-inflammatory manner, while $PPAD_{3\text{-}7\text{-}1}$ microgels directly consume ROS through its polyphenol structure. Moreover, when MCC950 is loaded in $PPAD_{3\text{-}7\text{-}1}$ microgels, a better ROS scavenging effect can be achieved due to the synergistic therapeutic effect.

In Vivo Curative Effect Against DED

Five days after topical treatment of different MCC950 formulas, the corneal epithelial damage was assessed by using corneal fluorescein staining and imaged using a slit lamp under cobalt blue light (Schmidl et al., 2020), which is one of the most important bases to evaluate the severity of DED (Osei et al., 2020; Wolffsohn et al., 2017). The corneal epithelial damage or defect was statistically scored based on the guidelines of the National Eye Institute/Industry Workshop, United States . As shown in **Figure 5A** Ⅰ, the corneal epithelium of healthy mice exhibited a clean and blue profile with negligible green dots. After 5 days of Scop treatment, dense and scattered green dots were observed, indicating severe corneal epithelial damage (**Figure 5A** Ⅱ). **Figure 5A** Ⅳ demonstrated that no obvious curative effect was observed when topically treated with free MCC950 aqueous solution (10 μM), probably due to the short retention time on the ocular surface (Lemp, 1995). On the contrary, topical application of the MCC950@$PPAD_{3\text{-}7\text{-}1}$ microgel significantly decreased the green dots of the cornea, and no significant difference was observed compared with the healthy cornea (**Figure 5A** Ⅵ). The curing effect of $PPAD_{3\text{-}7\text{-}1}$ microgels alone shown in **Figure 5A** Ⅲ proved that the ROS scavenging ability of $PPAD_{3\text{-}7\text{-}1}$ also contributed to the curing effect, confirming the synergistic treatment effect of MCC950@$PPAD_{3\text{-}7\text{-}1}$ microgels. In addition, the curing effect of a simple mixture of $PPAD_{3\text{-}7\text{-}1}$ and MCC950 was also evaluated, and a significantly lower curative effect was found (**Figure 5A** Ⅴ), demonstrating that a superior curative effect can be achieved when MCC950 was *in situ* encapsulated in $PPAD_{3\text{-}7\text{-}1}$ microgels. When MCC950 was simply mixed with $PPAD_{3\text{-}7\text{-}1}$ microgels, part of the MCC950 was not encapsulated inside the microgels and could be rapidly washed away after topical treatment, leading to a compromise of the curative effect.

The apoptosis of the corneal epithelium, an important part of DED pathogenesis (Kessal et al., 2021), was further investigated by using TUNEL assay. Frozen sections of corneal tissues were processed using an apoptosis detection kit and photographed by laser confocal microscopy. As shown in **Figures 5C,D**, only a small number of TUNEL-positive cells were found in the corneas of the NC mice, while a large number of TUNEL-positive cells were observed in the corneas of the mice subcutaneously injected with Scop for 5 days. This is consistent with that observed in previous studies (Park et al., 2018). When topically treated with $PPAD_{3\text{-}7\text{-}1}$ microgels, free MCC950, or a simple mixture of $PPAD_{3\text{-}7\text{-}1}$ microgels and MCC950, the number of TUNEL-positive HCECs was slightly decreased, indicating that the ocular surface damage was slightly alleviated. On the contrary, the apoptosis of the corneal epithelium was significantly inhibited after the topical treatment of MCC950@$PPAD_{3\text{-}7\text{-}1}$ microgels, indicating that a superior curative effect can be achieved when MCC950 was *in situ* encapsulated in $PPAD_{3\text{-}7\text{-}1}$ microgels rather than simple mixing. As shown in **Supplementary 3, 5**, effective inhibition of corneal epithelium apoptosis was achieved when treated with free MCC950 at a concentration up to 100 μM, which, however, may cause undesirable side effects due to the high dose. The superior therapeutic effect of MCC950@$PPAD_{3\text{-}7\text{-}1}$ microgels can be attributed to the synergistic effect by combining the ROS scavenging effect of $PPAD_{3\text{-}7\text{-}1}$ microgels and specific inhibition of NLRP3 by MCC950. In addition, the excellent adhesiveness of the $PPAD_{3\text{-}7\text{-}1}$ microgels significantly improved the bioavailability of MCC950 by prolonging the ocular surface retention time.

Effect of MCC950@$PPAD_{3\text{-}7\text{-}1}$ Microgels on Inflammatory Cytokine Expression in Ocular Surface

To further elucidate the therapeutic effects of MCC950@$PPAD_{3\text{-}7\text{-}1}$ microgels, real-time fluorescence quantitative PCR and Western blot experiments were used to evaluate the expression of several inflammation-related cytokines of DED at mRNA and protein levels (Ma et al., 2021; Zhang et al., 2021). As shown in **Figure 5F**, the mRNA expression level of several proinflammatory cytokines, such as IL6, NLRP3, and IL-1β, had significantly increased after Scop treatment (Kessal et al., 2021), suggesting the successful induction of ocular surface inflammation. This is consistent with the corneal fluorescein staining and TUNEL assay. The inhibition of expression at the mRNA level by free MCC950 exhibited a dose-dependent manner, which is shown in **Supplementary Figure 6**. Although the $PPAD_{3\text{-}7\text{-}1}$ microgel alone or free MCC950 exhibited an inhibitory effect on mRNA expression of these inflammatory factors, topical treatment of MCC950@$PPAD_{3\text{-}7\text{-}1}$ microgels showed superior inhibition of the expression than the simple mixture of MCC950 and the $PPAD_{3\text{-}7\text{-}1}$ microgel, indicating the synergistic therapeutic effect against DED. As shown in **Figure 5E**, IL6, NLRP3, and IL-1β expressions at the protein level greatly increased after Scop treatment, while the MCC950@$PPAD_{3\text{-}7\text{-}1}$ microgels markedly inhibited the expression of these inflammatory factors, which is well-consistent with PCR results.

CONCLUSION

In summary, a synergistic strategy for topical treatment of DED was achieved through a polydopamine-based microgel loaded with the NLRP3 inhibitor, MCC950, targeting the ROS-NLRP3-IL-1β signaling axis. The PPAD microgels were successfully synthesized *via* copolymerization of three kinds of monomers. Due to the excellent adhesiveness of polydopamine, the drug bioavailability was significantly improved by prolonging the ocular surface retention time. The *in vitro* assay demonstrated that the polydopamine-based microgels exhibited good biocompatibility and ROS scavenging effect. Moreover, the potentially toxic effects of MCC950 at a high dosage can be avoided. TUNEL assay revealed that compared with free MCC950, PPAD microgels *in situ* loaded with MCC950 significantly reduced ocular surface epithelial cell damage and apoptosis. PCR and WB results indicated that both mRNA and protein expression levels of inflammation-related cytokines were also significantly inhibited. We believe that this work will provide insightful guidance in the synergistic treatment of inflammation-related diseases by targeting the ROS-NLRP3-IL-1β signaling axis.

DATA AVAILABILITY STATEMENT

The original contributions presented in the study are included in the article/**Supplementary Material**, further inquiries can be directed to the corresponding authors.

ETHICS STATEMENT

The animal study was reviewed and approved by the Wenzhou Medical University.

AUTHOR CONTRIBUTIONS

All the authors contributed in conceptualization, methodology, and writing. ZZ, QC, DX, CP, WX, and LS conducted the investigation. ZZ and QC conducted the formal analysis. LS, JS, and WC contributed in supervision and funding acquisition.

FUNDING

This study was supported by the National Science Foundation for Young Scientists of China (Grant Nos 81970770, 82171021, and 51973161), the National Key Research and Development Program of China (2019YFC0840708), and Wenzhou Medical University (QTJ19035, 604090352/655).

SUPPLEMENTARY MATERIAL

The Supplementary Material for this article can be found online at: https://www.frontiersin.org/articles/10.3389/fbioe.2022.913648/full#supplementary-material

REFERENCES

Bao, X., Zhao, J., Sun, J., Hu, M., and Yang, X. (2018). Polydopamine Nanoparticles as Efficient Scavengers for Reactive Oxygen Species in Periodontal Disease. *ACS Nano* 12, 8882–8892. doi:10.1021/acsnano.8b04022

Barabino, S., Benitez-Del-Castillo, J. M., Fuchsluger, T., Labetoulle, M., Malachkova, N., Meloni, M., et al. (2020). Dry Eye Disease Treatment: The Role of Tear Substitutes, Their Future, and an Updated Classification. *Eur. Rev. Med. Pharmacol. Sci.* 24, 8642–8652. doi:10.26355/eurrev_202009_22801

Baudouin, C., Rolando, M., Benitez Del Castillo, J. M., Messmer, E. M., Figueiredo, F. C., Irkec, M., et al. (2019). Reconsidering the Central Role of Mucins in Dry Eye and Ocular Surface Diseases. *Prog. Retin. Eye Res.* 71, 68–87. doi:10.1016/j.preteyeres.2018.11.007

Bron, A. J., de Paiva, C. S., Chauhan, S. K., Bonini, S., Gabison, E. E., Jain, S., et al. (2017). TFOS DEWS II Pathophysiology Report. *Ocular Surf.* 15, 438–510. doi:10.1016/j.jtos.2017.05.011

Chen, Y., Chauhan, S. K., Lee, H. S., Stevenson, W., Schaumburg, C. S., Sadrai, Z., et al. (2013a). Effect of Desiccating Environmental Stress versus Systemic Muscarinic AChR Blockade on Dry Eye Immunopathogenesis. *Invest. Ophthalmol. Vis. Sci.* 54, 2457–2464. doi:10.1167/iovs.12-11121

Chen, Y., Li, M., Li, B., Wang, W., Lin, A., and Sheng, M. (2013b). Effect of Reactive Oxygen Species Generation in Rabbit Corneal Epithelial Cells on Inflammatory and Apoptotic Signaling Pathways in the Presence of High Osmotic Pressure. *Plos One* 8, e72900. doi:10.1371/journal.pone.0072900

Coll, R. C., Hill, J. R., Day, C. J., Zamoshnikova, A., Boucher, D., Massey, N. L., et al. (2019). MCC950 Directly Targets the NLRP3 ATP-Hydrolysis Motif for Inflammasome Inhibition. *Nat. Chem. Biol.* 15, 556–559. doi:10.1038/s41589-019-0277-7

Corcoran, S. E., Halai, R., and Cooper, M. A. (2021). Pharmacological Inhibition of the Nod-Like Receptor Family Pyrin Domain Containing 3 Inflammasome with MCC950. *Pharmacol. Rev.* 73, 968–1000. doi:10.1124/pharmrev.120.000171

Davis, J. L., Gilger, B. C., and Robinson, M. R. (2004). Novel Approaches to Ocular Drug Delivery. *Curr. Opin. Mol. Ther.* 6, 195–205.

Favero, G., Moretti, E., Krajčíková, K., Tomečková, V., and Rezzani, R. (2021). Evidence of Polyphenols Efficacy Against Dry Eye Disease. *Antioxidants* 10, 190. doi:10.3390/antiox10020190

Gao, R., Shi, H., Chang, S., Gao, Y., Li, X., Lv, C., et al. (2019). The Selective NLRP3-Inflammasome Inhibitor MCC950 Reduces Myocardial Fibrosis and Improves Cardiac Remodeling in a Mouse Model of Myocardial Infarction. *Int. Immunopharmacol.* 74, 105575. doi:10.1016/j.intimp.2019.04.022

Hu, J., Yang, L., Yang, P., Jiang, S., Liu, X., and Li, Y. (2020). Polydopamine Free Radical Scavengers. *Biomater. Sci.* 8, 4940–4950. doi:10.1039/d0bm01070g

Jia, X., Sheng, W.-b., Li, W., Tong, Y.-b., Liu, Z.-y., and Zhou, F. (2014). Adhesive Polydopamine Coated Avermectin Microcapsules for Prolonging Foliar Pesticide Retention. *ACS Appl. Mat. Interfaces* 6, 19552–19558. doi:10.1021/am506458t

Jiang, H., He, H., Chen, Y., Huang, W., Cheng, J., Ye, J., et al. (2017). Identification of a Selective and Direct NLRP3 Inhibitor to Treat Inflammatory Disorders. *J. Exp. Med.* 214, 3219–3238. doi:10.1084/jem.20171419

Jones, L., Downie, L. E., Korb, D., Benitez-Del-Castillo, J. M., Dana, R., Deng, S. X., et al. (2017). TFOS DEWS II Management and Therapy Report. *Ocular Surf.* 15, 575–628. doi:10.1016/j.jtos.2017.05.006

Kessal, K., Daull, P., Cimbolini, N., Feraille, L., Grillo, S., Docquier, M., et al. (2021). Comparison of Two Experimental Mouse Dry Eye Models Through Inflammatory Gene Set Enrichment Analysis Based on a Multiplexed Transcriptomic Approach. *Int. J. Mol. Sci.* 22, 10770. doi:10.3390/ijms221910770

Krishnan, S. M., Ling, Y. H., Huuskes, B. M., Ferens, D. M., Saini, N., Chan, C. T., et al. (2019). Pharmacological Inhibition of the NLRP3 Inflammasome Reduces Blood Pressure, Renal Damage, and Dysfunction in Salt-Sensitive Hypertension. *Cardiovasc. Res.* 115, 776–787. doi:10.1093/cvr/cvy252

Lemp, M. A. (1995). Report of the National Eye Institute/Industry Workshop on Clinical Trials in Dry Eyes. *CLAO J.* 21, 221–232.

Li, C.-C., Abrahamson, M., Kapoor, Y., and Chauhan, A. (2007). Timolol Transport From Microemulsions Trapped in HEMA Gels. *J. Colloid Interface Sci.* 315, 297–306. doi:10.1016/j.jcis.2007.06.054

Li, J.-a., Chen, L., Zhang, X.-q., and Guan, S.-k. (2020). Enhancing Biocompatibility and Corrosion Resistance of Biodegradable Mg-Zn-Y-Nd Alloy by Preparing PDA/HA Coating for Potential Application of Cardiovascular Biomaterials. *Mater. Sci. Eng. C* 109, 110607. doi:10.1016/j.msec.2019.110607

Lin, S., Ge, C., Wang, D., Xie, Q., Wu, B., Wang, J., et al. (2019). Overcoming the Anatomical and Physiological Barriers in Topical Eye Surface Medication Using a Peptide-Decorated Polymeric Micelle. *ACS Appl. Mat. Interfaces* 11, 39603–39612. doi:10.1021/acsami.9b13851

Liu, Y., Ai, K., Ji, X., Askhatova, D., Du, R., Lu, L., et al. (2017). Comprehensive Insights into the Multi-Antioxidative Mechanisms of Melanin Nanoparticles and Their Application to Protect Brain from Injury in Ischemic Stroke. *J. Am. Chem. Soc.* 139, 856–862. doi:10.1021/jacs.6b11013

Lv, Y., Chu, C., Liu, K., Ru, Y., Zhang, Y., Lu, X., et al. (2021). A Combination of CMC and α-MSH Inhibited ROS Activated NLRP3 Inflammasome in Hyperosmolarity Stressed HCECs and Scopolamine-Induced Dry Eye Rats. *Sci. Rep.* 11, 1184. doi:10.1038/s41598-020-80849-2

Ma, B., Zhou, Y., Liu, R., Zhang, K., Yang, T., Hu, C., et al. (2021). Pigment Epithelium-Derived Factor (PEDF) Plays Anti-Inflammatory Roles in the Pathogenesis of Dry Eye Disease. *Ocular Surf.* 20, 70–85. doi:10.1016/j.jtos.2020.12.007

Mason, L., Jafri, S., Dortonne, I., and Sheppard, J. D., Jr. (2021). Emerging Therapies for Dry Eye Disease. *Expert Opin. Emerg. Drugs* 26, 401–413. doi:10.1080/14728214.2021.2011858

Osei, K. A., Cox, S. M., and Nichols, K. K. (2020). Dry Eye Disease Practice in Ghana: Diagnostic Perspectives, Treatment Modalities, and Challenges. *Optom. Vis. Sci.* 97, 137–144. doi:10.1097/OPX.0000000000001487

Park, C. G., Kim, Y. K., Kim, M. J., Park, M., Kim, M. H., Lee, S. H., et al. (2015). Mucoadhesive Microparticles with a Nanostructured Surface for Enhanced Bioavailability of Glaucoma Drug. *J. Control. Release* 220, 180–188. doi:10.1016/j.jconrel.2015.10.027

Park, J. H., Moon, S.-H., Kang, D. H., Um, H. J., Kang, S.-S., Kim, J. Y., et al. (2018). Diquafosol Sodium Inhibits Apoptosis and Inflammation of Corneal Epithelial Cells via Activation of Erk1/2 and RSK: *In Vitro* and *In Vivo* Dry Eye Model. *Invest. Ophthalmol. Vis. Sci.* 59, 5108–5115. doi:10.1167/iovs.17-22925

Periman, L. M., Mah, F. S., and Karpecki, P. M. (2020). A Review of the Mechanism of Action of Cyclosporine A: The Role of Cyclosporine A in Dry Eye Disease and Recent Formulation Developments. *Clin. Ophthalmol.* 14, 4187–4200. doi:10.2147/OPTH.S279051

Pflugfelder, S. C., and de Paiva, C. S. (2017). The Pathophysiology of Dry Eye Disease. *Ophthalmology* 124, S4–S13. doi:10.1016/j.ophtha.2017.07.010

Reins, R. Y., Lema, C., Courson, J., Kunnen, C. M. E., and Redfern, R. L. (2018). MyD88 Deficiency Protects Against Dry Eye-Induced Damage. *Invest. Ophthalmol. Vis. Sci.* 59, 2967–2976. doi:10.1167/iovs.17-23397

Roberti, G., Oddone, F., Agnifili, L., Katsanos, A., Michelessi, M., Mastropasqua, L., et al. (2020). Steroid-Induced Glaucoma: Epidemiology, Pathophysiology, and Clinical Management. *Surv. Ophthalmol.* 65, 458–472. doi:10.1016/j.survophthal.2020.01.002

Schmidl, D., Schlatter, A., Chua, J., Tan, B., Garhöfer, G., and Schmetterer, L. (2020). Novel Approaches for Imaging-Based Diagnosis of Ocular Surface Disease. *Diagnostics* 10, 589. doi:10.3390/diagnostics10080589

Seen, S., and Tong, L. (2018). Dry Eye Disease and Oxidative Stress. *Acta Ophthalmol.* 96, e412–e420. doi:10.1111/aos.13526

Shao, Z., Hu, X., Cheng, W., Zhao, Y., Hou, J., Wu, M., et al. (2020). Degradable Self-Adhesive Epidermal Sensors Prepared from Conductive Nanocomposite Hydrogel. *Nanoscale* 12, 18771–18781. doi:10.1039/d0nr04666c

Sies, H. (2015). Oxidative Stress: A Concept in Redox Biology and Medicine. *Redox Biol.* 4, 180–183. doi:10.1016/j.redox.2015.01.002

Suneetha, M., Rao, K. M., and Han, S. S. (2019). Mussel-Inspired Cell/Tissue-Adhesive, Hemostatic Hydrogels for Tissue Engineering Applications. *ACS Omega* 4, 12647–12656. doi:10.1021/acsomega.9b01302

Tang, P., Han, L., Li, P., Jia, Z., Wang, K., Zhang, H., et al. (2019). Mussel-Inspired Electroactive and Antioxidative Scaffolds with Incorporation of Polydopamine-Reduced Graphene Oxide for Enhancing Skin Wound Healing. *ACS Appl. Mat. Interfaces* 11, 7703–7714. doi:10.1021/acsami.8b18931

Uchino, Y., Kawakita, T., Ishii, T., Ishii, N., and Tsubota, K. (2012). A New Mouse Model of Dry Eye Disease. *Cornea* 31 (Suppl. 1), S63–S67. doi:10.1097/ICO.0b013e31826a5de1

Wang, B., Zuo, X., Peng, L., Wang, X., Zeng, H., Zhong, J., et al. (2021). Melatonin Ameliorates Oxidative Stress-Mediated Injuries through Induction of HO-1 and Restores Autophagic Flux in Dry Eye. *Exp. Eye Res.* 205, 108491. doi:10.1016/j.exer.2021.108491

Wang, F., Song, Y., Huang, J., Wu, B., Wang, Y., Pang, Y., et al. (2021). Lollipop-Inspired Multilayered Drug Delivery Hydrogel for Dual Effective, Long-Term, and NIR-Defined Glaucoma Treatment. *Macromol. Biosci.* 21, 2100202. doi:10.1002/mabi.202100202

Wang, L., Lei, W., Zhang, S., and Yao, L. (2021). MCC950, a NLRP3 Inhibitor, Ameliorates Lipopolysaccharide-Induced Lung Inflammation in Mice. *Bioorg. Med. Chem.* 30, 115954. doi:10.1016/j.bmc.2020.115954

Wang, P., Sheng, M., Li, B., Jiang, Y., and Chen, Y. (2016). High Osmotic Pressure Increases Reactive Oxygen Species Generation in Rabbit Corneal Epithelial Cells by Endoplasmic Reticulum. *Am. J. Transl. Res.* 8, 860–870.

Wolffsohn, J. S., Arita, R., Chalmers, R., Djalilian, A., Dogru, M., Dumbleton, K., et al. (2017). TFOS DEWS II Diagnostic Methodology Report. *Ocular Surf.* 15, 539–574. doi:10.1016/j.jtos.2017.05.001

Wong, W.-T., Li, L.-H., Rao, Y. K., Yang, S.-P., Cheng, S.-M., Lin, W.-Y., et al. (2018). Repositioning of the β-Blocker Carvedilol as a Novel Autophagy Inducer that Inhibits the NLRP3 Inflammasome. *Front. Immunol.* 9, 1920. doi:10.3389/fimmu.2018.01920

Xue, J., Zhang, Z., Nie, J., and Du, B. (2017). Formation of Microgels by Utilizing the Reactivity of Catechols with Radicals. *Macromolecules* 50, 5285–5292. doi:10.1021/acs.macromol.7b01304

Yoon, S.-H., Hwang, I., Lee, E., Cho, H.-J., Ryu, J. H., Kim, T.-G., et al. (2021). Antimicrobial Peptide LL-37 Drives Rosacea-Like Skin Inflammation in an NLRP3-Dependent Manner. *J. Investigative Dermatology* 141, 2885–2894. e5. doi:10.1016/j.jid.2021.02.745

Yu, Q. H., Zhang, C. M., Jiang, Z. W., Qin, S. Y., and Zhang, A. Q. (2020). Mussel-Inspired Adhesive Polydopamine-Functionalized Hyaluronic Acid Hydrogel with Potential Bacterial Inhibition. *Glob. Challenges* 4, 1900068. doi:10.1002/gch2.201900068

Yu, W., Tao, M., Zhao, Y., Hu, X., and Wang, M. (2018). 4′-Methoxyresveratrol Alleviated AGE-Induced Inflammation via RAGE-Mediated NF-Kb and NLRP3 Inflammasome Pathway. *Molecules* 23, 1447. doi:10.3390/molecules23061447

Zhang, J., Dai, Y., Yang, Y., and Xu, J. (2021). Calcitriol Alleviates Hyperosmotic Stress-Induced Corneal Epithelial Cell Damage via Inhibiting the NLRP3-ASC-Caspase-1-GSDMD Pyroptosis Pathway in Dry Eye Disease. *J. Inflamm. Res.* Vol. 14, 2955–2962. doi:10.2147/JIR.S310116

Zhao, H., Zeng, Z., Liu, L., Chen, J., Zhou, H., Huang, L., et al. (2018). Polydopamine Nanoparticles for the Treatment of Acute Inflammation-Induced Injury. *Nanoscale* 10, 6981–6991. doi:10.1039/c8nr00838h

Zheng, Q., Ren, Y., Reinach, P. S., She, Y., Xiao, B., Hua, S., et al. (2014). Reactive Oxygen Species Activated NLRP3 Inflammasomes Prime Environment-Induced Murine Dry Eye. *Exp. Eye Res.* 125, 1–8. doi:10.1016/j.exer.2014.05.001

Zheng, Q., Ren, Y., Reinach, P. S., Xiao, B., Lu, H., Zhu, Y., et al. (2015). Reactive Oxygen Species Activated NLRP3 Inflammasomes Initiate Inflammation in Hyperosmolarity Stressed Human Corneal Epithelial Cells and Environment-Induced Dry Eye Patients. *Exp. Eye Res.* 134, 133–140. doi:10.1016/j.exer.2015.02.013

Zheng, Q., Tan, Q., Ren, Y., Reinach, P. S., Li, L., Ge, C., et al. (2018). Hyperosmotic Stress-Induced TRPM2 Channel Activation Stimulates NLRP3 Inflammasome Activity in Primary Human Corneal Epithelial Cells. *Invest. Ophthalmol. Vis. Sci.* 59, 3259–3268. doi:10.1167/iovs.18-23965

Conflict of Interest: The authors declare that the research was conducted in the absence of any commercial or financial relationships that could be construed as a potential conflict of interest.

Publisher's Note: All claims expressed in this article are solely those of the authors and do not necessarily represent those of their affiliated organizations, or those of the publisher, the editors, and the reviewers. Any product that may be evaluated in this article, or claim that may be made by its manufacturer, is not guaranteed or endorsed by the publisher.

frontiers | Frontiers in Bioengineering and Biotechnology

REVIEW
published: 16 June 2022
doi: 10.3389/fbioe.2022.920213

Application of Metal-Based Nanozymes in Inflammatory Disease: A Review

Ruifeng Li[1†], Xinyue Hou[2†], Lingrui Li[1], Jiancheng Guo[1], Wei Jiang[1]* and Wenjun Shang[2]**

[1]Application Center for Precision Medicine, Department of Molecular Pathology, The Second Affiliated Hospital of Zhengzhou University, Academy of Medical Sciences, Zhengzhou University, Zhengzhou, China, [2]Department of Kidney Transplantation, The First Affiliated Hospital of Zhengzhou University, Academy of Medical Sciences, Zhengzhou University, Zhengzhou, China

Reactive oxygen species (ROS) are metabolites of normal cells in organisms, and normal levels of ROS in cells are essential for maintaining cell signaling and other intracellular functions. However, excessive inflammation and ischemia-reperfusion can cause an imbalance of tissue redox balance, and oxidative stress occurs in a tissue, resulting in a large amount of ROS, causing direct tissue damage. The production of many diseases is associated with excess ROS, such as stroke, sepsis, Alzheimer's disease, and Parkinson's disease. With the rapid development of nanomedicine, nanomaterials have been widely used to effectively treat various inflammatory diseases due to their superior physical and chemical properties. In this review, we summarize the application of some representative metal-based nanozymes in inflammatory diseases. In addition, we discuss the application of various novel nanomaterials for different therapies and the prospects of using nanoparticles (NPs) as biomedical materials.

Keywords: reactive oxygen species, inflammatory diseases, antioxidant, metal-based nanozyme, enzyme mimic activity

OPEN ACCESS

Edited by:
Qitong Huang,
Gannan Medical University, China

Reviewed by:
Meiyan Wang,
Salk Institute for Biological Studies, United States
Chenhui Wang,
Chongqing University, China

***Correspondence:**
Jiancheng Guo
gjc@zzu.edu.cn
Wei Jiang
weijiang@zzu.edu.cn
Wenjun Shang
fccshangwj@zzu.edu.cn

†These authors have contributed equally to this work

Specialty section:
This article was submitted to Nanobiotechnology, a section of the journal Frontiers in Bioengineering and Biotechnology

Received: *14 April 2022*
Accepted: *02 May 2022*
Published: *16 June 2022*

Citation:
Li R, Hou X, Li L, Guo J, Jiang W and Shang W (2022) Application of Metal-Based Nanozymes in Inflammatory Disease: A Review. Front. Bioeng. Biotechnol. 10:920213. doi: 10.3389/fbioe.2022.920213

1 INTRODUCTION

The oxygen-containing mono-electron by-products produced by cells in the process of respiration and organism metabolism are called reactive oxygen species (ROS) (Panth et al., 2016). ROS are composed of superoxide-free radicals, hydroxyl-free radicals, peroxide-free radicals, hydrogen peroxide, hypochlorous acid, and ozone (Panth et al., 2016) (**Figure 1**). ROS production and scavenging maintain a dynamic balance. As a result, the cell's antioxidant system is disrupted, prompting the cell to produce excessive ROS, which destroys the redox state and causes oxidative stress. The oxidative stress can cause severe damage to cells, leading to cell structure damaged by an injury to the cell components, including the cell membrane and nucleus (Floyd and Carney, 1992; Cabiscol et al., 2000; Leutner et al., 2001). This damage to the cell structure leads to damage to cell function that results in a series of serious diseases, for instance, Parkinson's disease, heart/kidney ischemia-reperfusion injury, diabetes, inflammation, cardiovascular disease, and cancer (Barnham et al., 2004; Giordano, 2005; Rolo and Palmeira, 2006; Jaeschke, 2011; Wang and Choudhary, 2011).

ROS are generated by both intracellular and extracellular metabolic pathways (Gligorovski et al., 2015; Nosaka and Nosaka, 2016). Substances that eliminate, inhibit, and prevent ROS from reacting with cells are called antioxidants (Flora, 2007; D'Autréaux and Toledano, 2007; Lambeth, 2004). Antioxidants are used to remove excess reactive oxygen species produced in living organisms. There are a few free radical scavengers in organisms' antioxidant systems: endogenous free radical scavengers such as superoxide dismutase (SOD) and vitamin E, exogenous free radical

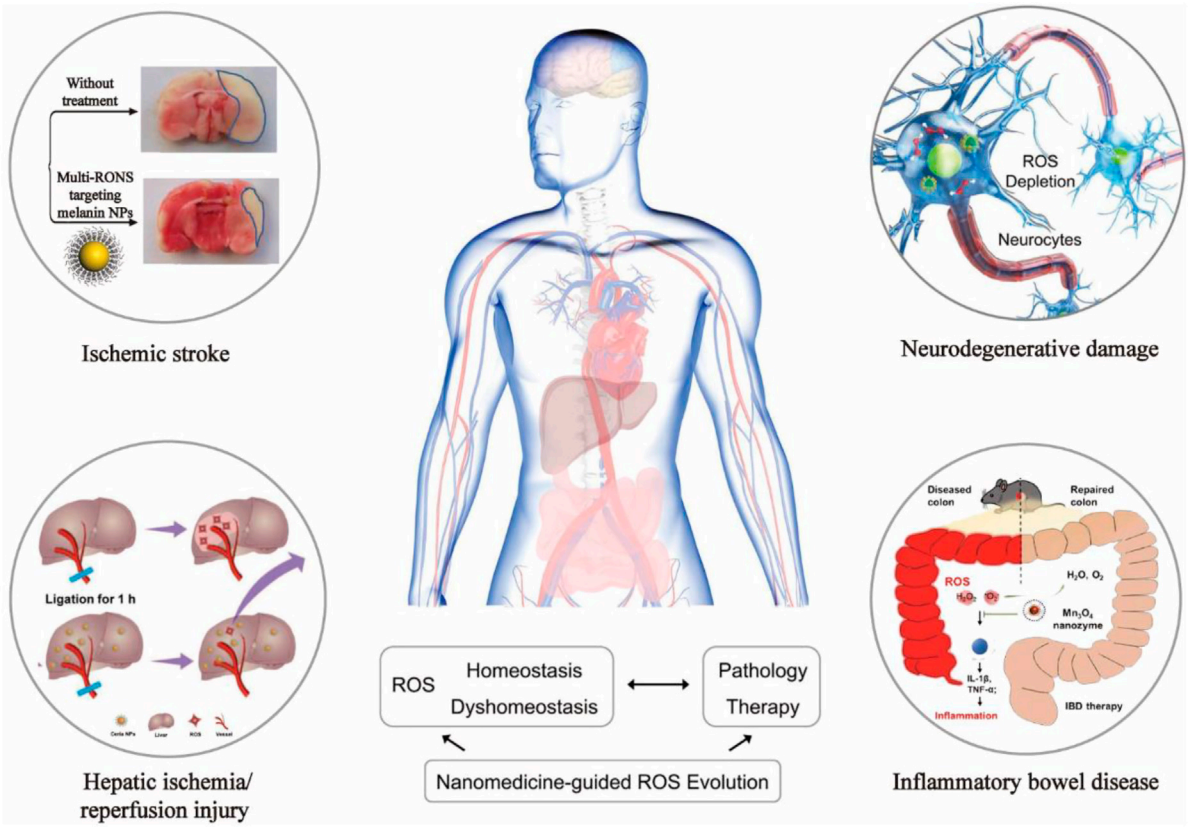

Graphical Abstract |

scavengers such as polyphenols, and Chinese herbal medicine that has antioxidation action similar to glossy *Ganoderma* and *Salvia miltiorrhiza*. Furthermore, the natural antioxidant enzyme system catalyzes free reactions to produce harmless products in removing ROS and reducing the damage caused by ROS. Among them, the leading natural antioxidant enzymes include superoxide dismutase (SOD), catalase (CAT), peroxidase (POD), and glutathione peroxidase (GPx) (Valko et al., 2006; Tidwell, 2013; Hamada et al., 2014; Kong et al., 2020; Hou et al., 2021). Although traditional natural enzymatic antioxidants are widely used, they are easily oxidized and have low bioavailability, poor modification, and stability. In addition, they are challenging to target scavenging oxygen free radicals, challenging to cross the blood–brain barrier, and easy to be neutralized by cell culture medium. To make up for the deficiency of traditional natural enzymes, several studies find the substitutes or mimic enzymes

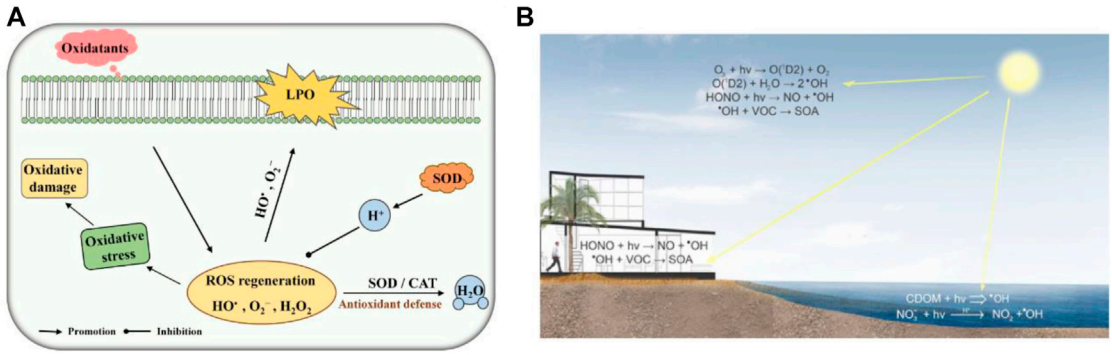

FIGURE 1 | (A) Schematic diagram of SOD and CAT toxicity against ROS. LPO, lipid peroxidation. Adapted with permission from ref.19. Copyright (2020) Frontiers in Microbiology. **(B)** ROS Material Chemistry. Adapted with permission from ref.11. Copyright (2016) American Chemical Society.

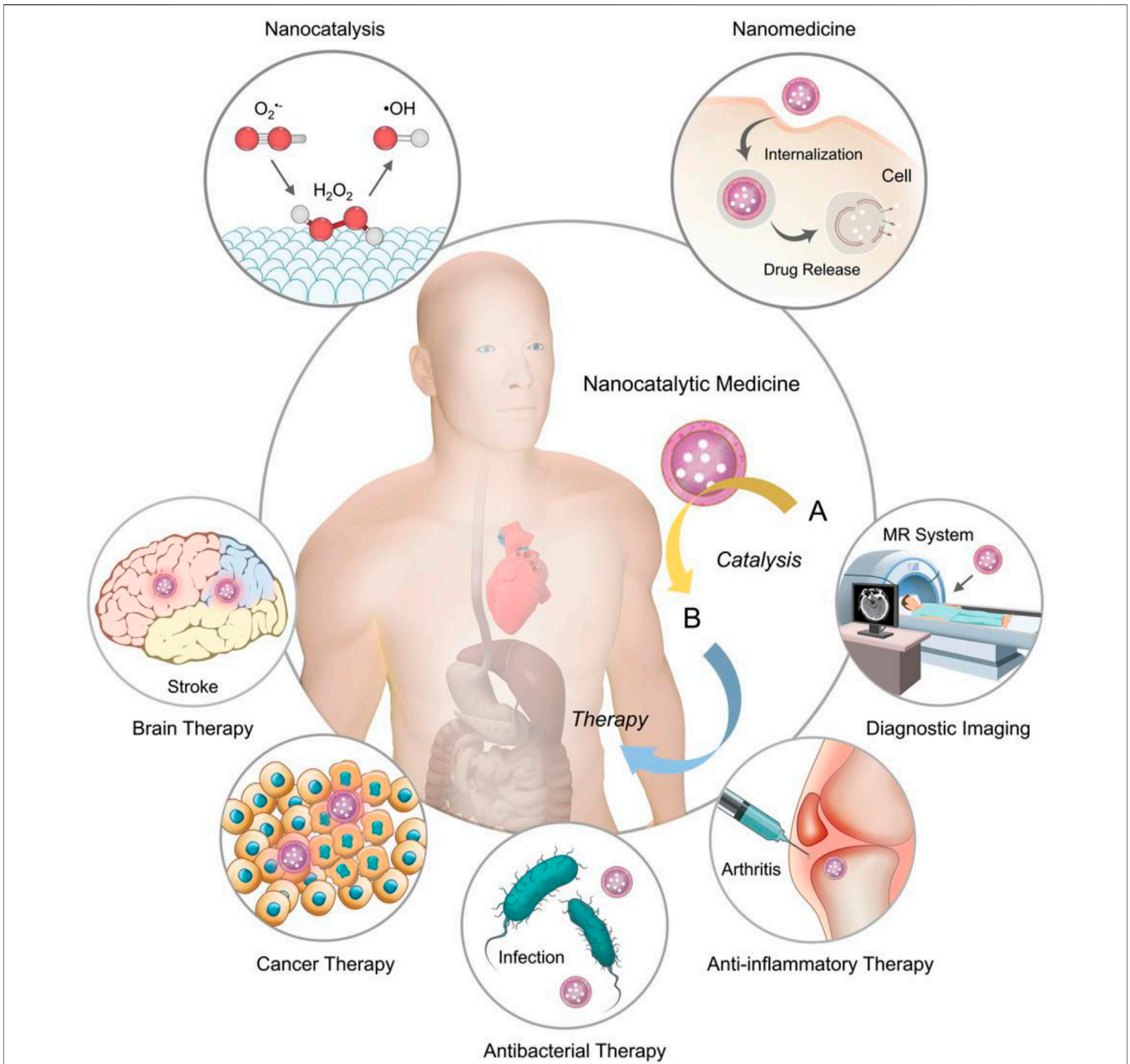

FIGURE 2 | Combining nanocatalysis with clinical medicine provides an advanced chemical modulation method for clinical treatment. MR, magnetic resonance. Adapted with permission from ref.17. Copyright (2019) John Wiley and Sons.

that can compensate for the shortcomings of natural enzymes and develop new antioxidants to make them better applied in production and life (Wu et al., 2019).

With the rapid development of nanotechnology, nanomaterials have been widely used in biomedical, optics, catalysis, and other fields because of their excellent physical and chemical properties, their ability to penetrate cell membranes, high activity, and low production cost (Yang et al., 2019; Liu et al., 2021; Yi et al., 2022). Because researchers found that these nanoparticles have the inherent ability to mimic the catalytic activity of certain biological enzymes, they are called nanomimicase enzymes, or nanozymes in short. In 2007, Xi Yunyan et al. found that iron tetroxide nanoparticles show natural HRP activity, which can catalyze the reaction between a substrate and hydrogen peroxide. Thus, they demonstrated that the nanomaterials themselves could simulate the functional activity of some biological enzymes (Gao et al., 2007). In previous studies, nanomaterials, such as fullerenes, gold nanoparticles, and ferromagnetic nanoparticles, also have been found to have the activity of

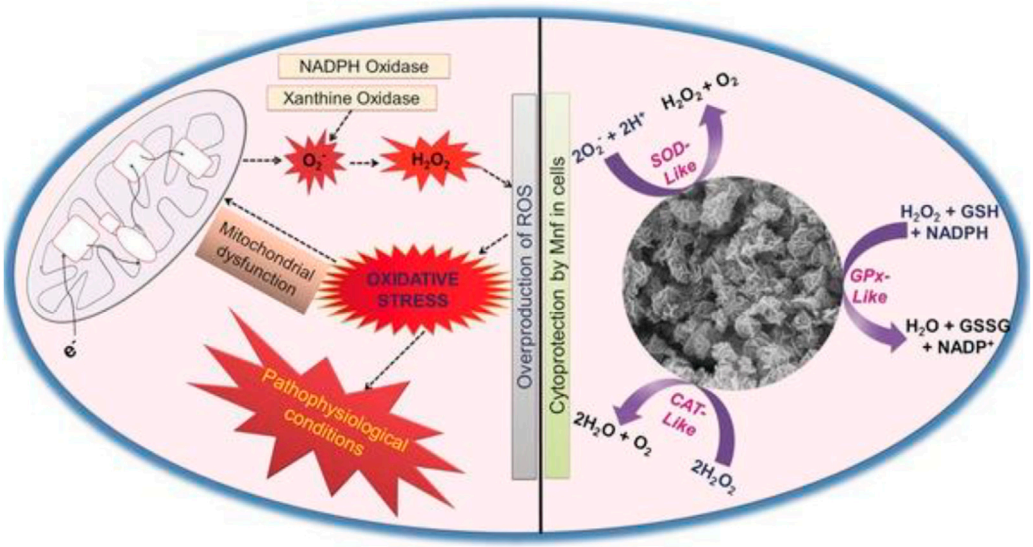

FIGURE 3 | Mn_3O_4 nanozyme (Mnf) modulates intracellular redox balance by mimicking the activities of catalase (CAT), glutathione peroxidase (GPx), and superoxide dismutase (SOD). Adapted with permission from ref.33. Copyright (2017) John Wiley and Sons.

some natural enzymes. These nanomaterials with the activity of natural enzymes are called nanozyme (Dugan et al., 1996; Comotti et al., 2004; Manea et al., 2004; Li et al., 2015), and nanozyme antioxidants, as nanozyme preparation, make up for the deficiency of traditional natural enzymes. In addition, nanozyme antioxidants have the advantages of low production cost, high modification degree and surface activity, targeted enrichment in specific tissues, high biocompatibility, and scale production. Thus, these advantages make the nanozyme antioxidants widely used in cancer treatment, biological science, drug carrier, biological antioxidant, and other fields. Nanoparticles could be a potential efficient therapeutic option for clinical treatment because they alter the biological distribution of antioxidants and have the inherent ability to remove electrons. According to the different catalytic substrates, the existing nanozymes can be divided into mimic peroxidase enzymes, mimic oxidase enzymes, catalase mimic enzymes, and superoxide dismutase mimic enzymes. Among them, peroxidase can catalyze the oxidation of hydrogen peroxide oxidation substrate; the oxide mimic enzyme catalyzes the oxidation of oxygen to the substrate; the CAT enzyme can catalyze the hydrogen peroxide decomposition reaction; and SOD enzymes can catalyze the superoxide anion disproportionation to produce hydrogen peroxide and oxygen. Therefore, these NPs could be applied to disease diagnosis, treatment, and biomedicine (Duan et al., 2015; Wang et al., 2016a; Cervadoro et al., 2018) (**Figure 2**).

According to recent studies, three kinds of nanozymes are commonly used: Prussian blue, nanocerium dioxide particles, and manganese-based analyses. In 1996, the Okuda team found that fullerenes could eliminate the superoxide radicals (Okuda et al., 1996); the Seal team (2005) showed that nanocerium dioxide (CeO_2) could prevent cell damage by radiation and attributed to the scavenging of free radicals (Okuda et al., 1996). Additionally, Gu et al. (2016) revealed that Prussian blue nanoparticles (PBNPs) have properties of catalase and superoxide dismutase (Watanabe et al., 2009). Qu Xiaogang and Ren Jinsong (2016) constructed a Donanamil complex system, which effectively eliminates overexpressed ROS in cells and prevents cells from oxidative stress damage (Huang et al., 2016). This article reviewed the types of nanoparticles with antioxidant capacity, the mechanism of action of nanozymes, and their clinical applications. This article mainly introduces the research progress of manganese NPs, ceria NPs, Prussian blue NPs, and other NPs in inflammation, Parkinson's disease, brain/liver ischemia/reperfusion, and other diseases.

1.1 Manganese-Based NPs

Manganese-based nanomaterials are nanomaterials with manganese as the active center and natural enzyme activity (Huang et al., 2016). In addition to playing an essential role in photosynthesis, divalent manganese plays a crucial role in hydrolysis and phosphotransferase. The more expensive manganese is the redox center of ribonucleotide reductase, catalase, peroxidase, and SOD in the mitochondria (Li et al., 2017; Wan et al., 2012). Manganese phosphate ($Mn_3(PO_4)_2$) is the first reported manganese nanoscale with superoxide dismutase activity (Miriyala et al., 2012). In 2014 (**Figure 3**), Wu et al. used bovine serum protein to wrap manganese dioxide (BSA-MnO_2), which can regulate the anaerobic status of the tumor microenvironment and has a specific effect on tumor treatment (Prasad et al., 2014). In 2016, researchers found that octahedral manganese oxide (MnO) nanomaterials have the properties of superoxide dismutase, and the relaxation time of MnO increases when it is in contact with superoxide radicals (Prasad et al., 2014). In addition, the researchers found that the

dendritic structure of Mn_3O_4 nanoparticles had a larger pore size and activities of superoxide dismutase and catalase (Yan et al., 2013).

Furthermore, the elimination rate of Mn_3O_4 on the superoxide anion can reach 50–60% (Singh et al., 2017). These advantages make up for the defects of natural enzyme antioxidants, so the researchers have researched the application of manganese-based nanozymes in treating clinical diseases and provided corresponding theoretical support for the application of manganese-based nanozymes in clinical treatment. Based on this, this article reviews the recent progress in synthesizing Mn_3O_4 nanoparticles by relevant teams in treating Parkinson's disease, inflammation, and other diseases.

Parkinson's disease (PD) is a neurodegenerative disease characterized by the substantia nigra striatum pathway degeneration, closely related to oxidative stress (Barnham et al., 2004). In the brain, dysregulation of redox balance can lead to oxidative stress in neuronal cells, resulting in neuronal loss (Yan et al., 2013; Li et al., 2020). Currently, there is no effective clinical treatment for PD. Moreover, the treatment for the disease is also the focus of clinicians and scientists. A few nanomaterials have been reported to mimic the activity of heme peroxidase, CAT, oxidases, or SOD enzymes (Gao et al., 2007; Asati et al., 2009; Wei and Wang, 2013; Dong et al., 2014). In addition, it has been reported that under pathophysiological conditions, the proper control of H_2O_2 levels through CAT–GPx cooperativity is essential (Baud et al., 2004). Given the *in vitro* antioxidant enzyme activity of the nanomaterials, Namrata Singh et al. combined the characteristics of enzyme-active nanomaterials to synthesize flower-shaped (Mnf) Mn_3O_4 nanoparticles. They established the cell model of Parkinson's disease in *in vitro* experiments, providing a clinical reference for treating Parkinson's and other neurological diseases. The activities of CAT, SOD, and Gpx of Mnf nanoparticles were verified by the comprehensive evaluation and characterization of Mnf nanoparticles' antioxidant capacity and different morphology Mn_3O_4 nanoparticles (Singh et al., 2017). The phase and morphology of Mnf did not change during the reaction, which proved that the high activity of Mnf was closely related to its morphology and multi-pore size. Human neuroblastoma-derived cell line SHSY-5Y was selected in the cell experiment, and the PD cell model was established by using the neurotoxin MPP^+ targeting dopamine neurons (Singh et al., 2017). MTT verified that Mnf nanoparticles were nontoxic, and the results of the DCFDA-H2 probe experiment showed that the loss of neuronal cell processes induced by MPP+ was repaired, confirming the protective effect of nanoparticles on cells. More importantly, the research results of Namrata Singh et al. proved that Mnf has better scavenging capacity of reactive oxygen species than traditional natural enzymes, which provides the effective reference data and theoretical guidance for the clinical application of Mnf in the treatment of neurodegenerative diseases caused by oxidative stress.

Inflammation has been demonstrated to cause various diseases, such as rheumatoid arthritis (Choy and Panayi, 2001), cardiovascular diseases (Taube et al., 2012), and even cancer (Colotta et al., 2009). The inflammatory response in the body is also closely related to reactive oxygen species. The production of free radicals in inflammatory sites is one of the pathogenesis of diseases. Mn_3O_4 nanoparticles (NPS) have a variety of enzyme activities to simulate the removal of oxygen free radicals, hydrogen peroxide, and hydroxyl radicals (Gorecki et al., 1991; Miriyala et al., 2012). Jia Yao et al. synthesized Mn_3O_4 NPs by the hydrothermal method and found that Mn_3O_4 NPs are more stable and have higher activity than natural enzymes, showing a good ROS scavenging effect *in vitro* (Yoshimura et al., 2021). These findings provide a basis for clinical studies on ROS-mediated inflammatory use of drugs. The DLS and zeta potential results proved that Mn_3O_4 NPs had good long-term storage stability. Also, the high crystallinity was confirmed by TEM detection (Yao et al., 2018; Yoshimura et al., 2021). The CO_2-specific probe hydroethidine (HE) was used to characterize the CO_2 scavenging capacity of Mn_3O_4 NPs. The experimental results showed that Mn_3O_4 NPs had a better SOD-like activity. Terephthalic acid (TA) reacted with hydrogen peroxide to prove that Mn_3O_4 NPs had a Catalin-like activity. The absorption spectrum and EPR spectrum were used to detect the hydroxyl group level in the presence of Mn_3O_4 NPs. In *in vitro* experiments, PMA was applied to the ears of mice, and the local inflammatory response was typical in the treated area. The fluorescence intensity of the DCFDA-H2 probe before and after comparison proved the scavenging ability of Mn_3O_4 NP reactive oxygen species, and HE staining showed that PMA induced lymphocytosis in the ear of mice, and the ear treated with Mn_3O_4 NPs could significantly alleviate the inflammatory symptoms. Jia Yao et al. not only demonstrated the scavenging activity of Mn_3O_4 analyses but also provided a promising therapeutic strategy for redox using the redox active analyses.

Inflammatory bowel disease (IBD) is a nonspecific chronic inflammatory disease of the intestinal tract, mainly including ulcerative colitis (UC) and Crohn's disease (Sheng et al., 2019; Chen and Shen, 2021). The pathogenesis of IBD is very complex and is generally believed to be related to immune, environmental factors, and genetic and genetic defects or changes (Podolsky, 2002). There are few effective treatments for IBD. Oxidative stress is a fundamental cause of IBD and plays an essential role in some of the characteristic signs and symptoms of IBD, such as abdominal pain, diarrhea, and big toxic colon (Zhao et al., 2019). Excessive ROS production leads to oxidative damage to the DNA, proteins, and lipids, which may promote the initiation and development of IBD (Mittler, 2017). Therefore, targeting inflammatory sites and scavenging reactive oxygen species may be effective strategies to reduce IBD. Natural enzymes in organisms, such as superoxide dismutase and catalase, can precisely remove O_2^- and H_2O_2, respectively, to protect the body from ROS damage. However, ROS in the focal area of IBD is often excessive, and natural enzymes in the organism are often tricky to control ROS in the normal physiological range, leading to the difficulty in clearing inflammation. At the same time, due to the high specificity of natural enzymes, a natural enzyme usually can selectively catalyze only one substrate, and it is challenging to remove multiple ROS simultaneously. In order to make Mn_3O_4@OLA@DSPE-PEG-COOH (hereinafter referred to as DPOMn_3O_4 nanoenzymes) which is stable in

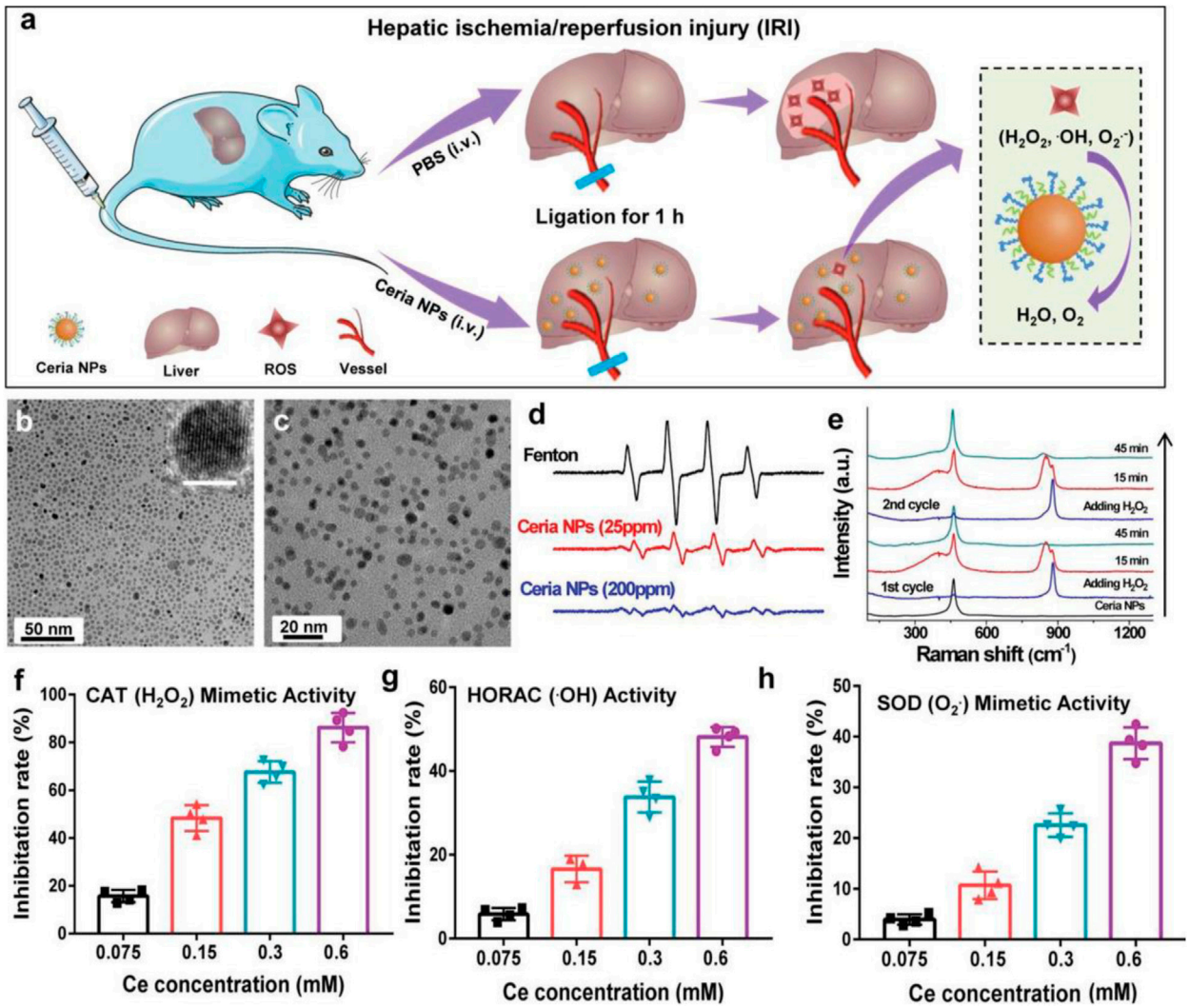

FIGURE 4 | Schematic diagram of ceria in the treatment of IRI and the antioxidant activity of ceria. **(A)** Schematic illustration of ceria for preventing IRI. **(B,C)** TEM images of ceria NPs. **(D)** ESR spectra of the different groups. **(E)** Raman spectra of ceria NPs reacting with H_2O_2. **(F–H)** Detection of ROS scavenging ability of ceria NPs. Adapted with permission from ref.60. Copyright (2019) John Wiley and Sons.

aqueous solution, Jia Yao et al. modified the surface of Mn_3O_4@OLA by using clear, good biocompatibility, and structure of small molecule lecithin derivative two stearic acyl phosphatidyl ethanolamine carboxy end group-polyethylene glycol (DSPEPEG-COOH) group. They confirmed the ability of the DPO-Mn_3O_4 nanoenzyme to scavenge superoxide anions *in vitro*. Subsequently, inflammatory bowel disease induced by dextran sulfate sodium (DSS) was established in mice (Mittler, 2017). Through enema administration of the DPO-Mn_3O_4 nanoenzyme, the therapeutic effect of DPO-Mn_3O_4 on the inflammatory bowel disease in mice was verified by the direct observation of the length and swelling degree of the colon of mice and the observation of colon tissue sections. Therefore, Yao Jia et al. demonstrated that Mn_3O_4 nanoenzyme could treat local *in vivo* inflammation by scavenging ROS.

1.2 Cerium-Based NPs

Cerium oxide (CeO_2) nanoparticles, also called nanoparticles of cerium oxide nanoparticles (CNPs), are well-known catalysts that show significant pharmacological potential due to their antioxidant properties (Ferreira et al., 2018). Cerium oxide itself has oxidation, as a combustion catalyst or catalyst carrier; which is widely used to remove industrial harmful gases or formaldehyde in the room, also is favored in the chemical industry. Compared with the oxidability of ceria, nanoceria has oxidability and reducibility. Oxygen in the nanometer cerium oxide lattice quickly falls off, resulting in oxygen hole defects. For the charge balance of the crystal, a small amount of Ce^{4+} is converted to Ce^{3+}. Ce^{3+} is reductive and will be oxidized to Ce^{4+} in the oxidation condition.

Consequently, Ce^{3+} is easy to be oxidized, and Ce^{3+} itself is reductive (Celardo et al., 2011). Therefore, CNPs scavenge free

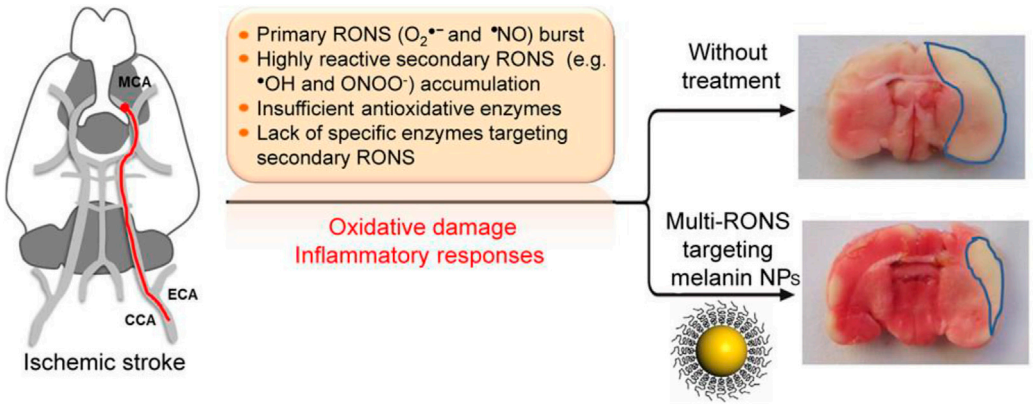

FIGURE 5 | Mechanism and effect of MeNPs in the treatment of ischemic stroke. Adapted with permission from ref.64. Copyright (2017) American Chemical Society.

radicals by reversibly binding oxygen through moving between Ce^{3+}(reduction) and Ce^{4+}(oxidation) forms on the particle surface. This ability is comparable to that of biological antioxidants. Because of this, CNPs are believed to exhibit the activity similar to dismutase and catalase, protecting cells from superoxide ions but hydrogen peroxide, two significant reactive oxygen species (Korsvik et al., 2007; Singh et al., 2011). Ceria nanoparticles are widely used in biomedicine for treating antioxidant-related diseases. Confirmed by the electron spin resonance, cerium oxide has the nature of the scavenging free radicals (Colon et al., 2009). In 2009, the United States, led by J Colon, consisting of the chemical, medical research team, provided in the United States "nano-drug" academic journals, published an article "using cerium oxide nanoparticles that protect normal cells from pneumonia caused by radioactive," which created new in the field of nanometer cerium oxide in biomedical applications (Colon et al., 2009; Colon et al., 2010). With the increasing popularity of cerium oxide nanoparticles in clinical use, the research team carried out relevant research on the application of cerium oxide in the treatment of liver ischemia/reperfusion. Moreover, the treatment of ischemic stroke also made significant progress. Consequently, this article reviewed the research results of relevant teams.

Hepatic ischemia-reperfusion injury (IRI) is one of the crucial causes of liver injury during liver transplantation, resection, and hypovolemic shock. Excessive production of reactive oxygen species is an essential factor leading to liver ischemia-reperfusion injury (IRI) (Eltzschig and Eckle, 2011; Zhai et al., 2013). Antioxidant treatment to improve the oxidative stress state of the injured liver is an effective therapeutic measure to improve IRI. The mononuclear phagocytic cell system (MPS) can affect the delivery of nanomaterials to the desired disease area (Bourquin et al., 2018; Feliu et al., 2016) (**Figure 4**). The direct prevention of liver ischemia-reperfusion injury (IRI) through nano-antioxidants with priority for liver uptake is an important research direction for applying nanomaterials in the treatment of liver IRI. Combining the redox activity characteristics of cerium oxide nanoparticles and the advantages of targeted enrichment in disease regions, Dalong Ni et al. selected representative nano-antioxidant cerium oxide nanoparticles (Ni et al., 2019). The establishment of the mouse liver IRI model specifically discussed the specific mechanism of cerium oxide NPs to prevent IRI and introduced the method of using the black box effect of nanomaterials to treat the live animal liver IRI. Positron emission tomography (PET) imaging real-time noninvasive assessment of cerium oxide NP biological distribution, using radionuclide 89 ^{zr} to mark ceria NPs, proves that polyethylene glycol (PEG) is changed to make these cerium oxides on the surface of the NPs with good blood circulation. Quantitative PET image analysis shows that NPs were cleared from the liver of mice from 1 to 21 days. These characteristics show that cerium oxide has the character of explicit according to the long-term accumulation in the liver to support the applications of cerium oxide in the body against hepatic IRI. The protective effect of cerium dioxide NPs on IRI in the mouse liver IRI model was compared. Aspartate aminotransferase (AST) and alanine aminotransferase (ALT) results showed liver injury in untreated IRI mice and effective prevention of IRI by cerium oxide NPs in the treated group. HE staining of the liver tissue showed liver sections of IRI mice in the PBS group, showing large areas of severe damage and significant lipolysis, necrosis, and bleeding of liver cells. The liver tissues of the IRI group treated with cerium oxide NPs were only slightly damaged, which indicated that cerium oxide NPs had a protective effect on IRI and proved the biocompatibility of cerium oxide NPs *in vivo*. The team's research will also provide references for the potential applications of nano-anticoagulants in preventing the liver IRI (Ni et al., 2019).

Acute ischemic cerebrovascular syndrome, also known as ischemic stroke, is a severe cerebrovascular disease that can lead to loss of brain function, disability, and even death. Oxidative damage is one of the important mechanisms leading to ischemic brain injury (Ngowi et al., 2021). During ischemia, the accumulation of superoxide anions, hydroxyl radicals, and hydrogen peroxide induces oxidative damage and leads to cell apoptosis (Barnham et al., 2004; Nathan and Cunningham-

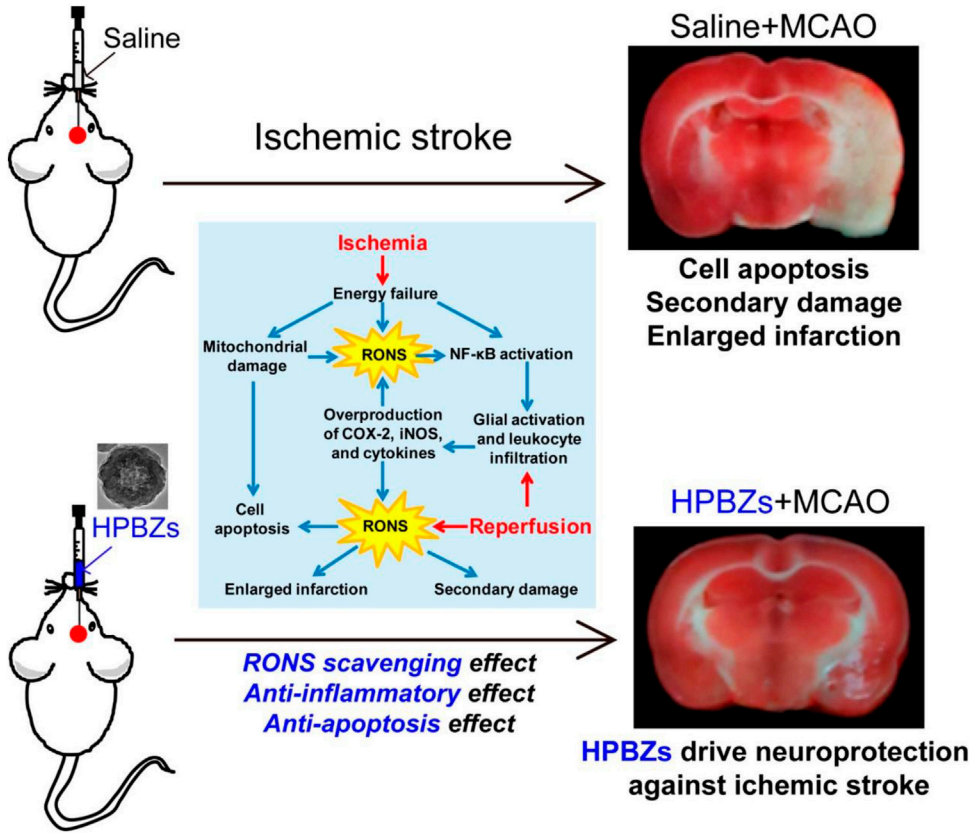

FIGURE 6 | Schematic illustration of HPBZs preventing ischemic stroke-induced neurological damage. Adapted with permission from ref.72. Copyright (2019) American Chemical Society.

Bussel, 2013). Yanlan Liu et al. studied the antioxidant effects of melanin nanoparticles (MeNPs) (Liu et al., 2017) (**Figure 5**). PEG-coated MeNPs were used to synthesize PEG-MeNPs with antioxidant and anti-inflammatory effects to conduct *in vitro* experiments and establish a rat model of ischemic stroke to study its antioxidant and anti-inflammatory effects *in vitro* and *in vivo*. Liu et al. first identified the antioxidant activity of MeNPs through comprehensive *in vivo* also *in vitro* experiments, demonstrating the feasibility of using these NPs as antioxidants *in vivo*. Liu et al. prepared the highly biocompatible cerium dioxide nanoparticles by coating them with PEG from nanoparticles dispersed in chloroform. TEM and DEPMPO characterized MeNPs and PEG-MeNPs, and SOD-like enzyme activity was found. X-ray photoelectron spectroscopy (XPS) found only a slight increase in the relative oxygen content of PEG-MeNPs. EPR analysis further confirmed the solid free radical signal of PEG-MeNPs. At the same time, PEG-MeNPs could maintain a high catalytic activity even after being stored at 4° for one year. These results indicate that PEG-MeNPs have good antioxidant stability. *In vitro*, neuro 2A cells were cultured using cobalt chloride ($CoCl_2$) to evaluate PEG-maps' neuroprotective effect on ischemia directly. Cobalt chloride ($CoCl_2$) is a common *in vitro* model used to investigate the mechanism of antioxidation therapy for the ischemia-related neuronal diseases. $CoCl_2$ significantly increased the ROS levels in neuro 2A, followed by cell death due to oxidative stress, while PEG-MeNPs significantly reduced the intracellular ROS levels, demonstrating the antioxidant capacity of PEG-MeNPs in cells. *In vivo*, PEG-MeNPs were injected into the lateral ventricles of experimental rats to evaluate their efficacy in the ischemic brain of experimental rats. The cerebral tissue sections of rats and TTC staining showed that the area of ischemic cerebral infarction of rats pretreated with PEG-MeNPs was about 14%.

Nevertheless, that of the control group was about 32%. The area of cerebral infarction of rats in the PEG-MeNPs-pretreated group was significantly lower than that in the control group. Accordingly, the generation of O_2 was also effectively inhibited, proving the possibility of treating ischemic brain injury with PEG-MeNPs. Through the tail vein injection of PEG–MeNPs, security in the body was assessed, and it was found that PEG-MeNPs have good blood compatibility, and do not change in serum alanine aminotransferase (ALT), aspartate aminotransferase (AST), and alkaline phosphatase (ALKP), blood in urine nitrogen (BUN), total protein (TP), or the level of albumin (propagated) in different organs of the histological analysis showed no NP morphological changes after the treatment or signs of inflammation, and proved that cerium oxide nanoparticles can be

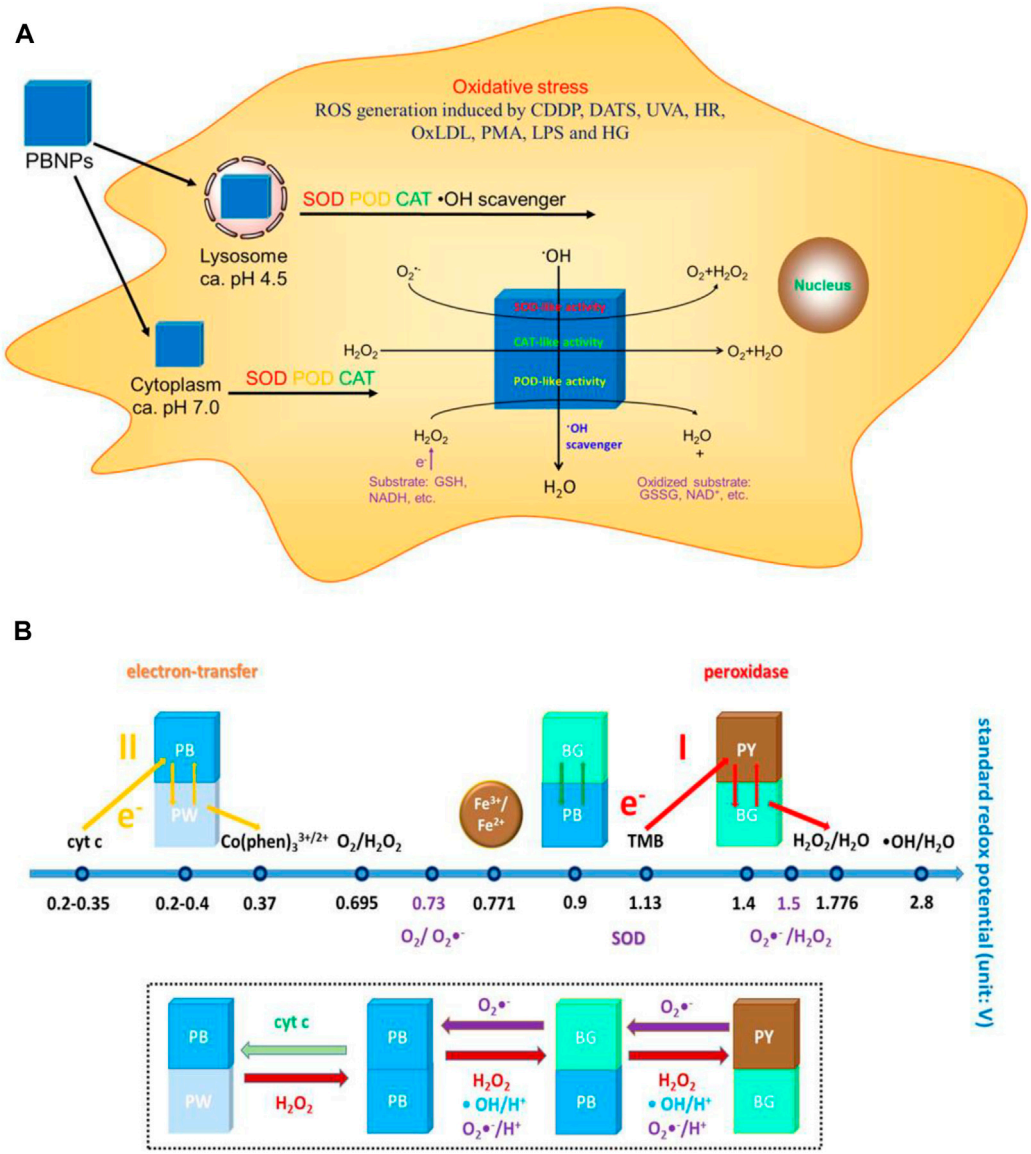

FIGURE 7 | (A) Schematic diagram of the mechanism of action of PBNPs in the cells. **(B)** Schematic diagram of the activity of PBNPs with different redox potentials of different compounds in different reaction systems. Adapted with permission from ref.27. Copyright (2016) American Chemical Society.

used as a safe and effective antioxidant for the feasibility of the application in the clinical treatment.

1.3 Iron-Based NPs

Prussian blue (PB), also known as ferric ferrocyanide, is the only antidote for clinical thallium poisoning, approved by the food and drug administration (FDA). In recent years, different types and functional nanomaterials based on PB have been widely used in inflammatory therapy, tumor therapy, molecular imaging, and other biomedical safety fields (Patra, 2016). PB can simulate various enzyme activities, including SOD, CAT, and POD. For example, Zhang W et al. found that Prussian blue nanoparticles (PBNs) can catalyze H_2O_2 with the artificial POD activity (Zhang et al., 2014). Further study by the team found that PBNP does not produce ROS such as OH through Fenton reaction, but has the POD activity of inhibiting the generation of OH, as well as a variety of biological enzyme activities such as CAT and SOD, which can effectively remove a variety of ROS ordinarily, and is widely used in inhibiting cell damage caused by ROS.

The mechanism of ROS scavenging by PB nanozyme particles shows that the surface volume of the nanozyme is a crucial factor in determining ROS scavenging efficiency. Consequently, hollow PB nanozyme is considered to have good ROS scavenging efficiency (Li and Shi, 2014; Wang et al., 2016b). The crystallinity of the hollow PB nanozyme particles synthesized by the microemulsion method is poor. Accordingly, they need to be synthesized in multiple steps at high temperatures. More importantly, it is not easy to achieve mass production (McHale et al., 2010; Roy et al., 2011). Under this

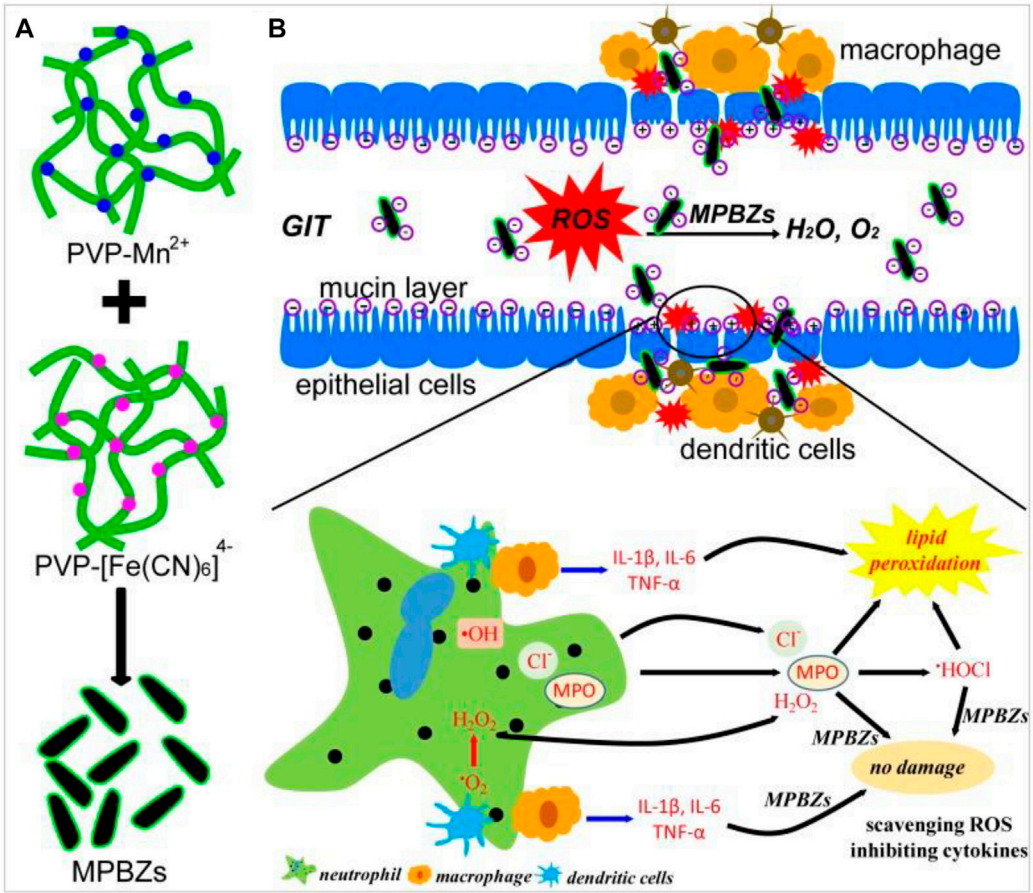

FIGURE 8 | (A) Schematic diagram of the synthetic production of MPBZs. **(B)** Schematic diagram of the mechanism of action of MPBZs *in vivo*. Adapted with permission from ref.56. Copyright (2019) Theranostics.

background, Kai Zhang et al. based on ischemic stroke disease pathogenesis with ROS, proved that the relationship between the development of the preparation of low cost also can be large-scale production of the artificial hollow nanozyme (HPBZs). The study of a new type of neural protection nano preparation provides the proof of the concept. Moreover, it may be helpful in the treatment of other ischemic stroke diseases related to ROS (Zhang et al., 2019) (**Figure 6**). The extensive characterization experiments by transmission electron microscopy showed that HPBZs had good crystallization. Accordingly, the changes in the hydrodynamic diameter of HPBZs at different time points proved the stability in the physiological environment and the potential for further application *in vivo* and *in vitro*. HPBZs can catalyze H_2O_2 to oxidize ABTS and TMB to nontoxic substances, which proves that HPBZs have an activity similar to peroxides. Choosing the TiO_2/UV system, HPBZs reduced the characteristic signal strength of BMPO/OH, indicating that HPBZs have good OH scavenging ability. To further demonstrate the antioxidant and anti-inflammatory activities of HPBZs, Kai Zhang et al. conducted cell and animal experiments *in vitro*. Using cobalt chloride ($CoCl_2$) to culture the SHSY-5Y cell line and construct an *in vitro* hypoxic model, it was found that HPBZs significantly promoted cell survival and also inhibited the production of reactive oxygen species. These results indicated that HPBZs could promote cell protection through antioxidant activity. Considering HPBZ *in vitro* antioxidant and anti-inflammatory activity, resistance to apoptosis, HPBZs' team further studied ischemic stroke in rats induced by the middle cerebral artery disease-modifying function in the model. Through the PET experiment, it was found that three pretreatment HPBZs lower ischemic injury in rats, cerebral infarction significantly less than the injected saline volume of MCAO rats, prompt HPBZ pretreatment can improve the nerve dysfunction; further comparing three groups of rats brain NO level and antioxidant capacity, HPBZ pretreatment can effectively suppress the RNS induced by MCAO generates, The anti-ROS activity of the brain tissue was significantly increased. Consequently, these results demonstrated the antioxidant properties of HPBZs in the treatment of ischemic stroke *in vivo*. In summary, Kai Zhang et al. constructed monodisperse HPBZs with good crystallization using a simple, formless synthesis strategy and applied it to treating ischemic stroke in rats, guiding the large-scale application of PB nanoparticles.

As mentioned previously, targeting intestinal inflammation and clearing ROS play key roles in IBD treatment. CAT, GPX,

SOD, POD, and other antioxidant enzymes are unique proteins with catalytic activity and high selectivity, and they all require the participation of the iron-containing auxiliary groups in the construction to exert excellent catalytic activity (Wu et al., 2019). Therefore, iron-based nanoenzymes have become the focus of research in recent years. On this basis, Zhang W et al. (Zhang et al., 2016) (**Figure 7**) designed a Prussian blue nanoparticle (PBNP) with a diameter of about 50 nm, which has activities of SOD, POD, CAT, and other enzymes, which can effectively remove ROS, and can effectively control the inflammation *in vivo* of lipopolysaccharide (LPS)-induced inflammatory mice by injection through the tail vein. PBNPs can target the aggregation of DSS-induced mouse colon inflammatory tissues, exert the activity of artificial nanozyme, effectively remove the excessive ROS produced in inflammatory tissues, block ROS-related inflammatory response and oxidative stress response, and inhibit the colon's progression, which improves the level of intestinal inflammation.

Later, Zhao Jiulong et al. (Zhao et al., 2019) (**Figure 8**) developed a new and effective strategy of nanoenzyme-catalyzed nanotherapy for IBD. Based on the activity of PBNPs, a novel manganese-Prussian blue nanoenzyme (MPBZs) was synthesized by using PBNPs as the basic framework and introducing Mn^{2+} with solid productivity. With the nanoscale size and good physiological stability, MPBZs can reach the inflammatory site of the colon smoothly through the robust acidic environment in the stomach and alkaline environment in the intestine, and specifically accumulate in the inflammatory site of the colon by using the EPR effect and charge effect of the intestinal epithelium. Due to the introduction of Mn^{2+} in MPBZs, the reducibility of MPBZs was more substantial than that of PBNPs, and the ROS scavenging ability was improved. Therefore, after the oral administration of MPBZs in DSS-induced acute IBD mice, the drugs can target intestinal inflammatory tissues, effectively remove ROS, and improve intestinal inflammation. At the same time, MPBZs can effectively reduce the expression levels of MPO, MDA, IL-1β, IL-6, IFN-γ, and TNF-α in the inflammatory colon tissue and effectively inhibit the progression of inflammation. Moreover, Zhao Jiulong synthetic MPBZs have many kinds of enzymes such as SOD and CAT activity, which can effectively eliminate ROS, are a high-quality artificial enzyme, inhibit oxidative stress in the process of inflammation reaction, and affect the oxidation of inflammatory-related signaling pathways and related critical molecular expression. Signaling pathway to reduce inflammation, especially for the ROS-related diseases, IBD provides a new thought of treatment, which has broad application prospects.

1.4 Other Nanomaterials

1.4.1 Platinum-Based NPs

Pt-NPs have activities similar to mitochondrial electron transport complexes and can be used as inhibitors of SOD and catalase. Watanabe et al. studied the antioxidant effects of PAA-protected platinum nanoparticles (PAA-Pt) (Watanabe et al., 2009). In *in vitro* evaluation, PAA-Pt cleared AOO generated by AAPH thermal decomposition in a dose-dependent manner. The concentration of NPs at 50% of any event was recovered (IC_{50}) 584 M, while the control showed no antioxidant activity. PAA-Pt is at least six times more active than other metal nanoparticles. The inhibition of PAA-Pt on linoleic acid peroxidation induced by AOO was further evaluated by determining the oxygen consumption and phenobarbital acid reactive substance (tar). Oxygen consumption decreased significantly after adding NPs, but there was no significant difference between oxygen consumption and the control group. The authors suggest that the peroxide inhibition mechanism of PAA-Pt particles may mainly be the elimination of toilets, which inhibits the peroxidation of linoleic acid. The thiobarbituric acid (TBA) test was designed to assess the production of free malondialdehyde (MDA) during lipid peroxidation. Accordingly, the results showed that PAA-Pt reduced the production of lipid peroxides by inhibiting the proliferation of the nitrite peroxidation chain induced by AOO. *In vivo*, Pt-NPs also act as a scavenger for RON. Katsumi et al. demonstrated for the first time in a mouse model that these NPs could protect against the hepatic ischemia-reperfusion injury (Katsumi et al., 2014). In their study, two Pt-NPs of different sizes were injected intravenously into mice, causing liver damage by blocking the portal vein, and consequently then reperfused for six hours. The results showed that both NPs were accumulated in the liver non-parenchymal cells after injection. The smaller the Pt-NPs, the more significant the decrease in alanine aminotransferase (ALT) and aspartic aminotransferase (AST). Small NPs also inhibited the increase in the ratio of oxidized GSH to reduced glutathione in the ischemic liver, effectively reducing the increase in lipid peroxides.

1.4.2 Selenium-Based NPs

As part of the liver's antioxidant defense system, selenium plays an essential role in antioxidative stress. Many studies have shown that supplementation with selenium can increase enzymes such as GPx, preventing the accumulation of free radicals and thus reducing cell damage (Tapiero et al., 2003; Qin et al., 2015). Therefore, nanomaterials containing selenium have intrinsic antioxidant properties. Zhai et al. used chitosan (CS) of different molecular weights to stabilize the synthesis of SeNPs, and then evaluated the antioxidant capacity of these nanoparticles (Zhai et al., 2017). The results of *in vitro* cell tests showed that the generation of intracellular electrons was inhibited by selenium concentration, also cs-sends; CS(l)-sends were stable by external or oral use, which effectively protected the glutathione peroxidase activity in mice and accordingly prevented the formation of lipofuscin induced by ultraviolet light. Se-doped carbon quantum dots (Se-CQDs) are also scavenger free radicals (Rosenkrans et al., 2020). In a recent study, the radical scavenging ability of SE-CQDs was investigated using the electron spin resonance (ESR) technique. The results showed that after the addition of SE-CQDs, the ESR signal of the DEMPO/OH adder disappeared, which indicated that it had an intense OH scavenging activity. The *in vitro* cell models

have shown that SE-CQDs can protect MDA-MB-231 cells from H_2O_2-induced oxidative stress. This was achieved by reducing H_2O_2-induced cell death consequently increasing cell viability (as determined by CCK8). In addition, quantitative analysis of ROS induction in MDA-MB-231 cells using the RONS fluorescent probe (DCFH-DA) showed that the fluorescence intensity of DCFH-DA significantly decreased after the addition, which confirmed the antioxidant capacity of SE-CQDs.

2 CONCLUSION

Reactive oxygen species (ROS) are metabolites of normal cells in organisms. Normal levels of ROS in cells are very important for maintaining cell signaling and other intracellular functions, so the dysregulation of ROS balance is involved in the pathophysiological processes of many diseases. The ideal antioxidant nanomaterials should be able to remove multiple primary and secondary electrons, maintain antioxidant activity against oxidative damage, be biocompatible, and have controllable properties such as size and modifiable surface. Choosing the proper nanomaterials for each disease is complicated because each disease has its unique process of oxidative stress, not the same, which is the most critical factor affecting the outcome of the disease. The selection of suitable nanomaterials for ROS scavenging should be based on their specific antioxidant capacity and their biological distribution, cyclic half-life, immunological properties, and other *in vivo* pharmacokinetics. With the development of nanometer research, various nanomaterials have been developed. Therefore, it is desirable to explore the antioxidant properties of these nanomaterials through a large number of *in vivo* studies.

AUTHOR CONTRIBUTIONS

WS, JG, and WJ conceived the idea, and critically revised and finalized the manuscript. RL and XH wrote the manuscript.

ACKNOWLEDGMENTS

We appreciate financial support from the Henan Province Medical Science and Technology Public Relations Plan Province Department Joint Construction project (SBGJ2018041, LHGJ20190329), and the Collaborative Innovation Project of Zhengzhou (Zhengzhou University) (No. 20XTZX05014).

REFERENCES

Asati, A., Santra, S., Kaittanis, C., Nath, S., and Perez, J. M. (2009). Oxidase-Like Activity of Polymer-Coated Cerium Oxide Nanoparticles. *Angew. Chem. Int. Ed.* 48 (13), 2308–2312. doi:10.1002/anie.200805279

Barnham, K. J., Masters, C. L., and Bush, A. I. (2004). Neurodegenerative Diseases and Oxidative Stress. *Nat. Rev. Drug Discov.* 3 (3), 205–214. doi:10.1038/nrd1330

Baud, O., Greene, A. E., Li, J., Wang, H., Volpe, J. J., and Rosenberg, P. A. (2004). Glutathione Peroxidase-Catalase Cooperativity Is Required for Resistance to Hydrogen Peroxide by Mature Rat Oligodendrocytes. *J. Neurosci.* 24 (7), 1531–1540. doi:10.1523/jneurosci.3989-03.2004

Bourquin, J., Milosevic, A., Hauser, D., Lehner, R., Blank, F., Petri-Fink, A., et al. (2018). Biodistribution, Clearance, and Long-Term Fate of Clinically Relevant Nanomaterials. *Adv. Mater* 30 (19), e1704307. doi:10.1002/adma.201704307

Cabiscol, E., Tamarit, J., and Ros, J. (2000). Oxidative Stress in Bacteria and Protein Damage by Reactive Oxygen Species. *Int. Microbiol.* 3 (1), 3–8.

Celardo, I., Pedersen, J. Z., Traversa, E., and Ghibelli, L. (2011). Pharmacological Potential of Cerium Oxide Nanoparticles. *Nanoscale* 3 (4), 1411–1420. doi:10.1039/c0nr00875c

Cervadoro, A., Palomba, R., Vergaro, G., Cecchi, R., Menichetti, L., Decuzzi, P., et al. (2018). Targeting Inflammation with Nanosized Drug Delivery Platforms in Cardiovascular Diseases: Immune Cell Modulation in Atherosclerosis. *Front. Bioeng. Biotechnol.* 6, 177. doi:10.3389/fbioe.2018.00177

Chen, G., and Shen, J. (2021). Artificial Intelligence Enhances Studies on Inflammatory Bowel Disease. *Front. Bioeng. Biotechnol.* 9, 635. doi:10.3389/fbioe.2021.635764

Choy, E. H. S., and Panayi, G. S. (2001). Cytokine Pathways and Joint Inflammation in Rheumatoid Arthritis. *N. Engl. J. Med.* 344 (12), 907–916. doi:10.1056/nejm200103223441207

Colon, J., Herrera, L., Smith, J., Patil, S., Komanski, C., Kupelian, P., et al. (2009). Protection from Radiation-Induced Pneumonitis Using Cerium Oxide Nanoparticles. *Nanomedicine Nanotechnol. Biol. Med.* 5 (2), 225–231. doi:10.1016/j.nano.2008.10.003

Colon, J., Hsieh, N., Ferguson, A., Kupelian, P., Seal, S., Jenkins, D. W., et al. (2010). Cerium Oxide Nanoparticles Protect Gastrointestinal Epithelium from Radiation-Induced Damage by Reduction of Reactive Oxygen Species and Upregulation of Superoxide Dismutase 2. *Nanomedicine Nanotechnol. Biol. Med.* 6 (5), 698–705. doi:10.1016/j.nano.2010.01.010

Colotta, F., Allavena, P., Sica, A., Garlanda, C., and Mantovani, A. (2009). Cancer-related Inflammation, the Seventh Hallmark of Cancer: Links to Genetic Instability. *Carcinogenesis* 30 (7), 1073–1081. doi:10.1093/carcin/bgp127

Comotti, M., Della Pina, C., Matarrese, R., and Rossi, M. (2004). The Catalytic Activity of ?Naked? Gold Particles. *Angew. Chem. Int. Ed.* 43 (43), 5812–5815. doi:10.1002/anie.200460446

D'Autréaux, B., and Toledano, M. B. (2007). ROS as Signalling Molecules: Mechanisms that Generate Specificity in ROS Homeostasis. *Nat. Rev. Mol. Cell. Biol.* 8 (10), 813–824. doi:10.1038/nrm2256

Dong, J., Song, L., Yin, J.-J., He, W., Wu, Y., Gu, N., et al. (2014). Co3O4 Nanoparticles with Multi-Enzyme Activities and Their Application in Immunohistochemical Assay. *ACS Appl. Mat. Interfaces* 6 (3), 1959–1970. doi:10.1021/am405009f

Duan, D., Fan, K., Zhang, D., Tan, S., Liang, M., Liu, Y., et al. (2015). Nanozyme-strip for Rapid Local Diagnosis of Ebola. *Biosens. Bioelectron.* 74, 134–141. doi:10.1016/j.bios.2015.05.025

Dugan, L. L., Gabrielsen, J. K., Yu, S. P., Lin, T.-S., and Choi, D. W. (1996). Buckminsterfullerenol Free Radical Scavengers Reduce Excitotoxic and Apoptotic Death of Cultured Cortical Neurons. *Neurobiol. Dis.* 3 (2), 129–135. doi:10.1006/nbdi.1996.0013

Eltzschig, H. K., and Eckle, T. (2011). Ischemia and Reperfusion-From Mechanism to Translation. *Nat. Med.* 17 (11), 1391–1401. doi:10.1038/nm.2507

Feliu, N., Docter, D., Heine, M., Del Pino, P., Ashraf, S., Kolosnjaj-Tabi, J., et al. (2016). *In Vivo* degeneration and the Fate of Inorganic Nanoparticles. *Chem. Soc. Rev.* 45 (9), 2440–2457. doi:10.1039/c5cs00699f

Ferreira, C. A., Ni, D., Rosenkrans, Z. T., and Cai, W. (2018). Scavenging of Reactive Oxygen and Nitrogen Species with Nanomaterials. *Nano Res.* 11 (10), 4955–4984. doi:10.1007/s12274-018-2092-y

Flora, S. J. (2007). Role of Free Radicals and Antioxidants in Health and Disease. *Cell. Mol. Biol. (Noisy-le-grand)* 53 (1), 1–2.

Floyd, R. A., and Carney, J. M. (1992). Free Radical Damage to Protein and DNA: Mechanisms Involved and Relevant Observations on Brain Undergoing Oxidative Stress. *Ann. Neurol.* 32 Suppl (Suppl. l), S22–S27. doi:10.1002/ana.410320706

Gao, L., Zhuang, J., Nie, L., Zhang, J., Zhang, Y., Gu, N., et al. (2007). Intrinsic Peroxidase-like Activity of Ferromagnetic Nanoparticles. *Nat. Nanotech* 2 (9), 577–583. doi:10.1038/nnano.2007.260

Giordano, F. J. (2005). Oxygen, Oxidative Stress, Hypoxia, and Heart Failure. *J. Clin. Invest.* 115 (3), 500–508. doi:10.1172/jci200524408

Gligorovski, S., Strekowski, R., Barbati, S., and Vione, D. (2015). Environmental Implications of Hydroxyl Radicals (OH). *Chem. Rev.* 115 (24), 13051–13092. doi:10.1021/cr500310b

Gorecki, M., Beck, Y., Hartman, J. R., Fischer, M., Weiss, L., Tochner, Z., et al. (1991). Recombinant Human Superoxide Dismutases: Production and Potential Therapeutical Uses. *Free Radic. Res. Commun.* 12-13 Pt 1 (Pt 1), 401–410. doi:10.3109/10715769109145810

Hamada, N., Fujimichi, Y., Iwasaki, T., Fujii, N., Furuhashi, M., Kubo, E., et al. (2014). Emerging Issues in Radiogenic Cataracts and Cardiovascular Disease. *J. Radiat. Res.* 55 (5), 831–846. doi:10.1093/jrr/rru036

Hou, X., Shi, J., Zhang, J., Wang, Z., Zhang, S., Li, R., et al. (2021). Treatment of Acute Kidney Injury Using a Dual Enzyme Embedded Zeolitic Imidazolate Frameworks Cascade that Catalyzes *In Vivo* Reactive Oxygen Species Scavenging. *Front. Bioeng. Biotechnol.* 9, 800428. doi:10.3389/fbioe.2021.800428

Huang, Y., Liu, Z., Liu, C., Ju, E., Zhang, Y., Ren, J., et al. (2016). Self-Assembly of Multi-Nanozymes to Mimic an Intracellular Antioxidant Defense System. *Angew. Chem. Int. Ed.* 55 (23), 6646–6650. doi:10.1002/anie.201600868

Jaeschke, H. (2011). Reactive Oxygen and Mechanisms of Inflammatory Liver Injury: Present Concepts. *J. Gastroenterol. Hepatol.* 26 (Suppl. 1), 173–179. doi:10.1111/j.1440-1746.2010.06592.x

Katsumi, H., Fukui, K., Sato, K., Maruyama, S., Yamashita, S., Mizumoto, E., et al. (2014). Pharmacokinetics and Preventive Effects of Platinum Nanoparticles as Reactive Oxygen Species Scavengers on Hepatic Ischemia/reperfusion Injury in Mice. *Metallomics* 6 (5), 1050–1056. doi:10.1039/c4mt00018h

Kong, L., Xiong, Z., Song, X., Xia, Y., Zhang, H., Yang, Y., et al. (2020). Enhanced Antioxidant Activity in Streptococcus Thermophilus by High-Level Expression of Superoxide Dismutase. *Front. Microbiol.* 11, 579804. doi:10.3389/fmicb.2020.579804

Korsvik, C., Patil, S., Seal, S., and Self, W. T. (2007). Superoxide Dismutase Mimetic Properties Exhibited by Vacancy Engineered Ceria Nanoparticles. *Chem. Commun.* (10), 1056–1058. doi:10.1039/b615134e

Lambeth, J. D. (2004). NOX Enzymes and the Biology of Reactive Oxygen. *Nat. Rev. Immunol.* 4 (3), 181–189. doi:10.1038/nri1312

Leutner, S., Eckert, A., and Müller, W. E. (2001). ROS Generation, Lipid Peroxidation and Antioxidant Enzyme Activities in the Aging Brain. *J. Neural Transm. (Vienna)* 108, 955–967. doi:10.1007/s007020170015

Li, C. W., Li, L. L., Chen, S., Zhang, J. X., and Lu, W. L. (2020). Antioxidant Nanotherapies for the Treatment of Inflammatory Diseases. *Front. Bioeng. Biotechnol.* 8, 200. doi:10.3389/fbioe.2020.00200

Li, W., Chen, B., Zhang, H., Sun, Y., Wang, J., Zhang, J., et al. (2015). BSA-stabilized Pt Nanozyme for Peroxidase Mimetics and its Application on Colorimetric Detection of Mercury(II) Ions. *Biosens. Bioelectron.* 66, 251–258. doi:10.1016/j.bios.2014.11.032

Li, W., Liu, Z., Liu, C., Guan, Y., Ren, J., and Qu, X. (2017). Manganese Dioxide Nanozymes as Responsive Cytoprotective Shells for Individual Living Cell Encapsulation. *Angew. Chem. Int. Ed.* 56 (44), 13661–13665. doi:10.1002/anie.201706910

Li, Y., and Shi, J. (2014). Hollow-structured Mesoporous Materials: Chemical Synthesis, Functionalization and Applications. *Adv. Mat.* 26 (20), 3176–3205. doi:10.1002/adma.201305319

Liu, H., Guo, C., Shang, Y., Zeng, L., Jia, H., and Wang, Z. (2021). A Supramolecular Nanoparticle of Pemetrexed Improves the Anti-tumor Effect by Inhibiting Mitochondrial Energy Metabolism. *Front. Bioeng. Biotechnol.* 9. doi:10.3389/fbioe.2021.804747

Liu, Y., Ai, K., Ji, X., Askhatova, D., Du, R., Lu, L., et al. (2017). Comprehensive Insights into the Multi-Antioxidative Mechanisms of Melanin Nanoparticles and Their Application to Protect Brain from Injury in Ischemic Stroke. *J. Am. Chem. Soc.* 139 (2), 856–862. doi:10.1021/jacs.6b11013

Manea, F., Houillon, F. B., Pasquato, L., and Scrimin, P. (2004). Nanozymes: Gold-Nanoparticle-Based Transphosphorylation Catalysts. *Angew. Chem. Int. Ed.* 43 (45), 6165–6169. doi:10.1002/anie.200460649

McHale, R., Ghasdian, N., Liu, Y., Ward, M. B., Hondow, N. S., Wang, H., et al. (2010). Prussian Blue Coordination Polymer Nanobox Synthesis Using Miniemulsion Periphery Polymerization (MEPP). *Chem. Commun.* 46 (25), 4574–4576. doi:10.1039/c0cc00003e

Miriyala, S., Spasojevic, I., Tovmasyan, A., Salvemini, D., Vujaskovic, Z., St. Clair, D., et al. (2012). Manganese Superoxide Dismutase, MnSOD and its Mimics. *Biochimica Biophysica Acta (BBA) - Mol. Basis Dis.* 1822 (5), 794–814. doi:10.1016/j.bbadis.2011.12.002

Mittler, R. (2017). ROS Are Good. *Trends Plant Sci.* 22 (1), 11–19. doi:10.1016/j.tplants.2016.08.002

Nathan, C., and Cunningham-Bussel, A. (2013). Beyond Oxidative Stress: an Immunologist's Guide to Reactive Oxygen Species. *Nat. Rev. Immunol.* 13 (5), 349–361. doi:10.1038/nri3423

Ngowi, E. E., Wang, Y.-Z., Qian, L., Helmy, Y. A. S. H., Anyomi, B., Li, T., et al. (2021). The Application of Nanotechnology for the Diagnosis and Treatment of Brain Diseases and Disorders. *Front. Bioeng. Biotechnol.* 9, 629832. doi:10.3389/fbioe.2021.629832

Ni, D., Wei, H., Chen, W., Bao, Q., Rosenkrans, Z. T., Barnhart, T. E., et al. (2019). Ceria Nanoparticles Meet Hepatic Ischemia-Reperfusion Injury: The Perfect Imperfection. *Adv. Mater* 31 (40), e1902956. doi:10.1002/adma.201902956

Nosaka, Y., and Nosaka, A. (2016). Understanding Hydroxyl Radical (OH) Generation Processes in Photocatalysis. *ACS Energy Lett.* 1 (2), 356–359. doi:10.1021/acsenergylett.6b00174

Okuda, K., Mashino, T., and Hirobe, M. (1996). Superoxide Radical Quenching and Cytochrome C Peroxidase-like Activity of C60-Dimalonic Acid, C62(COOH)4. *Bioorg. Med. Chem. Lett.* 6 (5), 539–542. doi:10.1016/0960-894x(96)00064-9

Panth, N., Paudel, K. R., and Parajuli, K. (2016). Reactive Oxygen Species: A Key Hallmark of Cardiovascular Disease. *Adv. Med.* 2016, 9152732. doi:10.1155/2016/9152732

Patra, C. R. (2016). Prussian Blue Nanoparticles and Their Analogues for Application to Cancer Theranostics. *Nanomedicine* 11 (6), 569–572. doi:10.2217/nnm.16.16

Podolsky, D. K. (2002). Inflammatory Bowel Disease. *N. Engl. J. Med.* 347 (6), 417–429. doi:10.1056/nejmra020831

Prasad, P., Gordijo, C. R., Abbasi, A. Z., Maeda, A., Ip, A., Rauth, A. M., et al. (2014). Multifunctional Albumin-MnO2 Nanoparticles Modulate Solid Tumor Microenvironment by Attenuating Hypoxia, Acidosis, Vascular Endothelial Growth Factor and Enhance Radiation Response. *ACS Nano* 8 (4), 3202–3212. doi:10.1021/nn405773r

Qin, S., Huang, B., Ma, J., Wang, X., Zhang, J., Li, L., et al. (2015). Effects of Selenium-Chitosan on Blood Selenium Concentration, Antioxidation Status, and Cellular and Humoral Immunity in Mice. *Biol. Trace Elem. Res.* 165 (2), 145–152. doi:10.1007/s12011-015-0243-5

Rolo, A. P., and Palmeira, C. M. (2006). Diabetes and Mitochondrial Function: Role of Hyperglycemia and Oxidative Stress. *Toxicol. Appl. Pharmacol.* 212 (2), 167–178. doi:10.1016/j.taap.2006.01.003

Rosenkrans, Z. T., Sun, T., Jiang, D., Chen, W., Barnhart, T. E., Zhang, Z., et al. (2020). Selenium-Doped Carbon Quantum Dots Act as Broad-Spectrum Antioxidants for Acute Kidney Injury Management. *Adv. Sci. (Weinh)* 7 (12), 2000420. doi:10.1002/advs.202000420

Roy, X., Hui, J. K.-H., Rabnawaz, M., Liu, G., and MacLachlan, M. J. (2011). Prussian Blue Nanocontainers: Selectively Permeable Hollow Metal-Organic Capsules from Block Ionomer Emulsion-Induced Assembly. *J. Am. Chem. Soc.* 133 (22), 8420–8423. doi:10.1021/ja2016075

Sheng, Y., Li, H., Liu, M., Xie, B., Wei, W., Wu, J., et al. (2019). A Manganese-Superoxide Dismutase from Thermus Thermophilus HB27 Suppresses Inflammatory Responses and Alleviates Experimentally Induced Colitis. *Inflamm. Bowel Dis.* 25 (10), 1644–1655. doi:10.1093/ibd/izz097

Singh, N., Savanur, M. A., Srivastava, S., D'Silva, P., and Mugesh, G. (2017). A Redox Modulatory Mn3 O4 Nanozyme with Multi-Enzyme Activity Provides Efficient Cytoprotection to Human Cells in a Parkinson's Disease Model. *Angew. Chem. Int. Ed.* 56 (45), 14267–14271. doi:10.1002/anie.201708573

Singh, S., Dosani, T., Karakoti, A. S., Kumar, A., Seal, S., and Self, W. T. (2011). A Phosphate-dependent Shift in Redox State of Cerium Oxide Nanoparticles and

its Effects on Catalytic Properties. *Biomaterials* 32 (28), 6745–6753. doi:10.1016/j.biomaterials.2011.05.073

Tapiero, H., Townsend, D. M., and Tew, K. D. (2003). The Antioxidant Role of Selenium and Seleno-Compounds. *Biomed. Pharmacother.* 57 (3-4), 134–144. doi:10.1016/s0753-3322(03)00035-0

Taube, A., Schlich, R., Sell, H., Eckardt, K., and Eckel, J. (2012). Inflammation and Metabolic Dysfunction: Links to Cardiovascular Diseases. *Am. J. Physiology-Heart Circulatory Physiology* 302 (11), H2148–H2165. doi:10.1152/ajpheart.00907.2011

Tidwell, T. (2013). Sunlight and Free Radicals. *Nat. Chem.* 5 (8), 637–639. doi:10.1038/nchem.1703

Valko, M., Rhodes, C. J., Moncol, J., Izakovic, M., and Mazur, M. (2006). Free Radicals, Metals and Antioxidants in Oxidative Stress-Induced Cancer. *Chemico-Biological Interact.* 160 (1), 1–40. doi:10.1016/j.cbi.2005.12.009

Wan, Y., Qi, P., Zhang, D., Wu, J., and Wang, Y. (2012). Manganese Oxide Nanowire-Mediated Enzyme-Linked Immunosorbent Assay. *Biosens. Bioelectron.* 33 (1), 69–74. doi:10.1016/j.bios.2011.12.033

Wang, H.-C. R., and Choudhary, S. (2011). Reactive Oxygen Species-Mediated Therapeutic Control of Bladder Cancer. *Nat. Rev. Urol.* 8 (11), 608–616. doi:10.1038/nrurol.2011.135

Wang, X., Feng, J., Bai, Y., Zhang, Q., and Yin, Y. (2016). Synthesis, Properties, and Applications of Hollow Micro-/Nanostructures. *Chem. Rev.* 116 (18), 10983–11060. doi:10.1021/acs.chemrev.5b00731

Wang, X., Hu, Y., and Wei, H. (2016). Nanozymes in Bionanotechnology: from Sensing to Therapeutics and beyond. *Inorg. Chem. Front.* 3 (1), 41–60. doi:10.1039/c5qi00240k

Watanabe, A., Kajita, M., Kim, J., Kanayama, A., Takahashi, K., Mashino, T., et al. (2009). In Vitrofree Radical Scavenging Activity of Platinum Nanoparticles. *Nanotechnology* 20 (45), 455105. doi:10.1088/0957-4484/20/45/455105

Wei, H., and Wang, E. (2013). Nanomaterials with Enzyme-like Characteristics (Nanozymes): Next-Generation Artificial Enzymes. *Chem. Soc. Rev.* 42 (14), 6060–6093. doi:10.1039/c3cs35486e

Wu, J., Wang, X., Wang, Q., Lou, Z., Li, S., Zhu, Y., et al. (2019). Nanomaterials with Enzyme-like Characteristics (Nanozymes): Next-Generation Artificial Enzymes (II). *Chem. Soc. Rev.* 48 (4), 1004–1076. doi:10.1039/c8cs00457a

Yan, M. H., Wang, X., and Zhu, X. (2013). Mitochondrial Defects and Oxidative Stress in Alzheimer Disease and Parkinson Disease. *Free Radic. Biol. Med.* 62, 90–101. doi:10.1016/j.freeradbiomed.2012.11.014

Yang, B., Chen, Y., and Shi, J. (2019). Nanocatalytic Medicine. *Adv. Mater* 31 (39), e1901778. doi:10.1002/adma.201901778

Yao, J., Cheng, Y., Zhou, M., Zhao, S., Lin, S., Wang, X., et al. (2018). ROS Scavenging Mn3O4nanozymes Forin Vivoanti-Inflammation. *Chem. Sci.* 9 (11), 2927–2933. doi:10.1039/c7sc05476a

Yi, X., Zeng, W., Wang, C., Chen, Y., Zheng, L., Zhu, X., et al. (2022). A Step-by-step Multiple Stimuli-Responsive Metal-Phenolic Network Prodrug Nanoparticles for Chemotherapy. *Nano Res.* 15 (2), 1205–1212. doi:10.1007/s12274-021-3626-2

Yoshimura, T., Mitsuyama, K., Sakemi, R., Takedatsu, H., Yoshioka, S., Kuwaki, K., et al. (2021). Evaluation of Serum Leucine-Rich Alpha-2 Glycoprotein as a New Inflammatory Biomarker of Inflammatory Bowel Disease. *Mediat. Inflamm.* 2021, 8825374. doi:10.1155/2021/8825374

Zhai, X., Zhang, C., Zhao, G., Stoll, S., Ren, F., and Leng, X. (2017). Antioxidant Capacities of the Selenium Nanoparticles Stabilized by Chitosan. *J. Nanobiotechnol* 15 (1), 4. doi:10.1186/s12951-016-0243-4

Zhai, Y., Petrowsky, H., Hong, J. C., Busuttil, R. W., and Kupiec-Weglinski, J. W. (2013). Ischaemia-reperfusion Injury in Liver Transplantation-From Bench to Bedside. *Nat. Rev. Gastroenterol. Hepatol.* 10 (2), 79–89. doi:10.1038/nrgastro.2012.225

Zhang, K., Tu, M., Gao, W., Cai, X., Song, F., Chen, Z., et al. (2019). Hollow Prussian Blue Nanozymes Drive Neuroprotection against Ischemic Stroke via Attenuating Oxidative Stress, Counteracting Inflammation, and Suppressing Cell Apoptosis. *Nano Lett.* 19 (5), 2812–2823. doi:10.1021/acs.nanolett.8b04729

Zhang, W., Hu, S., Yin, J.-J., He, W., Lu, W., Ma, M., et al. (2016). Prussian Blue Nanoparticles as Multienzyme Mimetics and Reactive Oxygen Species Scavengers. *J. Am. Chem. Soc.* 138 (18), 5860–5865. doi:10.1021/jacs.5b12070

Zhang, W., Ma, D., and Du, J. (2014). Prussian Blue Nanoparticles as Peroxidase Mimetics for Sensitive Colorimetric Detection of Hydrogen Peroxide and Glucose. *Talanta* 120, 362–367. doi:10.1016/j.talanta.2013.12.028

Zhao, J., Gao, W., Cai, X., Xu, J., Zou, D., Li, Z., et al. (2019). Nanozyme-mediated Catalytic Nanotherapy for Inflammatory Bowel Disease. *Theranostics* 9 (10), 2843–2855. doi:10.7150/thno.33727

Conflict of Interest: The authors declare that the research was conducted in the absence of any commercial or financial relationships that could be construed as a potential conflict of interest.

Publisher's Note: All claims expressed in this article are solely those of the authors and do not necessarily represent those of their affiliated organizations, or those of the publisher, the editors, and the reviewers. Any product that may be evaluated in this article, or claim that may be made by its manufacturer, is not guaranteed or endorsed by the publisher.

frontiers | Frontiers in Bioengineering and Biotechnology

ORIGINAL RESEARCH
published: 06 July 2022
doi: 10.3389/fbioe.2022.950146

Enhancing Drug Utilization Efficiency *via* Dish-Structured Triboelectric Nanogenerator

Qu Chen[1,2], Wenjing Deng[3], Jingjin He[2], Li Cheng[4], Pei-Gen Ren[5,6]* and Yang Xu[3]**

[1]Institute of Biomedicine and Biotechnology, Shenzhen Institute of Advanced Technology, Chinese Academy of Sciences, Shenzhen, China, [2]Shenzhen International Institute for Biomedical Research, Shenzhen, China, [3]School of Basic Medical Sciences, Southern Medical University, Guangzhou, China, [4]School of Materials and Energy, Lanzhou University, Lanzhou, China, [5]Center for Energy Metabolism and Reproduction, Shenzhen Institute of Advanced Technology, Chinese Academy of Sciences, Shenzhen, China, [6]Shenzhen College of Advanced Technology, University of Chinese Academy of Sciences, Shenzhen, China*

Due to the finding of severe side effects and low therapeutic efficacy with cancer chemotherapy, there still remains a great challenge to benefit patients with curative effect. In this work, we designed a self-powered drug delivery system comprising a current source derived from the disk TENG (D-TENG) and a pair of Au electrodes. Thus, cells seeded within the electrode gap could be stimulated by the current followed by D-TENG`s work. Under the rotation frequency of about 7.4 Hz, the peak output current and voltage of the D-TENG reached 3.7 μA and 135 V and achieved an average of 2.8 μA of output current. Furthermore, the D-TENG also showed its good stability to output steady current in a long-term condition. When applying the electric stimulation by this self-powered drug delivery system, a chemotherapy drug, doxorubicin (DOX), had significant uptake by cancer cells. Therefore, utilizing a novel TENG device as a part of chemotherapy would provide a new opportunity in future disease treatment.

Keywords: doxorubicin, dish-structure, triboelectric nanogenerator, drug utilization, enhanced efficiency

OPEN ACCESS

Edited by:
Qitong Huang,
Gannan Medical University, China

Reviewed by:
Xiang-Yu Kong,
Technical Institute of Physics and Chemistry (CAS), China
Guangqin Gu,
Henan University, China

****Correspondence:***
Li Cheng
chengl2007@live.cn
Pei-Gen Ren
pg.ren@siat.ac.cn
Yang Xu
yangxu@ucsd.edu

Specialty section:
This article was submitted to Nanobiotechnology, a section of the journal Frontiers in Bioengineering and Biotechnology

Received: *22 May 2022*
Accepted: *06 June 2022*
Published: *06 July 2022*

Citation:
Chen Q, Deng W, He J, Cheng L, Ren P-G and Xu Y (2022) Enhancing Drug Utilization Efficiency via Dish-Structured Triboelectric Nanogenerator. Front. Bioeng. Biotechnol. 10:950146. doi: 10.3389/fbioe.2022.950146

1 INTRODUCTION

Despite extensive efforts worldwide, cancer remains one of the leading causes of mortality (Sung et al., 2021). Surgery or radiotherapy is an effective strategy for the treatment of local tumors. In the remaining cases, chemotherapy is the main priority in cancer treatment (Chu and Sartorelli, 2018). However, chemotherapy is always accompanied by severe side effects and low therapeutic efficacy (Zhong et al., 2021). For example, a first-line clinical drug, doxorubicin (DOX) (Hai-wen et al., 2013), has been reported to result in all kinds of toxic side effects, including cardiotoxicity and alopecia, due to its low uptake by cancer cells (Zhao et al., 2019). Therefore, developing a new technology to enhance drug utilization is extremely urgent in order to reduce the side effects and improve efficacy.

Considering the physiological roles of bioelectrical signals in cell biology, electrical stimulation (ES) was introduced to improve some operations in many biological scenes. For example, a well-known microbiology technique called electroporation takes advantage of an electrical field to change the permeability of the cell membrane, allowing biomolecule transportation or even cell fusion (Zhang et al., 2018). Recently, ES has been demonstrated to have the potential to be a promising strategy for drug delivery and therapy. Karan Gulati's group combining electrical drug delivery and electrical stimulation therapy achieved beneficial results in bone implantation (Gulati et al., 2016). Cassandra L. Weaver's group developed a drug delivery nanocomposite controlled by electricity to meet various therapeutic needs (Weaver et al., 2014). With the concerted efforts of Pei-Chi Lee and

his colleagues, increased nanomedicine accumulation within tumor tissue stimulated by electrical single-walled carbon nanotubes helps to delay tumor growth (Lee et al., 2016). However, most of these techniques require an external power source, greatly increasing the cost and inconvenience, thereby limiting their further application.

Triboelectric nanogenerators (TENGs) (Fan et al., 2012a; Wang et al., 2014a; Zheng et al., 2014; Cheng et al., 2018; Qin et al., 2020; Zhang et al., 2020; Zhang et al., 2021a), which were invented to harvest unordered ambient mechanical energy on the basis of triboelectric effect and maxwell's displacement current (Wang, 2017), have been proved to be a simple, low-cost, and portable power source for self-powered devices and systems (Wang, 2013; Zheng et al., 2016; Cheng et al., 2017; Wang et al., 2018; Hao et al., 2021; Shang et al., 2021; Wang et al., 2021). A series of methods were investigated to increase the output performance of TENGs, such as material selection (Wang, 2013), surface roughness increment (Fan et al., 2012b; Zhang et al., 2015), surface charge injection (Wang et al., 2014a; Wang et al., 2014b), charge pump method (Cheng et al., 2018), step-down circuit (Qin et al., 2018), and multiple channel method (Zhang et al., 2022a). As a result, TENG's output voltage and peak current have been increased to more than ten thousand volts (Li et al., 2021) and hundreds of milliamperes (Cheng et al., 2013), and its output charge density is up to millicoulombs per square meter (Zhang et al., 2022a). As the output has been ameliorated to a very high level, TENGs are widely applied to establish self-powered nanodevices or nanosystems. For example, TENG's output changed under different driving forces, making it available to sense and detect these applied forces (Chen et al., 2022); through connecting TENGs together with sensors, UV light intensity, gas concentration, and other environmental information could be detected to realize the application of self-powered detection (Zheng et al., 2014; Su et al., 2018; Zhao et al., 2018; Zheng et al., 2022); using the current generated by TENGs, self-powered anticorrosion was realized (Wang et al., 2014a). Furthermore, through the use of display units or wireless transmission technology, the sensing result could be displayed directly or sent out for further processing (Zheng et al., 2014; Cheng et al., 2017; Zhang et al., 2022b). Using TENGs as a power source, many medical applications have been developed (Zhang et al., 2021b), and several self-powered systems have been designed for drug delivery (Wang et al., 2016; Bok et al., 2018; Liu et al., 2019). Among these systems, nanoneedles are considered one of the most effective methods for drug delivery, but bring up two problems: first, the active electrical area is usually very small, which makes it difficult to stimulate enough cells for therapy; second, fabrication of the nanoneedles and extra devices is always complicated and expensive. Thus, a simple and self-powered delivery system is required for current medicines.

In this work, we designed a very simple self-powered drug delivery system in order to reduce the severe side effects and enhance the therapeutic efficacy of chemotherapy. In this system, a disk TENG (D-TENG) is designed to provide a stable current, which performs the electrical stimulation towards cells/tissues

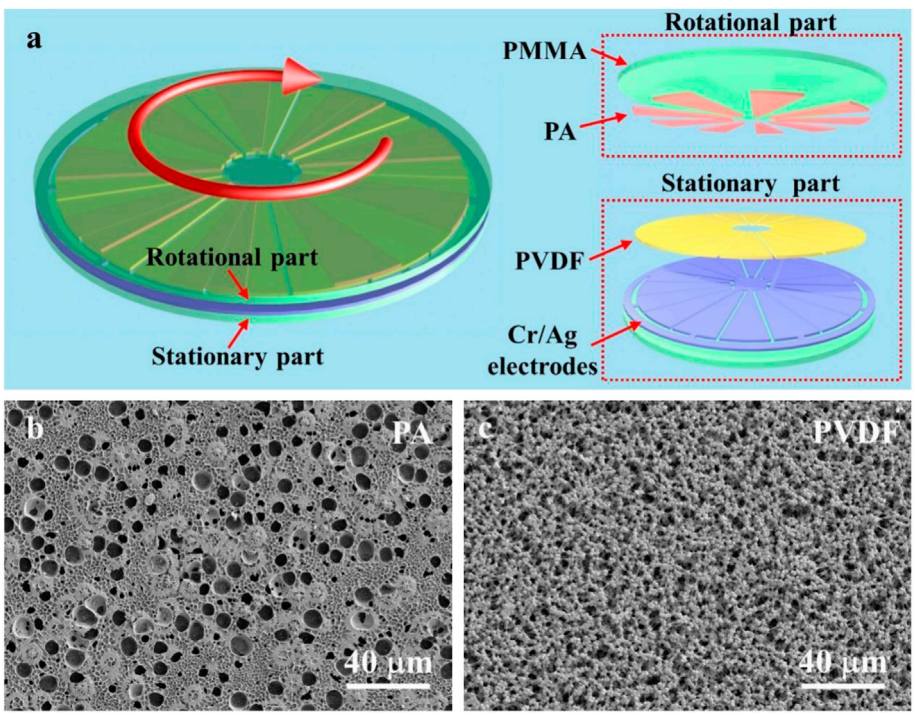

FIGURE 1 | Design of the D-TENG. **(A)** Schematic diagram of the D-TENG. **(B)** Scanning electron microscope (SEM) image of the spin-coated PA film. **(C)** SEM image of the spin-coated PVDF film.

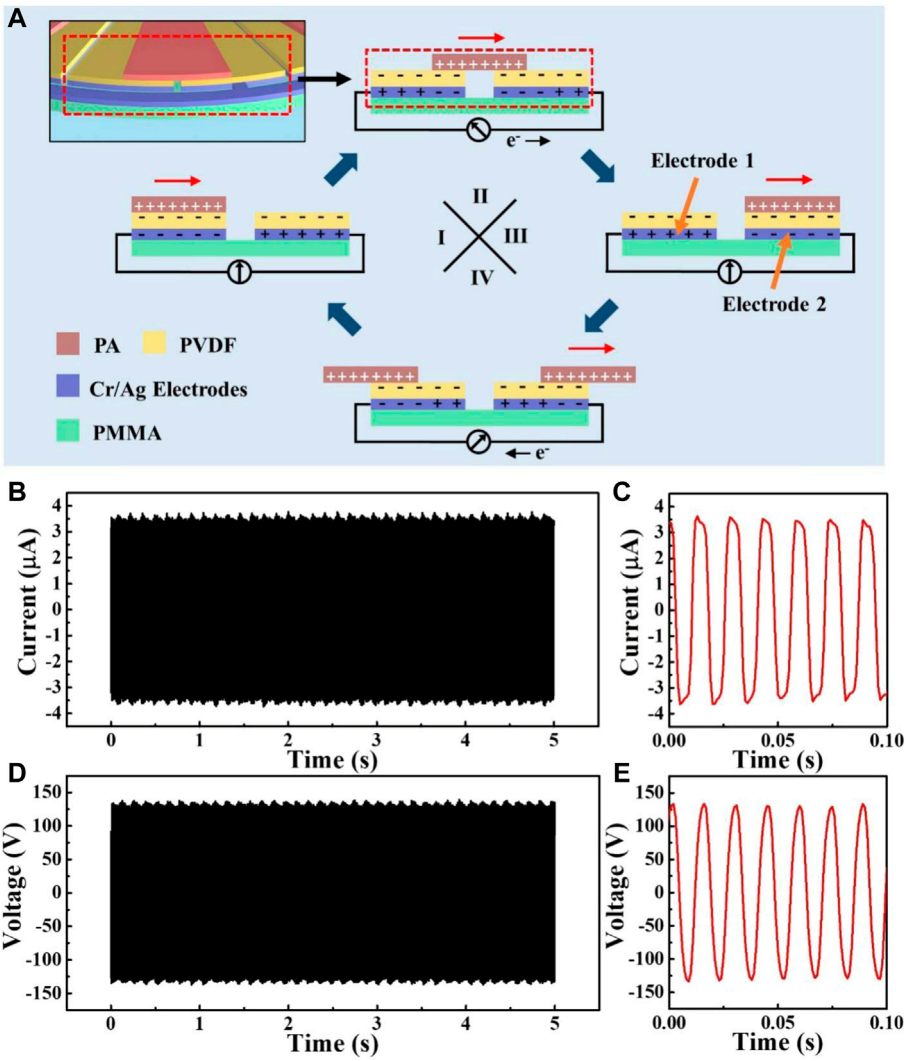

FIGURE 2 | Output of the D-TENG. **(A)** Schematic diagram of the working mechanism of the D-TENG. **(B)** Output current of the D-TENG. **(C)** Enlarged view of D-TENG's output current. **(D)** Output voltage of the D-TENG. **(E)** Enlarged view of D-TENG's output voltage.

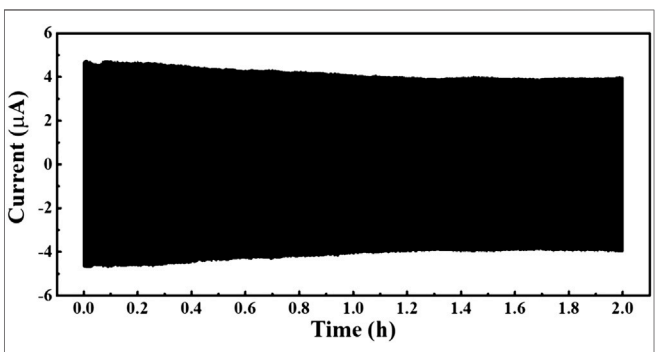

FIGURE 3 | Output current of the D-TENG working continuously for 2 h.

within two Au electrodes. An *in vitro* experiment showed that using this self-powered drug delivery system, the utilization efficiency of Dox was effectively increased.

2 MATERIALS AND METHODS

2.1 Materials

DOX was provided by Aladdin (Hangzhou, China). Mouse breast cancer cells (4T1 cell line) were purchased form the American Type Culture Collection (ATCC). PVDF powder was provided by Alfa Aesar (Shanghai, China). PA powder was provided by Macklin (Shanghai, China). All organic solvents were provided by Sinopharm Chemical Reagent (Shanghai, China).

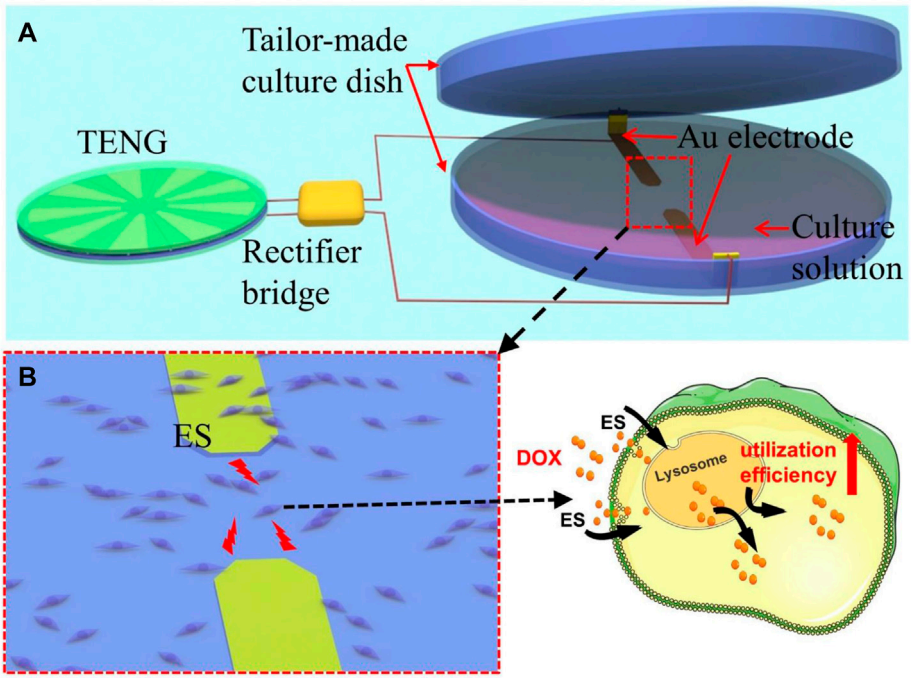

FIGURE 4 | *In vitro* self-powered drug delivery equipment. **(A)** Schematic diagram of the equipment. **(B)** Schematic diagram of the cells and Dox cocultured after electrical stimulation.

2.2 Preparation of PA and PVDF Solutions (Weaver et al., 2014)

To prepare the PA solution, 2 g of PA powder was added to 16 g of formic acid and then stirred for 30 min to make the PA powder dissolve. To prepare the PVDF solution, 3.75 g of PVDF powder was added to 8.5 g of N,N-dimethylacetamide (DMAC) and 12.75 g of acetone and then stirred at 60°C for 30 min to make the powder dissolve.

2.3 Fabrication of the D-TENG

Two pieces of PMMA sheet were first cleaned in sequence with ethanol and deionized water. The PA solution was spin-coated on one of the PMMA sheets at a speed of 1500 rpm for 60 s and then left for 30 min to make sure the solution is dry. The sheet was cut into the needed shape with 3 cm of radius to make the rotational part of the D-TENG. On the other piece of the PMMA sheet, Cr and Ag films were sputtered on one surface to make the Cr/Ag electrode, and PVDF solution was spin-coated on the Cr/Ag film at the speed of 1500 rpm for 60 s and then left for 30 min to make sure the solution is dry. The sheet was then cut into the needed shape; in this process, the Cr/Ag electrode was cut into two pieces, as shown in **Figure 1A** and two copper wires were connected to the two electrodes to make the stationary part of the D-TENG. At last, two parts of the D-TENG were assembled with the PA film in contact with the PVDF film and the center of the sheets aligned.

2.4 Fabrication of the Tailor-Made Culture Dish With Au Electrodes

Au electrodes with the needed shape were sputtered on the inner side of the bottom of an ordinary culture dish. Then, two copper wires were connected to the Au electrodes at the edge of the dish to make sure only the Au electrodes will contact the culture solution. The prepared culture dish with Au electrodes was sterilized with medicinal alcohol and UV light before cell culture.

2.5 Flow Cytometric Analysis of Drug Utilization Efficiency

4T1 cells were seeded in plates (3×10^5 cells/well) and cultured overnight. On the second day, media was changed and replaced with fresh media containing DOX. Cells were treated with/without TENG current stimulus for 1 h. The cells treated without DOX or ES were used for the control. 4T1 cells were cultured for another 24 h. Then, the cells were harvested and analyzed by a flow cytometer (BD Biosciences).

3 RESULTS AND DISCUSSION

As **Figure 1A** shows, the D-TENG comprises a rotational part and a stationary part. The rotational part contains a PMMA sheet as the substrate and nine PA films which act as a kind of friction layer and are attached to the PMMA sheet. The PA films are cut into circular sectors and ring-distributed on the PMMA sheet

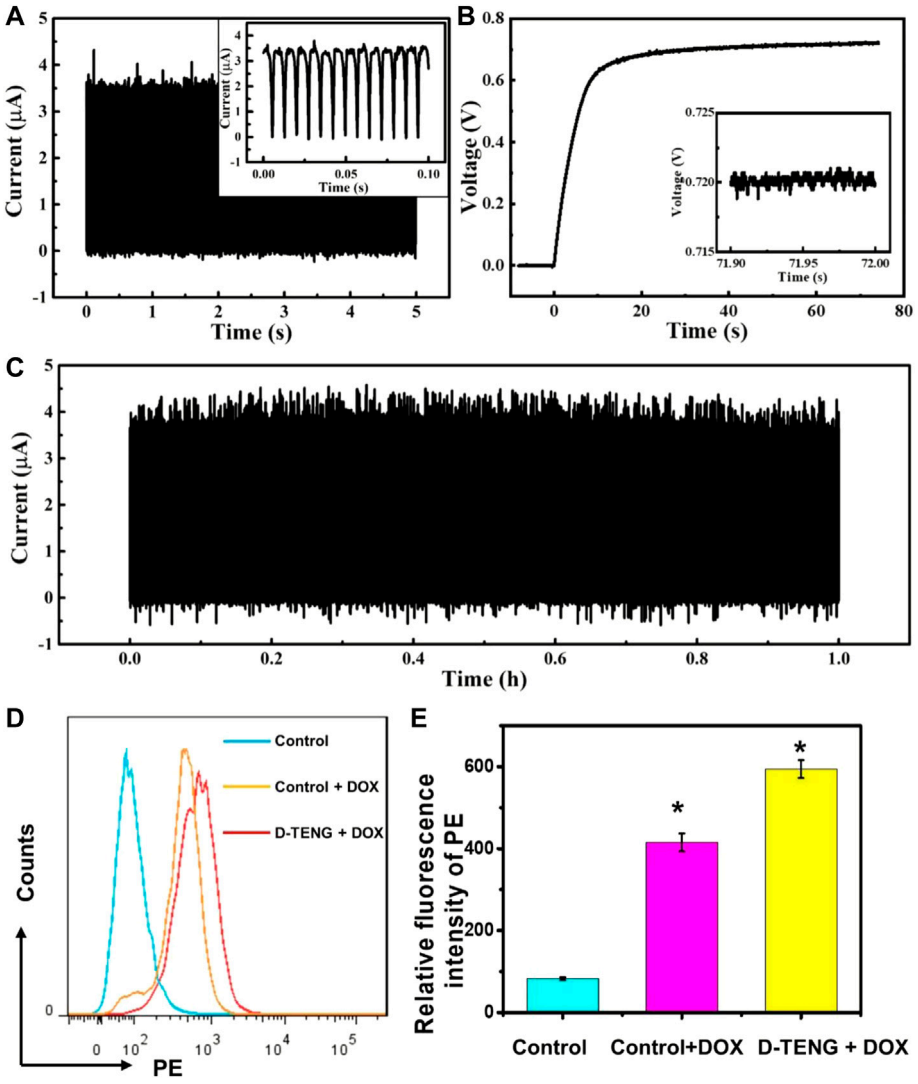

FIGURE 5 | *In vitro* enhancing drug utilization efficiency. **(A)** The current transmitted to the tailor-made culture dish. **(B)** The voltage between the Au electrodes. **(C)** The current is transmitted to the tailor-made culture dish in the simulation process. **(D)**. The uptake efficiency of 4T1 cells for Dox under 1 h stimulation was analyzed 24 h after stimulation. **(E)** Quantitative analysis of **(D)**. Unpaired *t* test. $n = 3$, $^*p < 0.05$, ns represents no significant difference.

with sectorial spaces of the same size. The stationary part contains a PMMA sheet as the substrate, two Cr/Ag electrodes and the sectorial PVDF films which act as the other kinds of friction layers attached to the electrodes. Each electrode contains nine sectorial units with the same size and distribution as the PA films. So, when the D-TENG is rotated, the PA films overlap with two electrodes alternately. To clearly observe the materials coating in the D-TENG, PA films (**Figure 1B**) and PVDF films (**Figure 1C**) were characterized using the scanning electron microscope (SEM). As the picture shows, rough surfaces with holes or particles formed naturally in the fabrication process of the films will help to increase the performance of the D-TENG. Details of the fabrication process are shown in the methods.

Figure 2A shows the working mechanism of the D-TENG. When the rotational part is rotated, PA films slide across the PVDF films. In this process, PA films rub with PVDF films. As a result, PA films take positive charges and PVDF films take negative charges. The total area of the PVDF films is twice that of the PA films', and charge density of the PA films is twice of the PVDF films'. When PA films overlap with electrode 1 (state I), though the positive charge on the PA film is partly offset by the negative charge, the residual charge will induce a negative charge in electrode 1. At electrode 2, the negative charge taken by the PVDF films on its surface will induce a positive charge in it. As a result, electrode 1 will take a negative charge and electrode 2 will take a positive charge. When PA films slide from electrode 1 to electrode 2 (state II), the overlapping area of electrode 1 with the PA films decreases, the overlapping area of electrode 2 increase, and electrons move from electrode 1 to electrode 2 through the external circuit and generate current in the circuit. When the PA films overlap with electrode 2 (state III), electrode 1 takes a positive charge and electrode 2 takes a negative charge.

And when PA films slide from electrode 2 to electrode 1 (state 4), electrons move from electrode 2 to electrode 1 and generate reversed current in the circuit. So, following the D-TENG work, one round from states I to IV will continue to the next round, which periodically generates alternating current in the circuit. As there are nine sectorial PA films in the device, each revolution of the D-TENG will generate nine forward and nine reversed current peaks in the circuit.

The D-TENG's output was then measured with a rotational frequency of about 7.4 Hz. Its output current was about 3.7 μA (**Figures 2B,C**), and its output voltage was about 135 V (**Figures 2D,E**). The frequency of the output current and voltage was about 67 Hz, which was about nine times the D-TENG's driving frequency. The integral results (**Supplementary Figure S1**) showed that the transferred charge of each peak was about 21 nC, and the D-TENG could export 2.8 μC in one second. This indicated the average output current of the D-TENG was about 2.8 μA, which achieved the comparable level commonly used in cell electrical stimulation (Macfelda et al., 2017; Yuan et al., 2021).

As a source of energy, the stability of the D-TENG is one of the most important properties. **Figure 3** shows the output current of the D-TENG working continuously for 2 hours. As expected, D-TENG's output decreased slightly in the first 1 hour, until its output current stabilized at about 4 μA. This good stability and intensity indicate the D-TENG has its own superiority for self-powered drug delivery.

Using this D-TENG as a power source, we designed a simple self-powered electrical stimulation system. The system contains the D-TENG, a rectifier bridge to convert the D-TENG's alternate current to direct current, and two Au electrodes to deliver the current. The Au electrode is used to prevent the possible electrochemical reaction. The cells/tissues stimulated by the current will increase the drug uptake efficiency.

An *in vitro* self-powered drug delivery experiment was then performed to check the effect of drug delivery using the simple drug delivery system. **Figure 4A** shows the equipment used in the *in vitro* experiment. In this equipment, the Au electrodes were deposited on the inner side of an ordinary culture disk (which consists of the tailor-made culture dish marked in the picture), which was used to culture and simulate the cells. Once the D-TENG is working, cells grow in the area between the two electrodes, which will be simulated. **Figure 4B** shows the mouse breast cancer cells (4T1 cell line) and Dox were cocultured in self-powered electrical stimulation system; after electrical stimulation, the uptake efficiency of cells for Dox will be determined.

In this experiment, mouse breast cancer cells (4T1 cell line) were seeded in culture plates. These cells were divided into three groups, including control, control with DOX (with no current stimulus), and D-TENG with DOX groups. In D-TENG with DOX groups, during the D-TENG 1 h continuous stimulation, the current transmitted to the tailor-made culture dish and the voltage between the Au electrodes were measured (**Figures 5A,B**). The D-TENG's output current was converted to direct current with a peak current of 3.5 μA and an average current of 2.9 μA (shown in **Supplementary Figure S2**). The voltage between the Au electrodes increases rapidly in the first 10 s and stabilizes at 0.72 V. **Figure 5C** shows that the current was stable during the stimulation process. Afterwards, 4T1 cells were cultured for another 24 h, and the cells were harvested and analyzed by flow cytometer (BD Biosciences). The flow cytometric results indicated that this self-powered drug delivery system could significantly improve the utilization efficiency of Dox (**Figures 5D,E**). Therefore, the electrical stimulation of D-TENG might be used to improve drug utilization efficiency for disease treatment in the future.

In conclusion, we designed a very simple self-powered drug delivery system that contains a D-TENG, a rectifier bridge, and two Au electrodes. At a working frequency of about 7.4 Hz, the D-TENG generates a peak current of 3.7 μA and an average output current of 2.8 μA. Considering the wide ranges were applied in previous works, the output of the D-TENG is powerful enough to stimulate the cells. Also, the D-TENG has good performance to provide stable current for a long time. The output current of the D-TENG is converted to direct current by the rectifier bridge to stimulate the cells/tissues between the Au electrode. An *in vitro* experiment showed this self-powered drug delivery system could significantly improve the utilization efficiency of Dox. The next step is to establish a biocompatible system to meet the wearable or transplantable needs in clinical trials. Taken together, we developed a stable and powerful D-TENG system for drug delivery, which will be part of chemotherapy in future treatment.

DATA AVAILABILITY STATEMENT

The raw data supporting the conclusions of this article will be made available by the authors without undue reservation.

AUTHOR CONTRIBUTIONS

P-GR, YX, and LC were responsible for the conceptualization. QC and LC designed the methodology. LC provided the scientific guidance for the experiment. QC, WD, and JH contributed to most of the biological studies, and LC to fabrication and characterization. The manuscript was organized and written by QC and LC and revised by JH, P-GR, and YX. All authors read and approved the final version.

FUNDING

This work was supported by the Shenzhen Science and Technology Program (no. JCYJ20210324122214039) and the National Natural Science Foundation of China (no. 52172203).

ACKNOWLEDGMENTS

The authors would like to thank the Yuan lab for providing the experimental platform.

SUPPLEMENTARY MATERIAL

The Supplementary Material for this article can be found online at https://www.frontiersin.org/articles/10.3389/fbioe.2022.950146/full#supplementary-material

Supplementary Figure S1 | The integral results of the D-TENG's output current. (a) The integral result of the D-TENG's output current without any additional process, which shows the output charge pure peak. (b) The integral result of the absolute values of D-TENG's output current, which shows the total output charge.

Supplementary Figure S2 | The integral results of the current transmitted to the tailor-made culture dish, which shows the total charge flowing through the culture solution.

REFERENCES

Bok, M., Lee, Y., Park, D., Shin, S., Zhao, Z.-J., Hwang, B., et al. (2018). Microneedles Integrated with a Triboelectric Nanogenerator: an Electrically Active Drug Delivery System. *Nanoscale* 10, 13502–13510. doi:10.1039/c8nr02192a

Chen, Y., Gao, Z., Zhang, F., Wen, Z., and Sun, X. (2022). Recent Progress in Self-powered Multifunctional E-skin for Advanced Applications. *Exploration* 2, 20210112. doi:10.1002/EXP.20210112

Cheng, G., Lin, Z.-H., Lin, L., Du, Z.-l., and Wang, Z. L. (2013). Pulsed Nanogenerator with Huge Instantaneous Output Power Density. *ACS Nano* 7, 7383–7391. doi:10.1021/nn403151t

Cheng, L., Xu, Q., Zheng, Y., Jia, X., and Qin, Y. (2018). A Self-Improving Triboelectric Nanogenerator with Improved Charge Density and Increased Charge Accumulation Speed. *Nat. Commun.* 9, 3773. doi:10.1038/s41467-018-06045-z

Cheng, L., Zheng, Y., Xu, Q., and Qin, Y. (2017). A Light Sensitive Nanogenerator for Self-Powered UV Detection with Two Measuring Ranges. *Adv. Opt. Mater.* 5, 1600623. doi:10.1002/adom.201600623

Chu, E., and Sartorelli, A. (2018). Cancer Chemotherapy. *Lange's Basic Clin. Pharmacol.*, 948–976. https://accessmedicine.mhmedical.com/content.aspx?bookid=2249&sectionid=175224452.

Fan, F.-R., Lin, L., Zhu, G., Wu, W., Zhang, R., and Wang, Z. L. (2012). Transparent Triboelectric Nanogenerators and Self-Powered Pressure Sensors Based on Micropatterned Plastic Films. *Nano Lett.* 12, 3109–3114. doi:10.1021/nl300988z

Fan, F.-R., Tian, Z.-Q., and Lin Wang, Z. (2012). Flexible Triboelectric Generator. *Nano Energy* 1, 328–334. doi:10.1016/j.nanoen.2012.01.004

Gulati, K., Maher, S., Chandrasekaran, S., Findlay, D. M., and Losic, D. (2016). Conversion of Titania (TiO2) into Conductive Titanium (Ti) Nanotube Arrays for Combined Drug-Delivery and Electrical Stimulation Therapy. *J. Mat. Chem. B* 4, 371–375. doi:10.1039/c5tb02108a

Hai-wen, Z., Li-qun, W., and Hong-liang, J. (2013). Chitosan-Based Cationic Micelles for Co-incorporation of Two Types of Drugs with Distinct Hydrophilicity. *Acta Polym. Sin.* 012, 1491–1499. doi:10.3724/SP.J.1105.2012.12115

Hao, M., Zhang, R., Jia, X., Gao, X., Gao, W., Cheng, L., et al. (2021). A Polymer Based Self-Powered Ethanol Gas Sensor to Eliminate the Interference of Ultraviolet Light. *Sensors Actuators A Phys.* 332, 113173. doi:10.1016/j.sna.2021.113173

Lee, P.-C., Peng, C.-L., and Shieh, M.-J. (2016). Combining the Single-Walled Carbon Nanotubes with Low Voltage Electrical Stimulation to Improve Accumulation of Nanomedicines in Tumor for Effective Cancer Therapy. *J. Control. Release* 225, 140–151. doi:10.1016/j.jconrel.2016.01.038

Li, Q., Liu, W., Yang, H., He, W., Long, L., Wu, M., et al. (2021). Ultra-stability High-Voltage Triboelectric Nanogenerator Designed by Ternary Dielectric Triboelectrification with Partial Soft-Contact and Non-contact Mode. *Nano Energy* 90, 106585. doi:10.1016/j.nanoen.2021.106585

Liu, Z., Nie, J., Miao, B., Li, J., Cui, Y., Wang, S., et al. (2019). Self-Powered Intracellular Drug Delivery by a Biomechanical Energy-Driven Triboelectric Nanogenerator. *Adv. Mat.* 31, 1807795. doi:10.1002/adma.201807795

Macfelda, K., Kapeller, B., Holly, A., Podesser, B. K., Losert, U., Brandes, K., et al. (2017). Bioelectrical Signals Improve Cardiac Function and Modify Gene Expression of Extracellular Matrix Components. *Esc. Heart Fail.* 4, 291–300. doi:10.1002/ehf2.12169

Qin, H., Cheng, G., Zi, Y., Gu, G., Zhang, B., Shang, W., et al. (2018). High Energy Storage Efficiency Triboelectric Nanogenerators with Unidirectional Switches and Passive Power Management Circuits. *Adv. Funct. Mat.* 28, 1805216. doi:10.1002/adfm.201805216

Qin, H., Gu, G., Shang, W., Luo, H., Zhang, W., Cui, P., et al. (2020). A Universal and Passive Power Management Circuit with High Efficiency for Pulsed Triboelectric Nanogenerator. *Nano Energy* 68, 104372. doi:10.1016/j.nanoen.2019.104372

Shang, W., Gu, G., Zhang, W., Luo, H., Wang, T., Zhang, B., et al. (2021). Rotational Pulsed Triboelectric Nanogenerators Integrated with Synchronously Triggered Mechanical Switches for High Efficiency Self-Powered Systems. *Nano Energy* 82, 105725. doi:10.1016/j.nanoen.2020.105725

Su, Y., Xie, G., Tai, H., Li, S., Yang, B., Wang, S., et al. (2018). Self-powered Room Temperature NO2 Detection Driven by Triboelectric Nanogenerator under UV Illumination. *Nano Energy* 47, 316–324. doi:10.1016/j.nanoen.2018.02.031

Sung, H., Ferlay, J., Siegel, R. L., Laversanne, M., Soerjomataram, I., Jemal, A., et al. (2021). Global Cancer Statistics 2020: GLOBOCAN Estimates of Incidence and Mortality Worldwide for 36 Cancers in 185 Countries. *CA A Cancer J. Clin.* 71, 209–249. doi:10.3322/caac.21660

Wang, H., Pastorin, G., and Lee, C. (2016). Toward Self-Powered Wearable Adhesive Skin Patch with Bendable Microneedle Array for Transdermal Drug Delivery. *Adv. Sci.* 3, 1500441. doi:10.1002/advs.201500441

Wang, M., Zhang, J., Tang, Y., Li, J., Zhang, B., Liang, E., et al. (2018). Air-Flow-Driven Triboelectric Nanogenerators for Self-Powered Real-Time Respiratory Monitoring. *ACS Nano* 12, 6156–6162. doi:10.1021/acsnano.8b02562

Wang, S., Xie, Y., Niu, S., Lin, L., Liu, C., Zhou, Y. S., et al. (2014). Maximum Surface Charge Density for Triboelectric Nanogenerators Achieved by Ionized-Air Injection: Methodology and Theoretical Understanding. *Adv. Mat.* 26, 6720–6728. doi:10.1002/adma.201402491

Wang, T., Gu, G., Shang, W., Gan, J., Zhang, W., Luo, H., et al. (2021). A Self-Powered Photodetector Using a Pulsed Triboelectric Nanogenerator for Actual Working Environments with Random Mechanical Stimuli. *Nano Energy* 90, 106518. doi:10.1016/j.nanoen.2021.106518

Wang, Z., Cheng, L., Zheng, Y., Qin, Y., and Wang, Z. L. (2014). Enhancing the Performance of Triboelectric Nanogenerator through Prior-Charge Injection and its Application on Self-Powered Anticorrosion. *Nano Energy* 10, 37–43. doi:10.1016/j.nanoen.2014.08.017

Wang, Z. L. (2017). On Maxwell's Displacement Current for Energy and Sensors: the Origin of Nanogenerators. *Mater. Today* 20, 74–82. doi:10.1016/j.mattod.2016.12.001

Wang, Z. L. (2013). Triboelectric Nanogenerators as New Energy Technology for Self-Powered Systems and as Active Mechanical and Chemical Sensors. *ACS Nano* 7, 9533–9557. doi:10.1021/nn404614z

Weaver, C. L., LaRosa, J. M., Luo, X., and Cui, X. T. (2014). Electrically Controlled Drug Delivery from Graphene Oxide Nanocomposite Films. *ACS Nano* 8, 1834–1843. doi:10.1021/nn406223e

Yuan, M., Li, X., Liu, J., Zheng, Y., Cheng, L., Tang, N., et al. (2021). Fully Integrated Self-Powered Electrical Stimulation Cell Culture Dish for Noncontact High-Efficiency Plasmid Transfection. *ACS Appl. Mat. Interfaces* 13, 54762–54769. doi:10.1021/acsami.1c16748

Zhang, C., Chen, J., Xuan, W., Huang, S., Shi, L., Cao, Z., et al. (2022). Triboelectric Nanogenerator-Enabled Fully Self-Powered Instantaneous Wireless Sensor Systems. *Nano Energy* 92, 106770. doi:10.1016/j.nanoen.2021.106770

Zhang, L., Cheng, L., Bai, S., Su, C., Chen, X., and Qin, Y. (2015). Controllable Fabrication of Ultrafine Oblique Organic Nanowire Arrays and Their Application in Energy Harvesting. *Nanoscale* 7, 1285–1289. doi:10.1039/c4nr06237j

Zhang, R., Hao, M., Bai, S., Song, P., Jia, X., Gao, W., et al. (2022). Multichannel Driving Triboelectric Nanogenerator for Enhancing the Output Charge Density. *Nano Energy* 98, 107272. doi:10.1016/j.nanoen.2022.107272

Zhang, W., Gu, G., Qin, H., Li, S., Shang, W., Wang, T., et al. (2020). Measuring the Actual Voltage of a Triboelectric Nanogenerator Using the Non-grounded Method. *Nano Energy* 77, 105108. doi:10.1016/j.nanoen.2020.105108

Zhang, W., Gu, G., Shang, W., Luo, H., Wang, T., Zhang, B., et al. (2021). A General Charge Compensation Strategy for Calibrating the Voltage of a Triboelectric

Nanogenerator Measured by a Capacitive Circuit. *Nano Energy* 86, 106056. doi:10.1016/j.nanoen.2021.106056

Zhang, Y., Gao, X., Wu, Y., Gui, J., Guo, S., Zheng, H., et al. (2021). Self-powered Technology Based on Nanogenerators for Biomedical Applications. *Exploration* 1, 90–114. doi:10.1002/EXP.20210152

Zhang, Z., Qiu, S., Zhang, X., and Chen, W. (2018). Optimized DNA Electroporation for Primary Human T Cell Engineering. *BMC Biotechnol.* 18, 4. doi:10.1186/s12896-018-0419-0

Zhao, C., Feng, H., Zhang, L., Li, Z., Zou, Y., Tan, P., et al. (2019). Highly Efficient *In Vivo* Cancer Therapy by an Implantable Magnet Triboelectric Nanogenerator. *Adv. Funct. Mat.* 29, 1808640. doi:10.1002/adfm.201808640

Zhao, K., Gu, G., Zhang, Y., Zhang, B., Yang, F., Zhao, L., et al. (2018). The Self-Powered CO2 Gas Sensor Based on Gas Discharge Induced by Triboelectric Nanogenerator. *Nano Energy* 53, 898–905. doi:10.1016/j.nanoen.2018.09.057

Zheng, Q., Zhang, H., Shi, B., Xue, X., Liu, Z., Jin, Y., et al. (2016). *In Vivo* Self-Powered Wireless Cardiac Monitoring via Implantable Triboelectric Nanogenerator. *ACS Nano* 10, 6510–6518. doi:10.1021/acsnano.6b02693

Zheng, Y., Cheng, L., Yuan, M., Wang, Z., Zhang, L., Qin, Y., et al. (2014). An Electrospun Nanowire-Based Triboelectric Nanogenerator and its Application in a Fully Self-Powered UV Detector. *Nanoscale* 6, 7842–7846. doi:10.1039/c4nr01934b

Zheng, Y., Ma, S., Benassi, E., Feng, Y., Xu, S., Luo, N., et al. (2022). Surface Engineering and On-Site Charge Neutralization for the Regulation of Contact Electrification. *Nano Energy* 91, 106687. doi:10.1016/j.nanoen.2021.106687

Zhong, L., Li, Y., Xiong, L., Wang, W., Wu, M., Yuan, T., et al. (2021). Small Molecules in Targeted Cancer Therapy: Advances, Challenges, and Future Perspectives. *Sig Transduct. Target Ther.* 6, 1–48. doi:10.1038/s41392-021-00572-w

Conflict of Interest: The authors declare that the research was conducted in the absence of any commercial or financial relationships that could be construed as a potential conflict of interest.

Publisher's Note: All claims expressed in this article are solely those of the authors and do not necessarily represent those of their affiliated organizations or those of the publisher, the editors, and the reviewers. Any product that may be evaluated in this article, or claim that may be made by its manufacturer, is not guaranteed or endorsed by the publisher.

frontiers | Frontiers in Bioengineering and Biotechnology

ORIGINAL RESEARCH
published: 08 July 2022
doi: 10.3389/fbioe.2022.940511

Visualization of Zika Virus Infection via a Light-Initiated Bio-Orthogonal Cycloaddition Labeling Strategy

Judun Zheng[1†], Rui Yue[1†], Ronghua Yang[2†], Qikang Wu[3,4†], Yunxia Wu[3,4], Mingxing Huang[5], Xu Chen[5], Weiqiang Lin[1], Jialin Huang[1], Xiaodong Chen[3,4], Yideng Jiang[6]*, Bin Yang[1]* and Yuhui Liao[1,5,6]**

[1]Molecular Diagnosis and Treatment Center for Infectious Diseases, Dermatology Hospital, Southern Medical University, Guangzhou, China, [2]Department of Burn and Plastic Surgery, Guangzhou First People's Hospital, South China University of Technology, Guangzhou, China, [3]Department of Clinical Laboratory, The First People's Hospital of Foshan, Foshan, China, [4]Department of Burn Surgery & Department of Rheumatology, The First People's Hospital of Foshan, Foshan, China, [5]Department of Infectious Disease, the Fifth Affiliated Hospital, Sun Yat-sen University, Zhuhai, China, [6]NHC Key Laboratory of Metabolic Cardiovascular Diseases Research, Ningxia Key Laboratory of Vascular Injury and Repair Research, Ningxia Medical University, Yinchuan, China

Zika virus (ZIKV) is a re-emerging flavivirus that leads to devastating consequences for fetal development. It is crucial to visualize the pathogenicity activities of ZIKV ranging from infection pathways to immunity processes, but the accurate labeling of ZIKV remains challenging due to the lack of a reliable labeling technique. We introduce the photo-activated bio-orthogonal cycloaddition to construct a fluorogenic probe for the labeling and visualizing of ZIKV. Via a simple UV photoirradiation, the fluorogenic probes could be effectively labeled on the ZIKV. We demonstrated that it can be used for investigating the interaction between ZIKV and diverse cells and avoiding the autofluorescence phenomenon in traditional immunofluorescence assay. Thus, this bioorthogonal-enabled labeling strategy can serve as a promising approach to monitor and understand the interaction between the ZIKV and host cells.

Keywords: Zika virus, quantum dots (DQs), light-initiated cycloaddition, fluorescent probe, phenanthrenequinone

OPEN ACCESS

Edited by:
Qitong Huang,
Gannan Medical University, China

Reviewed by:
Liewei Wen,
Jinan University, China
Zhixiong Wang,
National Institutes of Health (NIH), United States
Xiaofeng Lin,
Gannan Medical University, China

****Correspondence:***
Xiaodong Chen
cxd234@163.com
Yideng Jiang
jwcjyd@163.com
Bin Yang
yangbin1@smu.edu.cn
Yuhui Liao
liaoyh8@mail.sysu.edu.cn

†These authors have contributed equally to this work

Specialty section:
This article was submitted to Nanobiotechnology, a section of the journal Frontiers in Bioengineering and Biotechnology

Received: *10 May 2022*
Accepted: *30 May 2022*
Published: *08 July 2022*

Citation:
Zheng J, Yue R, Yang R, Wu Q, Wu Y, Huang M, Chen X, Lin W, Huang J, Chen X, Jiang Y, Yang B and Liao Y (2022) Visualization of Zika Virus Infection via a Light-Initiated Bio-Orthogonal Cycloaddition Labeling Strategy. Front. Bioeng. Biotechnol. 10:940511. doi: 10.3389/fbioe.2022.940511

1 INTRODUCTION

The mosquito-transmitted Zika virus (ZIKV), which belongs to the family Flaviviridae and genus flavivirus, can cause several Zika syndrome including ventriculomegaly and microcephaly (Miner and Diamond, 2017). Recent outbreaks of ZIKV have been reported in more than 30 countries or territories, emerging as a major threat to global health (Sampathkumar and Sanchez, 2016; Hills et al., 2017; Mengesha Tsegaye et al., 2018). The current diagnostic techniques available for ZIKV rely on the reverse transcriptase-polymerase chain reaction assay or ZIKV-specific IgM antibody testing, which play an important role in preventing the spread of disease (Ergünay et al., 2010; Barreiro, 2016; Kikuti et al., 2018; Low et al., 2021). The exploration of cellular signaling pathways on ZIKV infection has also attracted considerable research attention, greatly enriching the study of mechanisms of infection of RNA viruses (Grant et al., 2016; Chen et al., 2018; Chiramel and Best, 2018; Garcia et al., 2020). Among these, visualization of the Zika virus-host cell interactions is essential to comprehend the molecular mechanisms and pathogenesis of ZIKV disease.

Fluorescent dyes have been widely used in viral labeling and real-time imaging, which improve our understanding of the viral infection process (Zheng et al., 2019; Liao et al., 2020; Zhang et al.,

2020). Thus, the photobleaching and spectral overlaps of fluorophores are inescapable, greatly affecting the efficacy of fluorophores, greatly affecting the efficacy of tracking dye-labeled viruses, and limiting the application in bioimaging. Fluorescent quantum dots (QDs) can be rationally chosen as an alternative candidate because they have distinguishing optical properties including narrow-band and tunable fluorescence emission, high fluorescence quantum yields, and photostability (Matea et al., 2017; Pleskova et al., 2018). Currently, numerous efforts have been devoted to constructing the QDs–virus imaging modality and demonstrating its capabilities in providing meaningful information (You et al., 2006; Zhang et al., 2012; Ribeiro et al., 2019; Kuang et al., 2020; Chen et al., 2021; Chung and Zhang, 2021; Lin et al., 2021; He et al., 2022; Yi et al., 2022). It is crucial to reveal the real virus–host cell interaction transversion by maintaining viral infiltration after riveting the virus on QDs (Cui et al., 2011; Liu et al., 2012; Hong et al., 2015; Ma et al., 2017). However, riveting virus on QDs via the unmild and uncontrollable physical-chemical process remains challenging.

To address this, we rationally designed a novel strategy with the photo-click cycloaddition-based QDs to tag and track the ZIKV (Scheme1). The light-initiated bio-orthogonal photo-click reaction has been widely applied in numerous biolabeling and bioimaging, enabling visualization of specific biomolecules with precise spatiotemporal control in their native environment (Lim and Lin, 2011; Huang et al., 2013; Herner and Lin, 2016). With this strategy, ZIKV was successfully tracked and visualized after cell entry in different cell lines, such as A549 and SNB19. Moreover, the ZIKV-QDs can map the ZIKV–host cell interactions under chlorpromazine hydrochloride (CPZ)- or nocodazole-treated conditions. This strategy would provide a reliable toolbox to elucidate the virus–host cell interactions and develop potential rapid diagnosis and therapeutic approaches.

2 EXPERIMENTAL SECTION

2.1 Materials and Reagents

Syto13 was obtained from Sigma. Amino-labeled QDs were obtained from Wuhan Jiayuan Quantum Dots Co., Ltd (Wuhan, China). The cell counting kit-8 (CCK-8) was obtained from Dojindo Laboratories (Kumamoto, Japan). 1-ethyl-3-(3-dimethylaminopropyl) carbodiimide (EDCI), N-hydroxysuccinimid esters (NHS), and N,N-4-dimethylaminopyridine (DMAP) were purchased from Energy Chemical (Shanghai, China).

2.2 Cell Lines

A549 cell and SNB19 cell were purchased from ATCC. The cells were cultured in Dulbecco's modified Eagle medium (DMEM) (Gibco, Ltd., Grand Island, NY, USA). The media were supplemented with 10% FBS (Gibco), 50 U mL^{-1} penicillin, and 50 μg ml^{-1} streptomycin. The cells were maintained in a humidified 37°C incubator in 5% CO_2.

2.3 Modification of Zika Virus

9,10-phenanthrenequinone (PQ, 11 mg, $4.17*10^{-5}$ mol) was dispersed into 10 ml MES buffer, EDC (80 mg, $4.17*10^{-4}$ mol) and NHS (120 mg, $4.17*10^{-4}$ mol) were added, and then ultrasonic was applied for 15 s, the sealing film was sealed, and then it was shaken at 37°C for 15 min. Then, 100 μl of Zika virus (concentration is 2 mg/ml) was dispersed in 10 ml PBS. The liquid was added to the aforementioned MES buffer, shaken at 37°C overnight, and then purified by a NAP-5 desalting column to obtain Zika virus modified with the PQ group.

2.4 Modification of Quantum Dots

Take 1 μl of quantum dots (QDs) with the carboxyl group (molar concentration is $8*10^{-6}$), vinyl ether (VE) 1,000 μl, EDCI 15.3 mg, DAMP 9.8 mg, and put them into a 3-neck flask, respectively, then add 5 ml of dichloromethane to completely dissolve. Then, shake for 2 h at room temperature in a dark environment. Then, go through silica gel column chromatography to obtain quantum dots modified with vinyl ether group.

2.5 The Click Reaction of Zika Virus and Quantum Dots

The Zika viruses and the quantum dots were first modified with the PQ group and vinyl ether group, respectively. After that, these modified ZIKV and QDs were dissolved in a PBS solution and then irradiated with the LED lamp for 1 min to obtain the Zika virus modified with the quantum dots (ZIKV-QDs).

2.6 ZIKV-QD Internalization Assays

ZIKV-QDs and viral nucleic acid dye Syto13 were mixed and incubated for 1 h and then ultracentrifuged at 10,000 g for 0.5 h to remove the remaining dye. Then mixed with Vero or cells and shook 5 times with an interval of 15 min and then incubated in 5% carbon dioxide at 37°C for 24 h. Then, the cells were fixed with 4% paraformaldehyde, and the fluorescence imaging was observed under the confocal laser scanning microscope (CLSM).

2.7 Cell Culture and Cytotoxicity Evaluation *In Vitro*

SNB19 cells were cultured in DMEM containing 10% fetal bovine serum and 1% penicillin/streptomycin at 37°C in a humidified 5% CO_2 atmosphere. Cell density was determined using a hemocytometer before experimentation. Relative cell viabilities were determined by the standard CCK-8 assay. SNB19 cells were seeded into 96-well plates (10^4 cells per well). After cells were cultured for 12 h, they were added to a fresh culture medium and excited with a LED lamp (0.5 W/cm^2) at different times. After incubation at 37°C for 12 h, those cells were added containing 10% CCK-8 DMEM (100 μl). After incubation for 2 h at 37°C, OD_{450}, the absorbance value at 450 nm, was measured with a microplate reader to determine the cell viability.

2.8 Confocal Laser Scanning Microscope

The aforementioned fluorescent dye particles were photographed with a confocal laser scanning microscope (LSM880). The excitation wavelength of the quantum dots is 561 nm, and the emission wavelength is 605 nm. The excitation wavelength of Syto13 is 488 nm, and the emission wavelength is 509 nm.

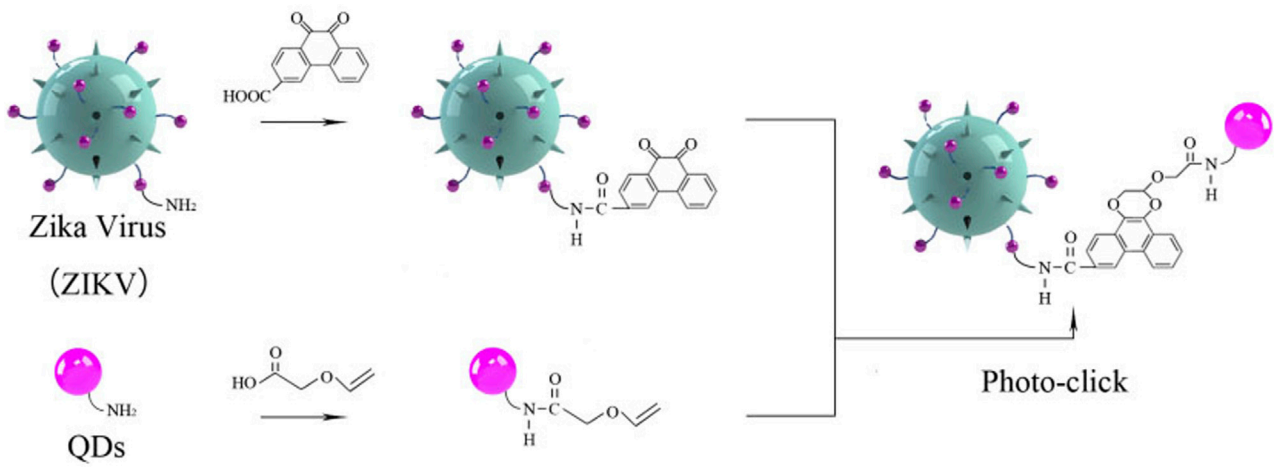

SCHEME 1 | Schematic illustration of Zika virus labeling and imaging via light-initiated photo-click cycloaddition.

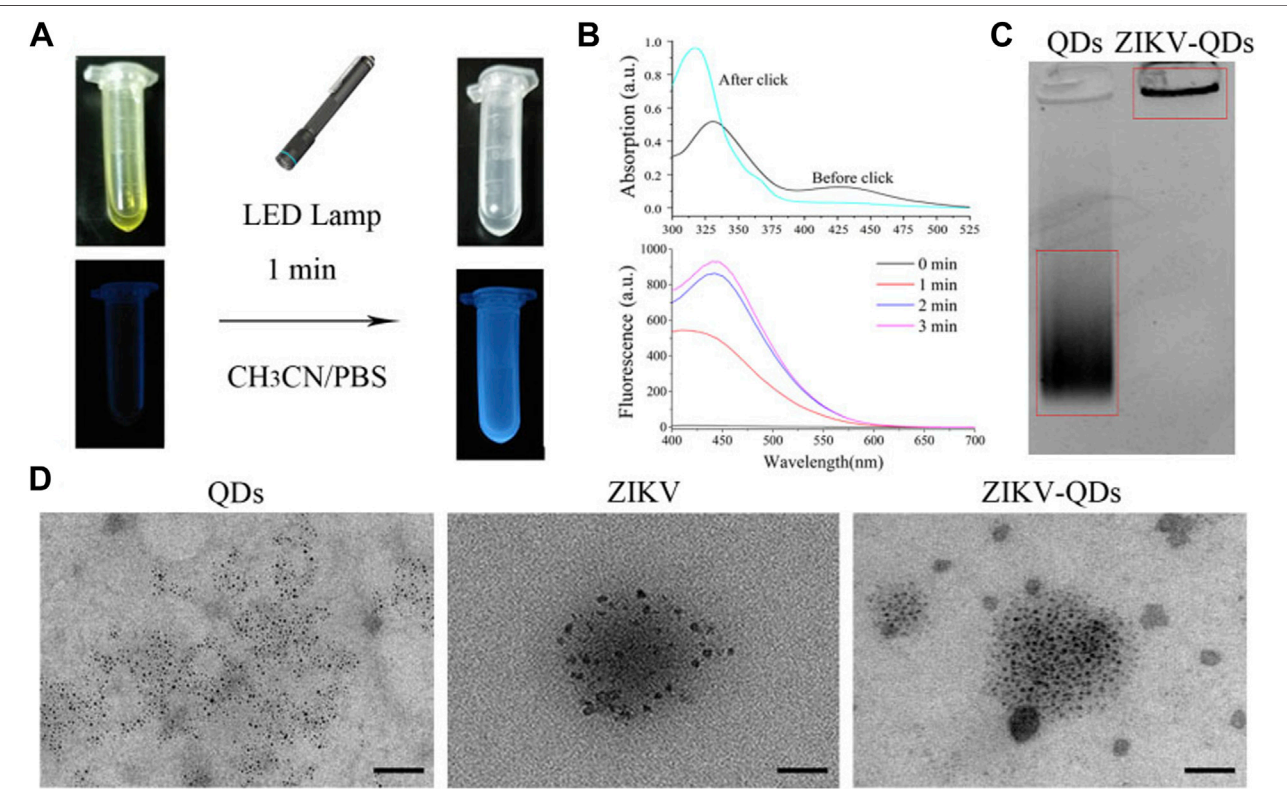

FIGURE 1 | Characterizations of Zika virus labeling and imaging via light-initiated bio-orthogonal photo-click cycloaddition. **(A)** Images of ZIKV and QD solution without (left) or with (right) the irradiation of the LED lamp. **(B)** Absorbance and fluorescence changes of ZIKV and QDs in CH3CN/PBS solution upon irradiation treatment. **(C)** Polyacrylamide gel electrophoresis analysis of QDs and ZIKV-QDs. **(D)** Transmission electron microscopy (TEM) of QDs, ZIKV, and ZIKV-QDs.

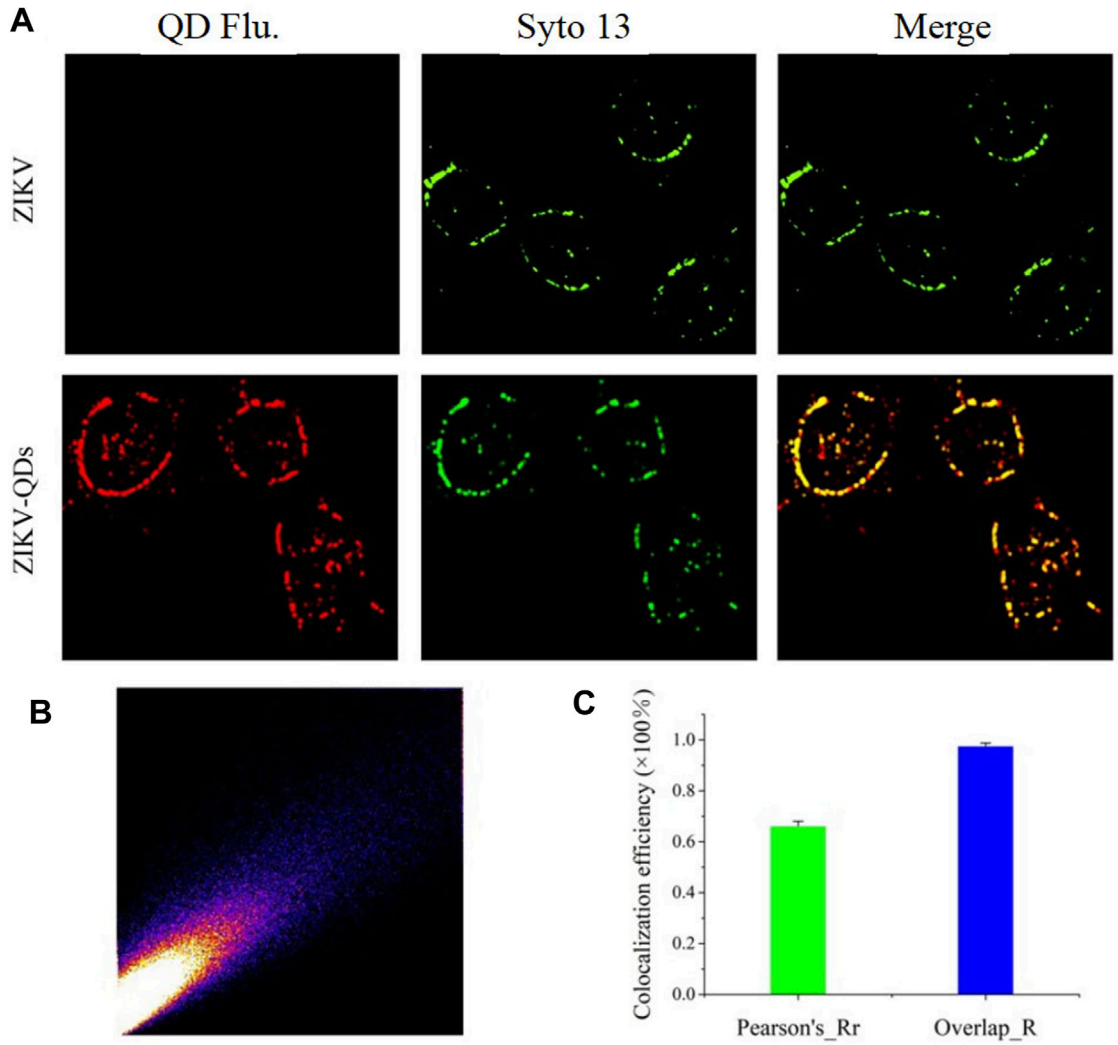

FIGURE 2 | (A) Confocal microscopic images of ZIKV nucleic acid colocalized with the commercially available organelle trackers Syto13 in SNB19 cells (Flu is the abbreviation for fluorescence). **(B)** Colocalization scatterplots of **(A)**. **(C)** Corresponding Pearson correlation coefficient of **(A)**.

3 RESULTS AND DISCUSSION

3.1 Feasibility and Characterizations of QD-Modified Zika Virus

Photo-click reaction has been developed as an alternative strategy for spatiotemporally labeling and imaging (Lim and Lin, 2011; Li et al., 2018). Among them, 9,10-phenanthrenequinone (PQ) and electron-rich vinyl ether were widely chosen as photo-click substrates (**Supplementary Figure S1, S2**). As previous reports revealed that the ZIKV could be chemically labeled with the chemical proteomics strategies owning to the ZIKV surface E proteins to understand the early-stage entry of ZIKV into host cells (Srivastava et al., 2020; King and Irigoyen, 2021). To prepare a fluorescent tracking method, PQ and vinyl ether were functionalized in the ZIKV and QDs, respectively. Then, the ZIKV was labeled with fluorescent QDs via the cyclization under the irradiation (**Scheme 1**). As shown in **Figure 1A**, the primary absorbance peak of the as-prepared 9,10-phenanthrenequinone exhibited a significant blue shift that goes from 330 to 310 nm (**Supplementary Figure S3**), and the absorbance band at 425 nm disappeared along with the irradiation of LED lamp, which was in accordance with the 9,10-phenanthrenequinone analog reported by Zhang group (Li et al., 2018).

Accordingly, the fluorescence intensity of PQ reacted with electron-rich vinyl ether at 450 nm was found to be greatly increased upon increasing irradiation time or concentration (**Supplementary Figure S4**), resulting in the photo-click reaction between PQ and electron-rich vinyl ether (Coelho et al., 2017). Meanwhile, the color of their mixed solution changed from yellow to colorless, and the blue light can be found, which was consistent with the antecedent results of absorbance and fluorescence (**Figure 1B**). In addition, the polyacrylamide gel electrophoresis analysis was chosen to validate whether the QDs were labeled on

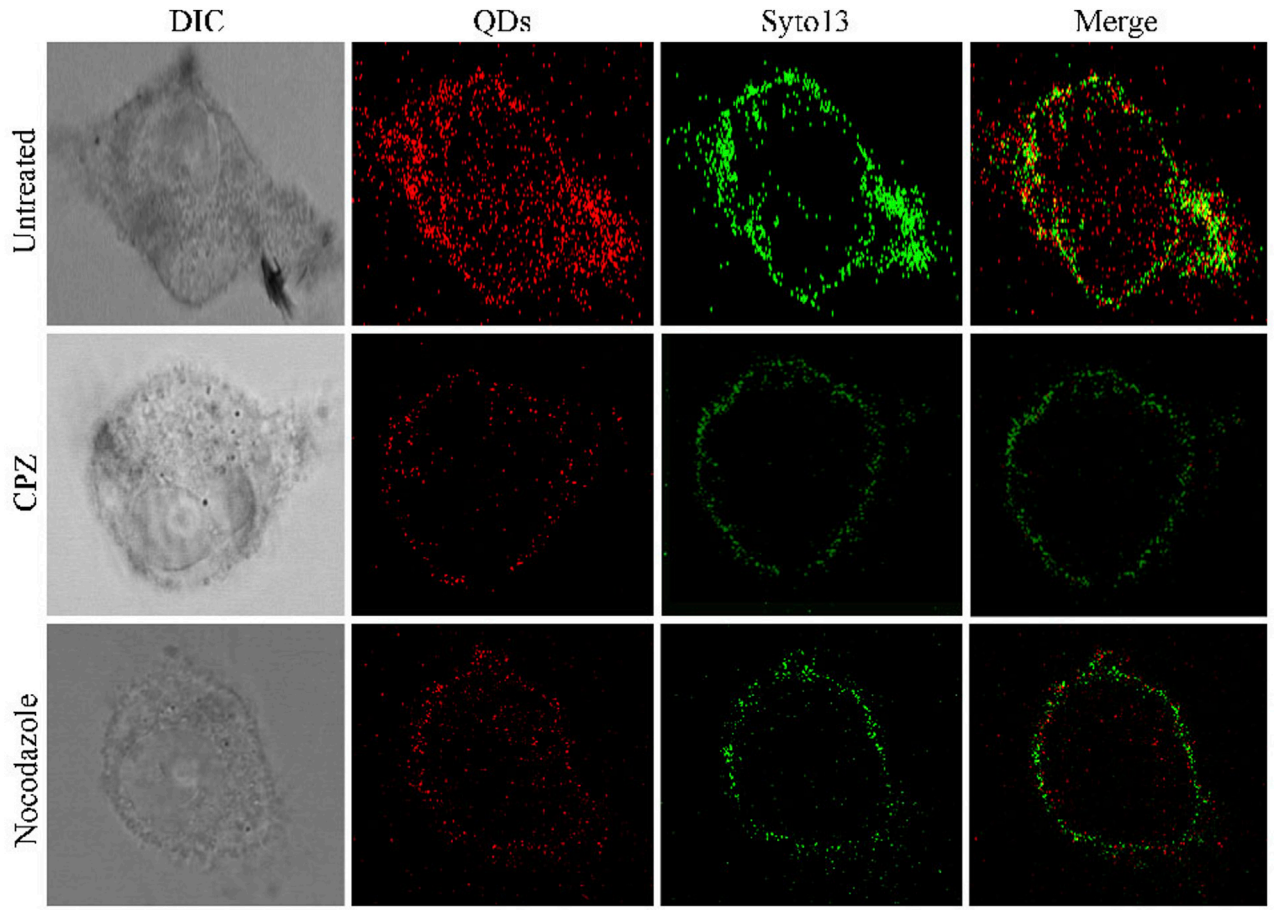

FIGURE 3 | Confocal microscopic images of ZIKV nucleic acid colocalized with the commercially available organelle trackers Syto13 in SNB19 cells treated with different drugs including chlorpromazine and nocodazole.

the ZIKV. As shown in **Figure 1C**, ZIKV-QDs held the original position compared to the QDs, which contributed to the macromolecular proteins of viruses conjugated with QDs by photo-click cycloaddition reaction. On the other hand, transmission electron microscopy (TEM) of ZIKV-QDs shows the typical ZIKV pattern functionalized with QDs, intuitively verifying that the QDs have been successfully decorated in the ZIKV (**Figure 1D**). Taken together, the photo-click cyclization between PQ and vinyl ether can be applied to label the ZIKV with QDs.

3.2 Quantitative Evaluation of QD-Modified Zika Virus

It is crucial to obtain high-purity viruses in various fields, ranging from virus pathogenesis to structure decomposition and vaccine development. Herein, the ZIKV particles were purified using a discontinuous sucrose gradient (Petruska et al., 2002), and all fractions were titrated by plaque assay. We observed the presence of ZIKV in all fractions, and the purified fraction has high titers above 10^8 PFU/ml (**Supplementary Figure S5**). In addition, a high RNA level was obtained at a sucrose concentration of 20%, resulting in 5.0 $\times$ 10^{10} RNA copies/ml (**Supplementary Figure S6**). To characterize the modification of QDs on ZIKV, we analyzed the particle sizes of ZIKV and ZIKV-QDs using the NanoSight NS300 equipment. As shown in **Supplementary Figures S7 and S8**, the average size increased from 108.9 ± 8.2 nm to 119.3 ± 11.5 nm, indicating that the QDs were successfully modified on ZIKV. Furthermore, the zeta potential data showed that the complex of ZIKV-QDs has a higher negative potential (−15.47 mV) than that of the individual QDs (−8.14 mV) and ZIKV (−12.03 mV) (**Supplementary Figure S9**). This result also indicated the successful modification of QDs on ZIKV through the amido bond between the carboxyl group and amino group. Additionally, no significant difference between the ZIKV and ZIKV-QDs viral titers was observed (**Supplementary Figure S10**), suggesting that the labeling process does not affect the infiltration performance.

3.3 Evaluation of Infiltration Capability With QD-Modified Zika Virus

Next, we evaluated its infiltration capability using the QD-modified ZIKV. In comparison absence of evidence for ZIKV infection in cells, we thus applied QD-modified ZIKV in mapping the infection process. The fluorescence imaging of A549 cells

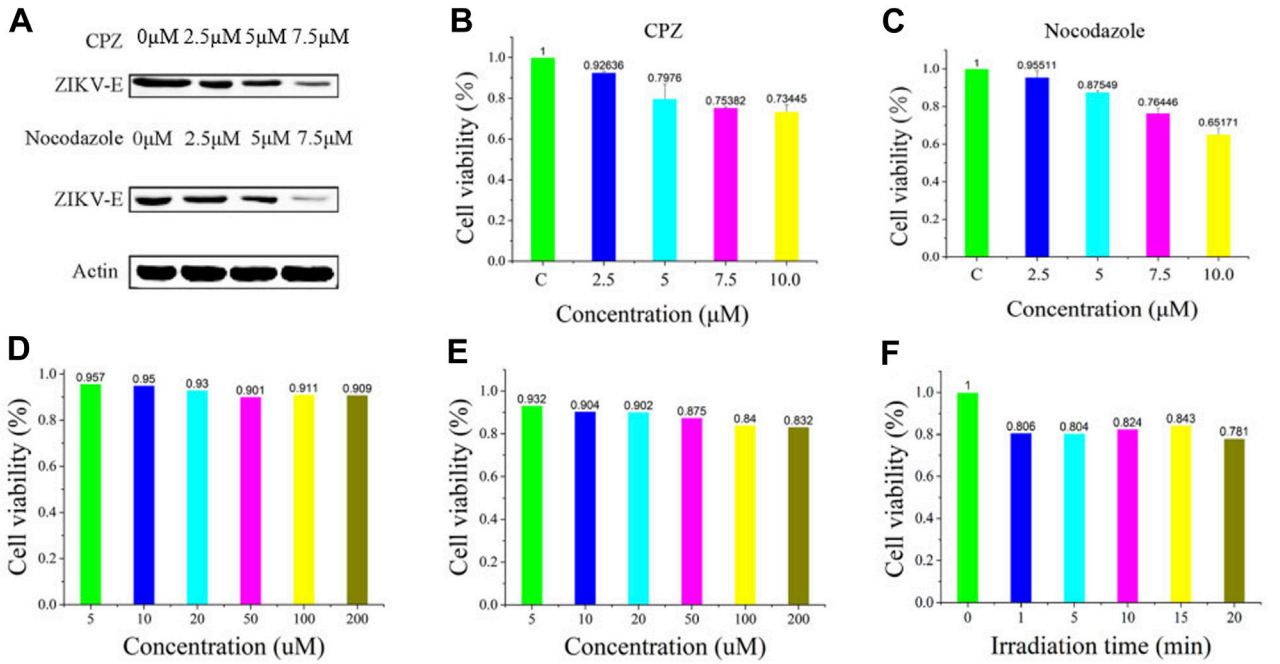

FIGURE 4 | (A) Levels of β-actin and ZIKV envelope protein E (ZIKV E) of SNB19 cells treated with CPZ or nocodazole. Cytotoxicity studies of **(B)** CPZ and **(C)** nocodazole. Cytotoxicity studies of **(D)** PQ and **(E)** VE, or **(F)** irradiation time.

incubated with ZIKV-QDs in the red channel was found to be much brighter compared to the ZIKV group without QDs, and no significant difference in the green emission of Syto13 dye was observed under both conditions (**Supplementary Figure S11A**). As expected, the fluorescence image of QDs overlaps well with that of a commercially available fluorescent dye of the nucleic acid tracking dye Syto13. Also, the corresponding Mander's overlap coefficient, a well-established colocation parameter, was performed as 0.94 for the ZIKV-QDs group (**Supplementary Figure S11B, S11C**). In order to confirm that the QDs were labeled on the ZIKV, ZIKV-QDs were first incubated with the nucleic acid dye Syto13. After that, Syto13-pretreated ZIKV-QDs mixed with cells and subsequently observed interaction behavior between ZIKV and host cell under the confocal laser scanning microscope. To verify the wide application of Syto13-pretreated ZIKV-QDs targeted tracing performance, we also obtained significant fluorescence colocalization experiments on the SNB19 cancer cell line via confocal fluorescence microscopy (**Figure 2A**). The Pearson correlation coefficient had been drawn via the confocal image (**Figure 2B**), and the corresponding Mander's overlap coefficient had also been calculated to be 0.97 (**Figure 2C**). These bioimaging results demonstrated that the ZIKV labeled with QDs could localize and trace the functions in virus infection procedures.

3.4 Evaluation of Drug Efficacy Through the QD-Modified Zika Virus

Furthermore, we demonstrated its applicability for assessing the efficacy of ZIKV-related treatments. Here, we introduced two typical kinds of antivirus drugs including CPZ and nocodazole, which could specifically inhibit clathrin-dependent endocytosis and formation of the microtubule, respectively (Xia and Liang, 2019; Sathyamoorthy et al., 2020). The cellular fluorescence intensity of QDs in the group treated with CPZ decreased compared to the control group (**Figure 3**). This was attributed to the less ZIKV crossing the monolayer of the barrier of Vero cells. In addition, the treatment of nocodazole also obviously abated the entry and infection of ZIKV at 2 h post-inoculation, providing direct evidence that the microtubule polymerization is required for intracellular trafficking of the ZIKV. These results prompt us to use the fluorescent nanoprobe QDs to trace the process of ZIKV infection and evaluate the treatment efficacy with the independent fluorescent signals.

To further validate the infiltration activity of the QD-labeled ZIKV, we chose the level of nascent protein synthesis to evaluate the ZIKV infection after being treated with CPZ or nocodazole. ZIKV envelope protein E (ZIKV E) is the major structural protein exposed on the cell surface of the particle, which is engaged in viral attachment, penetration, and membrane fusion. Thus, we chose the ZIKV E to study and evaluate the reason why hydrochloride and nocodazole could induce the infection of ZIKV. Western blot experiments indicate that ZIKV infection had a dramatic effect on the synthesis of ZIKV E (**Figure 4A**, top), similar to the case that cells infected with the translation inhibitor nocodazole (**Figure 4A**, bottom). At the same time, the CPZ and nocodazole exhibited some side effects (**Figures 4B, C**), which means these two drugs could not only inhibit the microtubule polymerization but also lead to the cellular apoptosis due to the disruption of intracellular trafficking (Liao et al., 2018). Furthermore, to test the biological application ability of pre-

QDs, the cytotoxicity of PQ and VE was tested with Vero cells. After incubation with different concentrations of PQ and VE, there was no significant change in SNB19 cells (**Figures 4D, E**). In order to evaluate the influence of light on cells, the effect of light was investigated by the standard CCK-8 assay. Following incubation of various times of light ranging from 0 to 5 min, the cellular viabilities were determined to exceed 80% (**Figure 4F**), indicating its low effect with the LED lamp laser. Taken together, these aforementioned findings indicated that ZIKV-QDs could accurately map and localize the ZIKV via monitoring the fluorescence of QDs under various conditions.

4 CONCLUSION

In this work, we developed a novel QD-based probe for reliable labeling and visualization of the Zika virus. This probe leverages photo-activated bio-orthogonal cycloaddition for high-efficient conjugation of ZIKV and QDs, exhibiting a simple labeling process and no influence on the infiltration performance. We verified that such a conjugation of ZIKV and QD probe can localize and trace the functions in the virus infection procedure. Moreover, the infiltration activity of the QD-labeled ZIKV is validated using the anti-ZIKV drugs including CPZ or nocodazole by monitoring the level of nascent protein synthesis. These findings suggest that the proposed QD probe could accurately map and localize the ZIKV via monitoring the fluorescence. Thus, this bioorthogonal-enabled QD probe might be a promising approach for monitoring the pathogenicity activities of ZIKV.

DATA AVAILABILITY STATEMENT

The datasets presented in this study can be found in online repositories. The names of the repository/repositories and accession number(s) can be found in the article/**Supplementary Material**.

AUTHOR CONTRIBUTIONS

JZ and RY designed and performed the experiment. RHY, QW, and YW were responsible for data collation and drafting the manuscript. MH, XC, and JH contributed to synthetic designs. WL, CX, and YJ, BY edited and revised the manuscript draft. JZ and YL were responsible for providing funds and unified management of work. All authors read and approved the final manuscript.

FUNDING

This work was supported by the National Natural Science Foundation of China (81972019, 21904145, 82002253, 81671970, 81772136, and 82102444), the Special Fund of Foshan Summit Plan (2020B019, 2020B012, 2020A015, 2019A006, 2019C002, and 2019D008), the Training Project of National Science Foundation for Outstanding/Excellent Young Scholars of Southern Medical University (C620PF0217), the China Postdoctoral Science Foundation (2020M682783 and 2021M693638), the Regional Joint Fund of Natural Science Foundation of Guangdong Province (2020A1515110529), the Guangdong Basic and Applied Basic Research Foundation (2020A1515010754), the Medical Research Fund of Guangdong Province (A2020322), Special Fund for Science and Technology Innovation Strategy of Guangdong Province (2020A1515011402), the Foundation of Foshan City (FS0AA-KJ218-1301-0034 and 2018AB003411), and the Young Scientists Project of the National Key Research and Development Program (2021YFC2302200).

SUPPLEMENTARY MATERIAL

The Supplementary Material for this article can be found online at: https://www.frontiersin.org/articles/10.3389/fbioe.2022.940511/full#supplementary-material

REFERENCES

Barreiro, P. (2016). Evolving RNA Virus Pandemics: HIV, HCV, Ebola, Dengue, Chikunguya, and Now Zika. *AIDS Rev.* 18 (1), 54–55.

Chen, J., Yang, Y.-f., Yang, Y., Zou, P., Chen, J., He, Y., et al. (2018). AXL Promotes Zika Virus Infection in Astrocytes by Antagonizing Type I Interferon Signalling. *Nat. Microbiol.* 3 (3), 302–309. doi:10.1038/s41564-017-0092-4

Chen, X., Zhu, J., Song, W., and Xiao, L.-P. (2021). Integrated Cascade Biorefinery Processes to Transform Woody Biomass into Phenolic Monomers and Carbon Quantum Dots. *Front. Bioeng. Biotechnol.* 9, 803138. doi:10.3389/fbioe.2021.803138

Chiramel, A. I., and Best, S. M. (2018). Role of Autophagy in Zika Virus Infection and Pathogenesis. *Virus Res.* 254, 34–40. doi:10.1016/j.virusres.2017.09.006

Chung, S., and Zhang, M. (2021). Microwave-Assisted Synthesis of Carbon Dot - Iron Oxide Nanoparticles for Fluorescence Imaging and Therapy. *Front. Bioeng. Biotechnol.* 9, 711534. doi:10.3389/fbioe.2021.711534

Coelho, S. V. A., Neris, R. L. S., Papa, M. P., Schnellrath, L. C., Meuren, L. M., Tschoeke, D. A., et al. (2017). Development of Standard Methods for Zika Virus Propagation, Titration, and Purification. *J. Virol. Methods* 246, 65–74. doi:10.1016/j.jviromet.2017.04.011

Cui, Z.-Q., Ren, Q., Wei, H.-P., Chen, Z., Deng, J.-Y., Zhang, Z.-P., et al. (2011). Quantum Dot-Aptamer Nanoprobes for Recognizing and Labeling Influenza A Virus Particles. *Nanoscale* 3 (6), 2454–2457. doi:10.1039/c1nr10218d

Ergünay, K., Saygan, M. B., Aydoğan, S., Litzba, N., Niedrig, M., Pınar, A., et al. (2010). Investigation of Dengue Virus and Yellow Fever Virus Seropositivities in Blood Donors from Central/Northern Anatolia, Turkey. *Mikrobiyol. Bul.* 44 (3), 415–424.

Garcia, G., Jr., Paul, S., Beshara, S., Ramanujan, V. K., Ramaiah, A., Nielsen-Saines, K., et al. (2020). Hippo Signaling Pathway Has a Critical Role in Zika Virus Replication and in the Pathogenesis of Neuroinflammation. *Am. J. Pathol.* 190 (4), 844–861. doi:10.1016/j.ajpath.2019.12.005

Grant, A., Ponia, S. S., Tripathi, S., Balasubramaniam, V., Miorin, L., Sourisseau, M., et al. (2016). Zika Virus Targets Human STAT2 to Inhibit Type I Interferon Signaling. *Cell Host Microbe* 19 (6), 882–890. doi:10.1016/j.chom.2016.05.009

He, C., Lin, X., Mei, Y., Luo, Y., Yang, M., Kuang, Y., et al. (2022). Recent Advances in Carbon Dots for *In Vitro*/Vivo Fluorescent Bioimaging: A Mini-Review. *Front. Chem.* 10, 905475. doi:10.3389/fchem.2022.905475

Herner, A., and Lin, Q. (2016). Photo-Triggered Click Chemistry for Biological Applications. *Top. Curr. Chem. (Z)* 374 (1), 77–107. doi:10.1007/s41061-015-0002-2

Hills, S. L., Fischer, M., and Petersen, L. R. (2017). Epidemiology of Zika Virus Infection. *J. Infect. Dis.* 216 (Suppl. l_10), S868–s874. doi:10.1093/infdis/jix434

Hong, Z.-Y., Lv, C., Liu, A.-A., Liu, S.-L., Sun, E.-Z., Zhang, Z.-L., et al. (2015). Clicking Hydrazine and Aldehyde: The Way to Labeling of Viruses with Quantum Dots. *ACS Nano* 9 (12), 11750–11760. doi:10.1021/acsnano.5b03256

Huang, L.-L., Lu, G.-H., Hao, J., Wang, H., Yin, D.-L., and Xie, H.-Y. (2013). Enveloped Virus Labeling via Both Intrinsic Biosynthesis and Metabolic Incorporation of Phospholipids in Host Cells. *Anal. Chem.* 85 (10), 5263–5270. doi:10.1021/ac4008144

Kikuti, M., Tauro, L. B., Moreira, P. S. S., Campos, G. S., Paploski, I. A. D., Weaver, S. C., et al. (2018). Diagnostic Performance of Commercial IgM and IgG Enzyme-Linked Immunoassays (ELISAs) for Diagnosis of Zika Virus Infection. *Virol. J.* 15 (1), 108. doi:10.1186/s12985-018-1015-6

King, E. L., and Irigoyen, N. (2021). Zika Virus and Neuropathogenesis: The Unanswered Question of Which Strain Is More Prone to Causing Microcephaly and Other Neurological Defects. *Front. Cell. Neurosci.* 15, 1–14. doi:10.3389/fncel.2021.695106

Kuang, Y., Zhang, J., Xiong, M., Zeng, W., Lin, X., Yi, X., et al. (2020). A Novel Nanosystem Realizing Curcumin Delivery Based on Fe3O4@Carbon Dots Nanocomposite for Alzheimer's Disease Therapy. *Front. Bioeng. Biotechnol.* 8, 614906–614916. doi:10.3389/fbioe.2020.614906

Li, J., Kong, H., Huang, L., Cheng, B., Qin, K., Zheng, M., et al. (2018). Visible Light-Initiated Bioorthogonal Photoclick Cycloaddition. *J. Am. Chem. Soc.* 140 (44), 14542–14546. doi:10.1021/jacs.8b08175

Liao, Y., Fan, Z., Deng, H., Yang, Y., Lin, J., Zhao, Z., et al. (2018). Zika Virus Liquid Biopsy: A Dendritic Ru(bpy)(3) (2+)-Polymer-Amplified ECL Diagnosis Strategy Using a Drop of Blood. *ACS Cent. Sci.* 4 (10), 1403–1411. doi:10.1021/acscentsci.8b00471

Liao, Y., Li, B., Zhao, Z., Fu, Y., Tan, Q., Li, X., et al. (2020). Targeted Theranostics for Tuberculosis: A Rifampicin-Loaded Aggregation-Induced Emission Carrier for Granulomas Tracking and Anti-infection. *ACS Nano* 14 (7), 8046–8058. doi:10.1021/acsnano.0c00586

Lim, R. K. V., and Lin, Q. (2011). Photoinducible Bioorthogonal Chemistry: a Spatiotemporally Controllable Tool to Visualize and Perturb Proteins in Live Cells. *Acc. Chem. Res.* 44 (9), 828–839. doi:10.1021/ar200021p

Lin, X., Xiong, M., Zhang, J., He, C., Ma, X., Zhang, H., et al. (2021). Carbon Dots Based on Natural Resources: Synthesis and Applications in Sensors. *Microchem. J.* 160, 105604. doi:10.1016/j.microc.2020.105604

Liu, S.-L., Zhang, Z.-L., Tian, Z.-Q., Zhao, H.-S., Liu, H., Sun, E.-Z., et al. (2012). Effectively and Efficiently Dissecting the Infection of Influenza Virus by Quantum-Dot-Based Single-Particle Tracking. *ACS Nano* 6 (1), 141–150. doi:10.1021/nn2031353

Low, S. L., Leo, Y. S., Lai, Y. L., Lam, S., Tan, H. H., Wong, J. C. C., et al. (2021). Evaluation of Eight Commercial Zika Virus IgM and IgG Serology Assays for Diagnostics and Research. *PLoS One* 16 (1), e0244601. doi:10.1371/journal.pone.0244601

Ma, Y., Wang, M., Li, W., Zhang, Z., Zhang, X., Tan, T., et al. (2017). Live Cell Imaging of Single Genomic Loci with Quantum Dot-Labeled TALEs. *Nat. Commun.* 8, 15318. doi:10.1038/ncomms15318

Matea, C., Mocan, T., Tabaran, F., Pop, T., Mosteanu, O., Puia, C., et al. (2017). Quantum Dots in Imaging, Drug Delivery and Sensor Applications. *Int. J. Nanomed.* 12, 5421–5431. doi:10.2147/ijn.S138624

Mengesha Tsegaye, M., Beyene, B., Ayele, W., Abebe, A., Tareke, I., Sall, A., et al. (2018). Sero-prevalence of Yellow Fever and Related Flavi Viruses in Ethiopia: a Public Health Perspective. *BMC Public Health* 18 (1), 1011. doi:10.1186/s12889-018-5726-9

Miner, J. J., and Diamond, M. S. (2017). Zika Virus Pathogenesis and Tissue Tropism. *Cell Host Microbe* 21 (2), 134–142. doi:10.1016/j.chom.2017.01.004

Petruska, J. M., Frank, D. W., Freeman, G. B., Evans, E. W., and MacDonald, J. S. (2002). Toxicity and Carcinogenicity Studies of Chlorpromazine Hydrochloride and P-Cresidine in the P53 Heterozygous Mouse Model. *Toxicol. Pathol.* 30 (6), 696–704. doi:10.1080/01926230290166788

Pleskova, S., Mikheeva, E., and Gornostaeva, E. (2018). Using of Quantum Dots in Biology and Medicine. *Adv. Exp. Med. Biol.* 1048, 323–334. doi:10.1007/978-3-319-72041-8_19

Ribeiro, J. F. F., Pereira, M. I. A., Assis, L. G., Cabral Filho, P. E., Santos, B. S., Pereira, G. A. L., et al. (2019). Quantum Dots-Based Fluoroimmunoassay for Anti-Zika Virus IgG Antibodies Detection. *J. Photochem. Photobiol. B Biol.* 194, 135–139. doi:10.1016/j.jphotobiol.2019.03.019

Sampathkumar, P., and Sanchez, J. L. (2016). Zika Virus in the Americas: A Review for Clinicians. *Mayo Clin. Proc.* 91 (4), 514–521. doi:10.1016/j.mayocp.2016.02.017

Sathyamoorthy, N., Chintamaneni, P. K., and Chinni, S. (2020). Plausible Role of Combination of Chlorpromazine Hydrochloride and Teicoplanin against COVID-19. *Med. Hypotheses* 144, 110011. doi:10.1016/j.mehy.2020.110011

Srivastava, M., Zhang, Y., Chen, J., Sirohi, D., Miller, A., Zhang, Y., et al. (2020). Chemical Proteomics Tracks Virus Entry and Uncovers NCAM1 as Zika Virus Receptor. *Nat. Commun.* 11 (1), 3896. doi:10.1038/s41467-020-17638-y

Xia, Y., and Liang, T. J. (2019). Development of Direct-Acting Antiviral and Host-Targeting Agents for Treatment of Hepatitis B Virus Infection. *Gastroenterology* 156 (2), 311–324. doi:10.1053/j.gastro.2018.07.057

Yi, X., Zeng, W., Wang, C., Chen, Y., Zheng, L., Zhu, X., et al. (2022). A Step-by-step Multiple Stimuli-Responsive Metal-Phenolic Network Prodrug Nanoparticles for Chemotherapy. *Nano Res.* 15, 1205–1212. doi:10.1007/s12274-021-3626-2

You, J.-O., Liu, Y.-S., Liu, Y.-C., Joo, K.-I., and Peng, C.-A. (2006). Incorporation of Quantum Dots on Virus in Polycationic Solution. *Int. J. Nanomed.* 1 (1), 59–64. doi:10.2147/nano.2006.1.1.59

Zhang, P., Liu, S., Gao, D., Hu, D., Gong, P., Sheng, Z., et al. (2012). Click-functionalized Compact Quantum Dots Protected by Multidentate-Imidazole Ligands: Conjugation-Ready Nanotags for Living-Virus Labeling and Imaging. *J. Am. Chem. Soc.* 134 (20), 8388–8391. doi:10.1021/ja302367s

Zhang, R., Zheng, J., and Zhang, T. (2020). *In Vivo* selective Imaging of Metabolic Glycosylation with a Tetrazine-Modified Upconversion Nanoprobe. *RSC Adv.* 10, 15990–15996. doi:10.1039/d0ra01832e

Zheng, J., Zeng, Q., Zhang, R., Xing, D., and Zhang, T. (2019). Dynamic-Reversible Photoacoustic Probe for Continuous Ratiometric Sensing and Imaging of Redox Status *In Vivo*. *J. Am. Chem. Soc.* 141 (49), 19226–19230. doi:10.1021/jacs.9b10353

Conflict of Interest: The authors declare that the research was conducted in the absence of any commercial or financial relationships that could be construed as a potential conflict of interest.

Publisher's Note: All claims expressed in this article are solely those of the authors and do not necessarily represent those of their affiliated organizations, or those of the publisher, the editors, and the reviewers. Any product that may be evaluated in this article, or claim that may be made by its manufacturer, is not guaranteed or endorsed by the publisher.

frontiers | Frontiers in Bioengineering and Biotechnology

MINI REVIEW
published: 15 July 2022
doi: 10.3389/fbioe.2022.952510

Recent Progresses in Electrochemical DNA Biosensors for SARS-CoV-2 Detection

Yanqiu Mei[1], Xiaofeng Lin[1,2], Chen He[2], Weijia Zeng[2], Yan Luo[2], Chenghao Liu[2], Zhehao Liu[1,2], Min Yang[1,2], Ying Kuang[1,2] and Qitong Huang[1,2]**

[1]Key Laboratory of Prevention and Treatment of Cardiovascular and Cerebrovascular Diseases, Ministry of Education, Key Laboratory of Biomaterials and Biofabrication in Tissue Engineering of Jiangxi Province, Key Laboratory of Biomedical Sensors of Ganzhou, School of Public Health and Health Management, School of Medical and Information Engineering, Gannan Medical University, Ganzhou, China, [2]Oil-Tea in Medical Health Care and Functional Product Development Engineering Research Center in Jiangxi, The Science Research Center, School of Pharmacy, Gannan Medical University, Ganzhou, China

Coronavirus disease 19 (COVID-19) is still a major public health concern in many nations today. COVID-19 transmission is now controlled mostly through early discovery, isolation, and therapy. Because of the severe acute respiratory syndrome coronavirus 2 (SARS-CoV-2) is the contributing factor to COVID-19, establishing timely, sensitive, accurate, simple, and budget detection technologies for the SARS-CoV-2 is urgent for epidemic prevention. Recently, several electrochemical DNA biosensors have been developed for the rapid monitoring and detection of SARS-CoV-2. This mini-review examines the latest improvements in the detection of SARS-COV-2 utilizing electrochemical DNA biosensors. Meanwhile, this mini-review summarizes the problems faced by the existing assays and puts an outlook on future trends in the development of new assays for SARS-CoV-2, to provide researchers with a borrowing role in the generation of different assays.

Keywords: COVID-19, SARS-CoV-2, electrochemical DNA biosensors, nucleic acid detection, virus/protein detection

OPEN ACCESS

Edited by:
Youbin Zheng,
Technion Israel Institute of Technology, Israel

Reviewed by:
Jia-Ming Liu,
Minnan Normal University, China
Boya Liu,
Boston Children's Hospital and Harvard Medical School, United States

***Correspondence:**
Xiaofeng Lin
Linxf@gmu.edu.cn
Qitong Huang
hqtblue@163.com

Specialty section:
This article was submitted to Nanobiotechnology, a section of the journal Frontiers in Bioengineering and Biotechnology

Received: *25 May 2022*
Accepted: *10 June 2022*
Published: *15 July 2022*

Citation:
Mei Y, Lin X, He C, Zeng W, Luo Y, Liu C, Liu Z, Yang M, Kuang Y and Huang Q (2022) Recent Progresses in Electrochemical DNA Biosensors for SARS-CoV-2 Detection. Front. Bioeng. Biotechnol. 10:952510. doi: 10.3389/fbioe.2022.952510

INTRODUCTION

The severe acute respiratory syndrome coronavirus 2 (SARS-CoV-2), a new member of the β-coronavirus genus, is closely related to SARS-CoV and is also the seventh coronavirus to infect humans (Akalin et al., 2020; Wiersinga et al., 2020; Zu et al., 2020), causing severe respiratory symptoms such as fever (37.3°C), cough and expectoration, nasal obstruction or even dyspnea in humans. A few people developed gastrointestinal symptoms (GI) (Jin et al., 2020a), such as nausea, vomiting, and diarrhea. Although the 2003 SARS-CoV, 2012 Middle East Respiratory Syndrome (MERS-COV), and the current epidemic of SARS-CoV-2 are all Human coronaviruse (HCoV) strains, SARS-CoV-2 is more infectious and pathogenic. At present, the main sources of infection of the disease include patients with COVID-19 patients, asymptomatic infections, and latent infections, which can be transmitted from person to person through droplets, contact, aerosols, and other transmission routes (Anderson et al., 2020; Kalbusch et al., 2020; Lin et al., 2020; Fu et al., 2021; Huang et al., 2021; Pan et al., 2021; Yip et al., 2021). It has been reported that one COVID-19 patient can transmit to three people at the same time (Qing et al., 2020), and the population is generally susceptible, especially elderly patients with chronic diseases who are more likely to become critically ill (Adhikari et al., 2020).

The single-stranded positive-stranded RNA virus, SARS-CoV-2, is 80–220 nm in diameter and has 12–24 nm vesicular rod like spikes. (**Figure 1A**) (Bullock and Tamin, 2020; Huang et al., 2020c;

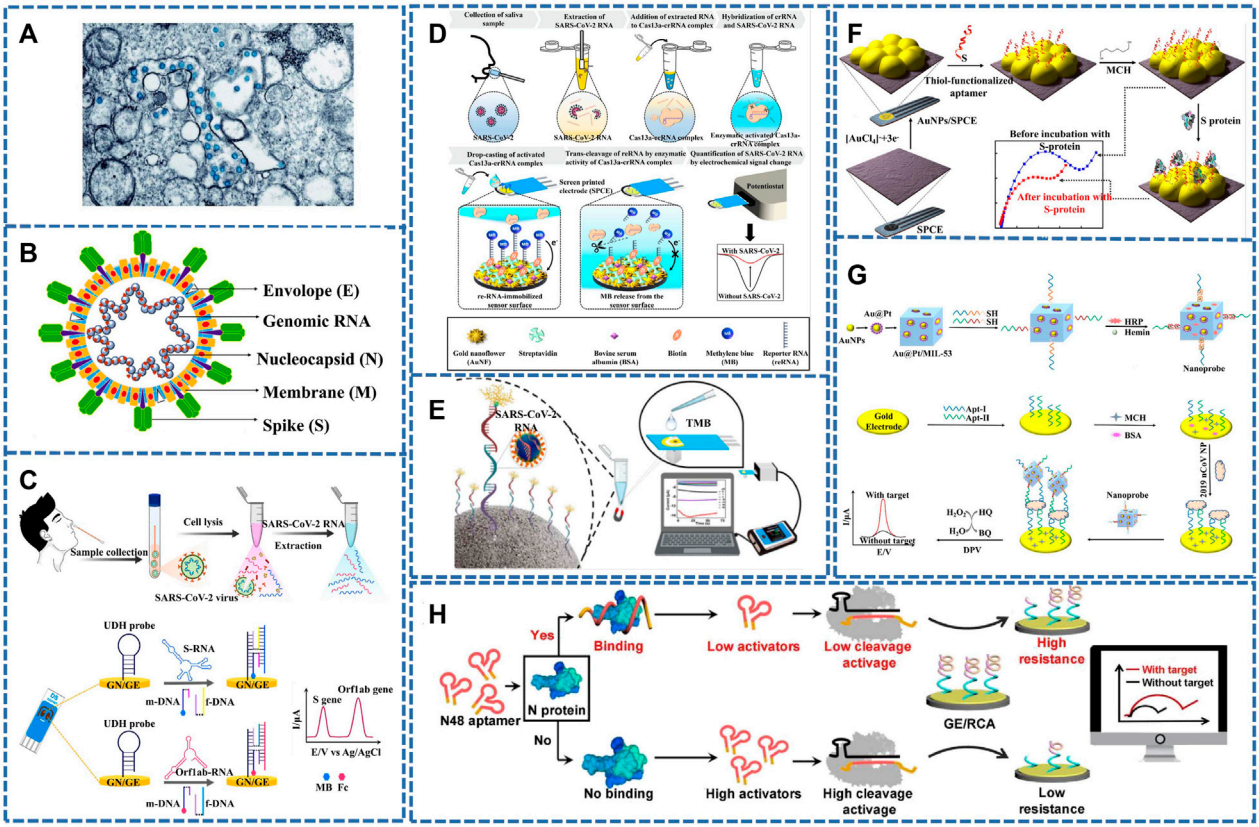

FIGURE 1 | (A) TEM image of SARS-CoV-2 (the blue globules) (Bullock and Tamin, 2020). **(B)** SARS-CoV-2's typical structure, S, M, E, and N proteins, encapsulates genomic RNA within virus particles (Kirtipal et al., 2020). **(C)** A detection workflow of SARS-CoV-2 RNA sequences from clinical samples using the electrochemical biosensor for detection of the S and Orf1ab genes (Kashefi-Kheyrabadi et al., 2022). **(D)** Schematic diagram of an electrochemical biosensing strategy for SARS-CoV-2 detection using CRISPR/Cas13a. (Heo et al., 2022). **(E)** Schematic diagram of an electrochemical gene sensor for detecting SARS-COV-2 (Cajigas et al., 2022). **(F)** Diagram of the preparation steps of the sensor for detecting SARS-CoV-2 S protein. (Abrego-Martinez et al., 2022). **(G)** Schematic diagram of constructing electrochemical sensor based on Au@Pt/MIL-53 (Tian et al., 2021). **(H)** Strategy and workflow of SARS-COV-2 antigen detection by CRISPR-based electrochemical sensor (Liu et al., 2022).

Lu et al., 2020; Zhou et al., 2020). At the same time, it is also a single-stranded positive-stranded RNA virus with typical "coronavirus" morphological characteristics. Its homology with SARS-COV and MERS genome sequences is close to 79% and 50%, respectively (Lu et al., 2020; Zhou et al., 2020), so it can be modified to detect SARS-CoV-2 by referring to previous detection methods of SARS-COV. The genome of SARS-CoV-2 consists of two noncoding (5′-terminal noncoding region and 3′-terminal noncoding region) and five coding regions (an open reading box 1a/b (ORF1a/b), the S region encoding spinous glycoprotein (S protein), the E region encoding envelope protein (E protein), the M region encoding membrane protein (M protein) and the N region encoding nucleocapsid protein (N protein)) (Xu et al., 2020; Yang and Wang, 2020) (**Figure 1B**). Among them, ORF1a/b genes are responsible for viral genome replication, transcription and translation (Jalandra et al., 2020; Kirtipal et al., 2020; Udugama et al., 2020; Yang and Wang, 2020). The virus on the surface of the outer coating is mainly composed of four structural proteins, the S protein, the E protein, the M protein and the N protein (Nie et al., 2020). S protein, which enables the virus to enter the host cell, can be used for vaccine, research and development of therapeutic antibodies and diagnosis depending on its advantages. Proteins M and E are responsible for forming the envelope of the virus, whereas the N protein participates in the assembly of viruses (Jalandra et al., 2020; Udugama et al., 2020; Yang and Wang, 2020).

At the early stage of the outbreak, metagenomic sequencing obtained the whole genome sequence of the SARS-CoV-2 virus, which provided the basis for the classification of SARS-CoV-2 as a new member of the genus β-coronavirus. Although metagenomic sequencing is costly, it not only provides technical support for the analysis of the origin and pathogenesis of SARS-CoV-2 but also lays the foundation for the development of novel SARS-CoV-2 detection methods (Lu et al., 2020; Wu et al., 2020). As detection methods have improved, the commonly used methods include polymerase chain reaction (PCR) (Yuan et al., 2020), reverse transcription PCR (RT-PCR) (Huang et al., 2020a; Hu et al., 2020; Xie et al., 2020), reverse transcription loop-mediated isothermal amplification (RT-LAMP) (Baek et al., 2020; Yan et al., 2020),

regularly interspaced short palindromic repeats-CRISPR-associated (CRISPR-Cas) (Broughton et al., 2020; Ding et al., 2020) and nucleic acid biosensors (Alafeef et al., 2020; Zhu et al., 2020). Currently, Although PCR can yield results with less viral genetic material. However, we still need more sensitive, simple, accurate, and inexpensive rapid assays for SARS-CoV-2 detection.

Electrochemical biosensors could provide the possibility for rapid medical diagnosis by rapid detection of biomarkers (Chen et al., 2018; Huang et al., 2020b; Lu et al., 2021; Raza et al., 2021; Huang et al., 2022), which have been used to detect Zika virus (Afsahi et al., 2018), Ebola virus (Ilkhani and Farhad, 2018), HIV(Nandi et al., 2020), influenza virus (Krishna et al., 2016; Chowdhury et al., 2019), etc. With the advancement of COVID-19 research, electrochemical biosensors, especially electrochemical DNA biosensors, have been widely studied in the detection of SARS-CoV-2.

This mini-review covers the recent progress of the rapid detection of SARS-COV-2 by using electrochemical DNA biosensors for the first time. What's more, this mini-review summarizes the problems faced by the existing assays and puts an outlook on future trends in the development of new assays for SARS-CoV-2, which can provide researchers with a borrowing role in the development of new assays.

ELECTROCHEMICAL DNA SENSOR DETECTION OF SARS-COV-2

Electrochemical DNA biosensors for the detection of viruses and bacteria are now widely used due to their advantages of higher sensitivity, less sample size, low cost, simplicity, and portability (Adam et al., 2020; Lin et al., 2021; Huang et al., 2022; Mei et al., 2022). The electrochemical DNA biosensors are based on the single-strand DNA or complementary target DNA fixed on the electrode and the target DNA through the principle of base complementarity, resulting in changes in concentration, energy, and other aspects, and this change can be converted into visual electrical signals through the appropriate conversion elements on the sensor (Huang et al., 2020b; Karimi-Maleh et al., 2021). Therefore, they combine biological specific recognition with electrochemical high sensitivity analysis to further realize the detection and analysis of the target, so that it has the potential of immediate detection and diagnosis.

Specific Detection of SARS-COV-2 Nucleic Acid

Recently, nanomaterials have been extensively applied in life science, energy science and other fields (Xu et al., 2019; Zhuang et al., 2019; Kuang et al., 2020; Wen et al., 2020; Chen et al., 2021; He et al., 2021; Liu et al., 2021; Savchenko et al., 2021; Schultz et al., 2021; Wu et al., 2021; Xu and Liu, 2021; He et al., 2022; Yi et al., 2022; Zhuang et al., 2022). At present, nanomaterials in electrochemical biosensors have also been broadly concerned for gauging SARS-COV-2. Graphene (G) is considered one of the suitable materials for sensor applications due to its special good properties such as physical properties, electronics as well as oxygen-containing groups, which are introduced in the construction of biosensors and can improve the analytical parameters of electrochemical biosensors (Abdel-Haleem et al., 2021; Meng et al., 2021). Alafeef et al. developed an electrochemical biosensor chip constructed by G that can selectively recognize SARS-CoV-2 RNA (N gene) (Alafeef et al., 2020). It was obtained by immobilizing highly specific ssDNA (antisense oligonucleotides)-capped gold nanoparticles (AuNPs) probes of viral N gene onto G coated filter paper. AuNPs achieve the goal of improving the electrochemical response of the sensor to the target by enhancing the electron transfer process and providing a large surface area for the ssDNA probe. G-ssDNA-AuNPs-built monitoring platform can read the results in 5 min with a handheld reader. When combined with benchtop devices, point-of-care (POC) testing can be offered to economically lag, resource-poor areas. Zhao et al. 2021) synthesized an ultra-sensitive sandwich electrochemical sensor using calixarene functionalized go and SARS-CoV-2 targeted RNA with limit of detection (LOD) as low as 200 copies/mL for clinical samples. Based on this sensor, a smartphone can detect SARS-CoV-2. Moreover, the detection process can detect SARS-CoV-2 samples sensitively, accurately and rapidly without RNA amplification, which also provides effective suggestions for low-cost and simple POC diagnosis.

Rolling circle amplification (RCA) and catalytic hairpin assembly (CHA) in the nucleic acid amplification strategy can be combined with electrochemical analysis to accurately amplify electrochemical signals. Chaibun et al. (2021) designed the electrochemical biosensor for SARS-CoV-2 (S or N gene) RNA based on RCA. The technique can detect viruses as low as one copy/μl in 2 h by differential pulse voltammetry (DPV). It was evaluated in conjunction with quantitative RT-PCR (qRT-PCR) on 106 clinical samples, of which 41 were positive (SARS-COV-2) and nine other samples were positive for other respiratory viruses, with 100% agreement between the two methods. Peng et al. (2021) prepared an electrochemical sensor based on CHA and terminal deoxynucleotidyl transferase (TdT) induced polymerization. When the target gene (ORF1ab gene) combined with hairpin HP1 and HP2 to form a Y-type DNA structure, TdT induced polymerization was further activated. A great quantity of long single-stranded DNA products are generated in the dNTP pool, during which a large number of $Ru(NH_3)_6^{3+}$ adsorbs on the DNA phosphoric acid skeleton through strong electrostatic interaction. Therefore, this method can be used to obtain evidently boosted electrochemical signals for sensitive monitoring of SARS-COV-2. Kashefi-kheyrabadi et al. (2022) developed an electrochemical sensor without nucleic acid amplification. The detection process is shown in **Figure 1C**, the S and ORF1ab genes of SARS-CoV-2 can be detected simultaneously within 1 h with LOD as low as 5.0 and 6.8 ag/μl.

Heo et al. (2022) combined CRISPR/Cas13a with the electrochemical biosensor. The detection process is shown in **Figure 1D**. When the single-stranded RNA (ssRNA) probe was recognized by the SARS-CoV-2 RNA phase, the Cas13a-crRNA complex was formed, which was then introduced into the

TABLE 1 | Comparison of SARS-CoV-2 electrochemical genetic sensor detection methods.

Targets for detection	Methods	Linear range	LOD	References
S protein	EIS	0–10^5 pM	1.30 pM	Abrego-Martinez et al. (2022)
N gene	Microcontrollers	585.4–5.854 × 10^7 copies/μl	6.9 copies/μl	Alafeef et al. (2020)
RBD protein	EIS	10–6.4 × 10^4 nM	7 nM	Amouzadeh Tabrizi and Acedo, (2022)
RdRP gene	DPV	10^{-10}–10^{-5} M	1.86 × 10^{-7} M	Ang et al. (2022)
N gene	CV	800–4,000 copies/μl	258.01 copies/μl	Avelino et al. (2021)
SARS-CoV-2 RNA (H)	I-t	0–1,000 pM	0.73 pM	Cajigas et al. (2022)
N or S gene	DPV	1–10^9 copies/μl	1 copies/μl	Chaibun et al. (2021)
N gene	EIS	0.1–10^6 fg/ml	0.59 fg/ml	Cui et al. (2022)
S1 protein	DPV	0.3–300 nM	7 nM	Curti et al. (2022)
ORF1ab gene	DPV	10^2–10^9 fg/ml	100 fg/ml	Damiati et al. (2021)
ORF1a gene	CV	—	2.3 copies/μl	Najjar et al. (2021)
RdRP gene	DPV	100–3 × 10^6 fM	45 fM	Deng et al. (2022)
RdRP gene	ECL	1–10^5 fM	2.67 fM	Fan et al. (2021)
RdRP gene	ECL	10–10^7 aM	7.8 aM	Fan et al. (2022)
RdRP gene	CV	1–8 × 10^3 pM	0.3 pM	Farzin et al. (2021)
ORF1ab gene	ECL	50–10^8 fM	0.514 fM	Gutiérrez-Gálvez et al. (2022)
N protein	DPV	50–10^5 pg/ml	16.5 pg/ml	Han et al. (2022)
ORF1ab gene	DPV	1–10^9 aM	0.48 aM	Hatamluyi et al. (2022)
ORF and S genes	DPV	1.0 × 10^{-1}–1.0 × 10^5 fg/ml	ORF gene: 4.4 × 10^{-2} fg/ml. S gene: 8.1 × 10^{-2} fg/ml	Heo et al. (2022)
S protein	SWV	10^{-4}–10^2 nM	10 nM	Idili et al. (2021)
ORF1ab gene	ECL	0.1–10^{11} fM	0.1 fM	Jiang et al. (2022)
ORF1ab and S genes	SWV	10^{-16}–10^{-11} M	ORF1ab gene: 5.0 ag/μl. S gene: 6.8 ag/μl	Kashefi-Kheyrabadi et al. (2022)
RdRP and N genes	DPV	10^3–10^9 copies	RdRP gene: 0.972 fg/μl. N gene: 3.925 fg/μl,	Kim et al. (2021)
N gene	DPV	10–200 pg/μl	10 pg/μl	Kumar et al. (2021)
N protein	EIS	0.05–125 ng/ml	0.077 ng/ml	Liu et al. (2022)
ORF1ab gene	DPV	0–100 pM	1.01 pM	Martínez-Periñán et al. (2021)
SARS-CoV-2 RNA	Chronoamperometric	1–10^4 pM	1 pM	Pang et al. (2021)
ORF1ab gene	DPV	10^2–10^6 pM	26 fM	Peng et al. (2021)
ORF1ab and N genes	SWV	10^{-3}–10 ng/μl	3.8 × 10^{-5} ng/μl	Ramírez-Chavarría et al. (2022)
S protein	DPV	10–50 ng/ml	2.63 ng/ml	Sari et al. (2022)
N gene	DPV	10–10^6 fM	3.5 fM	Song et al. (2021)
N protein	DPV	25–5 × 10^4 pg/ml	8.33 pg/ml	Tian et al. (2021)
RdRP gene	ECL	1–10^5 fM	0.21 fM	Yao et al. (2021)
RdRp gene	ECL	0–2000 aM	43.70 aM	Zhang et al. (2022a)
RdRP gene	ECL	0–1,000 aM	32.8 aM	Zhang et al. (2022b)
RdRP gene	ECL	0–10^3 aM	12.8 aM	Zhang et al. (2022c)
RdRP gene	ECL	0–3,000 aM	59 aM	Zhang et al. (2022d)
ORF1ab gene	DPV	10^3–10^9 copies/ml	200 copies/ml	Zhao et al. (2021)

Abbreviation: CV, Cyclic voltammetry; DPV, Differential pulse voltammery; EIS, Electrochemical impedance spectroscopy; SWV, Square wave voltammetry; ECL, Electrochemiluminescence; I-t, Amperometric.

reporter RNA (reRNA)-coupled electrochemical sensor to activate RNase, thereby cutting reRNA. In this process, redox molecules released by reRNA will cause changes in their current, thus achieving the purpose of sensitive detection. Amplification-free sensors designed by the team enable ultra-low concentration testing of SARS-CoV-2 RNA. This opens the possibility of on-site and high-speed diagnostic COVID-19 testing.

Although many sensors are available to monitor SARS-COV-2, false-positive results from its homologous viruses cannot be ruled out. Cajigas et al. (2022) reported an electrochemical biosensor that can specifically detect SARS-COV-2 and distinguish the homologous viruses of SARS-CoV, Middle East Respiratory Syndrome (MERS), and Human Coronavirus (HKU1) (**Figure 1E**). Biosensors with immobilized capture probes were combined with modified magnetic beads (MMBS), while the capture probes were first hybridized with the targets and then hybridized with biotinylated signal probes in a sandwich format. The biotinylated signal probe allowed interaction with one of three distinct protein-enzyme compounds containing distinct numbers of horse radish peroxidase (HRP) molecules to generate visual electrical signals by the timing current method. The prepared biosensor provides the possibility to check infected and asymptomatic patients. At the same time, it will also contribute to resisting the COVID-19 pandemic.

Specific Detection of SARS-COV-2 VIRUS/PROTEIN

With the development of nucleic acid testing, there are broad prospects for virus detection, but if the viral RNA is mutated, it

can produce false-negative results, so researchers switched to detecting SARS-CoV-2-related proteins. Such as receptor-binding domain (RBD) (Jalandra et al., 2020; Udugama et al., 2020), S protein (Jin et al., 2020b; Wu et al., 2020) and N protein. Therefore, Abrego-Martinez et al. (2022) prepared a biosensor for detecting SARS-CoV-2 (S protein) by fixing probe ssDNA on gold nanoparticles (**Figure 1F**). Its advantages were fast detection speed, low detection limit (1.30 p.m.), and results that could be obtained in 40 min, but SARS-CoV had a certain response to it, which was negligible compared to SARS-CoV-2. The direct detection of SARS-CoV-2 was achieved by immobilizing ssDNA AuNPs on screen-printed electrode, which was also applied in a handheld potentiostat linked to a smartphone. To further reduce costs, Curti et al. prepared a biosensor targeting SARS-CoV-2 S1 by using an inexpensive and highly conductive single-wall carbon nanotube screen-printed electrode (SWCNT-SPE). The adapted ssDNA can block virus infection *in vitro*. It is possible to prepare multifunctional sensors (Curti et al., 2022).

Designing a highly sensitive assay is urgent for the early diagnosis and treatment of SARS-CoV-2. Tian et al. (2021) designed a diaptamer sensor for highly selective recognition of SARS-CoV-2 N protein using the metal-organic framework MIL-53 Au@Pt Nanoparticles and enzymes, as shown in the **Figure 1G**. The detection limit was as low as 8.33 pg/ml.

CRISPR-Cas is an efficient, simple and powerful gene targeting technology (Liu and Fan, 2014), and the nucleic acid detection of CRISPR/Cas nuclease holds great promise for the development of SARS-COV-2 diagnostics under high sensitivity, specificity and reliability (Chertow Daniel, 2018; Li et al., 2019). Liu et al. (2022) combined this method with electrochemical analysis to prepare a sensor for SARS-COV-2 virus detection (**Figure 1H**). the signal of electrochemical impedance spectroscopy (EIS) signal was linked to the morphology and presence of the RCA-DNA structure, which was determined by the DNA cleavage activity of Cas12a attachment regulated by target-induced competition. Therefore the sensor was also responsible for its ability to test SARS-COV-2 with high specificity.

The nucleic acid and virus/protein determinations are summarised in **Table 1**. Compared to the traditional testing methods (PCR, RT-PCR), electrochemical DNA sensors have demonstrated their ability to detect SARS-CoV-2 with ease of use, no need for expensive instruments, lower detection limits, higher sensitivity, and specificity. In particular, it has the advantage of shorter detection times, demonstrating its ability to detect and control outbreaks rapidly. The miniaturised electrochemical biosensor can be combined with lateral flow assay (LFA), loop-mediated isothermal amplification (LAMP), RT-LAMP approaches, clustered regularly interspaced short palindromic repeats (CRISPR) and other methods to further increase sensitivity. In fact, we also hope that by comparing the different assays, other researchers will be able to create more sensitive, rapid, economical, and accurate COVID-19 assays.

CONCLUSION AND PERSPECTIVES

The rapid, sensitive and accurate determination of SARS-CoV-2 is crucial for the prevention and control of the epidemic. Electrochemical DNA biosensors have the advantages of high sensitivity, high selectivity, and economical portability, et al., which have been gradually applied to SARS-CoV-2 detection. In this mini-review, the latest researches on electrochemical DNA biosensors for the monitoring of SARS-CoV-2 in recent years have been summarized. Although there are many electrochemical DNA biosensors for SARS-CoV-2 detection, there are still some opportunities and challenges: 1) the preparation of working electrode materials should be simpler; 2) the stability of the electrochemical DNA biosensors should be guaranteed; 3) how to achieve simultaneous detection of multiple different genes? Of course, with the further in-depth research, the above problems will be effectively solved, which will provide the possibility for the commercial application of electrochemical biosensors for SARS-CoV-2 detection.

AUTHOR CONTRIBUTIONS

YM: defined the focus of the review. CH, WZ, and YL: writing. CL, and ZL: editing. MY and YK: reviewing. XL and QH: writing, reviewing and editing.

FUNDING

This work has been supported by the National Natural Science Foundation of China (No. 82060599), the Natural Science Foundation of Jiangxi (No. 20202BABL213018), the Science and Technology Project of the Education Department of Jiangxi Province (Nos. GJJ190795 and GJJ211517), the Science and Technology Project of Jiangxi Health Committee (No. 202131033), the Research Fund of Gannan Medical University (Nos. ZD201901, YQ202003, and YB201911), the Open Fund of Fujian Provincial Key Laboratory of Modern Analytical Science and Separation Technology and the Science and Technology (No. K2017-01), the Plan Post-subsidy Project of Ganzhou (No. 2019-60-174) and the Special Fund for Graduate Innovation in Jiangxi Province (No. YC2021-S796).

REFERENCES

Abdel-Haleem, F. M., Gamal, E., Rizk, M. S., Madbouly, A., El Nashar, R. M., Anis, B., et al. (2021). Molecularly Imprinted Electrochemical Sensor-Based Fe2O3@MWCNTs for Ivabradine Drug Determination in Pharmaceutical Formulation, Serum, and Urine Samples. *Front. Bioeng. Biotechnol.* 9, 648704. doi:10.3389/fbioe.2021.648704

Abrego-Martinez, J. C., Jafari, M., Chergui, S., Pavel, C., Che, D., and Siaj, M. (2022). Aptamer-based Electrochemical Biosensor for Rapid Detection of SARS-CoV-2: Nanoscale Electrode-Aptamer-SARS-CoV-2 Imaging by Photo-Induced Force Microscopy. *Biosens. Bioelectron.* 195, 113595. doi:10.1016/j.bios.2021.113595

Adam, N., Schlicht, S., Han, Y., Bechelany, M., Bachmann, J., and Perner, M. (2020). Metagenomics Meets Electrochemistry: Utilizing the Huge Catalytic

Potential from the Uncultured Microbial Majority for Energy-Storage. *Front. Bioeng. Biotechnol.* 8, 567. doi:10.3389/fbioe.2020.00567

Adhikari, S. P., Meng, S., Wu, Y.-J., Mao, Y.-P., Ye, R.-X., Wang, Q.-Z., et al. (2020). Epidemiology, Causes, Clinical Manifestation and Diagnosis, Prevention and Control of Coronavirus Disease (COVID-19) during the Early Outbreak Period: a Scoping Review. *Infect. Dis. Poverty* 9, 29. doi:10.1186/s40249-020-00646-x

Afsahi, S., Lerner, M. B., Goldstein, J. M., Lee, J., Tang, X., Bagarozzi, D. A., et al. (2018). Novel Graphene-Based Biosensor for Early Detection of Zika Virus Infection. *Biosens. Bioelectron.* 100, 85–88. doi:10.1016/j.bios.2017.08.051

Akalin, E., Azzi, Y., Bartash, R., Seethamraju, H., Parides, M., Hemmige, V., et al. (2020). Covid-19 and Kidney Transplantation. *N. Engl. J. Med.* 382 (25), 2475–2477. doi:10.1056/NEJMc2011117

Alafeef, M., Dighe, K., Moitra, P., and Pan, D. (2020). Rapid, Ultrasensitive, and Quantitative Detection of SARS-CoV-2 Using Antisense Oligonucleotides Directed Electrochemical Biosensor Chip. *ACS Nano* 14 (12), 17028–17045. doi:10.1021/acsnano.0c06392

Amouzadeh Tabrizi, M., and Acedo, P. (2022). An Electrochemical Impedance Spectroscopy-Based Aptasensor for the Determination of SARS-CoV-2-RBD Using a Carbon Nanofiber–Gold Nanocomposite Modified Screen-Printed Electrode. *Biosensors* 12 (3), 142. doi:10.3390/bios12030142

Anderson, R. M., Hollingsworth, T. D., Baggaley, R. F., Maddren, R., and Vegvari, C. (2020). COVID-19 Spread in the UK: the End of the Beginning? *Lancet* 396 (10251), 587–590. doi:10.1016/S0140-6736(20)31689-5

Ang, W. L., Lim, R. R. X., Ambrosi, A., and Bonanni, A. (2022). Rapid Electrochemical Detection of COVID-19 Genomic Sequence with Dual-Function Graphene Nanocolloids Based Biosensor. *FlatChem* 32, 100336. doi:10.1016/j.flatc.2022.100336

Avelino, K. Y. P. S., Dos Santos, G. S., Frías, I. A. M., Silva-Junior, A. G., Pereira, M. C., Pitta, M. G. R., et al. (2021). Nanostructured Sensor Platform Based on Organic Polymer Conjugated to Metallic Nanoparticle for the Impedimetric Detection of SARS-CoV-2 at Various Stages of Viral Infection. *J. Pharm. Biomed. Analysis* 206, 114392. doi:10.1016/j.jpba.2021.114392

Baek, Y. H., Um, J., Antigua, K. J. C., Park, J.-H., Kim, Y., Oh, S., et al. (2020). Development of a Reverse Transcription-Loop-Mediated Isothermal Amplification as a Rapid Early-Detection Method for Novel SARS-CoV-2. *Emerg. Microbes Infect.* 9 (1), 998–1007. doi:10.1080/22221751.2020.1756698

Broughton, J. P., Deng, X., Yu, G., Fasching, C. L., Servellita, V., Singh, J., et al. (2020). CRISPR-Cas12-based Detection of SARS-CoV-2. *Nat. Biotechnol.* 38 (7), 870–874. doi:10.1038/s41587-020-0513-4

Bullock, H. A., and Tamin, A. (2020). *Transmission Electron Microscopic Image of an Isolate from the First U.S. Case of COVID-19, Formerly Known as 2019-nCoV. The Spherical Viral Particles, Colorized Blue, Contain Cross-Sections through the Viral Genome, Seen as Black Dots*. CDC 2020. Available at: https://phil.cdc.gov/Details.aspx?pid=23354.

Cajigas, S., Alzate, D., Fernández, M., Muskus, C., and Orozco, J. (2022). Electrochemical Genosensor for the Specific Detection of SARS-CoV-2. *Talanta* 245, 123482. doi:10.1016/j.talanta.2022.123482

Chaibun, T., Puenpa, J., Ngamdee, T., Boonapatcharoen, N., Athamanolap, P., O'Mullane, A. P., et al. (2021). Rapid Electrochemical Detection of Coronavirus SARS-CoV-2. *Nat. Commun.* 12 (1), 802. doi:10.1038/s41467-021-21121-7

Chen, B., Chen, D., Li, F., Lin, X., and Huang, Q. (2018). Graphitic Porous Carbon: Efficient Synthesis by a Combustion Method and Application as a Highly Selective Biosensor. *J. Mat. Chem. B* 6 (46), 7684–7691. doi:10.1039/c8tb02139b

Chen, Z., Liao, T., Wan, L., Kuang, Y., Liu, C., Duan, J., et al. (2021). Dual-stimuli Responsive Near-Infrared Emissive Carbon Dots/hollow Mesoporous Silica-Based Integrated Theranostics Platform for Real-Time Visualized Drug Delivery. *Nano Res.* 14 (11), 4264–4273. doi:10.1007/s12274-021-3624-4

Chertow, D. S. (2018). Next-generation Diagnostics with CRISPR. *Science* 360 (6387), 381–382. doi:10.1126/science.aat4982

Chowdhury, A. D., Takemura, K., Li, T.-C., Suzuki, T., and Park, E. Y. (2019). Electrical Pulse-Induced Electrochemical Biosensor for Hepatitis E Virus Detection. *Nat. Commun.* 10 (1), 3737. doi:10.1038/s41467-019-11644-5

Cui, J., Kan, L., Cheng, F., Liu, J., He, L., Xue, Y., et al. (2022). Construction of Bifunctional Electrochemical Biosensors for the Sensitive Detection of the SARS-CoV-2 N-Gene Based on Porphyrin Porous Organic Polymers. *Dalton Trans.* 51 (5), 2094–2104. doi:10.1039/D1DT03869A

Curti, F., Fortunati, S., Knoll, W., Giannetto, M., Corradini, R., Bertucci, A., et al. (2022). A Folding-Based Electrochemical Aptasensor for the Single-step Detection of the SARS-CoV-2 Spike Protein. *ACS Appl. Mat. Interfaces* 14 (17), 19204–19211. doi:10.1021/acsami.2c02405

Damiati, S., Sopstad, S., Peacock, M., Akhtar, A. S., Pinto, I., Soares, R. R. G., et al. (2021). Flex Printed Circuit Board Implemented Graphene-Based DNA Sensor for Detection of SARS-CoV-2. *IEEE Sensors J.* 21 (12), 13060–13067. doi:10.1109/JSEN.2021.3068922

Deng, Y., Peng, Y., Wang, L., Wang, M., Zhou, T., Xiang, L., et al. (2022). Target-triggered Cascade Signal Amplification for Sensitive Electrochemical Detection of SARS-CoV-2 with Clinical Application. *Anal. Chim. Acta* 1208, 339846. doi:10.1016/j.aca.2022.339846

Ding, X., Yin, K., Li, Z., Lalla, R. V., Ballesteros, E., Sfeir, M. M., et al. (2020). Ultrasensitive and Visual Detection of SARS-CoV-2 Using All-In-One Dual CRISPR-Cas12a Assay. *Nat. Commun.* 11 (1), 4711. doi:10.1038/s41467-020-18575-6

Fan, Z., Yao, B., Ding, Y., Xu, D., Zhao, J., and Zhang, K. (2022). Rational Engineering the DNA Tetrahedrons of Dual Wavelength Ratiometric Electrochemiluminescence Biosensor for High Efficient Detection of SARS-CoV-2 RdRp Gene by Using Entropy-Driven and Bipedal DNA Walker Amplification Strategy. *Chem. Eng. J.* 427, 131686. doi:10.1016/j.cej.2021.131686

Fan, Z., Yao, B., Ding, Y., Zhao, J., Xie, M., and Zhang, K. (2021). Entropy-driven Amplified Electrochemiluminescence Biosensor for RdRp Gene of SARS-CoV-2 Detection with Self-Assembled DNA Tetrahedron Scaffolds. *Biosens. Bioelectron.* 178, 113015. doi:10.1016/j.bios.2021.113015

Farzin, L., Sadjadi, S., Sheini, A., and Mohagheghpour, E. (2021). A Nanoscale Genosensor for Early Detection of COVID-19 by Voltammetric Determination of RNA-dependent RNA Polymerase (RdRP) Sequence of SARS-CoV-2 Virus. *Microchim. Acta* 188 (4), 121. doi:10.1007/s00604-021-04773-6

Fu, L., Liu, X., Su, Y., Ma, J., and Hong, K. (2021). Prevalence and Impact of Cardiac Injury on COVID -19: A Systematic Review and Meta-analysis. *Clin. Cardiol.* 44 (2), 276–283. doi:10.1002/clc.23540

Gutiérrez-Gálvez, L., del Caño, R., Menéndez-Luque, I., García-Nieto, D., Rodríguez-Peña, M., Luna, M., et al. (2022). Electrochemiluminescent Nanostructured DNA Biosensor for SARS-CoV-2 Detection. *Talanta* 240, 123203. doi:10.1016/j.talanta.2021.123203

Han, C., Li, W., Li, Q., Xing, W., Luo, H., Ji, H., et al. (2022). CRISPR/Cas12a-Derived Electrochemical Aptasensor for Ultrasensitive Detection of COVID-19 Nucleocapsid Protein. *Biosens. Bioelectron.* 200, 113922. doi:10.1016/j.bios.2021.113922

Hatamluyi, B., Rezayi, M., Amel Jamehdar, S., Rizi, K. S., Mojarrad, M., Meshkat, Z., et al. (2022). Sensitive and Specific Clinically Diagnosis of SARS-CoV-2 Employing a Novel Biosensor Based on Boron Nitride Quantum Dots/flower-like Gold Nanostructures Signal Amplification. *Biosens. Bioelectron.* 207, 114209. doi:10.1016/j.bios.2022.114209

He, C., Lin, X., Mei, Y., Luo, Y., Yang, M., Kuang, Y., et al. (2022). Recent Advances in Carbon Dots for *In Vitro*/Vivo Fluorescent Bioimaging: A Mini-Review. *Front. Chem.* 10, 905475. doi:10.3389/fchem.2022.905475

He, S., Huang, Q., Zhang, Y., Zhang, H., Xu, H., Li, X., et al. (2021). Magnetic Beads-Based Multicolor Colorimetric Immunoassay for Ultrasensitive Detection of Aflatoxin B1. *Chin. Chem. Lett.* 32 (4), 1462–1465. doi:10.1016/j.cclet.2020.09.047

Heo, W., Lee, K., Park, S., Hyun, K.-A., and Jung, H.-I. (2022). Electrochemical Biosensor for Nucleic Acid Amplification-free and Sensitive Detection of Severe Acute Respiratory Syndrome Coronavirus 2 (SARS-CoV-2) RNA via CRISPR/Cas13a Trans-cleavage Reaction. *Biosens. Bioelectron.* 201, 113960. doi:10.1016/j.bios.2021.113960

Hu, X., Zhu, L., Luo, Y., Zhao, Q., Tan, C., Chen, X., et al. (2020). Evaluation of the Clinical Performance of Single-, Dual-, and Triple-Target SARS-CoV-2 RT-qPCR Methods. *Clin. Chim. Acta* 511, 143–148. doi:10.1016/j.cca.2020.10.008

Huang, P., Liu, T., Huang, L., Liu, H., Lei, M., Xu, W., et al. (2020a). Use of Chest CT in Combination with Negative RT-PCR Assay for the 2019 Novel Coronavirus but High Clinical Suspicion. *Radiology* 295 (1), 22–23. doi:10.1148/radiol.2020200330

Huang, Q., Lin, X., Chen, D., and Tong, Q.-X. (2022). Carbon Dots/α-Fe2O3-Fe3O4 Nanocomposite: Efficient Synthesis and Application as a Novel

Electrochemical Aptasensor for the Ultrasensitive Determination of Aflatoxin B1. *Food Chem.* 373, 131415. doi:10.1016/j.foodchem.2021.131415

Huang, Q., Lin, X., Tong, L., and Tong, Q.-X. (2020b). Graphene Quantum Dots/Multiwalled Carbon Nanotubes Composite-Based Electrochemical Sensor for Detecting Dopamine Release from Living Cells. *ACS Sustain. Chem. Eng.* 8 (3), 1644–1650. doi:10.1021/acssuschemeng.9b06623

Huang, Y., Liu, G. D., and Zhang, X. J. (2020c). Detection and Diagnosis of COVID-19. *Prog. Chem.* 32 (9), 1241–1251. doi:10.7536/PC200522

Huang, Z., Huang, P., Du, B., Kong, L., Zhang, W., Zhang, Y., et al. (2021). Prevalence and Clinical Outcomes of Cardiac Injury in Patients with COVID-19: A Systematic Review and Meta-Analysis. *Nutr. Metabolism Cardiovasc. Dis.* 31 (1), 2–13. doi:10.1016/j.numecd.2020.09.004

Idili, A., Parolo, C., Alvarez-Diduk, R., and Merkoçi, A. (2021). Rapid and Efficient Detection of the SARS-CoV-2 Spike Protein Using an Electrochemical Aptamer-Based Sensor. *ACS Sens.* 6 (8), 3093–3101. doi:10.1021/acssensors.1c01222

Ilkhani, H., and Farhad, S. (2018). A Novel Electrochemical DNA Biosensor for Ebola Virus Detection. *Anal. Biochem.* 557, 151–155. doi:10.1016/j.ab.2018.06.010

Jalandra, R., Yadav, A. K., Verma, D., Dalal, N., Sharma, M., Singh, R., et al. (2020). Strategies and Perspectives to Develop SARS-CoV-2 Detection Methods and Diagnostics. *Biomed. Pharmacother.* 129, 110446. doi:10.1016/j.biopha.2020.110446

Jiang, C., Mu, X., Liu, S., Liu, Z., Du, B., Wang, J., et al. (2022). A Study of the Detection of SARS-CoV-2 ORF1ab Gene by the Use of Electrochemiluminescent Biosensor Based on Dual-Probe Hybridization. *Sensors* 22 (6), 2402. doi:10.3390/s22062402

Jin, X., Lian, J.-S., Hu, J.-H., Gao, J., Zheng, L., Zhang, Y.-M., et al. (2020a). Epidemiological, Clinical and Virological Characteristics of 74 Cases of Coronavirus-Infected Disease 2019 (COVID-19) with Gastrointestinal Symptoms. *Gut* 69 (6), 1002–1009. doi:10.1136/gutjnl-2020-320926

Jin, Y.-H., Cai, L., Cai, L., Cheng, Z.-S., Cheng, H., Deng, T., et al. (2020b). A Rapid Advice Guideline for the Diagnosis and Treatment of 2019 Novel Coronavirus (2019-nCoV) Infected Pneumonia (Standard Version). *Mil. Med. Res.* 7 (1), 4. doi:10.1186/s40779-020-0233-6

Kalbusch, A., Henning, E., Brikalski, M. P., Luca, F. V. d., and Konrath, A. C. (2020). Impact of Coronavirus (COVID-19) Spread-Prevention Actions on Urban Water Consumption. *Resour. Conservation Recycl.* 163, 105098. doi:10.1016/j.resconrec.2020.105098

Karimi-Maleh, H., Alizadeh, M., Orooji, Y., Karimi, F., Baghayeri, M., Rouhi, J., et al. (2021). Guanine-Based DNA Biosensor Amplified with Pt/SWCNTs Nanocomposite as Analytical Tool for Nanomolar Determination of Daunorubicin as an Anticancer Drug: A Docking/Experimental Investigation. *Ind. Eng. Chem. Res.* 60 (2), 816–823. doi:10.1021/acs.iecr.0c04698

Kashefi-Kheyrabadi, L., Nguyen, H. V., Go, A., Baek, C., Jang, N., Lee, J. M., et al. (2022). Rapid, Multiplexed, and Nucleic Acid Amplification-free Detection of SARS-CoV-2 RNA Using an Electrochemical Biosensor. *Biosens. Bioelectron.* 195, 113649. doi:10.1016/j.bios.2021.113649

Kim, H. E., Schuck, A., Lee, S. H., Lee, Y., Kang, M., and Kim, Y.-S. (2021). Sensitive Electrochemical Biosensor Combined with Isothermal Amplification for Point-Of-Care COVID-19 Tests. *Biosens. Bioelectron.* 182, 113168. doi:10.1016/j.bios.2021.113168

Kirtipal, N., Bharadwaj, S., and Kang, S. G. (2020). From SARS to SARS-CoV-2, Insights on Structure, Pathogenicity and Immunity Aspects of Pandemic Human Coronaviruses. *Infect. Genet. Evol.* 85, 104502. doi:10.1016/j.meegid.2020.104502

Krishna, V. D., Wu, K., Perez, A. M., and Wang, J.-P. (2016). Giant Magnetoresistance-Based Biosensor for Detection of Influenza A Virus. *Front. Microbiol.* 7, 400. doi:10.3389/fmicb.2016.00400

Kuang, Y., Zhang, J., Xiong, M., Zeng, W., Lin, X., Yi, X., et al. (2020). A Novel Nanosystem Realizing Curcumin Delivery Based on Fe3O4@Carbon Dots Nanocomposite for Alzheimer's Disease Therapy. *Front. Bioeng. Biotechnol.* 8, 614906. doi:10.3389/fbioe.2020.614906

Kumar, M. S., Nandeshwar, R., Lad, S. B., Megha, K., Mangat, M., Butterworth, A., et al. (2021). Electrochemical Sensing of SARS-CoV-2 Amplicons with PCB Electrodes. *Sensors Actuators B Chem.* 343, 130169. doi:10.1016/j.snb.2021.130169

Kurnia Sari, A., Yeni Wahyuni Hartati, Y. W., Shabarni Gaffar, S., Isa Anshori, I., Darmawan Hidayat, D., and Hesti Lina Wiraswati, H. L. (2022). The Optimization of an Electrochemical Aptasensor to Detect RBD Protein S SARS-CoV-2 as a Biomarker of COVID-19 Using Screen-Printed Carbon electrode/AuNP. *J. Electrochem. Sci. Eng.* 12 (1), 219–235. doi:10.5599/jese.1206

Li, Y., Li, S., Wang, J., and Liu, G. (2019). CRISPR/Cas Systems towards Next-Generation Biosensing. *Trends Biotechnol.* 37 (7), 730–743. doi:10.1016/j.tibtech.2018.12.005

Lin, L., Hu, K., Cai, S., Deng, X., Shao, X., Liang, Y., et al. (2020). Hypoproteinemia Is an Independent Risk Factor for the Prognosis of Severe COVID-19 Patients. *J. Clin. Biochem. Nutr.* 67 (2), 126–130. doi:10.3164/jcbn.20-75

Lin, X., Mei, Y., He, C., Luo, Y., Yang, M., Kuang, Y., et al. (2021). Electrochemical Biosensing Interface Based on Carbon Dots-Fe3O4 Nanomaterial for the Determination of *Escherichia coli* O157:H7. *Front. Chem.* 9 (903), 769648. doi:10.3389/fchem.2021.769648

Liu, L., and Fan, X.-D. (2014). CRISPR-cas System: a Powerful Tool for Genome Engineering. *Plant Mol. Biol.* 85 (3), 209–218. doi:10.1007/s11103-014-0188-7

Liu, N., Liu, R., and Zhang, J. (2022). CRISPR-Cas12a-mediated Label-free Electrochemical Aptamer-Based Sensor for SARS-CoV-2 Antigen Detection. *Bioelectrochemistry* 146, 108105. doi:10.1016/j.bioelechem.2022.108105

Liu, Z., Du, Y., Zhang, P., Zhuang, Z., and Wang, D. (2021). Bringing Catalytic Order Out of Chaos with Nitrogen-Doped Ordered Mesoporous Carbon. *Matter* 4 (10), 3161–3194. doi:10.1016/j.matt.2021.07.019

Lu, R., Zhao, X., Li, J., Niu, P., Yang, B., Wu, H., et al. (2020). Genomic Characterisation and Epidemiology of 2019 Novel Coronavirus: Implications for Virus Origins and Receptor Binding. *Lancet* 395 (10224), 565–574. doi:10.1016/S0140-6736(20)30251-8

Lu, Y., Zhou, Q., and Xu, L. (2021). Non-Invasive Electrochemical Biosensors for TNF-α Cytokines Detection in Body Fluids. *Front. Bioeng. Biotechnol.* 9, 701045. doi:10.3389/fbioe.2021.701045

Martínez-Periñán, E., García-Mendiola, T., Enebral-Romero, E., del Caño, R., Vera-Hidalgo, M., Vázquez Sulleiro, M., et al. (2021). A MoS2 Platform and Thionine-Carbon Nanodots for Sensitive and Selective Detection of Pathogens. *Biosens. Bioelectron.* 189, 113375. doi:10.1016/j.bios.2021.113375

Mei, Y., He, C., Zeng, W., Luo, Y., Liu, C., Yang, M., et al. (2022). Electrochemical Biosensors for Foodborne Pathogens Detection Based on Carbon Nanomaterials: Recent Advances and Challenges. *Food Bioprocess Technol.* 15 (3), 498–513. doi:10.1007/s11947-022-02759-7

Meng, S., Liu, Y., Wang, L., Ji, X., Chen, Y., Zheng, T., et al. (2021). Graphene-Based Flexible Sensors for Simultaneous Detection of Ascorbic Acid, Dopamine, and Uric Acid. *Front. Bioeng. Biotechnol.* 9, 726071. doi:10.3389/fbioe.2021.726071

Najjar, D., Rainbow, J., Timilsina, S. S., Jolly, P., de Puig, H., Yafia, M., et al. (2021). Lab-on-a-chip Multiplexed Electrochemical Sensor Enables Simultaneous Detection of SARS-CoV-2 RNA and Host Antibodies. *MedRxiv*. doi:10.1101/2021.09.01.21262387

Nandi, S., Mondal, A., Roberts, A., and Gandhi, S. (2020). Biosensor Platforms for Rapid HIV Detection. *Adv. Clin. Chem.* 98, 1–34. doi:10.1016/bs.acc.2020.02.001

Nie, J., Li, Q., Wu, J., Zhao, C., Hao, H., Liu, H., et al. (2020). Establishment and Validation of a Pseudovirus Neutralization Assay for SARS-CoV-2. *Emerg. Microbes Infect.* 9 (1), 680–686. doi:10.1080/22221751.2020.1743767

Pan, L., Huang, P., Xie, X., Xu, J., Guo, D., and Jiang, Y. (2021). Metabolic Associated Fatty Liver Disease Increases the Severity of COVID-19: A Meta-Analysis. *Dig. Liver Dis.* 53 (2), 153–157. doi:10.1016/j.dld.2020.09.007

Pang, S.-N., Lin, Y.-L., Yu, K.-J., Chiou, Y.-E., Leung, W.-H., and Weng, W.-H. (2021). An Effective SARS-CoV-2 Electrochemical Biosensor with Modifiable Dual Probes Using a Modified Screen-Printed Carbon Electrode. *Micromachines* 12 (10), 1171. doi:10.3390/mi12101171

Peng, Y., Pan, Y., Sun, Z., Li, J., Yi, Y., Yang, J., et al. (2021). An Electrochemical Biosensor for Sensitive Analysis of the SARS-CoV-2 RNA. *Biosens. Bioelectron.* 186, 113309. doi:10.1016/j.bios.2021.113309

Qing, W., Chen, K., Yang, Y., Wang, Y., and Liu, X. (2020). Cu2+-doped Carbon Dots as Fluorescence Probe for Specific Recognition of Cr(VI) and its Antimicrobial Activity. *Microchem. J.* 152, 104262. doi:10.1016/j.microc.2019.104262

Ramírez-Chavarría, R. G., Castillo-Villanueva, E., Alvarez-Serna, B. E., Carrillo-Reyes, J., Ramírez-Zamora, R. M., Buitrón, G., et al. (2022). Loop-mediated Isothermal Amplification-Based Electrochemical Sensor for Detecting SARS-

CoV-2 in Wastewater Samples. *J. Environ. Chem. Eng.* 10 (3), 107488. doi:10.1016/j.jece.2022.107488

Raza, T., Qu, L., Khokhar, W. A., Andrews, B., Ali, A., and Tian, M. (2021). Progress of Wearable and Flexible Electrochemical Biosensors with the Aid of Conductive Nanomaterials. *Front. Bioeng. Biotechnol.* 9, 761020. doi:10.3389/fbioe.2021.761020

Savchenko, A., Yin, R. T., Kireev, D., Efimov, I. R., and Molokanova, E. (2021). Graphene-Based Scaffolds: Fundamentals and Applications for Cardiovascular Tissue Engineering. *Front. Bioeng. Biotechnol.* 9, 797340. doi:10.3389/fbioe.2021.797340

Schultz, A., Knoll, T., Urban, A., Schuck, H., Von Briesen, H., Germann, A., et al. (2021). Novel Cost-Efficient Graphene-Based Impedance Biosensor for the Analysis of Viral Cytopathogenicity and the Effect of Antiviral Drugs. *Front. Bioeng. Biotechnol.* 9, 718889. doi:10.3389/fbioe.2021.718889

Song, Z., Ma, Y., Chen, M., Ambrosi, A., Ding, C., and Luo, X. (2021). Electrochemical Biosensor with Enhanced Antifouling Capability for COVID-19 Nucleic Acid Detection in Complex Biological Media. *Anal. Chem.* 93 (14), 5963–5971. doi:10.1021/acs.analchem.1c00724

Tian, J., Liang, Z., Hu, O., He, Q., Sun, D., and Chen, Z. (2021). An Electrochemical Dual-Aptamer Biosensor Based on Metal-Organic Frameworks MIL-53 Decorated with Au@Pt Nanoparticles and Enzymes for Detection of COVID-19 Nucleocapsid Protein. *Electrochimica Acta* 387, 138553. doi:10.1016/j.electacta.2021.138553

Udugama, B., Kadhiresan, P., Kozlowski, H. N., Malekjahani, A., Osborne, M., Li, V. Y. C., et al. (2020). Diagnosing COVID-19: The Disease and Tools for Detection. *ACS Nano* 14 (4), 3822–3835. doi:10.1021/acsnano.0c02624

Wen, L., Wen, C., Zhang, F., Wang, K., Yuan, H., and Hu, F. (2020). siRNA and Chemotherapeutic Molecules Entrapped into a Redox-Responsive Platform for Targeted Synergistic Combination Therapy of Glioma. *Nanomedicine Nanotechnol. Biol. Med.* 28, 102218. doi:10.1016/j.nano.2020.102218

Wiersinga, W. J., Rhodes, A., Cheng, A. C., Peacock, S. J., and Prescott, H. C. (2020). Pathophysiology, Transmission, Diagnosis, and Treatment of Coronavirus Disease 2019 (COVID-19). *JAMA* 324 (8), 782–793. doi:10.1001/jama.2020.12839

Wu, F., Zhao, S., Yu, B., Chen, Y.-M., Wang, W., Song, Z.-G., et al. (2020). A New Coronavirus Associated with Human Respiratory Disease in China. *Nature* 579 (7798), 265–269. doi:10.1038/s41586-020-2008-3

Wu, J., Wang, Q., Dong, X., Xu, M., Yang, J., Yi, X., et al. (2021). Biocompatible AIEgen/p-Glycoprotein siRNA@reduction-Sensitive Paclitaxel Polymeric Prodrug Nanoparticles for Overcoming Chemotherapy Resistance in Ovarian Cancer. *Theranostics* 11 (8), 3710–3724. doi:10.7150/thno.53828

Xie, X., Zhong, Z., Zhao, W., Zheng, C., Wang, F., and Liu, J. (2020). Chest CT for Typical Coronavirus Disease 2019 (COVID-19) Pneumonia: Relationship to Negative RT-PCR Testing. *Radiology* 296 (2), E41–E45. doi:10.1148/radiol.2020200343

Xu, L., Li, D., Ramadan, S., Li, Y., and Klein, N. (2020). Facile Biosensors for Rapid Detection of COVID-19. *Biosens. Bioelectron.* 170, 112673. doi:10.1016/j.bios.2020.112673

Xu, Z., He, H., Zhang, S., Wang, B., Jin, J., Li, C., et al. (2019). Mechanistic Studies on the Antibacterial Behavior of Ag Nanoparticles Decorated with Carbon Dots Having Different Oxidation Degrees. *Environ. Sci. Nano* 6 (4), 1168–1179. doi:10.1039/C8EN01090K

Xu, Z., and Liu, Y. (2021). The Behavior of Carbonized Polymer Dots at the Nano-Bio Interface and Their Luminescent Mechanism: A Physical Chemistry Perspective. *Chin. J. Chem.* 39 (2), 265–273. doi:10.1002/cjoc.202000334

Yan, C., Cui, J., Huang, L., Du, B., Chen, L., Xue, G., et al. (2020). Rapid and Visual Detection of 2019 Novel Coronavirus (SARS-CoV-2) by a Reverse Transcription Loop-Mediated Isothermal Amplification Assay. *Clin. Microbiol. Infect.* 26 (6), 773–779. doi:10.1016/j.cmi.2020.04.001

Yang, P., and Wang, X. (2020). COVID-19: a New Challenge for Human Beings. *Cell Mol. Immunol.* 17 (5), 555–557. doi:10.1038/s41423-020-0407-x

Yao, B., Zhang, J., Fan, Z., Ding, Y., Zhou, B., Yang, R., et al. (2021). Rational Engineering of the DNA Walker Amplification Strategy by Using a Au@Ti3C2@PEI-Ru(dcbpy)32+ Nanocomposite Biosensor for Detection of the SARS-CoV-2 RdRp Gene. *ACS Appl. Mat. Interfaces* 13 (17), 19816–19824. doi:10.1021/acsami.1c04453

Yi, X., Zeng, W., Wang, C., Chen, Y., Zheng, L., Zhu, X., et al. (2022). A Step-by-step Multiple Stimuli-Responsive Metal-Phenolic Network Prodrug Nanoparticles for Chemotherapy. *Nano Res.* 15 (2), 1205–1212. doi:10.1007/s12274-021-3626-2

Yip, T. L., Huang, Y., and Liang, C. (2021). Built Environment and the Metropolitan Pandemic: Analysis of the COVID-19 Spread in Hong Kong. *Build. Environ.* 188, 107471. doi:10.1016/j.buildenv.2020.107471

Yuan, J., Kou, S., Liang, Y., Zeng, J., Pan, Y., and Liu, L. (2020). Polymerase Chain Reaction Assays Reverted to Positive in 25 Discharged Patients with COVID-19. *Clin. Infect. Dis.* 71 (16), 2230–2232. doi:10.1093/cid/ciaa398

Zhang, K., Fan, Z., Ding, Y., and Xie, M. (2022a). A pH-Engineering Regenerative DNA Tetrahedron ECL Biosensor for the Assay of SARS-CoV-2 RdRp Gene Based on CRISPR/Cas12a Trans-activity. *Chem. Eng. J.* 429, 132472. doi:10.1016/j.cej.2021.132472

Zhang, K., Fan, Z., Ding, Y., Zhu, S., Xie, M., and Hao, N. (2022b). Exploring the Entropy-Driven Amplification Reaction and Trans-cleavage Activity of CRISPR-Cas12a for the Development of an Electrochemiluminescence Biosensor for the Detection of the SARS-CoV-2 RdRp Gene in Real Samples and Environmental Surveillance. *Environ. Sci. Nano* 9 (1), 162–172. doi:10.1039/D1EN00645B

Zhang, K., Fan, Z., Huang, Y., Ding, Y., and Xie, M. (2022c). A Strategy Combining 3D-DNA Walker and CRISPR-Cas12a Trans-cleavage Activity Applied to MXene Based Electrochemiluminescent Sensor for SARS-CoV-2 RdRp Gene Detection. *Talanta* 236, 122868. doi:10.1016/j.talanta.2021.122868

Zhang, K., Fan, Z., Huang, Y., Ding, Y., Xie, M., and Wang, M. (2022d). Hybridization Chain Reaction Circuit-Based Electrochemiluminescent Biosensor for SARS-Cov-2 RdRp Gene Assay. *Talanta* 240, 123207. doi:10.1016/j.talanta.2022.123207

Zhao, H., Liu, F., Xie, W., Zhou, T.-C., Ouyang, J., Jin, L., et al. (2021). Ultrasensitive Supersandwich-type Electrochemical Sensor for SARS-CoV-2 from the Infected COVID-19 Patients Using a Smartphone. *Sensors Actuators B Chem.* 327, 128899. doi:10.1016/j.snb.2020.128899

Zhou, P., Yang, X.-L., Wang, X.-G., Hu, B., Zhang, L., Zhang, W., et al. (2020). A Pneumonia Outbreak Associated with a New Coronavirus of Probable Bat Origin. *Nature* 579 (7798), 270–273. doi:10.1038/s41586-020-2012-7

Zhu, X., Wang, X., Han, L., Chen, T., Wang, L., Li, H., et al. (2020). Multiplex Reverse Transcription Loop-Mediated Isothermal Amplification Combined with Nanoparticle-Based Lateral Flow Biosensor for the Diagnosis of COVID-19. *Biosens. Bioelectron.* 166, 112437. doi:10.1016/j.bios.2020.112437

Zhuang, Z., Li, Y., Huang, J., Li, Z., Zhao, K., Zhao, Y., et al. (2019). Sisyphus Effects in Hydrogen Electrochemistry on Metal Silicides Enabled by Silicene Subunit Edge. *Sci. Bull.* 64 (9), 617–624. doi:10.1016/j.scib.2019.04.005

Zhuang, Z., Li, Y., Yu, R., Xia, L., Yang, J., Lang, Z., et al. (2022). Reversely Trapping Atoms from a Perovskite Surface for High-Performance and Durable Fuel Cell Cathodes. *Nat. Catal.* 5 (4), 300–310. doi:10.1038/s41929-022-00764-9

Zu, Z. Y., Jiang, M. D., Xu, P. P., Chen, W., Ni, Q. Q., Lu, G. M., et al. (2020). Coronavirus Disease 2019 (COVID-19): A Perspective from China. *Radiology* 296 (2), E15–E25. doi:10.1148/radiol.2020200490

Conflict of Interest: The authors declare that the research was conducted in the absence of any commercial or financial relationships that could be construed as a potential conflict of interest.

frontiers | Frontiers in Bioengineering and Biotechnology

TYPE Original Research
PUBLISHED 31 August 2022
DOI 10.3389/fbioe.2022.991949

OPEN ACCESS

EDITED BY
Qitong Huang,
Gannan Medical University, China

REVIEWED BY
Zhijin Fan,
Sun Yat-sen University, China
Hani Nasser Abdelhamid,
Assiut University, Egypt

*CORRESPONDENCE
Xiaojun Liu,
drliuxiaojun@163.com
Hao Tang,
tangpku_zzuhao@zzu.edu.cn
Qian Bai,
baiqian@zzu.edu.cn

†These authors have contributed equally to this work

SPECIALTY SECTION
This article was submitted to Nanobiotechnology, a section of the journal Frontiers in Bioengineering and Biotechnology

RECEIVED 12 July 2022
ACCEPTED 03 August 2022
PUBLISHED 31 August 2022

CITATION
Li Q, Feng R, Chang Z, Liu X, Tang H and Bai Q (2022), Hybrid biomimetic assembly enzymes based on ZIF-8 as "intracellular scavenger" mitigating neuronal damage caused by oxidative stress.
Front. Bioeng. Biotechnol. 10:991949.
doi: 10.3389/fbioe.2022.991949

Hybrid biomimetic assembly enzymes based on ZIF-8 as "intracellular scavenger" mitigating neuronal damage caused by oxidative stress

Qing Li[1†], Ruixia Feng[2†], Zhaohui Chang[1†], Xiaojun Liu[2*], Hao Tang[3*] and Qian Bai[2*]

[1]Department of Molecular Pathology, Application Center for Precision Medicine, The Second Affiliated Hospital of Zhengzhou University, Zhengzhou, China, [2]Department of Critical Care Medicine, Second Affiliated Hospital of Zhengzhou University, Zhengzhou, China, [3]National Health Commission Key Laboratory of Cardiovascular Regenerative Medicine, Heart Center of Henan Provincial People's Hospital, Central China Fuwai Hospital of Zhengzhou University, Fuwai Central China Cardiovascular Hospital and Central China Branch of National Center for Cardiovascular Diseases, Zhengzhou, China

Superoxide dismutase (SOD) was immobilized in zeolite imidazolate framework-8 (ZIF-8) through biomimetic mineralization method, namely SOD@ZIF-8, which was then used in the treatment of nerve damage by eliminating reactive oxygen species (ROS). A series of chemical characterization and enzymatic activity researches revealed that SOD was successfully embedded into ZIF-8 without apparent influence on the antioxidant activity of SOD. Cell level experiments showed that SOD@ZIF-8 could be effectively endocytosed by cells. The activity of SOD@ZIF-8 in scavenging ROS played a critical role in protecting SHSY-5Y cells from MPP^+-induced cell model and relieving cell apoptosis, indicating that SOD@ZIF-8 could effectively rescue ROS-mediated neurological disorders though removing excessive ROS produced *in vitro*.

KEYWORDS

biomimetic mineralization, SOD@ZIF-8, nerve damage, ROS scavenging, neurological disorders

Introduction

Reactive oxygen species (ROS), which is frequently mentioned in the field of biology and medicine, refers to oxygen-containing substances with high reactivity, specific including superoxide anion (O_2^-), hydrogen peroxide (H_2O_2), hydroxyl radical (OH), singlet oxygen ($^1O_2$), peroxide free radical (LOO), hydrogen peroxide lipid (LOOH), peroxynitro group ($ONOO^-$), hypochlorous acid (HOCl), ozone (O_3) and so on. ROS generated in the process of oxygen metabolism are essential for cell signaling and immune response (Finkel, 2011; Sena and Chandel, 2012). However, the excessive expression of ROS is deleterious especially in the brain, since it induces oxidative damage of protein,

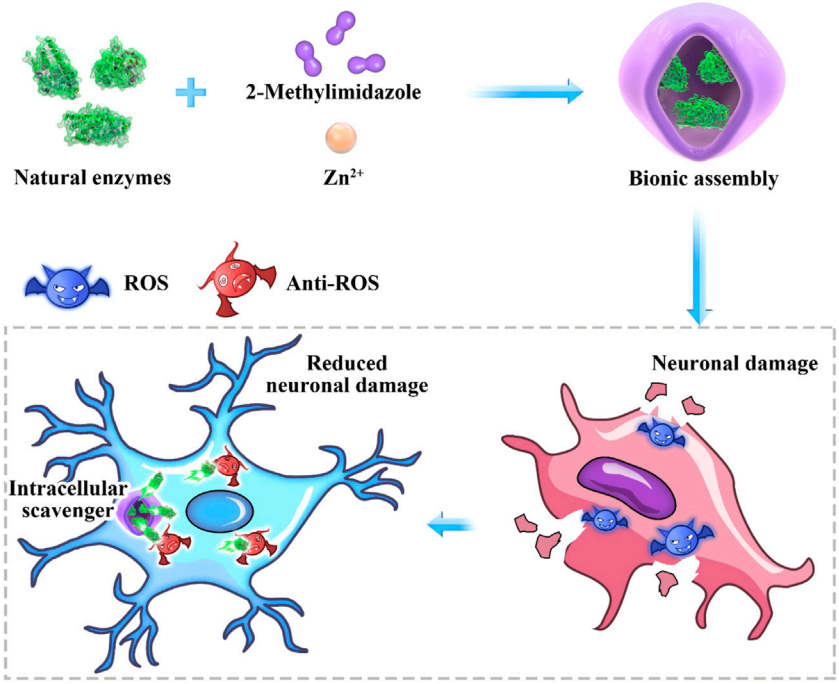

SCHEME 1
Antioxidant biomimetic assembly as "intracellular scavenger" for the treatment of neuronal damage.

lipid and DNA. As such, ROS are highly responsible for the development of many nerve damage such as cerebral palsy, Alzheimer's diseases, schizophrenia and Parkinson's diseases (PD) (Dietrich-Muszalska and Kontek, 2010; Popa-Wagner et al., 2013; Yan et al., 2013). Superoxide dismutase (SOD), as a crucial member of the antioxidant system, can efficiently catalyze the decomposition of superoxide radical to hydrogen peroxide and oxygen (Hall et al., 2010; Hu and Tirelli, 2012; Van Raamsdonk and Hekimi, 2012). Therefore, it has demonstrated therapeutic potential in the treatment of ROS-mediated diseases including inflammation, diabetes, radiation injuries, and central nervous system (CNS) disorders (Seshadri et al., 2010; Wang et al., 2010). However, due to the relatively instability character and short intracellular half-lives of proteins, direct use of SOD has been hampered by poor pharmacokinetics, rapid renal clearance, degradation by proteases in the serum and low cellular membranes penetrating ability (Tong et al., 2012; Chen et al., 2013; Liu et al., 2021a; Li et al., 2022a). Thus, to enhance SOD stability and bioavailability with desirable catalytic activity, immobilization method has been investigated by using different solid supports such as organic polymers, magnetic nanoparticles and mesoporous silica (Wu and Yang, 2017; Li et al., 2021). Among these materials, metal-organic frameworks (MOFs), consisting by metal ions nodes and organic ligands, have been increasingly proven to be a robust solid support in the enzyme immobilization due to its large surface area, tunable porosity and functionality, favorable excellent thermal/mechanical stability (Orellana-Tavra et al., 2015; Lian et al., 2016; Lian et al., 2017; Abdelhamid, 2021; Hoseinpour and Shariatinia, 2021; Li et al., 2022b). Generally, MOF-based immobilization approaches are mainly included by physical adsorption or entrapment, which have demonstrated unique advantages such as high loading efficiency of enzymes and excellent stability against high temperature and organic solvents (Ding et al., 2021). Nevertheless, these strategies are not able to achieve the size control of enzyme-MOF composites and maintain the enzymatic activity due to MOF-induced destabilization of enzymes' conformation. Recently, biomimetic mineralization approach for MOF synthesis has been adopted to encapsulate the enzyme molecules within protective exteriors through self-assembly process (Liang et al., 2015; Chen and Ma, 2016; Liang et al., 2016; Mehta et al., 2016; Abdelhamid, 2020; Fan et al., 2021). These enzyme-MOF composites are able to solve the unfavorable solvent effect of enzymatic structure and limited loading of large enzyme into MOF pores. Unlike other encapsulation approaches such as coprecipitation, enzyme molecules can trigger nucleation of porous crystals by concentrating the MOF building blocks in the process of biomimetic mineralization (Xie et al., 2010; He et al., 2016; Jiang et al., 2017; Zhu et al., 2022). Notably, enzyme-

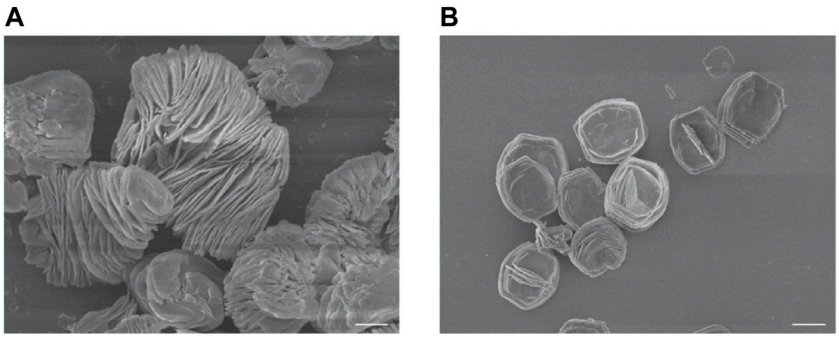

FIGURE 1
SEM images of ZIF-8 with the molar ratios of 2-dimethylimidazole and zinc acetate at 4:1 **(A)** and 24:1 **(B)**. The scale bars are 5 μm.

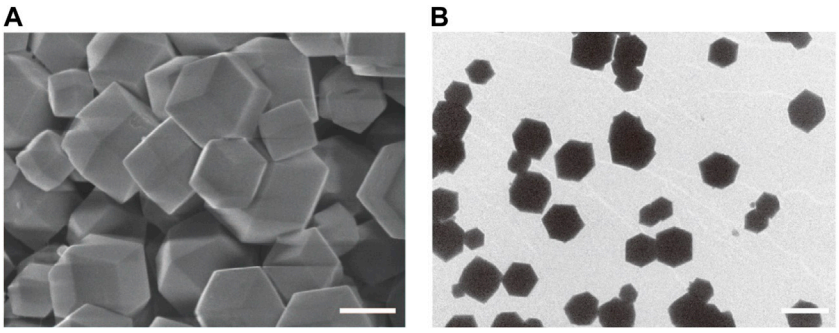

FIGURE 2
SEM images **(A)** and TEM images **(B)** of SOD@ZIF-8. The scale bars are 100 nm for A and 200 nm for **(B)**

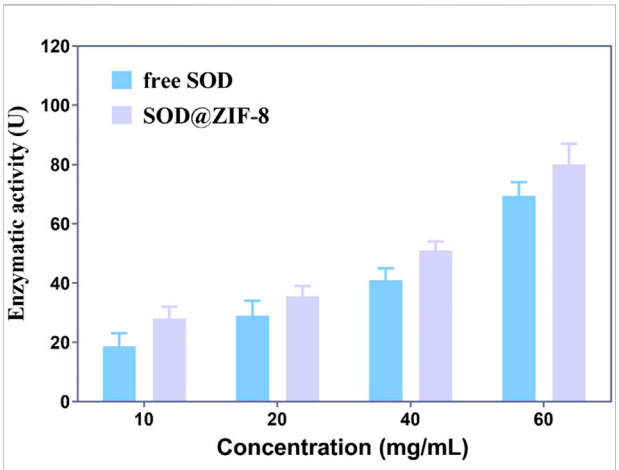

FIGURE 3
The enzymatic activities of free SOD and SOD@ZIF-8 under various concentrations.

MOF composites obtained from this method can enlarge the bioactive temperature range of enzyme and enhance the stability in a facile manner, demonstrating a great promise in the biomedical application (Montanari et al., 2012; Tabrez et al., 2012; Zhu et al., 2012; Li et al., 2020; Yang et al., 2020).

Herein, SOD was embedded into zeolite imidazolate framework-8 (ZIF-8) through biomimetic mineralization method (denoted as SOD@ZIF-8). The SOD@ZIF-8 assembly was then employed as ROS scavenger in neuronal damage treatment. Significantly, a n neuronal damage cell model was established to evaluate the therapeutic effect of SOD@ZIF-8 (Scheme 1).

Results and discussion

Firstly, ZIF-8 with various molar ratios of 2-dimethylimidazole/Zn^{2+} (4:1, 24:1 and 48:1) were synthesized

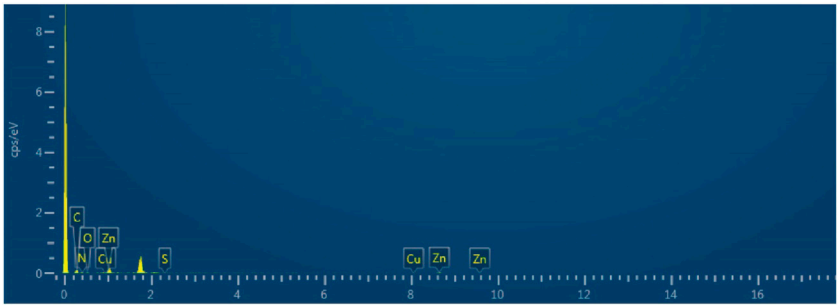

FIGURE 4
Elemental analysis of SOD@ZIF-8.

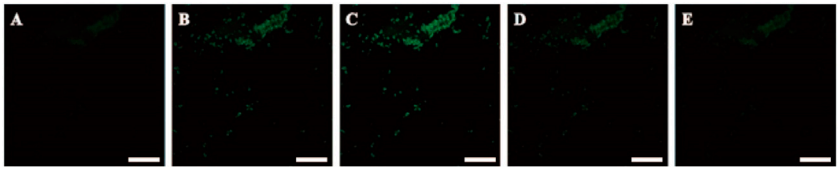

FIGURE 5
CLSM photographs of FITC-SOD@ZIF-8 with various depth at the z-axis of **(A)** 50 nm, **(B)** 100 nm, **(C)** 150 nm, **(D)** 200 nm, **(E)** 250 nm. 488 and 530 nm were chosen as the wavelengths for the detection of the fluorescence of FITC. The scale bars are 200 μm.

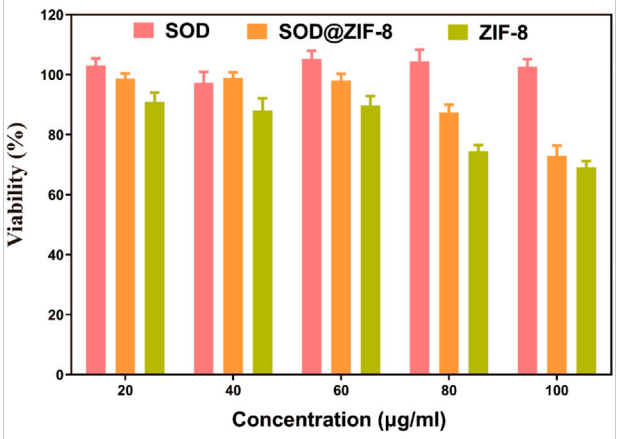

FIGURE 6
Toxicity of drugs with the same SOD content on SHSY-5Y cells. The concentrations of SOD@ZIF-8 varied from 20 to 100 μg/ml.

to investigate the suitable morphology and particle size for biomedical applications. As shown in Figure 1, micro-scaled SOD@ZIF-8 composites with size of more than 3 μm were obtained at the molar ratios of 4:1 and 24:1, respectively. Moreover, their morphology is too irregular to illustrate a single assembly enzyme complex. When the molar ratio was fixed at 48:1, regular dodecahedron structure and smaller size of SOD@ZIF-8 with 150–200 nm was achieved, which was preferable for the biomedical applications. Further, SOD was immobilized into ZIF-8 through biomimetic mineralization method. SEM and TEM images (Figure 2) suggested that the morphology and particle size did not change significantly compared with me-ZIF-8. Importantly, after ZIF-8 immobilization, the SOD activity was improved compared with free SOD (Figure 3), suggesting the biomimetic mineralization stategies could help enhance the enzymatic activities of SOD. This phenomenon might result from the fact that ZIF-8 benefit the dispersion of SOD, thus exposing more enzyme-activity centers and promoting enzymatic activity.

Meanwhile, chemical elements analysis of SOD@ZIF-8 showed the presence of Cu signal in the composites, presenting immobilization of enzyme harboring Cu element in ZIF-8 through biomimetic mineralization (Figure 4). To further validate the efficient assembly of SOD enzyme, SOD was labeled with fluorescein isothiocyanate (FITC) and then incorporated into ZIF-8 to construct FITC-labeled SOD@ZIF-8 through biomimetic mineralization. As shown in (Figure 5), green fluorescence of FITC-labeled SOD was clearly shown in the SOD@ZIF-8 assembling enzyme through laser confocal

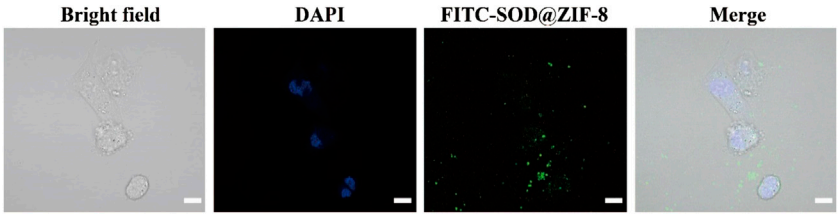

FIGURE 7
Cellular uptake ability of SOD@ZIF-8 detected by CLSM.

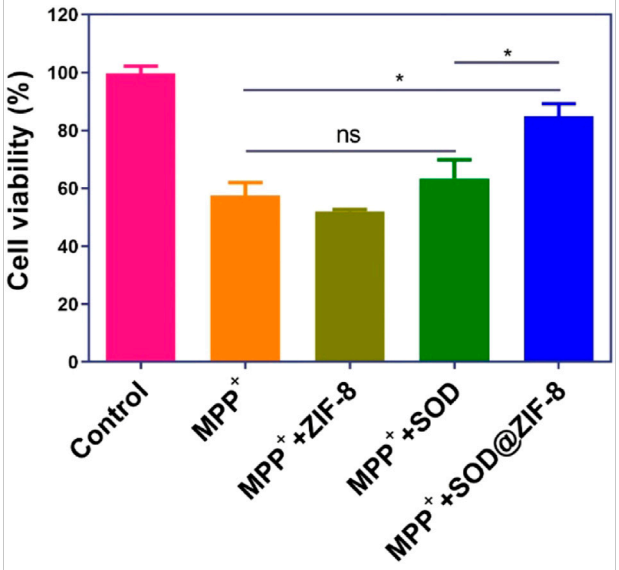

FIGURE 8
Viability of SHSY-5Y cells exposed to MPP^+ after different treatments.

microscope. The fluorescence intensity of FITC showed a gradually increasing trend from the peak to the middle and then reduced to the bottom, indicating the successful incorporation of SOD into ZIF-8. Besides, The BCA result suggested that the loading efficiency of SOD in SOD@ZIF-8 was 23.43 wt%, which was a relatively high level among the reports of SOD immobilization.

To investigate the applications of SOD@ZIF-8 composites *in vitro*, cell viability was examined to determine their potential cytotoxicity through MTT assay. As shown in Figure 6, compared with pure ZIF-8, the entrapment of SOD into ZIF-8 through biomimetic mineralization significantly reduced the cytotoxicity of ZIF-8 at various concentrations of 20–100 μg/ml. Negligible cytotoxicity was observed in SOD@ZIF-8 composites at the concentration of 60 μg/ml, indicating that SOD@ZIF-8 presented a satisfactory biocompatibility against cells. Subsequently, SOD was labeled with FITC and then employed to determine the cellular uptake of SOD@ZIF-8 by fluorescence microscope. As shown in Figure 7, strong green fluorescence was observed in FITC-SOD@ZIF-8 nanocomposites-treated cells, and It can be clearly found that the particles are located in the cell rather than on the cell surface, verifying that SOD@

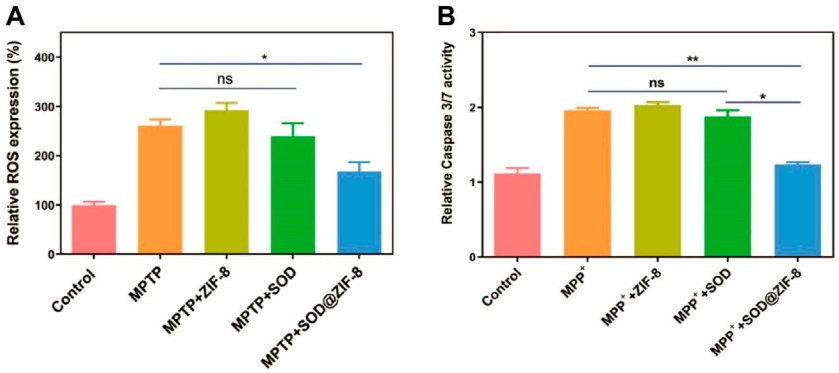

FIGURE 9
ROS scavenging activity of various nanomaterials in MPP^+ treated SHSY-5Y cells detected by flow cytometry with DCFDA-H2 dye **(A)** and the detection of apoptosis by measuring the activity of effector caspase-3/7 **(B)**.

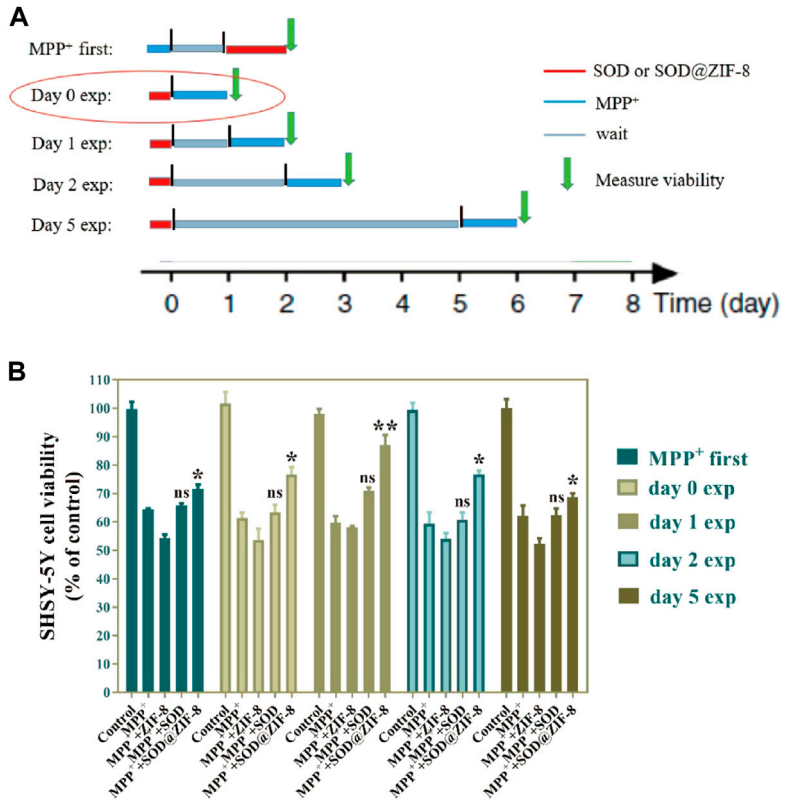

FIGURE 10
Long-term persistence effect of SOD@ZIF-8. Cells were pretreated with MPP^+ (MPP^+ first)or pretreated with SOD@ZIF-8 (Day 0 exp to Day 5 exp), washed and continued to culture for several days (gray time period in schematic diagram) and then exposed to MPP^+ for 24 h. Cell viability was quantified by MTT assay.

TABLE 1 Study on the diagnosis and treatment of oxidization-related diseases based on ZIF-8 nanomaterials.

Nanomaterials	Particle sizes	Antioxidants	Antioxidant activity	Treatment of disease	References
CeO_2@ZIF-8	About 100 nm	CeO_2	SOD, CAT	ischemic stroke	He et al. (2020)
SOD@ZIF-8	About 150 nm	SOD	SOD	Noise-induced hearing loss	Zhang et al. (2022)
ZIF-8@PB-QCT	About 100 nm	PB-QCT	SOD, CAT	Parkinson's disease	Liu et al. (2021b)

ZIF-8 were efficiently uptake by cells. The superior endocytosis of SOD@ZIF-8 composites by cells was mainly attributed to the nanosized structure, which was essential for intracellular release of SOD to cleave ROS *in vitro*.

For these encouraging advantages, we then investigated the ROS scavenging ability of SOD@ZIF-8 composites. 1-Methyl-4-phenylpyridinium (MPP^+) as a neurotoxin was able to cause cell death in human neuroblastoma SH-SY5Y cells due to the intracellular elevation of ROS and apoptosis induction, which typically was used to resemble nerve damage phenotype (Ding et al., 2021). As shown in Figure 8, obvious cell death was exhibited after SH-SY5Y cells were incubated with 2 mM MPP^+. In contrast, cells pre-treated with SOD@ZIF-8 composites demonstrated an increasing viability after exposure to MPP^+, confirming the protection afforded by SOD@ZIF-8 composites against neurotoxin. Subsequently, 2′-7′-dichlorodihydrofluorescein diacetate (DCFH-DA), which was used to directly measure the redox state of cells, were adopted to detect ROS generation of SH-SY5Y cells. As shown in Figure 9A, SH-SY5Y cells treated with MPP^+

exhibited an enhanced expression of ROS, leading to the cell death. Meanwhile, a significant decrease of ROS expression was achieved after SOD@ZIF-8 composites treatment, which was in agreement with MTT results. To confirm the protective effect of SOD@ZIF-8 composites, the activity of caspase-3 was detected. As illustrated in Figure 9B, compared with untreated cells, MPP^+ treatment triggered caspase-3 activation, leading to the apoptotic death of SH-SY5Y cells. However, a significant decrease of caspase-3 expression was achieved in SOD@ZIF-8 treatment, revealing that SOD@ZIF-8 composites inhibited apoptotic effect by downregulation of caspase-3.

To assess the long-term therapeutic effect of SOD@ZIF-8 composites, SH-SY5Y cells were incubated with SOD@ZIF-8 in advance, subsequently treated with MPP^+ following several days. As shown in Figure 10, SOD@ZIF-8 composites achieved a better protective effect compared with free SOD during 1, 2 and 5 days. Meanwhile, the protective effect afforded by SOD@ZIF-8 composites was gradually decreased in a time-dependent manner, where still 70% cell viability was achieved after 5-days treatment. These results could confirm that biomimetically mineralized enzymes maintained a persistent protective effect for cells. Interestingly, simultaneous administration of SOD@ZIF-8 composites and MPP^+ demonstrated a little lower protective effect, which was probably caused by the delayed release of SOD from SOD@ZIF-8 composites after cellular uptake. Similarly, less protective effect was achieved when cells were pre-incubated with MPP^+ and then treated with SOD@ZIF-8, indicating that SOD@ZIF-8 composites was attributed to prevention of MPP^+-induced cell damage. These results demonstrated that biomimetically mineralized SOD@ZIF-8 provided a strong therapeutic efficacy and possessed a persistent protective effect in SH-SY5Y cells. In comparison with other reports concerning about treatment of oxidative damage diseases based on ZIF-8 nanomaterials, our study exhibits satisfactory antioxidant duration and therapeutic effects (Table 1) (He, 2020; Zhang, 2022; Liu, 2021b). We believe that this study has important implications for the application of ZIF-8-based antioxidant nanomaterials in neurodegenerative diseases, as well as other diseases associated with oxidative damage.

Conclusion

In summary, SOD was successfully immobilized in the ZIF-8 through biomimetic mineralization method. The composite SOD@ZIF-8 showed satisfactory enzymatic activity and excellent stability against temperature, pH and ion environment. Moreover, compared with free SOD, SOD@ZIF-8 composites were capable of realizing efficient cellular uptake to scavenge intracellular ROS induced by MPP^+ in neuroblasts, benefiting the cell survival state and cell activity significantly. Our study suggested that SOD@ZIF-8 composites could be employed as a potential approach for the treatment of nerve damage and other oxidative stress-stimulated neurological disorders.

Methods

Construction of SOD@ZIF-8 through biomimetic mineralization

The SOD@ZIF-8 composites through biomimetic mineralization was constructed according to previous reports (Fan et al., 2021; Zhu et al., 2022). Briefly, 2 ml of 2-methylimidazole (HMeIM) solution (15.68 mg/ml) was mixed with 2 ml of $Zn(OAc)_2$ solution (8.76 mg/ml), 200 μL of methanol and 1 ml of SOD solution (1 mg/ml). The compound was incubated at room temperature for 24 h, and then solids were collected by centrifugation and washed until no absorbance at 280 nm could be detected in the supernatant. Subsequently, solids were lyophilized to obtain SOD@ZIF-8 composites. The SOD loading in ZIF-8 was determine by BCA assay kit (Beyotime, Nanjing, China). Synthesis of FITC–SOD@ZIF-8.

20 mg SOD and 10 mg FITC were dissolved in 50 ml of PBS (50 mM, pH 8.0) and the mixture was stirred at room temperature for 24 h in the dark. The mixture was dialyzed against distilled water using Amicon® Ultra-15 ultrafiltration tube (Millipore, MA) until no absorbance at 488 nm could be detected in the supernatant and then lyophilized to obtain FITC–SOD. Compound FITC–SOD@ZIF-8 was constructed as described in the above section.

SOD enzymatic activity detection

SOD enzymatic activity was determined by nitro blue tetrazolium (NBT) assay and pyrogallol autoxidation assay. For NBT assay, solution containing 75 μM NBT, 13 mM methionine, 20 μM riboflavin, and free SOD or SOD@ZIF-8 were mixed in PBS buffer (25 mM, pH 7.4), respectively. The mixtures were detected at the absorbance at 560 nm using UV-2700 spectrophotometer (Shimadzu, Kyoto, Japan). For pyrogallol autoxidation assay, 240 μL enzyme solutions (1 mg/ml) was added to 750 μL Tris-HCL (pH 8.2) and incubated for 20 min 10 μL pyrogallol solution (50 mM) was then mixed into the enzyme solutions and the absorbance at 325 nm was measured for 1 min by UV-2700 spectrometer (Shimadzu, Kyoto, Japan). Characterization of SOD@ZIF-8 Composites.

After depositing samples evenly onto a rigorously cleaved silicon wafer surface, scanning electron microscopy (SEM)

images and elemental analysis of SOD@ZIF-8 were obtained on a Hitachi FE-SEM S-4800 instrument with an acceleration voltage of 3 kV. Transmission electron microscopy (TEM) was carried on a JEM-2100F filed emission electron microscope with an acceleration voltage of 200 kV.

Cell viability assay

SH-SY5Y cells were seeded into 96-well plates at a density of 7,000 cells/well overnight. Different formulations were added into the cells for 6 h and 2 mM MPP^+ was subsequently added for 24 h. 20 μL of MTT solution (5 mg/ml) was added into each well and incubated at 37°C for another 4 h. Finally, dimethyl sulfoxide (DMSO) was used to dissolve the formed formazan crystal and the absorbance at 492 nm was measured by a GF-M3000 microplate reader (CAIHONG, Shandong, China).

ROS detection of SH-SY5Y cells

ROS levels in SHSY-5Y cells were determined according to Reactive Oxygen Species Assay Kit (Beyotime, Nanjing, China). SH-SY5Y cells were seeded into 6-well plates at a density of 2.0×10^5 cells per well and pre-treated with different formulations for 6 h. Cells were then exposed to 2 mM MPP^+ for 2 h at 37°C and stained with 10 μM DCFH-DA for 20 min at 37°C. ROS expression was detected by flow cytometry (Accuri C6, Beckman, NJ) and analyzed using Beckman Coulter software.

Statistical analysis

GraphPad Prism 8.0.2 was utilized for all statistical analyses. The outcomes were compared via Student's *t*-tests. $^*p < 0.01$, $^{**}p < 0.005$, $^{***}p < 0.001$.

Data availability statement

The original contributions presented in the study are included in the article/supplementary material, further inquiries can be directed to the corresponding authors.

Author contributions

QL, RF, ZC: Complete research and manuscript writing, XL, HT, QB: Propose design concepts and review manuscripts.

Funding

The authors are grateful for the financial support from the Henan Medical Science and Technology Research Youth Project Co-Sponsored by the Province and Ministry in China (No: SBGJ202103088). Young and middle-aged academic leaders of health in Henan Province (No: HNSWJW-2021001).

Conflict of interest

The authors declare that the research was conducted in the absence of any commercial or financial relationships that could be construed as a potential conflict of interest.

Publisher's note

All claims expressed in this article are solely those of the authors and do not necessarily represent those of their affiliated organizations, or those of the publisher, the editors and the reviewers. Any product that may be evaluated in this article, or claim that may be made by its manufacturer, is not guaranteed or endorsed by the publisher.

References

Abdelhamid, H. N (2020) Biointerface between ZIF-8 and biomolecules and their applications. *Biointerface Res. Appl. Chem.* 11 (1), 8283–8297.

Abdelhamid, H. N. (2021). Zeolitic imidazolate frameworks (ZIF-8) for biomedical applications: A review. *Curr. Med. Chem.* 28 (34), 7023–7075. doi:10.2174/0929867328666210608143703

Chen, Y.-P., Chen, C.-T., Hung, Y., Chou, C.-M., Liu, T.-P., Liang, M.-R., et al. (2013). A new strategy for intracellular delivery of enzyme using mesoporous silica nanoparticles: Superoxide dismutase. *J. Am. Chem. Soc.* 135 (4), 1516–1523. doi:10.1021/ja3105208

Chen, Y., and Ma, S. (2016). Biomimetic catalysis of metal--organic frameworks. *Dalton Trans.* 45 (24), 9744–9753. doi:10.1039/c6dt00325g

Dietrich-Muszalska, A., and Kontek, B. (2010). Lipid peroxidation in patients with schizophrenia. *Psychiatry Clin. Neurosci.* 64 (5), 469–475. doi:10.1111/j.1440-1819.2010.02132.x

Ding, S., Liu, Z., Huang, C., Zeng, N., Jiang, W., and Li, Q. (2021). Novel engineered bacterium/black phosphorus quantum dot hybrid system for hypoxic tumor targeting and efficient photodynamic therapy. *ACS Appl. Mat. Interfaces* 13, 10564–10573. doi:10.1021/acsami.0c20254

Fan, Z., Liu, H., Xue, Y., Lin, J., Fu, Y., Xia, Z., et al. (2021). Reversing cold tumors to hot: An immunoadjuvant-functionalized metal-organic framework for multimodal imaging-guided synergistic photo-immunotherapy. *Bioact. Mat.* 6 (2), 312–325. doi:10.1016/j.bioactmat.2020.08.005

Finkel, T. (2011). Signal transduction by reactive oxygen species. *J. Cell Biol.* 194 (1), 7–15. doi:10.1083/jcb.201102095

Hall, E. D., Vaishnav, R. A., and Mustafa, A. G. (2010). Antioxidant therapies for traumatic brain injury. *Neurotherapeutics* 7 (1), 51–61. doi:10.1016/j.nurt.2009.10.021

He, H., Han, H., Shi, H., Tian, Y., Sun, F., Song, Y., et al. (2016). Construction of thermophilic lipase-embedded metal--organic frameworks via biomimetic mineralization: A biocatalyst for ester hydrolysis and kinetic resolution. *ACS Appl. Mat. Interfaces* 8 (37), 24517–24524. doi:10.1021/acsami.6b05538

He, L., Huang, G., Liu, H., Sang, C., Liu, X., and Chen, T. (2020). Highly bioactive zeolitic imidazolate framework-8-capped nanotherapeutics for efficient reversal of reperfusion-induced injury in ischemic stroke. *Sci. Adv.* 6 (12), eaay9751. doi:10.1126/sciadv.aay9751

Hoseinpour, V., and Shariatinia, Z. (2021). Applications of zeolitic imidazolate framework-8 (ZIF-8) in bone tissue engineering: A review. *Tissue Cell* 72, 101588. doi:10.1016/j.tice.2021.101588

Hu, P., and Tirelli, N. (2012). Scavenging ROS: Superoxide dismutase/catalase mimetics by the use of an oxidation-sensitive nanocarrier/enzyme conjugate. *Bioconjug. Chem.* 23 (3), 438–449. doi:10.1021/bc200449k

Jiang, W., Wang, X., Chen, J., Liu, Y., Han, H., Ding, Y., et al. (2017). Deuterohemin-peptide enzyme mimic-embedded metal-organic frameworks through biomimetic mineralization with efficient ATRP catalytic activity. *ACS Appl. Mat. Interfaces* 9 (32), 26948–26957. doi:10.1021/acsami.7b09218

Li, Q., Chen, Y., Bai, S., Shao, X., Jiang, L., and Li, Q. (2020). Immobilized lipase in bio-based metal-organic frameworks constructed by biomimetic mineralization: A sustainable biocatalyst for biodiesel synthesis. *Colloids Surfaces B Biointerfaces* 188, 110812. doi:10.1016/j.colsurfb.2020.110812

Li, Q., Liu, Y., Dai, X., Jiang, W., and Zhao, H. (2021). Nanozymes regulate redox homeostasis in ROS-related inflammation. *Front. Chem.* 9, 740607. doi:10.3389/fchem.2021.740607

Li, Q., Liu, Y., Zhang, Y., and Jiang, W. (2022). Immunogenicity-boosted cancer immunotherapy based on nanoscale metal-organic frameworks. *J. Control. Release* 347, 183–198. doi:10.1016/j.jconrel.2022.05.003

Li, Q., Shao, X., Dai, X., Guo, Q., Yuan, B., Liu, Y., et al. (2022). Recent trends in the development of hydrogel therapeutics for the treatment of central nervous system disorders. *NPG Asia Mat.* 14, 14. doi:10.1038/s41427-022-00362-y

Lian, X., Chen, Y.-P., Liu, T.-F., and Zhou, H.-C. (2016). Coupling two enzymes into a tandem nanoreactor utilizing a hierarchically structured MOF. *Chem. Sci.* 7 (12), 6969–6973. doi:10.1039/c6sc01438k

Lian, X., Fang, Y., Joseph, E., Wang, Q., Li, J., Banerjee, S., et al. (2017). Enzyme--MOF (Metal--Organic framework) composites. *Chem. Soc. Rev.* 46 (11), 3386–3401. doi:10.1039/c7cs00058h

Liang, K., Coghlan, C. J., Bell, S. G., Doonan, C., and Falcaro, P. (2016). Enzyme encapsulation in zeolitic imidazolate frameworks: A comparison between controlled Co-precipitation and biomimetic mineralisation. *Chem. Commun.* 52 (3), 473–476. doi:10.1039/c5cc07577g

Liang, K., Ricco, R., Doherty, C. M., Styles, M. J., Bell, S., Kirby, N., et al. (2015). Biomimetic mineralization of metal-organic frameworks as protective coatings for biomacromolecules. *Nat. Commun.* 6, 7240. doi:10.1038/ncomms8240

Liu, Y., Hong, H., Xue, J., Luo, J., Liu, Q., Chen, X., et al. (2021). Near-infrared radiation-assisted drug delivery nanoplatform to realize blood-brain barrier crossing and protection for parkinsonian therapy. *ACS Appl. Mat. Interfaces* 13 (31), 37746–37760. doi:10.1021/acsami.1c12675

Liu, Y., Li, Q., Bai, Q., and Jiang, W. (2021). Advances of smart nano-drug delivery systems in osteosarcoma treatment. *J. Mat. Chem. B* 9, 5439–5450. doi:10.1039/d1tb00566a

Mehta, J., Bhardwaj, N., Bhardwaj, S. K., Kim, K.-H., and Deep, A. (2016). Recent advances in enzyme immobilization techniques: Metal-organic frameworks as novel substrates. *Coord. Chem. Rev.* 322, 30–40. doi:10.1016/j.ccr.2016.05.007

Montanari, R. M., Barbosa, L. C. A., Demuner, A. J., Silva, C. J., Andrade, N. J., Ismail, F., et al. (2012). Exposure to anacardiaceae volatile oils and their constituents induces lipid peroxidation within food-borne bacteria cells. *Molecules* 17 (8), 9728–9740. doi:10.3390/molecules17089728

Orellana-Tavra, C., Baxter, E. F., Tian, T., Bennett, T. D., Slater, N. K. H., Cheetham, A. K., et al. (2015). Amorphous metal--organic frameworks for drug delivery. *Chem. Commun.* 51 (73), 13878–13881. doi:10.1039/c5cc05237h

Popa-Wagner, A., Mitran, S., Sivanesan, S., Chang, E., and Buga, A.-M. (2013). ROS and brain diseases: The good, the bad, and the ugly. *Oxid. Med. Cell. Longev.* 2013, 1–14. doi:10.1155/2013/963520

Sena, L. A., and Chandel, N. S. (2012). Physiological roles of mitochondrial reactive oxygen species. *Mol. Cell* 48 (2), 158–167. doi:10.1016/j.molcel.2012.09.025

Seshadri, G., Sy, J. C., Brown, M., Dikalov, S., Yang, S. C., Murthy, N., et al. (2010). The delivery of superoxide dismutase encapsulated in polyketal microparticles to rat myocardium and protection from myocardial ischemia-reperfusion injury. *Biomaterials* 31 (6), 1372–1379. doi:10.1016/j.biomaterials.2009.10.045

Tabrez, S., R Jabir, N., Shakil, S., H Greig, N., Alam, Q., M Abuzenadah, A., et al. (2012). A synopsis on the role of tyrosine hydroxylase in Parkinson's disease. *CNS Neurol. Disord. Targets (Formerly Curr. Drug Targets-CNS Neurol. Disord.* 11 (4), 395–409. doi:10.2174/187152712800792785

Tong, J., Yi, X., Luxenhofer, R., Banks, W. A., Jordan, R., Zimmerman, M. C., et al. (2012). Conjugates of superoxide dismutase 1 with amphiphilic poly (2-oxazoline) block copolymers for enhanced brain delivery: Synthesis, characterization and evaluation *in vitro* and *in vivo*. *Mol. Pharm.* 10 (1), 360–377. doi:10.1021/mp300496x

Van Raamsdonk, J. M., and Hekimi, S. (2012). Superoxide dismutase is dispensable for normal animal lifespan. *Proc. Natl. Acad. Sci. U. S. A.* 109 (15), 5785–5790. doi:10.1073/pnas.1116158109

Wang, G., Liu, X., Guo, Q., and Namura, S. (2010). Chronic treatment with fibrates elevates superoxide dismutase in adult mouse brain microvessels. *Brain Res.* 1359, 247–255. doi:10.1016/j.brainres.2010.08.075

Wu, M.-X., and Yang, Y.-W. (2017). Metal--Organic framework (MOF)-Based drug/cargo delivery and cancer therapy. *Adv. Mat.* 29 (23), 1606134. doi:10.1002/adma.201606134

Xie, H., Hu, L., and Li, G. S. H-S. Y5Y. (2010). SH-SY5Y human neuroblastoma cell line: *In vitro* cell model of dopaminergic neurons in Parkinson's disease. *Chin. Med. J.* 123 (8), 1086–1092.

Yan, M. H., Wang, X., and Zhu, X. (2013). Mitochondrial defects and oxidative stress in alzheimer disease and Parkinson disease. *Free Radic. Biol. Med.* 62, 90–101. doi:10.1016/j.freeradbiomed.2012.11.014

Yang, Y., Zhu, D., Liu, Y., Jiang, B., Jiang, W., Yan, X., et al. (2020). Platinum-carbon-integrated nanozymes for enhanced tumor photodynamic and photothermal therapy. *Nanoscale* 12, 13548–13557. doi:10.1039/d0nr02800b

Zhang, Y., Li, Q., Han, C., Geng, F., Zhang, S., Qu, Y., et al. (2022). Superoxide dismutase@zeolite imidazolate framework-8 attenuates noise-induced hearing loss in rats. *Front. Pharmacol.* 13, 885113. doi:10.3389/fphar.2022.885113

Zhu, D., Ling, R., Chen, H., Lyu, M., Qian, H., Wu, K., et al. (2022). Biomimetic copper single-atom nanozyme system for self-enhanced nanocatalytic tumor therapy. *Nano Res.* 15 (8), 7320–7328. doi:10.1007/s12274-022-4359-6

Zhu, Y., Zhang, J., and Zeng, Y. (2012). Overview of tyrosine hydroxylase in Parkinson's disease. *CNS Neurol. Disord. Targets (Formerly Curr. Drug Targets-CNS Neurol. Disord.* 11 (4), 350–358. doi:10.2174/187152712800792901

frontiers | Frontiers in Bioengineering and Biotechnology

TYPE Mini Review
PUBLISHED 09 September 2022
DOI 10.3389/fbioe.2022.993015

OPEN ACCESS

EDITED BY
Qitong Huang,
Gannan Medical University, China

REVIEWED BY
Manoj Nayak,
CSIR-Central Scientific Instruments Organisation (CSIR-CSIO), India
Shirong Hu,
Minnan Normal University, China

*CORRESPONDENCE
Xin Du,
xdu@sdnu.edu.cn
Zhenguo Zhang,
zhangzg@sdnu.edu.cn

SPECIALTY SECTION
This article was submitted to Nanobiotechnology, a section of the journal Frontiers in Bioengineering and Biotechnology

RECEIVED 13 July 2022
ACCEPTED 12 August 2022
PUBLISHED 09 September 2022

CITATION
Zhang T, Du X and Zhang Z (2022), Advances in electrochemical sensors based on nanomaterials for the detection of lipid hormone. *Front. Bioeng. Biotechnol.* 10:993015. doi: 10.3389/fbioe.2022.993015

Advances in electrochemical sensors based on nanomaterials for the detection of lipid hormone

Tingting Zhang, Xin Du* and Zhenguo Zhang*

Shandong Provincial Key Laboratory of Animal Resistance Biology, College of Life Sciences, Shandong Normal University, Jinan, Shandong, China

Lipid hormone is produced by highly differentiated endocrine cells and directly secretes into the blood circulation or tissue fluid to act as information transmission. It influences the physiological functions of the human body by controlling the metabolic processes of multiple tissue cells. Monitoring the levels of lipid hormone is of great importance for maintaining human health. The electrochemical sensor is considered as an ideal tool to detect lipid hormone owing to its advantages such as quick response, convenience and low economic costs. In recent 3 years, researchers have developed various electrochemical sensors for the detection of lipid hormone to improve their sensitivity or selectivity. The use of nanomaterials (such as carbon nanomaterials, precious metal and polymer) is a key research object and a breakthrough for improving the sensing performance of electrochemical sensors for detection of lipid hormone. This paper reviews and discusses the basic principle, nanomaterials, actuality and future development trend of electrochemical sensors for the detection of lipid hormone in the past 3 years.

KEYWORDS

lipid hormone, electrochemical biosensor, detection principles, research progress, nanomaterials

1 Introduction

A range of hormones, including steroid and fatty acid derivative hormone, are classified as lipid hormone because of their lipid chemical makeup. Sex hormone, adrenocortical hormone and vitamin D (VD) are three primary subtypes of steroid hormones. The three primary types of fatty acid derivative hormones are prostaglandin, leukotriene, and iso-prostaglandin. Although the human body contains relatively little of these compounds, they can have a big physiological impact such as regulating menstruation (Critchley et al., 2020), preventing anxiety (McHenry et al., 2014) and regulating blood sugar levels (Vargas et al., 2020). Hormonal imbalances can be harmful to human health (Adegoke et al., 2021). Levels of all lipid hormones are significant diagnostic indicators for possible disease status (Pelizzaro et al., 2021). Thus, early detection by measuring the level of hormone has important significance for the identification of human diseases and the advancement of medical science.

Currently, the traditional analysis methods of lipid hormone are high-performance liquid chromatography (Ozgocer et al., 2017), liquid chromatography-mass spectrometry (Zhang et al., 2021), chemical luminescence method (Abdulsattar and Greenway, 2019) and enzyme-linked immunosorbent assay (Yin et al., 2019). However, these traditional detection techniques have the limitations of complex preparation steps, high analysis costs and time-consuming. Under these circumstances, electrochemical biosensors offer certain benefits over conventional analytical techniques, including simplicity, portability and quick detection. (Felix and Angnes, 2018) which has been applied in the fields of drug research, clinical diagnosis, food safety testing, environmental monitoring and other fields (Aydin et al., 2019). The types of the electrochemical sensor of lipid hormone that have been reported including electrochemical immunosensors (Mathew et al., 2020), electrochemical aptamer sensing (Tang et al., 2022) and electrochemical molecular imprinted polymer (MIP) sensors (Rebelo et al., 2020). Many nanomaterials including graphene, carbon nanotubes, gold nanoparticles (AuNPs) and adapters were applied in the preparation of the sensor.

This paper mainly reviews the application of electrochemical biosensors in lipid hormone detection in the past 3 years, including various kinds of detection principles, the application of nanomaterials, performance and advantages of these electrochemical sensors. We also summarize the future direction of electrochemical biosensors in lipid hormone detection, containing the challenges of current techniques and emerging applications.

2 Principle of electrochemical sensors for detection of lipid hormone

The biosensor is an instrument that uses immobilized bio-sensitive materials (antibodies, enzymes, receptors, cells, microorganisms, nucleic acids, etc.) as biometric elements to recognize the required target molecule and converts the analyte concentration into electrical signals for detection (Ronkainen et al., 2010). In general, an electrochemical biosensor has three components including biometric elements, sensors and electronic systems.

Nanomaterials are often applied to modify the electrode to amplify the detection signal. Commonly used nanomaterials include carbon nanomaterials (such as carbon nanotubes, carbon quantum dots and graphene), precious metal nanomaterials [such as gold (Au) and silver (Ag)], metal oxides (such as copper oxide and titanium oxide), polymer nanomaterials (such as MIP and conducting polymers) and biological nanomaterials (such as adapters) (Raza et al., 2021). Furthermore, the synergistic effect of multi-component nanomaterials can provide more obvious additional advantages.

The common detection methods of electrochemical sensors are cyclic voltammetry (CV), differential pulse voltammetry (DPV), square wave voltammetry (SWV) and electrochemical impedance spectrum (EIS). These detection methods all have their own uses and characteristics: CV may be used to verify both the reversibility of a reaction and the existence of intermediates in redox processes. With DPV and SWV, target analytes can even be detected at picomolar or femtomolar concentrations (Goud et al., 2021). EIS may be used to determine if the electrode/electrolyte interface impedance changes when the target is bound to the surface-immobilized biorecognition element. It has broad measured range and high detection stability as its main traits (Li et al., 2019). With the progress of electrochemical sensors, the detection method has gradually developed from desktop to portable and wearable biosensors (Samson and Koh, 2020). The schematic representation of the electrochemical biosensor for detection of lipid hormone is shown in Figure 1.

3 Research on the electrochemical sensor of lipid hormone

Electrochemical sensors for the detection of lipid hormone have had significant success recently. A summary of electrochemical sensors for the detection of lipid hormone is listed in Table 1.

3.1 Electrochemical sensors for the detection of steroid hormone

Current electrochemical sensing technology to detect steroid hormone is mainly used for early diagnosis of disease, pregnancy research, food toxicity and pollution levels (Kelch et al., 2020). The following is a review of the electrochemical sensors of progesterone, 17β-estradiol, testosterone, cortisol, and VD.

3.1.1 Electrochemical sensors for the detection of progesterone

Progesterone is most commonly used as a pregnancy biomarker (Goh et al., 2016), which also has a central role in biology and medicine (Kanninen et al., 2019; Polat et al., 2020). Monitoring progesterone concentrations has been reported to be important in the autoimmune disease in women during menstruation (Chang and Wang, 2020), the dairy industry that can supply trustworthy data on mammalian reproduction by keeping track of progesterone levels (Yu and Maeda, 2017) and the environmental health protection by monitoring the progesterone in the wastewater (Cui et al., 2021).

Naderi and Jalali modified glassy carbon electrode (GCE) for progesterone accurately trace analysis in human serum samples and medicines using multi-wall carbon nanotubes (MWCNTs),

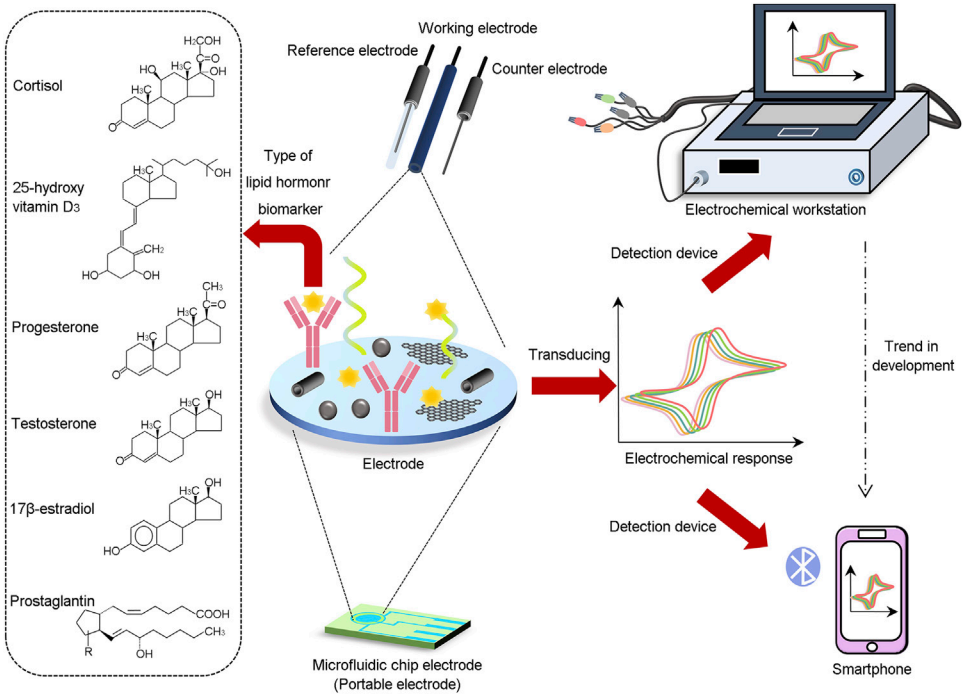

FIGURE 1
Schematic representation of the electrochemical biosensor for detection of lipid hormone.

AuNPs and poly-L-serine (Naderi and Jalali, 2020). DishaKumari et al. (2021) used magnetic graphene oxide (MGO) nanocomposite as an electrode material for the loading of bio-receptors. The increased surface area with strong electric conductivity improved sensor responsiveness. This design amplified the electrochemical signal and avoided the requirement of labeling enzymes and substrates.

Recently, progesterone detection has been accomplished using a variety of aptamer-based sensor designs. A photo-electrochemical sensor was created by Li et al. (2020) using magnetic-optical $Fe_3O_4@SiO_2@TiO_2$-NH_2-aptamer-nanoparticles. The sensor could selectively capture progesterone in complex biological samples. Samie and Arvand prepared a label-free electrochemical progesterone aptamer sensor using graphene quantum dots-NiO-Au hybrid nanofibers/NH_2 functionalized MWCNTs (GQDs-NiO-AuNFs/f-MWCNTs) and was successfully used to determine progesterone in human serum samples and pharmaceutical preparations (Samie and Arvand, 2020). Moreover, Zhu's team simultaneously used antibodies and aptamer together to propose a progesterone sandwich assay, designing a sandwich-structured cathode photochemical biosensor (Zhu et al., 2020). The advantages of the sensor were easier progesterone determination, higher sensitivity and selectivity.

3.1.2 Electrochemical sensors for the detection of estradiol

So far, multiple electrochemical sensors of estradiol were aiming for 17β-estradiol, which is a natural estrogen secreted by humans and domestic animals with the strongest estrogen activity. Even trace amounts of exogenous 17β-estradiol entering the body can cause significant damage to our health (Pu et al., 2019). So, effective 17β-estradiol monitoring is important.

In the research field of 17β-estradiol electrochemical sensor, composite nanomaterials made of carbon nanomaterials and other nanomaterials have been widely used. Tanrikut's team prepared a highly efficient sensor to detect 17β-estradiol by using the $NiFe_2O_4$-mesoporous carbon ($NiFe_2O_4$-MC) nanocomposite which displayed an optimal electron transfer rate (Tanrikut et al., 2020). Supchocksoonthorn et al. designed a 17β-estradiol sensor employing carbon dots/polyaniline (CDs/PANI) composite (Supchocksoonthorn et al., 2021). 17β-estradiol and CDs/PANI are connected by hydrogen bonds and stacking to govern adsorption. Chang et al. demonstrated a split aptamer-based electrochemical estradiol aptamer sensor, with the first piece functionalized with adamantane and the second piece that had gold nanoparticles label (Chang et al., 2021). The disposable laser-scribed graphene electrode strip

TABLE 1 A summary of electrochemical sensors for the detection of lipid hormone.

Lipid hormone	Nanomaterials	Electrochemical Method	Sample	Linear range (nM)	Detection limit (nM)	Reference
progesterone	poly-L-serine/AuNPs/MWCNTs	CV, EIS	human serum	1–2000	200	Naderi and Jalali, (2020)
progesterone	MGO	DPV, CV	tap water	1×10^{-4}–1000	1.5×10^{-4}	DishaKumari et al. (2021)
progesterone	Fe_3O_4@SiO_2@ TiO_2–NH_2–aptamer–cDNA	EIS	milk	0.001–6	3×10^{-4}	Li et al. (2020)
progesterone	BSA/aptamer/GQDs-NiO-AuNFs/f-MWCNTs	DPV	human serum, pharmaceutical products	10–100	1.8×10^{3}	Samie and Arvand, (2020)
progesterone	aptamer-Au-CuO-Cu_2O/ progesterone/Ab/CDs-GO	photoelectrochemical	human serum	0.5–180	0.17	Zhu et al. (2020)
17β-estradiol	$NiFe_2O_4$-MC	CV, DPV, SWV	drug tablets	20–566	6.88	Tanrikut et al. (2020)
17β-estradiol	CDs-PANI	CV	human serum, water	$1\text{-}1 \times 10^{5}$	43	Supchocksoonthorn et al. (2021)
17β-estradiol	poly(β-CD)/AF1-ADA/ON1/ AF2-Au	DPV, EIS	milk	0.001–10	7×10^{-7}	Chang et al. (2021)
17β-estradiol	EIPs/WS_2	CV	eel serum	0.37–3,671.34	2.08×10^{-7}	Lee et al. (2020)
17β-estradiol	MIP/CB	DPV	river water	100–2.3×10^{4}	30	da Silva and Pereira, (2022)
17β-estradiol	MIP	CV, SWV	real water	0.01–100	0.06	Regasa and Nyokong, (2022)
testosterone	TIECP	CV	human urine	0.35–346.72	~pM	Liu et al. (2020)
testosterone	Ab/pBDBT	amperometric	synthetic urine and serum	34.67–1733.58	58.08	Bulut et al. (2020)
cortisol	ALP/1-NPP	CV	human serum	0–1091.46	63.03	Vargas et al. (2020)
cortisol	AuNPs/MWCNTs	CV, DPV	human sweat	2.73×10^{-6}-273	8.19×10^{-7}	Liu et al. (2021)
cortisol	DTSP/AuNPs/graphene	CV	artificial sweat	0.03–212.87	0.03	Naik et al. (2021)
cortisol	MIP	CV	artificial sweat	10–1000	0.2	Tang et al. (2021)
cortisol	poly(GMA-co-EGDMA)/ CNC/CNT	CV, EIS	human sweat	27.29–180.09	5.46 ± 1.09	Mugo and Alberkant, (2020)
cortisol	MWCNTs/CMK-3/AgNPs	CV, DPV	human saliva	2.7×10^{-4}–2.7×10^{-2}	2.5×10^{-4}	Huang et al. (2021)
cortisol	MIP-aptamer/N-CQDs-FG	CV, DPV, EIS	human saliva	0.001-10	3.3×10^{-4}	Yu et al. (2022)
VD	graphene/Nafion	CV, SWV, EIS	food	113.64–5681.82	35.79	Thangphatthanarungruang et al. (2020)
25(OH)D_3	BSA/Ab-25(OH)D_3/EDC-NHS/ GCN-β-CD@AuNPs	CV, DPV, EIS	serum	0.25–1247.97	0.03	Anusha et al. (2022)
25(OH)D_3	Ab/Cys/Au/MoS_2	CV, DPV, EIS	human serum	0.0025–249.59	9×10^{-4}	Kaur et al. (2021)
VD_3	GQD-Au/aptamer-VD_3	EIS	human serum	1–500	0.7	Wadhwa et al. (2020)
25(OH)D_3	CHA/DNA tetrahedron	CV, SWV, EIS	human serum	0.1–1000	0.026	Shuo et al. (2021)
VD_3	Co-Ag/PANI-PPY/IL	CV, SWV, EIS	human serum and urine	12.5–22,500	7.3	Anusha et al. (2021)
PGE2	anti-PGE2/DSP	EIS	human urine	0.28–11.35		Ganguly et al. (2021)

1-NPP, 1-Naphthyl phosphate; DTSP, dithiobis (succinimidyl propionate); GA, glutaraldehyde; CNC, carbon nanotube; CNT, cellulose nanocrystal; CMK-3, ordered mesoporous carbon CMK-3; Cys, Cysteamine; DSP, thiol cross-linker.

with exceptional sensitivity was successfully created from the sensing platform. In order to find 17β-estradiol in the eel Lee et al. (2020) serum, developed a screen-printed carbon electrode (SPCE) with 17β-estradiol-imprinted poly (aniline-co-metanilic acid) (EIPs) and tungsten disulfide (WS_2). Da Silva and Pereira modified the electrode with MIP and carbon black (CB) to improve the sensitivity of the electrode by more than 173% compared with GCE (da Silva and Pereira, 2022). This electrochemical sensor could be easily fabricated and detect 17β-estradiol rapidly with a limit of detection (LOD) of 30 nM.

In addition to MIP electrochemical sensors based on carbon nanomaterials, Regasa and Nyokong created an electrochemical sensor based on MIP supported by AgNPs capped with 2-mercaptobenzoxazole (Regasa and Nyokong, 2022). The sensor was used to measure 17β-estradiol in actual

water samples without the need of sample preconcentration processes, resulting in satisfactory selectivity, sensitivity, reusability and storage stability performances.

3.1.3 Electrochemical sensors for the detection of testosterone

Testosterone is the most essential steroid released by testicular stromal cells (Gugoasa and Stefan-van Staden, 2018) whose levels are related to many male hormone disorders and cardiovascular diseases.

To create a testosterone-imprinted electronically conductive polymer (TIECP) on the sensing electrodes, Liu et al. optimized the synthetic self-assembly of poly (aniline-co-metanilic acid) and testosterone using an electrochemical method (Liu et al., 2020). This technique optimized the conductivity of nanomaterials. Moreover, Bulut's team synthesized a new phenylenediamine-benzodithiophene polymer (pBDBT) used to manufacture biosensors for testosterone detection (Bulut et al., 2020). A platform for real-time field detection was provided by glutaraldehyde-fixed testosterone antibodies on the polymer-coated SPCE surface. It can be used for testosterone analysis in illicit drugs.

3.1.4 Electrochemical sensor for the detection of cortisol

Cortisol is an important glucocorticoid found in a variety of biological fluids. Abnormally elevated cortisol levels can cause hypertension, damage to muscle tissue and immune system.

Now, more and more studies of electrochemical sensors for cortisol are being developed. For example, Vargas et al. (2020) developed a dual-electrochemical immunosensor based on gold microchip for the simultaneous detection of insulin and cortisol, which relied on competitive immunoassays with alkaline phosphatase (ALP) labeling . In addition, Liu et al. (2021) designed the electrochemical immunosensor for flexible AuNPs/MWCNTs/polydimethylsiloxane thin films and Naik et al. (2021) designed the "smart bandage" microfluidic platform sensor for graphene/silver solution. These three sensors are all used to detect cortisol and have the potential for instant applications.

In the study of cortisol molecularly imprinted polymers sensors, Tang et al. (2021). used a high permeability sweat-absorbing porous hydrogel to prepare a non-invasive, touch-based MIP electrochemical sensor Besides, poly glycidylmethacrylate-co ethylene glycol dimethacrylate (GMA-co-EGDMA) were used for the research of flexible MIP biosensor (Mugo and Alberkant, 2020). These two sensors have the advantages of being stretchable, small-portable and without sampling, and can serve as human wearable devices and instant application devices.

In addition to using a single biometric element to develop sensors, Huang et al. (2021) presented a highly sensitive and selective electrochemical sensor with an aptamer-antibody sandwich mode A specific combination of antibodies and aptamers was utilized to identify the target cortisol. Whereafter, Yu et al. (2022) suggested a novel electrochemical aptamer sensor using functionalized graphene (FG) and nitrogen-deqcarbon quantum dots (N-CQDs) integrating MIP techniques for trace analysis of cortisol in saliva samples.

3.1.5 Electrochemical sensors for the detection of VD

VD is not only a lipid-soluble vitamin but also an immunomodulatory hormone that has two present forms of VD_2 and VD_3 (Charoenngam and Holick, 2020). As the best marker for the monitoring of VD levels, 25-hydroxy VD (25(OH) D) is frequently employed in clinical diagnosis (Binkley et al., 2010; Farrell and Herrmann, 2013).

In the field of VD electrochemical sensors based on carbon nanomaterials, Thangphatthanarungruang prepared a graphene nanocomposite sensor for simultaneously measuring vitamins (A, D, E and K) that are lipid-soluble in various matrix samples (infant milk, yogurt and parsley) (Thangphatthanarungruang et al., 2020). Anusha designed a label-free impedance sensor using ethyl-3-(3-dimethyl aminopropyl) carbodiimide-N-hydroxysuccinimide/graphitic carbon nitride-β-cyclodextrin (EDC-NHS/GCN-β-CD) @AuNPs composite to assay serum samples for the presence of $25(OH)D_3$ (Anusha et al., 2022). It is less destructive to its biomolecular activity, thus improving the sensitivity of detection. Kaur et al. (2021) designed a voltammetric immunosensor based on molybdenum sulfur MoS_2/AuNPs/tin fluoride oxide with $25(OH)D_3$ as the target molecule The result showed that the MoS_2-modified AuNPs model demonstrated excellent detection conductivity, sensitivity and stability.

Some electrochemical sensors using VD_3 aptamer were also reported. Wadhwa's team prepared a portable electrochemical aptamer sensor to identify VD_3 employing graphene quantum dot-gold hybrid nanoparticles (GQD-Au) with a LOD of 0.70 nM (Wadhwa et al., 2020). Subsequently, Shuo et al. (2021) proposed a novel electrochemical aptamer sensor for sensitively detecting $25(OH)D_3$ by fixing DNA tetrahedra on Au surfaces and a technique for catalytic hairpin assembly (CHA) amplification.

In addition, Anusha's group synthesized a new composite material based on polyaniline-polypyrrole (PANI-PPY) copolymer doped with silver-cobalt (Co-Ag) and ionic liquid (IL) (Anusha et al., 2021). The composite material was first used to modify the GCE. Later, a manual paper sensor was created using the suggested material. And using two different tests to detect VD_3 in serum and urine samples.

3.2 Electrochemical sensors for the detection of fatty acid derivative hormone

The fatty acid derivative hormone is a metabolite produced by lipids through oxidative and enzymatic metabolic pathways including iso-prostaglandin and prostaglandin. Prostaglandin regulates pathological processes in female reproductive function (Niringiyumukiza et al., 2018), inflammation, and tissue repair (Rael, 2016). The lipid peroxidation biomarker 8-iso-prostaglandin F2α and carotid subclinical atherosclerosis showed a significant positive connection (Alharby et al., 2019).

In previous reports, electrochemical sensors of prostaglandin E1 (Zheng et al., 2016) and 8-iso-prostaglandin F2α (Sanchez-Tirado et al., 2017) have been successively reported. With the deepening understanding of the fatty acid derivative hormone and the development of electrochemical sensors, Ganguly et al. (2021) developed a three-electrode planar gold microelectrode system with flow-based nanopore membranes for electrochemical immunosensors for detecting prostaglandin E2 (PGE2). This sensor can be used in both clinical and home settings for a more immediate, fast and accurate diagnosis of urinary tract infection.

4 Conclusion and future perspectives

This paper mainly describes the recent research progress of electrochemical biosensors in the field of lipid hormone detection in the past 3 years. This could help the future development of such sensors in medicine and science. Furthermore, combined with the important role and significance of lipid hormones such as progesterone, estradiol, testosterone, cortisol, VD, prostaglandin in regulating human life activities and disease control, and the easy application of electrochemical sensors, the development of lipid hormone electrochemical sensors has attracted more and more attention in recent years.

Overall, so far, there are more comprehensive and mature studies of steroid electrochemical sensors than those of fatty acid derivative. Current electrochemical biosensors for fatty acid derivative hormone use only antibodies as recognition elements. In the future, electrochemical sensors will have considerable potential for development and applications in the detection of lipid hormone. A key opportunity for the development of electrochemical sensor and biosensor platforms is the introduction of innovative functional nanomaterials and analytical technologies. Such as new electrode materials with more selectivity and sensitivity, more portable wearable sensors and instant application sensors still need to be continuously explored by researchers.

Author contributions

TZ: conceptualization and writing—original draft preparation. XD and ZZ: validation, writing—review and editing, and project administration. All authors contributed to the article and approved the submitted version.

Funding

This work was supported by grants from the National Natural Science Foundation of China (32170921 and 32170734), and the Young Talent of Lifting Engineering for Science and Technology in Shandong, China (SDAST2021qt07).

Conflict of interest

The authors declare that the research was conducted in the absence of any commercial or financial relationships that could be construed as a potential conflict of interest.

Publisher's note

All claims expressed in this article are solely those of the authors and do not necessarily represent those of their affiliated organizations, or those of the publisher, the editors and the reviewers. Any product that may be evaluated in this article, or claim that may be made by its manufacturer, is not guaranteed or endorsed by the publisher.

References

Abdulsattar, J. O., and Greenway, G. M. (2019). A sensitive chemiluminescence based immunoassay for the detection of cortisol and cortisone as stress biomarkers. *J. Anal. Sci. Technol.* 10 (1), 34. doi:10.1186/s40543-019-0196-y

Adegoke, E. O., Rahman, M. S., Park, Y.-J., Kim, Y. J., and Pang, M.-G. (2021). Endocrine-disrupting chemicals and infectious diseases: From endocrine disruption to immunosuppression. *Int. J. Mol. Sci.* 22 (8), 3939. doi:10.3390/ijms22083939

Alharby, H., Abdelati, T., Rizk, M., Youssef, E., Moghazy, K., Gaber, N., et al. (2019). Association of lipid peroxidation and interleukin-6 with carotid atherosclerosis in type 2 diabetes. *Cardiovasc. Endocrinol. Metab.* 8 (3), 73–76. doi:10.1097/XCE.0000000000000175

Anusha, T., Bhavani, K. S., Kumar, J. V. S., Bonanni, A., and Brahman, P. K. (2021). Fabrication of handmade paper sensor based on silver-cobalt doped copolymer-ionic liquid composite for monitoring of vitamin D-3 level in real samples. *Microchem. J.* 161, 105789. doi:10.1016/j.microc.2020.105789

Anusha, T., Bhavani, K. S., Kumar, J. V. S., Brahman, P. K., and Hassan, R. Y. A. (2022). Fabrication of electrochemical immunosensor based on GCN-beta-CD/Au nanocomposite for the monitoring of vitamin D deficiency. *Bioelectrochemistry* 143, 107935. doi:10.1016/j.bioelechem.2021.107935

Aydin, E. B., Aydin, M., and Sezginturk, M. K. (2019). Advances in electrochemical immunosensors. *Adv. Clin. Chem.* 92, 1–57. doi:10.1016/bs.acc.2019.04.006

Binkley, N., Krueger, D. C., Morgan, S., and Wiebe, D. (2010). Current status of clinical 25-hydroxyvitamin D measurement: An assessment of between-laboratory agreement. *Clin. Chim. Acta* 411, 1976–1982. doi:10.1016/j.cca.2010.08.018

Bulut, U., Sanli, S., Cevher, S. C., Cirpan, A., Donmez, S., and Timur, S. (2020). A biosensor platform based on amine functionalized conjugated benzenediamine-benzodithiophene polymer for testosterone analysis. *J. Appl. Polym. Sci.* 137, 49332. doi:10.1002/app.49332

Chang, Y., and Wang, M. (2020). Recurrent erythema before menses: Autoimmune progesterone dermatitis caused by hypersensitivity to progesterone. *Am. J. Obstetrics Gynecol.* 222 (5), 501–502. doi:10.1016/j.ajog.2019.08.033

Chang, Z., Zhu, B., Liu, J., Zhu, X., Xu, M., and Travas-Sejdic, J. (2021). Electrochemical aptasensor for 17 beta-estradiol using disposable laser scribed graphene electrodes. *Biosens. Bioelectron. X.* 185, 113247. doi:10.1016/j.bios.2021.113247

Charoenngam, N., and Holick, M. A.-O. (2020). Immunologic effects of vitamin D on human health and disease. *Nutrients* 12, 2097. doi:10.3390/nu12072097

Critchley, H. O. D., Maybin, J. A., Armstrong, G. M., and Williams, A. R. W. (2020). Physiology of the endometrium and regulation of menstruation. *Physiol. Rev.* 100 (3), 1149–1179. doi:10.1152/physrev.00031.2019

Cui, X., Shu, H., Wang, L., Chen, G., Han, J., Hu, Q., et al. (2021). Methacrylic functionalized hybrid carbon nanomaterial for the selective adsorption and detection of progesterone in wastewater. *Environ. Sci. Pollut. Res.* 28 (44), 62306–62320. doi:10.1007/s11356-021-15056-1

da Silva, D. N., and Pereira, A. C. (2022). An electrochemical sensor modified with a molecularly imprinted polymer and carbon black for 17-β-estradiol detection. *Anal. Methods* 14, 1208–1213. doi:10.1039/d1ay02062e

DishaKumari, P., Nayak, M. K., and Kumar, P. (2021). An electrochemical biosensing platform for progesterone hormone detection using magnetic graphene oxide. *J. Mat. Chem. B* 9 (26), 5264–5271. doi:10.1039/d1tb00380a

Farrell, C.-J., and Herrmann, M. (2013). Determination of vitamin D and its metabolites. *Best Pract. Res. Clin. Endocrinol. Metabolism* 27, 675–688. doi:10.1016/j.beem.2013.06.001

Felix, F. S., and Angnes, L. (2018). Electrochemical immunosensors - a powerful tool for analytical applications. *Biosens. Bioelectron. X.* 102, 470–478. doi:10.1016/j.bios.2017.11.029

Ganguly, A., Ebrahimzadeh, T., Zimmern, P. E., De Nisco, N. J., and Prasad, S. (2021). Label free, lateral flow prostaglandin E2 electrochemical immunosensor for urinary tract infection diagnosis. *Chemosensors* 9 (9), 271. doi:10.3390/chemosensors9090271

Goh, J. Y., He, S., Allen, J. C., Malhotra, R., and Tan, T. C. (2016). Maternal obesity is associated with a low serum progesterone level in early pregnancy. *Horm. Mol. Biol. Clin. Investig.* 27 (3), 97–100. doi:10.1515/hmbci-2015-0030

Goud, K. Y., Reddy, K. K., Khorshed, A., Kumar, V. S., Mishra, R. K., Oraby, M., et al. (2021). Electrochemical diagnostics of infectious viral diseases: Trends and challenges. *Biosens. Bioelectron.* 180, 113112. doi:10.1016/j.bios.2021.113112

Gugoasa, L. A., and Stefan-van Staden, R.-I. (2018). Advanced methods for the analysis of testosterone. *Curr. Med. Chem.* 25 (33), 4037–4049. doi:10.2174/0929867324666170724102602

Huang, Z., Chen, H., Ye, H., Chen, Z., Jaffrezic-Renault, N., and Guo, Z. (2021). An ultrasensitive aptamer-antibody sandwich cortisol sensor for the noninvasive monitoring of stress state. *Biosens. Bioelectron. X.* 190, 113451. doi:10.1016/j.bios.2021.113451

Kanninen, T. T., Moretti, M. L., and Lakhi, N. A. (2019). Autoimmune progesterone dermatitis following vaginal progesterone exposure in pregnancy. *Obstet. Med.* 12 (2), 100–102. doi:10.1177/1753495X18771255

Kaur, A., Rana, S., Bharti, A., Chaudhary, G. R., and Prabhakar, N. (2021). Voltammetric detection of vitamin D employing Au-MoS2 hybrid as immunosensing platform. *Microchim. Acta* 188 (7), 222. doi:10.1007/s00604-021-04862-6

Kelch, J., Delaney, A., Kelleher, F., Baker, P., Iwuoha, E., and Dempsey, E. (2020). Impedimetric and electrochemical evaluation of a new redox active steroid derivative for hormone immunosensing. *Biosens. Bioelectron. X.* 150, 111876. doi:10.1016/j.bios.2019.111876

Lee, M.-H., Thomas, J. L., Su, Z.-L., Zhang, Z.-X., Lin, C.-Y., Huang, Y.-S., et al. (2020). Doping of transition metal dichalcogenides in molecularly imprinted conductive polymers for the ultrasensitive determination of 17 beta-estradiol in eel serum. *Biosens. Bioelectron. X.* 150, 111901. doi:10.1016/j.bios.2019.111901

Li, F., Yu, Z., Han, X., and Lai, R. Y. (2019). Electrochemical aptamer-based sensors for food and water analysis: A review. *Anal. Chim. Acta* 1051, 1–23. doi:10.1016/j.aca.2018.10.058

Li, H., Li, Y., Li, J., Yang, F., Xu, L., Wang, W., et al. (2020). Magnetic-optical core-shell nanostructures for highly selective photoelectrochemical aptasensing. *Anal. Chem.* 92 (5), 4094–4100. doi:10.1021/acs.analchem.9b05762

Liu, K.-H., O'Hare, D., Thomas, J. L., Guo, H.-Z., Yang, C.-H., and Lee, M.-H. (2020). Self-assembly synthesis of molecularly imprinted polymers for the ultrasensitive electrochemical determination of testosterone. *Biosens. (Basel).* 10 (3), 16. doi:10.3390/bios10030016

Liu, Q., Shi, W., Tian, L., Su, M., Jiang, M., Li, J., et al. (2021). Preparation of nanostructured PDMS film as flexible immunosensor for cortisol analysis in human sweat. *Anal. Chim. Acta* 1184, 339010. doi:10.1016/j.aca.2021.339010

Mathew, M., Radhakrishnan, S., Vaidyanathan, A., Chakraborty, B., and Rout, C. S. (2020). Flexible and wearable electrochemical biosensors based on two-dimensional materials: Recent developments. *Anal. Bioanal. Chem.* 413, 727–762. doi:10.1007/s00216-020-03002-y

McHenry, J., Carrier, N., Hull, E., and Kabbaj, M. (2014). Sex differences in anxiety and depression: Role of testosterone. *Front. Neuroendocrinol.* 35 (1), 42–57. doi:10.1016/j.yfrne.2013.09.001

Mugo, S. M., and Alberkant, J. (2020). Flexible molecularly imprinted electrochemical sensor for cortisol monitoring in sweat. *Anal. Bioanal. Chem.* 412 (8), 1825–1833. doi:10.1007/s00216-020-02430-0

Naderi, P., and Jalali, F. (2020). Poly-L-serine/AuNPs/MWCNTs as a platform for sensitive voltammetric determination of progesterone. *J. Electrochem. Soc.* 167 (2), 027524. doi:10.1149/1945-7111/ab6a7f

Naik, A. R., Zhou, Y., Dey, A. A., Arellano, D. L. G., Okoroanyanwu, U., Secor, E. B., et al. (2021). Printed microfluidic sweat sensing platform for cortisol and glucose detection. *Lab. Chip* 22 (1), 156–169. doi:10.1039/d1lc00633a

Niringiyumukiza, J. D., Cai, H., and Xiang, W. (2018). Prostaglandin E2 involvement in mammalian female fertility: Ovulation, fertilization, embryo development and early implantation. *Reprod. Biol. Endocrinol.* 16, 43. doi:10.1186/s12958-018-0359-5

Ozgocer, T., Yildiz, S., and Ucar, C. (2017). Development and validation of an enzyme-linked immunosorbent assay for detection of cortisol in human saliva. *J. Immunoass. Immunochem.* 38 (2), 147–164. doi:10.1080/15321819.2016.1230130

Pelizzaro, F., Kitenge, M. P., Cardin, R., Ponzoni, A., Cillo, U., Vitale, A., et al. (2021). Circulating prostaglandin E-2: A novel potential prognostic biomarker in patients with hepatocellular carcinoma. *Clin. Exp. Med.* 21 (4), 675–682. doi:10.1007/s10238-021-00705-z

Polat, M., Mumusoglu, S., Bozdag, G., Ozbek, I.Y., Humaidan, P., and Yarali, H. (2020). Virgo: Addition of intramuscular progesterone to vaginal progesterone in hormone replacement therapy in vitrified-warmed blastocyst transfer cycles. *Reprod. Biomed. Online* 40 (6), 812–818. doi:10.1016/j.rbmo.2020.01.0311472-6483

Pu, H., Huang, Z., Sun, D.-W., and Fu, H. (2019). Recent advances in the detection of 17 beta-estradiol in food matrices: A review. *Crit. Rev. Food Sci. Nutr.* 59 (13), 2144–2157. doi:10.1080/10408398.2019.1611539

Rael, E. (2016). Unraveling the complexity of leukotriene and prostaglandin inflammatory signaling. *J. Allergy Clin. Immunol.* 137 (1), 299–300. doi:10.1016/j.jaci.2015.09.003

Raza, T., Qu, L., Khokhar, W. A., Andrews, B., Ali, A., and Tian, M. (2021). Progress of wearable and flexible electrochemical biosensors with the aid of conductive nanomaterials. *Front. Bioeng. Biotechnol.* 9, 761020. doi:10.3389/fbioe.2021.761020

Rebelo, P., Costa-Rama, E., Seguro, I., Pacheco, J. G., Nouws, H. P. A., Cordeiro, M. N. D. S., et al. (2020). Molecularly imprinted polymer-based electrochemical sensors for environmental analysis. *Biosens. Bioelectron.* 172, 112719. doi:10.1016/j.bios.2020.112719

Regasa, M. B., and Nyokong, T. (2022). Design and fabrication of electrochemical sensor based on molecularly imprinted polymer loaded onto silver nanoparticles for the detection of 17-β-estradiol. *J. Mol. Recognit.* 2022, e2978. doi:10.1002/jmr.2978

Ronkainen, N. J., Halsall, H. B., and Heineman, W. R. (2010). Electrochemical biosensors. *Chem. Soc. Rev.* 39 (5), 1747–1763. doi:10.1039/b714449k

Samie, H. A., and Arvand, M. (2020). Label-free electrochemical aptasensor for progesterone detection in biological fluids. *Bioelectrochemistry* 133, 107489. doi:10.1016/j.bioelechem.2020.107489

Samson, C., and Koh, A. (2020). Stress monitoring and recent advancements in wearable biosensors. *Front. Bioeng. Biotechnol.* 8, 1037. doi:10.3389/fbioe.2020.01037

Sanchez-Tirado, E., Gonzalez-Cortes, A., Yudasaka, M., Iijima, S., Langa, F., Yanez-Sedeno, P., et al. (2017). Electrochemical immunosensor for the determination of 8-isoprostane aging biomarker using carbon nanohorns-modified disposable electrodes. *J. Electroanal. Chem.* 793, 197–202. doi:10.1016/j.jelechem.2016.11.003

Shuo, Y., Hossain, M. N., Yongxin, L., Chengjun, S., and Heinz-Bernhard, K. (2021). Development of a novel electrochemical aptasensor based on catalytic hairpin assembly and DNA tetrahedron for the detection of 25-hydroxyvitamin D3. *Sensors Actuators B Chem.* 354, 131217. doi:10.1016/j.snb.2021.131217

Supchocksoonthorn, P., Alvior Sinoy, M. C., de Luna, M. D. G., and Paoprasert, P. (2021). Facile fabrication of 17β-estradiol electrochemical sensor using polyaniline/carbon dot-coated glassy carbon electrode with synergistically enhanced electrochemical stability. *Talanta* 235, 122782. doi:10.1016/j.talanta.2021.122782

Tang, T., Liu, Y., and Jiang, Y. (2022). Recent progress on highly selective and sensitive electrochemical aptamer-based sensors. *Chem. Res. Chin. Univ.* 38, 866–878. doi:10.1007/s40242-022-2084-z

Tang, W., Yin, L., Sempionatto, J. R., Moon, J.-M., Teymourian, H., and Wang, J. (2021). Touch-based stressless cortisol sensing. *Adv. Mat.* 33 (18), 2008465. doi:10.1002/adma.202008465

Tanrikut, E., Ozcan, I., Sel, E., Koytepe, S., and Savan, E. K. (2020). Simultaneous electrochemical detection of estradiol and testosterone using nickel ferrite oxide doped mesoporous carbon nanocomposite modified sensor. *J. Electrochem. Soc.* 167 (8), 087509. doi:10.1149/1945-7111/ab927f

Thangphatthanarungruang, J., Yakoh, A., Laocharoensuk, R., Chotsuwan, C., Chailapakul, O., and Siangproh, W. (2020). High-efficient of graphene nanocomposite: Application to rapidly simultaneous identification and quantitation of fat-soluble vitamins in different matric samples. *J. Electroanal. Chem.* 873, 114361. doi:10.1016/j.jelechem.2020.114361

Vargas, E., Povedano, E., Krishnan, S., Teymourian, H., Tehrani, F., Campuzano, S., et al. (2020). Simultaneous cortisol/insulin microchip detection using dual enzyme tagging. *Biosens. Bioelectron. X.* 167, 112512. doi:10.1016/j.bios.2020.112512

Wadhwa, S., John, A. T., Nagabooshanam, S., Mathur, A., and Narang, J. (2020). Graphene quantum dot-gold hybrid nanoparticles integrated aptasensor for ultra-sensitive detection of vitamin D-3 towards point-of-care application. *Appl. Surf. Sci.* 521, 146427. doi:10.1016/j.apsusc.2020.146427

Yin, S., Yang, Y., Wu, L., Li, Y., and Sun, C. (2019). Recent advances in sample preparation and analysis methods for vitamin D and its analogues in different matrices. *TrAC Trends Anal. Chem.* 110, 204–220. doi:10.1016/j.trac.2018.11.008

Yu, C., Li, L., Ding, Y., Liu, H., and Cui, H. (2022). Molecularly imprinted electrochemical aptasensor based on functionalized graphene and nitrogen-doped carbon quantum dots for trace cortisol assay. *Analyst* 147 (4), 744–752. doi:10.1039/d1an01838h

Yu, G.-M., and Maeda, T. (2017). Inline progesterone monitoring in the dairy industry. *Trends Biotechnol.* 35 (7), 579–582. doi:10.1016/j.tibtech.2017.02.007

Zhang, H., Cui, Z., Yang, B., Fang, D., Liu, Y., and Wang, Z. (2021). Integrated recombinant gene yeast bioassay and HPLC-MS analysis for detection of low-dose multi-component residue of hormone-like compounds in environment. *Sci. Total Environ.* 773, 145569. doi:10.1016/j.scitotenv.2021.145569

Zheng, H., Zhang, Q., Hong, Z., Lin, Y., and Dai, H. (2016). A bifunctional catalyst based ECL immunosensor for a cardiac biomarker regulated by oxygen evolution reaction. *Electrochimica Acta* 215, 326–333. doi:10.1016/j.electacta.2016.08.120

Zhu, Y., Xu, Z., Gao, J., Ji, W., and Zhang, J. (2020). An antibody-aptamer sandwich cathodic photoelectrochemical biosensor for the detection of progesterone. *Biosens. Bioelectron. X.* 160, 112210. doi:10.1016/j.bios.2020.112210

frontiers | Frontiers in Bioengineering and Biotechnology

TYPE Review
PUBLISHED 12 October 2022
DOI 10.3389/fbioe.2022.1042625

OPEN ACCESS

EDITED BY
Qitong Huang,
Gannan Medical University, China

REVIEWED BY
Zhijin Fan,
Sun Yat-sen University, China
Boya Liu,
Boston Children's Hospital and Harvard Medical School, United States

*CORRESPONDENCE
Jinrui Zhang,
jlzhangjr@jlu.edu.cn
Jianlin Zuo,
zuojl@jlu.edu.cn

SPECIALTY SECTION
This article was submitted to Nanobiotechnology, a section of the journal Frontiers in Bioengineering and Biotechnology

RECEIVED 12 September 2022
ACCEPTED 29 September 2022
PUBLISHED 12 October 2022

CITATION
Tian H, Wu R, Feng N, Zhang J and Zuo J (2022), Recent advances in hydrogels-based osteosarcoma therapy. *Front. Bioeng. Biotechnol.* 10:1042625. doi: 10.3389/fbioe.2022.1042625

Recent advances in hydrogels-based osteosarcoma therapy

Hao Tian[1], Ronghui Wu[2], Na Feng[3], Jinrui Zhang[1,4]* and Jianlin Zuo[1]*

[1]Department of Orthopedics, China-Japan Union Hospital of Jilin University, Changchun, China, [2]Department of Dermatology, China-Japan Union Hospital of Jilin University, Changchun, China, [3]Department of Laboratory Medicine, Nanfang Hospital, Southern Medical University, Guangzhou, China, [4]State Key Laboratory of Magnetic Resonance and Atomic and Molecular Physics, National Center for Magnetic Resonance in Wuhan, Innovation Academy for Precision Measurement Science and Technology, Chinese Academy of Science, Wuhan, China

Osteosarcoma (OS), as a typical kind of bone tumors, has a high incidence among adolescents. Traditional tumor eradication avenues for OS such as chemotherapy, surgical therapy and radiation therapy usually have their own drawbacks including recurrence and metastasis. In addition, another serious issue in the treatment of OS is bone repair because the bone after tumor invasion usually has difficulty in repairing itself. Hydrogels, as a synthetic or natural platform with a porous three-dimensional structure, can be applied as desirable platforms for OS treatment. They can not only be used as carriers for tumor therapeutic drugs but mimic the extracellular matrix for the growth and differentiation of mesenchymal stem cells (MSCs), thus providing tumor treatment and enhancing bone regeneration at the same time. This review focuses the application of hydrogels in OS suppression and bone regeneration, and give some suggests on future development.

KEYWORDS

osteosarcoma, bone repair, hydrogels, OS suppression, bone regeneration

Introduction

Osteosarcoma (OS), as a well-known primary bone tumor, involves the invasion of tumors into bone tissue and often occurs in children and adolescents (Mann et al., 2022). Reports suggested that OS has become the second leading cause of death among young cancer patients, especially to the stage of tumor lung metastasis (Siclari and Qin, 2010; Roessner et al., 2021). OS patients may suffer from disability and even death, eliciting heavy blows and losses to the society. Although developing quickly, there are often no obvious clinical signs or severe pain in the early stage of OS. Therefore, it's critical but tricky for the diagnosis and treatment of OS. To date, clinical treatment strategies include allogeneic bone transplantation and mechanically processed prosthesis (Gianferante et al., 2017; Simpson and Brown, 2018). However, defects such as insufficient allogeneic bone sources and poor biocompatibility severely limit their applications. Besides, most OS can be clean

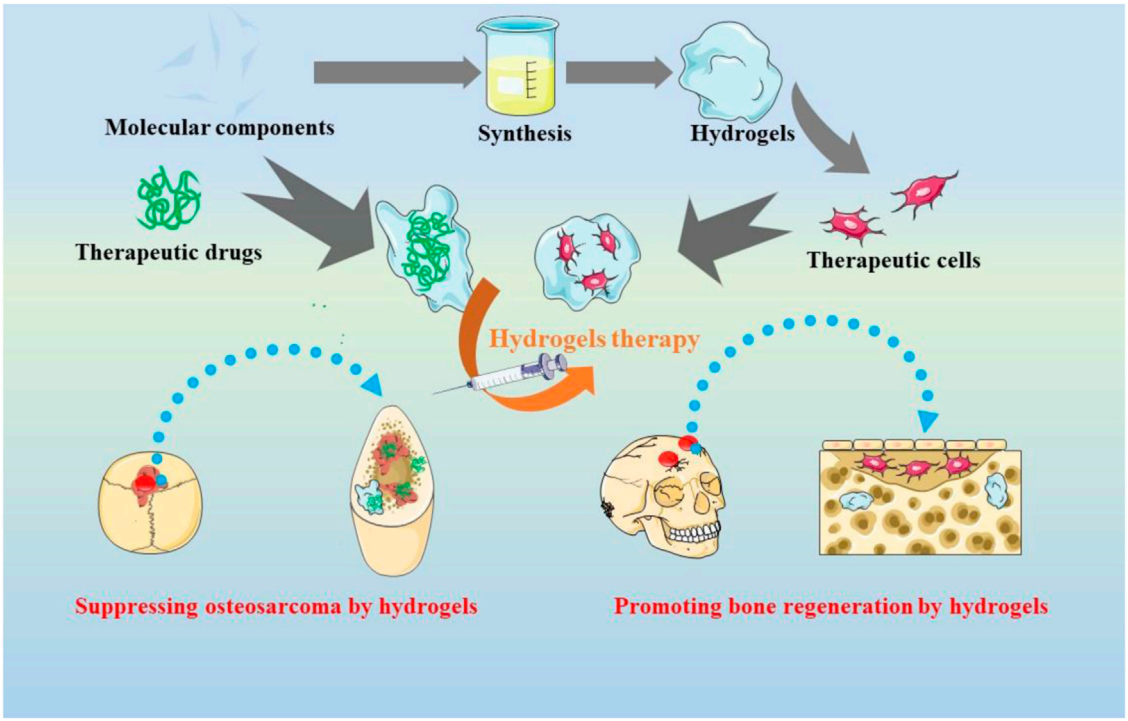

SCHEME 1
The applications of hydrogels-based therapeutics for suppressing the tumors and promoting bone regeneration in osteosarcoma treatment.

up by surgical intervention, but usually fails to completely ablate the tumor, thus causing post-surgery recurrence and metastasis (Lin et al., 2015; Chen et al., 2017; Friesenbichler et al., 2017; Haghiralsadat et al., 2017; Liu et al., 2021; Wang et al., 2021; Xu et al., 2022). Thus, to avoid postoperative recurrence and metastasis as much as possible, chemotherapy and radiotherapy are combined after surgery. Unfortunately, radiotherapy is reluctant to exert effect in OS and OS is susceptible to chemotherapy resistance (Bohnke et al., 2007; Campbell, 2009; Gianferante et al., 2017; Shoag et al., 2019; Pattee et al., 2020). What's more, the patients receiving chemotherapy often suffer from side effects including hair loss and vomiting, which will obviously decrease the quality of life (Bosma et al., 2018). At the same time, patients suffered from OS and surgical resection will have bone defects, eliciting acute pain and disability. Thus, implementing the development of OS therapy is a pretty tough work. Correspondingly, innovative and effective methods are urgently needed to guide the therapy of OS in clinical problems (Liao et al., 2021a).

As discussed above, it's vital to ensure the complete resection of OS after surgery but remains difficulty. Besides, radical resection is dangerous because of the complex anatomical structure and blood vessels in the bone tissues (Wang et al., 2018a; Liu et al., 2019; Wang et al., 2019; Zhang et al., 2019; Yang et al., 2020a; Pan et al., 2020). Along with the development of biotechnology and nanotechnology, novel alternative strategies with less side effects are developed. Specifically, photothermal therapy (PTT) is becoming a promising method that can covert near-infrared (NIR) light into thermal damage in tumor tissues (Chu and Dupuy, 2014; Chen et al., 2016; Liu et al., 2019; Wang et al., 2020; Xu et al., 2021), rejecting tumor region without damaging other organs or tissues (Xing et al., 2016; Shan et al., 2018; Pan et al., 2019; Hou et al., 2020; Jiang et al., 2020). PTT is based on various nanoparticles such as gold (Li Volsi et al., 2017; Mahmoodzadeh et al., 2018; Liao et al., 2019), carbon (Du et al., 2019; Farzin et al., 2019; Guo et al., 2022; Zhang et al., 2022) and copper nanomaterials (Liu et al., 2018). For example, PTT using gold nanoparticles has desirable therapeutic efficacy for prostate cancer in clinical trials (Rastinehad et al., 2019; Taneja, 2020). However, these nanomaterials usually have unsatisfactory biocompatibility and limited bioavailability. Thus, an appropriate carrier is needed to avoid these defects of nanoparticles and benefit their biological applications. More importantly, bone metabolism is becoming unbalanced because of the invasion of tumors into bone, leading to bone defect that is difficult to repair itself (Velasco et al., 2015; Wang et al., 2018b; Khajuria et al., 2018; Zhang et al., 2018). Therefore,

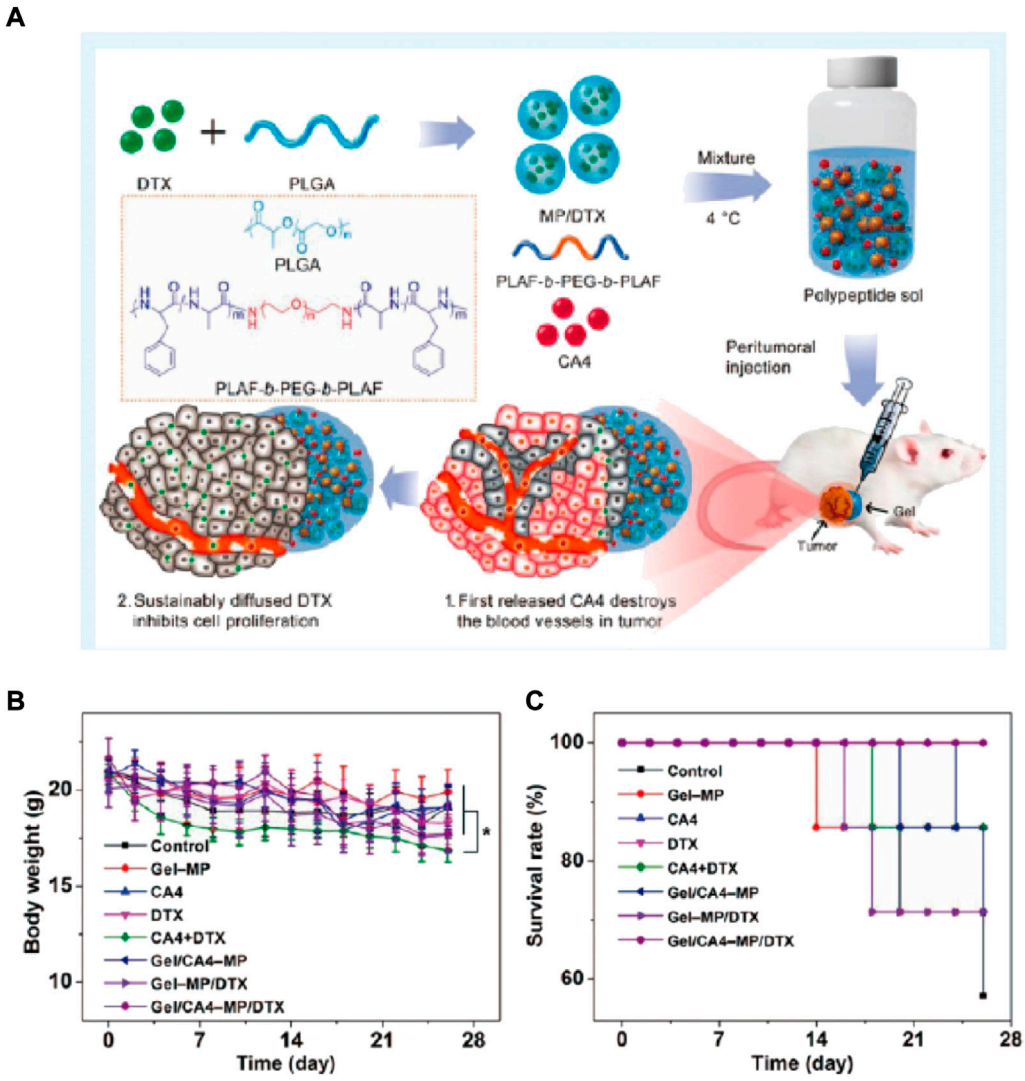

FIGURE 1
(A) Sequential Drug Delivery with Gel-MP Construct, Showing Preparation of Gel/CA4–MP/DTX for Two-Pronged Locally Synergistic Chemotherapy of Osteosarcoma. **(B)** Variations of body weight and survival rate. **(A)** Change of body weight and **(B)** survival rate of K7 osteosarcoma-grafted mice after treatment of PBS as control, Gel–MP, CA4, DTX, CA4+DTX, Gel/CA4–MP, Gel–MP/DTX, or Gel/CA4–MP/DTX. [Data were represented as mean ± SD (n = 10; (*) $p < 0.05$)].

therapeutic drugs, growth factors and/or stem cells are urgently needed. Benefiting from the continuous development in biomaterials science, bone tissue engineering scaffolds become a fascinating material with great hope to bone regeneration (Gong et al., 2009; Ni et al., 2014; Li et al., 2018a; Shi et al., 2019). Among various tissue engineering scaffolds, hydrogels with excellent bioactivity, biocompatibility and biodegradability have attracted much attention of researchers. Hydrogels are three-dimensional porous mesh gel with abundant water absorbance (Xu et al., 2020). It can not only afford a vehicle for tumor therapeutic drug but mimic the extracellular matrix (ECM) for the growth and differentiation of mesenchymal stem cells (MSCs), thus providing tumor treatment and enhancing bone regeneration at the same time (Chen et al., 2020). Moreover, when integrating hydrogels with other drug delivery systems such as liposomes and microspheres, carriers with better performance can be created by synergism.

Herein, we discussed the recent advances in the use of hydrogels to achieve OS therapy, with emphasis on suppressing the tumors and Promoting bone regeneration (Scheme 1). We believe that This review will provide a useful reference for hydrogels-based OS therapy and the field of

10.3389/fbioe.2022.1042625

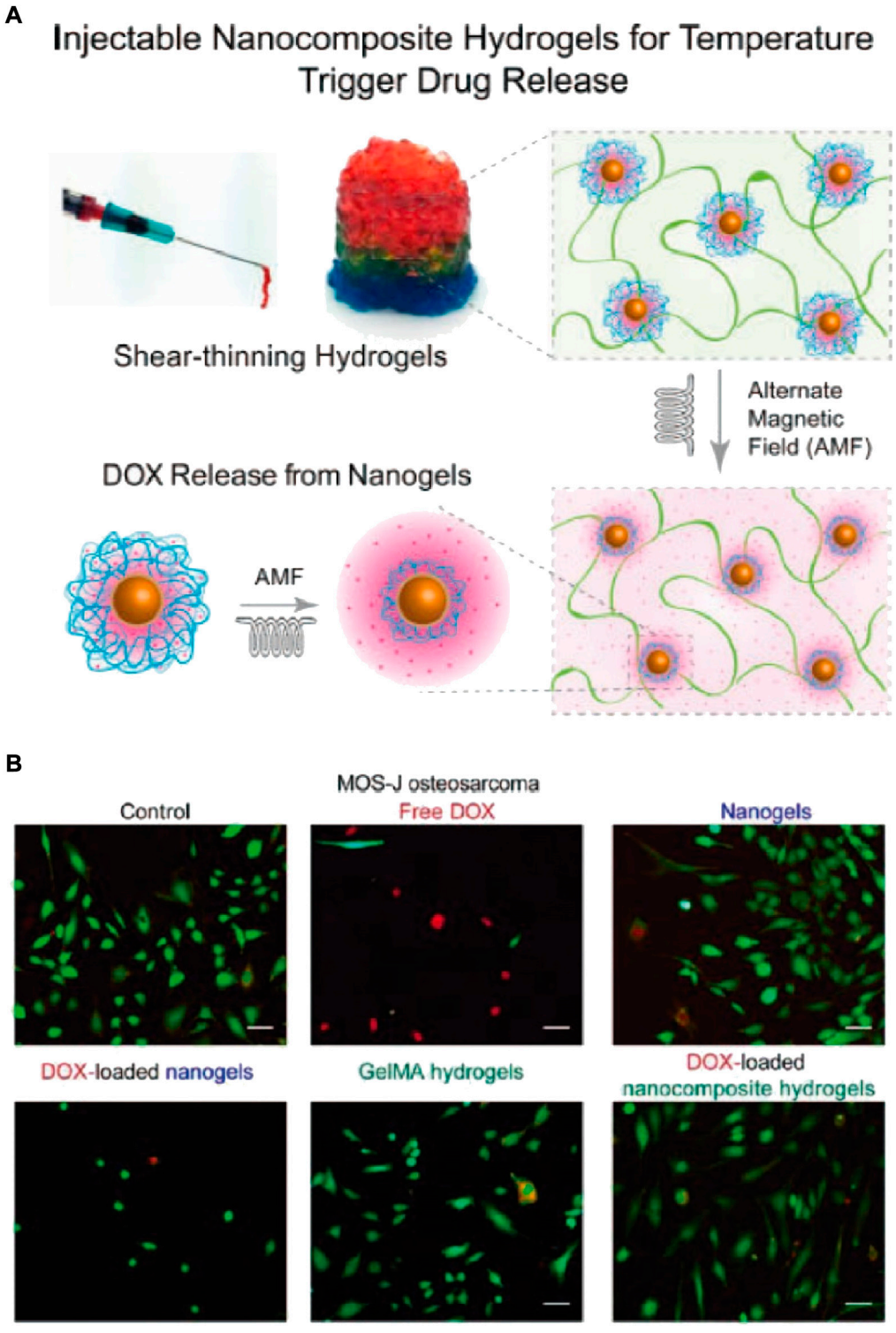

FIGURE 2
(A) Schematic depiction of nanocomposite hydrogels fabrication that can be injected for drug release in response to stimuli. **(B)** MOS-Js, live or dead staining indicated more dead cells upon exposure with free DOX than nanogels and nanocomposites loaded DOX (Scale bar 100 μm).

complex diseases to combine tumor therapy and tissue engineering.

Suppressing the tumors by hydrogels

The conventional therapy strategies for OS comprise the combination of chemotherapy with surgical methods (Dou et al., 2013). Chemotherapy for OS began in the 1970s, which includes doxorubicin (DOX), cisplatin et al. Despite great expectations are expected in chemotherapy, the overall efficacy of which are no more than 60% (Lai et al., 2007) attributing to the high toxic effects of chemotherapy and drug resistance in secondary cancer. Therefore, it's crucial to construct an artificial implant for the local administration and controlled-release of chemical drugs (Wu et al., 2018).

Several researches have demonstrated that hydrogels are capable of treating tumors due to their porous structure and versatile biocompatibility. It's acceptable to administer therapeutic drugs or functional cells into the resected OS area with the help of hydrogels (Yang et al., 2020b). With the advantages of providing continuous drug release for tumor illumination, hydrogels encapsulated with drugs can afford localized tumor therapy, replacing systemic chemotherapy administered intravenously (Zheng et al., 2017; Yang et al., 2018; Chen et al., 2019; Peng et al., 2022). As an example, chitosan-based hydrogels are designed for therapeutic agents and cell delivery for tumor therapy (Pan et al., 2019). Besides, thermoresponsive hydrogel based on PEG-g-chitosan (PCgel) can benefit T lymphocyte infiltration into the gel and allow a sustainable release of cells (Jiang et al., 2020). Further, reports have suggested the gelatin gel for the release of anti-carcinogenic drugs (Hu et al., 2018). Wu et al. united gelatin methacryloyl (GelMA) hydrogel with gemcitabine hydrochloride loaded liposomes for OS ablation, which exhibited desirable properties in antitumor and sustained release (Wu et al., 2018). Specifically, the hydrogel system showed feasible application in eradicating OS *in vivo* by MG63-bearing mice.

Because of the complexity and diversity of tumor pathogenesis, the effect of single chemical drug may be compromised. Thus, synergistic chemotherapy is needed to solve the problem. For instance, Combretastatin A-4 (CA4) are able to bind the tubulin of endothelial cells, disturbing the formation of blood vessel and ultimately, eliciting tumor necrosis through inhibiting the supply of oxygen and nutrients (Perez-Perez et al., 2016). Unfortunately, CA4 can only work on the internal tumors with rich vascular, but often fail to treat the edge of the tumor tissues. Nevertheless, the peripheral tumor tissues are sensitive to traditional drugs like DOX and docetaxel (DTX). For this issue, Zheng et al. developed an injectable thermosensitive hydrogel system for the co-encapsulation and sequential release of CA4 and DTX (Figure 1A) (Zheng et al., 2017). CA4 was released preferentially, which could damage the neovascularization system and inhibit the exchange of nutrients. The followed release of DTX could clean up the surface cells of tumor tissues and lead to apoptosis of the tumor (Figures 1B,C). Likewise, Sun et al. co-loaded Oxaliplatin (OXA) and Alendronate (ALN) onto mPEG45-PLV19 thermosensitive hydrogel (Sun et al., 2020). OXA is a widely accepted anticancer drug, which can induce immunogenic death (ICD) for tumor elimination. ALN have bone affinity as well as the effect of inhibiting bone destruction. Studies found that the system could inhibit the progress of OS and prevent tumor lung metastasis.

Currently, the OS treatment regimen is mostly DOX, methotrexate (MTX), and cisplatin (CDDP) based. The clinical efficacy of this regimen was proved by the systemic administration of the aforementioned drugs (Bielack et al., 2009). Ma et al. successfully established a system based on poly (L-lactide-*co*-glycolide)-poly (ethylene glycol)-poly (lactide-*co*-glycolide) (PLGA-PEG-PLGA) for delivering CDDP, MTX, and DOX (Ma et al., 2015). In the human osteosarcoma model of nude mice, the triple-delivery system could induce enhanced tumor apoptosis, displaying high tumor suppression efficacy. Furthermore, the evaluation of alteration in mice's bodies and their organs histological analysis in *ex vivo* experiment revealed less toxic effects and obvious organ damage after localized treatment. Therefore, local co-delivery of CDDP, MTX, and DOX *via* thermos-sensitive hydrogels might be a promising option for better osteosarcoma treatment. "Smart" hydrogels are novel biomaterials that are influenced by external stimuli. Thus, multiple investigations have been carried out to determine the scope of bio-medical implementations, for instance, regenerative engineering and therapeutic delivery. Jalili et al. established nano-engineered hydrogel comprising poly (NIPAM-co-AM)/MNPs, for local and on-demand injection for delivering drugs (doxorubicin (DOX)) (Figure 2A). In this investigation, shear-thinning hydrogels capable of self-recovering were engineered by manipulating gelatin methacrylate (GelMA) network's crosslinking density. Prior to this crosslinking GelMA pre-polymer solution was mixed with DOX-loaded Poly (NIPAM-*co*-AM)/MNP nanogels (GelMA/(poly (NIPAM-*co*-AM)/MNPs)). The magnetic field and temperature-dependent DOX release from (GelMA/(poly (NIPAM-*co*-AM)/MNPs)) were evaluated. Lastly, the efficacy of this new form of DOX-carrying drug on pre-osteoblast and osteosarcoma cells was investigated *in vivo* (Figure 2B).

Currently, the therapeutic drug's maximum tolerated dose (MTD) is not only important for determining the formulation's concentration, but also for predicting its success in the clinical setting (Kim et al., 2010; Ranade et al., 2014). Even though the MTD of some drugs showed improvement to some extent through the polymer-regulated delivery mechanism, the MTD of drugs that are delivered by hydrogel still needs additional research. For localized OS treatment, Yang et al. used thermo-

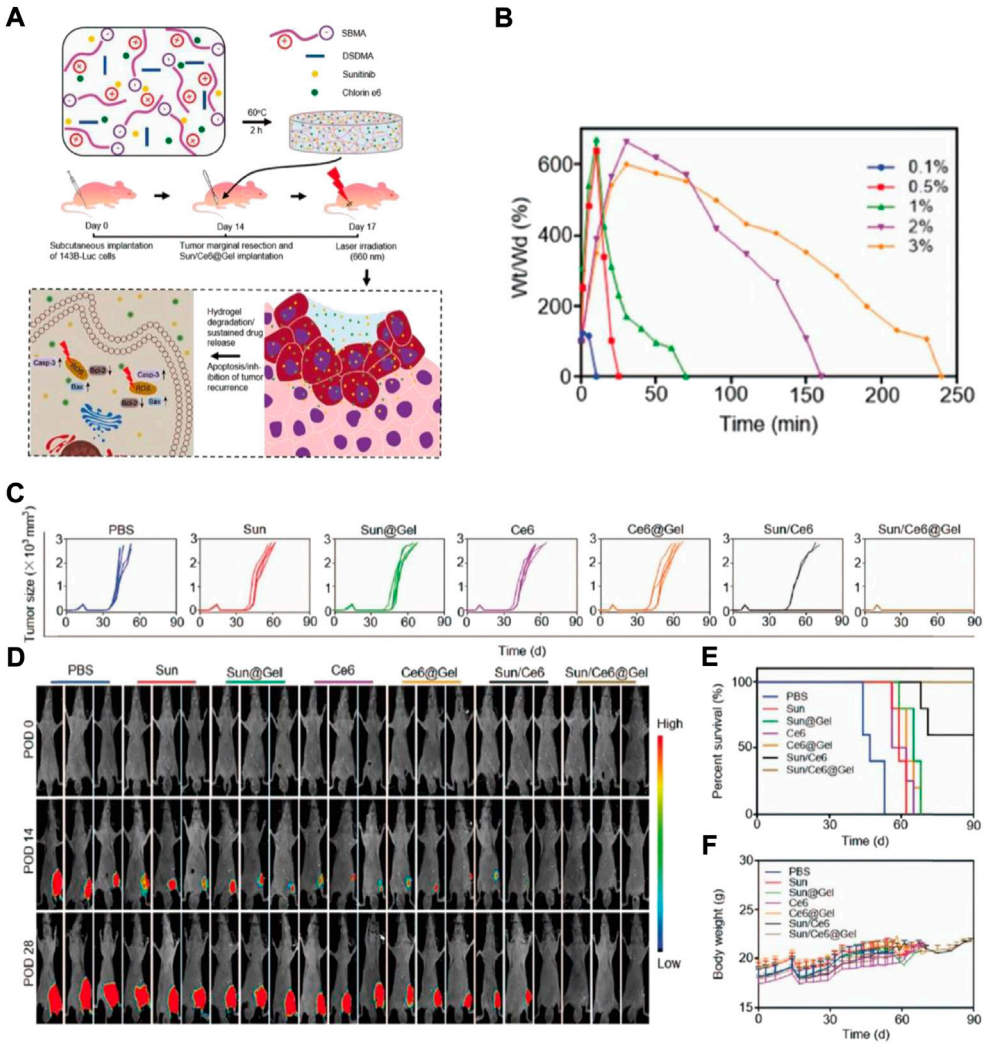

FIGURE 3
(A) Schematic depiction of Sun/Ce6@Gel synthesis and Sun and Ce6 synergistic antitumor impact in inhibiting mice tumor recurrence. Sun/Ce6@gel was generated by fusing Ce6, Sun, DSDMA, and SBMA for 2 h, and was administered in the residual cavity, thereby it inhibited tumor relapse post osteosarcoma marginal eradication. Casp-3: caspase-3. The degeneration and DSDMA–SBMA hydrogels release data. **(B)** Hydrated DSDMA–SBMA hydrogels weight alternations in the solution of PBS supplemented with DTT (100 mM). **(C)** Individual tumor growth kinetics during the treatment. **(D)** *Invivo* nude mice tumor recurrence bioluminescence images. POD, postoperative days. **(E)** Survival rates **(F)** Mice's body weights were measured, and the effective doses of Sun and Ce65 were selected as 5mg and 1 mg per kg, respectively.

sensitive hydrogel to incorporate DOX into the poly (D,Llactide-co-glycolide)-poly (ethylene glycol)-poly (D,L-lactide-co-glycolide) (PLGA-PEG-PLGA) (Yang et al., 2018). The PLGA-PEG-PLGA triblock copolymer was successfully prepared and proved by 1H NMR. Furthermore, hydrogel characters, including rheological evaluation, sol-gel phase transition, and drug release in the *in vitro* experiment were studied. The DOX-packed hydrogel's cytotoxicity was evaluated *in vitro*, in K-7 (mouse osteosarcoma cancer) and Saos-2 (human osteosarcoma cancer) cells. Lastly, the DOX-loaded hydrogel's antitumor efficacy was determined *in vivo* in the K-7 mice tumor model. DOX-loaded hydrogel's systemic toxicity and the safety of its local delivery were assessed by mice's organ pathological analysis and their survival rate. Similarly, Yu et al. suggested a procedure for local Sun and chlorin e6 (Ce6) delivery by zwitterionic redox-responsive hydrogels for preventing the relapse of osteosarcoma (Figure 3A) (Yu et al., 2020). Yu synthesized hydrogels using a redox-responsive cross-linker (DSDMA), in which drugs Ce6 and Sun were introduced, a complex called Sun/Ce6@Gel (Figure 3B). This composite was administered in the residual cavity instantly post tumor eradication. Ce6 and Sun are liberated from the zwitterionic hydrogels because of redox sensitivity post-implantation at the surgery site (Figure 3C). This should result in reduced anti-apoptotic and increased

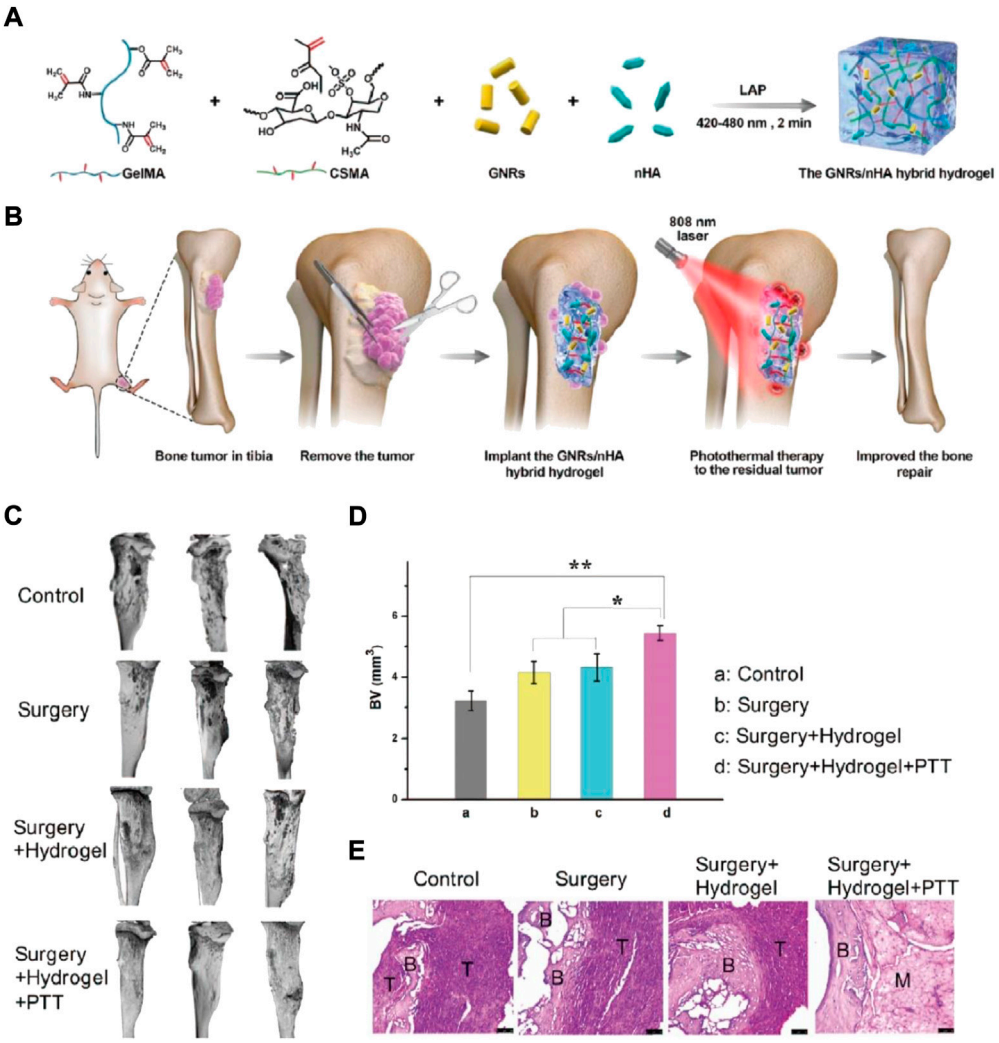

FIGURE 4
(A) The diagrammatic GNRs/nHA hybrid hydrogel preparation. **(B)** The hybrid GNRs/nHA hydrogel application for photothermal treatment and regeneration of bone tumor. **(C)** The micro-CT reconstruction in each group of mice after treatment for 2 weeks; **(D)** The bone volume (BV) parameter in each mice group (*$p < 0.05$, **$p < 0.01$); **(E)** The tibia bone tumor H&E stained images of different groups.

pro-apoptotic gene expression. The potency of Ce6-and Sun-packed hydrogel as a postoperative osteosarcoma therapy was determined in both *in vitro* and *in vivo* conditions (Figures 3D–F).

Promoting bone regeneration by hydrogels

Osteosarcoma originates at the epiphyseal end with a rich blood supply. The osteosarcoma effect on bone is huge, and the body takes time to repair or heal itself. Therefore, stem cells, small-molecule, external scaffolds, or growth factor drugs are required (Velasco et al., 2015; Wang et al., 2018b). Recently, computer-assisted digital technology, material mechanics, and bone tissue engineering scaffolds (e.g., 3D printed scaffolds, microspheres, and hydrogels) have progressed a lot with the continuous advancement in the field of biomaterials (Li et al., 2017; Xu et al., 2017). Hydrogels can imitate extracellular matrix (ECM) and improve bone repair by proliferating and differentiating MSCs (Liu et al., 2022). Thus, bone regeneration has widely been studied because of its outstanding osteoinductivity and bio-compatibility, -activity, and—degradability (Feng et al., 2019). Yap et al. established a novel thermoreversible hydrogel scaffold comprising glyoxal (Gx), PLuronic F127, and carboxymethyl hexanoyl chitosan

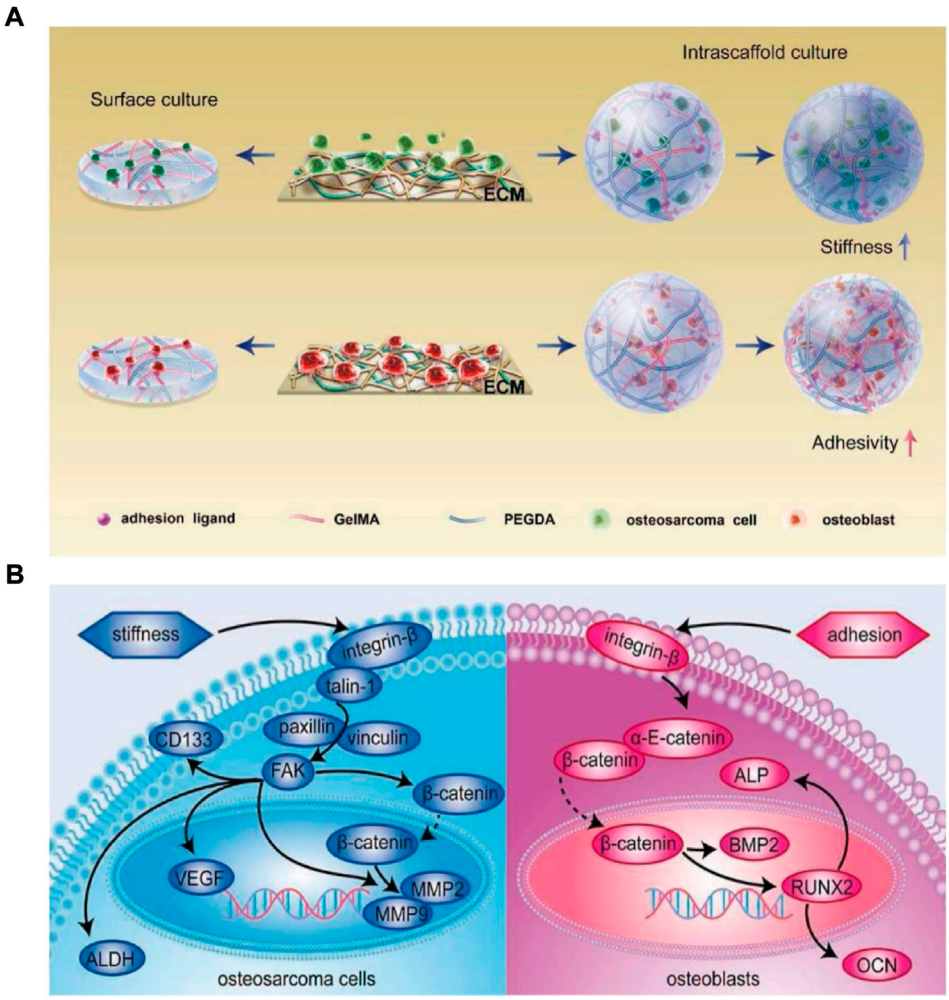

FIGURE 5
(A) Schematic illustration of various anchorage-independent osteosarcoma cells and anchorage-dependent osteoblasts responses to adhesive activity and stiffness of scaffold **(B)** Respond of osteoblasts and osteosarcoma cell's mechanisms to stiffness and adhesion ligands of ECM, respectively. ECM's stiffness and not the matrix adhesion influences the growth of osteosarcoma cells by regulating the integrin-induced FA signaling pathway, while osteoblasts are primarily influenced by ECM adhesion ligands *via* the integrin-induced AJ signaling pathway modulation.

TABLE 1 Recent summary of therapeutic strategies for hydrogel osteosarcoma.

Components	Models	Strategies	References
Chitosan	Tumor	Therapeutic drug delivery	33
PEG-g-chitosan	Tumor	Immunotherapy	31
Gelatin methacryloyl	OS	Therapeutic drug delivery synergy therapy	56
Injectable thermosensitive hydrogel	OS	Co-encapsulation and sequential release of CA4 and DTX	61
Poly (NIPAM-co-AM)/MNPs	OS	Local and on-demand injection for delivering drugs [doxorubicin (DOX)]	66
GNRs/nHA	Bone regeneration	Healing defects after bone tumor surgical resection	80
Poly (ethylene glycol) diacrylate (PEGDA) and GelMA	Bone regeneration	Modulating the integrin-induced pathway of adherens junction	86

(CA), injected for encapsulating human osteosarcoma MG-63 cells. These hydrogel encapsulated cells proliferated >400% during a 5-day incubation period. The results suggest that F127/CA/Gx hydrogel can envelop cells for tissue engineering (Yap and Yang, 2020). Prosthodontic-inspired photopolymerization stimulated by blue light is a gentle process for initiating the polymerization of monomers (Chen et al., 2020; Downs et al., 2020; Feng et al., 2022), The blue light initiator in the hydrogel system commences hydrogel cross-linking. Human Bone contains 50%–70% inorganic calcium and phosphorus. Nano hydroxyapatite ($Ca_{10}(PO_4)_6(OH)_2$, nHA) has been proven to provide nutrition for bone defects and also help repair bone (Li et al., 2018b; Tan et al., 2021). However, nHA can also inhibit tumors (Barbanente et al., 2021). The hybrid nHA hydrogel is hypothesized to furnish an ECM mimic post osteosarcoma eradication and stimulate bone defect restoration. Liao et al. used light-induced photopolymerization for developing GNRs/nHA hybrid hydrogel (Figure 4A) (Liao et al., 2021b). To generate a biocompatible hydrogel, methacrylate gelatin (GelMA) and methacrylated chondroitin sulfate (CSMA) were used. The nHA and GNRs dissipated easily in the hydrogel. The developed GelMA/CSMA hydrogel, GNRs/nHA hybrid were used for eradicating the residual tumor after surgery *via* PTT and for healing defects after bone tumor surgical resection (Figure 4B). The GelMA/CSMA hydrogel photothermally treated tumors residues left after surgery and repaired the bone deformities in a tibia osteosarcoma mice model (Figures 4C–E).

Osteocytes are crucial for the bone remodeling process, during which the trapped osteoblasts phenotypically alter to mature as osteocytes. The underlying osteocyte mechanisms are still debatable, and it has few study models. E. J. Lee et al. studied how alterations in the mechanical features of bone matrix that lack minerals can affect the phenotypic transformation of osteoblast to osteocyte in a 3D setting *via* bioprinting-based technology called Combing Extrusion printing on Cellulose scaffolds with Lamination (ExCeL) (Lee et al., 2019). Similarly, Vashisth et al. established a biomimetic 3D hybrid scaffold after studying the natural bone architecture with nano-microscale features, favorable porous interconnected structure, and mechanical strength (Vashisth and Bellare, 2018). The key hybrid scaffold constituents are core-sheath nanofibers and hydrogel, which are organized suitably to generate a microenvironment that resembles bone. The core-sheath nanofibers are specifically coiled tightly into a ring to imitate the osteon and reinforced in a hydrogel matrix.

In comparison with traditional biometal scaffolds (like that of titanium and titanium-based alloys), Young's polyetheretherketone (PEEK) model resembles more human cortical bone, thereby, alleviating osteoporosis and osteonecrosis risk triggered by stress shielding (Wang et al., 2014; Torstrick et al., 2018). Based on this, Yin et al. fabricated a novel and versatile coating made from GelMA hydrogels and TOB-laden MXene nanosheets on an inert orthopedic PEEK material, to eliminate remaining cancerous cells, prevent infection related to bacteria, and guide the regeneration of bone tissues (Yin et al., 2020).

How cancerous cells and their normal counterparts have anchorage-dependency and react to the stiffness and adhesion ligand density of the same ECM is still unclear. Jiang et al. analyzed the impact of ECM adhesion ligand density and stiffness on osteosarcoma cells (bone cancerous cells) and osteoblasts (bone-producing cells) *via* poly (ethylene glycol) diacrylate (PEGDA) and GelMA hydrogels (Figure 5A) (Jiang et al., 2019). When osteosarcoma cells were cultured in 3D PEGDA/GelMA hydrogel matrix, they showed high dependence on the stiffness of the matrix by modulating the integrin-induced pathway of focal adhesion (FA), whereas osteoblasts showed high sensitivity toward matrix adhesion ligand density by modulating the integrin-induced pathway of adherens junction (AJ) (Figure 5B). But in the 2D hydrogels surface culture, bone cancerous cells presented a different behavior and showed sensitivity to the matrix adhesion ligand density due to their "forced" attachment to the substrate, similar to anchorage-dependent osteoblasts.

Conclusion and prospects

Hydrogels are enormous water meshes that characteristically resemble extracellular matrix. These are very porous and have excellent biological compatibility and degradability. They are capable of introducing growth factors that can repair bone defects (Torstrick et al., 2018; Zhang et al., 2018). Therefore, they are good suiters for repairing bone. Literature indicates potential hydrogels application for regenerating bone tissue. For potential bone cancer therapy, these should first be capable of curing tumors. Administering drugs or other molecules directly at the resected tumor site for treatment is highly advised. Hydrogels provide sustainable drug release for tumor eradication (Ali Gumustas et al., 2016; Hu et al., 2020). Some act by delivering the drug directly to the specific system 126. Localized hydrogel therapy for cancer treatment can replace systemic chemotherapy given orally or intravenously (Zheng et al., 2017; Yang et al., 2018; Chen et al., 2019). With the discovery of new hydrogel functions, their implementations are no longer limited to repairing tissues, it has extended to bone repair and tumor eradication (Table 1).

However, hydrogel's application in osteosarcoma is limited for the following reasons, first, despite extensive literature research on hydrogels, clinical applications have encountered bottlenecks, and only a few hydrogels have been approved and commercialized (Fan et al., 2022; Li et al., 2022). Additionally, cytotoxicity is often stimulated because of the hydrogel's inorganic nature and the metal ions involved. Hydrogels are mainly developed from raw

materials that are non-essential to organisms. With further investigations solving the aforementioned issues associated with osteosarcoma therapy-related hydrogels, it is expected that a promising candidate might be discovered that would contribute to human health and well-being.

Author contributions

HT and JZ: manuscript preparation, figures and tables preparation, and manuscript editing and revision. JZ: literature collection and evaluation, and draft manuscript preparation. RW and NF: figure legend preparation, references insertion, and graphic abstract preparation.

Acknowledgments

We greatly acknowledge the financial support from Science and Technology Development Program of Jilin Provinces (Nos. YDZJ202201ZYTS043, and YDZJ202201ZYTS520), State Key Laboratory of Magnetic Resonance and Atomic and Molecular Physics, National Center for Magnetic Resonance in Wuhan, Innovation Academy for Precision Measurement Science and Technology (T152205).

Conflict of interest

The authors declare that the research was conducted in the absence of any commercial or financial relationships that could be construed as a potential conflict of interest.

Publisher's note

All claims expressed in this article are solely those of the authors and do not necessarily represent those of their affiliated organizations, or those of the publisher, the editors and the reviewers. Any product that may be evaluated in this article, or claim that may be made by its manufacturer, is not guaranteed or endorsed by the publisher.

References

Ali Gumustas, S., Isyar, M., Topuk, S., Yilmaz, I., Oznam, K., Onay, T., et al. (2016). Systematic evaluation of drug-loaded hydrogels for application in osteosarcoma treatment. *Curr. Pharm. Biotechnol.* 17 (10), 866–872. doi:10.2174/1389201017666160519113104

Barbanente, A., Palazzo, B., Esposti, L. D., Adamiano, A., Iafisco, M., Ditaranto, N., et al. (2021). Selenium-doped hydroxyapatite nanoparticles for potential application in bone tumor therapy. *J. Inorg. Biochem.* 215, 111334. doi:10.1016/j.jinorgbio.2020.111334

Bielack, S., Jurgens, H., Jundt, G., Kevric, M., Kuhne, T., Reichardt, P., et al. (2009). Osteosarcoma: The COSS experience. *Cancer Treat. Res.* 152, 289–308. doi:10.1007/978-1-4419-0284-9_15

Bohnke, A., Jung, J., Taubert, H., Hauptmann, S., and Bartel, F. (2007). Both somatic and germline genetics of the TP53-pathway influence ovarian cancer incidence and survival. *Verh. Dtsch. Ges. Pathol.* 91, 233–242.

Bosma, S. E., Wong, K. C., Paul, L., Gerbers, J. G., and Jutte, P. C. (2018). A cadaveric comparative study on the surgical accuracy of freehand, computer navigation, and patient-specific instruments in joint-preserving bone tumor resections. *Sarcoma* 2018, 1–9. doi:10.1155/2018/4065846

Campbell, P. J. (2009). Somatic and germline genetics at the JAK2 locus. *Nat. Genet.* 41 (4), 385–386. doi:10.1038/ng0409-385

Chen, Q., Xu, L., Liang, C., Wang, C., Peng, R., and Liu, Z. (2016). Photothermal therapy with immune-adjuvant nanoparticles together with checkpoint blockade for effective cancer immunotherapy. *Nat. Commun.* 7, 13193. doi:10.1038/ncomms13193

Chen, X., Chen, Y., Jiang, J., Wu, L., Yin, S., Miao, X., et al. (2017). Nano-pulse stimulation (NPS) ablate tumors and inhibit lung metastasis on both canine spontaneous osteosarcoma and murine transplanted hepatocellular carcinoma with high metastatic potential. *Oncotarget* 8 (27), 44032–44039. doi:10.18632/oncotarget.17178

Chen, Y., Hao, Y., Huang, Y., Wu, W., Liu, X., Li, Y., et al. (2019). An injectable, near-infrared light-responsive click cross-linked azobenzene hydrogel for breast cancer chemotherapy. *J. Biomed. Nanotechnol.* 15 (9), 1923–1936. doi:10.1166/jbn.2019.2821

Chen, Y., Zhang, J., Liu, X., Wang, S., Tao, J., Huang, Y., et al. (2020). Noninvasive *in vivo* 3D bioprinting. *Sci. Adv.* 6 (23), eaba7406. doi:10.1126/sciadv.aba7406

Chu, K. F., and Dupuy, D. E. (2014). Thermal ablation of tumours: Biological mechanisms and advances in therapy. *Nat. Rev. Cancer* 14 (3), 199–208. doi:10.1038/nrc3672

Dou, X. Q., Zhang, D., and Feng, C. L. (2013). Wettability of supramolecular nanofibers for controlled cell adhesion and proliferation. *Langmuir* 29 (49), 15359–15366. doi:10.1021/la4040276

Downs, F. G., Lunn, D. J., Booth, M. J., Sauer, J. B., Ramsay, W. J., Klemperer, R. G., et al. (2020). Multi-responsive hydrogel structures from patterned droplet networks. *Nat. Chem.* 12 (4), 363–371. doi:10.1038/s41557-020-0444-1

Du, Y., Liu, X., Liang, Q., Liang, X. J., and Tian, J. (2019). Optimization and design of magnetic ferrite nanoparticles with uniform tumor distribution for highly sensitive MRI/MPI performance and improved magnetic hyperthermia therapy. *Nano Lett.* 19 (6), 3618–3626. doi:10.1021/acs.nanolett.9b00630

Fan, Z., Jiang, C., Wang, Y., Wang, K., Marsh, J., Zhang, D., et al. (2022). Engineered extracellular vesicles as intelligent nanosystems for next-generation nanomedicine. *Nanoscale Horiz.* 7 (7), 682–714. doi:10.1039/d2nh00070a

Farzin, A., Hassan, S., Emadi, R., Etesami, S. A., and Ai, J. (2019). Comparative evaluation of magnetic hyperthermia performance and biocompatibility of magnetite and novel Fe-doped hardystonite nanoparticles for potential bone cancer therapy. *Mater. Sci. Eng. C* 98, 930–938. doi:10.1016/j.msec.2019.01.038

Feng, Q., Xu, J., Zhang, K., Yao, H., Zheng, N., Zheng, L., et al. (2019). Dynamic and cell-infiltratable hydrogels as injectable carrier of therapeutic cells and drugs for treating challenging bone defects. *ACS Cent. Sci.* 5 (3), 440–450. doi:10.1021/acscentsci.8b00764

Feng, T., Wu, H., Ma, W., Wang, Z., Wang, C., Wang, Y., et al. (2022). An injectable thermosensitive hydrogel with a self-assembled peptide coupled with an antimicrobial peptide for enhanced wound healing. *J. Mat. Chem. B* 10 (32), 6143–6157. doi:10.1039/d2tb00644h

Friesenbichler, J., Maurer-Ertl, W., Bergovec, M., Holzer, L. A., Ogris, K., Leitner, L., et al. (2017). Clinical experience with the artificial bone graft substitute Calcibon used following curettage of benign and low-grade malignant bone tumors. *Sci. Rep.* 7 (1), 1736. doi:10.1038/s41598-017-02048-w

Gianferante, D. M., Mirabello, L., and Savage, S. A. (2017). Germline and somatic genetics of osteosarcoma - connecting aetiology, biology and therapy. *Nat. Rev. Endocrinol.* 13 (8), 480–491. doi:10.1038/nrendo.2017.16

Gong, C. Y., Shi, S., Peng, X. Y., Kan, B., Yang, L., Huang, M. J., et al. (2009). Biodegradable thermosensitive injectable PEG-PCL-PEG hydrogel for bFGF antigen delivery to improve humoral immunity. *Growth factors.* 27 (6), 377–383. doi:10.3109/08977190903159938

Guo, J., Wei, W., Zhao, Y., and Dai, H. (2022). Iron oxide nanoparticles with photothermal performance and enhanced nanozyme activity for bacteria-infected wound therapy. *Regen. Biomater.* 9, rbac041. doi:10.1093/rb/rbac041

Haghiralsadat, F., Amoabediny, G., Sheikhha, M. H., Forouzanfar, T., Helder, M. N., and Zandieh-Doulabi, B. (2017). A novel approach on drug delivery: Investigation of A new nano-formulation of liposomal doxorubicin and biological evaluation of entrapped doxorubicin on various osteosarcoma cell lines. *Cell J.* 19 (1), 55–65. doi:10.22074/cellj.2017.4502

Hou, M., Liu, W., Zhang, L., Zhang, L., Xu, Z., Cao, Y., et al. (2020). Responsive agarose hydrogel incorporated with natural humic acid and MnO2 nanoparticles for effective relief of tumor hypoxia and enhanced photo-induced tumor therapy. *Biomater. Sci.* 8 (1), 353–369. doi:10.1039/c9bm01472a

Hu, Q., Liu, M., Chen, G., Xu, Z., and Lv, Y. (2018). Demineralized bone scaffolds with tunable matrix stiffness for efficient bone integration. *ACS Appl. Mat. Interfaces* 10 (33), 27669–27680. doi:10.1021/acsami.8b08668

Hu, Y., Chen, X., Li, Z., Zheng, S., and Cheng, Y. (2020). Thermosensitive *in situ* gel containing luteolin micelles is a promising efficient agent for colorectal cancer peritoneal metastasis treatment. *J. Biomed. Nanotechnol.* 16 (1), 54–64. doi:10.1166/jbn.2020.2870

Jiang, T., Zhao, J., Yu, S., Mao, Z., Gao, C., Zhu, Y., et al. (2019). Untangling the response of bone tumor cells and bone forming cells to matrix stiffness and adhesion ligand density by means of hydrogels. *Biomaterials* 188, 130–143. doi:10.1016/j.biomaterials.2018.10.015

Jiang, Y. W., Gao, G., Hu, P., Liu, J. B., Guo, Y., Zhang, X., et al. (2020). Palladium nanosheet-knotted injectable hydrogels formed via palladium-sulfur bonding for synergistic chemo-photothermal therapy. *Nanoscale* 12 (1), 210–219. doi:10.1039/c9nr08454a

Khajuria, D. K., Kumar, V. B., Gigi, D., Gedanken, A., and Karasik, D. (2018). Accelerated bone regeneration by nitrogen-doped carbon dots functionalized with hydroxyapatite nanoparticles. *ACS Appl. Mat. Interfaces* 10 (23), 19373–19385. doi:10.1021/acsami.8b02792

Kim, S., Nishimoto, S. K., Bumgardner, J. D., Haggard, W. O., Gaber, M. W., and Yang, Y. (2010). A chitosan/β-glycerophosphate thermo-sensitive gel for the delivery of ellagic acid for the treatment of brain cancer. *Biomaterials* 31 (14), 4157–4166. doi:10.1016/j.biomaterials.2010.01.139

Lai, D., Chen, C. M., Chiu, F. Y., Chang, M. C., and Chen, T. H. (2007). Reconstruction of juxta-articular huge defects of distal femur with vascularized fibular bone graft and Ilizarov's distraction osteogenesis. *J. Trauma Inj. Infect. Crit. Care* 62 (1), 166–173. doi:10.1097/ta.0b013e31802dccdb

Lee, B. E. J., Shahin-Shamsabadi, A., Wong, M. K., Raha, S., Selvaganapathy, P. R., and Grandfield, K. (2019). A bioprinted *in vitro* model for osteoblast to osteocyte transformation by changing mechanical properties of the ECM. *Adv. Biosyst.* 3 (10), e1900126. doi:10.1002/adbi.201900126

Li, C., Armstrong, J. P., Pence, I. J., Kit-Anan, W., Puetzer, J. L., Correia Carreira, S., et al. (2018). Glycosylated superparamagnetic nanoparticle gradients for osteochondral tissue engineering. *Biomaterials* 176, 24–33. doi:10.1016/j.biomaterials.2018.05.029

Li, D., Nie, W., Chen, L., McCoul, D., Liu, D., Zhang, X., et al. (2018). Self-Assembled hydroxyapatite-graphene scaffold for photothermal cancer therapy and bone regeneration. *J. Biomed. Nanotechnol.* 14 (12), 2003–2017. doi:10.1166/jbn.2018.2646

Li, Qing, Shao, Xinxin, Dai, Xianglin, Guo, Qiong, Yuan, Bolei, Liu, Ying, et al. (2022). Recent trends in the development of hydrogel therapeutics for the treatment of central nervous system disorders. *NPG Asia Mat.* 14, 14. doi:10.1038/s41427-022-00362-y

Li Volsi, A., Scialabba, C., Vetri, V., Cavallaro, G., Licciardi, M., and Giammona, G. (2017). Near-infrared light responsive folate targeted gold nanorods for combined photothermal-chemotherapy of osteosarcoma. *ACS Appl. Mat. Interfaces* 9 (16), 14453–14469. doi:10.1021/acsami.7b03711

Li, Y., Xiao, Y., and Liu, C. (2017). The horizon of materiobiology: A perspective on material-guided cell behaviors and tissue engineering. *Chem. Rev.* 117 (5), 4376–4421. doi:10.1021/acs.chemrev.6b00654

Liao, J., Han, R., Wu, Y., and Qian, Z. (2021). Review of a new bone tumor therapy strategy based on bifunctional biomaterials. *Bone Res.* 9 (1), 18. doi:10.1038/s41413-021-00139-z

Liao, J., Jia, Y., Chen, L., Zhou, L., Li, Q., Qian, Z., et al. (2019). Magnetic/gold core-shell hybrid particles for targeting and imaging-guided photothermal cancer therapy. *J. Biomed. Nanotechnol.* 15 (10), 2072–2089. doi:10.1166/jbn.2019.2839

Liao, J., Shi, K., Jia, Y., Wu, Y., and Qian, Z. (2021). Gold nanorods and nanohydroxyapatite hybrid hydrogel for preventing bone tumor recurrence via postoperative photothermal therapy and bone regeneration promotion. *Bioact. Mat.* 6 (8), 2221–2230. doi:10.1016/j.bioactmat.2021.01.006

Lin, L., Hao, R., Xiong, W., and Zhong, J. (2015). Quantitative analyses of the effect of silk fibroin/nano-hydroxyapatite composites on osteogenic differentiation of MG-63 human osteosarcoma cells. *J. Biosci. Bioeng.* 119 (5), 591–595. doi:10.1016/j.jbiosc.2014.10.009

Liu, Q., Qian, Y., Li, P., Zhang, S., Wang, Z., Liu, J., et al. (2018). The combined therapeutic effects of (131)iodine-labeled multifunctional copper sulfide-loaded microspheres in treating breast cancer. *Acta Pharm. Sin. B* 8 (3), 371–380. doi:10.1016/j.apsb.2018.04.001

Liu, Y., Bhattarai, P., Dai, Z., and Chen, X. (2019). Photothermal therapy and photoacoustic imaging via nanotheranostics in fighting cancer. *Chem. Soc. Rev.* 48 (7), 2053–2108. doi:10.1039/c8cs00618k

Liu, Y., Li, Q., Bai, Q., and Jiang, W. (2021). Advances of smart nano-drug delivery systems in osteosarcoma treatment. *J. Mat. Chem. B* 9 (27), 5439–5450. doi:10.1039/d1tb00566a

Liu, Y., Wang, Q., Liu, X., Nakielski, P., Pierini, F., Li, X., et al. (2022). Highly adhesive, stretchable and breathable gelatin methacryloyl-based nanofibrous hydrogels for wound dressings. *ACS Appl. Bio Mat.* 5 (3), 1047–1056. doi:10.1021/acsabm.1c01087

Ma, H., He, C., Cheng, Y., Yang, Z., Zang, J., Liu, J., et al. (2015). Localized Co-delivery of doxorubicin, cisplatin, and methotrexate by thermosensitive hydrogels for enhanced osteosarcoma treatment. *ACS Appl. Mat. Interfaces* 7 (49), 27040–27048. doi:10.1021/acsami.5b09112

Mahmoodzadeh, F., Abbasian, M., Jaymand, M., Salehi, R., and Bagherzadeh-Khajehmarjan, E. (2018). A novel gold-based stimuli-responsive theranostic nanomedicine for chemo-photothermal therapy of solid tumors. *Mater. Sci. Eng. C* 93, 880–889. doi:10.1016/j.msec.2018.08.067

Mann, K., Waters, A. R., Park, E. R., Perez, G. K., Vaca Lopez, P. L., Kaddas, H. K., et al. (2022). HIAYA CHAT study protocol: A randomized controlled trial of a health insurance education intervention for newly diagnosed adolescent and young adult cancer patients. *Trials* 23 (1), 682. doi:10.1186/s13063-022-06590-5

Ni, P., Ding, Q., Fan, M., Liao, J., Qian, Z., Luo, J., et al. (2014). Injectable thermosensitive PEG-PCL-PEG hydrogel/acellular bone matrix composite for bone regeneration in cranial defects. *Biomaterials* 35 (1), 236–248. doi:10.1016/j.biomaterials.2013.10.016

Pan, H., Zhang, C., Wang, T., Chen, J., and Sun, S. K. (2019). *In situ* fabrication of intelligent photothermal indocyanine green-alginate hydrogel for localized tumor ablation. *ACS Appl. Mat. Interfaces* 11 (3), 2782–2789. doi:10.1021/acsami.8b16517

Pan, S., Yin, J., Yu, L., Zhang, C., Zhu, Y., Gao, Y., et al. (2020). 2D MXene-integrated 3D-printing scaffolds for augmented osteosarcoma phototherapy and accelerated tissue reconstruction. *Adv. Sci. (Weinh).* 7 (2), 1901511. doi:10.1002/advs.201901511

Pattee, J., Zhan, X., Xiao, G., and Pan, W. (2020). Integrating germline and somatic genetics to identify genes associated with lung cancer. *Genet. Epidemiol.* 44 (3), 233–247. doi:10.1002/gepi.22275

Peng, Z., Li, M., Wang, Y., Yang, H., Wei, W., Liang, M., et al. (2022). Self-assembling imageable silk hydrogels for the focal treatment of osteosarcoma. *Front. Cell Dev. Biol.* 10, 698282. doi:10.3389/fcell.2022.698282

Perez-Perez, M. J., Priego, E. M., Bueno, O., Martins, M. S., Canela, M. D., and Liekens, S. (2016). Blocking blood flow to solid tumors by destabilizing tubulin: An approach to targeting tumor growth. *J. Med. Chem.* 59 (19), 8685–8711. doi:10.1021/acs.jmedchem.6b00463

Ranade, A. N., Ranpise, N. S., and Ramesh, C. (2014). Exploring the potential of gastro retentive dosage form in delivery of ellagic acid and aloe vera gel powder for treatment of gastric ulcers. *Curr. Drug Deliv.* 11 (2), 287–297. doi:10.2174/1567201810666131122153041

Rastinehad, A. R., Anastos, H., Wajswol, E., Winoker, J. S., Sfakianos, J. P., Doppalapudi, S. K., et al. (2019). Gold nanoshell-localized photothermal ablation of prostate tumors in a clinical pilot device study. *Proc. Natl. Acad. Sci. U. S. A.* 116 (37), 18590–18596. doi:10.1073/pnas.1906929116

Roessner, A., Lohmann, C., and Jechorek, D. (2021). Translational cell biology of highly malignant osteosarcoma. *Pathol. Int.* 71 (5), 291–303. doi:10.1111/pin.13080

Shan, W., Chen, R., Zhang, Q., Zhao, J., Chen, B., Zhou, X., et al. (2018). Improved stable indocyanine green (ICG)-Mediated cancer optotheranostics with naturalized hepatitis B core particles. *Adv. Mat.* 30 (28), e1707567. doi:10.1002/adma.201707567

Shi, R., Gong, M., Chi, C., Huang, Y., Li, W., Li, G., et al. (2019). Nano twin-fiber membrane with osteogenic and antibacterial dual functions as artificial periosteum for long bone repairing. *J. Biomed. Nanotechnol.* 15 (2), 272–287. doi:10.1166/jbn.2019.2687

Shoag, J. E., Wise, D. R., Sharaf, R. N., and Sternberg, C. N. (2019). Somatic and germline sequencing in genitourinary oncology: Genetics for the clinician. *Curr. Opin. Urol.* 29 (4), 315–318. doi:10.1097/mou.0000000000000643

Siclari, V. A., and Qin, L. (2010). Targeting the osteosarcoma cancer stem cell. *J. Orthop. Surg. Res.* 5, 78. doi:10.1186/1749-799x-5-78

Simpson, E., and Brown, H. L. (2018). Understanding osteosarcomas. *J. Am. Acad. Physician Assist.* 31 (8), 15–19. doi:10.1097/01.jaa.0000541477.24116.8d

Sun, Y., Li, K., Li, C., Zhang, Y., and Zhao, D. (2020). Thermogel delivers Oxaliplatin and alendronate *in situ* for synergistic osteosarcoma therapy. *Front. Bioeng. Biotechnol.* 8, 573962. doi:10.3389/fbioe.2020.573962

Tan, W., Gao, C., Feng, P., Liu, Q., Liu, C., Wang, Z., et al. (2021). Dual-functional scaffolds of poly(L-lactic acid)/nanohydroxyapatite encapsulated with metformin: Simultaneous enhancement of bone repair and bone tumor inhibition. *Mater. Sci. Eng. C* 120, 111592. doi:10.1016/j.msec.2020.111592

Taneja, S. S. (2020). Re: Gold nanoshell-localized photothermal ablation of prostate tumors in a clinical pilot device study. *J. Urology* 203 (1), 31. doi:10.1097/ju.0000000000000614

Torstrick, F. B., Lin, A. S. P., Potter, D., Safranski, D. L., Sulchek, T. A., Gall, K., et al. (2018). Porous PEEK improves the bone-implant interface compared to plasma-sprayed titanium coating on PEEK. *Biomaterials* 185, 106–116. doi:10.1016/j.biomaterials.2018.09.009

Vashisth, P., and Bellare, J. R. (2018). Development of hybrid scaffold with biomimetic 3D architecture for bone regeneration. *Nanomedicine Nanotechnol. Biol. Med.* 14 (4), 1325–1336. doi:10.1016/j.nano.2018.03.011

Velasco, M. A., Narvaez-Tovar, C. A., and Garzon-Alvarado, D. A. (2015). Design, materials, and mechanobiology of biodegradable scaffolds for bone tissue engineering. *Biomed. Res. Int.* 2015, 1–21. doi:10.1155/2015/729076

Wang, L., He, S., Wu, X., Liang, S., Mu, Z., Wei, J., et al. (2014). Polyetheretherketone/nano-fluorohydroxyapatite composite with antimicrobial activity and osseointegration properties. *Biomaterials* 35 (25), 6758–6775. doi:10.1016/j.biomaterials.2014.04.085

Wang, L., Long, N. J., Li, L., Lu, Y., Li, M., Cao, J., et al. (2019). Correction: Multi-functional bismuth-doped bioglasses: Combining bioactivity and photothermal response for bone tumor treatment and tissue repair. *Light. Sci. Appl.* 8, 54. doi:10.1038/s41377-019-0165-7

Wang, L., Long, N. J., Li, L., Lu, Y., Li, M., Cao, J., et al. (2018). Multi-functional bismuth-doped bioglasses: Combining bioactivity and photothermal response for bone tumor treatment and tissue repair. *Light. Sci. Appl.* 7, 1. doi:10.1038/s41377-018-0007-z

Wang, X., Shao, J., Abd El Raouf, M., Xie, H., Huang, H., Wang, H., et al. (2018). Near-infrared light-triggered drug delivery system based on black phosphorus for *in vivo* bone regeneration. *Biomaterials* 179, 164–174. doi:10.1016/j.biomaterials.2018.06.039

Wang, Y. C., Dai, H. L., Li, Z. H., Meng, Z. Y., Xiao, Y., and Zhao, Z. (2021). Mesoporous polydopamine-coated hydroxyapatite nano-composites for ROS-triggered nitric oxide-enhanced photothermal therapy of osteosarcoma. *J. Mat. Chem. B* 9 (36), 7401–7408. doi:10.1039/d1tb01084k

Wang, Z., Jia, T., Sun, Q., Kuang, Y., Liu, B., Xu, M., et al. (2020). Construction of Bi/phthalocyanine manganese nanocomposite for trimodal imaging directed photodynamic and photothermal therapy mediated by 808nm light. *Biomaterials* 228, 119569. doi:10.1016/j.biomaterials.2019.119569

Wu, W., Dai, Y., Liu, H., Cheng, R., Ni, Q., Ye, T., et al. (2018). Local release of gemcitabine via *in situ* UV-crosslinked lipid-strengthened hydrogel for inhibiting osteosarcoma. *Drug Deliv. (Lond).* 25 (1), 1642–1651. doi:10.1080/10717544.2018.1497105

Xing, R., Liu, K., Jiao, T., Zhang, N., Ma, K., Zhang, R., et al. (2016). An injectable self-assembling collagen-gold hybrid hydrogel for combinatorial antitumor photothermal/photodynamic therapy. *Adv. Mat.* 28 (19), 3669–3676. doi:10.1002/adma.201600284

Xu, B., Ye, J., Yuan, F. Z., Zhang, J. Y., Chen, Y. R., Fan, B. S., et al. (2020). Advances of stem cell-laden hydrogels with biomimetic microenvironment for osteochondral repair. *Front. Bioeng. Biotechnol.* 8, 247. doi:10.3389/fbioe.2020.00247

Xu, P., Hu, L., Yu, C., Yang, W., Kang, F., Zhang, M., et al. (2021). Unsymmetrical cyanine dye via *in vivo* hitchhiking endogenous albumin affords high-performance NIR-II/photoacoustic imaging and photothermal therapy. *J. Nanobiotechnology* 19 (1), 334. doi:10.1186/s12951-021-01075-0

Xu, T., Yang, H., Yang, D., and Yu, Z. Z. (2017). Polylactic acid nanofiber scaffold decorated with chitosan islandlike topography for bone tissue engineering. *ACS Appl. Mat. Interfaces* 9 (25), 21094–21104. doi:10.1021/acsami.7b01176

Xu, Y., Qi, J., Sun, W., Zhong, W., and Wu, H. (2022). Therapeutic effects of zoledronic acid-loaded hyaluronic acid/polyethylene glycol/nano-hydroxyapatite nanoparticles on osteosarcoma. *Front. Bioeng. Biotechnol.* 10, 897641. doi:10.3389/fbioe.2022.897641

Yang, Q., Yin, H., Xu, T., Zhu, D., Yin, J., Chen, Y., et al. (2020). Engineering 2D mesoporous Silica@MXene-integrated 3D-printing scaffolds for combinatory osteosarcoma therapy and NO-augmented bone regeneration. *Small* 16 (14), e1906814. doi:10.1002/smll.201906814

Yang, Z., Liu, J., and Lu, Y. (2020). Doxorubicin and CDCUR inclusion complex coloaded in thermosensitive hydrogel PLGAPEGPLGA localized administration for osteosarcoma. *Int. J. Oncol.* 57 (2), 433–444. doi:10.3892/ijo.2020.5067

Yang, Z., Yu, S., Li, D., Gong, Y., Zang, J., Liu, J., et al. (2018). The effect of PLGA-based hydrogel scaffold for improving the drug maximum-tolerated dose for *in situ* osteosarcoma treatment. *Colloids Surfaces B Biointerfaces* 172, 387–394. doi:10.1016/j.colsurfb.2018.08.048

Yap, L. S., and Yang, M. C. (2020). Thermo-reversible injectable hydrogel composing of pluronic F127 and carboxymethyl hexanoyl chitosan for cell-encapsulation. *Colloids Surfaces B Biointerfaces* 185, 110606. doi:10.1016/j.colsurfb.2019.110606

Yin, J., Han, Q., Zhang, J., Liu, Y., Gan, X., Xie, K., et al. (2020). MXene-based hydrogels endow polyetheretherketone with effective osteogenicity and combined treatment of osteosarcoma and bacterial infection. *ACS Appl. Mat. Interfaces* 12 (41), 45891–45903. doi:10.1021/acsami.0c14752

Yu, Z., Xiao, Z., Shuai, X., and Tian, J. (2020). Local delivery of sunitinib and Ce6 via redox-responsive zwitterionic hydrogels effectively prevents osteosarcoma recurrence. *J. Mat. Chem. B* 8 (30), 6418–6428. doi:10.1039/d0tb00970a

Zhang, K., Jia, Z., Yang, B., Feng, Q., Xu, X., Yuan, W., et al. (2018). Adaptable hydrogels mediate cofactor-assisted activation of biomarker-responsive drug delivery via positive feedback for enhanced tissue regeneration. *Adv. Sci. (Weinh).* 5 (12), 1800875. doi:10.1002/advs.201800875

Zhang, W., Gu, J., Li, K., Zhao, J., Ma, H., Wu, C., et al. (2019). A hydrogenated black TiO2 coating with excellent effects for photothermal therapy of bone tumor and bone regeneration. *Mater. Sci. Eng. C* 102, 458–470. doi:10.1016/j.msec.2019.04.025

Zhang, Y., Guo, Z., Zhu, H., Xing, W., Tao, P., Shang, W., et al. (2022). Synthesis of liquid Gallium@Reduced graphene oxide core-shell nanoparticles with enhanced photoacoustic and photothermal performance. *J. Am. Chem. Soc.* 144 (15), 6779–6790. doi:10.1021/jacs.2c00162

Zheng, Y., Cheng, Y., Chen, J., Ding, J., Li, M., Li, C., et al. (2017). Injectable hydrogel-microsphere construct with sequential degradation for locally synergistic chemotherapy. *ACS Appl. Mat. Interfaces* 9 (4), 3487–3496. doi:10.1021/acsami.6b15245

frontiers | Frontiers in Bioengineering and Biotechnology

TYPE Original Research
PUBLISHED 24 October 2022
DOI 10.3389/fbioe.2022.1042646

OPEN ACCESS

EDITED BY
Qitong Huang,
Gannan Medical University, China

REVIEWED BY
Boya Liu,
Boston Children's Hospital, Harvard Medical School, United States
Ju Jiao,
Third Affiliated Hospital of Sun Yat-sen University, China

*CORRESPONDENCE
Qing Li,
lq1515012032@163.com
Ying Liu,
lydyzjj@163.com
Huihua Xiong,
lizaabear@tjh.tjmu.edu.cn

SPECIALTY SECTION
This article was submitted to Nanobiotechnology, a section of the journal Frontiers in Bioengineering and Biotechnology

RECEIVED 12 September 2022
ACCEPTED 12 October 2022
PUBLISHED 24 October 2022

CITATION
Li R, Zhao W, Wu T, Wang A, Li Q, Liu Y and Xiong H (2022), Tantalum-carbon-integrated nanozymes as a nano-radiosensitizer for radiotherapy enhancement. *Front. Bioeng. Biotechnol.* 10:1042646. doi: 10.3389/fbioe.2022.1042646

Tantalum-carbon-integrated nanozymes as a nano-radiosensitizer for radiotherapy enhancement

Rui Li[1], Weiheng Zhao[1], Tingting Wu[2], Aifeng Wang[2], Qing Li[2]*, Ying Liu[2]* and Huihua Xiong[1]*

[1]Department of Oncology, Tongji Hospital, Huazhong University of Science and Technology, Wuhan, China, [2]Department of Pharmacy, Henan Provincial People's Hospital, Department of Pharmacy of Centeral China Fuwai Hospital, Centeral China Fuwai Hospital of Zhengzhou University, Zheng Zhou, China

Radiotherapy (RT) plays a pivotal role in the comprehensive treatment of multiple malignant tumors, exerting its anti-tumor effects through direct induction of double-strand breaks (DSBs) or indirect induction of reactive oxygen species (ROS) production. However, RT resistance remains a therapeutic obstacle that leads to cancer recurrence and treatment failure. In this study, we synthesised a tantalum-carbon-integrated nanozyme with excellent catalase-like (CAT-like) activity and radiosensitivity by immobilising an ultrasmall tantalum nanozyme into a metal-organic framework (MOF)-derived carbon nanozyme through *in situ* reduction. The integrated tantalum nanozyme significantly increased the CAT activity of the carbon nanozyme, which promoted the production of more oxygen and increased the ROS levels. By improving hypoxia and increasing the level of ROS, more DNA DSBs occur at the cellular level, which, in turn, improves the sensitivity of RT. Moreover, tantalum–carbon-integrated nanozymes combined with RT have demonstrated notable anti-tumor activity *in vivo*. Therefore, exploiting the enzymatic activity and the effect of ROS amplification of this nanozyme has the potential to overcome resistance to RT, which may offer new horizons for nanozyme-based remedies for biomedical applications.

KEYWORDS

hypoxia, nanozyme, radiotherapy, ROS, tantalum

1 Introduction

Malignant tumors are refractory diseases with high morbidity and mortality rates, which seriously threatens human health (Sung et al., 2021). Radiotherapy (RT) is a commonly used treatment modality (Gong et al., 2021) that achieves locoregional tumor control mainly through direct physical damage to DNA or indirect damage from reactive oxygen species (ROS) (Schaue and McBride, 2015). However, in clinical practice, patients can develop different degrees of resistance to RT, leading to treatment failure and recurrence of metastasis, thus limiting the efficacy of RT for treatment of tumors

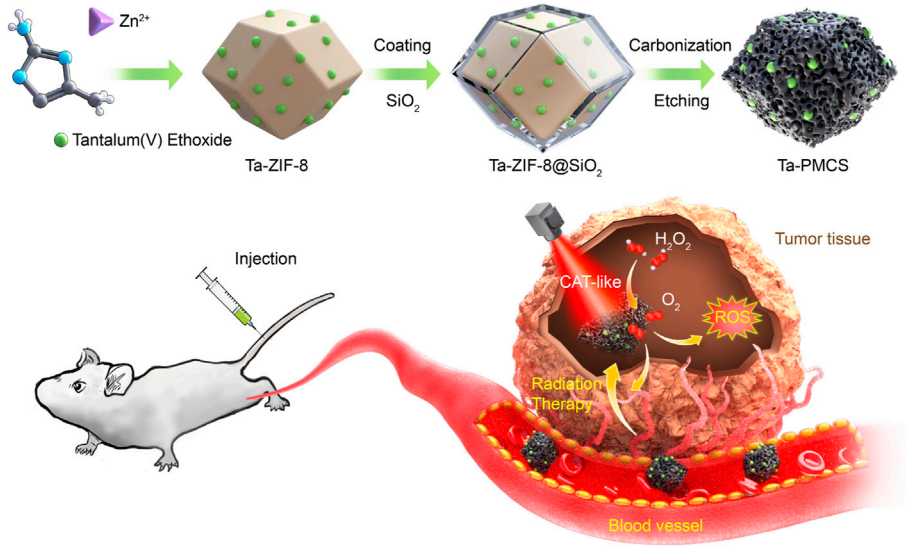

SCHEME 1
Illustration of the design and synthesis of Ta-PMCS for radiation therapy enhancement.

(Makhov et al., 2018). Addressing the sensitivity of RT has become a pivotal issue in the efficacy of RT in patients with tumors (Huang and Zhou, 2020; Thielhelm et al., 2021; Li et al., 2022).

Thus far, the possible mechanisms of radiation resistance include ROS levels, tumor cell hypoxia, DNA radiation damage repair, glutathione (GSH) content, cell proliferation, cycle regulation, and the activation of related RT resistance signaling pathways (Song et al., 2017a; Xie et al., 2019; Chen et al., 2020; Suo et al., 2020; Huang et al., 2021a). The free radicals generated during RT treatment are the main source of ROS, which promote the effects of RT by acting on DNA double-strand breaks (DSBs) (Cheng et al., 2018; Sun et al., 2018; Srinivas et al., 2019; Huang and Pan, 2020). In addition, the supply of oxygen in the tumor microenvironment is a crucial factor in the killing effect of RT (Dou et al., 2018). Studies have revealed that the tumor microenvironment is in a hypoxic state, which induces large secretion of vascular production factors, chemokines, and biologically active mediators, promoting tumor progression and metastasis (Gilkes et al., 2014; Hompland et al., 2021; Kopecka et al., 2021). The radiosensitivity of cells irradiated in the presence of oxygen is approximately three times higher than that in the absence of oxygen; therefore, the radiation dose required to kill oxygen-depleted cells is significantly higher than that required to kill fully oxygenated cells (Kabakov and Yakimova, 2021; Telarovic et al., 2021). The existence of a hypoxic tumor microenvironment enables the broken single-stranded DNA structure to be repaired by moieties such as sulfhydryl groups, resulting in fewer DNA damage sites, reduced tumor cell apoptosis, and ultimately radioresistance. In contrast, RT generates a large amount of ROS, which are produced by bombarding oxygen molecules with high-energy electrons. Thus, some tumors are less sensitive to RT owing to their high levels of internal hypoxia and low oxygen content (Graham and Unger, 2018; Bolland et al., 2021).

In recent years, owing to the excellent biocompatibility and safety of nanomaterials, nanotechnology-based RT sensitisation has garnered considerable attention and has exhibited promising potential for improving the effectiveness of RT, reducing toxic side effects, and improving prognosis (Gao et al., 2017; Chen et al., 2019; Huang et al., 2021b; Sun et al., 2021). Several metal element nanoparticles with high atomic numbers exhibit RT sensitising properties (Guo et al., 2017; Feng et al., 2018; Huang et al., 2019; Lu et al., 2021; Yang et al., 2021; Yang et al., 2022). It has a high X-ray absorption capacity, which can increase the dose of precipitated RT. When the metal nanoparticles reach the tumor site, they are subjected to radioactive irradiation, and after the particles absorb radiation, various effects (such as the photoelectric and Compton effects) occur, releasing a diverse range of particles such as photoelectrons, Compton electrons, and Auger electrons, which react with organic molecules or water in cancer cells to generate a large number of free radicals, thus improving the effect of RT. In addition, nanoparticles can achieve nano-RT sensitisation by regulating the cell cycle, depleting GSH, remoulding tumor vasculature, relieving hypoxia in the tumor microenvironment, and loading chemotherapeutic drugs (Zhang et al., 2019; Lyu et al., 2020; Wang et al., 2021; Zhou et al., 2021; Gao et al., 2022). For instance, Pei Pan et al. (2022) exploited an integrated nanosystem (Bac@BNP) that enhances the sensitivity of RT by modulating the cell cycle and increasing the level of ROS. In a study by Ma et al.

(2021), a bismuth nitrate-loaded cisplatin prodrug (NP@PVP) was synthesised to enhance DNA damage after RT by improving the amount of ROS production; meanwhile, cisplatin in NP@PVP can be released slowly to inhibit DNA damage repair, with temporal and spatial synchronisation.

Tantalum (Ta) is a non-toxic, biologically inert element with a large atomic number (Z = 73) and is a "biophilic metal" with excellent biocompatibility, and it has been widely used in medical implants in the human body (Koshevaya et al., 2021; Mani et al., 2022). According to previous studies, Ta-based nanomaterials can not only be applied as low-toxicity and high-efficiency radiosensitizers but can also be utilised as excellent functional group carriers for loading drugs to modulate the biological behaviour of tumors, which has the advantage of "multi-functional integration" and exhibits considerable potential for biomedical applications (Song et al., 2017b; Chen et al., 2017). In this study, a Ta–carbon nanozyme was used as a logical layout, as shown in Scheme 1, and it demonstrated outstanding catalase-like (CAT-like) activity. It alleviates the hypoxic tumor microenvironment by catalysing hydrogen peroxide and increasing ROS levels to cause more DNA DSBs, thus producing a highly potent anti-tumor effect in the presence of RT. In a human HeLa cancer model, the tumor suppression rate of Ta–carbon nanozyme combined with RT was greater than 81%, which was significantly higher than that of RT alone. In addition, no noticeable side effects of Ta–carbon nanozyme were identified in this study.

Based on these findings, Ta–carbon nanozyme boosted the effectiveness of RT, suggesting that a new treatment strategy was developed to overcome the limitations of RT by combining the enzymatic activity and radiosensitizer properties of nanozymes.

2 Materials and methods

2.1 Materials

$Zn(NO_3)_2{\cdot}6H_2O$, 2-methylimidazole, hexadecyl trimethyl ammonium bromide (CTAB), Tantalum(V) ethoxide, and human cervical cancer HeLa cells were acquired from Shanghai Cell Bank and cultured in DMEM medium (Solarbio, China) with 10% foetal bovine serum (FBS, Gibco, United States) and 1% penicillin/streptomycin (Sangon Biotech) in a humidified environment at 37°C and 5% CO_2. 6-week-old female BALB/c nude mice (17–21 g) were provided by Jiangsu Jicui Yaokang Biotechnology.

2.2 Construction of Ta-carbon nanozyme and characterization synthesis of Ta-ZIF-8 nanoparticles

A solution of $Zn(NO_3)_2{\cdot}6H_2O$ (32 mmol in 500 ml CH_3OH) was poured into a solution containing 135 mmol 2-methylimidazole, tantalum(V) ethoxide, and 0.3 mmol CTAB in methanol (400 ml), and the resulting solution was stirred for 2 h at room temperature. The white solid precipitate was separated *via* centrifugation and washed with methanol.

2.3 Synthesis of Ta-zif-8@msio$_2$ core@shell nanoparticles

ZIF-8 was dispersed in 240 ml of a 10 vol% methanol solution that had already been adjusted to pH using NaOH; subsequently, 6 ml of an aqueous CTAB (0.068 mol/L) solution was added. Thereafter, TEOS (1.2 ml) was added dropwise to the solution, and the resulting dispersion was stirred for 0.5 h. The resulting core-shell nanoparticles were separated through centrifugation and washed with ethanol.

2.4 Synthesis of porphyrin-like mesoporous carbon nanozyme

The Ta-ZIF-8@mSiO_2 core@shell sample was pyrolysed at 800°C for 2 h under flowing N_2 and thereafter allowed to cool slowly to room temperature. The pyrolysed sample was subsequently etched with a 4 M NaOH solution to remove the mSiO_2 shell, followed by centrifugation and washing with deionised water several times until the supernatant was neutral.

2.5 Characterization

The morphology of the nanozyme was characterised using transmission electron microscopy (TEM; JEM-2010 ES500W, Japan) and field emission scanning electron microscopy (SEM; Zeiss Merlin Compact). SEM images were captured, and energy-dispersive spectrometry (EDS) mapping was performed using a TESCAN MIRA4 instrument. TEM was performed using a Titan G260-300 field-emission electron microscope. Particle distribution analysis was performed on a Malvern Zetasizer Nano ZS90 instrument. Powder X-ray diffraction patterns were measured on a Bruker D8 Advance 25, and the data were collected in the range of 5–45° at a scan rate of 15 min^{-1}. Fourier-transform infrared spectroscopy was performed using a Thermo Scientific Nicolet 6700 spectrometer.

2.6 Cell counting kit-8 assay (CCK8 assay)

HeLa cells were seeded into 96-well plates at a density of 4000 cells/well and incubated overnight. Thereafter, the cells were treated with Ta–carbon nanozyme and administered 0 or 6 Gy RT. Cell viability was detected using CCK8 reagent (HY-K0301, MCE), as instructed. Briefly, 10 μL CCK8 reagent with

90 μL serum free medium was added to each well and cultured for 1 h in a 37°C incubator. Optical density values at 450 nm were measured using a microplate reader (ELx800, BioTek, United States).

2.7 Colony formation and cell cycle assays

Colony formation assays were used to assess the effectiveness of Ta–carbon nanozyme for radiosensitisation. Cells were evenly seeded into 6-well plates (1000 per well) and incubated for 10–14 days after different treatments. Thereafter, the cells were fixed in methanol for 20 min, stained with crystal violet solution for 15 min, washed in PBS, air-dried, and photographed. Finally, colonies (more than 50 cells) were counted manually using a microscope (0D140BC, Ningbo Shunyu Instrument Co., Ltd.). For cell cycle distribution, cells were collected, fixed overnight in 75% ice-cold ethanol, and incubated with propidium iodide (PI) solution (Seville, Wuhan, China) with RNase for 30 min at 37°C protected from light. The cell cycle distribution was examined using a CytoFLEX flow cytometer (Beckman Coulter, United States) and visualised using Modfit software (Version 3.1).

2.8 Transwell migration and invasion assay

Transwell assays were performed to determine the migration and invasion abilities of HeLa cells. Cells in a suspension containing 200 μL of serum-free DMEM medium at a density of 5×10^5/ml were inoculated in Transwell chambers (Corning, NY, United States) with or without matrix gel coating, subsequently placed in 600 μL of DMEM medium with 20% FBS, and incubated for 24 h in a 37°C incubator. Thereafter, the cells were fixed in 4% paraformaldehyde, stained with 0.1% crystalline violet, and the inside of the chambers was wiped off with a swab. Five random fields from each chamber were selected for analysis. The images were photographed and collected using an inverted microscope.

2.9 Apoptosis and live/dead assay

To detect the cell apoptosis rate, we used the Annexin V-FITC/PI (#KGA108, KeyGen Biotech, China) double staining method. A total of 106 cells were suspended in 500 μL binding buffer containing 5 μL AnnexinV-FITC and 5 μL PI. The cells were incubated in the dark at room temperature for 15 min and quantified using FACS analysis. The data were analysed using FlowJo software (version 10). To distinguish living cells from dead cells, a Calcein/PI Cell Viability/Cytotoxicity Assay Kit (#C2015M, Beyotime Biotechnology, China) was used to perform the live/dead assay. Cells were incubated with Calcein AM/PI assay solution at 37°C for 30 min and thereafter observed under a fluorescence microscope, where Calcein AM stained live cells with green fluorescence and PI stained dead cells with red fluorescence.

2.10 Intracellular reactive oxygen species (ROS) generation

An ROS assay kit (#S0033S, Beyotime, China) using the fluorescent probe DCFH-DA was used to assess the intracellular levels of ROS. The DCFH-DA probe was diluted with 1:1000 in serum-free medium and incubated with cells at 37°C for 30 min before detection of ROS levels through flow cytometry or fluorescence microscopy.

2.11 γ-H2AX immunofluorescence analysis

To assess the extent of DNA damage, we performed immunofluorescence analysis to detect phospho-histone-H2AX (γ-H2AX) foci. After RT, the cells were incubated for 2 h and thereafter fixed with 4% paraformaldehyde and Triton X-100 permeated cells. After three washes with PBS, add anti-phosphorylated histone γ-H2AX rabbit monoclonal antibody (#9718, CST, United States) diluted 1:1000 and incubated overnight at 4°C. The next day, the sections were incubated with cy5-conjugated goat anti-rabbit secondary antibody (#GB27303, Servicebio, China) for 1 h at room temperature, stained with DAPI (#C1006, Beyotime, China) for 5 min, and observed under a fluorescent microscope (DMI3000B, Leica, Germany).

2.12 *In Vivo* anti-tumor study

All experiments involving mice were approved by the ethics committee of Tongji Hospital. Six-week-old female BALB/c nude mice were purchased from Jiangsu Jicui Yaokang Biotechnology and bred in-house under specific-pathogen-free conditions. HeLa cells (1×10^6/100 μL) were subcutaneously injected into the right lower buttocks of the mice. When the volume of the tumor reached approximately 200 mm^3, the mice were randomly grouped into four groups (five mice per group): 1) saline; 2) Ta–carbon nanozyme; 3) saline + RT; and 4) Ta–carbon nanozyme + RT. Tumor volume and body weight of the mice were recorded every other day and maintained until the 14th day. Tumor volume was measured as follows: tumor volume (mm^3) = maximum length (mm) × vertical width (Gong et al., 2021) (mm^2)/2. At the end of the experiment, orbital blood was extracted from the mice and they were sacrificed through cervical dislocation. Tumor tissue and major tissue organs were removed and fixed with formalin or frozen directly in an

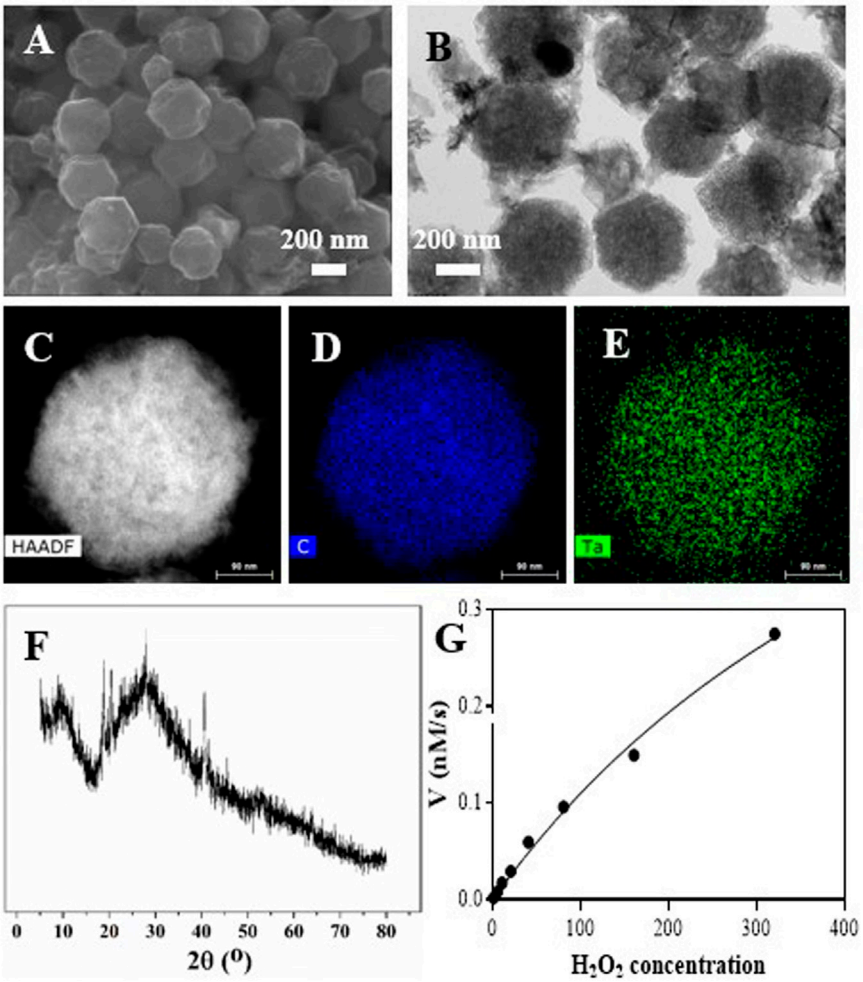

FIGURE 1
Characterization of the Ta-PMCS. **(A)** SEM image of the Ta-PMCS; **(B)** TEM image of the Ta-PMCS; **(C)** HAADF image of Ta-PMCS; **(D,E)** Elemental mapping images of C, and Ta. **(F)** PXRD of Ta-PMCS; **(G)** catalase-like activity of Ta-PMCS.

80°C refrigerator to prepare paraffin or frozen sections, respectively.

2.13 H&E staining, immunohistochemistry, DHE and HIF-1a

Paraffin sections of tumor tissues were stained with haematoxylin and eosin (H&E) to examine the morphology, structure, apoptosis, and necrosis of the tumor cells. For the proliferation ability of cells, we detected the expression level of Ki-67 through immunohistochemical staining with a Ki67 antibody (#27309-1-AP, 1/400 dilution, Proteintech, China). Dihydroethidium (DHE) and immunofluorescence of HIF-1A were performed to assess oxidative stress and hypoxia levels in tumor tissues.

2.14 Biosafety evaluation

To determine the biosafety of Ta–carbon nanozyme, the blood supernatant of mice was collected to detect liver and kidney functions. In addition, paraffin sections of heart, liver, spleen, lung, and kidney were stained with H&E.

Statistical analysis

All statistical analyses were performed using the GraphPad Prism 8.0.2 software. Data are presented as the mean ± standard deviation. Two-way analysis of variance (ANOVA) or two-tailed Student's t-test were used to evaluate statistical significance. A p value less than 0.05 were regarded as statistically significant ($^{*}p < 0.05$, $^{**}p < 0.01$, and $^{***}p < 0.005$).

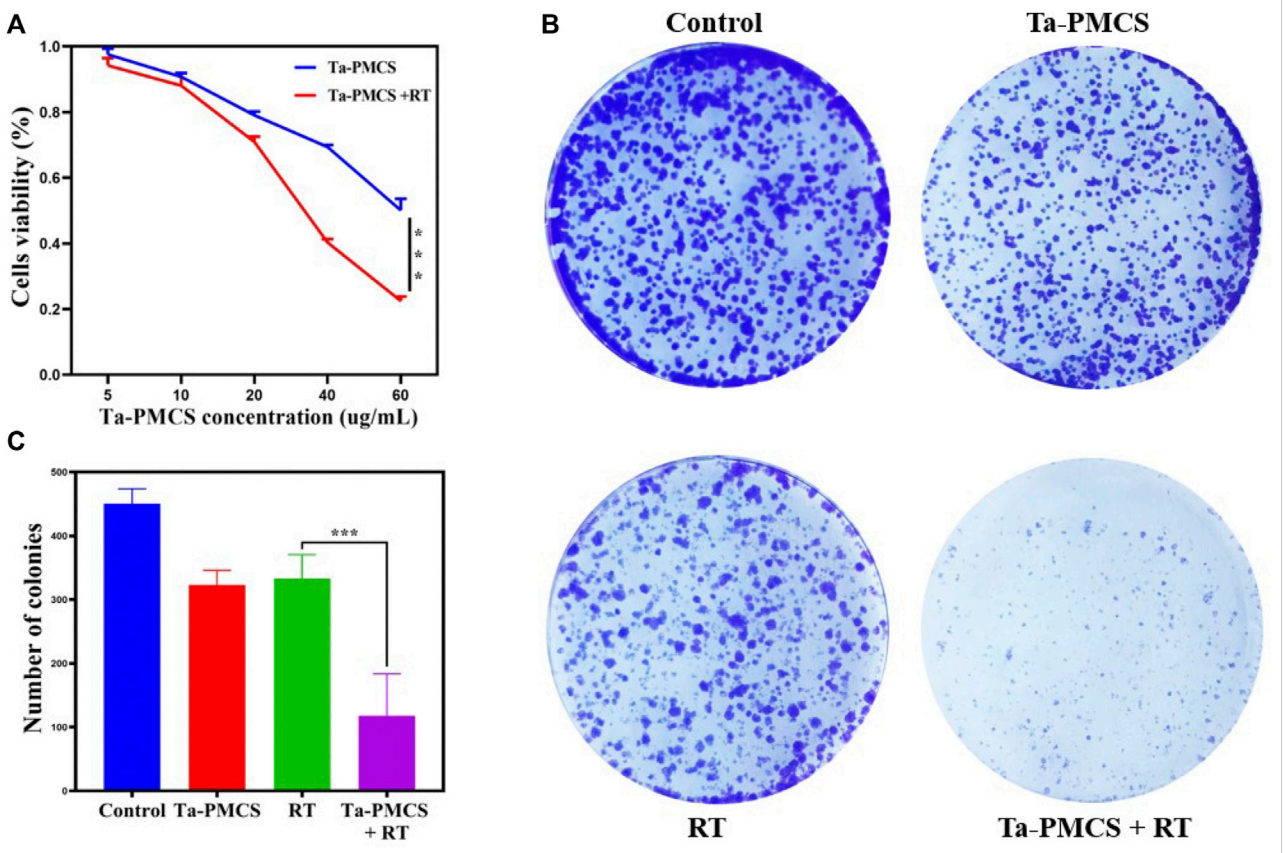

FIGURE 2
Assessment of the anti-proliferation ability of Ta-PMCS *in vitro*. **(A)** CCK-8 assay of HeLa cells treat with Ta-PMCS or Ta-PMCS + RT at different concentration gradients. **(B,C)** Colony formation assays were used to detect the proliferation of HeLa cells treated with the control, Ta-PMCS, RT or Ta-PMCS + RT. *$p < 0.05$, **$p < 0.01$, ***$p < 0.005$.

3 Results and discussion

3.1 Synthesis and characterization of Ta-carbon nanozyme

The synthesis of Ta–carbon nanozyme is illustrated in Scheme 1. In previous studies, Ta-modified MOF-derived mesoporous carbon nanozymes were first synthesised. The complete synthesis procedure did not involve complex conditions for the steady synthesis of Ta–carbon nanozymes. First, the surface morphology and composition of the Ta–carbon nanozyme were characterised by SEM, TEM, and EDS. As shown in Figure 1A, the prepared Ta–carbon nanozyme had a uniform spherical structure with an average size of approximately 300 nm, which was also confirmed by the TEM image (Figure 1B) and dynamic light scattering (Supplementary Figure S1). The composition distribution was investigated in detail through high-angle annular dark-field scanning TEM mapping, as shown in Figures 1C–E. The EDS data showed that C and Ta were present in the Ta–carbon nanozyme (Supplementary Figure S2). The activity of Ta-carbon nanozyme before and after soaking in water for 14 days indicating its good stability (Supplementary Figure S3). The crystal structure of the Ta–carbon nanozyme was characterised by X-ray diffraction (XRD). The XRD pattern (Figure 1F) exhibited a wide diffraction peak indexed to carbon. After investigating the nanozyme activity, the Ta–carbon nanozyme was observed to have CAT-like activity that can catalyse the decomposition of H_2O_2 to generate O_2 and H_2O. The amount of O_2 produced in the system depended on the concentration of H_2O_2 in the reaction system. As shown in Figure 1G, with increasing H_2O_2 concentration, the rate of oxygen generation also increased.

3.2 Ta-carbon nanozyme exerts radiosensitization *in vitro*

The CCK-8 assay detected the cell viability of Ta–carbon nanozyme at 0 and 6 Gy with different concentration gradients (Figure 2A). When the Ta–carbon nanozyme concentration reached

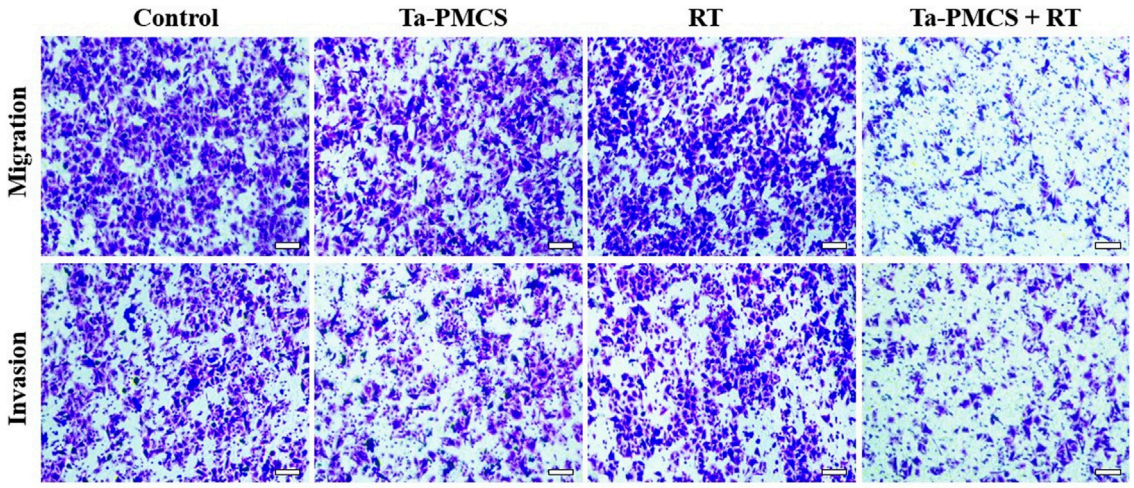

FIGURE 3
The migration and invasion ability of HeLa cells treated with the control, Ta-PMCS, RT or Ta-PMCS + RT were detected by Transwell assay (scale bar: 50 μm).

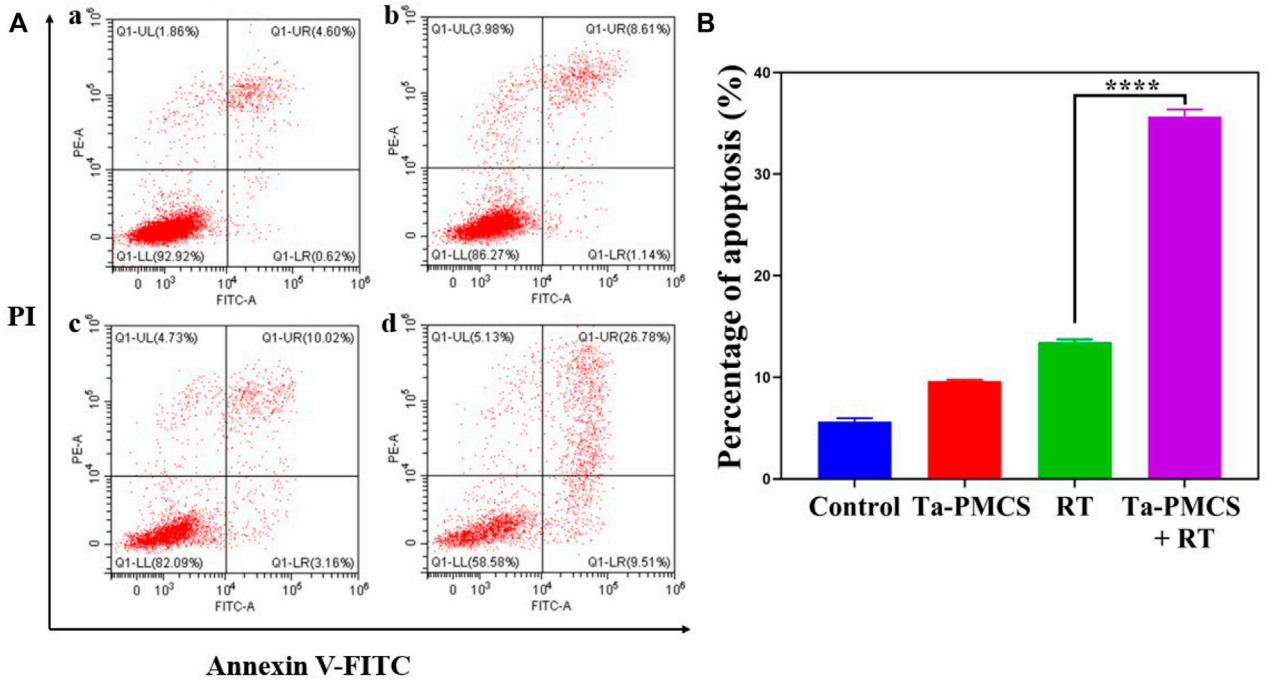

FIGURE 4
Annexin V-FITC/PI dual-staining was used to assess the apoptosis rates of HeLa cells. **(A)** Control; **(B)** Ta-PMSC (20 ug/mL); **(C)** RT (6 gy); **(D)** Ta-PMSC (20 ug/mL) + RT (6 gy). *$p < 0.05$, **$p < 0.01$, ***$p < 0.005$.

60 μg/ml, the cell survival rate decreased to approximately 50%, whereas only 22% of the Ta–carbon nanozyme combined with the RT group. These results suggest that the exposure of HeLa cells to Ta–carbon nanozyme following combined RT can significantly reduce the proliferative activity of the cells. Thereafter, we used a concentration of 30 μg/ml of Ta–carbon nanozyme and 6 Gy as the

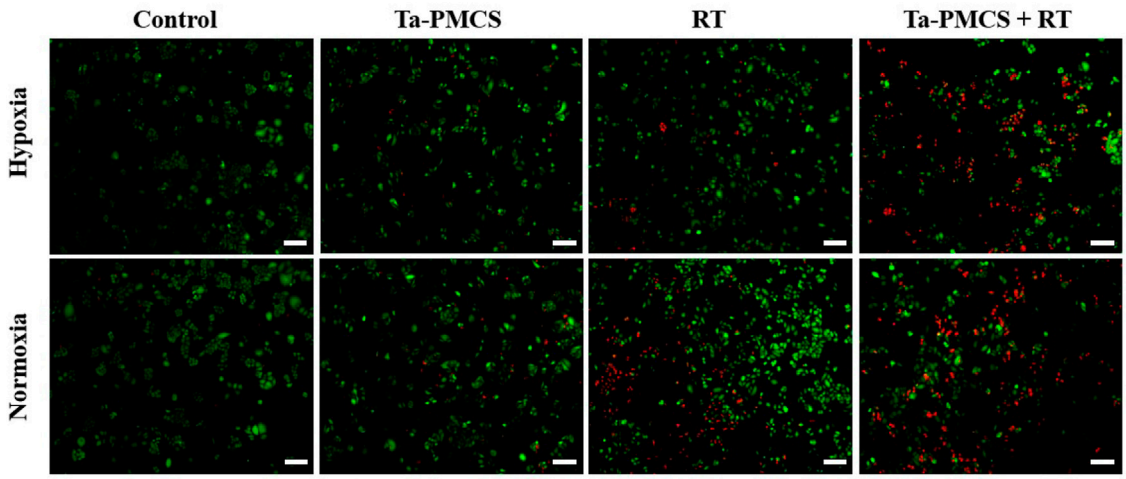

FIGURE 5
Fluorescence images of HeLa cells co-stained with Calcein AM (live cells, green) and PI (dead cells, red) treat with the control, Ta-PMCS, RT or Ta-PMCS + RT under hypoxia (1% O2) and normoxia (21% O2) conditions (scale bar: 50 μm).

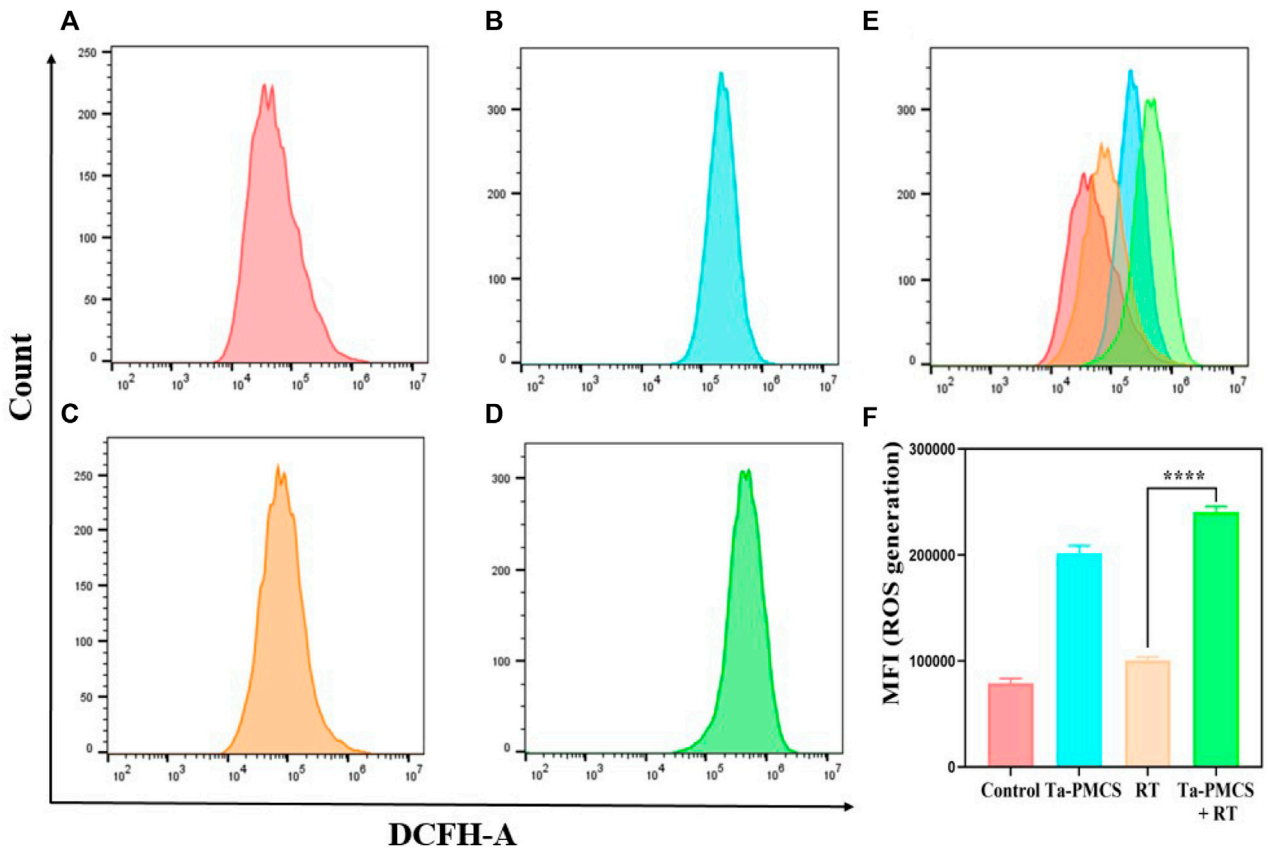

FIGURE 6
ROS levels were measured by flow cytometry after treat with different treatments. **(A)** Control; **(B)** Ta-PMSC; **(C)** RT; **(D)** Ta-PMSC + RT; **(E)** merged imaged of **(A)**, **(B)**, **(C)** and **(D)**. **(F)** Mean fluorescence intensity of ROS generation. *$p < 0.05$, **$p < 0.01$, ***$p < 0.005$.

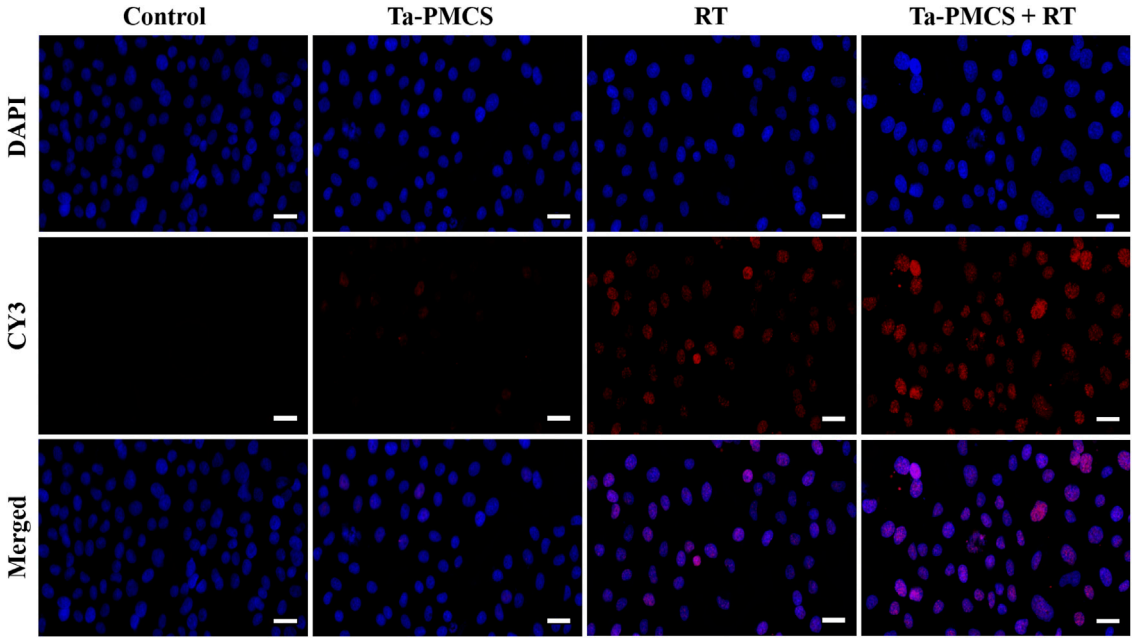

FIGURE 7
Immunofluorescence staining of γ-H2AX of HeLa cells treated with the control, Ta-PMCS, RT or Ta-PMCS + RT to assess DNA damage (scale bar: 50 μm).

radiation dose for subsequent experimental validation. Meanwhile, the clone formation assays (Figure 2B) indicated that pretreatment with Ta–carbon nanozyme combined with RT significantly inhibited proliferation and colony formation, with an inhibition rate of 74%, which was 26% and 28% in the RT and Ta–carbon nanozyme groups, respectively (Figure 2C). These results support the view that Ta–carbon nanozyme combined with RT has a greater inhibitory effect on HeLa cell proliferation than either Ta–carbon nanoparticles or irradiation alone, indicating that Ta–carbon nanozyme and RT can both suppress cell proliferation and have a synergistic effect. In addition, given that the capacity of tumor cells to migrate and invade is closely related to cancer progression, metastasis, recurrence, and poor prognosis, we conducted transwell experiments to assess the effect of Ta–carbon nanozyme combined with RT on the invasive and migratory capacity of HeLa cells. As anticipated, compared with exposure to Ta–carbon nanozyme or RT alone, after treatment with Ta–carbon nanozyme and RT, the ability of HeLa cells to migrate and invade was significantly weakened (Figure 3). To assess the anti-tumor effect, the apoptosis rate and cell cycle arrest induced by the control, Ta–carbon nanozyme, RT, and Ta–carbon nanozyme + RT were evaluated through flow cytometry. Apoptosis is a key mechanism underlying anticancer effects and radiosensitivity in tumor therapy. In Figures 4A,B, the apoptosis results and apoptosis rates of the different treatment groups are illustrated. When the cells were exposed to Ta–carbon nanozyme and RT separately, the apoptosis rates were 9.75 and 13.18%, respectively. When the two were used in combination, the apoptosis rate increased further and reached 36.29%, indicating that the Ta–carbon nanozyme has a RT-enhancing effect. The cell cycle distribution of the different treatment groups is shown in Supplementary Figure S4. The Ta–carbon nanozyme alone did not block the cell cycle in the G2/M phase before radiation treatment. In comparison to the RT group, Ta–carbon nanozyme combined with RT slightly arrested the cell cycle in the G2/M phase, and it is widely believed that blockade in the G2/M phase triggers the apoptotic cell death. To further evaluate the therapeutic effect of Ta–carbon nanozyme under normoxic and hypoxic conditions, calcein-AM (live cells) and PI (dead cells) staining was performed on HeLa cells. Under normoxia, green fluorescence was observed in almost the entire field of vision, with nearly no cell death in the control group. Under hypoxic conditions, the tumor cell-killing ability of the RT group was weaker than that of the normoxic group. However, the killing ability of the Ta–carbon nanozyme + RT group was comparable to that of the normoxic state, indicating that the Ta–carbon nanozyme has a CAT-like catalytic ability to alleviate the hypoxic state of tumor cells (Figure 5). To understand the sensitisation mechanism of RT in depth, ROS and γ-H2AX levels were measured. ROS are mainly derived from mitochondria and contribute to the level of oxidative stress in cells. Previous studies have reported that ROS can damage proteins, cause DNA damage, and induce apoptosis. Thus, we measured ROS levels in each group, as shown in Figure 6. According to the FCM results, intracellular ROS levels were

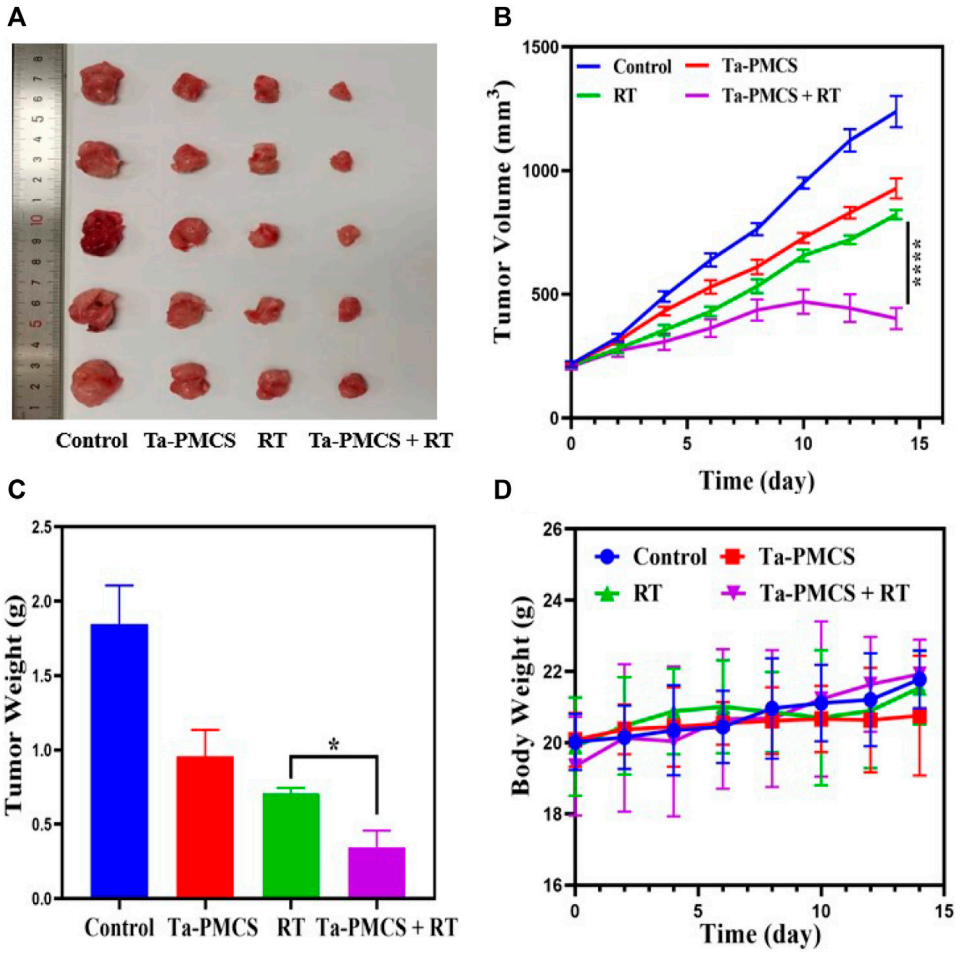

FIGURE 8
Tumor growth inhibition after treated with the control, Ta-PMCS, RT or Ta-PMCS + RT *in vivo*. **(A)** The gross tumor appearance after treat with different treatments; **(B)** tumor volume changes in different groups; **(C)** tumor weight; **(D)** body weight changes. *$p < 0.05$, **$p < 0.01$, ***$p < 0.005$.

elevated in cells treated with Ta–carbon nanozyme alone, 2.5 times higher than in the control group and 2 times higher than in the RT alone treatment group. When Ta–carbon nanozyme was combined with RT, ROS levels were 2.4 times higher than those in the RT group. Fluorescence microscopy images confirmed this change in the ROS levels (Supplementary Figure S5). This implies that more DNA DSBs can be generated, resulting in a sensitising effect of RT. The generation of DSBs in cancer cells offers a deeper understanding of radiation-induced lesion development within these cells, and the measurement of γ-H2AX levels is a highly sensitive tool for identifying DSB generation in response to irradiation. Therefore, nuclear γ-H2AX foci were measured through immunofluorescence staining with different treatment groups (Figure 7). Cells treated with Ta–carbon nanozyme + RT demonstrated a significant increase in the number of DSBs compared to cells treated with Ta–carbon nanozyme or RT alone. The observed increase in DNA damage may be due to cellular uptake of Ta nanoparticles, increasing the dose of RT precipitation, and relieving intracellular hypoxia in tumor cells, leading to the formation of more γ-H2AX lesion. The quantitative assessment of γ-H2AX foci density revealed that the γ-H2AX foci levels were 1.6-fold higher in the Ta–carbon nanozyme + RT treatment group than in the RT treatment group, illustrating the potential of Ta–carbon nanozyme as an effective radiosensitizer.

3.3 Tantalum-carbon nanozyme composites inhibited tumor growth *in vivo*

Considering the biological properties of Ta–carbon nanozyme, such as favourable anti-tumor effects *in vitro* by increasing ROS levels and alleviating hypoxia in the tumor microenvironment, we further investigated the inhibitory effect and biosafety of Ta–carbon nanozyme in a HeLa cancer-bearing mouse model. A total of 10^6 cells were

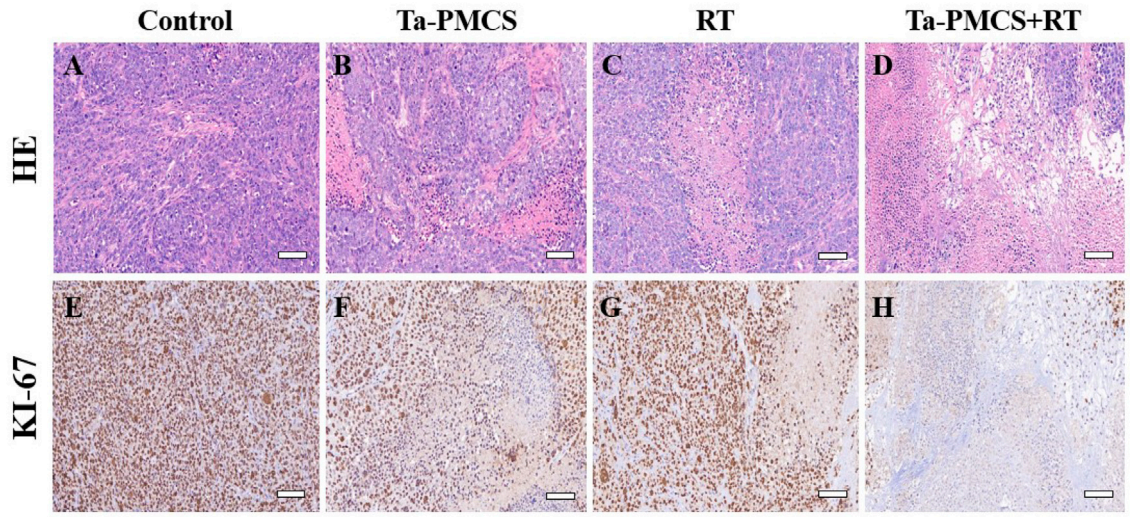

FIGURE 9
HE and Ki67 staining of tumor sections in different groups (scale bar: 50 μm). **(A,E)** Control; **(B,F)** Ta-PMCS; **(C,G)** RT; **(D,H)** Ta-PMCS+RT.

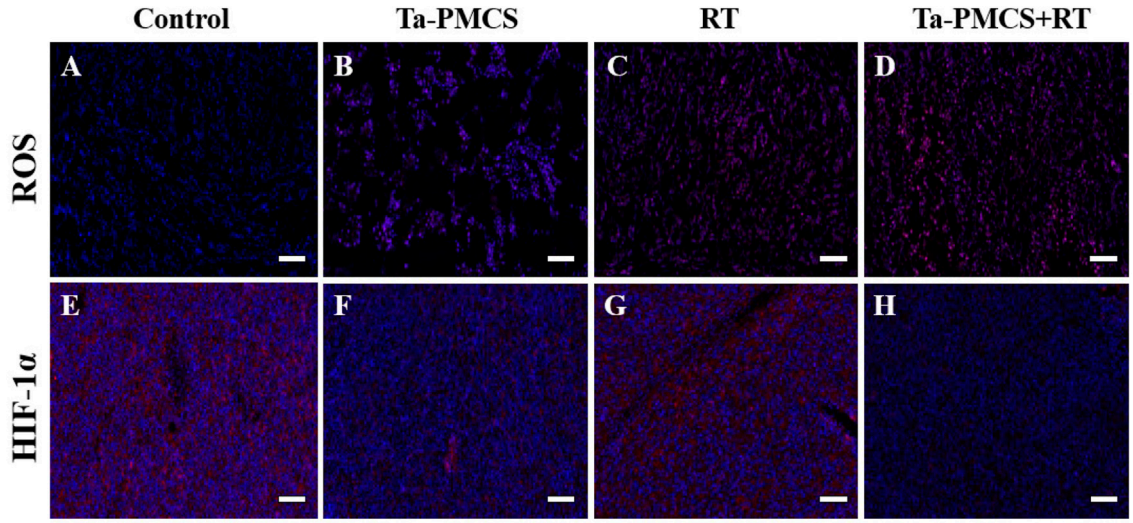

FIGURE 10
ROS and HIF-1α staining of tumor sections in different groups (scale bar: 50 μm). **(A,E)** Control; **(B,F)** Ta-PMCS; **(C,G)** RT; **(D,H)** Ta-PMCS+RT.

subcutaneously injected into the mice to construct HeLa tumor-bearing BALB/c nude mice. At the time point when the tumor volume was 200 mm^3, the mice were divided into four groups (n = 4): 1) saline solution group, 2) Ta–carbon nanozyme group (8 mg/kg), 3) RT group (6 Gy), and 4) Ta–carbon nanozyme + RT group (8 mg/kg, 6 Gy). The mice were administered saline or Ta–carbon nanozyme *via* the tail vein at a dose of 8 mg/kg once every other day three times, followed by 0 or 6 Gy RT 24 h later, respectively. Tumor volume and body weight were measured every alternate day for each group of mice. Thereafter, the mice were sacrificed on day 14, and the tumors were weighed simultaneously. The gross appearance of the tumor is shown in Figure 8A. As shown in Figures 8B,C, the tumor volume in the saline group (control group) increased rapidly. The Ta–carbon nanozyme and RT alone group exhibited a certain tumor inhibition

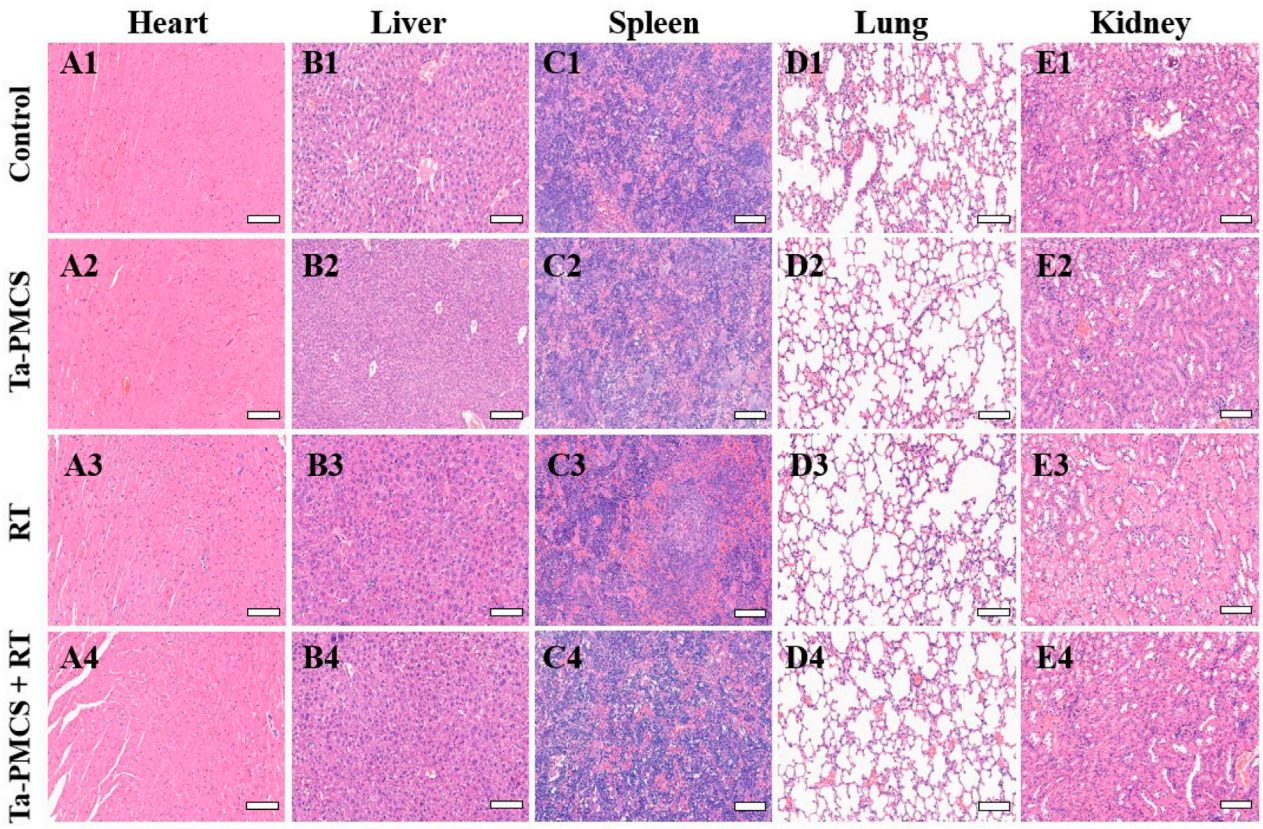

FIGURE 11
HE staining of major organs in mice injected with different treatments (scale bar: 50 μm).

effect, and the Ta–carbon nanozyme + RT group exhibited the best tumor suppression effect (82%), suggesting that Ta–carbon nanozyme can fully improve the efficiency of RT. There was no severe body weight loss during the observation period among the four groups, indicating minimal systemic toxicity and no significant side effects (Figure 8D). Thereafter, H&E, Ki-67, ROS, and HIF-1a staining were collected from each group of tumor sections. H&E (Figures 9A–D) staining revealed that the Ta–carbon nanozyme combined with RT induced a significant reduction in the number of tumor cells and an increase in the rate of apoptosis or necrosis compared with other treatment modalities. In Figures 9E–H, immunohistochemistry Ki-67 staining results confirmed that the Ta–carbon nanozyme + RT group was the most effective in inhibiting proliferation. We then assessed the oxidative stress and hypoxia levels in the tumor tissue. Measurement of intratumoral ROS generation in mice treated with the DCF exhibited significantly enhanced staining in mice that had been treated with the Ta–carbon nanozyme + RT combination (Figures 10A–D). Because the neoplastic microenvironment in solid tumors is characterised by a typical hypoxic state, it promotes tumor progression and resistance to RT, and HIF-1α is an important regulator of hypoxia. Therefore, we assessed the expression levels of HIF-1α in tumor tissues using immunofluorescence staining. In comparison with the control group, HIF expression was reduced in the Ta–carbon nanozyme group, indicating that the Ta–carbon nanozyme exhibits peroxidase activity, alleviates hypoxia in the tumor microenvironment, and has the potential for RT sensitisation (Figures 10E–H). These results suggest that the combination of Ta–carbon nanozyme and RT effectively overcomes intratumor hypoxia and enhances oxidative stress levels, thereby enhancing DNA DBS and antitumor effects. In recent years, the excellent performance of nanomaterials in drug delivery, molecular imaging, tumor therapy, and several other applications makes them a promising biomedical application material. The underlying toxicity *in vivo* is a considerable concern for the use of nanomaterials in pharmaceutical and clinical applications. Thus, at the end of this study, we evaluated the biosafety of the Ta–carbon nanozyme in mice. As shown in Figure 11, the tissue structure and cell morphology of the main organs (heart, liver, spleen, lung, and kidney) stained by H&E confirmed that these nanoparticles

had little or no systemic toxicity when administered *in vivo*. Moreover, the plasma biochemical indices of the different treatment groups were within the normal range, and serum aspartate aminotransferase, alanine aminotransferase, alkaline phosphatase, creatinine, and blood urea nitrogen of the mice did not exhibit any significant abnormalities, implying that the liver and kidney functions were normal (Supplementary Figure S6). The obtained results suggest that the Ta–carbon nanozyme exhibits excellent biocompatibility and may offer a promising strategy for RT.

4 Conclusion

In this study, we successfully constructed a viable and efficient Ta–carbon nanozyme with prominent CAT-like activity and ROS amplification to enhance tumor RT by alleviating hypoxia and generating ROS. The synthesis of Ta–carbon nanozymes is simple, convenient, and low-cost, without the requirement of multiple enzymes and complicated reactions. It exhibits CAT-like activity and catalyses the decomposition of H_2O_2 to generate O_2 and H_2O, improving the production of oxygen in the tumor microenvironment. Additionally, with a higher atomic number of TA, its absorption capacity for X-rays is strong, which can increase the dose of radiation precipitation, and the ROS produced can cause more DNA DSBs, thereby enhancing the effect of RT. In a human cervical cancer model, the tumor suppression rate of the Ta–carbon nanozyme combined with the RT group was more than 80%, which was markedly higher than that of RT alone group (62%). In addition, H&E staining of important organs and liver and kidney functions demonstrated that the Ta–carbon nanozyme had no clear toxic side effects *in vivo*. Therefore, this study provides a simple, feasible, clinically valuable, safe, and effective RT treatment strategy for overcoming RT resistance.

Data availability statement

The original contributions presented in the study are included in the article/Supplementary Material, further inquiries can be directed to the corresponding authors.

Ethics statement

The animal study was reviewed and approved by Tongji Medical College, Huazhong University of Science and Technology.

Author contributions

RL conceived this study, conducted the experiments and drafted this article. HX provided funding and revised the manuscript. YL, QL, WZ, TW, and AW carried out the statistical analysis and adjusted the figures. All authors contributed to the article and endorsed the submitted version.

Funding

This work was supported by the Chinese Society of Clinical Oncology (Grant No. 2021014).

Conflict of interest

The authors declare that the research was conducted in the absence of any commercial or financial relationships that could be construed as a potential conflict of interest.

Publisher's note

All claims expressed in this article are solely those of the authors and do not necessarily represent those of their affiliated organizations, or those of the publisher, the editors and the reviewers. Any product that may be evaluated in this article, or claim that may be made by its manufacturer, is not guaranteed or endorsed by the publisher.

Supplementary material

The Supplementary Material for this article can be found online at: https://www.frontiersin.org/articles/10.3389/fbioe.2022.1042646/full#supplementary-material

References

Bolland, H., Ma, T. S., Ramlee, S., Ramadan, K., and Hammond, E. M. (2021). Links between the unfolded protein response and the DNA damage response in hypoxia: A systematic review. *Biochem. Soc. Trans.* 49 (3), 1251–1263. doi:10.1042/bst20200861

Chen, Q., Chen, J., Yang, Z., Xu, J., Xu, L., Liang, C., et al. (2019). Nanoparticle-enhanced radiotherapy to trigger robust cancer immunotherapy. *Adv. Mat.* 31 (10), e1802228. doi:10.1002/adma.201802228

Chen, Y., Gao, P., Wu, T., Pan, W., Li, N., and Tang, B. (2020). Organelle-localized radiosensitizers. *Chem. Commun.* 56 (73), 10621–10630. doi:10.1039/d0cc03245j

Chen, Y., Song, G., Dong, Z., Yi, X., Chao, Y., Liang, C., et al. (2017). Drug-loaded mesoporous tantalum oxide nanoparticles for enhanced synergetic chemoradiotherapy with reduced systemic toxicity. *Small* 13 (8), 1602869. doi:10.1002/smll.201602869

Cheng, K., Sano, M., Jenkins, C. H., Zhang, G., Vernekohl, D., Zhao, W., et al. (2018). Synergistically enhancing the therapeutic effect of radiation therapy with radiation activatable and reactive oxygen species-releasing nanostructures. *ACS Nano* 12 (5), 4946–4958. doi:10.1021/acsnano.8b02038

Dou, Y., Liu, Y., Zhao, F., Guo, Y., Li, X., Wu, M., et al. (2018). Radiation-responsive scintillating nanotheranostics for reduced hypoxic radioresistance under ROS/NO-mediated tumor microenvironment regulation. *Theranostics* 8 (21), 5870–5889. doi:10.7150/thno.27351

Feng, L., Dong, Z., Liang, C., Chen, M., Tao, D., Cheng, L., et al. (2018). Iridium nanocrystals encapsulated liposomes as near-infrared light controllable nanozymes for enhanced cancer radiotherapy. *Biomaterials* 181, 81–91. doi:10.1016/j.biomaterials.2018.07.049

Gao, J., Wang, Z., Guo, Q., Tang, H., and Yang, C. (2022). Mitochondrion-targeted supramolecular "nano-boat" simultaneously inhibiting dual energy metabolism for tumor selective and synergistic chemo-radiotherapy. *Theranostics* 12 (3), 1286–1302. doi:10.7150/thno.67543

Gao, M., Liang, C., Song, X., Chen, Q., Jin, Q., Wang, C., et al. (2017). Erythrocyte-membrane-enveloped perfluorocarbon as nanoscale Artificial red blood cells to relieve tumor hypoxia and enhance cancer radiotherapy. *Adv. Mat.* 29 (35), 1701429. doi:10.1002/adma.201701429

Gilkes, D. M., Semenza, G. L., and Wirtz, D. (2014). Hypoxia and the extracellular matrix: Drivers of tumour metastasis. *Nat. Rev. Cancer* 14 (6), 430–439. doi:10.1038/nrc3726

Gong, L., Zhang, Y., Liu, C., Zhang, M., and Han, S. (2021). Application of radiosensitizers in cancer radiotherapy. *Int. J. Nanomedicine* 16, 1083–1102. doi:10.2147/ijn.s290438

Graham, K., and Unger, E. (2018). Overcoming tumor hypoxia as a barrier to radiotherapy, chemotherapy and immunotherapy in cancer treatment. *Int. J. Nanomedicine* 13, 6049–6058. doi:10.2147/ijn.s140462

Guo, Z., Zhu, S., Yong, Y., Zhang, X., Dong, X., Du, J., et al. (2017). Synthesis of BSA-coated BiOI@Bi(2) S(3) semiconductor heterojunction nanoparticles and their applications for radio/photodynamic/photothermal synergistic therapy of tumor. *Adv. Mat.* 29 (44), 1704136. doi:10.1002/adma.201704136

Hompland, T., Fjeldbo, C. S., and Lyng, H. (2021). Tumor hypoxia as a barrier in cancer therapy: Why levels matter. *Cancers (Basel)* 13 (3), 499. doi:10.3390/cancers13030499

Huang, C., Ding, S., Jiang, W., and Wang, F. B. (2021). Glutathione-depleting nanoplatelets for enhanced sonodynamic cancer therapy. *Nanoscale* 13 (8), 4512–4518. doi:10.1039/d0nr08440a

Huang, G., and Pan, S. T. (2020). ROS-mediated therapeutic strategy in chemo-/radiotherapy of head and neck cancer. *Oxid. Med. Cell. Longev.* 2020, 1–30. doi:10.1155/2020/5047987

Huang, Q., Zhang, S., Zhang, H., Han, Y., Liu, H., Ren, F., et al. (2019). Boosting the radiosensitizing and photothermal performance of Cu(2- x)Se nanocrystals for synergetic radiophotothermal therapy of orthotopic breast cancer. *ACS Nano* 13 (2), 1342–1353. doi:10.1021/acsnano.8b06795

Huang, R. X., and Zhou, P. K. (2020). DNA damage response signaling pathways and targets for radiotherapy sensitization in cancer. *Signal Transduct. Target. Ther.* 5 (1), 60. doi:10.1038/s41392-020-0150-x

Huang, Z., Wang, Y., Yao, D., Wu, J., Hu, Y., and Yuan, A. (2021). Nanoscale coordination polymers induce immunogenic cell death by amplifying radiation therapy mediated oxidative stress. *Nat. Commun.* 12 (1), 145. doi:10.1038/s41467-020-20243-8

Kabakov, A. E., and Yakimova, A. O. (2021). Hypoxia-induced cancer cell responses driving radioresistance of hypoxic tumors: Approaches to targeting and radiosensitizing. *Cancers (Basel)* 13 (5), 1102. doi:10.3390/cancers13051102

Kopecka, J., Salaroglio, I. C., Perez-Ruiz, E., Sarmento-Ribeiro, A. B., Saponara, S., De Las Rivas, J., et al. (2021). Hypoxia as a driver of resistance to immunotherapy. *Drug resist. updat.* 59, 100787. doi:10.1016/j.drup.2021.100787

Koshevaya, E., Krivoshapkina, E., and Krivoshapkin, P. (2021). Tantalum oxide nanoparticles as an advanced platform for cancer diagnostics: A review and perspective. *J. Mat. Chem. B* 9 (25), 5008–5024. doi:10.1039/d1tb00570g

Li, R., Wang, H., Liang, Q., Chen, L., and Ren, J. (2022). Radiotherapy for glioblastoma: Clinical issues and nanotechnology strategies. *Biomater. Sci.* 10 (4), 892–908. doi:10.1039/d1bm01401c

Lu, J., Guo, Z., Xie, W., Chi, Y., Zhang, J., Xu, W., et al. (2021). Gold-iron selenide nanocomposites for amplified tumor oxidative stress-augmented photo-radiotherapy. *Biomater. Sci.* 9 (11), 3979–3988. doi:10.1039/d1bm00306b

Lyu, M., Zhu, D., Kong, X., Yang, Y., Ding, S., Zhou, Y., et al. (2020). Glutathione-depleting nanoenzyme and glucose oxidase combination for hypoxia modulation and radiotherapy enhancement. *Adv. Healthc. Mat.* 9 (11), e1901819. doi:10.1002/adhm.201901819

Ma, Y. C., Tang, X. F., Xu, Y. C., Jiang, W., Xin, Y. J., Zhao, W., et al. (2021). Nano-enabled coordination platform of bismuth nitrate and cisplatin prodrug potentiates cancer chemoradiotherapy via DNA damage enhancement. *Biomater. Sci.* 9 (9), 3401–3409. doi:10.1039/d1bm00157d

Makhov, P., Joshi, S., Ghatalia, P., Kutikov, A., Uzzo, R. G., and Kolenko, V. M. (2018). Resistance to systemic therapies in clear cell renal cell carcinoma: Mechanisms and management strategies. *Mol. Cancer Ther.* 17 (7), 1355–1364. doi:10.1158/1535-7163.mct-17-1299

Mani, G., Porter, D., Grove, K., Collins, S., Ornberg, A., and Shulfer, R. (2022). A comprehensive review of biological and materials properties of Tantalum and its alloys. *J. Biomed. Mat. Res. A* 110 (6), 1291–1306. doi:10.1002/jbm.a.37373

Pan, P., Dong, X., Chen, Y., Zeng, X., and Zhang, X. Z. (2022). Engineered bacteria for enhanced radiotherapy against breast carcinoma. *ACS Nano* 16, 801–812. doi:10.1021/acsnano.1c08350

Schaue, D., and McBride, W. H. (2015). Opportunities and challenges of radiotherapy for treating cancer. *Nat. Rev. Clin. Oncol.* 12 (9), 527–540. doi:10.1038/nrclinonc.2015.120

Song, G., Cheng, L., Chao, Y., Yang, K., and Liu, Z. (2017). Emerging nanotechnology and advanced materials for cancer radiation therapy. *Adv. Mat.* 29 (32), 1700996. doi:10.1002/adma.201700996

Song, G., Ji, C., Liang, C., Song, X., Yi, X., Dong, Z., et al. (2017). TaOx decorated perfluorocarbon nanodroplets as oxygen reservoirs to overcome tumor hypoxia and enhance cancer radiotherapy. *Biomaterials* 112, 257–263. doi:10.1016/j.biomaterials.2016.10.020

Srinivas, U. S., Tan, B. W. Q., Vellayappan, B. A., and Jeyasekharan, A. D. (2019). ROS and the DNA damage response in cancer. *Redox Biol.* 25, 101084. doi:10.1016/j.redox.2018.101084

Sun, L., Shen, F., Tian, L., Tao, H., Xiong, Z., Xu, J., et al. (2021). ATP-responsive smart hydrogel releasing immune adjuvant synchronized with repeated chemotherapy or radiotherapy to boost antitumor immunity. *Adv. Mat.* 33 (18), e2007910. doi:10.1002/adma.202007910

Sun, Y., Miao, H., Ma, S., Zhang, L., You, C., Tang, F., et al. (2018). FePt-Cys nanoparticles induce ROS-dependent cell toxicity, and enhance chemo-radiation sensitivity of NSCLC cells *in vivo* and *in vitro*. *Cancer Lett.* 418, 27–40. doi:10.1016/j.canlet.2018.01.024

Sung, H., Ferlay, J., Siegel, R. L., Laversanne, M., Soerjomataram, I., Jemal, A., et al. (2021). Global cancer statistics 2020: GLOBOCAN estimates of incidence and mortality worldwide for 36 cancers in 185 countries. *Ca. A Cancer J. Clin.* 71 (3), 209–249. doi:10.3322/caac.21660

Suo, M., Liu, Z., Tang, W., Guo, J., Jiang, W., Liu, Y., et al. (2020). Development of a novel oxidative stress-amplifying nanocomposite capable of supplying intratumoral H(2)O(2) and O(2) for enhanced chemodynamic therapy and radiotherapy in patient-derived xenograft (PDX) models. *Nanoscale* 12 (45), 23259–23265. doi:10.1039/d0nr06594c

Telarovic, I., Wenger, R. H., and Pruschy, M. (2021). Interfering with tumor hypoxia for radiotherapy optimization. *J. Exp. Clin. Cancer Res.* 40 (1), 197. doi:10.1186/s13046-021-02000-x

Thielhelm, T. P., Goncalves, S., Welford, S. M., Mellon, E. A., Cohen, E. R., Nourbakhsh, A., et al. (2021). Understanding the radiobiology of vestibular schwannomas to overcome radiation resistance. *Cancers (Basel)* 13 (18), 4575. doi:10.3390/cancers13184575

Wang, X., Niu, X., Sha, W., Feng, X., Yu, L., Zhang, Z., et al. (2021). An oxidation responsive nano-radiosensitizer increases radiotherapy efficacy by remolding tumor vasculature. *Biomater. Sci.* 9 (18), 6308–6324. doi:10.1039/d1bm00834j

Xie, J., Gong, L., Zhu, S., Yong, Y., Gu, Z., and Zhao, Y. (2019). Emerging strategies of nanomaterial-mediated tumor radiosensitization. *Adv. Mat.* 31 (3), e1802244. doi:10.1002/adma.201802244

Yang, S., Han, G., Chen, Q., Yu, L., Wang, P., Zhang, Q., et al. (2021). Au-Pt nanoparticle formulation as a radiosensitizer for radiotherapy with dual effects. *Int. J. Nanomedicine* 16, 239–248. doi:10.2147/ijn.s287523

Yang, Y., Liu, B., Liu, Y., Chen, J., Sun, Y., Pan, X., et al. (2022). DNA-based MXFs to enhance radiotherapy and stimulate robust antitumor immune responses. *Nano Lett.* 22 (7), 2826–2834. doi:10.1021/acs.nanolett.1c04888

Zhang, L., Su, H., Wang, H., Li, Q., Li, X., Zhou, C., et al. (2019). Tumor chemo-radiotherapy with rod-shaped and spherical gold nano probes: Shape and active targeting both matter. *Theranostics* 9 (7), 1893–1908. doi:10.7150/thno.30523

Zhou, X., You, M., Wang, F., Wang, Z., Gao, X., Jing, C., et al. (2021). Multifunctional graphdiyne-cerium oxide nanozymes facilitate MicroRNA delivery and attenuate tumor hypoxia for highly efficient radiotherapy of esophageal cancer. *Adv. Mat.* 33 (24), e2100556. doi:10.1002/adma.202100556

Frontiers in
Bioengineering and Biotechnology

Accelerates the development of therapies, devices, and technologies to improve our lives

A multidisciplinary journal that accelerates the development of biological therapies, devices, processes and technologies to improve our lives by bridging the gap between discoveries and their application.

Discover the latest Research Topics

See more →

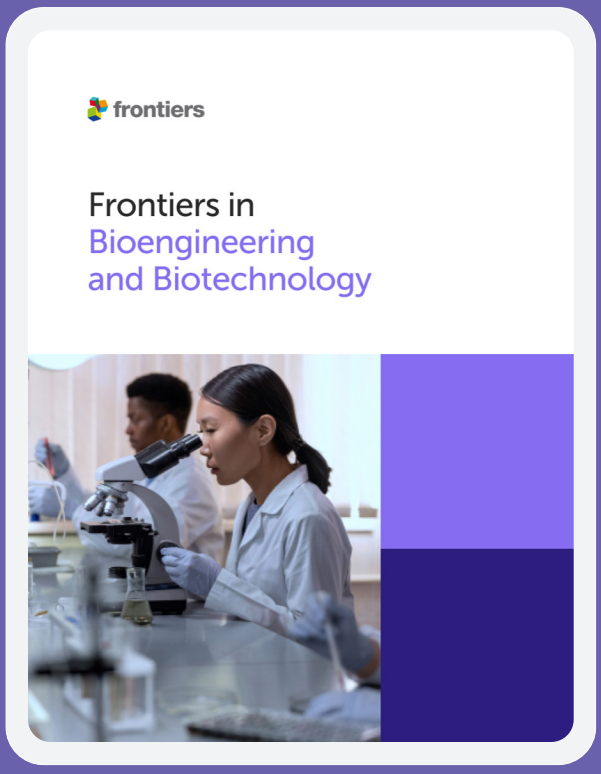

Frontiers

Avenue du Tribunal-Fédéral 34
1005 Lausanne, Switzerland
frontiersin.org

Contact us

+41 (0)21 510 17 00
frontiersin.org/about/contact